Radioactive Atoms and Molecules for Fundamental Physics

by

Silviu-Marian Udrescu

B.Sc., New York University Abu Dhabi (2018)

Submitted to the Department of Physics
in partial fulfillment of the requirements for the degree of

DOCTOR OF PHILOSOPHY IN PHYSICS

at the

MASSACHUSETTS INSTITUTE OF TECHNOLOGY

September 2024

Authored by:	Silviu-Marian Udrescu Department of Physics Aug 16, 2024
Certified by:	Ronald F. Garcia Ruiz Assistant Professor of Physics, Thesis Supervisor
Accepted by:	Lindley Winslow Associate Department Head

Radioactive Atoms and Molecules for Fundamental Physics

by

Silviu-Marian Udrescu

Submitted to the Department of Physics
on Aug 16, 2024 in partial fulfillment of the requirements for the degree of

DOCTOR OF PHILOSOPHY IN PHYSICS

ABSTRACT

The Standard Model (SM) of particle physics and the theory of General Relativity represent two of the greatest achievements in physics in the past century. However, despite their success, many experimental observations remain unanswered: What is the nature of Dark Matter and Dark Energy? Why is there so little antimatter in the Universe? Why is gravity so weak compared to the other fundamental forces? These questions point to the existence of new phenomena waiting to be discovered. High-precision laser spectroscopy experiments using atoms and molecules emerged as a fruitful approach for searching for new physics effects. Recently, atoms and molecules containing short-lived radioactive isotopes have been proposed as particularly sensitive laboratories to search for physics beyond the SM, especially at the nuclear level. However, many atoms containing very short-lived isotopes are still out of reach for spectroscopic investigations, while radioactive molecules have been completely inaccessible experimentally until recently.

In this thesis, I will present a series of pioneering experiments aimed at harnessing the power of radioactive atoms and molecules to explore nuclear phenomena, both within and beyond the SM. I will start by describing the first-ever precision laser spectroscopy investigation of a radioactive molecule, radium monofluoride (RaF). I will present measurements of the vibrational, rotational, and hyperfine spectrum of RaF, proving its high sensitivity to minuscule nuclear effects. These experiments allowed the quantification of a feasible laser-cooling scheme for RaF and the observation of the effect of the distribution of nuclear magnetization inside the Ra nucleus on the energy levels of RaF. To our knowledge, this is the first time this effect was observed in a molecule, opening the way for using molecules to benchmark *ab initio* nuclear theory. Finally, I will present measurements of the ionization potential of RaF, showing its suitability for Rydberg states studies and precise quantum control using external electric fields.

I will then present the theoretical calculations and the status of an experiment aiming to measure hadronic parity violation using single molecular ions inside a Penning trap. The experiment's goal is to use the external magnetic field provided by the trap to fine-tune molecular energy levels of opposite parity close to degeneracy, thus increasing the signal produced by parity violating nuclear properties. The sensitivity to the sought-after signal is expected to be increased by more than twelve orders of magnitude compared to atoms. This amplification will allow the observation of yet-to-be-measured parity violating effects in a molecule. These measurements will be critical to guide our understanding of electroweak nuclear phenomena.

Finally, I will show preliminary results obtained from a novel experiment with the goal of enabling laser spectroscopy studies of atoms and molecules containing radioactive nuclei with lifetimes of 1 ms and below. Such isotopes can't be currently studied spectroscopically. Using an event-by-event Doppler reconstruction, our approach could overcome most of the challenges encountered by state-of-the-art experimental techniques, allowing us to extend our reach toward unexplored regions of the nuclear chart. Such short-lived isotopes are of great importance for our microscopic understanding of nuclei as well as for constraining the properties of nuclear matter.

Thesis supervisor: Ronald F. Garcia Ruiz
Title: Assistant Professor of Physics

Acknowledgments

I would like to thank my supervisor, Ronald Fernando Garcia Ruiz. The results presented in this thesis would not have been possible without his continuous support. Ronald was willing to take me in his research group when I was unsure of what path to follow during my PhD. I am extremely grateful for his trust in me and willingness to allow me to explore new ideas and get involved in new projects. Ronald has always been open to discussing at any hour of the day or night, and no question has ever been too big or too small for that. Throughout my PhD, he has been a source of optimism, giving me not only scientific advice but also moral support when I needed it.

I would also like to thank Ronald's group at MIT for all the help and good times, inside and outside the lab, as well as all our collaborators, both on the experimental and theoretical side. I would like to thank in particular Prof. David DeMille, from whom I had the opportunity to learn a lot while working together, as well as Prof. Max Tegmark, with whom I had a lot of fun trying to make neural networks more interpretable during my first two years of PhD.

I would like to thank my English teacher, Roxana-Georgeta Bratu, for her invaluable help while I was applying for colleges in my last year of high school and for her continuous support since then. I would also like to thank my math teacher from Romania, Marius Mîinea, who strengthened my love for mathematics and made me push my skills to a competitive level.

Most of all, I want to thank my loving and supportive family, my parents, Elza-Crina and Pompiliu, my grandparents, Elena and Vasile, my aunt and uncle, Mihaela and Marian-Guzi, and my beloved wife, Elif. None of this would have been possible without your continuous support and sacrifices during my physics journey. I hope I made you proud, wherever you are.

Contents

List of Figures

List of Tables

Chapter 1

Why Radioactive Molecules?

Great progress has been made over the last century in our understanding of the Universe due to the development of new theoretical ideas and mathematical tools, as well as complex experiments able to test such theories and guide further research directions. This work culminated with the development of the Standard Model of particle physics, the most complete description to date of the building blocks of our Universe [1]. Throughout the years, the Standard Model successfully withstood more and more precise experimental tests [2] and its consistency culminated with the discovery of the Higgs boson in 2012 [3, 4].

However, despite all these decades-long successes, the Standard Model is not a complete theory of our Universe, and a deeper, more fundamental theory awaits to be discovered, of which the Standard Model is just a lower energy approximation (or effective field theory as physicists call it). There are still many observations about the Universe that can't be answered within the Standard Model. For example, there is no explanation for the values of the Standard Model parameters, which leads to unanswered questions about the relative strengths of the fundamental forces and particles masses [1, 5, 6]. The Standard Model predictions do not tell us if there are more fundamental forces or particles besides the ones we discovered so far [1]. The Standard Model also does not provide a quantum description of gravity and fails to explain cosmological observations such as the nature of dark matter and dark energy or the overwhelming imbalance between matter and antimatter in our Universe [1, 7]. All these shortcomings lead physicists to search for new physics beyond the Standard Model.

However, even within the physics of the Standard Model, certain phenomena have evaded a proper theoretical description. For example, despite a well understood theory of quantum chromodynamics (QCD), describing the strong force between quarks and gluons, its direct application to the atomic nucleus is out of reach for most nuclei, due to the non-perturbative nature of QCD in these systems [1, 8, 9]. A closely related issue is solving the nuclear many-body problem. Even if we could derive interactions between nucleons starting from the QCD description of strong force, solving the associated Schrödinger equation is still a formidable challenge for most nuclei and most observables [1, 8–10]. It's been only recently that progress was made in both of these directions, with the development of nuclear interactions derived through the use of chiral effective field theory, the development of new techniques to tackle the nuclear many-body problem, and significant progress on the available computational power [11–15]. However, much work remains to be done both theoretically and

experimentally, where the measurement of electroweak properties of key nuclei can provide critical information to guide our fundamental understanding of the atomic nucleus [14, 15].

In the past few decades, atoms proved to be valuable laboratories for exploring a wide range of the phenomena mentioned above [14–19]. The interaction between the electronic cloud of an atom and its nucleus can teach us about the inner structure of that nucleus, while deviations of the measured physical quantities from the Standard Model predictions can hint towards new physics, such as new particles or new forces [14, 15, 17]. For instance, measurement of atomic electronic transitions between different isotopes can teach us about changes in the nuclear size when neutrons are added/removed to/from the atomic nucleus [15, 16, 20–22], while the hyperfine structure provides information about the nuclear electromagnetic moments. These observations tell us about the distribution of matter and currents inside the nucleus, and often, unexpected trends along isotopic chains force us to rethink our understanding of the atomic nucleus and thus bring us closer to a better understanding of the nuclear force [15, 19, 23]. Atomic parity violation measurements have also represented an active area of research, providing valuable information about the weak interaction between electrons and nucleons or even between the nucleons inside a nucleus, thereby facilitating some of the most stringent tests of the Standard Model at low energy [24, 25]. In addition, atoms proved to be also very useful for searches of parity and time-reversal (P,T) symmetry violating effects, whose observation, given our current experimental sensitivities, could explain the matter-antimatter asymmetry in the Universe, the nature of Dark Matter, and can help us solve the strong CP problem [18].

Recently, molecules have emerged as a new platform upon which fundamental physics studies can be performed [26–29]. While their advantages over atoms have been predicted since the sixties [30], their experimental investigation targeted towards the phenomena described above was hindered by their complex energy spectrum due to their extra degrees of freedom, such as vibrational and rotational [31]. However, the recent progress made in the AMO community facilitated the use of molecules for new physics searches [28, 29], which allowed us to use their complexity to our advantage and often achieve higher sensitivity to symmetry-violating properties compared to experiments with atoms [14, 17, 32–42]. As discussed in great detail in Chapters 2 and 3, molecules have levels of opposite parity which can be more than 5 orders of magnitude closer to each other compared to atoms [14, 17, 26, 27, 31, 43]. Given that many of the effects mentioned above, particularly those violating parity, scale as the inverse of such an energy difference, performing a measurement in a molecule can enhance sensitivity to the sought-after effects compared to the same measurement done in an atom. This has led to molecules setting the most stringent bounds on the P,T-violating electron electric dipole moment (EDM), more than three orders of magnitude tighter than the ones obtained using atoms, and allowed tests of C,P-violation physics at the tens of TeV energy scale, comparable to the energy scales probed by the Large Hadron Collider [28, 29], at CERN.

While the enhancement in sensitivity to a wide range of physics scenarios of interest offered by molecules compared to atoms is clear, it turns out that placing the right nucleus inside a molecule can provide even further enhancements. In particular, it was suggested that many symmetry-violating effects could be significantly enhanced, by as much as five orders of magnitude, in quadrupole and octupole (pear-shaped) deformed nuclei, compared to nuclei that do not possess octupole deformation [14, 17, 44–46]. However, large nuclear

deformations, in particular octupole deformation, are only present in short-lived, radioactive isotopes [47]. Building molecules out of such isotopes takes us to the realm of radioactive molecules. Hence, using these systems for fundamental physics experiments represents a compelling choice [14, 17, 44–46]. However, working with radioactive molecules poses additional challenges (on top of the inherent complexity of molecules in general). They often do not occur naturally and instead need to be produced artificially at specific radioactive beam facilities, such as FRIB [48], ISOLDE [49] or RIKEN [50] and even then, they can only be produced in tiny amounts (on the order of 10^7 molecules per second and below), in very contaminated environments, and can have relatively short lifetimes (from days to below milliseconds) [51–54]. Thus, sensitive techniques need to be employed for their spectroscopic studies, and in some cases, the experiments need to be performed online, i.e., the molecules should be investigated as soon as they are produced [51–54]. All these challenges prevented spectroscopic studies of radioactive molecules until recent years.

This thesis presents the first precision laser spectroscopy investigation of a radioactive molecule, radium monofluoride (RaF). The obtained results represent the building blocks upon which future measurements of symmetry-violating phenomena can be performed using this molecule, as well as other radioactive molecules of interest. The thesis is organized as follows. In Chapter 2, the molecular structure theory needed to explain the measured spectra, as well as to extract the fundamental physics of interest from it, is introduced. Chapter 3 discusses various electroweak nuclear properties of interest that can be measured using atoms and molecules and the physics that can be learned from them, emphasizing the ones observed in our work and presented in greater detail in the later chapters of this thesis. Chapter 4 describes the first precision laser spectroscopy study of a radioactive molecule, radium monofluoride (RaF), presenting the measurement and analysis of its electronic [52], vibrational [52], rotational [53, 54] and hyperfine [54] structure, as well as its ionization potential. These measurements allowed the quantification of a laser cooling scheme for RaF and proved the high sensitivity of this molecule to different nuclear spin-dependent and spin-independent effects. Chapter 5 describes a new experimental proposal (and the progress on its implementation in practice) to measure hadronic parity violation using single molecular ions inside a Penning trap [55]. This approach will allow the investigation of electroweak nuclear properties in a wide range of molecules, being particularly suited for short-lived, radioactive species. Chapter 6 presents a new experiment and exciting preliminary results, built to study very short-lived isotopes (lifetimes < 1 ms) of great importance for nuclear structure and new physics searches, but until now, out of reach for existing spectroscopic techniques [56]. Finally, Chapter 7 presents the conclusions of this work with an exciting outlook on the many new research opportunities laid out for the future in the field of radioactive atoms and molecules.

Chapter 2

Molecular Structure Theory

Molecules are excellent laboratories for fundamental physics studies, including exciting searches for new physics effects, such as violations of the fundamental symmetries of nature [26, 28, 29, 43]. One of the main reasons for this is the existence of closely spaced levels of opposite parity, which translates into a high sensitivity to parity violating effects [17, 31, 43]. However, molecules' complex energy level structure poses additional challenges to investigate and describe theoretically compared to atoms. The interplay between the various degrees of freedom, such as electronic, vibrational, and rotational, on top of which, in many cases, one needs to account for the electron and nuclear intrinsic spins, can make analyzing any experimentally measured data a daunting task. Fortunately, decades of hard work, both on the experimental and theoretical side, led to significant progress in allowing us to disentangle the complicated dynamics of these systems [31]. This chapter gives a brief description of the properties of diatomic molecules, the notation commonly used, and, more importantly, the math needed to understand their structure and, therefore, their experimentally measured energy spectra.

2.1 Spherical Tensors and Angular Momentum

Understanding the energy levels of a molecule is closely related to understanding spherical tensors and their application to the various angular momenta encountered in practice. One can think of a molecule as a rotating rigid body. Thus, in most calculations, a difference must be made between the lab frame and the molecule's internal (co-rotating) frame [31, 57, 58]. This distinction has important consequences. For example, the angular momentum operators in the lab frame J_X, J_Y, and J_Z obey the well-known commutation relationship:

$$[J_i, J_j] = i\epsilon_{ijk}J_k, \tag{2.1}$$

where the indices i, j and k can be any of X, Y or Z and ϵ_{ijk} is the Levi-Civita tensor. However, if we look at the same operators in the rest frame of the molecule (J_x, J_y and J_z), i.e., defining rotations around the co-rotating frame axis, we obtain that [31, 57]:

$$[J_i, J_j] = -i\epsilon_{ijk}J_k, \tag{2.2}$$

where the indices i, j and k can be any of x, y or z. This anomalous commutation relationship for the angular momentum operator in the body frame means that the usual angular momentum algebra, built upon the usual commutation relationship, Eq. 2.1, can't be directly applied to angular momentum calculations in the rest frame of the molecule. This is important given that, very often, one needs to combine vectors defined in the lab frame with vectors defined in the frame of the molecule [27–29, 31]. Often encountered examples of this are the Stark Hamiltonian, given by the product between the intrinsic dipole moment of the molecule $\mathbf{d}$ and an externally applied electric field $\mathbf{E}$, or the electron Zeeman Hamiltonian, given by the product between the electron spin $\mathbf{S}$ and an externally applied magnetic field $\mathbf{B}$.

One way to overcome this challenge is based on the formalism described in Ref. [31], which allows us to easily go back and forth between the lab frame and the intrinsic frame of the molecule. Thus, one can take a vector from the body frame of the molecule to the lab frame, perform all the needed calculations there (using the standard tensor algebra tools), and at the end, rotate that vector back to the rest frame of the molecule. This is a very powerful approach which facilitates the calculation of most (if not all) matrix elements encountered in the characterization of diatomic molecules [31].

As the calculations we will perform will use spherical tensors, it is worth relating these objects with the more commonly used vectors. For a general vector $\mathbf{V}$, with components in a given frame V_x, V_y and V_z, we can build an associated spherical tensor (of rank 1 in this case), $T^1(\mathbf{V})$, with the associated components [31]:

$$\begin{aligned} T^1_0(\mathbf{V}) &= V_z \\ T^1_\pm(\mathbf{V}) &= \mp\frac{1}{\sqrt{2}}\left(V_x \pm iV_y\right). \end{aligned} \tag{2.3}$$

Using these, for example, the common dot product between 2 vectors $\mathbf{V}$ and $\mathbf{W}$ becomes:

$$\mathbf{V}\cdot\mathbf{W} = T^1(\mathbf{V})\cdot T^1(\mathbf{W}) = \sum_p (-1)^p T^1_p(\mathbf{V}) T^1_{-p}(\mathbf{W}). \tag{2.4}$$

This can be extended straightforwardly to higher rank tensors [31]. To achieve the goal of transforming a spherical tensor from the molecule to the lab frame and the other way around, there is one more quantity that needs to be introduced, which will be often used in our calculations moving forward: the Wigner rotation matrix [59]. If we apply a rotation operator $R(\phi,\theta,\chi)$ to an eigenvector of the angular momentum operator, $|J,M\rangle$, moving it between two different frames related to each other by rotations through the Euler angles $\omega \equiv (\phi,\theta,\chi)$, we have:

$$R(\omega)\,|J,M\rangle = \sum_{M'} |J,M'\rangle\, \mathcal{D}^J_{M'M}(\omega). \tag{2.5}$$

The resulting $(2J+1)\times(2J+1)$ matrix, $\mathcal{D}^J_{M'M}(\omega)$, is called the Wigner rotation matrix. Using it, we can now write the expression relating the components of a spherical tensor (in general of rank k) from the lab frame to the body frame of the molecule and back [31]:

$$
\begin{aligned}
T_p^k(\mathbf{V}) &= \sum_q \mathcal{D}_{pq}^{(k)}(\omega)^* T_q^k(\mathbf{V}) \\
T_q^k(\mathbf{V}) &= \sum_p \mathcal{D}_{pq}^{(k)}(\omega) T_p^k(\mathbf{V}),
\end{aligned}
\tag{2.6}
$$

where p and q refer to the lab and molecular frame, respectively. Before proceeding to look into calculating matrix elements of spherical tensors and thus matrix elements of the various molecular Hamiltonians of interest, which is the ultimate goal in calculating molecular properties, two more very important mathematical objects need to be introduced: the Wigner 3-j symbol and the Wigner-Eckart theorem [31, 60].

In molecular physics, coupling of the angular momenta plays a fundamental role (e.g., see Sec. 2.2 about Hund's cases). In performing calculations, introducing the so-called Wigner 3-j symbols proves to be of great help. In general, a coupled angular momentum eigenstate $|J, M\rangle$ and the associated uncoupled eigenstate $|J_1, M_1\rangle\,|J_2, M_2\rangle$ can be related as:

$$
|J, M\rangle = \sum_{M_1, M_2} |J_1, M_1\rangle\,|J_2, M_2\rangle\,\langle J_1, J_2, M_1, M_2|J, M\rangle\,, \tag{2.7}
$$

using the Clebsch–Gordan coefficients, $\langle J_1, J_2, M_1, M_2|J, M\rangle$. The values for these coefficients are tabulated and can also be calculated for any values of $J's$ and $M's$. Given their properties, the above relationship can also be easily inverted, giving:

$$
|J_1, M_1\rangle\,|J_2, M_2\rangle = \sum_{J, M} |J, M\rangle\,\langle J_1, J_2, M_1, M_2|J, M\rangle\,. \tag{2.8}
$$

Using the Clebsch–Gordan coefficients, one can then define the Wigner 3-J symbol as [31]:

$$
\begin{pmatrix} J_1 & J_1 & J_3 \\ M_1 & M_2 & M_3 \end{pmatrix} \equiv (-1)^{J_1 - J_2 - M_3} (2J_3 + 1)^{-1/2}\,\langle J_1, J_2, M_1, M_2|J_3, -M_3\rangle\,. \tag{2.9}
$$

Next, we will mention the famous Wigner-Eckart theorem and its importance in applying tensor algebra to quantum mechanical calculations. This theorem states that:

$$
\langle J, M|T_q^k(\mathbf{V})|J', M'\rangle = (-1)^{J-M} \begin{pmatrix} J & k & J' \\ -M & q & M' \end{pmatrix} \langle J||T^k(\mathbf{V})||J'\rangle\,, \tag{2.10}
$$

with the reduced matrix element $\langle J||T^k(\mathbf{V})||J'\rangle$ defined as:

$$
\langle J||T^k(\mathbf{V})||J'\rangle \equiv \sum_{N, N', p} (-1)^{J-N} \begin{pmatrix} J & k & J' \\ -N & p & N' \end{pmatrix} \langle J, N|T_p^k(\mathbf{V})|J', N'\rangle\,. \tag{2.11}
$$

The meaning of this theorem is that, in order to calculate a given matrix element, one needs to calculate a reduced matrix element, which doesn't depend on M, M', or k, and it thus needs to be calculated only once for all $(2J+1) \times (2k+1) \times (2J'+1)$ possible $\langle J, M|T_q^k(\mathbf{V})|J', M\rangle$ matrix elements and a Wigner 3-j symbol, which is different for different M, M', or k but can be easily computed (or looked for in existing tables).

2.1.1 Useful Formula for Calculations of Matrix Elements of Spherical Tensors

Using the tools described in the previous section, together with formulas which can be derived from them (see Ref. [31] for more details on various derivations of formulas used in this section), we can calculate a wide range of matrix elements of interest (with or without external fields present), some of which will prove to be useful in the upcoming chapters. Before deriving some of these matrix elements, I will briefly mention below several formulas that appear often and thus are very useful in various calculations.

For a first-rank tensor, the reduced matrix element is given by:

$$\langle J||T^1(\mathbf{J})||J'\rangle = \delta_{J,J'}\left[J(J+1)(2J+1)\right]^{1/2}. \tag{2.12}$$

If we have two angular momenta $\mathbf{J_1}$ and $\mathbf{J_2}$ which couple to give a total angular momentum $\mathbf{J}$ and an operator acting only on one of the angular momenta (say $\mathbf{J_1}$), $T^k(\mathbf{V_1})$, we have [31]:

$$\langle J_1, J_2, J, M_J|T^k_p(\mathbf{V_1})|J_1', J_2', J', M_J'\rangle = (-1)^{J-M_J}\begin{pmatrix} J & k & J' \\ -M_J & p & M_J'\end{pmatrix}\langle J_1, J_2, J||T^k(\mathbf{V_1})||J_1', J_2', J'\rangle, \tag{2.13}$$

with

$$\langle J_1, J_2, J||T^k(\mathbf{V_1})||J_1', J_2', J'\rangle = \delta_{J_2J_2'}(-1)^{J'+J_1+J_2+k}\left[(2J+1)(2J'+1)\right]^{1/2}\begin{Bmatrix} J_1' & J' & J_2 \\ J & J_1 & k\end{Bmatrix}\langle J_1||T^k(\mathbf{V_1})||J_1'\rangle. \tag{2.14}$$

The $\begin{Bmatrix} J_1' & J' & J_2 \\ J & J_1 & k\end{Bmatrix}$ term is a Wigner 6-j symbol, which is the extension of the Wigner 3-j symbol, which is used when two angular momenta are coupled, $|J_1, M_1\rangle|J_2, M_2\rangle$, to the case of 3 angular momenta coupling $|J_1, M_1\rangle|J_2, M_2\rangle|J_3, M_3\rangle$. We can also have Wigner 9-j symbols appearing when four angular momenta are coupled, and so on. Their expressions become increasingly complicated, but they can be easily calculated numerically and are usually available in many packages, for example, in Python.

A closely related formula involving the scalar product of 2 spherical tensors, each acting on one of the two angular momenta involved, $\mathbf{J_1}$ and $\mathbf{J_2}$ (more general results can be obtained, but they are not needed for calculations performed in this thesis) is given by [31]:

$$\begin{aligned}&\langle J_1, J_2, J, M_J|T^k(\mathbf{V_1})\cdot T^k(\mathbf{V_2})|J_1', J_2', J', M_J'\rangle = \\ &(-1)^{J_1'+J+J_2}\delta_{J,J'}\delta_{M_J,M_J'}\begin{Bmatrix} J_2' & J_1' & J \\ J_1 & J_2 & k\end{Bmatrix}\langle J_1||T^1(\mathbf{V_1})||J_1'\rangle\langle J_2||T^1(\mathbf{V_2})||J_2'\rangle.\end{aligned} \tag{2.15}$$

Useful formulas often needed when computing products between two spherical tensors, one defined in the lab and the other in the molecule's frame also involve matrix elements of the Wigner function. Below, we list some of which will be used in the derivations presented below [31]:

$$\langle J, M, \Omega | \mathcal{D}^{(k)}_{pq}(\omega)^* | J', M', \Omega' \rangle = (-1)^{M-\Omega} \left[(2J+1)(2J'+1)\right]^{1/2} \begin{pmatrix} J & k & J' \\ -\Omega & q & \Omega' \end{pmatrix} \begin{pmatrix} J & k & J' \\ -M & p & M' \end{pmatrix}, \tag{2.16}$$

$$\langle J, M, \Omega | \mathcal{D}^{(k)}_{pq}(\omega)^* | J', M', \Omega' \rangle = (-1)^{J-M} \begin{pmatrix} J & k & J' \\ -M & p & M' \end{pmatrix} \langle J, \Omega || \mathcal{D}^{(k)}_{.q}(\omega)^* || J', \Omega' \rangle , \tag{2.17}$$

where $\mathcal{D}^{(k)}_{.q}$ means that the matrix element is reduced only relative to the lab frame system (not the rotating one). From the previous two equations, we also get:

$$\langle J, \Omega || \mathcal{D}^{(k)}_{.q}(\omega)^* || J', \Omega' \rangle = (-1)^{J-\Omega} \begin{pmatrix} J & k & J' \\ -\Omega & q & -\Omega' \end{pmatrix} \left[(2J+1)(2J'+1)\right]^{1/2} . \tag{2.18}$$

There are other useful formulas one can derive, and many of them are presented in Ref. [31]. The ones shown above, however, are enough to allow us to calculate a wide range of matrix elements of interest, some of which I will derive below. I will limit the calculations only to $^2\Sigma^+$ and $^2\Pi_{1/2}$ states, which are the electronic levels appearing in the experiments/calculations presented in this thesis. Still, they can be extended straightforwardly (eventually using equivalent formulas for higher-order tensor ranks) to other kinds of electronic states. The purpose of these derivations is not to cover all possible cases one can encounter in practice but to provide explicit examples of using spherical tensors for molecular calculations in a wide range of scenarios, helpful in calculating the matrix elements of many Hamiltonians of interest. As these derivations will depend on the basis used, the reader might first want to read Sec. 2.2 first, in which the various Hund's cases and associated good quantum numbers are introduced.

2.1.2 Zeeman Interaction in a $^2\Sigma^+$ State

The associated Hamiltonian, in this case, is given by:

$$H_S = -g_S \mu_B \mathbf{B} \cdot \mathbf{S}, \tag{2.19}$$

where g_S is the electron g-factor, μ_B is the Bohr magneton, and we will use a Hund's case (b) basis for our calculations (see Sec. 2.2). The obtained matrix element is:

$$M = -g_s \mu_B \left\langle ^2\Sigma^+, \Lambda = 0, S, N, J, M_J | T^1(\mathbf{B}) \cdot T^1(\mathbf{S}) | ^2\Sigma^+, \Lambda = 0, S, N', J', M'_J \right\rangle . \tag{2.20}$$

If we take the direction of the magnetic field as the z-axis of the laboratory frame and denote its magnitude by B_z, the expression above becomes:

$$M = -g_s \mu_B B_z \left\langle S, N, J, M_J | T^1_{p=0}(\mathbf{S}) | S, N', J', M'_J \right\rangle , \tag{2.21}$$

where we dropped the $^2\Sigma^+$ and $\Lambda = 0$ parts i.e. the electronic state doesn't change. This has the same form as Eq. 2.13 with the notation $J_1 \to S$ and $J_2 \to N$. Thus, the matrix element becomes:

$$M = -g_s \mu_B B_z (-1)^{J-M_J} \begin{pmatrix} J & 1 & J' \\ -M_J & 0 & M'_J \end{pmatrix} \langle S, N, J || T^1(\mathbf{S}) || S, N', J' \rangle \,. \tag{2.22}$$

Then, using Eq. 2.14 we get:

$$\begin{aligned} M = &- g_s \mu_B B_z (-1)^{J-M_J} \begin{pmatrix} J & 1 & J' \\ -M_J & 0 & M'_J \end{pmatrix} \delta_{N,N'} (-1)^{J'+S+N+1} \left[(2J+1)(2J'+1)\right]^{1/2} \\ &\times \begin{Bmatrix} S & J' & N \\ J & S & 1 \end{Bmatrix} \langle S || T^1(\mathbf{S}) || S \rangle \,. \end{aligned} \tag{2.23}$$

Finally, using Eq. 2.12, we get the final form of this matrix element:

$$\begin{aligned} M = &- g_s \mu_B B_z (-1)^{J-M_J} \begin{pmatrix} J & 1 & J' \\ -M_J & 0 & M'_J \end{pmatrix} \delta_{N,N'} (-1)^{J'+S+N+1} \begin{Bmatrix} S & J' & N \\ J & S & 1 \end{Bmatrix} \times \\ &\times \left[(2J+1)(2J'+1) S(S+1)(2S+1)\right]^{1/2} . \end{aligned} \tag{2.24}$$

Cumbersome as it looks, this expression can now be easily evaluated for any pair of spin-rotational levels in a molecule. For example, for the ground rotational level, $N = N' = 0$ and $J = J' = 1/2$, and a magnetic field of 1 Gauss, we obtain $M \approx 1.4$ MHz.

2.1.3 Zeeman Interaction in a $^2\Pi_{1/2}$ State

It is instructive to also calculate the matrix element of the Zeeman Hamiltonian in a $^2\Pi_{1/2}$ state, where the commonly used angular momenta coupling corresponds to Hund's case (a) (see Sec. 2.2), with the basis:

$$|\Lambda, S, \Sigma, J, \Omega, M_J\rangle \,. \tag{2.25}$$

The corresponding Zeeman Hamiltonian now is (we are ignoring, as in the previous derivation, the contribution due to the molecular rotation):

$$H = -g_S \mu_B \mathbf{S} \cdot \mathbf{B} - g_L \mu_B \mathbf{L} \cdot \mathbf{B}, \tag{2.26}$$

where $\mathbf{L}$ is the electron orbital angular momentum and g_L the associated g-factor. We will first treat the first term in the Hamiltonian and assume that the magnetic field is pointing along the z-axis of the lab frame. We then get for the corresponding matrix element:

$$M = -g_S \mu_B \langle \Lambda, S, \Sigma, J, \Omega, M_J | B_z T^1_{p=0}(S) | \Lambda', S', \Sigma', J', \Omega', M'_J \rangle \,. \tag{2.27}$$

However, unlike the previous case, the electron spin is better described in the rest frame of the molecule rather than in the lab frame. Therefore, we will write $T^1_{p=0}(\mathbf{S})$ as $T^1_{p=0}(\mathbf{S}) = \sum_q \mathcal{D}^1_{0q}(\omega)^* T^1_q(\mathbf{S})$. The matrix element then becomes:

$$
\begin{aligned}
M &= -g_S \mu_B B_z \sum_q \langle \Lambda, S, \Sigma, J, \Omega, M_J | \mathcal{D}^1_{0q}(\omega)^* T^1_q(\mathbf{S}) | \Lambda', S', \Sigma', J', \Omega', M'_J \rangle \\
&= -g_S \mu_B B_z \sum_q \langle J, \Omega, M_J | \mathcal{D}^1_{0q}(\omega)^* | J', \Omega', M'_J \rangle \langle \Lambda, S, \Sigma | T^1_q(\mathbf{S}) | \Lambda', S', \Sigma' \rangle .
\end{aligned}
\tag{2.28}
$$

Using Eq. 2.16 we get:

$$
\langle J, \Omega, M_J | \mathcal{D}^1_{0,q}(\omega)^* | J', \Omega', M'_J \rangle = (-1)^{M_J - \Omega} \left[(2J+1)(2J'+1) \right]^{1/2} \begin{pmatrix} J & 1 & J' \\ -\Omega & q & \Omega' \end{pmatrix} \begin{pmatrix} J & 1 & J' \\ -M_J & 0 & M'_J \end{pmatrix},
\tag{2.29}
$$

and from the Wigner-Eckart theorem together with Eq. 2.12:

$$
\begin{aligned}
\langle \Lambda, S, \Sigma | T^1_q(\mathbf{S}) | \Lambda', S', \Sigma' \rangle &= \langle \Lambda | \Lambda' \rangle \langle S, \Sigma | T^1_q(\mathbf{S}) | S', \Sigma' \rangle \\
&= \delta_{\Lambda,\Lambda'} \delta_{SS'} (-1)^{S-\Sigma} \begin{pmatrix} S & 1 & S' \\ -\Sigma & q & \Sigma' \end{pmatrix} \left[S(S+1)(2S+1) \right]^{1/2} .
\end{aligned}
\tag{2.30}
$$

Thus, we obtain:

$$
\begin{aligned}
M = -g_S \mu_B B_z \sum_q (-1)^{M_J - \Omega} \left[(2J+1)(2J'+1) \right]^{1/2} \begin{pmatrix} J & 1 & J' \\ -\Omega & q & \Omega' \end{pmatrix} \begin{pmatrix} J & 1 & J' \\ -M_J & 0 & M_J \end{pmatrix} \times \\
\delta_{\Lambda,\Lambda'} \delta_{SS'} (-1)^{S-\Sigma} \begin{pmatrix} S & 1 & S' \\ -\Sigma & q & \Sigma' \end{pmatrix} \left[S(S+1)(2S+1) \right]^{1/2} .
\end{aligned}
\tag{2.31}
$$

In this case, all values of $q = 0, \pm 1$ contribute. If we restrict ourselves to the $q = 0$ case and let $J = J'$, the above expression greatly simplifies to:

$$
\begin{aligned}
M = -g_S \mu_B B_z (-1)^{M_J - \Omega + S - \Sigma} (2J+1) \left[S(S+1)(2S+1) \right]^{1/2} \times \\
\begin{pmatrix} J & 1 & J \\ -\Omega & 0 & \Omega \end{pmatrix} \begin{pmatrix} J & 1 & J \\ -M_J & 0 & M_J \end{pmatrix} \begin{pmatrix} S & 1 & S \\ -\Sigma & 0 & \Sigma \end{pmatrix},
\end{aligned}
\tag{2.32}
$$

which, upon using the general formula:

$$
\begin{pmatrix} J & 1 & J \\ -M & 0 & M \end{pmatrix} = (-1)^{J-M} \frac{M}{\left(J(J+1)(2J+1) \right)^{1/2}},
\tag{2.33}
$$

gives:

$$
\begin{aligned}
M = -g_S \mu_B B_z (-1)^{-2(J-\Omega)+2(S-\Sigma)} (2J+1) \left[S(S+1)(2S+1) \right]^{1/2} \times \\
\frac{\Omega}{\left(J(J+1)(2J+1) \right)^{1/2}} \frac{M_J}{\left(J(J+1)(2J+1) \right)^{1/2}} \frac{\Sigma}{\left(S(S+1)(2S+1) \right)^{1/2}} \\
= -g_S \mu_B B_z \frac{\Omega M_J \Sigma}{J(J+1)}.
\end{aligned}
\tag{2.34}
$$

Similar results are obtained for the second term of Eq. 2.26, with $g_S \to g_L$ and $\Sigma \to \Lambda$ which in the end gives for the matrix element for the Hamiltonian in Eq. 2.26 the very simple expression:

$$\langle \Lambda, S, \Sigma, J, \Omega, M_J | H | \Lambda, S, \Sigma, J, \Omega, M_J \rangle = -\mu_B B_z \left(g_S \Sigma + g_L \Lambda \right) \frac{\Omega M_J}{J(J+1)}. \tag{2.35}$$

Given that we have $g_S \approx -2$ and $g_L \approx -1$ (the exact values depend on the exact molecular state under consideration), for a $^2\Pi_{1/2}$ state with $\Lambda = 1$ and $\Sigma = -1/2$ we get that $g_S\Sigma + g_L\Lambda \approx 0$ and thus the calculated matrix element in this case is also ≈ 0.

2.1.4 Stark Interaction in a $^2\Sigma^+$ State

The Hamiltonian for the Stark interaction, between the intrinsic dipole moment of the molecule, $\mathbf{d}$, and an externally applied electric field $\mathbf{E}$ is:

$$H_S = -\mathbf{d} \cdot \mathbf{E}. \tag{2.36}$$

We will use Hund's case (b) and take the direction of the electric field to be along the lab frame z-axis, whose magnitude we denote by E_z. The matrix element is then given by:

$$\begin{aligned} M &= -E_z \langle \Lambda = 0, S, N, J, M_J | T^1_{p=0}(\mathbf{d}) | \Lambda = 0, S, N', J', M'_J \rangle \\ &= -E_z \sum_q \langle \Lambda = 0, S, N, J, M_J | T^1_q(\mathbf{d}) \mathcal{D}^{(1)}_{00}(\omega)^* | \Lambda = 0, S, N', J', M'_J \rangle . \end{aligned} \tag{2.37}$$

Since we work in a given electronic state, we only need the $q = 0$ term. Thus we get:

$$\begin{aligned} M &= -E_z \langle \Lambda = 0, S, N, J, M_J | T^1_{q=0}(\mathbf{d}) \mathcal{D}^{(1)}_{00}(\omega)^* | \Lambda = 0, S, N', J', M'_J \rangle \\ &= -E_Z \langle \Lambda = 0 | T^1_{q=0}(\mathbf{d}) | \Lambda = 0 \rangle \langle \Lambda = 0, S, N, J, M_J | \mathcal{D}^{(1)}_{00}(\omega)^* | \Lambda = 0, S, N', J', M'_J \rangle . \end{aligned} \tag{2.38}$$

The $D \equiv \langle \Lambda = 0 | T^1_0(\mathbf{d}) | \Lambda = 0 \rangle$ term represents the z-component of the matrix element of the dipole moment in the rest frame of the molecule (this value needs to be measured experimentally or calculated numerically, but it is a constant for a given electronic state), we get:

$$
\begin{aligned}
M &= -E_Z D \left\langle \Lambda=0, S, N, J, M_J | \mathcal{D}^{(1)}_{00}(\omega)^* | \Lambda=0, S, N', J', M'_J \right\rangle \\
&= -E_z D (-1)^{J-M_J} \begin{pmatrix} J & 1 & J' \\ -M_J & 0 & M_J \end{pmatrix} \left\langle N, S, \Lambda=0, J || \mathcal{D}^{(1)}_{\cdot 0}(\omega)^* || N', S, \Lambda=0, J' \right\rangle \\
&= -E_z D (-1)^{J-M_J} \begin{pmatrix} J & 1 & J' \\ -M_J & 0 & M_J \end{pmatrix} (-1)^{J'+S+N+1} \left[(2J+1)(2J'+1)\right]^{1/2} \times \\
&\begin{Bmatrix} J & N & S \\ N' & J' & 1 \end{Bmatrix} \left\langle N, \Lambda || \mathcal{D}^{(1)}_{\cdot 0}(\omega)^* || N', \Lambda \right\rangle \\
&= E_z D (-1)^{J-M_J+J'+S+2N-\Lambda} \begin{pmatrix} J & 1 & J' \\ -M_J & 0 & M_J \end{pmatrix} \left[(2J+1)(2J'+1)\right]^{1/2} \times \\
&\begin{Bmatrix} J & N & S \\ N' & J' & 1 \end{Bmatrix} \begin{pmatrix} N & 1 & N' \\ -\Lambda & 0 & \Lambda \end{pmatrix} \left[(2N+1)(2N'+1)\right]^{1/2},
\end{aligned}
\tag{2.39}
$$

where to obtain the expression in the second line, we used Eq. 2.14, 2.17 and 2.18. For example, for $N' = N+1 = 1$, $J' = J = 1/2$, $D = 3$ MHz/(V/cm) and $E_z = 1$ kV/cm, we get $M = 1$ GHz.

Using this expression for the matrix element, we can also extract the selection rules for electric dipole transitions between rotational levels within the same electronic (and vibrational) level, based on the properties of the Wigner 3-j symbols (of course, for such transitions, we need a time-varying field, but the derivation remains the same). For the considered $^2\Sigma^+$ state (i.e. $\Lambda = 0$) they are given by: $\Delta N = N' - N = \pm 1$ and $\Delta J = J' - J = 1/2, \pm 1$.

2.1.5 Stark Interaction in a $^2\Pi_{1/2}$ State

As in the Zeeman interaction case, we also show, for comparative purposes relative to the $^2\Sigma^+$ case, the matrix elements of the Stark Hamiltonian in a $^2\Pi_{1/2}$ state. We will use again a Hund's case a basis (Eq. 2.25) and take the direction of the electric field as the z-axis of the laboratory frame, whose magnitude we denote E_z. Then, the matrix element becomes:

$$
M = -E_z \left\langle \Lambda, S, \Sigma, J, \Omega, M_J | T^1_{p=0}(\mathbf{d}) | \Lambda', S', \Sigma', J', \Omega', M'_J \right\rangle . \tag{2.40}
$$

Again, it is more convenient to express the dipole moment in the rest frame of the molecule:

$$
\begin{aligned}
M &= -E_z \sum_q \left\langle \Lambda, S, \Sigma, J, \Omega, M_J | \mathcal{D}^{(1)}_{0q}(\omega)^* T^1_q(\mathbf{d}) | \Lambda', S', \Sigma', J', \Omega', M'_J \right\rangle \\
&= -E_z \sum_q \left\langle J, \Omega, M_J | \mathcal{D}^{(1)}_{0q}(\omega)^* | J', \Omega', M'_J \right\rangle \left\langle \Lambda | T^1_q(\mathbf{d}) | \Lambda' \right\rangle \delta_{SS'} \delta_{\Sigma\Sigma'} \\
&= -E_z \sum_q (-1)^{2J-M_J-\Omega} \left[(2J+1)(2J'+1)\right]^{1/2} \begin{pmatrix} J & 1 & J' \\ -\Omega & q & \Omega' \end{pmatrix} \begin{pmatrix} J & 1 & J' \\ -M_J & 0 & M'_J \end{pmatrix} \left\langle \Lambda | T^1_q(\mathbf{d}) | \Lambda' \right\rangle \delta_{SS'} \delta_{\Sigma\Sigma'},
\end{aligned}
\tag{2.41}
$$

where we used Eq. 2.16, together with the fact that the dipole moment doesn't act on the electron spin, thus it doesn't change S and Σ (an important consequence of this fact is discussed in more detail in Chapter 5, in the context of the Stark interference technique). If we keep as before only the $q = 0$ component and denote the molecule frame electric dipole moment by $D \equiv \langle \Lambda | T^1_0(\mathbf{d}) | \Lambda' \rangle$ we get:

$$\langle \Lambda, S, \Sigma, J, \Omega, M_J | H_S | \Lambda, S, \Sigma, J', \Omega', M'_J \rangle = -DE_z(-1)^{2J-M_J-\Omega} \left[(2J+1)(2J'+1)\right]^{1/2} \times \begin{pmatrix} J & 1 & J' \\ -\Omega & 0 & \Omega' \end{pmatrix} \begin{pmatrix} J & 1 & J' \\ -M_J & 0 & M'_J \end{pmatrix}. \tag{2.42}$$

If we take $J = J' = 1/2$, $D = 3$ MHz/(V/cm) and $E_z = 1$ kV/cm, we get $M = 1$ GHz. We can again use this matrix element to extract the selection rules for electric dipole transitions between rotational levels within an electronic (and vibrational) state of the molecule. In the considered case, the transition is allowed only if $\Delta J = J' - J = 0, \pm 1$ and $\Delta\Omega = \Delta M_J = 0$.

2.1.6 Fermi Contact Interaction in a $^2\Sigma^+$ State

Hyperfine interactions play an important role in understanding the spectra of molecules in which one of the constituent nuclei has a spin greater than zero. It can even provide valuable information about the inner structure of the nucleus itself (this topic will be described in detail in Chapter 4, in the context of the hyperfine structure measurement of ^{225}RaF [54]). One of the terms appearing in the hyperfine Hamiltonian, the so-called Fermi contact interaction term, is given by [31]:

$$H_{Fermi} = b_F T^1(\mathbf{S}) \cdot T^1(\mathbf{I}), \tag{2.43}$$

where b_F is a hyperfine structure constant quantifying the coupling strength between the electron spin $\mathbf{S}$ and the nuclear spin $\mathbf{I}$. Given that for the ^{225}RaF case, which will be of interest to us, the interesting hyperfine structure effects come from the ground electronic state, which is a $^2\Sigma^+$, we will calculate the matrix element of the above Hamiltonian in this state, assuming a Hund's case b coupling (see Sec. 2.2). The matrix element of interest then becomes:

$$M_{Fermi} = b_F \langle \Lambda, N, S, J, I, F, M_F | T^1(\mathbf{S}) \cdot T^1(\mathbf{I}) | \Lambda, N', S, J', I, F', M'_F \rangle, \tag{2.44}$$

where F is the total angular momentum of the molecule, including the nuclear spin. Given that we are interested only in a given electronic manifold, $^2\Sigma^+$, we assumed from the start that Λ and S don't change. Also, the spin of the nucleus is constant (it doesn't depend on the electronic state of the molecule). Using Eq. 2.15, the above matrix element becomes [31]:

$$M_{Fermi} = b_F(-1)^{J'+F+I}\delta_{F,F'}\delta_{M_F,M'_F}\begin{Bmatrix} I & J' & F \\ J & I & 1 \end{Bmatrix}\langle N,S,J||T^1(\mathbf{S})||N',S,J'\rangle\langle I||T^1(\mathbf{I})||I\rangle$$
$$= b_F(-1)^{J'+F+I}\delta_{F,F'}\delta_{M_F,M'_F}\begin{Bmatrix} I & J' & F \\ J & I & 1 \end{Bmatrix}[I(I+1)(2I+1)]^{1/2}\langle N,S,J||T^1(\mathbf{S})||N',S,J'\rangle . \tag{2.45}$$

Now, using Eq. 2.14, this becomes:

$$M_{Fermi} = b_F(-1)^{J'+F+I}\delta_{F,F'}\delta_{M_F,M'_F}\begin{Bmatrix} I & J' & F \\ J & I & 1 \end{Bmatrix}[I(I+1)(2I+1)]^{1/2}\times$$
$$\delta_{N,N'}(-1)^{J+N+1+S}[(2J+1)(2J'+1)]^{1/2}\begin{Bmatrix} S & J' & N \\ J & S & 1 \end{Bmatrix}\langle S||T^1(\mathbf{S})||S\rangle$$
$$= b_F\delta_{N,N'}\delta_{F,F'}\delta_{M_F,M'_F}(-1)^{J+J'+F+S+N+I+1}[(2J+1)(2J'+1)I(I+1)(2I+1)S(S+1)(2S+1)]^{1/2}$$
$$\begin{Bmatrix} I & J' & F \\ J & I & 1 \end{Bmatrix}\begin{Bmatrix} S & J' & N \\ J & S & 1 \end{Bmatrix}, \tag{2.46}$$

which can be easily calculated for a given spin-rotational/hyperfine level.

2.2 Angular Momentum Couplings and the Hund's Cases

Various angular momenta are present in a diatomic molecule, and their interactions lead to the observed rich spectra [31, 57, 58, 61]. It is often the case that some of these interaction are (much) stronger than others, and a specific basis can be chosen to reflect that, such that the off-diagonal matrix elements of the Hamiltonian under consideration in that basis are as small as possible [31, 57, 58, 61]. Each such situation (and an associated basis) corresponds to a Hund's case and they will be described below [31, 57, 58, 61, 62]. There are five Hund's cases usually considered in literature, labeled alphabetically from "a" to "e" and the classification of electronic states into one of these cases is based on the relative magnitude of 3 energy scales: electronic, spin-orbit and rotational [31, 57, 58, 61, 62]. The involved angular momenta used in this classification are:

S - the electronic spin angular momentum

L - the electronic orbital angular momentum

R - the rotational angular momentum of the nuclei

N - the total angular momentum, exclusive of electron/nuclear spin ($\mathbf{N} = \mathbf{L} + \mathbf{R}$)

$\mathbf{J_e}$ - the total electronic angular momentum ($\mathbf{J_e} = \mathbf{L} + \mathbf{S}$)

J - the total angular momentum of the molecule, exclusive of nuclear spin ($\mathbf{J} = \mathbf{N} + \mathbf{S}$)

Note that this classification of Hund's cases doesn't depend on the nuclear spin.

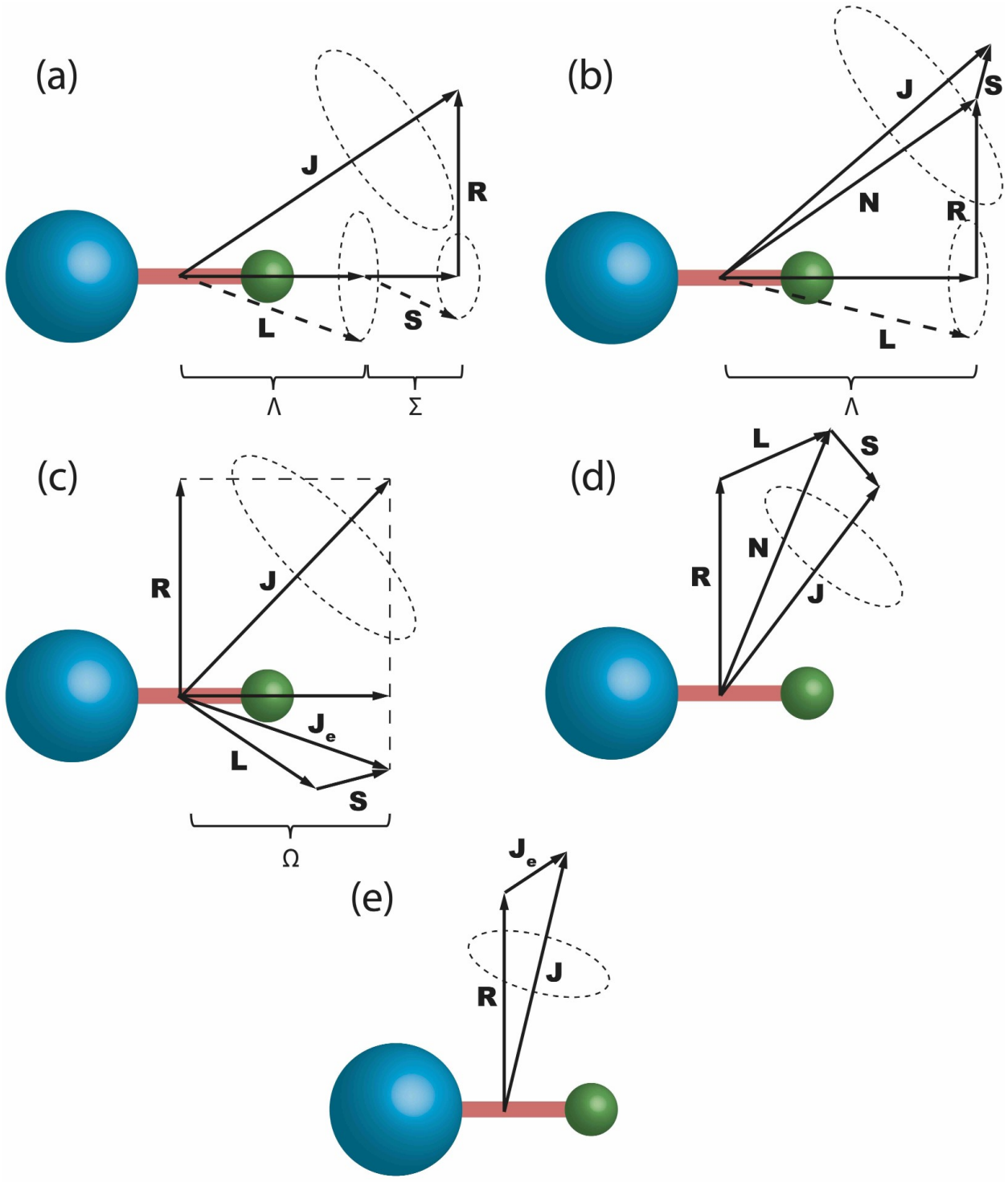

Figure 2.1: Angular momentum coupling in a diatomic molecule for Hund's cases (a), (b), (c), (d) and (e). See main text for details.

2.2.1 Hund's Case (a)

This situation is useful when strong electrostatic forces make the orbital angular momentum of the electron $\mathbf{L}$ to be coupled to the internuclear axis around which it precesses, while the electron spin, $\mathbf{S}$, is coupled to $\mathbf{L}$ through a strong spin-orbit interaction. The projections of $\mathbf{L}$ and $\mathbf{S}$ on the internuclear axis are denoted by Λ and Σ, while their sum, which is well defined in this Hund's case, is $\Omega = \Lambda + \Sigma$. The total angular momentum of the molecule, $\mathbf{J}$, is then the result of the coupling of Ω with $\mathbf{R}$ [31, 57, 58, 61, 62]. Figure 2.1 shows a diagram of the vectors coupling in this Hund's case.

Hund's case (a) is most useful when the spin-orbit interaction is much larger than the rotational one, parameterized as:

$$A\Lambda \gg BJ, \tag{2.47}$$

with A and B being the spin-orbit and rotational constants, respectively. This shows that for high enough rotational quantum numbers, J, the Hund's case (a) becomes a worse description of the system, and a different Hund's case or an intermediate description between two such cases could be more appropriate. Assuming the condition in Eq. 2.47 holds, the wavefunction used as the basis in the Hund's case (a), written in terms of the good quantum numbers, is $|\Lambda, S, \Sigma, J, \Omega, M_J\rangle$ [31].

It should be emphasized again that this basis doesn't diagonalize the molecular Hamiltonian (and the diagram in Fig. 2.1 is an idealized scenario associated with this angular momentum coupling scheme). While it leads to a Hamiltonian matrix with off-diagonal terms as small as possible, there are usually terms in the molecular Hamiltonian mixing different Hund's case (a) basis wavefunctions. For example, the so-called spin uncoupling term, $\mathbf{J} \cdot \mathbf{S}$, which arises from the rotational Hamiltonian [31]:

$$H_{rot} = B\mathbf{R}^2 = B\left[\mathbf{J} - \mathbf{L} - \mathbf{S}\right]^2, \tag{2.48}$$

can couple wavefunctions with Σ or Ω differing by ± 1. While small, such terms must be accounted for when trying to understand a molecular spectrum, especially at high enough spectroscopic resolution.

Finally, in a Hund's case (a) description of an electronic manifold, we have $2S + 1$ fine-structure levels, as a result of the spin-orbit interaction, of energy $A\Sigma\Lambda$ (and labeled by their Ω), on top of which we have the much smaller rotational splitting, with rotational levels of energy $BJ(J+1)$ [31]. Hund's case (a) is used to describe the first excited electronic level of the RaF molecule, $^2\Pi_{1/2}$, in Chapter 4 [52–54].

2.2.2 Hund's Case (b)

This situation applies to cases where $\Lambda = 0$ or $\Lambda \neq 0$ but the spin-orbit coupling is so weak (usually much weaker than the rotational interaction) that the electron spin $\mathbf{S}$ is not coupled to the internuclear axis. In this case, Σ and therefore Ω are not well defined, and a different coupling scheme (shown in Fig. 2.1) is used to characterize this Hund's case. Here, the projection of $\mathbf{L}$ (which is still strongly coupled to the internuclear axis and rapidly precesses around it) first couple to the rotation of the nuclei, $\mathbf{R}$, forming the

vector **N**. Finally, the electron spin **S** couples to **N** to form the total angular momentum of the molecule, **J**. The corresponding basis wavefunctions, together with the good quantum numbers in this basis are: $|\Lambda, N, S, J, M_J\rangle$ [31, 57, 58, 61, 62]. Hund's case (b) is used to describe the ground electronic level of the RaF molecule, $^2\Sigma^+$, in Chapter 4 [52–54].

It should be mentioned at this point that both Hund's case (a) and (b) basis are complete, and in general, calculating molecular Hamiltonian matrix elements (see Sec. 2.1) can be done in either (although, as mentioned, one is usually significantly easier to use than the other depending on the electronic state). It is often the case that calculations need to be performed (e.g., transition probabilities) involving spin-rotational levels of two electronic manifolds [53, 54], each of which is better described by a different Hund's case among the two considered so far. In this case, one needs to perform a transformation from one basis to the other. The formula for converting from Hund's case (b) to Hund's case (a) is [31, 63]:

$$|\Lambda, N, S, J, M_J\rangle = \sum_{\Omega=-1/2}^{1/2} \sum_{\Sigma=-1/2}^{1/2} (-1)^{J+\Omega} \sqrt{2N+1} \begin{pmatrix} S & N & J \\ \Sigma & \Lambda & -\Omega \end{pmatrix} |\Lambda, S, \Sigma, J, \Omega, M_J\rangle \,. \quad (2.49)$$

The other 3 Hund's cases left are not used for the analysis of the measured spectra presented in this thesis, therefore they will just be briefly described below for completeness.

2.2.3 Hund's Case (c)

In the previous two cases, the Coulomb electrostatic interaction was assumed to be strong enough to force the electronic orbital angular momentum **L** to precess around the internuclear axis. In Hund's case (c), the spin-orbit interaction is so strong that that **L** first couples to **S** to form $\mathbf{J_e}$, which then precesses around the internuclear axis (see Fig. 2.1 for the coupling scheme in this case). This is usually the case in heavy molecules [31]. The projection of this vector on the internuclear axis Ω (which is again a good quantum number as in Hund's case (a)) combines with the molecular frame rotation, **R** to form **J** [31, 57, 58, 61, 62]. It should be emphasized that, unlike Hund's cases (a) and (b), in Hund's case (c) Λ is not good quantum number anymore. Thus, the electronic levels can't be labeled using it anymore (e.g., Σ, Π). The basis wavefunctions in this case, together with the good quantum numbers, are $|J_e, J, \Omega, M_J\rangle$ [31].

The next 2 Hund's cases are less commonly used, but they can be useful in the description of higher lying, Rydberg molecular states [31, 57, 58, 61, 62]. While this might appear not very relevant to the topics presented in this thesis, as described in detail in Chapter 3, the RaF molecule presents some peculiar properties that could allow the investigation and quantum control of such Rydberg states, which could be very useful in future measurements using this molecule [14].

2.2.4 Hund's Case (d)

In this case, the rotational interaction dominates over the electrostatic and spin-orbit one, the latter one being particularly weak. Then, the coupling in Fig. 2.1 emerges where the electronic angular momentum, **L**, couples directly to the rotation frame of the molecule,

R, forming **N**, which subsequently couples to the electron spin **S** (assuming $S > 0$) to form **J** [31, 57, 58, 61, 62]. In this case the basis wavefunctions, together with the associated good quantum numbers, are: $|R, L, N, S, J\rangle$ [31]. Note that there is no projection on the molecular axis good quantum number in this case.

2.2.5 Hund's Case (e)

This case is similar to the previous one, in that the Coulomb electronic interaction is very weak (mainly because the electronic levels under consideration are high-lying ones), leading again to no molecular axis projection good quantum numbers. However, unlike Hund's case (d), the spin-orbit coupling can have an energy comparable to the rotational one. In this situation, we have the coupling scheme shown in Fig. 2.1, where **L** and **S** couple to form $\mathbf{J_e}$, which then couples to the molecular rotation, **R**, to form **J** [31, 57, 58, 61, 62]. The basis wavefunction and the associated good quantum numbers are then: $|R, J_a, J\rangle$ [31].

2.3 Spectroscopic Notation for Molecules

Labeling different electronic levels in a molecule depends on the Hund's case best suitable to describe that state. For example, in a Hund's case (a) or (c), Ω is a good quantum number, and hence it is used to label the state, but this is not the case for a Hund's case (b) (we won't be looking at Hund's cases (d) and (e) in this thesis moving forward). Generally, when naming a molecular electronic level, one starts with a Roman letter. By convention, for the ground state, this is X. Then, going higher in energy, the states are labeled in alphabetical order, using uppercase letters (A, B, C ...) for the states with the same multiplicity (total intrinsic electronic spin) as the ground electronic state and using lowercase letters (a, b, c ...) for states with a different multiplicity compared to the ground state [31, 57, 58].

Following this, for a Hund's case (a), the notation takes the form [31, 57, 58]:

$$^{2S+1}\Lambda^{\pm}_{\Omega}, \tag{2.50}$$

where S is the electronic spin, Λ is the electronic orbital angular momentum projection along the internuclear axis denoted as Σ for $\Lambda = 0$, Π for $|\Lambda| = 1$, Δ for $|\Lambda| = 2$, Φ for $|\Lambda| = 3$ and so on, while $\Omega = \Lambda + \Sigma$ is the total projection of the electron angular momentum ($J_e = L + S$) along the internuclear axis. Finally, the superscript $\pm$ is related to the symmetry of the electronic wavefunction when reflected through a plane passing through the internuclear axis. An example of this notation is the first excited electronic state of the RaF molecule, $^2\Pi_{1/2}$ [51–54]. The same notation is also used for a Hund's case (b) electronic level, with the exception that Ω (which is not well defined in this case) is omitted. For example, the ground electronic state of RaF is $^2\Sigma^+$ [51–54]. For Hund's case (c), Λ is not a good quantum number anymore, but often, in labeling electronic levels in this case, the closest Hund's case (a) or (b) that can describe them is mentioned in square brackets. For example, the first excited electronic state in PbO is labeled as a(1) [$^3\Sigma^+$] [64]. Note the lowercase letter used here, a, due to the fact that the ground state of PbO, $X^1\Sigma^+$, has a different multiplicity than the considered state [64].

2.4 Parity of the Molecular Wavefunctions

Before starting to talk about the molecular Hamiltonian, it is worth mentioning the behavior of the molecular wavefunctions under the parity operation, which flips the sign of the spatial coordinates in the lab frame (not in the molecule's rest frame):

$$P : \begin{pmatrix} x \\ y \\ z \end{pmatrix} \rightarrow \begin{pmatrix} -x \\ -y \\ -z \end{pmatrix} . \tag{2.51}$$

The derivation is straightforward but a little tedious, so here we will present the final results for Hund's cases (a) and (b), which will be of interest to us in the rest of the thesis (a detailed derivation can be found in Ref. [31]). For a Hund's case (a), we have [31]:

$$P \left|\Lambda, S, \Sigma, J, \Omega, M\right\rangle = (-1)^{J-S} \left|-\Lambda, S, -\Sigma, J, -\Omega, M\right\rangle . \tag{2.52}$$

This is true for all values of Λ, except for the Σ^- states, where the expression on the right must be multiplied by -1. While the Hund's case (a) wavefunction is not an eigenstate of the parity operator, the eigenstates can be built as linear combinations of such wavefunctions. For example, for the excited $^2\Pi_{1/2}$ electronic state of the RaF molecule [51–54], the positive parity states are:

$$\left|+\right\rangle = \frac{1}{\sqrt{2}} \left(\left|\Lambda = 1, S, \Sigma = -1/2, J, \Omega = 1/2, M\right\rangle + (-1)^{J-1/2} \left|\Lambda = -1, S, \Sigma = 1/2, J, \Omega = -1/2, M\right\rangle\right) , \tag{2.53}$$

and the negative parity ones:

$$\left|-\right\rangle = \frac{1}{\sqrt{2}} \left(\left|\Lambda = 1, S, \Sigma = -1/2, J, \Omega = 1/2, M\right\rangle - (-1)^{J-1/2} \left|\Lambda = -1, S, \Sigma = 1/2, J, \Omega = -1/2, M\right\rangle\right) . \tag{2.54}$$

For a Hund's case (b) wavefunction, we have [31]:

$$P \left|\Lambda, N, S, J, M_J\right\rangle = (-1)^N \left|-\Lambda, N, S, J, M_J\right\rangle , \tag{2.55}$$

again, with an extra -1 factor on the right for Σ^- states. For the $^2\Sigma^+$ electronic state, describing the ground electronic levels of RaF and SiO^+ described in Chapters 4 and 5 [51–55], given that $\Lambda = 0$, we have levels of opposite parity alternating with N. In both Hund's cases, the vibrational wavefunction, which depends only on the magnitude of the internuclear distance and not on its orientation, doesn't change under parity, and therefore, the vibrational quantum number is not included in the expressions above.

Finally, it should be mentioned that the labels e and f are also commonly used to denote the parity of molecular levels instead of $\pm$ (e.g., the default setting in the PGOPHER software used to simulate molecular spectra) [65]. The label e is used for states of parity $(-1)^J$ if J is an integer or $(-1)^{J-1/2}$ if J is a half-integer. The label f is used for states of parity $-(-1)^J$ if J is an integer or $-(-1)^{J-1/2}$ if J is a half-integer.

2.5 Molecular Hamiltonian and the Born-Oppenheimer Approximation

A diatomic molecule consists of two nuclei and several electrons, interacting with each other electromagnetically. While the weak interaction can play a measurable role in diatomic molecules, as described in detail in Chapter 5, it will not be discussed for now, as its effect is much smaller than the ones due to the electromagnetic interaction [26, 27, 43, 55]. Therefore, the Hamiltonian for a diatomic molecule in free space can be written as [31]:

$$H_{mol} = -\hbar^2 \sum_{\alpha=1}^{2} \frac{1}{2M_\alpha} \nabla_\alpha^2 - \frac{\hbar^2}{2m} \sum_{i=1}^{n} \nabla_i^2 + \sum_{i<j} \frac{e^2}{4\pi\epsilon_0 r_{ij}} - \sum_{\alpha,i} \frac{Z_\alpha e^2}{4\pi\epsilon_0 r_{i\alpha}} + \frac{Z_1 Z_2 e^2}{4\pi\epsilon_0 R} + H(\mathbf{S}_i), \quad (2.56)$$

where $\hbar$ is the reduced Plank constant, ϵ_0 is the electric permitivity of vacuum, M_α and Z_α are the mass and atomic number of the nucleus. α, m and e are the electron mass and charge, r_{ij} is the distance between electrons i and j, $r_{i\alpha}$ is the distance between the electron i and nucleus α. R is the distance between the two nuclei. The first two terms are the kinetic energy of the nuclei and electrons, respectively. The third term is the electrostatic energy due to electron-electron interaction. The fourth term is the electrostatic interaction between electrons and nuclei. The fifth term is the electrostatic interaction between the two nuclei. Finally, $H(\mathbf{S}_i)$ is the Hamiltonian containing interactions involving the electron spin (for now, we ignore the Hamiltonian related to the nuclear spin), leading to the fine structure of the molecule.

We can remove the translational motion energy from the above Hamiltonian (which doesn't change the measured spectrum of the molecules in an isotropic space) by moving to a frame with the origin at the center of mass of the two nuclei (note that this frame is still fixed, i.e., not rotating with the molecule) [66, 67]. In this case, the Hamiltonian becomes [31]:

$$\begin{aligned} H_{mol} = &- \frac{\hbar^2}{2m} \sum_{i=1}^{n} \nabla_i^2 - \frac{\hbar^2}{2(M_1+M_2)} \sum_{i,j} \nabla_i \cdot \nabla_j + \sum_{i<j} \frac{e^2}{4\pi\epsilon_0 r_{ij}} - \sum_{\alpha,i} \frac{Z_\alpha e^2}{4\pi\epsilon_0 r_{i\alpha}} + H(\mathbf{S}_i) \\ &- \frac{\hbar}{2\mu} \nabla_R + \frac{Z_1 Z_2 e^2}{4\pi\epsilon_0 R}, \end{aligned} \quad (2.57)$$

where $\mu = \frac{M_1 M_2}{M_1+M_2}$ is the reduced nuclear mass. Notice the new term appearing in the Hamiltonian in this new frame, $-\frac{\hbar^2}{2(M_1+M_2)} \sum_{i,j} \nabla_i \cdot \nabla_j$, called the mass polarization term. While this is the full molecular Hamiltonian in the stationary, lab frame, calculations involving this Hamiltonian (using the formalism of effective Hamiltonian described in Sec. 2.7) are greatly simplified if the electrons' coordinates are expressed in a frame rotating with the molecule (which makes sense intuitively, as the electrons rotate with the nuclei in the lab frame). If we express the electronic coordinates (as well as its spin) in the rotating frame, the molecular Hamiltonian becomes (we will separate the kinetic term of the nuclear part of the Hamiltonian moving on, similar to Ref. [31]):

$$
\begin{aligned}
H_{mol} &= H_e + H_N \\
H_e &= -\frac{\hbar^2}{2m}\sum_{i=1}^{n}\nabla_i^2 - \frac{\hbar^2}{2(M_1+M_2)}\sum_{i,j}\nabla_i\cdot\nabla_j + \sum_{i<j}\frac{e^2}{4\pi\epsilon_0 r_{ij}} - \sum_{\alpha,i}\frac{Z_\alpha e^2}{4\pi\epsilon_0 r_{i\alpha}} + H(\mathbf{S}_i) + \frac{Z_1 Z_2 e^2}{4\pi\epsilon_0 R} \\
H_N &= -\frac{\hbar^2}{2\mu R^2}\frac{\partial}{\partial R}\left(R^2\frac{\partial}{\partial R}\right) + \frac{\hbar^2}{2\mu R^2}(\mathbf{J}-\mathbf{L}-\mathbf{S})^2.
\end{aligned}
\tag{2.58}
$$

The first term in H_N corresponds to the vibrational energy of the molecule, and the second term to the rotational energy. Note that the form of the operator $\mathbf{J}-\mathbf{L}-\mathbf{S}$ comes from expressing the electron spin $\mathbf{S}$ in the rotating frame (which corresponds to Hund's case (a)). If we were to express it in the lab frame (corresponding to Hund's case (b)), that operator would become $\mathbf{N}-\mathbf{L}$, where $\mathbf{N}$ is the total angular momentum of the molecule except for the electron spin $\mathbf{S}$. This distinction is important in practice when performing calculations using electronic levels described by different Hund's cases.

Now that the Hamiltonian is expressed in the frame most convenient for future calculations (Eq. 2.58), the ultimate goal is to solve the Schrodinger equation associated with this Hamiltonian:

$$
H_{mol}\psi_{Ne} = E_{Ne}\psi_{Ne}, \tag{2.59}
$$

from which all the molecular energy levels, E_{Ne}, can be obtained, as well as any other operator of interest, using the wavefunction, ψ_{Ne}. Here, the "Ne" subscript denotes the fact that the wavefunction and the associated energy depend both on the electrons and nuclei. In general, any solution of Eq. 2.59 can be written as an infinite sum [31, 57]:

$$
\psi_{Ne} = \sum_i \psi_e^i(\mathbf{r}_i, R)\psi_N^i(R,\theta,\phi), \tag{2.60}
$$

where ψ_e^i are orthonormal eigenstates of the electronic Hamiltonian, H_e, and thus they depend only on the electrons coordinates (in the rotating frame), $\mathbf{r}_i$. This dependence varies as a function of R, while the dependence on the rotation angles, θ, and ϕ of the molecular frame is taken entirely by the functions ψ_N^i. In general, this equation cannot be solved exactly. A main challenge to solving this equation arises from the fact that the nuclear motion couples different electronic levels together, so in order to solve the Schrodinger equation exactly, one would need to include all these (infinite number of) electronic states and solve for them simultaneously [31, 57]. Thus, a perturbative approach is taken, which doesn't include all the physics contained in the Hamiltonian in Eq. 2.57, but which can explain the data with high precision (assuming enough terms are accounted for in the perturbative expansion) [31]. This is the main idea behind the effective Hamiltonian formulation described in Sec. 2.7. For now, we will follow a simpler approach and solve the Schrodinger equation (Eq. 2.59) using the famous Born-Oppenheimer approximation [68], which is able to retain a good amount of the physics of interest while allowing us to express the total molecular wavefunction as a product between an electronic (in the rotating frame of the molecule), a vibrational, and a rotational wavefunction [31, 57, 68]. Deviations from this simple picture

and couplings between these wavefunctions, as well as the effect of the electronic spin, $\mathbf{S}$, will be discussed in Sec. 2.7.

In order to get to the Born-Oppenheimer approximation [68], one begins by ignoring all couplings due to the nuclear motion between different electronic levels. This is a valid approximation, as usually, these couplings are small, given that the mass of the nuclei is much larger than the electrons, and thus one can imagine that the electrons are able to follow the nuclear motion adiabatically and, therefore, the electronic eigenstates of the system do not change [31, 57]. In this case, the molecular eigenfunction can be written simply as the product between an electronic wavefunction (which is an eigenstate of the H_e in Eq. 2.57) and a nuclear wavefunction, $\phi_N(R,\theta,\phi)$, which is, in general, different than the ones appearing in Eq. 2.60 [31, 57]:

$$\psi_{Ne} = \psi_e(\mathbf{r}, R)\phi_N(R,\theta,\phi), \tag{2.61}$$

and the associated Schrodinger equation becomes:

$$\begin{aligned}(H_e + H_N)\psi_e(\mathbf{r}, R)\phi_N(R,\theta,\phi) &= E_{Ne}\psi_e(\mathbf{r}, R)\phi(R,\theta,\phi)\\ H_e\psi_e(\mathbf{r}, R) &= E_e(R)\psi_e(\mathbf{r}, R),\end{aligned} \tag{2.62}$$

from which we obtain [31]:

$$\left(E_e(R) + H_N - \frac{\hbar}{2\mu}\int \psi_e^*\nabla_R^2\psi_e d\mathbf{r}\right)\phi_N(R,\theta,\phi) = E_{Ne}(R)\phi_N(R,\theta,\phi). \tag{2.63}$$

If the $\frac{\hbar}{2\mu}\int \psi_e^*\nabla_R^2\psi_e d\mathbf{r}$ term is kept, we obtain the adiabatic approximation [31, 57]. However, if we go one step further in our simplifications and ignore this term, thus removing any motional coupling between the nuclei and the electrons, we obtain the Born-Oppenheimer approximation [31, 57, 68]:

$$\left(E_e(R) + H_N\right)\phi_N(R,\theta,\phi) = E_{Ne}\phi_N(R,\theta,\phi). \tag{2.64}$$

Despite its multiple layers of simplifications, this equation can provide a very good picture of the different degrees of freedom in molecules, and it is usually a very good approximation for closed-shell molecules [31, 57]. Moreover, it represents an excellent starting point for the analysis of the data presented in Article 1 of Chapter 4 [52], in which the effects of replacing one of the nuclei in the molecules with its isotopes are investigated.

By solving Eq. 2.64, we can quantify the rovibrational motion of the nuclei in the potential created by the electronic cloud, $E_e(R)$, and thus compare it to the experiment. The rotational part can be extracted relatively easily, with the energy given by [31]:

$$E_{rot}(R) = \frac{\hbar^2}{2\mu R^2}\left[J(J+1) - \Omega^2\right], \tag{2.65}$$

where Ω is the projection (in a Hund's case (a) picture) of the total angular momentum of the molecule, J, on the internuclear axis. Note that this rotational energy still depends on R, which means that in order to get the full contribution of this term to the nuclear energy,

we need to average it over the vibrational wavefunction, which is achieved by adding Eq. 2.65 to $E_e(R)$ in the vibrational Schrodinger equation.

One main challenge in solving the vibrational Schrodinger equation is the fact that $E_e(R)$ doesn't have, in general, a closed form. Often, the shape of $E_e(R)$ is obtained by performing complex, numerical, many-body calculations to solve the electronic Schrodinger equation (second line in Eq. 2.62) for various values of R (for each calculation, the value of R is kept fixed). This problem can be solved in practice either by using an analytical formula able to reproduce the shape of the potential, with as few free parameters as possible or by writing the function $E_e(R)$ as a Taylor expansion around the equilibrium geometry (which can also be obtained from numerical calculations) of the given electronic state, R_e. One example of the former approach (which will be used to calculate the vibrational wavefunctions of the ground and excited RaF electronic levels in Article 2 of Chapter 4 [53]) is the Morse potential, expressed as [69]:

$$V(R) = D_e \left(1 - e^{-a(R-R_e)}\right)^2, \tag{2.66}$$

where D_e is the dissociation energy of the molecule in the electronic state under consideration, and $a = \sqrt{k_e/(2D_e)}$. k_e is the force constant of the electronic state at the equilibrium internuclear distance. The second approach is based on the Dunham parameterization [70]:

$$E_e(R) = a_0\xi^2 \left(1 + a_1\xi + a_2\xi^2 + a_3\xi^3 + ...\right), \tag{2.67}$$

where $a_0 = \frac{h\omega_e^2}{4B_e}$, with ω_e the vibrational constant of the electronic state. a_i, $i > 0$, are parameters that can be fit to measured data. The expansion parameter is:

$$\xi \equiv \frac{R - R_e}{R_e}. \tag{2.68}$$

This approach is used in Article 1 of Chapter 4 in order to study the isotope shift effects in RaF molecules [52]). Note that this parameterization is valid for $|\xi| < 1$, but the formula can, in principle, be extended beyond this using analytical continuation [71]. These two ways of expressing the effective electronic potential felt by the nuclei, $E_e(R)$, can also be used if the term $\frac{\hbar}{2\mu}\int \psi_e^* \nabla_R^2 \psi_e d\mathbf{r}$ in Eq. 2.63 is kept i.e. we work in the adiabatic approximation. However, in this case, the values of the various parameters will be slightly different. Following the Dunham approach [70] and combining Eq. 2.58, 2.63, 2.65 and 2.67, we obtain the following formula for the rovibrational energy levels of the molecule (in terms of the vibrational quantum number, ν and rotational quantum number, J) [70]:

$$\begin{aligned} E_{\nu,J} &= \sum_{kl} Y_{kl}(\nu + 1/2)^k \left[J(J+1)\right]^l \\ &= Y_{00} + Y_{10}(\nu + 1/2) + Y_{20}(\nu + 1/2)^2 + ...Y_{01}J(J+1) + Y_{02}\left[J(J+1)\right]^2 + ... \\ &+ Y_{11}(\nu + 1/2)J(J+1). \end{aligned} \tag{2.69}$$

The Y_{kl}'s can then be fit to measured rotational and vibrational transitions in molecules (the number of needed parameters depends on the precision of the measured data) and, for example, their obtained values compared to the theoretically predicted ones or used to

predict the energy of not yet measured molecular states. It is worth mentioning at this point that these parameters carry an isotopic dependence, which is useful in extracting information about the nuclei contained in the molecule [72], as described in great detail in Article 1 of Chapter 4 [52].To lowest order, this isotopic dependence is simply [70]:

$$Y_{kl} \propto \mu^{-(k/2+l)}, \tag{2.70}$$

where μ is the reduced mass of the molecule. However, higher-order corrections in the expansion of the Y_{kl} parameters lead to [52, 72]:

$$Y_{kl} \propto \mu^{-(k/2+l)} \left[1 + m_e \left(\frac{\Delta_{kl}^A}{M_A} + \frac{\Delta_{kl}^B}{M_B}\right) + V_{kl}^A \left\langle r^2 \right\rangle_A + V_{kl}^B \left\langle r^2 \right\rangle_B + ...\right], \tag{2.71}$$

where M_A (M_B) and $\left\langle r^2 \right\rangle_A$ ($\left\langle r^2 \right\rangle_B$) are the mass and charge radius of the nucleus A (B) in the molecule, m_e is the electron mass, $\Delta_{kl}^{A,B}$ and $V_{kl}^{A,B}$ are isotope independent electronic parameters and the "..." stands for higher order terms in the mass and charge radius expansion. From this, it can be seen that by performing measurements in several isotopologues (molecules in which one of the nuclei is replaced with an isotope), we can extract the change in the charge radius between pairs of isotopes, A and A', $\delta \left\langle r^2 \right\rangle_{AA'}$ [52].

Before moving to a more detailed description of the non-adiabatic corrections to the obtained results through the use of the effective Hamiltonian (as well as the inclusion of electronic and eventually nuclear spins), it is worth writing down the formula for the energy levels obtained using the Morse potential (Eq. 2.66) to represent the electronic potential, which is often easier to work with [31, 57, 58, 69]:

$$E_{\nu,J} = \omega_e(\nu+1/2) - x_e\omega_e(\nu+1/2)^2 + B_e J(J+1) - D_e \left[J(J+1)\right]^2 - \alpha_e(\nu+1/2)J(J+1). \tag{2.72}$$

Ignoring higher order corrections, usually on the order of $\frac{B_e^2}{\omega_e^2}$ or smaller ($B_e \ll \omega_e$ for most molecules), it can be shown that: $\omega_e = Y_{10}$, $B_e = Y_{01}$, $x_e\omega_e = -Y_{20}$, $D_e = -Y_{02}$ and $\alpha_e = -Y_{11}$ [72].

2.6 Franck Condon Factors

The transition probability between two electronic levels in a molecule, in the electric dipole approximation, is proportional to the square of the transition electric dipole moment matrix element between the two levels [31, 57, 58]. The dipole moment operator in the rest frame of the molecule can be written as [31, 57, 58]:

$$\mathbf{d} = e\left(Z_1\mathbf{R_1} + Z_2\mathbf{R_2} - \sum_i \mathbf{r_i}\right), \tag{2.73}$$

where the sum is over all the electron positions and the transition dipole moment matrix element in the Born-Oppenheimer approximation, $\mathbf{D}_{if}$, is then:

$$\mathbf{D}_{if} \propto \left\langle \psi_e^f \right| \left\langle \psi_v^f \right| e \left(Z_1\mathbf{R_1} + Z_2\mathbf{R_2} - \sum_i \mathbf{r_i}\right) \left|\psi_v^i\right\rangle \left|\psi_e^i\right\rangle, \tag{2.74}$$

where ψ_e^i (ψ_e^f) and ψ_v^i (ψ_v^f) stand for the initial (final) electronic and vibrational levels, respectively. Note that $\mathbf{D}_{if}$ also depends on the initial and final rotational levels, but these contributions can be easily calculated (together with the associated selection rules) as described in Sec. 2.1.4 and 2.1.5. We then have:

$$\begin{aligned}\mathbf{D}_{if} &\propto \left[e \left\langle \psi_e^f \right| \left\langle \psi_v^f \right| \left(Z_1 \mathbf{R_1} + Z_2 \mathbf{R_2} \right) \left| \psi_v^i \right\rangle \left| \psi_e^i \right\rangle - e \left\langle \psi_e^f \right| \left\langle \psi_v^f \right| \sum_i \mathbf{r_i} \left| \psi_v^i \right\rangle \left| \psi_e^i \right\rangle \right] \\ &\propto \left[e \left\langle \psi_e^f | \psi_e^i \right\rangle \left\langle \psi_v^f \right| \left(Z_1 \mathbf{R_1} + Z_2 \mathbf{R_2} \right) \left| \psi_v^i \right\rangle - e \left\langle \psi_e^f \right| \sum_i \mathbf{r_i} | \psi_e^f \rangle \left\langle \psi_v^f | \psi_v^i \right\rangle \right] .\end{aligned} \tag{2.75}$$

This first term above is zero, as we assume that the (different) initial and final electronic levels are orthonormal. Thus we are left with:

$$\begin{aligned}\mathbf{D}_{if} &\propto - e \left\langle \psi_e^f \right| \sum_i \mathbf{r_i} | \psi_e^f \rangle \left\langle \psi_v^f | \psi_v^i \right\rangle \\ \mathbf{D}_{if} &\propto \left\langle \psi_v^f | \psi_v^i \right\rangle ,\end{aligned} \tag{2.76}$$

The obtained term $\langle \psi_v^f | \psi_v^i \rangle$ is equal to the overlap integral of the ground and excited vibrational levels under considerations, and its square is called the Franck-Condon factor [73–75]. It reflects the probability of driving transitions between different vibrational levels in different electronic states, but, more relevant for us, as described in detail in Chapter 4 [53], it gives the probability for a vibrational level in an excited electronic state, to decay to a given vibrational level in the ground electronic state. This is very important for laser cooling, as ideally, one wants the decay to be back to the initial vibrational level upon an excitation [33]. Since there are no selection rules for transitions between vibrational levels in different electronic states, the Franck-Condon factors are solely responsible for this vibrational branching [33].

2.7 Effective Hamiltonian

In Sec. 2.5, we showed that, to a good degree of approximation, we can write the molecular wavefunction as the product between the electronic, vibrational, and rotational parts. This is possible due to the large difference in the energy scales associated with each of these terms. However, in doing so, we completely ignored (both in the adiabatic and Born-Oppenheimer approximation) the coupling between different electronic eigenstates due to the nuclear motion. If we want to fully understand the measured spectra in most molecules (including the ones described in Chapters 4 and 5 [52–55]), these couplings need to be included in our description of the molecular energy levels [31, 57, 58].

While fully accounting for all the levels present in a molecule is computationally intractable, the large energy gap between the electronic, vibrational, and rotational motions allows us to include, order by order, any previously ignored effects in a perturbative way. This is the main idea behind the effective Hamiltonian description of the molecular energy

levels [31]. In particular, in our measurements, we are often interested only in the spin-rotational and hyperfine levels of a given vibrational level of a particular electronic state. The effective Hamiltonian is, therefore, an operator acting only on these levels of interest, obtained by absorbing the effects of the other vibrational and rotational molecular levels present in the full Hamiltonian in the form of effective parameters [31], as described below. Very important is the fact that, in the way they are built, the eigenvalues of the effective Hamiltonian (the difference between which is measured experimentally) are equal to the corresponding eigenvalues of the full Hamiltonian to any desired order and hence precision in perturbation theory. The derivations presented below are based on the formalism described in Ref. [31]. This reference is strongly recommended for a more in-depth explanation of effective Hamiltonians for diatomic molecules.

The appeal of the effective Hamiltonian is that it allows for a straightforward interpretation of the experimental data in terms of a small number of effective molecular parameters, which would be impossible if the full Hamiltonian was to be used [31, 57, 58]. While the physical meaning of the effective parameters is not clear anymore in this approach, given that each of them can be decomposed into various perturbative terms, including the effects of the other vibrational and electronic levels, one can compare the experimentally obtained values to their predictions, at any desired (or feasible) order in the perturbative expansion [31]. As shown in great detail in Chapter 4, this is a very fruitful approach to gauge the quality of *ab initio* molecular calculations and their reliability for predicting electronic parameters associated with (not yet measured) new physics effects [54].

A detailed and general derivation of the effective Hamiltonian from the full molecular Hamiltonian can be found in Ref. [31]. It should be emphasized that, while in this formalism, one uses a perturbative approach, the final result is different relative to the usual perturbation theory used in quantum mechanics. Instead of obtaining corrections to a given energy and/or wavefunction due to the other terms in the perturbing Hamiltonian, the final result in this case is a new Hamiltonian, but acting in a smaller space than the original one [31]. While this new Hamiltonian allows us to interpret our measured spectra without worrying about the other vibrational and electronic molecular levels, it is not, in general, a diagonal matrix in the space spanned by the spin-rotational/hyperfine basis commonly used in practical calculations (e.g., Hund's case (a) or (b) basis). However, the eigenvalues obtained by diagonalizing this reduced space Hamiltonian will be identical to the equivalent ones in the original, full Hamiltonian, at the perturbative level used [31]. In this section, I will present this approach applied to terms in the molecular Hamiltonian relevant to the diatomic molecules studied in the rest of this thesis, in particular for $^2\Sigma^+$ and $^2\Pi_{1/2}$ electronic levels.

The full molecular Hamiltonian, which is an extension of the one in Eq. 2.58, by including the effect of fine and hyperfine interactions, is (note that moving forward, we set $\hbar = c = 1$) [31]:

$$H = -\frac{1}{2m}\sum_i^n \nabla_i^2 + \sum_{i<j}\frac{e^2}{4\pi\epsilon_0 r_{ij}} - \sum_i \frac{Z_1 e^2}{4\pi\epsilon_0 r_{i1}} - \sum_i \frac{Z_2 e^2}{4\pi\epsilon_0 r_{i2}} + \frac{Z_1 Z_2 e^2}{4\pi\epsilon_0 R}$$
$$- \frac{1}{2\mu R^2}\frac{\partial}{\partial R}\left(R^2\frac{\partial}{\partial R}\right) + B(R)(\mathbf{N}-\mathbf{L})^2 - \frac{1}{2M}\sum_{i,j}\nabla_i\cdot\nabla_j + H_{SO}^e + H_{SO}^n + H_{hf}, \tag{2.77}$$

where on the first line, we have the kinetic electronic energy together with the potential energy from electron-electron pairwise interactions, interactions between the electrons, and the two nuclei (of atomic number Z_1 and Z_2), as well as the interactions between the two nuclei. $M = M_1 + M_2$ is the total mass of the two nuclei. On the second line we have the kinetic energy of the nuclei and the mass polarization term. H_{SO}^e is the term responsible for the spin-orbit coupling interaction, which can be written as (see Ref. [31] for a derivation):

$$H_{SO}^e = \frac{e^2 g_S}{16\pi\epsilon_0 m_e^2}\sum_i \mathbf{s_i}\cdot\left(\frac{Z_1}{r_{i1}^3}\mathbf{r}_{i1}\times\mathbf{p_i} + \frac{Z_2}{r_{i2}^3}\mathbf{r}_{i2}\times\mathbf{p_i}\right), \tag{2.78}$$

where $\mathbf{s_i}$ and $\mathbf{p_i}$ are the intrinsic spin and linear momentum of the i-th electron. The next term, H_{SO}^n, is responsible for the effective coupling between the electron spin and the molecular rotation, and it can be written as (see Ref. [31] for a derivation):

$$H_{SO}^n = -\frac{e^2 g_S}{8\pi\epsilon_0 m_e}\sum_i \mathbf{s_i}\cdot\left(\frac{Z_1}{M_1 r_{i1}^3}\mathbf{r}_{i1}\times\mathbf{P_1} + \frac{Z_2}{M_2 r_{i2}^3}\mathbf{r}_{i2}\times\mathbf{P_2}\right), \tag{2.79}$$

where $\mathbf{P_1}$ and $\mathbf{P_2}$ are the linear momentum of the two nuclei. The last term contains all the hyperfine interaction, and its exact form depends on the spin of the two nuclei inside the molecule. If we choose as our reference Hamiltonian, H_0, on top of which we perform the perturbative expansion leading towards the effective Hamiltonian, to be the first line in Eq. 2.77:

$$H_0 = -\frac{1}{2m}\sum_i^n \nabla_i^2 + \sum_{i<j}\frac{e^2}{4\pi\epsilon_0 r_{ij}} - \sum_i \frac{Z_1 e^2}{4\pi\epsilon_0 r_{i1}} - \sum_i \frac{Z_2 e^2}{4\pi\epsilon_0 r_{i2}} + \frac{Z_1 Z_2 e^2}{4\pi\epsilon_0 R}, \tag{2.80}$$

we can denote by $|e\rangle|\nu\rangle|r\rangle$ the eigenstates of this Hamiltonian, such that [31]:

$$H_0|e\rangle|\nu\rangle|r\rangle = V_e(R)|e\rangle|\nu\rangle|r\rangle. \tag{2.81}$$

This notation emphasizes that at this level of approximation (i.e., ignoring all the Hamiltonian terms in the second line of Eq. 2.77), the electronic $|e\rangle$, vibrational $|\nu\rangle$ and rotational $|r\rangle$ wavefunctions can be separated exactly (i.e., there is no coupling between them). Note that here by $|r\rangle$ we mean all the spin-rotational and hyperfine quantum numbers needed to fully describe the state of interest. In practice, $|r\rangle$ will be chosen as one of Hund's cases basis. It is important to note that at this point all the vibrational and rotational energy levels within a given electronic manifold are degenerate. We can first remove the vibrational

levels degeneracy by including the effects of the $-\frac{1}{2\mu R^2}\frac{\partial}{\partial R}\left(R^2\frac{\partial}{\partial R}\right)$ term in Eq. 2.77 [31]. The vibrational Hamiltonian at this level of approximation then becomes [31]:

$$\left[-\frac{1}{2\mu R^2}\frac{\partial}{\partial R}\left(R^2\frac{\partial}{\partial R}\right)+V_e(R)\right]|e\rangle\,|\nu\rangle=(T_e+G_{e\nu})\,|e\rangle\,|\nu\rangle\,, \tag{2.82}$$

where T_e is the value of the minimum of the potential curve of $V_e(R)$ and in general, $G_{e\nu}$ can be written as [31]:

$$G_{e\nu}=\omega_e\,(\nu+1/2)-\omega_e x_e\,(\nu+1/2)^2+\omega_e y_e\,(\nu+1/2)^3+.... \tag{2.83}$$

At this point, different vibrational levels have different energies, but all the rotational states in a given vibrational level are still degenerate. This degeneracy can, of course, be lifted by including the remaining terms in Eq. 2.77 through the effective Hamiltonian [31], which we denote by H_e^{eff}. This acts on the spin-rotational and hyperfine states of the electronic level $|e\rangle$ (in the first part of the derivation, we can ignore the vibrational wavefunction). Following the derivation in Ref. [31], the connection between the effective Hamiltonian and the original one, Eq. 2.77, (to second order in perturbation theory) is:

$$H_e^{eff}=\langle e|\,H\,|e\rangle+\sum_{e\neq e'}\frac{\langle e|\,H\,|e'\rangle\,\langle e'|\,H\,|e\rangle}{V_e(R)-V_{e'}(R)}. \tag{2.84}$$

Note that at this step, the effective Hamiltonian still depends on the internuclear distance. This will be removed once we average over the vibrational wavefunction. When talking about an electronic level, we consider the states with both positive and negative Ω values (for a Hund's case (a) case), or Λ values (for a Hund's case (b) case), so, if $|e\rangle = {}^2\Pi_{1/2}$, we would have both states: $|{}^2\Pi_{1/2}, \Lambda=1, \Sigma=-1/2, \Omega=1/2\rangle$ and $|{}^2\Pi_{1/2}, \Lambda=-1, \Sigma=1/2, \Omega=-1/2\rangle$. Using Eq. 2.84, we can see the beauty of using the effective Hamiltonian in practice by starting with the rotational energy term in the full Hamiltonian: $B(R)(\mathbf{N}-\mathbf{L})^2$. This form is useful for Hund's case (b) (and it will be used later to describe the ground electronic state of RaF and SiO^+ [52–55]). The formalism described below can be just as well applied to a Hund's case (a), in which case the rotational operator takes the form $B(\mathbf{J}-\mathbf{L}-\mathbf{S})^2$, but the advantage of using the effective Hamiltonian is more clear using the Hund's case (b) form of the rotational Hamiltonian [31]. This can be expanded as:

$$H_{rot}=B(R)(\mathbf{N}^2+\mathbf{L}^2-2L_zN_z-N_+L_--L_-N_+). \tag{2.85}$$

The main complication in evaluating matrix elements using this Hamiltonian is related to the fact that the $L_\pm$ operators connect different electronic levels, and computing their matrix elements between such levels is challenging, as the electronic orbital angular momentum is not a conserved quantity in the rest frame of the molecule (where we perform our calculations). The L_zN_z term is a constant for a given electronic and vibrational state, as $L_z=N_z=\Lambda$ and $\mathbf{L}^2$, while challenging to compute for different electronic states, it can be absorbed as a correction to the electronic/vibrational energies, without influencing the relative spacing between rotational levels in a given electronic (and vibrational) manifold. Thus, the operator of interest for describing the rotational motion of a molecule is $B(R)(\mathbf{N}^2-N_+L_--N_-L_+)$. We can now compute the effect of this operator in a perturbative manner. To first order in our

perturbative expansion, for a given electronic state, $|e\rangle$, the effective rotational Hamiltonian, $H^{(1)}_{rot,eff}$ is [31]:

$$\begin{aligned} H^{(1)}_{rot,eff} &= \langle e|B(R)\mathbf{N^2}|e\rangle \\ &= \langle e|B(R)|e\rangle\, \mathbf{N^2}. \end{aligned} \tag{2.86}$$

If we stopped here, the effective molecular parameter associated with the rotational motion would be $B^{(1)}(R) = \langle e|B(R)|e\rangle$, and the operator $\mathbf{N}^2$. If we go to second order in perturbation theory, we have the term [31]:

$$\sum_{e'\neq e} \frac{\langle e|B(R)(N_+L_- + N_-L_+)|e'\rangle\, \langle e'|B(R)(N_+L_- + N_-L_+)|e\rangle}{V_e(R) - V_{e'}(R)}. \tag{2.87}$$

Now there are two cases, leading to two different effects in the effective Hamiltonian. In the first one, the electron orbital angular operator in the matrix element on the left is opposite to the one from the right, leading to an overall operator of the form $L_-L_+N_-N_+$. As we will show below, this contributes to the rotational energy of the molecule [31]. In the other case, the two operators are the same, so we have $L_-L_-N_+N_+$ or $L_+L_+N_-N_-$, which leads to the so-called Λ-doubling, which will be discussed later [31].

Working in the first case above, we have [31]:

$$\begin{aligned} H^{(2)}_{rot,eff} &= \sum_{e'\neq e} \frac{\langle e|B(R)L_\pm|e'\rangle\, \langle e'|B(R)L_\mp|e\rangle}{V_e(R) - V_{e'}(R)} N_\mp N_\pm \\ &= \sum_{e'\neq e} \frac{\langle e|B(R)L_\pm|e'\rangle\, \langle e'|B(R)L_\mp|e\rangle}{V_e(R) - V_{e'}(R)} (\mathbf{N}^2 - N_z^2). \end{aligned} \tag{2.88}$$

Thus, besides the N_z^2 which is a constant for a given electronic and vibrational level and thus can be ignored for our purposes, we ended up with an effective term whose operator $\mathbf{N}^2$ is exactly the same as before. Thus, if we write $B^{(2)}(R) \equiv \sum_{e'\neq e} \frac{\langle e|B(R)L_\pm|e'\rangle\langle e'|B(R)L_\mp|e\rangle}{V_e(R)-V_{e'}(R)}$, the effective rotational operator becomes, to second order in perturbation theory [31]:

$$H_{rot,eff} = (B^{(1)} + B^{(2)})\mathbf{N^2}. \tag{2.89}$$

The effect of all the other electronic levels is simply absorbed in a redefinition of the rotational parameter. Thus, in practice, when trying to make sense of our data, we just need to find the best parameter $B \equiv B^{(1)} + B^{(2)}$ reproducing our results without worrying about all the complicated electronic matrix elements that enter in the definition of this parameter [31]. Once B is fit to the data, predicting any other rotational level in the given electronic and vibrational state becomes trivial. However, the price to pay for this is that giving a physical interpretation of the B parameter becomes practically impossible. While the $B^{(1)} = \frac{1}{2\mu R^2}$ can be thought of in terms of the moment of inertia of the molecule, the $B^{(2)}$ term has no clear interpretation.

Now, we can tackle the remaining situation mentioned above, related to the operators $L_-L_-N_+N_+$ and $L_+L_+N_-N_-$. In this case, the associated term in the effective Hamiltonian is given by [31]:

$$H_{\Lambda-doubling} = \sum_{e'\neq e} \frac{\langle e|B(R)L_-|e'\rangle \langle e'|B(R)L_-|e\rangle}{V_e(R) - V_{e'}(R)} N_+N_+ + \sum_{e'\neq e} \frac{\langle e|B(R)L_+|e'\rangle \langle e'|B(R)L_+|e\rangle}{V_e(R) - V_{e'}(R)} N_-N_-. \tag{2.90}$$

As can be seen, in this case, two electronic levels with $\Delta\Lambda = 2$ are connected. This is the case, for example, for a $^2\Pi_{1/2}$ electronic state, in which the $|\Lambda = 1\rangle$ and $|\Lambda = -1\rangle$ states are mixed through a $|^2\Sigma\rangle$ state. Eq. 2.90 can be simplified to an effective operator (see Ref. [31] for a derivation):

$$H_{\Lambda-doubling}(R) = -q(R) \sum_{q=\pm1} e^{-2iq\phi} \left[T^2_{2q}(\mathbf{N}, \mathbf{N})\right], \tag{2.91}$$

with

$$\begin{aligned} T^2_{\pm2}(\mathbf{N}, \mathbf{N}) &= T^1_{\pm1}(\mathbf{N}) T^1_{\pm1}(\mathbf{N}), \\ q(R) &\equiv 4 \sum_{e'} \frac{|\langle e, \Lambda = 1|B(R)T^1_1(\mathbf{L})|e', \Lambda = 0\rangle|^2}{V_e(R) - V_{e'}(R)}. \end{aligned} \tag{2.92}$$

The second expression above is valid for a $^2\Sigma^+$ intermediate state but requires an extra minus sign for a $^2\Sigma^-$ intermediate electronic level. ϕ is the orbital azimuthal angle of the electron in the molecular rest frame. While the new effective term, Eq. 2.91, can't be combined with the rotational one (Eq. 2.89), it can be easily evaluated as a separate term, from which the value of the Λ-doubling parameter, q, can be extracted.

As mentioned in Sec. 2.4 (Eq. 2.53 and 2.54), the levels of opposite parity in a Π electronic level are linear combinations of $\Lambda = \pm1$ states. The effect of the Λ-doubling effective Hamiltonian is to lift the degeneracy between these two levels, such that for each rotational level, J, we have two states of opposite parity separated by an amount given (in part) by this Hamiltonian. It should be noted that, besides the rotational Hamiltonian, the H^e_{SO} term in the original Hamiltonian, whose effect can be shown to be proportional to the operator $\mathbf{L} \cdot \mathbf{S}$ (see Ref. [31]), also contributes to the Λ-doubling. This contribution can be entirely due to H^e_{SO}, in which case the effective operator is of the form $L_\pm L_\pm S_\mp S_\mp$. This term doesn't play a role in doublet electronic states, and this can be easily shown using the Wigner-Eckart theorem [31]. The contribution can also be caused by the interference between the rotational Hamiltonian and H^e_{SO}, in which case the operator is of the form $L_\pm L_\pm S_\mp N_\mp$ [31]. While this effect is visible for a Π state at second order in perturbation theory, if we look at a Δ state, the connection between the $\Lambda = 2$ and $\Lambda = -2$ levels is possible through the Λ-doubling effective Hamiltonian only at the fourth order in perturbation theory, leading to a very small splitting between opposite parity levels in a given rotational state [31]. These levels can be easily polarized in small electric fields (usually < 100 V/cm) and play a crucial role in searches for CP-violation using molecules [14, 17, 28, 29].

The same formalism as above can be applied, in a straightforward manner, to all the other terms left in Eq. 2.77, giving us several (usually very few, to second order in perturbation theory) effective Hamiltonian terms, which can be easily and very conveniently used to explain our data, without us having to ever worry about the complicated interplay between electronic and nuclear degrees of freedom in the molecule. The main operators of importance for us are the spin-orbit interaction [31]:

$$H_{SO,eff} = A(R)T^1_{q=0}(L)T^1_{q=0}(S), \tag{2.93}$$

and the spin-rotational interaction [31]:

$$H_{SR,eff} = \gamma(R)\mathbf{N}\cdot\mathbf{S}. \tag{2.94}$$

These, together with the rotational and Λ-doubling operators as well as the hyperfine structure (when a nuclear spin is present), are enough to describe the measured rotational spectra of a wide range of diatomic molecules such as the molecules studied in this thesis [31].

However, as a last step to be able to use these operators, the dependence of the effective molecular parameters on the internuclear distance, R, should be removed. This can be done by including the effect of the vibrational motion of the molecule in a perturbative way, equivalent to the one used in the case of the electronic wavefunctions [31]. If we follow the Dunham parameterization (see Eq. 2.67), it can be shown that for any operator $O(R)$, its first order vibrational correction is given by [31, 71]:

$$O_\nu = \langle\nu|O(R)|\nu\rangle = O_e + \frac{B_e}{\omega_e}\left(\frac{d^2O(R)}{d\xi^2}\Big|_{R_e} - 3a_1\frac{dO(R)}{d\xi}\Big|_{R_e}\right)(\nu+1/2) + ..., \tag{2.95}$$

where $B_e = \frac{1}{2\mu R_e}$, with R_e the radius corresponding to the minimum of the electronic potential, $V_e(R)$. The derivatives are taken with respect to $\xi \equiv \frac{R-R_e}{R_e}$, evaluated at $R = R_e$. Here, $|\nu\rangle$ are the vibrational wavefunctions obtained from Eq. 2.82, and given our formalism so far, it is implied that the operators and vibrational wavefunctions are all defined with respect to only a single electronic manifold. Thus, the values of the rotational and hyperfine parameters depend on the vibrational levels in which the measurement is performed, dependence which is, to lowest order, linear in the vibrational quantum number, ν [31].

We can go one step further (and this is needed for most measurements of the rotational energy [53, 54]) and use second-order perturbation theory relative to the vibrational energy levels, i.e., include the effect of vibrational levels, other than the one we are working in, into the operators appearing in the effective Hamiltonian [31]. For example, for the rotational energy, we can have a new effective operator [31]:

$$\sum_{\nu'}\frac{\langle\nu|B(R)\mathbf{N}^2|\nu'\rangle\langle\nu'|B(R)\mathbf{N}^2|\nu\rangle}{G_\nu - G_{\nu'}} \to -D_\nu\mathbf{N^4}, \tag{2.96}$$

with [31]:

$$D_\nu \equiv -\sum_{\nu'}\frac{\langle\nu|B(R)|\nu'\rangle\langle\nu'|B(R)|\nu\rangle}{G_\nu - G_{\nu'}}. \tag{2.97}$$

The minus sign is by convention. Similar corrections can be obtained for the other effective Hamiltonian parameters, but they are less relevant for the analysis performed in this thesis, and in general, their effects are less pronounced than those discussed above [31].

Chapter 3

Nuclear Electroweak Properties and Molecules

Many body systems have fascinated physicists for hundreds of years. One system in particular, whose understanding posed a formidable challenge to even the brightest minds in the field, is the atomic nucleus [76–81]. Despite a well-understood theory of Quantum Chromodynamics (QCD) [1], an explanation of various nuclear phenomena observed experimentally has eluded physicists, mainly due to the non-perturbative nature of the problem [1]. Giving a theoretical explanation for the emergence of collective nuclear behaviors in individual nuclei or across isotopic chains, starting from the underlying nucleonic degrees of freedom, seemed like a daunting challenge. Even more far-fetched seemed the possibility of going even deeper and connect the observed nuclear effects to the fundamental quarks and gluons.

However, major developments, both on the theoretical and experimental side, made in the last few years, allowed us to shine light on many of these questions and even lay down a systematic path for improving our understanding of nuclei in the years to come [11–13, 15, 16, 19–22, 24, 51–54, 82–86]. On the theoretical side, this was mainly achieved due to the development of new, more computationally efficient quantum many-body methods, the development of effective nucleon-nucleon interactions starting from the Chiral Effective Field Theory (ch-EFT), as well as due to the massive progress made in the computational power available to researchers [11–13, 83, 84, 86]. On the experimental side, the ability to perform spectroscopic studies on atoms containing nuclei at the extreme of stability, facilitated by the continuous developments made at radioactive beam facilities [48–50], opened the way for systematic investigations of long isotopic chains [15, 16, 19–22, 24, 82]. This revealed new, unexpected trends in various nuclear properties, such as charge radii and electromagnetic moments, forcing us to rethink our understanding of the atomic nucleus [16, 19–22]. Concurrently, the rapid advancement made in our ability to quantum control the degrees of freedom of molecules, opened the way to investigating parity and time-reversal violating nuclear electroweak properties, with orders of magnitude higher sensitivity compared to atoms [14, 17, 32–42]. A non-zero measurement of such effects would give us not only a better grasp of some of the least known parts of the Standard Model (SM) [14, 17, 26, 27, 43], but can even allow for searches for new physics [14, 17, 28, 29].

In this chapter, I will discuss various nuclear electroweak properties, in particular

ground state ones, whose investigation greatly benefited from the development of AMO techniques [15], as well as the advantages of using diatomic molecules for exploring such properties [14, 17, 43]. The first half of the chapter discusses P,T-even nuclear properties, such as the nuclear mean-square charge radius, $\langle r^2 \rangle$, magnetic dipole moment, $\boldsymbol{\mu}$, and electric quadrupole moment, $\mathbf{Q}$. The second half of the chapter will be focused on P-odd, T-even nuclear properties, such as the nuclear weak charge, Q_W, and the nuclear anapole moment, $\mathbf{a}$.

3.1 P,T-even Ground State Nuclear Properties

The Coulomb interaction between the electronic cloud and a point-like nucleus can give us a good understanding of the measured atomic and molecular spectra, and this played a major role in the development of quantum mechanics in its infancy [87]. However, in practice, the nucleus is not a point-like object, and the spatial distribution of the charge and currents inside of it has measurable effects on the surrounding electrons and thus on the observed patterns in the spectra of atoms and molecules [15]. Despite these effects being very small (on the order of 10^{-6} of the usual electronic transitions) they can be measured with current laser technology and they can provide us valuable information about the structure of nuclei [15, 16, 19, 23, 52, 54].

3.1.1 Isotope Shifts

The first consequence of accounting for the finite size of the nucleus is the fact that the electric field felt by the electrons changes relative to a point-like nucleus, especially for electrons in $s_{1/2}$ and $p_{1/2}$ orbitals which have a non-negligible probability to be found inside the nucleus [15, 88, 89]. Thus, a difference will be found if an electronic transition is measured between two such electronic levels in two different isotopes. If we denote the two isotopes by A and A', this difference called the isotope shift, is denoted as:

$$\delta\nu_{IS}^{A,A'} = \nu_{A'} - \nu_A. \tag{3.1}$$

Two main effects contribute to $\delta\nu_{IS}^{A,A'}$, the change in the nuclear size, $\delta\nu_{FS}^{A,A'}$, and the changes in the nuclear mass, $\delta\nu_{MS}^{A,A'}$, when going from on isotope to the other, which leads to a change in the nuclear kinetic energy, in the center of mass frame of the nucleus-electrons system [15, 88, 89]:

$$\delta\nu_{IS}^{A,A'} = \delta\nu_{FS}^{A,A'} + \delta\nu_{MS}^{A,A'}, \tag{3.2}$$

where $\delta\nu_{FS}^{A,A'}$ is called the volume (or field) shift, and it is related to the first effect mentioned above, while the $\delta\nu_{MS}^{A,A'}$ term is the nuclear mass shift, given by the second effect described. While the masses of a wide range of isotopes are known with exquisite precision (e.g., from Penning trap measurements [90, 91]), information about the nuclear size requires precise and sensitive laser spectroscopy studies. Currently, isotope shift measurements provide a unique tool for extracting information about the evolution of nuclear size away from stability [15].

It can be shown that, for a given electronic level, the shift in energy due to the finite nuclear size for an isotope of mass A can be expressed as [15, 89]:

$$E_r = \frac{Ze^2}{6\epsilon_0} \langle r^2 \rangle_A |\psi(0)|^2, \tag{3.3}$$

where ϵ_0 is the vacuum electric permittivity, and $\langle r^2 \rangle_A$ is the nuclear mean-square charge radius of the isotope given by:

$$\langle r^2 \rangle_A = \frac{1}{Ze} \int \rho_c(r) r^2 dV, \tag{3.4}$$

with the nuclear charge density, $\rho_c(r)$, defined such that its integral over the nuclear volume equals the nuclear charge:

$$\int \rho_c(r) dV = Ze. \tag{3.5}$$

$|\psi(0)|^2$ is the probability for the electron to be found at the center of the nucleus for the given electronic level. Note that we assume this probability to be constant within the nucleus, and its value is the same for all isotopes. Thus, the effect of the nuclear size on the transition between two electronic levels, $\nu^{i \to f}$, can be expressed as:

$$\begin{aligned} \nu^{i \to f} &= \frac{Ze^2}{6\epsilon_0} \langle r^2 \rangle_A \left(|\psi(0)^f|^2 - |\psi(0)^i|^2 \right) \\ &= \frac{Ze^2}{6\epsilon_0} \langle r^2 \rangle_A \Delta |\psi(0)|^2, \end{aligned} \tag{3.6}$$

where $\Delta|\psi(0)|^2$ is the difference in electron density inside the nucleus between the final and initial electronic states. Finally, by measuring this transition in two isotopes, A and A', the energy shift caused by the change in the nuclear size can be expressed as:

$$\begin{aligned} \delta\nu_{FS}^{A,A'} &= \frac{Ze^2}{6\epsilon_0} \Delta|\psi(0)|^2 (\langle r^2 \rangle_{A'} - \langle r^2 \rangle_A) \\ &= \frac{Ze^2}{6\epsilon_0} \Delta|\psi(0)|^2 \delta \langle r^2 \rangle^{A,A'} \\ &= F \delta \langle r^2 \rangle^{A,A'}, \end{aligned} \tag{3.7}$$

where $\langle r^2 \rangle^{A,A'} = \langle r^2 \rangle_{A'} - \langle r^2 \rangle_A$ is the change in the mean-square charge radius between the two isotopes. To first order, the electron probability density inside of the nucleus is assumed to be constant, and the electronic part of the field shift is given by $F \equiv \frac{Ze^2}{6\epsilon_0} \Delta|\psi(0)|^2$ [15, 89]. Variations of the electron density inside the nucleus and relativistic contributions can have measurable effects, particularly in heavy nuclei, leading to modifications of the F parameter defined above. Moreover, in general, higher-order radial moments, beyond $\langle r^2 \rangle$, need to be accounted for, following the relation [15, 89]:

$$\delta\nu_{FS}^{A,A'} = F\left(\delta\left\langle r^2\right\rangle^{A,A'} + a\delta\left\langle r^4\right\rangle^{A,A'} + b\delta\left\langle r^6\right\rangle^{A,A'} + ...\right). \tag{3.8}$$

Such moments, in particular $\delta\left\langle r^4\right\rangle^{A,A'}$, are expected to become visible in high-precision measurements and they can provide valuable information about the nucleus, such as the diffuseness of the nuclear density near the surface of the nucleus (also called the surface thickness) [92], and limit the sensitivity for new physics searches [93, 94].

We will now look at the mass shift contribution to the isotope shift, whose effect can be explained as follows. We can write the non-relativistic motion of the nucleus in the center of mass frame as [89]:

$$E = \frac{\mathbf{P}^2}{2M}, \tag{3.9}$$

where $\mathbf{P}$ and M are the nuclear momentum and mass. From this, we get:

$$E = \frac{(\sum_i \mathbf{p_i})^2}{2M} = \frac{1}{2M}\left(\sum_i \mathbf{p_i}^2 + \sum_{i\neq j} \mathbf{p_i}\cdot\mathbf{p_j}\right), \tag{3.10}$$

where $\mathbf{p_i}$ is the momentum of the i-th electron. When an electron goes to a different energy level and thus changes its momentum, the change in energy due to the term above (and thus the photon needed to induce this transition) will have a dependence on the mass of the nucleus, M, and thus lead to an isotopic dependence [89]. The mass shift is usually written as [15, 89]:

$$\delta\nu_{MS}^{A,A'} = \frac{M_A - M_{A'}}{M_A M_{A'}}(K_{NMS} + K_{SMS}). \tag{3.11}$$

The first term, called the normal mass shift, comes from the $\sum_i \mathbf{p_i}^2$ contribution in Eq. 3.10, and it can be calculated using the measured transition frequency, ν (in the non-relativistic case, $K_{NMS} = m_e\nu$, with m_e the electron mass). The second term, called the specific mass term, comes from the $\sum_{i\neq j} \mathbf{p_i}\cdot\mathbf{p_j}$ term in Eq. 3.10, and it is thus the result of pairwise correlation effects between all the electrons. Calculating this term is more challenging than the normal mass shift term, and it usually requires complex, many-body quantum chemistry calculations [15, 89].

Therefore, the total isotope shift to leading order in the isotope mass and change in the mean square charge radius is given by [15, 88, 89]:

$$\delta\nu_{IS}^{A,A'} = F\delta\left\langle r^2\right\rangle^{A,A'} + \frac{M_A - M_{A'}}{M_A M_{A'}}(K_{NMS} + K_{SMS}). \tag{3.12}$$

One way to extract the quantity of interest from here, $\delta\left\langle r^2\right\rangle^{A,A'}$, is to numerically calculate F and K_{SMS} and use the measured value of $\delta\nu_{IS}^{A,A'}$, together with the known isotope masses and extracted K_{NMS} values. This approach is used for the analysis performed in Article 1 from Chapter 4 [52]. In Article 1, we also took advantage of the fact that the mass shift is much smaller than the field shift as the nuclear mass increases, and for the case of RaF, the mass shift was shown to be significantly smaller than the measurement uncertainties. On the other hand, if independent mean-squared charge radii measurements are available for at

least three isotopes of the element of interest, the parameters F and K_{SMS} can be extracted directly from a King plot analysis [88], from the plot of $\delta\nu_{IS}^{A,A'}$ as a function of $\delta\langle r^2\rangle^{A,A'}$. The extracted values can then be used to compute $\delta\langle r^2\rangle^{A,A'}$ for other isotopes of interest [15, 89]. Finally, it should be noted that, given the form of Eq. 3.12, if isotope shift measurements are performed for two different transitions, $\delta\nu_{IS,1}^{A,A'}$ and $\delta\nu_{IS,2}^{A,A'}$, they must follow the linear relationship:

$$\widetilde{\delta\nu_{IS,2}^{A,A'}} = \left(K_2 - \frac{F_2}{F_1}K_1\right) + \frac{F_2}{F_1}\widetilde{\delta\nu_{IS,1}^{A,A'}}, \tag{3.13}$$

where $K \equiv K_{SMS} + K_{NMS}$, and $\widetilde{\delta\nu_{IS,i}^{A,A'}} = \delta\nu_{IS,i}^{A,A'}\frac{M_A M_{A'}}{M_A - M_{A'}}$. Thus, if the isotope shift is measured in a system where F and K can be more easily calculated (e.g., a system with only one electron outside a closed shell), from the linear formula above, the corresponding values of F and K can be obtained in any other system [15, 88, 89]. It should also be mentioned that searches for deviations from linearity in Eq. 3.13 are currently used to look for the existence of new fundamental forces, mediating interactions between electrons and neutrons [93, 94]. Standard Model contributions can induce higher order moments in the nuclear charge radius expansion (see Eq. 3.8) and thus act as a background in such searches.

We end this section by mentioning that formulas equivalent to Eq. 3.12 exist in diatomic molecules not only for the electronic but also vibrational and rotational transitions [70, 72]. For example, ignoring the coupling between different degrees of motion in a molecule (see Chapter 2 for details), the energy of a rovibrational level in a molecule, specified by the quantum numbers ν and J, is given by (to lowest order in ν and J):

$$\begin{aligned} E_{A'}(\nu, J) = &\left(Y_{00} + \delta_{00}\frac{\Delta M_{A'}}{M_{A'}} + f_{00}\delta\langle r^2\rangle^{A,A'}\right) + \\ &\left(Y_{10} + \delta_{10}\frac{\Delta M_{A'}}{M_{A'}} + f_{10}\delta\langle r^2\rangle^{A,A'}\right)\left(\frac{\mu_A}{\mu_{A'}}\right)^{1/2}(\nu + 1/2) + \\ &\left(Y_{01} + \delta_{01}\frac{\Delta M_{A'}}{M_{A'}} + f_{01}\delta\langle r^2\rangle^{A,A'}\right)\frac{\mu_A}{\mu_{A'}}\left[J(J+1)\right], \end{aligned} \tag{3.14}$$

where Y_{ij}, δ_{ij}, and f_{ij} are electronic structure parameters. μ_A ($\mu_{A'}$) is the reduced mass of the molecule containing the isotope A (A'). $\Delta M_{A'} = M_{A'} - M_A$, with A being the reference isotope. The formalism discussed above is valid when only one nucleus in the molecule is replaced by an isotope, but it can be extended to both nuclei. This shows that molecules, compared to atoms, can offer complementary information for exploring nuclear properties and searches for new physics. More details about this approach and the sensitivity of diatomic molecules to nuclear effects are provided in Article 1 of Chapter 4, where it is applied to study RaF isotopologues [52].

3.1.2 Nuclear Magnetic Dipole and Electric Quadrupole

The isotope shift effects mentioned above exist for all nuclei. However, if the nucleus has a spin different from zero, additional nuclear properties can contribute to the observed

spectra [15, 85, 95–97]. For a spin $I \geq 1/2$, the nucleus possess a magnetic dipole moment, $\boldsymbol{\mu}$. The interaction between this dipole moment and the magnetic field generated by the moving electrons at the location of the nucleus, $\mathbf{B_e}$, leads to the magnetic hyperfine interaction given by [15, 97, 98]:

$$H_\mu = -\boldsymbol{B_e} \cdot \boldsymbol{\mu} = A\mathbf{I} \cdot \mathbf{J}, \tag{3.15}$$

where A is a parameter quantifying the strength of this interaction ($A = \frac{B_e \mu}{IJ}$). The magnetic field generated by the electrons is proportional to the total electronic angular momentum, $\mathbf{J}$ [15]. The effect of this interaction in molecules, as well as its matrix elements for specific angular momentum couplings, have been discussed in Chapter 2, and the calculations are similar in the atomic case [31]. From measurements of the hyperfine splitting, one can extract the parameter A, and then, from independent calculations of the electronic structure parameter B_e, the dipole moment of the nucleus can be extracted. This can then be compared to various nuclear many-body calculations, guiding thus our microscopic understanding of the nucleus [15, 19].

However, above, we implicitly assumed that the nucleus is a point-like object (in this case, a point magnetic dipole). But we know this is not the case. As we showed in the previous section, the size of the nucleus has a visible influence on the Coulomb potential felt by the electrons. It is thus expected that this spatial extend will also play a role in the measured hyperfine interaction [54, 99–103]. In particular, one needs to account for the distribution of the nuclear magnetization over the entire nuclear volume and for the fact that the electronic cloud, when penetrating the nucleus, samples this (usually non-uniform) distribution. In this case, the nuclear dipole moment changes as [104]:

$$\boldsymbol{\mu} \rightarrow \boldsymbol{\mu}(\mathbf{r}) = \boldsymbol{\mu} f(\mathbf{r}), \tag{3.16}$$

where $f(\mathbf{r})$ is a function (normalized to 1) describing the distribution of magnetization inside the nucleus, which is identically equal to 1 for a point like dipole moment. Thus, the exact separation of the nuclear and electronic parts in Eq. 3.15 needs to be replaced by an integral over the nuclear volume, i.e. $\int \mathbf{B_e}(\mathbf{r}) \cdot d\boldsymbol{\mu}(\mathbf{r})$. Measurements of this effect can provide a deeper understanding of the electroweak currents inside the nucleus, compared to the point-like dipole case [54, 104] and can offer a test of various nuclear many-body models. However, to observe this effect (i.e., tell it apart from the point dipole case), sufficiently high precision is needed in the hyperfine structure measurement, as well as in the calculations of electronic form factor $\mathbf{B_e}(\mathbf{r})$. Article 3, presented in Chapter 4, describes the experiment, together with electronic structure calculations, that allowed, for the first time, an observation of the effect of the distribution of the nuclear magnetization inside a molecule [54, 104].

When the nuclear spin is larger than half ($I \geq 1$), the nucleus possesses an electric quadrupole moment, $\mathbf{Q}$, which interacts with the electric field gradient produced by the electron cloud at the nucleus, leading to quadrupole hyperfine interaction, expressed as [15, 31]:

$$H_Q = -eT^2(\nabla \mathbf{E}) \cdot T^2(\mathbf{Q}). \tag{3.17}$$

The nuclear quadrupole moment provides information about the collective effects inside the nucleus, as well as the nuclear deformation [15, 95, 97].

From the form of its electronic operator, it can be seen that the matrix element of the Hamiltonian in Eq. 3.17 is zero for electronic states with total angular momentum $J < 1$. This can make the measurement of the nuclear quadrupole moment challenging, if not impossible, for specific elements if their electronic ground state has $J < 1$ and the excited electronic states with $J \geq 1$ have a lifetime too short to allow a precise measurement of the splitting due to the nuclear quadrupole hyperfine interaction. This is the case, for example, for potassium isotopes [105–109]. However, if a molecule contains the nucleus of interest, measurements of the nuclear quadrupole moment become possible even in the electronic ground state. On the one hand, given that the electronic wavefunction in a molecule is not an eigenstate of the electron angular momentum operator (see Chapter 2) [31], values of $J \geq 1$ will be present in the electronic ground state, thus leading to a nonzero matrix element. On the other hand, rotational and hyperfine levels in the ground electronic state of a molecule are long-lived (on the order of seconds or larger). Thus, these states can allow for precise measurements of the hyperfine splitting due to the nuclear electric quadrupole moment [31, 57, 58]. For example, precise measurements of the nuclear moment in ^{39,40,41}K isotopes have been obtained through spectroscopic measurements of potassium-containing molecules [110]. Thus, molecules represent a promising avenue for investigating higher-order nuclear moments (even higher than the ones considered above) that would be challenging to measure through other techniques, further contributing to our understanding of the structure of nuclei.

3.2 Parity Violation in Atoms, Molecules and Nuclei

Parity violating (PV) interactions in atoms and molecules can be broadly classified in two categories: nuclear spin-independent (NSI), and nuclear spin-dependent (NSD) [17]. These interactions can arise either from a direct PV coupling between electrons and nucleons or from PV interactions between nucleons inside the nucleus, which can later interact electromagnetically with the electron [14, 17].

3.2.1 Nuclear-Spin Independent Parity Violation

In atoms and molecules, the parity violating interaction between an electron and a nucleon is mediated by the exchange of a Z^0 boson. Due to its short range, compared to the atomic/molecular size, the interaction can be approximated as a contact interaction, with the associated P-odd, T-even Hamiltonian given by [111]:

$$H = \frac{G_F}{\sqrt{2}} \left\{ C_1 \bar{N} \gamma_\mu N \bar{e} \gamma_\mu \gamma_5 e + C_2 \bar{e} \gamma_\mu e \bar{N} \gamma_\mu \gamma_5 N \right\}, \tag{3.18}$$

where $G_F \approx 2.22 \times 10^{-14}$ a.u. is the Fermi constant, e and N are the electron and nuclear field operators, and $\bar{e}$ and $\bar{N}$ their conjugate transpose. γ_μ ($\mu = 0, 1, 2, 3$) are the usual Dirac gamma matrices and $\gamma_5 \equiv i\gamma^0\gamma^1\gamma^2\gamma^3$. C_1 quantifies the coupling between the nucleon vector current and the electron axial-vector current. It is defined in terms of the equivalent couplings of the electron to the up ($C_{1,u}$) and down ($C_{1,d}$) quarks as [1, 112–114]:

$$
\begin{aligned}
C_{1,p} &\equiv 2C_{1,u} + C_{1,d} \approx \frac{1}{2}\left(1 - 4\sin^2\theta_W\right) \\
C_{1,n} &\equiv C_{1,u} + 2C_{1,d} \approx -\frac{1}{2}.
\end{aligned}
\tag{3.19}
$$

The C_2 constant quantifies the coupling between the nucleon axial-vector current and electron vector current, being given by [1, 112–114]:

$$
\begin{aligned}
C_{2,p} &\approx g_A \frac{1}{2}\left(1 - 4\sin^2\theta_W\right) \\
C_{2,n} &\approx -g_A \frac{1}{2}\left(1 - 4\sin^2\theta_W\right),
\end{aligned}
\tag{3.20}
$$

with $g_A \approx 1.26$ [17], $\sin^2\theta_W \approx 0.23$ [1], with θ_W being the Weinberg angle and the "$\approx$" sign emphasizing that the expressions are valid only at the tree level in the SM. Radiative corrections to these expressions can be calculated as described, for example, in Refs. [1, 114].

Given their large mass relative to the electron, the nucleons can be treated nonrelativistically, in which case the PV Hamiltonian above can be written as the following effective Hamiltonian acting only on the electron [17, 111, 115]:

$$
H = \frac{G_F}{\sqrt{2}}\gamma_5\left[ZC_{1,p}\rho_p(\mathbf{r}) + NC_{1,n}\rho_n(\mathbf{r})\right] + \frac{G_F}{\sqrt{2}}\left[C_{2,p}\rho_p(\mathbf{r})\boldsymbol{\alpha}\cdot\sum_p \boldsymbol{\sigma}_p + C_{2,n}\rho_n(\mathbf{r})\boldsymbol{\alpha}\cdot\sum_n \boldsymbol{\sigma}_n\right],
\tag{3.21}
$$

where $\rho_p(\mathbf{r})$ and $\rho_n(\mathbf{r})$ are the protons and neutrons density distributions normalized to unity, Z and N are the proton and neutron number, respectively. $\boldsymbol{\sigma}_p$ and $\boldsymbol{\sigma}_n$ are the proton and neutron Pauli matrices, and $\boldsymbol{\alpha} = \gamma_0\boldsymbol{\gamma}$ is the electron velocity operator. One of the goals of atomic/molecular PV experiments is to extract, with high precision, the values of the four constants in this Hamiltonian: $C_{1,p}$, $C_{1,n}$, $C_{2,p}$ and $C_{2,n}$ and compare them against the SM predictions, from which information about possible new physics effects can be extracted.

The first term in Eq. 3.21 is responsible for the nuclear spin-independent (NSI) PV effects in atoms and molecules. The proton and neutron densities in this equation can be written in a multipole expansion using spherical harmonics [116]:

$$
\begin{aligned}
\rho_n(\mathbf{r}) &\approx \rho_{0n}(r) + \sum_{q=-2}^{2}(-1)^q\rho_{2n,q}(r)Y_{2,q}(\theta,\phi) + ... \\
\rho_p(\mathbf{r}) &\approx \rho_{0p}(r) + \sum_{q=-2}^{2}(-1)^q\rho_{2p,q}(r)Y_{2,q}(\theta,\phi) + ...,
\end{aligned}
\tag{3.22}
$$

where "..." stand for higher order terms in the expansion, while the $\rho_{2n,q}$ and $\rho_{2p,q}$ are coefficients of the multipole expansion for the neutron and proton density, respectively. The second nonzero term in these expansions gives rise to the nuclear spin-dependent parity

violating weak quadrupole moment of the nucleus, which can provide us information about the neutron spatial distribution inside the nucleus [116–120]. If we focus only the monopole term, the effective NSI PV hamiltonian becomes:

$$H_{NSI}^{PV} = \frac{G_F}{\sqrt{2}}\gamma_5 \left[ZC_{1,p}\rho_{0p}(r) + NC_{1,n}\rho_{0n}(r)\right]. \tag{3.23}$$

In general, in a real nucleus, the proton and neutron densities are different, which leads to the so-called neutron skin effect [121], defined as the difference between the root-mean-square radii of the neutrons and protons (see Eq. 3.4). This property is of high interest for understanding the equation of state of the nuclear matter and predicting properties of neutron stars [122, 123], as well as due to its effect on extracting weak nuclear properties from atomic measurements [121, 124, 125]. For now, we will ignore this difference and let $\rho(r) \equiv \rho_{0p} = \rho_{0n}$. With these assumptions, we end up with the commonly used form for the effective NSI PV Hamiltonian acting in the electron space:

$$H_{NSI}^{PV} = \frac{G_F}{2\sqrt{2}} Q_W \gamma_5 \rho(r), \tag{3.24}$$

where $Q_W(Z,N)$ is the nuclear weak charge, which, at the tree level, takes the form (higher order electroweak radiative corrections can be calculated) [1, 114, 126–129]:

$$Q_W^{\text{tree}}(Z,N) \equiv 2\left[ZC_{1,p} + NC_{1,n}\right]. \tag{3.25}$$

It can be seen from Eq. 3.19 and 3.25 that the magnitude of Q_W increases with the neutron number, $Q_W \approx -N$.

This NSI PV interaction is the dominant PV interaction in atoms and adds small but measurable changes to the transition amplitudes between different atomic energy levels. Given that the NSI PV Hamiltonian is nonzero only inside the nuclear volume (i.e., where $\rho(r) \neq 0$), the biggest effect in atoms comes from mixing $s_{1/2}$ and $p_{1/2}$ atomic orbitals. In this case, the sought-for effects scale as Z^3, and thus, it can be significantly enhanced in heavy systems. The goal of atomic PV experiments is to extract the weak charge of the nucleus, Q_W, and from there the Weinberg angle and compare them against electroweak theory predictions, thus allowing for stringent tests of the SM at low energy. While not observed yet, a deviation from the SM predictions can allow the exploration of a wide range of exciting new physics scenarios [130–133], such as the existence of new massive Z' bosons, with a mass at the TeV scale [134–137], or of a lighter "dark" boson (with a mass in the MeV-GeV range), weakly coupled to the SM particles [130, 131, 138, 139]. These measurements can also be used to explore vacuum polarization corrections to the SM W and Z bosons self-energies due to new particles beyond the SM [136, 140, 141] or interactions between electrons and cosmic fields (such as the axion field) [142–144]. Even in the absence of new physics, setting bounds on exotic physics scenarios is of great importance.

The nuclear weak charge has been measured so far in several nuclei: ^{209}Bi [145], ^{208}Pb [146, 147], ^{205}Tl [148, 149], ^{170,172,174,176}Yb [24]. For Yb, the isotopic dependence of the nuclear weak charge was observed for the first time and showed to be in agreement with the SM. Measurements in ^{133}Cs, with a 0.35% relative precision [25], have allowed the most stringent low-energy test of the SM to date [136, 150, 151].

3.2.2 Nuclear-Spin Dependent Parity Violation

In molecules, however, the contribution of this NSI PV term is significantly suppressed [17, 111], thus offering sensitivity to the poorly known NSD PV effects [17]. One such NSD PV effect comes from the second term of the Hamiltonian in Eq. 3.21, and it represents the Z^0 boson exchange between nucleon axial-vector and the electron vector currents ($A_n V_e$):

$$H_{axial} = \frac{G_F}{\sqrt{2}} \left[C_{2,p} \rho(r) \boldsymbol{\alpha} \cdot \sum_p \boldsymbol{\sigma}_p + C_{2,n} \rho(r) \boldsymbol{\alpha} \cdot \sum_n \boldsymbol{\sigma}_n \right], \tag{3.26}$$

where we ignored the difference between the proton and neutron densities, as well as higher order terms in the expansion in Eq. 3.22, i.e. $\rho(r) = \rho_p(\mathbf{r}) = \rho_n(\mathbf{r})$. Averaging over the nuclear part, this can be written as [152–156]:

$$H_{\text{axial}} = \frac{G_F}{\sqrt{2}} \eta_{\text{axial}} \left(\boldsymbol{\alpha} \cdot \boldsymbol{I} \right) \rho(r), \tag{3.27}$$

where $\boldsymbol{I}$ is the nuclear spin and η_{axial} is the physics parameter of interest. This parameter depends on the structure of the nucleus under consideration, as well as on the $C_{2,n}$ and $C_{2,p}$ parameters of the SM. In the shell model, single particle picture, the nuclear part can be estimated as [153]:

$$\eta_{axial} = C_2 \frac{1/2 - K}{I(I+1)}, \tag{3.28}$$

where $C_2 = C_{2,p}$ ($C_2 = C_{2,n}$) is used for the unpaired proton (neutron) and

$$K \equiv (I + 1/2) (-1)^{I + l_i + 1/2}, \tag{3.29}$$

with l_i the orbital angular momentum of the unpaired nucleon. While these single-particle results are useful for an order of magnitude estimation of the effect, they can deviate significantly from detailed, *ab initio* nuclear calculations by as much as 100% [12]. Therefore, such sophisticated calculations are needed, in most cases, for extracting the SM parameters of interest (C_2) from the experiment or for searches for new physics (such as leptophobic Z' bosons [157]).

Another NSD PV effect, which is of high importance from the point of view of electroweak nuclear structure, is due to the nuclear anapole moment. This P-odd, T-even moment arises from the PV interactions between nucleons inside the nucleus, more specifically from meson exchange mediated nucleon-nucleon interactions, with one of the nucleon-meson vertex being P-violating while the other is a strong interaction vertex [158]. One of the main goals of NSD PV measurements is to extract the coupling constants characterizing the weak, P-violating vertex and thus give us a better understanding of hadronic PV [17, 156, 159]. The electrons can interact electromagnetically with this anapole moment, giving rise to PV effects at the atomic or molecular level. This interaction can be expressed in terms of the following Hamiltonian acting in the electron space [154–156]:

$$H_{\text{anapole}} = \frac{G_F}{\sqrt{2}} \eta_{\text{anapole}} \left(\boldsymbol{\alpha} \cdot \boldsymbol{I} \right) \rho(r), \tag{3.30}$$

where η_{anapole} quantifies the hadronic weak interaction inside the nucleus, being the parameter we want to extract experimentally to be confronted with nuclear structure calculations.

A simple way to estimate η_{anapole} can be obtained assuming a single particle (SP) shell model approximation. In this case, one considers the interaction between one unpaired nucleon and the rest of the nucleus, which can be parameterized as [160]:

$$V_{NN,SP}^{PV} = \frac{G_F}{\sqrt{2}} \frac{g_i}{2m} \left[\boldsymbol{\sigma} \cdot \mathbf{p} \rho(r) + \mathbf{p} \cdot \boldsymbol{\sigma} \rho(r) \right], \tag{3.31}$$

from which $\eta_{anapole}$ can be expressed as [154, 155]:

$$\eta_{\text{anapole}} = \frac{9}{10} \frac{\alpha \mu_i}{m r_0} g_i A^{2/3} \frac{K}{I(I+1)} \approx 1.15 \times 10^{-3} \mu_i g_i A^{2/3} \frac{K}{I(I+1)}, \tag{3.32}$$

where g_i is the nucleon-nucleus weak interaction coupling for a proton ($i = p$) or neutron ($i = n$), m is the nucleon mass, α is the fine structure constant, $r_0 \approx 1.2$ fm, A is the atomic number and μ_i is the unpaired nucleon magnetic moment. However, as before, this single particle picture is useful just for order of magnitude estimates, as well as for gauging the scaling of the effect with the atomic number. To extract the fundamental parameters of interest (weak nucleon-meson couplings) reliably from experiments, more detailed (ideally *ab initio)* nuclear structure calculations are needed, which can significantly deviate from the shell model estimates (by as much as 400% [12]). In general, for these calculations, the nuclear ground state wavefunction, $|\psi_{gs}\rangle$, is computed in the presence of the NN PV weak interaction, V_{NN}^{PV} [12]:

$$|\psi_{gs}\rangle = |\psi_{gs}, P\rangle + \sum_i \frac{\langle \psi_i, -P | V_{NN}^{PNC} | \psi_{gs}, P \rangle}{E_{gs} - E_i} |\psi_i, -P\rangle, \tag{3.33}$$

with $|\psi_{gs}, P\rangle$ and E_{gs} the ground state wavefunction of fixed parity, P, and energy in the absence of any PV effects. $|\psi_i, -P\rangle$ and E_i are the other nuclear eigenstates of opposite parity relative to the ground state and their associated energies. Calculating this demands complex nuclear many-body methods, and it represents a major challenge for most nuclei. One also needs the V_{NN}^{PNC}, which is usually parametrized, in the one-meson-exchange model, in terms of six meson-nucleon weak couplings: f_π, h_ρ^0, h_ρ^1, h_ρ^2, h_ω^0, h_ω^1 [159, 161–163], where π, ρ and ω indicate the mediating meson, while the superscripts indicate whether the weak vertex is an isoscalar (0), isovector (1) or isotensor (2) [159, 161]. Note that the g_i coupling constants considered in the single-particle picture can be expressed in terms of these six constants [154, 160, 161, 164]. Standard Model estimates for the values of these couplings have been calculated by Donoghue, Desplanques, and Holstein [161], who provided "best values" and "reasonable ranges" for them. The broad "reasonable ranges", which can be as big as hundreds of percent of the "best value", show the large degree of uncertainty in computing these values [159, 161]. One of the main goals of anapole moments measurements is to extract the values of these weak coupling constants. V_{NN}^{PNC} can also be obtained with different parametrizations of the weak coupling constants, using PV nuclear interactions derived using perturbative chiral effective field theory [11, 165–168]. Once $|\psi_{gs}\rangle$ is computed, the anapole moment $\mathbf{a}$ is calculated as the expectation value of the anapole moment operator $\hat{\mathbf{a}}$ over $|\psi_{gs}\rangle$, with [160]:

$$\hat{\mathbf{a}} = \sum_i^A \frac{\pi e}{m} \left[\mu_i \left(\mathbf{r_i} \times \boldsymbol{\sigma_i} \right) - \frac{q}{2} \left(\mathbf{p_i} r_i^2 + r_i^2 \mathbf{p_i} \right) \right], \tag{3.34}$$

where μ_i, $\mathbf{r_i}$, $\mathbf{p_i}$, $\boldsymbol{\sigma_i}$ are the magnetic moment, position, momentum, and spin operator of the i-th nucleon and q = 1 (0) for a proton (neutron). Usually, the first term in the bracket is significantly bigger than the second one [12, 160]. Note that higher order terms can be added to the anapole moment operator shown above, such as two-body currents [12, 169]. Two-body currents have been shown to play a significant role in correctly calculating the magnetic dipole moment of nuclei [85], and one would expect they can also be important for anapole moment calculations.

Finally, η_{anapole} can be extracted using [12, 160]:

$$\mathbf{a} = \frac{G_F}{\sqrt{2}|e|} \eta_{\text{anapole}} \mathbf{I}, \tag{3.35}$$

and it contains the information about the nucleon-meson weak coupling constants described above. The fact that the anapole moment vector $\mathbf{a}$ points along the nuclear spin $\mathbf{I}$ follows from the Wigner-Eckart theorem.

A third contribution to the NSD PV effects comes from the interference between the NSI Z^0 boson exchange with the hyperfine interaction, and it is given (with a good degree of approximation [170]) by [154–156]:

$$H_{\text{hf}} = \frac{G_F}{\sqrt{2}} \eta_{\text{hf}} \left(\boldsymbol{\alpha} \cdot \boldsymbol{I} \right) \rho(r), \tag{3.36}$$

In the single particle approximation η_{hf} is equal to [155, 156]:

$$\eta_{\text{hf}} = -\frac{1}{3} Q_W \frac{\alpha \mu}{m_p r_0 A^{1/3}} \approx 2.5 \times 10^{-4} A^{2/3} \mu, \tag{3.37}$$

where Q_W is the weak charge, and μ is the magnetic moment of the nucleus. Due to its numerical prefactor, this NSD effect is usually much smaller than the two previously considered. If needed, more detailed calculations of η_{hf} can be performed, accurate to below 10% relative uncertainty [158, 170], which will be necessary if NSD PV effects are to be measured at the 1% level in the future.

It can be noticed that the three NSD PV effects considered so far can be easily combined to get:

$$H_{NSD}^{PV} = \frac{G_F}{\sqrt{2}} \eta \left(\boldsymbol{\alpha} \cdot \boldsymbol{I} \right) \rho(r), \tag{3.38}$$

with $\eta = \eta_{\text{axial}} + \eta_{\text{anapole}} + \eta_{\text{hf}}$. η_{hf} is smaller than the other two terms, and it can be calculated with enough precision [170] and subtracted from η. However, separating the effects of η_{anapole} and η_{axial} is not possible with only one measurement. However, given that the η_{anapole} scales with $A^{2/3}$, while η_{axial} is expected to be constant, measuring η in several isotopes should allow disentangling the two contributions. The same $A^{2/3}$ scaling also shows that η_{anapole} is the dominant NSD PV in heavy nuclei, while η_{axial} dominates in lighter nuclei [43].

Despite several measurements of the weak charge in several nuclei (some of them with sub-percent accuracy [25]), so far, the only nonzero measurement of an NSD-PV effect in an atom was observed in the ^{133}Cs experiment [25], where the dominant contribution comes from the anapole moment [160]. However, there is tension between the obtained values for the meson-nucleon weak couplings obtained from this experiment and other accelerator-based studies, motivating further experiments in this direction [160, 171]. The goal of one of our experiments, which will be introduced in Chapter 5, is to extend the measurement of NSD PV effects to nuclei across the entire nuclear chart, including radioactive, octupole-deformed ones, where the anapole moment effect is expected to be largely enhanced [14]. This would allow us to better constrain the different parameters characterizing the weak nucleon-meson coupling, as well as to provide stringent tests for the development of microscopic nuclear theory. At the same time, measurements in light nuclei would allow us to measure with better precision the $C_{2,p}$ and $C_{2,n}$ parameters, which are poorly constrained parameters of the SM [14, 17, 27].

Chapter 4

First Precision Laser Spectroscopy Investigation of a Radioactive Molecule: Radium Monofluoride

Molecules hold a great promise in our exploration of new physics, in particular violations of the fundamental symmetries of nature, such as parity and time reversal [14, 17]. One of the main reasons for this enhanced sensitivity to the sought-after effects in molecules is the fact that molecules contain energy levels of opposite parity, which can be much closer to each other compared to those in atoms [17, 31]. For example, the main energy scale between opposite parity levels in atoms is typically on the order of ~ 1 eV, while the spacing between two opposite parity rotational levels in a molecule can be five orders of magnitude smaller [14, 31, 172, 173].

This enhancement alone makes the molecules very appealing for new physics searches. In addition, however, most of the effects we are interested in can be written, to a good degree of approximation (usually to first order in perturbation theory), as the product between an electronic operator, O_e, and a nuclear operator, O_n [14, 17]. While the enhancements due to O_e are the ones described above, it turns out that one can also gain large enhancements in sensitivity to symmetry-violating nuclear properties for specific nuclei, where large values of O_n can be achieved. [14, 17, 44–46, 174, 175]. The nuclear properties of interest scale as a power of the proton number and mass of the heaviest nucleus inside the molecule, and can be further enhanced for deformed nuclei [14, 45, 46]. Certain nuclear symmetry violating effects are expected to show already large enhancements due to the nuclear quadrupole deformation alone (e.g. the P,T-odd nuclear magnetic quadrupole moment) [44, 172, 176–178], while others get further enhanced if the nuclei have an octupole deformation, such as the P,T-odd nuclear Schiff moment, which can be expressed as[14, 17, 44–46, 174, 175]:

$$S \propto Z A^{2/3} \beta_2 \beta_3^2, \tag{4.1}$$

where Z and A are the atomic and mass numbers and β_2 and β_3 quantify the magnitude of the nuclear quadrupole and octupole deformations, respectively. An enhancement of about three orders of magnitude of this effect is expected for the octupole deformed ^{223,225}Ra nuclei compared to ^{199}Hg nucleus [45, 46], where the most stringent limits to date on C,P-violation

in the hadronic sector have been set [179], while two additional orders of magnitude are expected in the octupole deformed ^{229}Pa nucleus [14, 45].

Evidence of octupole deformation has so far only been observed and predicted to have a non-zero value for particular short-lived radioactive isotopes such as ^{221}Rn ($\tau = 26$ mins), ^{223}Rn ($\tau = 24$ mins), ^{223}Ra ($\tau = 11.4$ days), ^{223}Fr ($\tau = 22$ mins), ^{225}Ra ($\tau = 14.9$ days) or ^{229}Pa ($\tau = 1.5$ days) [47, 180]. Therefore, to take advantage of the large enhancements due to both O_e and O_n, radioactive molecules emerge as a natural and leading candidate for future fundamental physics studies, in particular, violations of the fundamental symmetries of nature in the hadronic sector.

However, only recently have spectroscopy studies of radioactive molecules become possible [51]. This is because, unlike the case of non-radioactive species, the study of radioactive molecules brings numerous challenges (but also rewards, as described above) [51–54]. Most radioactive molecules do not occur naturally, so they need to be produced at specialized facilities such as ISOLDE [49] at CERN in Switzerland, FRIB [48] in the U.S., or RIKEN [50] in Japan. Moreover, handling radioactive elements requires specialized training and infrastructure, which can prove difficult to fulfill on a university campus. However, progress in this direction, for studying radioactive molecules such as RaF, RaOH, $RaOH^+$, and $RaOCH_3^+$ is underway [14, 181]. Finally, even if radioactive molecules can be produced, they may have lifetimes of only a few days or below [51–54]. Therefore, they have to be studied online, i.e., close to the place where they are produced and ideally as soon as they are produced. Thus, many such experiments need to be performed on-site at the facilities able to produce the molecules of interest [51–54]. Finally, even if the previous challenges are overcome, only a small amount of radioactive molecules of interest can be produced, typically from $\sim 10^6$ per second, down to a few per minute and usually among a much larger number of other molecules, which act as a contaminant/background for the measurement. Therefore, specialized, highly sensitive, and selective techniques need to be developed to study such species [51–54].

This chapter describes the first precision laser spectroscopy investigations of a radioactive molecule, radium monofluoride (RaF) [51–54]. During my PhD, we achieved the measurement and characterization of its electronic and vibrational [52] (Article 1), rotational [53, 54] (Article 2) and hyperfine [54] (Article 3) structure, as well as the measurement of its ionization potential (Article 4). These results provided a laser cooling scheme for these molecules [51, 53] (Article 2) and allowed the identification of the low-lying rotational and hyperfine energy levels suitable for future symmetry violation studies [53, 54] (Articles 2 and 3). Our results proved the large sensitivity of this molecule to nuclear spin-independent and dependent effects [52, 54] (Articles 1 and 3). Complementary to our experimental findings, our results were accompanied by *ab initio* many-body electronic calculations, confirming the ability of these calculations to properly characterize the electronic structure properties of this molecule [52–54] (Articles 1, 3 and 4). These results are pioneering in the field of spectroscopy of radioactive molecules, representing the stepping stone towards using these species for future fundamental physics studies.

4.1 Article 1: Isotope Shifts of Radium Monofluoride Molecules

This article (S.-M. Udrescu et al., "Isotope shifts of radium monofluoride molecules", Phys. Rev. Lett. 127, 033001 (2021)) presents the first observation of the isotope shift effect in a radioactive isotopologue chain (molecules in which a nucleus is replaced with one of its isotopes), proving experimentally the high sensitivity of the RaF molecules to nuclear effects, in particular changes in the nuclear size upon isotopic substitution of the Ra nucleus. Comparison with the experiment proves the accuracy of quantum chemistry many-body calculations at below 10% level. For this article, published in Physical Review Letters (2021), I led the data analysis and the analytical theoretical calculations. I prepared the figures and the different drafts of the manuscript, including the initially submitted version, as well as the subsequent revisions. I was in charge of the submission process.

Editors' Suggestion | Featured in Physics

Isotope Shifts of Radium Monofluoride Molecules

S. M. Udrescu,[1,*] A. J. Brinson,[1] R. F. Garcia Ruiz,[1,2,†] K. Gaul,[3] R. Berger,[3,‡] J. Billowes,[4] C. L. Binnersley,[4] M. L. Bissell,[4] A. A. Breier,[5] K. Chrysalidis,[2] T. E. Cocolios,[6] B. S. Cooper,[4] K. T. Flanagan,[4,7] T. F. Giesen,[5] R. P. de Groote,[8] S. Franchoo,[9] F. P. Gustafsson,[6] T. A. Isaev,[10] Á. Koszorús,[6] G. Neyens,[2,6] H. A. Perrett,[4] C. M. Ricketts,[4] S. Rothe,[2] A. R. Vernon,[4] K. D. A. Wendt,[11] F. Wienholtz,[2,12] S. G. Wilkins,[1,2] and X. F. Yang[13]

[1]*Massachusetts Institute of Technology, Cambridge, Massachusetts 02139, USA*
[2]*CERN, CH-1211 Geneva 23, Switzerland*
[3]*Fachbereich Chemie, Philipps-Universität Marburg, Hans-Meerwein-Straße 4, 35032 Marburg, Germany*
[4]*School of Physics and Astronomy, The University of Manchester, Manchester M13 9PL, United Kingdom*
[5]*Laboratory for Astrophysics, Institute of Physics, University of Kassel, 34132 Kassel, Germany*
[6]*KU Leuven, Instituut voor Kern- en Stralingsfysica, B-3001 Leuven, Belgium*
[7]*Photon Science Institute, The University of Manchester, Manchester M13 9PY, United Kingdom*
[8]*Department of Physics, University of Jyväskylä, Survontie 9, Jyväskylä FI-40014, Finland*
[9]*Institut de Physique Nucleaire d'Orsay, F-91406 Orsay, France*
[10]*NRC Kurchatov Institute-PNPI, Gatchina, Leningrad district 188300, Russia*
[11]*Institut für Physik, Johannes Gutenberg-Universität Mainz, D-55128 Mainz, Germany*
[12]*Institut für Physik, Universität Greifswald, D-17487 Greifswald, Germany*
[13]*School of Physics and State Key Laboratory of Nuclear Physics and Technology, Peking University, Beijing 100971, China*

(Received 4 December 2020; revised 21 April 2021; accepted 19 May 2021; published 14 July 2021)

Isotope shifts of $^{223–226,228}$Ra^{19}F were measured for different vibrational levels in the electronic transition $A^2\Pi_{1/2} \leftarrow X^2\Sigma^+$. The observed isotope shifts demonstrate the particularly high sensitivity of radium monofluoride to nuclear size effects, offering a stringent test of models describing the electronic density within the radium nucleus. *Ab initio* quantum chemical calculations are in excellent agreement with experimental observations. These results highlight some of the unique opportunities that short-lived molecules could offer in nuclear structure and in fundamental symmetry studies.

DOI: 10.1103/PhysRevLett.127.033001

Introduction.—The study of electron-nucleus interactions offers a powerful tool in the exploration of the atomic nucleus and of the fundamental particles and interactions of nature [1]. In recent years, the immense progress of theoretical and experimental molecular spectroscopy is breaking new ground in fundamental physics research. The structure of well-chosen molecular systems can offer exceptionally high sensitivity to investigate the violation of fundamental symmetries, which can be enhanced by more than 5 orders of magnitude with respect to atomic systems [1–5]. Ongoing developments pave the way for distinct approaches to measure symmetry-violating effects that could rigorously test the standard model at low energy, and constrain the existence of new physics [6–8].

Electronic states in atoms and molecules can be highly sensitive to the structure of their atomic nuclei, and enable detailed investigations into the electron-nucleon interaction [9–12]. Adding or removing neutrons to or from an atomic nucleus results in small differences in the energies of its bound electrons, known as isotope shifts. In atoms, isotope shift measurements have provided unique access to study the evolution of nuclear charge radii in exotic nuclei [13–18]. Precision measurements along isotopic chains can be used to separate electronic and nuclear effects, thereby placing powerful constraints on the violation of fundamental symmetries and the search for new physics beyond the standard model [9–11,19,20]. The possibility of performing precision measurements over long chains of isotopologues—molecules of the same elements that differ by the number of neutrons in their nuclei—offers an ideal scenario to investigate nuclear structure phenomena, nuclear-spin-dependent parity violation interactions, and probe fine details of the electron-nucleon interaction in so far unexplored regimes.

A separation of so-called mass and volume effects from isotope shift measurements requires at least two relative measurements (three isotopologues), but no heavy element beyond Pb possesses more than two long-lived isotopes [21,22]. This has been a major experimental obstacle, limiting our knowledge of molecules containing heavy

nuclei, as radioactive molecules can often only be produced in small quantities (typically less than 10^7 molecules/s). Thus, their study requires exceptionally sensitive experimental techniques, which have not been available until very recently [23].

In parallel to experimental advances in molecular physics, the development of molecular theory is of critical importance. Accurate determination of molecular parameters is important not only to guide experiments, but also essential to extract nuclear structure and new physics observables from experimental results. The interpretation of molecular experiments relies upon computations of molecular enhancement parameters, which strongly depend on the description of the electron wave function at the nucleus. Hence, measurements of molecular isotope shifts, which are highly sensitive to the electron-nucleus interaction at the nucleus, provide an important test for the reliability of quantum chemical calculations. However, until now, comparatively little was known about electronic shifts in isotopologues [24]. To our knowledge, isotope shift measurements have neither been reported yet in molecules containing isotopes of elements heavier than lead (Pb, $Z = 82$) [25], nor for molecules containing short-lived isotopes.

In this Letter we investigate, theoretically and experimentally, the changes in the molecular energy levels when neutrons are added to (or removed from) the radium nucleus of RaF molecules. RaF molecules are of special interest for fundamental physics research as their electronic structure is predicted to provide a large enhancement of both parity and time-reversal violating effects [4,8,26–28]. Moreover, some nuclei in the very long isotope chain of Ra ($Z = 88$) exhibit octupole deformation [29,30], which results in a significant amplification of their symmetry-violating nuclear properties, relative to light molecules [2,3].

Experimental technique.—Our experimental approach was described in detail in Ref. [23]. Briefly, Ra isotopes were produced at the ISOLDE facility at CERN, by impinging 1.4-GeV protons onto a uranium-carbide target. Upon injection of CF_4 gas into the target material, radium molecules were formed through reactive collisions of the evaporated Ra atoms. RaF^+ molecules were created by surface ionization and extracted using an electrostatic field. The desired isotopologue was selected using a high-resolution magnetic mass separator (HRS). After that, ions were collisionally cooled for up to 10 ms in a radio-frequency quadrupole (RFQ) trap, filled with helium gas at room temperature. Bunches of RaF^+ of 4 μs temporal width were released and accelerated to 39 998(1) eV, and then sent to the Collinear Resonance Ionization Spectroscopy (CRIS) setup [31–35].

At the CRIS beam line, the ions were passed through a charge-exchange cell where they were neutralized in flight by collisions with a sodium vapor, primarily by the reaction $RaF^+ + Na \rightarrow RaF + Na^+$. The estimated ionization energy of RaF is close to that of the atomic Na (5.14 eV), hence the RaF molecules predominately populated the $X^2\Sigma^+$ electronic ground state in the neutralization process [36]. After this step, any remaining ions were deflected from the main, neutral molecular beam, which was then collinearly overlapped in space and time with two pulsed laser beams in an ultrahigh-vacuum (10^{-10} mbar) laser-molecule interaction region.

The RaF molecules were resonantly ionized in two steps. First, one laser pulse of tunable wavelength was used to resonantly excite the electronic transition of interest, $A^2\Pi_{1/2} \leftarrow X^2\Sigma^+$. The electronically excited RaF molecules were then ionized using a high-power, 355-nm pulsed laser. Subsequently, the resonantly ionized RaF^+ ions were deflected from the bunch and detected by an ion detector. The wavelength of the ionization laser was set such that RaF molecules can be ionized if they are already in an excited electronic state, i.e., if the frequency of the first laser was on resonance with a transition in the RaF molecule. Hence, the low-lying electronic and vibrational spectra were obtained by counting the number of ions detected as a function of the wavelength of the first laser pulse.

Computational methods.—Electronic transition wave numbers $\tilde{\nu}$ for different isotopologues of RaF were calculated at the level of relativistic Fock-space Coupled Cluster including Singles and Doubles amplitudes (FSCCSD) with the program package DIRAC19 [37], correlating 17 electrons [FSCCSD(17e)]. Isotope shift constants $F = [(\partial\delta\tilde{\nu})/(\partial\delta\langle r^2\rangle)]$ were deduced by calculation of transition wave numbers for different mean-square nuclear charge radii $\langle r^2\rangle$ with a Gaussian nuclear charge distribution model and computation of the slope within a linear fit model.

In order to estimate the quality of this method, FSCCSD calculations with an extended basis set and 27 correlated electrons [FSCCSD(27e)] were carried out for three nuclear charge radii at an internuclear distance of $4.3a_0$ (close to the RaF ground state bond length, see Ref. [27]). This extended basis set was also used in atomic calculations of Ra^+, in which 19 electrons ($5d$, $6s$, $6p$, and $7s$ shells) were correlated. These atomic calculations were used to directly compare our measurements and previous isotope shift measurements in the radium ion [38]. To account for the effect of the larger basis and active space in the other calculations, the FSCCSD(17e) isotope shifts were corrected by a factor $\{[F_{\mathrm{FSCCSD(27e)}}(4.3a_0)]/[F_{\mathrm{FSCCSD(17e)}}(4.3a_0)]\}$, to which we will refer as FSCCSDc in the following.

Isotope shift constants $F(r_{\mathrm{RaF}}) = [(\partial\delta\tilde{\nu})/(\partial\delta\langle r^2\rangle)](r_{\mathrm{RaF}})$ were calculated for bond lengths of $r_{\mathrm{RaF}} = 4.0$, 4.1, 4.2, 4.25, 4.3, and $4.4\,a_0$, which covers the region around the equilibrium structure of the electronic ground state. From this, we determined F as a function of r_{RaF} from a fourth-degree polynomial fit. Vibrational corrections to F were calculated within a one-dimensional discrete variable

representation (DVR) approach. In DVR calculations, potentials of the electronic ground and excited states calculated in Ref. [27] were employed. For more details on the applied active space in FSCCSD calculations, used basis sets, the employed Gaussian model, and the vibrational corrections, see the Supplemental Material [39].

Results and discussion.—The measured isovibrational spectra of the $A^2\Pi_{1/2} \leftarrow X^2\Sigma^+$ electronic manifold for two of the investigated isotopologues, $^{224}Ra^{19}F$ (top) and $^{228}Ra^{19}F$ (bottom), are shown in Fig. 1(a). The reported wave numbers have been transformed to the molecular rest frame to account for the Doppler shift between the lab frame and the molecular bunch velocity. Each spectrum was fitted with a sum of four skewed-Voigt profiles in addition to a constant background, from which the centers of the $0 \leftarrow 0$, $1 \leftarrow 1$, $2 \leftarrow 2$, and $3 \leftarrow 3$ transitions were extracted. Wave number values are shown relative to the $0 \leftarrow 0$ transition of $^{226}Ra^{19}F$. The continuous curves show the best fits to the data. The vertical lines indicate the central value of each of the four transitions, with the widths indicating the associated uncertainty. A close-up view of the spectra corresponding to the $0 \leftarrow 0$ transition of the five isotopologues $^{223–226,228}Ra^{19}F$ can be seen in Fig. 1(b). The plot at the bottom shows the position of the center of each peak relative to the one corresponding to $^{226}Ra^{19}F$. Each vertical band corresponds to a given isotopologue according to the color used in the top plot, and the width of the band shows the uncertainty on the given central value. A shift of the central values between the measured isotopologues can be clearly observed. The obtained isotope shifts for all five isotopologues are shown in Table I.

At a bond length of $4.3a_0$, the isotope shift constant F is computed to be -0.797 at the level of FSCCSD(17e) and -0.825 at the level of FSCCSD(27e), respectively. From a comparison of these two values we estimate the relative uncertainty of the FSCCSD(17e) approach due to the basis set and the size of the active space to be less than 4%. Comparison of the isotope shift constant in the $7p^2P_{1/2} \leftarrow 7s^2S_{1/2}$ transition in Ra^+ calculated at the level of FSCCSD (27e) $[F = -1.283(3)\ (\mathrm{cm}^{-1}/\mathrm{fm}^2)]$ to atomic calculations with a comparable method but a different nuclear model in Ref. [38] $[F = -1.328\ (\mathrm{cm}^{-1}/\mathrm{fm}^2)]$ shows a deviation of about 3%. Assuming that this deviation is mainly due the use of a different model for the nuclear charge distribution we estimate the error due to the Gaussian nuclear model to be about 3%. Thereby, we note that the shape of the potential of a Gaussian nuclear charge distribution is rather similar to the shape of the potential of a homogeneously charged solid sphere nuclear model used as the starting point in Ref. [38], as well as to the shape of the potential of a Fermi nuclear model (see Ref. [48] for a review). Finally, from CC calculations of hyperfine couplings in the $X^2\Sigma^+$ state [4] and the $A^2\Pi_{1/2}$ state [12] we assume contributions of excitations involving three electrons as characterized by

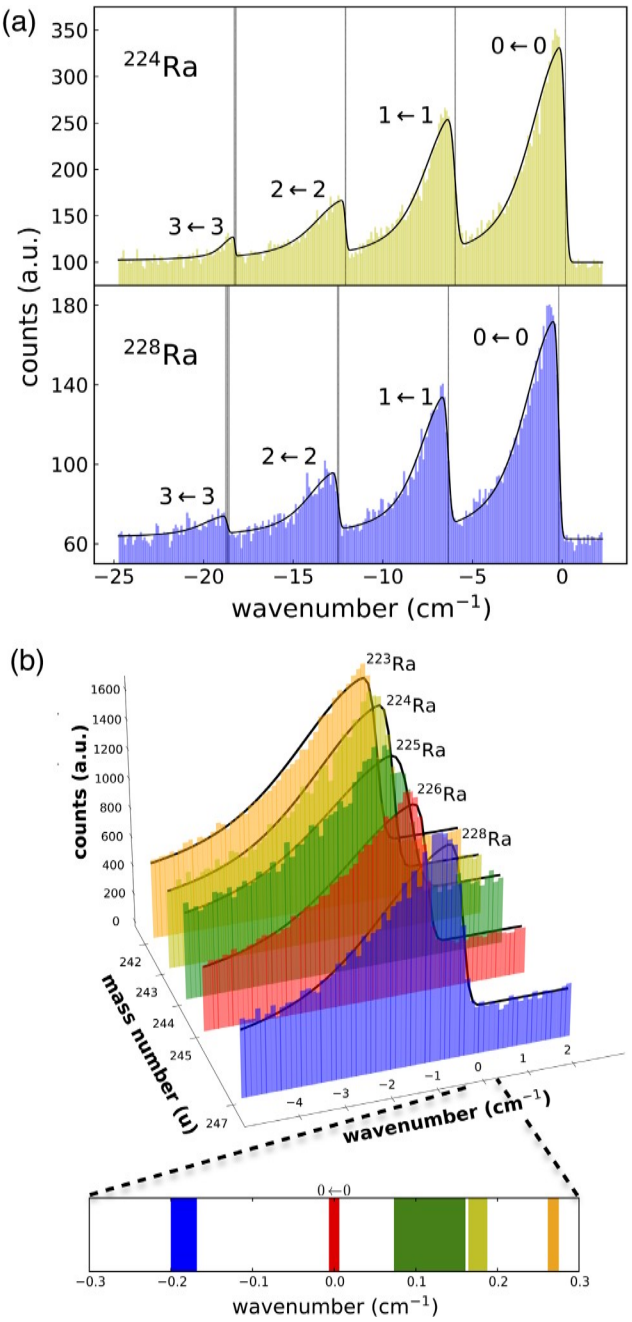

FIG. 1. Isovibrational spectra of the $A^2\Pi_{1/2} \leftarrow X^2\Sigma^+$ electronic transition. (a) Spectra of the $^{224}Ra^{19}F$ (top) and $^{228}Ra^{19}F$ (bottom) isotopologues. The wave number axis was shifted such that the origin coincides with the center of the $0 \leftarrow 0$ transition of the reference $^{226}Ra^{19}F$ isotopologue. Moving in the negative direction on the wave number axis, the four peaks correspond to the $0 \leftarrow 0$, $1 \leftarrow 1$, $2 \leftarrow 2$, and $3 \leftarrow 3$ vibrational transitions. The histograms represent the experimental data, while the continuous black curves depict the best fits for each isotopologue. The vertical bands mark the central values of the transitions, while the width of each band corresponds to the associated uncertainty. (b) $0 \leftarrow 0$ peaks of the five isotopologues $^{223–226,228}Ra^{19}F$. The plot at the bottom marks the position of the center of each peak relative to the one corresponding to $^{226}Ra^{19}F$. The width of each vertical band shows the uncertainty on the given central value.

TABLE I. Measured isotope shifts of the $A^2\Pi_{1/2} \leftarrow X^2\Sigma^+$ vibrational transitions for the isotopologues $^{223-226,228}Ra^{19}F$ (in units of cm^{-1}). The isotope shifts are given relative to $^{226}Ra^{19}F$.

M	$\delta\tilde{\nu}^{245,M}_{0\leftarrow0}$	$\delta\tilde{\nu}^{245,M}_{1\leftarrow1}$	$\delta\tilde{\nu}^{245,M}_{2\leftarrow2}$	$\delta\tilde{\nu}^{245,M}_{3\leftarrow3}$
242	0.269(9)	0.278(14)	0.274(30)	0.298(63)
243	0.176(13)	0.177(28)	0.178(31)	0.064(80)
244	0.117(46)	0.100(74)	0.121(75)	0.001(131)
245	0	0	0	0
247	−0.184(17)	−0.179(26)	−0.251(60)	−0.374(123)

the T_3 CC amplitudes to be less than 3%. Errors from other sources, such as the vibrational description employed in comparison, are expected to be negligible. Thus, an overall uncertainty of about 10% is estimated for the calculated isotope shift constants.

Results of *ab initio* calculations of isotope shift constants F for the electronic states $X^2\Sigma_{1/2}$ and $A^2\Pi_{1/2}$ for the first four vibrational levels in RaF and a comparison to experimentally determined isotope shift constants (see details below) are shown in Table II. Within the 10% uncertainty of the theoretical methods discussed above, the predictions are in agreement with experiment. This is also shown in the inset of Fig. 2.

Similar to atoms, the isotopic shifts of the electronic energy levels in molecules can be highly sensitive to the electron density at the nucleus and to changes of the nuclear size [49–51]. This in turn can provide valuable constraints for quantum chemical calculations, such as determination of the ground-state electronic wave function. However, molecules also possess vibrational and rotational degrees of freedom [24,52,53]. Changes in the nuclear volume between different isotopes can yield measurable deviations to the parameters associated with these degrees of freedom.

TABLE II. Calculated isotope shift constants $F = [(\partial\delta\tilde{\nu})/(\partial\delta\langle r^2\rangle)]$ of vibrational levels v for the $X^2\Sigma_{1/2}$ and $A^2\Pi_{1/2}$ electronic states are shown at the FSCCSD(17e) level of theory, with vibrational corrections at the level of DVR. FSCCSDc values shown in squared brackets in the fourth column. Comparison of the theoretically determined isotope shift constants to experimentally obtained F are presented in the last two columns. Theoretical values are estimated to have a relative error of approximately 10% (see text).

	$F(cm^{-1}/fm^2)$			
v	$X^2\Sigma_{1/2}$	$A^2\Pi_{1/2}$	$A^2\Pi_{1/2}, v \leftarrow X^2\Sigma_{1/2}, v$	
			Theory	Experiment
0	0.764	−0.033	−0.797 [−0.825]	−0.845(24)
1	0.766	−0.034	−0.800 [−0.828]	−0.868(39)
2	0.769	−0.035	−0.803 [−0.831]	−0.876(75)
3	0.771	−0.036	−0.807 [−0.835]	−0.862(166)

Vibrational and rotational isotope shifts are sensitive to the first and second derivatives of the electronic density with respect to internuclear distance [49–51].

By accounting for the finite nuclear size in addition to the breakdown of the Born-Oppenheimer approximation, the isotope shift can be approximately related to changes in the nuclear charge radius (see Supplemental Material [39] for derivation and further details) [49–51,54–57]:

$$\delta\nu^{A,A',\Pi,\Sigma,\nu} = \left(\Delta V_{00}^{A,\Pi-\Sigma} + \frac{\Delta V_{10}^{A,\Pi-\Sigma}}{\sqrt{\mu_A}}(\nu+1/2)\right)\delta\langle r^2\rangle_{AA'} \tag{1}$$

where μ_A is the reduced mass of the reference isotopologue, ΔV_{00}^A and ΔV_{10}^A represent corrections to the Y_{00} and Y_{10} Dunham parameters due to finite nuclear size. These are related to the effective electronic density at the Ra nucleus, $\bar{\rho}_e^A$, as well as the first and second derivatives of this density with respect to the internuclear distance (see Ref. [51], for a detailed discussion).

Empirical values of the molecular parameters in Eq. (1) can be extracted from the dependence of the measured molecular isotope shifts on the change in the mean-square charge radius, $\delta\langle r^2\rangle$, of the Ra nucleus [38,58]. The values used for $\delta\langle r^2\rangle$ were obtained from literature values of

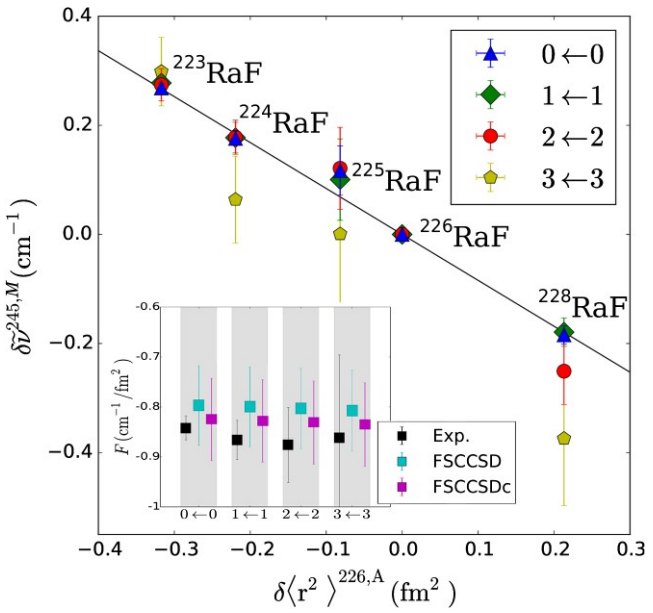

FIG. 2. Isotope shifts as a function of the changes in the charge radius of the five analyzed RaF isotopologues with respect to the reference $^{226}Ra^{19}F$ molecule. Each color corresponds to one of the four investigated transitions and the black line shows the best linear fit to the $0 \leftarrow 0$ transition. The inset in the bottom left shows the values of the slope of this fit, F, corresponding to experimental data (black) and theoretical predictions (cyan for FSCCSD method and magenta for FSCCSDc). See main text for details.

TABLE III. Corrections to the Y_{00} and Y_{10} Dunham parameters due to the finite size of the nucleus (in units of $\mathrm{cm}^{-1}/\mathrm{fm}^2$, and $\mathrm{u}.^{1/2}\ \mathrm{cm}^{-1}/\mathrm{fm}^2$, respectively). The last column shows the variation of the effective electron density between the Π and Σ states (in units of $\mathrm{Å}^{-3}$).

Method	$\Delta V_{00}^{A,\Pi-\Sigma}$	$\Delta V_{10}^{A,\Pi-\Sigma}$	$\Delta(\bar{\rho}_e^A)^{\Pi-\Sigma}$
Experiment	−0.839(33)	−0.065(120)	392(15)
FSCCSD	−0.795(82)	−0.014(150)	371(38)
FSCCSDc	−0.823(85)	−0.014(155)	385(40)

the $7p^2P_{1/2} \leftarrow 7s^2S_{1/2}$ transition measured in Ra^+ [38], and using our calculated field shift, $F = -1.283(3)\ (\mathrm{cm}^{-1}/\mathrm{fm}^2)$. Mass-shift contributions to the isotope shift which are below 30 MHz were neglected and were included as an additional uncertainty. Figure 2 shows the four measured transitions for RaF isotopologues as a function of the changes in the root-mean-square charge radius, $\delta\langle r^2\rangle^{226,A}$, of the Ra nucleus with respect to the ^{226}Ra isotope.

A fit to Eq. (1) was performed for each of the four transitions. The extracted molecular parameters and theoretical results are shown in Table III. The change in electron density at the nucleus between the Π and Σ states was obtained using $V_{00}^A = [(Z_A e^2)/(6\epsilon_0)]\bar{\rho}_e^A$, with Z_A being the atomic number of the Ra nucleus, e the electron charge, and ϵ_0 the electric constant [50,51]. As seen in Table III, an excellent agreement between experimental and theoretical results is obtained. The isotope shifts in these molecules are dominated by the product between the changes of the nuclear size, $\delta\langle r^2\rangle$, and the molecular parameter $\Delta(V_{00}^A)^{\Pi-\Sigma} = -0.839(33)\ \mathrm{cm}^{-1}/\mathrm{fm}^2$. This notably large sensitivity to nuclear size effects indicates that even for relatively low precision isotope shift measurements (uncertainty better than $0.02\ \mathrm{cm}^{-1}$), values of $\delta\langle r^2\rangle$ could be extracted with better than 10% precision. Thus, such kind of molecules combined with the present method could offer sensitive routes to investigate nuclear structure properties of exotic actinide nuclei. These elements are highly reactive and challenging to produce and study in their atomic or ionic forms. However, their chemical properties facilitate the formation of molecular compounds. Hence, the extension of these studies to actinide molecules could provide new access to yet-unexplored nuclear properties in these nuclei.

Summary and outlook.—Isotope shift measurements of different RaF isotopologues were determined for the first time, exhibiting a remarkably high sensitivity to changes in the nuclear charge radius of the Ra nucleus. The effective electronic density at the Ra nucleus was obtained by combining our results with previous independent measurements of the mean-square charge radii of Ra isotopes. *Ab initio* quantum chemical calculations show an excellent agreement with the experimental findings, confirming the high sensitivity that this molecule offers to study the electron-nucleon interaction in the proximity of the Ra nucleus.

As illustrated in this work, measurements of molecular isotope shifts offer complementary information to test the reliability of quantum chemical calculations, and provide empirical input by which the accuracy of theoretical models can be gauged. Quantum chemical calculations are essential to extract nuclear structure and fundamental physics parameters from precision measurements. Such information is especially interesting for molecules containing exotic isotopes of the heaviest elements of the periodic table. These species are of marked interest for nuclear physics and fundamental symmetry studies [2,12,59–69], but until now the experimental knowledge of their molecular spectra and nuclear properties has been lacking. Our findings offer important information to understand nuclear structure and symmetry-violating effects in this kind of molecules.

This work was supported by the ERC Consolidator Grant No. 648381 (FNPMLS); the Office of Nuclear Physics, U.S. Department of Energy, under Grants No. DE-SC0021176 and No. DE-SC0021179; the MIT international and technology initiatives Global Seed Funds; Deutsche Forschungsgemeinschaft (DFG, German Research Foundation)—Projektnummer 328961117—SFB 1319 ELCH; STFC Grants No. ST/L005794/1, No. ST/P004423/1, and No. ST/L005786/1 and Ernest Rutherford Grant No. ST/L002868/1; projects from FWO-Vlaanderen, Geconcerteerde Onderzoeks Actie 15/010 from KU Leuven; the European Unions Grant Agreement 654002 (ENSAR2); the Russian Science Foundation under Grant No. 18-12-00227 (2020); the BMBF Grants No. 05P15HGCIA and No. 05P18HGCIA. The National Key RD Program of China (No. 2018YFA0404403) and the National Natural Science Foundation of China (No. 11875073). We thank J. P. Ramos, J. Ballof, and T. Stora for their support in the production of RaF molecules. We would also like to thank the ISOLDE technical group for their support and assistance. Computer time provided by the Center for Scientific Computing (CSC) Frankfurt is gratefully acknowledged.

*sudrescu@mit.edu
†rgarciar@mit.edu
‡robert.berger@uni-marburg.de

[1] M. S. Safronova, D. Budker, D. DeMille, Kimball, D. F. Jackson, A. Derevianko, and C. W. Clark, Search for new physics with atoms and molecules, Rev. Mod. Phys. **90**, 025008 (2018).

[2] V. V. Flambaum, Enhanced nuclear schiff moment and time-reversal violation in ^{229}Th-containing molecules, Phys. Rev. C **99**, 035501 (2019).

[3] N. Auerbach, V. V. Flambaum, and V. Spevak, Collective t-and p-Odd Electromagnetic Moments in Nuclei with Octupole Deformations, Phys. Rev. Lett. **76**, 4316 (1996).

[4] A. D. Kudashov, A. N. Petrov, L. V. Skripnikov, N. S. Mosyagin, T. A. Isaev, R. Berger, and A. V. Titov, Ab initio study of radium monofluoride (RaF) as a candidate to search for parity-and time-and-parity–violation effects, Phys. Rev. A **90**, 052513 (2014).

[5] A. N. Petrov and L. V. Skripnikov, Energy levels of radium monofluoride RaF in external electric and magnetic fields to search for P- and T, P-violation effects, Phys. Rev. A **102**, 062801 (2020).

[6] V. V. Flambaum, D. DeMille, and M. G. Kozlov, Time-Reversal Symmetry Violation in Molecules Induced by Nuclear Magnetic Quadrupole Moments, Phys. Rev. Lett. **113**, 103003 (2014).

[7] E. Altuntaş, J. Ammon, S. B. Cahn, and D. DeMille, Demonstration of a Sensitive Method to Measure Nuclear-Spin-Dependent Parity Violation, Phys. Rev. Lett. **120**, 142501 (2018).

[8] K. Gaul, S. Marquardt, T. Isaev, and R. Berger, Systematic study of relativistic and chemical enhancements of P, T-odd effects in polar diatomic radicals, Phys. Rev. A **99**, 032509 (2019).

[9] C. Delaunay, R. Ozeri, G. Perez, and Y. Soreq, Probing atomic Higgs-like forces at the precision frontier, Phys. Rev. D **96**, 093001 (2017).

[10] C. Delaunay, C. Frugiuele, E. Fuchs, and Y. Soreq, Probing new spin-independent interactions through precision spectroscopy in atoms with few electrons, Phys. Rev. D **96**, 115002 (2017).

[11] J. C. Berengut, D. Budker, C. Delaunay, V. V. Flambaum, C. Frugiuele, E. Fuchs, C. Grojean, R. Harnik, R. Ozeri, G. Perez, and Y. Soreq, Probing New Long-Range Interactions by Isotope Shift Spectroscopy, Phys. Rev. Lett. **120**, 091801 (2018).

[12] L. V. Skripnikov, Nuclear magnetization distribution effect in molecules: Ra^+ and RaF hyperfine structure, J. Chem. Phys. **153**, 114114 (2020).

[13] R. F. Garcia Ruiz *et al.*, Unexpectedly large charge radii of neutron-rich calcium isotopes, Nat. Phys. **12**, 594 (2016).

[14] P. Campbell, I. D. D. Moore, and M. R. R. Pearson, Laser spectroscopy for nuclear structure physics, Prog. Part. Nucl. Phys. **86**, 127 (2016).

[15] G. Hagen *et al.*, Neutron and weak-charge distributions of the ^{48}Ca nucleus, Nat. Phys. **12**, 186 (2016).

[16] B. A. Marsh, T. Day Goodacre, S. Sels, Y. Tsunoda, B. Andel, A. N. Andreyev, N. A. Althubiti, D. Atanasov, A. E. Barzakh, J. Billowes *et al.*, Characterization of the shape-staggering effect in mercury nuclei, Nat. Phys. **14**, 1163 (2018).

[17] R. de Groote *et al.*, Measurement and microscopic description of odd-even staggering of charge radii of exotic copper isotopes, Nat. Phys. **16**, 620 (2020).

[18] S. Kaufmann, J. Simonis, S. Bacca, J. Billowes, M. L. Bissell, K. Blaum, B. Cheal, R. F. G. Ruiz, W. Gins, C. Gorges *et al.*, Charge Radius of the Short-Lived Ni-68 and Correlation With the Dipole Polarizability, Phys. Rev. Lett. **124**, 132502 (2020).

[19] D. Antypas, A. Fabricant, J. E. Stalnaker, K. Tsigutkin, V. V. Flambaum, and D. Budker, Isotopic variation of parity violation in atomic ytterbium, Nat. Phys. **15**, 120 (2019).

[20] I. Counts, J. Hur, D. P. L. Aude Craik, H. Jeon, C. Leung, J. C. Berengut, A. Geddes, A. Kawasaki, W. Jhe, and V. Vuletić, Evidence for Nonlinear Isotope Shift in Yb^+ Search for New Boson, Phys. Rev. Lett. **125**, 123002 (2020).

[21] A. A. Sonzogni, Nudat 2.0: Nuclear structure and decay data on the internet, in *AIP Conference Proceedings*, Vol. 769 (American Institute of Physics, College Park, 2005), pp. 574–577.

[22] T. E. Cocolios, A new perspective on charge radii around $z = 82$, Hyperfine Interact. **238**, 16 (2017).

[23] R. F. Garcia Ruiz, R. Berger, J. Billowes, C. L. Binnersley, M. L. Bissell, A. A. Breier, A. J. Brinson, K. Chrysalidis, T. Cocolios, B. Cooper *et al.*, Spectroscopy of short-lived radioactive molecules, Nature (London) **581**, 396 (2020).

[24] J. L. McHale, *Molecular Spectroscopy* (CRC Press, Florida, 2017).

[25] H. Knöckel, T. Kröckertskothen, E. Tiemann *et al.*, Molecular-beam-laser studies of the states $X^1\Sigma^+$ and $A0^+$ of PbS, Chem. Phys. **93**, 349 (1985).

[26] T. A. Isaev, S. Hoekstra, and R. Berger, Laser-cooled RaF as a promising candidate to measure molecular parity violation, Phys. Rev. A **82**, 052521 (2010).

[27] T. A. Isaev and R. Berger, Lasercooled radium monofluoride: A molecular all-in-one probe for new physics, arXiv:1302.5682.

[28] K. Gaul and R. Berger, Toolbox approach for quasi-relativistic calculation of molecular properties for precision tests of fundamental physics, J. Chem. Phys. **152**, 044101 (2020).

[29] L. P. Gaffney, P. A. Butler, M. Scheck, A. B. Hayes, F. Wenander, M. Albers, B. Bastin, C. Bauer, A. Blazhev, S. Bönig *et al.*, Studies of pear-shaped nuclei using accelerated radioactive beams, Nature (London) **497**, 199 (2013).

[30] P. A. Butler, L. P. Gaffney, P. Spagnoletti, K. Abrahams, M. Bowry, J. Cederkäll, G. DeAngelis, H. DeWitte, P. E. Garrett, A Goldkuhle *et al.*, Evolution of Octupole Deformation in Radium Nuclei from Coulomb Excitation of Radioactive ^{222}Ra and ^{228}Ra Beams, Phys. Rev. Lett. **124**, 042503 (2020).

[31] K. T. Flanagan, K. M. Lynch, J. Billowes, M. L. Bissell, I. Budinčević, T. E. Cocolios, R. P. DeGroote, S. DeSchepper, V. N. Fedosseev, S. Franchoo *et al.*, Collinear Resonance Ionization Spectroscopy of Neutron-Deficient Francium Isotopes, Phys. Rev. Lett. **111**, 212501 (2013).

[32] R. P. De Groote, I. Budinčević, J. Billowes, M. L. Bissell, T. E. Cocolios, G. J. Farooq-Smith, V. N. Fedosseev, K. T. Flanagan, S. Franchoo, R. F. Garcia Ruiz *et al.*, Use of a Continuous Wave Laser and Pockels Cell for Sensitive High-Resolution Collinear Resonance Ionization Spectroscopy, Phys. Rev. Lett. **115**, 132501 (2015).

[33] R. F. Garcia Ruiz, A. R. Vernon, C. L. Binnersley, B. K. Sahoo, M. Bissell, J. Billowes, T. E. Cocolios, W. Gins, R. P. deGroote, K. T. Flanagan *et al.*, High-Precision Multiphoton Ionization of Accelerated Laser-Ablated Species, Phys. Rev. X **8**, 041005 (2018).

[34] A. R. Vernon, R. P. deGroote, J. Billowes, C. L. Binnersley, T. E. Cocolios, G. J. Farooq-Smith, K. T. Flanagan, R. F. Garcia Ruiz, W. Gins, Á. Koszorús *et al.*, Optimising the Collinear Resonance Ionisation Spectroscopy (CRIS) experiment at CERN-ISOLDE, Nucl. Instrum. Methods Phys. Res., Sect. B **463**, 384 (2020).

[35] K. Ágota, J. Billowes, C. L. Binnersley, M. L. Bissell, T. E. Cocolios, B. S. Cooper, R. P. deGroote, G. J. Farooq-Smith, V. N. Fedosseev, K. T. Flanagan *et al.*, Resonance ionization schemes for high resolution and high efficiency studies of exotic nuclei at the CRIS experiment, Nucl. Instrum. Methods Phys. Res., Sect. B **463**, 398 (2020).

[36] T. A. Isaev, S. Hoekstra, L. Willmann, and R. Berger, Ion neutralisation mass-spectrometry route to radium monofluoride (RaF), arXiv:1310.1511.

[37] A. S. P. Gomes *et al.*, DIRAC a relativistic *ab initio* electronic structure program, Release DIRAC19, https://doi.org/10.5281/zenodo.3572669 (2019); see also http://www.diracprogram.org.

[38] L. W. Wansbeek, S. Schlesser, B. K. Sahoo, A. E. L. Dieperink, C. J. G. Onderwater, and R. G. E. Timmermans, Charge radii of radium isotopes, Phys. Rev. C **86**, 015503 (2012).

[39] See Supplemental Material at http://link.aps.org/supplemental/10.1103/PhysRevLett.127.033001 for more details regarding the calculations of the isotope shift constants, as well as the derivations of the equations relating the isotope shift to the changes in the nuclear charge radius in molecules, which includes Refs. [40–47].

[40] L. Visscher and K. G. Dyall, Dirac-Fock atomic electronic structure calculations using different nuclear charge distributions, At. Data Nucl. Data Tables **67**, 207 (1997).

[41] R. Meyer, Trigonometric interpolation method for one dimensional quantum mechanical problems, J. Chem. Phys. **52**, 2053 (1970).

[42] J. L. Dunham, The energy levels of a rotating vibrator, Phys. Rev. **41**, 721 (1932).

[43] H. Jeffreys, On certain approximate solutions of linear differential equations of the second order, Proc. London Math. Soc. **2**, 428 (1925).

[44] G. Wentzel, Eine verallgemeinerung der quantenbedingungen fr die zwecke der wellenmechanik, Z. Phys. **38**, 518 (1926).

[45] H. A. Kramers, Wellenmechanik und halbzahlige quantisierung, Z. Phys. **39**, 828 (1926).

[46] L. Brillouin, The wave mechanics of Schrödinger; A general method of solution by successive approximations, C.R. Hebd. Seances Acad. Sci. **183**, 24 (1926).

[47] H. Knöckel and E. Tiemann, Isotopic field shift in the transition $A0^+ - X^1\Sigma^+$ of PbS, Chem. Phys. **68**, 13 (1982).

[48] D. Andrae, Finite nuclear charge density distributions in electronic structure calculations for atoms and molecules, Phys. Rep. **336**, 413 (2000).

[49] J. Schlembach and E. Tiemann, Isotopic field shift of the rotational energy of the Pb-chalcogenides and Tl-halides, Chem. Phys. **68**, 21 (1982).

[50] S. Knecht and T. Saue, Nuclear size effects in rotational spectra: A tale with a twist, Chem. Phys. **401**, 103 (2012).

[51] A. Almoukhalalati, A. Shee, and T. Saue, Nuclear size effects in vibrational spectra, Phys. Chem. Chem. Phys. **18**, 15406 (2016).

[52] C. N. Banwell, E. M. McCash *et al.*, *Fundamentals of Molecular Spectroscopy*, Vol. 851 (McGraw-Hill, New York, 1994).

[53] R. F. Barrow, D. A. Long, and D. James Millen, *Molecular Spectroscopy*, Vol. 3 (Royal Society of Chemistry, Amsterdam, 1975).

[54] A. H. M. Ross, R. S. Eng, and H. Kildal, Heterodyne measurements of $^{12}C^{18}O$, $^{13}C^{16}O$, and $^{13}C^{18}O$ laser frequencies; mass dependence of Dunham coefficients, Opt. Commun. **12**, 433 (1974).

[55] Ph. R. Bunker, The nuclear mass dependence of the Dunham coefficients and the breakdown of the Born-Oppenheimer approximation, J. Mol. Spectrosc. **68**, 367 (1977).

[56] J. K. G. Watson, The isotope dependence of diatomic Dunham coefficients, J. Mol. Spectrosc. **80**, 411 (1980).

[57] R. J. LeRoy, Improved parameterization for combined isotopomer analysis of diatomic spectra and its application to HF and DF, J. Mol. Spectrosc. **194**, 189 (1999).

[58] K. M. Lynch, S. G. Wilkins, J. Billowes, C. L. Binnersley, M. L. Bissell, K. Chrysalidis, T. E. Cocolios, T. D. Goodacre, R. P. de Groote, G. J. Farooq-Smith *et al.*, Laser-spectroscopy studies of the nuclear structure of neutron-rich radium, Phys. Rev. C **97**, 024309 (2018).

[59] V. V. Flambaum, D. W. Murray, and S. R. Orton, Time invariance violating nuclear electric octupole moments, Phys. Rev. C **56**, 2820 (1997).

[60] V. V. Flambaum, Electric dipole moments of actinide atoms and RaO molecule, Phys. Rev. A **77**, 024501 (2008).

[61] J. Engel, M. J. Ramsey-Musolf, and U. V. Kolck, Electric dipole moments of nucleons, nuclei, and atoms: The standard model and beyond, Prog. Part. Nucl. Phys. **71**, 21 (2013).

[62] J. Baron, W. C. Campbell, D. DeMille, J. M. Doyle, G. Gabrielse, Y. V. Gurevich, P. W. Hess, N. R. Hutzler, E. Kirilov, I. Kozyryev *et al.*, Order of magnitude smaller limit on the electric dipole moment of the electron, Science **343**, 269 (2014).

[63] J. Dobaczewski, J. Engel, M. Kortelainen, and P. Becker, Correlating Schiff Moments in the Light Actinides with Octupole Moments, Phys. Rev. Lett. **121**, 232501 (2018).

[64] V. Andreev *et al.*, Improved limit on the electric dipole moment of the electron, Nature (London) **562**, 355 (2018).

[65] L. V. Skripnikov, N. S. Mosyagin, A. V. Titov, and V. V. Flambaum, Actinide and lanthanide molecules to search for strong CP-violation, arXiv:2003.10885.

[66] V. V. Flambaum and V. A. Dzuba, Electric dipole moments of atoms and molecules produced by enhanced nuclear schiff moments, Phys. Rev. A **101**, 042504 (2020).

[67] R. F. Garcia Ruiz, Designer molecules for fundamental-symmetry tests, Physics **14**, 3 (2021).

[68] M. Fan, C. A. Holliman, X. Shi, H. Zhang, M. W. Straus, X. Li, S. W. Buechele, and A. M. Jayich, Optical Mass Spectrometry of Cold $RaOH^+$ and $RaOCH_3{}^+$, Phys. Rev. Lett. **126**, 023002 (2021).

[69] P. Yu and N. R. Hutzler, Probing Fundamental Symmetries of Deformed Nuclei in Symmetric Top Molecules, Phys. Rev. Lett. **126**, 023003 (2021).

Isotope Shifts of Radium Monofluoride Molecules

S.M. Udrescu,[1,*] A.J. Brinson,[1] R.F. Garcia Ruiz,[1,2,†] K. Gaul,[3] R. Berger,[3,‡] J. Billowes,[4] C.L. Binnersley,[4] M.L. Bissell,[4] A.A. Breier,[5] K. Chrysalidis,[2] T.E. Cocolios,[6] B.S. Cooper,[4] K.T. Flanagan,[4,7] T.F. Giesen,[5] R.P. de Groote,[8] S. Franchoo,[9] F.P. Gustafsson,[6] T.A. Isaev,[10] Á. Koszorús,[6] G. Neyens,[2,6] H.A. Perrett,[4] C.M. Ricketts,[4] S. Rothe,[2] A.R. Vernon,[4] K.D.A. Wendt,[11] F. Wienholtz,[2,12] S.G. Wilkins,[2] and X.F. Yang[13]

[1] *Massachusetts Institute of Technology, Cambridge, MA 02139, USA*
[2] *CERN, CH − 1211 Geneva 23, Switzerland*
[3] *Fachbereich Chemie, Philipps − Universität Marburg, Hans − Meerwein − Straße 4, 35032 Marburg, Germany*
[4] *School of Physics and Astronomy, The University of Manchester, Manchester M13 9PL, United Kingdom*
[5] *Laboratory for Astrophysics, Institute of Physics, University of Kassel, 34132 Kassel, Germany*
[6] *KU Leuven, Instituut voor Kern − en Stralingsfysica, B − 3001 Leuven, Belgium*
[7] *Photon Science Institute, The University of Manchester, Manchester M13 9PY, United Kingdom*
[8] *Department of Physics, University of Jyväskylä, Survontie 9, Jyväskylä, FI − 40014, Finland*
[9] *Institut de Physique Nucleaire d'Orsay, F − 91406 Orsay, France*
[10] *NRC Kurchatov Institute-PNPI, Gatchina, Leningrad district 188300, Russia*
[11] *Institut für Physik, Johannes Gutenberg − Universität Mainz, D − 55128 Mainz, Germany*
[12] *Institut für Physik, Universität Greifswald, D − 17487 Greifswald, Germany*
[13] *School of Physics and State Key Laboratory of Nuclear Physics and Technology, Peking University, Beijing 100971, China*

(Dated: December 4, 2020)

THEORETICAL METHODS

Transition energies for different isotopologues of RaF were calculated at the level of relativistic Fock-Space Coupled Cluster including Singles and Doubles amplitudes (FSCCSD). These calculations were carried out with the program package DIRAC19 [1]. The nuclear charge density of nucleus A was described by a normalized Gaussian function $\rho_A(\vec{r}_i) = \rho_0 \mathrm{e}^{-\zeta|\vec{r}_i-\vec{r}_A|^2}$ with $\zeta = \frac{3}{2\langle r^2\rangle}$ being characterized by an empirically determined root-mean-square nuclear radius of $\langle r^2\rangle^{1/2} = \left[0.836A^{1/3}+0.570\right]$ fm [2], instead of a homogeneously charged solid sphere as was assumed as a starting point in previous atomic calculations used to determine the experimental nuclear charge radii in Radium isotopes [3, 4]. Here $\vec{r}_i$ and $\vec{r}_A$ denote the position vector of electron i and nucleus A, respectively. Calculations were carried out for different root-mean-square nuclear radii that within this model correspond to isotopologues of ^{A}Ra^{19}F, with even values for the Ra nucleus mass, A, ranging from $A = 212$ up to $A = 232$, in addition to the isotopologues with $A = 213, 223, 225$.

Calculations were performed using the s,p,d,f-subset of the ANO-RCC basis on Ra and the s,p,d-subset of the ANO-RCC basis on F. In these calculations, the 6s, 6p and 7s shells of Ra and the 2s and 2p shells of F are correlated (17 electrons) and are therefore denoted as FSCCSD(17e). All calculations were repeated for bond lengths of $r_{\mathrm{RaF}} = 4.0, 4.1, 4.2, 4.25, 4.3$ and $4.4\ a_0$, which covers the region around the equilibrium structure of the electronic ground state. For each bond length, the isotope shift constant $F(r_{\mathrm{RaF}}) = \frac{\partial\delta\widetilde{\nu}}{\partial\delta\langle r^2\rangle}(r_{\mathrm{RaF}})$ is determined by a linear fit of the total energy of RaF for different electronic states in dependence of the Ra mass (see Fig. 1).

TABLE I. Isotope shift constants $F = \frac{\partial\delta\tilde{\nu}}{\partial\delta\langle r^2\rangle}$ of electronic states in RaF for different bond lengths at the FSCCSD(17e) level. FSCCSD(27e) calculations are shown in square brackets for a bond length of $r_{\mathrm{RaF}} = 4.3\,a_0$. Isotope shift constants F of the $A^2\Pi_{1/2} \leftarrow X^2\Sigma_{1/2}$ transition correspond to the slopes in Fig. 1. For all calculated isotope shifts fit errors are $< 10^{-3}\ \frac{\mathrm{cm}^{-1}}{\mathrm{fm}^2}$.

r_{RaF} (a_0)	$F\ \left(\frac{\mathrm{cm}^{-1}}{\mathrm{fm}^2}\right)$		
	$X^2\Sigma_{1/2}$	$A^2\Pi_{1/2}$	$A^2\Pi_{1/2} \leftarrow X^2\Sigma_{1/2}$
4.0	0.756	−0.015	−0.771
4.1	0.758	−0.021	−0.778
4.2	0.760	−0.027	−0.787
4.25	0.762	−0.030	−0.792
4.3	0.764	−0.033	−0.797 [−0.825]
4.4	0.769	−0.039	−0.808

In order to estimate the quality of this method, FSCSSD calculations with an extended basis set of 33 s, 29 p, 20 d, 14 f, 7 g, and 6 h functions for Ra and additionally correlating the 5d shell of Ra (27 correlated electrons) (FSCCSD(27e)) were carried out for the isotopologues ^{224}Ra^{19}F, ^{226}Ra^{19}F and ^{228}Ra^{19}F at a bond length of $4.3\ a_0$. The resulting isotope shifts constants for different bond lengths of RaF are shown in Table I.

The same basis set that was employed in the FSCCSD(27e) calculations was used in an atomic FSCCSD calculation of Ra^+, in which 19 electrons (5d, 6s, 6p and 7s shells) were correlated. These atomic calculations were used to allow a direct comparison between our measurements and previous isotope shift measure-

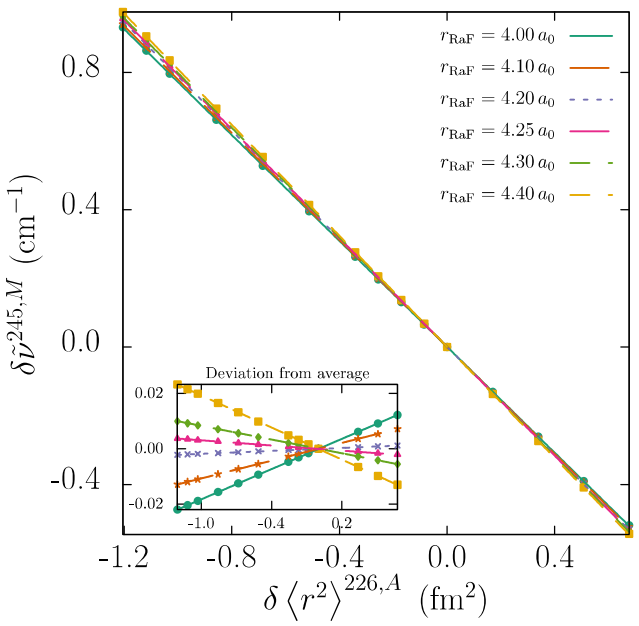

FIG. 1. Isotope shifts as a function of the changes in the charge radius with respect to the reference charge radius that corresponds within the applied model to the isotopologue ^{226}Ra^{19}F molecule calculated at the level of FSCCSD(17e). Each color corresponds to one of the six different bond lengths. In the inset (bottom left), the deviation from the average over all bond lengths is shown for each bond length. The slopes of the linear fits for each bond length are given in Table I.

ments in the radium ion. In the present work, the nucleus is modeled as a Gaussian distribution. In all FSCCSD calculations, the active space was restricted to virtual orbitals below 1000 E_h.

Vibrational corrections to isotope shift constants were calculated from a fourth-degree polynomial fit of the bond length dependence of isotope shifts:

$$F(r_{\mathrm{RaF}}) \approx \sum_{k=0} c_k r_{\mathrm{RaF}}^k \,. \tag{1}$$

Vibrational wave functions were received in a one-dimensional discrete variable representation (DVR) scheme [5] employing the potentials of the electronic ground and excited states calculated in Ref. [6] using the the reference isotopologue ^{226}Ra^{19}F. The dependence of the vibrational wave functions on different masses of Ra was determined to be $\ll 1\,\%$. A sketch of the electronic potentials of the $X^2\Sigma^+$ and $A^2\Pi_{1/2}$ from Ref. [6] are shown in Fig. 2. The linear moments in the figure are shown for the first four vibrational levels to illustrate for which bond lengths the vibronic expectation values are evaluated. The bond length dependence of the isotope shift of the $X^2\Sigma^+$ and $A^2\Pi_{1/2}$ states is given relative to that of the 0th vibrational level. The vibronic expectation value is calculated as

$$F = \langle v|F(r_{\mathrm{RaF}})|v\rangle = \sum_{k=0} \langle v|r_{\mathrm{RaF}}^k|v\rangle c_k \,, \tag{2}$$

with c_k being coefficients of the fourth-order polynomial fit of the bond length dependence of isotope shifts. The crossing points of $\langle \frac{\partial \delta\tilde{\nu}}{\partial \delta\langle r^2\rangle}\rangle$ (points and stars) with the linear moments (gray vertical lines) give the leading-order contribution to the vibronic expectation values. For the $A^2\Pi_{1/2}$ state this is almost identical to the full expectation values (orange dotted/dashed lines), whereas for the $X^2\Sigma^+$ state non-linear contributions are much more important.

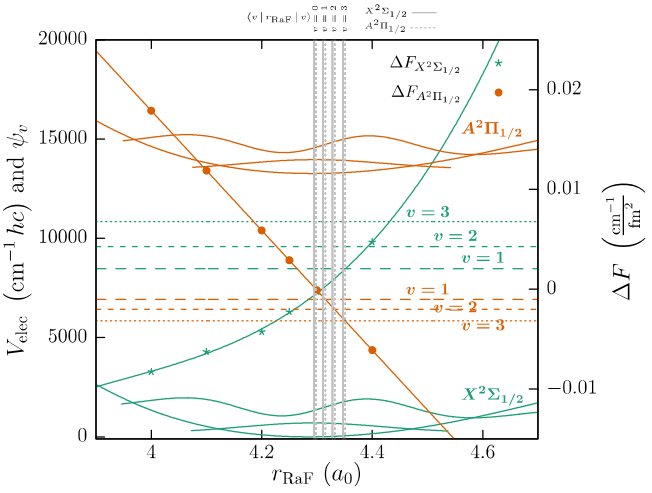

FIG. 2. Electronic potentials of the $X^2\Sigma^+$ and $A^2\Pi_{1/2}$ states. The vibrational wave functions are shown for the zeroth and third vibrational states, respectively. Wave functions are shifted to the energy of the vibrational level and scaled arbitrarily for better representation (see text for more details). Isotope shift constants are shown relative to the vibrational ground state ($\Delta F = (F - \langle v=0|F(r_{\mathrm{RaF}})|v=0\rangle)$) for both electronic states as function of r_{RaF} (dots and stars) alongside polynomial approximations and vibronic expectation values (horizontal dotted lines).

ISOTOPE SHIFT DERIVATION

In the Dunham model [7], the rovibrational energy levels of a diatomic molecule are given by

$$E_{\nu,J} = \sum_{k,l\geq 0} Y_{kl} \left(\nu + \frac{1}{2}\right)^k [J(J+1)]^l, \tag{3}$$

where ν and J are the vibrational and rotational quantum numbers, respectively, for a given electronic level, and Y_{kl} are the Dunham coefficients in units of frequency.

It can be shown [8, 9] that these coefficients have an explicit dependence on the reduced mass of the molecule expressed as

$$Y_{kl} = \mu^{-(k/2+l)} U_{kl}. \tag{4}$$

Ross et al. [10] showed that further isotope-dependent corrections are needed for the expression above, to account for the breakdown of the Born-Oppenheimer approximation and the Jeffreys-Wentzel-Brillouin-Kramers (JWBK) approximation [11–14] used in the Dunham model derivation [15–17]. The size of the nuclei of the atoms in the molecule produces a further shift of the energy levels [8, 9, 18, 19], introducing a field shift correction. The modified expression is given by

$$\begin{aligned} Y_{kl} = \mu^{-(k/2+l)} U_{kl} \Bigg[1 + m_\mathrm{e} \left(\frac{\Delta_{kl}^A}{M_A} + \frac{\Delta_{kl}^B}{M_B} \right) \\ + V_{kl}^A \langle r^2 \rangle_A + V_{kl}^B \langle r^2 \rangle_B \Bigg], \end{aligned} \tag{5}$$

where M_A and M_B are the masses of the two atoms in the molecule, while Δ_{kl}^α and Δ_{kl}^B are mass-independent corrections for each of the two atoms. $\langle r^2 \rangle_A$ and $\langle r^2 \rangle_B$ are the nuclear mean-squared charge radii of the two nuclei in the molecule, while V_{kl}^A and V_{kl}^B quantify the magnitude of the change of a given Dunham parameter due to the nuclear size. These parameters can be related to the electron density at the given nucleus, as well as the first and second derivative of this density with respect to internuclear axis (see [9] for a more detailed discussion).

In our case, given that we are interested in variations between molecules in which only the radium nucleus is changed, the fluorine nucleus contributions can be neglected ($\mathcal{O}(M_\mathrm{F}, \langle r^2 \rangle_\mathrm{F})$). Eq. 5 reduces to:

$$\begin{aligned} Y_{kl} = \mu_\mathrm{RaF}^{-(k/2+l)} U_{kl} \left[1 + m_\mathrm{e} \frac{\Delta_{kl}^\mathrm{Ra}}{M_\mathrm{Ra}} + V_{kl}^\mathrm{Ra} \langle r^2 \rangle_\mathrm{Ra} \right] \\ + \mathcal{O}(M_\mathrm{F}, \langle r^2 \rangle_\mathrm{F}). \end{aligned} \tag{6}$$

In this approach, the parameter U_{kl} is independent of mass or volume effects, being the same for all isotopes. At the energy resolution of our experiment, we are mainly sensitive to changes in the electronic energy E_el, associated to Y_{00} and the first-order vibrational energy E_vib, linked to Y_{10}. So that the transition energy E is given by

$$E = \overbrace{Y_{00}' - Y_{00}''}^{E_\mathrm{el}} + \overbrace{Y_{10}' - Y_{10}''}^{E_\mathrm{vib}}. \tag{7}$$

Thus, the energy of the electronic transition between the $X^2\Sigma^+$ and $A^2\Pi_{1/2}$ state for a given RaF isotopologue, α, is given by

$$\begin{aligned} E_\mathrm{el}^{\alpha,\Pi,\Sigma} &= Y_{00}^{\alpha,\Pi} - Y_{00}^{\alpha,\Sigma} \\ &= U_{00}^\Pi \left[1 + m_\mathrm{e} \frac{\Delta_{00}^{\alpha,\Pi}}{M_\alpha} + V_{00}^{\alpha,\Pi} \langle r^2 \rangle_\alpha \right] \\ &\quad - U_{00}^\Sigma \left[1 + m_\mathrm{e} \frac{\Delta_{00}^{\alpha,\Sigma}}{M_\alpha} + V_{00}^{\alpha,\Sigma} \langle r^2 \rangle_\alpha \right] \\ &= U_{00}^\Pi - U_{00}^\Sigma + \frac{m_\mathrm{e}}{M_\alpha} (\Delta_{00}^{\alpha,\Pi} U_{00}^\Pi - \Delta_{00}^{\alpha,\Sigma} U_{00}^\Sigma) \\ &\quad + (V_{00}^{\alpha,\Pi} U_{00}^\Pi - V_{00}^{\alpha,\Sigma} U_{00}^\Sigma) \langle r^2 \rangle_\alpha. \end{aligned} \tag{8}$$

This expression can be re-written as

$$E_\mathrm{el}^{\alpha,\Pi,\Sigma} = U_{00}^\Pi - U_{00}^\Sigma + \frac{\Delta(\Delta_{00}^{\alpha,\Pi-\Sigma})}{M_\alpha} + \Delta V_{00}^{\alpha,\Pi-\Sigma} \langle r^2 \rangle_\alpha, \tag{9}$$

with

$$\Delta(\Delta_{00}^{\alpha,\Pi-\Sigma}) \equiv m_\mathrm{e} (\Delta_{00}^{\alpha,\Pi} U_{00}^\Pi - \Delta_{00}^{\alpha,\Sigma} U_{00}^\Sigma), \tag{10}$$

and

$$\Delta V_{00} \equiv V_{00}^{\alpha,\Pi} U_{00}^\Pi - V_{00}^{\alpha,\Sigma} U_{00}^\Sigma. \tag{11}$$

The equivalent formula for the vibrational energy E_vib, for the same vibrational excitation, ν, of the $X^2\Sigma^+$ and $A^2\Pi_{1/2}$ electronic levels is given by

$$\begin{aligned} &E_\mathrm{vib}^{\alpha,\Pi,\Sigma,\nu} \\ &= (Y_{10}^{\alpha,\Pi} - Y_{10}^{\alpha,\Sigma})(\nu + 1/2) \\ &= \mu_\alpha^{-1/2} U_{10}^\Pi \left[1 + m_\mathrm{e} \frac{\Delta_{10}^{\alpha,\Pi}}{M_\alpha} + V_{10}^{\alpha,\Pi} \langle r^2 \rangle_\alpha \right] (\nu + 1/2) \\ &\quad - \mu_\alpha^{-1/2} U_{10}^\Sigma \left[1 + m_\mathrm{e} \frac{\Delta_{10}^{\alpha,\Sigma}}{M_\alpha} + V_{10}^{\alpha,\Sigma} \langle r^2 \rangle_\alpha \right] (\nu + 1/2), \end{aligned} \tag{12}$$

and

$$\begin{aligned} E_\mathrm{vib}^{\alpha,\Pi,\Sigma,\nu} &= \mu_\alpha^{-1/2} (U_{10}^\Pi - U_{10}^\Sigma)(\nu + 1/2) \\ &\quad + \mu_\alpha^{-1/2} \frac{m_\mathrm{e}}{M_\alpha} (\Delta_{10}^{\alpha,\Pi} U_{10}^\Pi - \Delta_{10}^{\alpha,\Sigma} U_{10}^\Sigma)(\nu + 1/2) \\ &\quad + \mu_\alpha^{-1/2} (V_{10}^{\alpha,\Pi} U_{10}^\Pi - V_{10}^{\alpha,\Sigma} U_{10}^\Sigma)(\nu + 1/2) \langle r^2 \rangle_\alpha. \end{aligned} \tag{13}$$

Similarly, it can be expressed as

$$\begin{aligned} E_\mathrm{vib}^{\alpha,\Pi,\Sigma,\nu} &= \mu_\alpha^{-1/2} (U_{10}^\Pi - U_{10}^\Sigma)(\nu + 1/2) \\ &\quad + \mu_\alpha^{-1/2} \frac{\Delta(\Delta_{10}^{\alpha,\Pi-\Sigma})}{M_\alpha} (\nu + 1/2) + \mu_\alpha^{-1/2} \Delta V_{10}^{\alpha,\Pi-\Sigma} (\nu + 1/2) \langle r^2 \rangle_\alpha, \end{aligned} \tag{14}$$

where

$$\Delta(\Delta_{10}^{\alpha,\Pi-\Sigma}) \equiv m_\mathrm{e} (\Delta_{10}^{\alpha,\Pi} U_{10}^\Pi - \Delta_{10}^{\alpha,\Sigma} U_{10}^\Sigma), \tag{15}$$

and

$$\Delta V_{10} \equiv V_{10}^{\alpha,\Pi} U_{10}^{\Pi} - V_{10}^{\alpha,\Sigma} U_{10}^{\Sigma}. \tag{16}$$

Using Eq. 9, the isotope shift between two isotopologues α and α' associated to the electronic energy between the Π and Σ state is given by

$$\begin{aligned} E_{\rm el}^{\alpha',\Pi,\Sigma} - E_{\rm el}^{\alpha,\Pi,\Sigma} &= \Delta(\Delta_{00}^{\alpha,\Pi-\Sigma}) \left(\frac{1}{M_{\alpha'}} - \frac{1}{M_\alpha} \right) \\ &\quad + \Delta V_{00}^{\alpha,\Pi-\Sigma} (\langle r^2 \rangle_{\alpha'} - \langle r^2 \rangle_\alpha) \\ &= \Delta(\Delta_{00}^{\alpha,\Pi-\Sigma}) \left(\frac{M_\alpha - M_{\alpha'}}{M_\alpha M_{\alpha'}} \right) \\ &\quad + \Delta V_{00}^{\alpha,\Pi-\Sigma} \delta\langle r^2 \rangle_{\alpha\alpha'} \end{aligned} \tag{17}$$

Similarly, Eq. 14 gives the isotope shift associated with the vibrational energy

$$\begin{aligned} &E_{\rm vib}^{\alpha',\Pi,\Sigma,\nu} - E_{\rm vib}^{\alpha,\Pi,\Sigma,\nu} \\ &= \Delta(\Delta_{10}^{\alpha,\Pi-\Sigma}) \left(\frac{M_\alpha {\mu'_\alpha}^{-1/2} - M_{\alpha'} \mu_\alpha^{-1/2}}{M_\alpha M_{\alpha'}} \right) (\nu + 1/2) \\ &+ \Delta V_{10}^{\alpha,\Pi-\Sigma} \left(\frac{\langle r^2 \rangle_{\alpha'}}{\sqrt{\mu_{\alpha'}}} - \frac{\langle r^2 \rangle_\alpha}{\sqrt{\mu_\alpha}} \right) (\nu + 1/2). \end{aligned} \tag{18}$$

Therefore, the overall energy shift due to electronic and vibrational energy is given by

$$\begin{aligned} &\Delta E^{\alpha,\alpha',\Pi,\Sigma,\nu} \\ &= E_{\rm el}^{\alpha',\Pi,\Sigma} - E_{\rm el}^{\alpha,\Pi,\Sigma} + E_{\rm vib}^{\alpha',\Pi,\Sigma,\nu} - E_{\rm vib}^{\alpha,\Pi,\Sigma,\nu} \\ &= \Delta(\Delta_{00}^{\alpha,\Pi-\Sigma}) \left(\frac{M_\alpha - M_{\alpha'}}{M_\alpha M_{\alpha'}} \right) + \Delta V_{00}^{\alpha,\Pi-\Sigma} \delta\langle r^2 \rangle_{\alpha\alpha'} \\ &\quad + \Delta(\Delta_{10}^{\alpha,\Pi-\Sigma}) \left(\frac{M_\alpha \mu_{\alpha'}^{-1/2} - M_{\alpha'} \mu_\alpha^{-1/2}}{M_\alpha M_{\alpha'}} \right) (\nu + 1/2) \\ &+ \Delta V_{10}^{\alpha,\Pi-\Sigma} \left(\frac{\langle r^2 \rangle_{\alpha'}}{\sqrt{\mu_{\alpha'}}} - \frac{\langle r^2 \rangle_\alpha}{\sqrt{\mu_\alpha}} \right) (\nu + 1/2) \\ &\approx \Delta V_{00}^{\alpha,\Pi-\Sigma} \delta\langle r^2 \rangle_{\alpha\alpha'} + \Delta V_{10}^{\alpha,\Pi-\Sigma} \left(\frac{\langle r^2 \rangle_{\alpha'}}{\sqrt{\mu_{\alpha'}}} - \frac{\langle r^2 \rangle_\alpha}{\sqrt{\mu_\alpha}} \right) (\nu + 1/2). \end{aligned} \tag{19}$$

The terms containing $\Delta(\Delta_{00}^{\alpha,\Pi-\Sigma})$ and $\Delta(\Delta_{10}^{\alpha,\Pi-\Sigma})$ are expected to be less than 0.001 cm^{-1} in magnitude, based on mass shift values from Ra^+ [3], and the $\widetilde{\omega}_e$ values of the $A^2\Pi_{1/2}$ and $X^2\Sigma^+$ states in $^{226}Ra^{19}F$ [20]. Hence they are neglected in the present study. When the term $\frac{\delta\langle r^2 \rangle_{\alpha\alpha'}}{\sqrt{\mu_\alpha}}$ is used instead of $\left(\frac{\langle r^2 \rangle_{\alpha'}}{\sqrt{\mu_{\alpha'}}} - \frac{\langle r^2 \rangle_\alpha}{\sqrt{\mu_\alpha}} \right)$, a correction factor of up to 1.5% should be taken into account.

* sudrescu@mit.edu
† rgarciar@mit.edu
‡ robert.berger@uni-marburg.de

[1] DIRAC, a relativistic ab initio electronic structure program, Release DIRAC19 (2019), written by A. S. P. Gomes, T. Saue, L. Visscher, H. J. Aa. Jensen, and R. Bast, with contributions from I. A. Aucar, V. Bakken, K. G. Dyall, S. Dubillard, U. Ekström, E. Eliav, T. Enevoldsen, E. Faßhauer, T. Fleig, O. Fossgaard, L. Halbert, E. D. Hedegård, B. Heimlich–Paris, T. Helgaker, J. Henriksson, M. Iliaš, Ch. R. Jacob, S. Knecht, S. Komorovský, O. Kullie, J. K. Lærdahl, C. V. Larsen, Y. S. Lee, H. S. Nataraj, M. K. Nayak, P. Norman, G. Olejniczak, J. Olsen, J. M. H. Olsen, Y. C. Park, J. K. Pedersen, M. Pernpointner, R. di Remigio, K. Ruud, P. Sałek, B. Schimmelpfennig, B. Senjean, A. Shee, J. Sikkema, A. J. Thorvaldsen, J. Thyssen, J. van Stralen, M. L. Vidal, S. Villaume, O. Visser, T. Winther, and S. Yamamoto (available at http://dx.doi.org/10.5281/zenodo.3572669, see also http://www.diracprogram.org).
[2] L. Visscher and K. G. Dyall, "Dirac-fock atomic electronic structure calculations using different nuclear charge distributions," At. Data Nucl. Data Tables **67**, 207–224 (1997).
[3] L. W. Wansbeek, S. Schlesser, B. K. Sahoo, A. E. L. Dieperink, C. J. G. Onderwater, and R. G. E. Timmermans, "Charge radii of radium isotopes," Phys. Rev. C **86**, 015503 (2012).
[4] KM Lynch, SG Wilkins, J Billowes, CL Binnersley, ML Bissell, K Chrysalidis, Thomas Elias Cocolios, T Day Goodacre, RP de Groote, Gregory James Farooq-Smith, *et al.*, "Laser-spectroscopy studies of the nuclear structure of neutron-rich radium," Phys. Rev. C **97**, 024309 (2018).
[5] R. Meyer, "Trigonometric interpolation method for one-dimensional quantum-mechanical problems," J. Chem. Phys. **52**, 2053–2059 (1970), https://doi.org/10.1063/1.1673259.
[6] TA Isaev and R Berger, "Lasercooled radium monofluoride: A molecular all-in-one probe for new physics," arXiv preprint arXiv:1302.5682 (2013).
[7] JL Dunham, "The energy levels of a rotating vibrator," Phys. Rev. **41**, 721 (1932).
[8] Stefan Knecht and Trond Saue, "Nuclear size effects in rotational spectra: A tale with a twist," Chem. Phys. **401**, 103–112 (2012).
[9] Adel Almoukhalalati, Avijit Shee, and Trond Saue, "Nuclear size effects in vibrational spectra," Phys. Chem. Chem. Phys. **18**, 15406–15417 (2016).
[10] AHM Ross, RS Eng, and H Kildal, "Heterodyne measurements of $^{12}C^{18}O$, $^{13}C^{16}O$, and $^{13}C^{18}O$ laser frequencies; mass dependence of Dunham coefficients," Opti. Comm. **12**, 433–438 (1974).
[11] Harold Jeffreys, "On certain approximate solutions of lineae differential equations of the second order," Proceedings of the London Mathematical Society **2**, 428–436 (1925).
[12] Gregor Wentzel, "Eine Verallgemeinerung der Quantenbedingungen für die Zwecke der Wellenmechanik," Z. Phys. **38**, 518–529 (1926).
[13] Hendrik Anthony Kramers, "Wellenmechanik und hal-

bzahlige Quantisierung," Z. Phys. **39**, 828–840 (1926).
[14] Leon Brillouin, "The wave mechanics of schrödinger; a general method of solution by successive approximations," Account Give back. Weekly. Seances Acad. Sci. **183**, 24–26 (1926).
[15] Ph R Bunker, "The nuclear mass dependence of the dunham coefficients and the breakdown of the born-oppenheimer approximation," J. Mol. Spectrosc. **68**, 367–371 (1977).
[16] James KG Watson, "The isotope dependence of diatomic dunham coefficients," J. Mol. Spectrosc. **80**, 411–421 (1980).
[17] Robert J Le Roy, "Improved parameterization for combined isotopomer analysis of diatomic spectra and its application to hf and df," J. Mol. Spectrosc. **194**, 189–196 (1999).
[18] H Knöckel and E Tiemann, "Isotopic field shift in the transition $A0^+ - X^1\Sigma^+$ of PbS," Chem. Phys. **68**, 13–19 (1982).
[19] J Schlembach and E Tiemann, "Isotopic field shift of the rotational energy of the pb-chalcogenides and tl-halides," Chem. Phys. **68**, 21–28 (1982).
[20] RF Garcia Ruiz, R Berger, J Billowes, CL Binnersley, ML Bissell, AA Breier, AJ Brinson, K Chrysalidis, T Cocolios, B Cooper, *et al.*, "Spectroscopy of short-lived radioactive molecules," Nature **581**, 396 (2020).

4.2 Article 2: Precision Spectroscopy and Laser-Cooling Scheme of a Radium-Containing Molecule

This article (S.-M. Udrescu, et al., "Precision spectroscopy and laser-cooling scheme of a radium-containing molecule", Nature Physics 20, 202– 207 (2024).) presents the first high-resolution, rotationally resolved spectroscopy of a radioactive molecule, ^{226}RaF. This measurement provided a quantitative laser cooling scheme for this molecule (for the first time in a radioactive molecule), as well as the location of the low-lying rotational levels suitable for future fundamental physics studies using this molecule. For this article, published in Nature Physics (2024), I was involved in the experiment, I led the data analysis and the theoretical calculations, I prepared the figures and the different drafts of the manuscript, including the initially submitted version, as well as the subsequent, revised ones and I was in charge of the submission process.

Reproduced with permission from Springer Nature.

nature physics

Article

https://doi.org/10.1038/s41567-023-02296-w

Precision spectroscopy and laser-cooling scheme of a radium-containing molecule

Received: 2 March 2023

Accepted: 19 October 2023

Published online: 9 January 2024

Check for updates

S. M. Udrescu[1] ✉, S. G. Wilkins[1] ✉, A. A. Breier[2], M. Athanasakis-Kaklamanakis[3,4], R. F. Garcia Ruiz[1] ✉, M. Au[5,6], I. Belošević[7], R. Berger[8], M. L. Bissell[9], C. L. Binnersley[9], A. J. Brinson[1], K. Chrysalidis[5], T. E. Cocolios[4], R. P. de Groote[4], A. Dorne[4], K. T. Flanagan[9,10], S. Franchoo[11], K. Gaul[8], S. Geldhof[4], T. F. Giesen[2], D. Hanstorp[12], R. Heinke[5], Á. Koszorús[3], S. Kujanpää[13], L. Lalanne[4], G. Neyens[4], M. Nichols[12], H. A. Perrett[9], J. R. Reilly[9], S. Rothe[5], B. van den Borne[4], A. R. Vernon[9], Q. Wang[14], J. Wessolek[9], X. F. Yang[15] & C. Zülch[8]

Molecules containing heavy radioactive nuclei are predicted to be extremely sensitive to violations of the fundamental symmetries of nature. The nuclear octupole deformation of certain radium isotopes massively boosts the sensitivity of radium monofluoride molecules to symmetry-violating nuclear properties. Moreover, these molecules are predicted to be laser coolable. Here we report measurements of the rovibronic structure of radium monofluoride molecules, which allow the determination of their laser cooling scheme. We demonstrate an improvement in resolution of more than two orders of magnitude compared to the state of the art. Our developments allowed measurements of minuscule amounts of hot molecules, with only a few hundred per second produced in a particular rotational state. The combined precision and sensitivity achieved in this work offer opportunities for studies of radioactive molecules of interest in fundamental physics, chemistry and astrophysics.

The Standard Model of particle physics has been spectacularly successful at explaining the fundamental interactions of the known elementary particles of the universe up to TeV-scale energies. However, the Standard Model is not a complete theory of nature, as it cannot account for observations related to dark matter, dark energy, the matter–antimatter asymmetry of the universe or the spectrum of elementary particle masses[1]. Numerous Standard Model extensions have been proposed to explain these observations, often predicting stronger violations of fundamental symmetries, such as parity or time reversal, or the existence of new forces and particles[1]. A great deal of attention is therefore now focused on constraining these effects in precision experiments conducted across different energy scales.

In the last few years, precision molecular studies have emerged as a compelling platform upon which to perform these investigations[2–9]. Symmetry-violating properties of fundamental particles can add minuscule but measurable perturbations to the energies of molecular states.

[1]Massachusetts Institute of Technology, Cambridge, MA, USA. [2]Laboratory for Astrophysics, Institute of Physics, University of Kassel, Kassel, Germany. [3]Experimental Physics Department, CERN, Geneva 23, Switzerland. [4]KU Leuven, Instituut voor Kern - en Stralingsfysica, Leuven, Belgium. [5]Systems Department, CERN, Geneva 23, Switzerland. [6]Department Chemie, Johannes Gutenberg-Universitat Mainz, Mainz, Germany. [7]TRIUMF, Vancouver, British Columbia, Canada. [8]Fachbereich Chemie, Philipps-Universität Marburg, Marburg, Germany. [9]School of Physics and Astronomy, The University of Manchester, Manchester, UK. [10]Photon Science Institute, The University of Manchester, Manchester, UK. [11]Laboratoire Irène Joliot-Curie, Orsay, France. [12]Department of Physics, University of Gothenburg, Gothenburg, Sweden. [13]Department of Physics, Accelerator laboratory, University of Jyväskylä, Jyväskylä, Finland. [14]School of Nuclear Science and Technology, Lanzhou University, Lanzhou, P. R. China. [15]School of Physics and State Key Laboratory of Nuclear Physics and Technology, Peking University, Beijing, China. ✉e-mail: sudrescu@mit.edu; wilkinss@mit.edu; rgarciar@mit.edu

https://doi.org/10.1038/s41567-023-02296-w

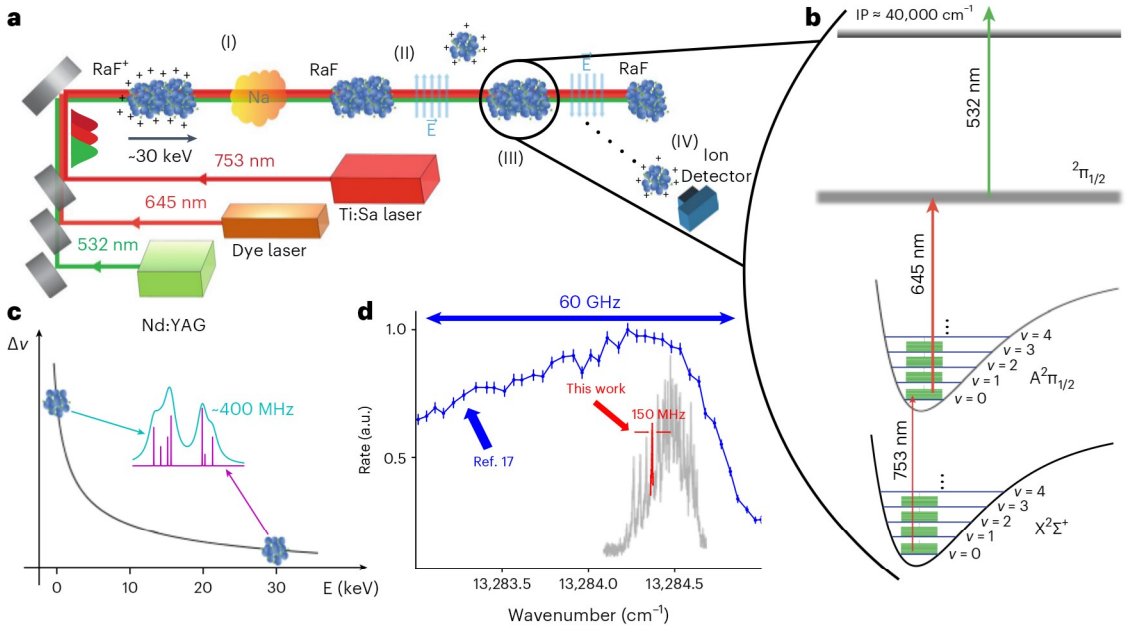

Fig. 1 | Illustration of the experimental setup. a, Mass-selected RaF^+ ions accelerated to ~30 keV are partially neutralized in a Na vapour (I). Residual ions are removed using a static electric field (II), and neutral molecules are overlapped collinearly with three pulsed laser beams (III). The three lasers used are shown as coloured cuboids. Their approximate wavelengths and relative timings (coloured Gaussian shapes) are indicated. Resonantly ionized molecules are deflected and detected on an ion detector (IV). **b**, Three-step ionization scheme for the RaF molecules. The first Ti:Sa laser excites the molecules from the ground $X^2\Sigma^+$ to the excited $A^2\Pi_{1/2}$ electronic state. Potential curves of the two states, vibrational (blue) and rotational (green) energy levels are shown, not to scale (v labels the vibrational quantum numbers). A second dye laser further excites the molecules to a higher-lying $^2\Pi_{1/2}$ electronic state. Finally, a neodymium-doped yttrium-aluminium-garnet (Nd:YAG) pulsed laser ionizes the molecules. The value of the ionization potential (IP) as well as the wavelengths of the lasers used are shown. **c**, At zero centre-of-mass kinetic energy, the simulated rovibronic spectra have transition linewidths, $\Delta\nu$, at $T = 500$ K, of ~400 MHz (cyan line). At 30 keV, the linewidths can be reduced by up to three orders of magnitude (magenta line), limited by the natural linewidth of the transition. **d**, A spectrum of our current results (red and grey lines) is compared with previous results (blue dots)[17], displaying the linewidth reduction from ~60 GHz to ~150 MHz. The x axis shows the wavenumber of the first-step laser in cm^{-1}. The y axis shows the ion count rate in arbitrary units (a.u.). The error bars represent one standard deviation statistical uncertainty.

Due to their close-lying rotational states of opposite parity, molecules can be imbued with an enhanced sensitivity, of more than 11 orders of magnitude, to symmetry-violating properties, relative to atoms[5,6]. In addition, as the strength of symmetry-violating effects rapidly scales with atomic number, nuclear spin and nuclear deformation, molecules containing heavy, radioactive nuclei, such as the pear-shaped radium (Ra)[10], are predicted to further provide more than two orders of magnitude enhancement, relative to non-radioactive systems[11–16].

Radium monofluoride (RaF) molecules are particularly attractive systems to study the aforementioned physical phenomena, as their molecular structure has been suggested to be favourable for laser cooling, paving the way towards highly sensitive studies, and a diverse range of opportunities in fundamental physics research[13,17–19]. However, in contrast to atoms, laser-cooling molecules is substantially more complex. Due to their rotational and vibrational degrees of freedom, finding appropriate cycling transitions for laser cooling poses a major experimental challenge[20–27].

Here we performed precision studies of the rovibronic structure of $^{226}Ra^{19}F$. We present a three-step resonance ionization scheme that allows very sensitive measurements with a high rotational-state selectivity, while also improving the spectral resolution of our measurements by more than two orders of magnitude (Fig. 1d) with respect to previous experiments[17,19]. This allowed for precise measurements of the structure of these molecules and their energy levels that are suitable for fundamental physics studies. By employing a combination of narrow- and broad-band laser systems, we were able to address molecules in specific rotational levels, populated with yields as low as a few hundred per second, and immersed within a highly congested spectrum. Our achieved combination of experimental resolution, high sensitivity and low background is critical for the study of radioactive molecules, which are produced with small fluxes (<10^6 molecules per s), high temperatures (>2,000 K) and in contaminated environments. Additionally, our results provide an unambiguous identification and quantification of a laser cooling scheme of this molecule, which can be achieved by using only three lasers. This is an essential step towards achieving ultra-cold temperatures and performing symmetry-violating measurements with these molecules in dedicated future experiments.

Isotopes of radium were produced by impinging 1.4-GeV protons onto a uranium-carbide target. Following reactions with a CF_4 gas introduced into the target container, RaF^+ molecules were formed, extracted, mass separated and injected into a room-temperature radio-frequency trap, filled with He gas, which cooled and bunched them. Bunches of RaF^+, accelerated to 29.908(1) keV, were then sent towards the Collinear Resonance Ionization Spectroscopy (CRIS) setup at the Isotope Separator On Line Device Radioactive Ion Beam Facility at the European Organization for Nuclear Research (ISOLDE-CERN)[17,19,28] once every 20 ms. The high translational energy of the molecular bunch allows a significant reduction of the transitions' linewidth (Fig. 1c)[29,30]. The ions were neutralized in-flight by passing through a charge-exchange cell filled with a sodium vapour at a temperature of ~500 K, predominantly populating the $X^2\Sigma^+$ electronic ground state in the neutralization process[17,19]. The remaining ions were deflected from the neutral beam, which was then collinearly overlapped with three pulsed laser beams in an ultra high-vacuum (5×10^{-10} mbar) interaction region (Fig. 1a). Further details of the experimental setup can be found in Methods.

https://doi.org/10.1038/s41567-023-02296-w

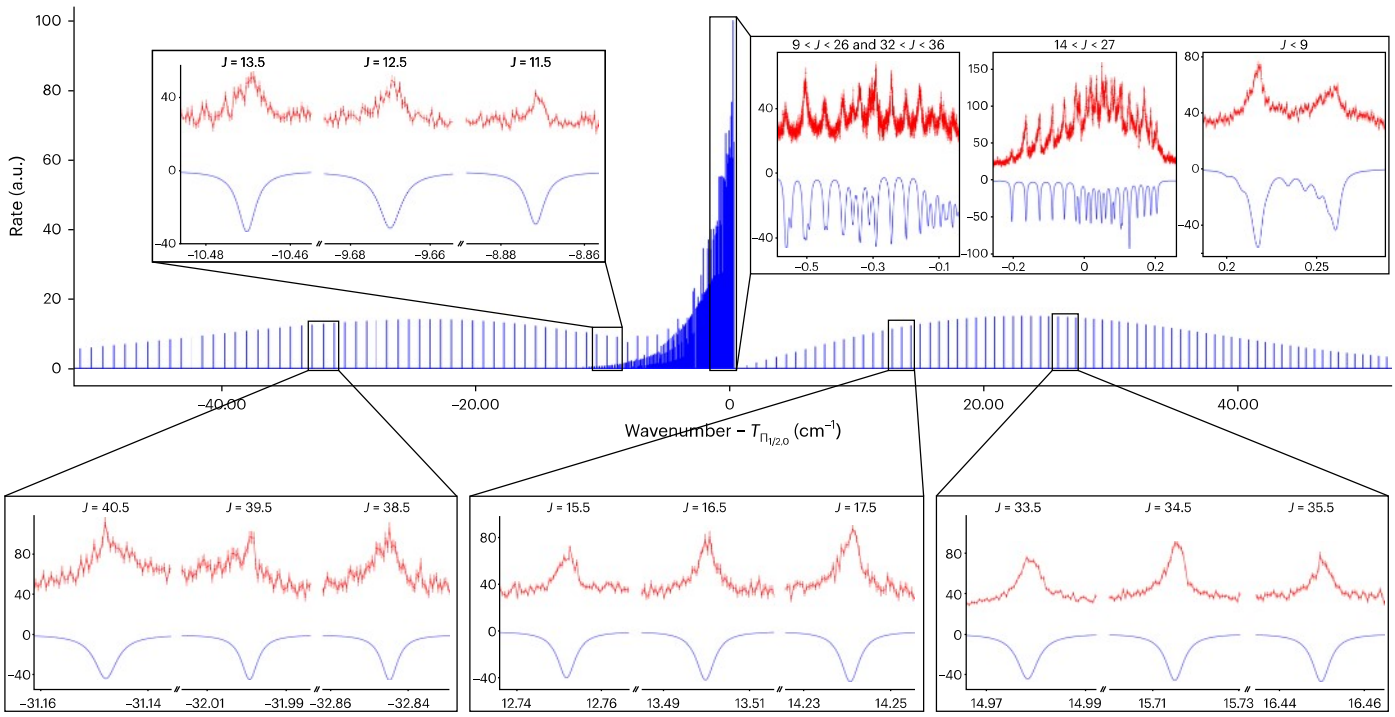

Fig. 2 | Example of measured spectra for the $0' \leftarrow 0''$ transitions. In the centre, in blue, we present the simulated RaF rovibronic spectrum obtained for $J \leq 100$, over a range of ~100 cm^{-1} (J is the rotational quantum number of the rotational levels in the $X^2\Sigma^+$ electronic level). Figures in magnified views show measured spectra for different regions (note the broken x axis present in some of the figures). The connected red dots show the experimental data, whereas the continuous blue line represents the best fit to the data. The error bars indicate one standard deviation statistical uncertainty. For each spectrum, we also show the covered range of J values (see the main text and Methods for the details of the fit). The values on the x axis correspond to the wavenumber of the first laser used in the excitation-ionization scheme, Doppler-corrected to the molecular rest frame and shifted by $T_{\Pi_{1/2},0} = 13284.427$ cm^{-1}. The rate on the y axis is given in arbitrary units (a.u.).

The RaF molecules were resonantly ionized by a stepwise three-photon process. Firstly, an injection-seeded Titanium:Sapphire (Ti:Sa) laser of tunable wavelength, with a linewidth of 20 MHz, was used to resonantly excite the rovibronic transitions of interest, between the vibrational ground or first-excited states of $X^2\Sigma^+$ and $A^2\Pi_{1/2}$, denoted as $0' \leftarrow 0''$ and $1' \leftarrow 1''$, respectively. Then, a tunable pulsed dye laser, with a linewidth of 10 GHz and wavenumber around 15,500 cm^{-1} (645 nm), resonantly excited molecules in the $A^2\Pi_{1/2}$ state to a higher-lying electronic state, tentatively assigned as a $^2\Pi_{1/2}$ (ref. 31) (an example of the spectra of the seconds step transition is shown in Extended Data Fig. 1). Finally, the electronically excited RaF molecules were ionized using a high-power (40 mJ per pulse) neodymium-doped yttrium-aluminium-garnet pulsed laser (Nd:YAG) at 532 nm (Fig. 1b). For a given wavelength of the first laser, the second laser wavelength, as well as the timing of the three lasers, were adjusted to maximize the measured ion signal. Resonant excitation to the higher-lying $^2\Pi_{1/2}$ electronic state, that lies closer to the ionization potential, enabled a longer-wavelength non-resonant laser to be used for the ionization step in this three-step scheme. This significantly reduced the non-resonant laser background, increasing the signal-to-noise ratio by an order of magnitude, compared to a two-step scheme[17,19], and facilitating an almost three orders of magnitude improved spectroscopic resolution.

The resonantly ionized RaF^+ molecules were deflected from the neutral bunch and detected by a MagneTOF ion detector. The wavelength of the ionization laser was chosen such that RaF molecules can only be ionized if they exist in the intermediate highly-excited electronic state, that is if the frequency of the first- and second-step lasers were on resonance with sequential transitions in the RaF molecule. The rovibronic spectra were obtained by counting the number of detected ions as a function of the wavelength of the first laser.

Figure 2 shows examples of experimental spectra, where the data are shown as red points and the fitted peak positions are shown in blue (similar spectra for the $1' \leftarrow 1''$ transitions, as well as more details about the $0' \leftarrow 0''$ transitions are shown in Extended Data Fig. 2 and Extended Data Fig. 3, respectively). In the centre, in blue, we show the full simulated spectrum of RaF for $J \leq 100$ and $T = 500$ K, over a range of ~100 cm^{-1} (J represents the rotational quantum number of the rotational levels in the $X^2\Sigma^+$ electronic level and T represents the temperature). For each measured spectrum, we also indicate the range of J values contained within it. The x axis shows the wavenumber of the first excitation laser, Doppler-corrected to the molecular rest frame and shifted by $T_{\Pi_{1/2},0} = 13284.427$ cm^{-1}. The temperature of the simulations was estimated based on the distribution of the population of the rotational levels in the $0' \leftarrow 0''$ vibrational spectrum. At this temperature, no states with $J > 100$ are expected to be observed in our experiment. However, the extraction of the physical parameters from the data depends only on the location of the measured transitions in frequency space and not on their intensity. Therefore, the obtained results are not affected by the choice of temperature.

We fitted the $0' \leftarrow 0''$ and $1' \leftarrow 1''$ transitions using an effective rotational Hamiltonian for each of the two electronic states. The fit was performed using the publicly available software PGOPHER[32]. For the fit, we used 60 spin-rotation transitions with values of J ranging from 1.5 to 40.5 for $0' \leftarrow 0''$ and 32 spin-rotation transitions with J values from 5.5 to 36.5 for $1' \leftarrow 1''$. The values of the molecular parameters obtained from the fitting procedure are shown in the second and third column of Table 1, for the $v = 0$ and $v = 1$ vibrational levels of the $X^2\Sigma^+$ and $A^2\Pi_{1/2}$ states, respectively (the resulting vibrational independent parameters are shown in Extended Data Table 1). A comparison with theoretical predictions, where available, is displayed in the last column.

https://doi.org/10.1038/s41567-023-02296-w

Table 1 | Fitted rotational parameters

Parameter	v=0 (cm^{-1})	v=1 (cm^{-1})	Theory[a] (cm^{-1})
B''_v	0.191985(5)[15]	0.19092(4)[6]	0.192[b]
			0.1909[c]
$10^7 \times D''_v$	1.40(5)[10]	1.2(3)[4]	
γ_v	0.00585(3)[7]	0.00581(5)[15]	0.006[d]
B'_v	0.191015(5)[15]	0.18997(4)[6]	0.192[b]
			0.1902[c]
$10^7 \times D'_v$	1.40(5)[10]	1.5(3)[4]	
p_v	−0.41071(3)[7]	−0.40978(10)[20]	
$10^7 \times p_{D,v}$	1.9(2)[5]	4.4(20)[15]	
$T_{\Pi_{1/2},v}$	13284.427(1)[20]	13278.316(1)[20]	13300[c]

In the first column, we list the parameter names, while the second and third columns show their values for the ground and first-excited vibrational states of the $X^2\Sigma^+$ and $A^2\Pi_{1/2}$ electronic manifolds. We show the 1σ statistical and systematic uncertainties in round and square brackets, respectively. In the last column we present the available theoretical predictions. [a] The theoretical studies report the equilibrium rotational parameters: $B_e \approx \frac{3}{2}B_0 - \frac{1}{2}B_1$ and $\gamma_e \approx \frac{3}{2}\gamma_0 - \frac{1}{2}\gamma_1$. [b] Ref. 14 [c] Ref. 33 [d] Ref. 34

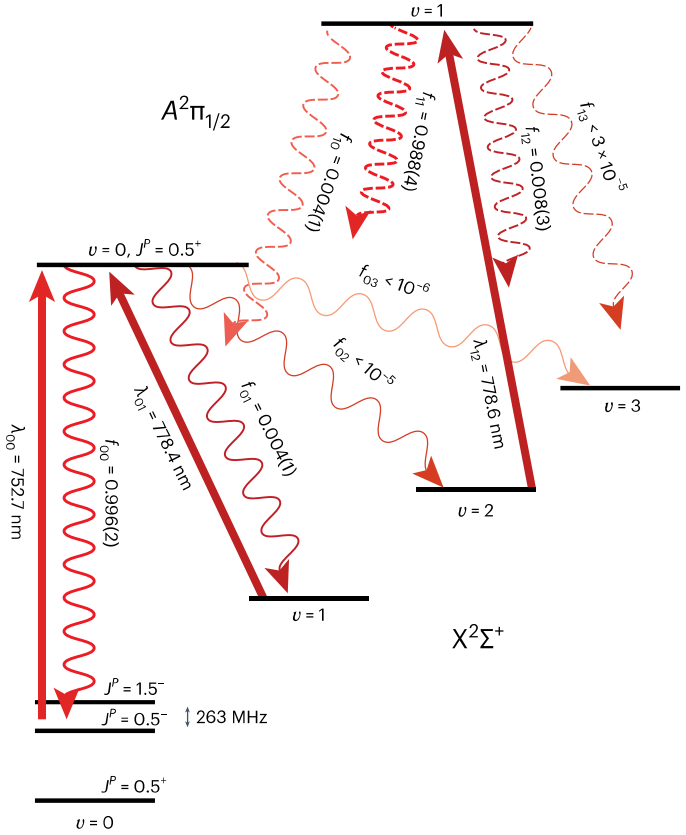

Fig. 3 | Proposed laser cooling scheme for RaF. The upwards-pointing arrows represent laser excitations between the ground, $X^2\Sigma^+$, and excited, $A^2\Pi_{1/2}$, electronic states. The wavelength of each laser ($\lambda_{v'v''}$) is shown (energy levels not shown to scale). The wavy, downwards-pointing arrows represent spontaneous emission from the $v' = 0$ (continuous lines) and $v' = 1$ (dashed lines) vibrational levels, including the associated Franck–Condon factors ($f_{v'v''}$). The labels v' and v'' represent the vibrational quantum number of the excited and ground electronic manifolds, respectively. The vibrational (v) and rotational (J) quantum numbers as well as the parity (+/−) are shown for the states of interest. Similar colours indicate similar values of the transition frequencies. We show in brackets the uncertainty associated with the calculated Franck–Condon factors (see Methods for details).

An excellent agreement is seen between the experimentally determined values and previous ab initio calculations[14,33,34]. A detailed description of the data analysis, as well as an in-depth explanation of the effective Hamiltonians employed, are presented in Methods.

In Fig. 3, we show a laser cooling scheme for RaF, requiring only three lasers. The location of the relevant spin-rotational levels in frequency space was obtained from the fitted rotational parameters. The Franck–Condon factors, $f_{v',v''}$, between the $X^2\Sigma^+$ and $A^2\Pi_{1/2}$ vibrational levels were calculated assuming a Morse potential for each of the two electronic states, parameterized using the rotational constants obtained in this work, B'_e and B''_e (Methods), as well as the vibrational constants and dissociation energies from ref. 17. The solid, upwards-pointing arrows represent laser excitations, while the sinusoidal ones represent spontaneous emission. One laser will be used to pump the main cooling transitions between the $J^P = 0.5^-$, $v = 0$ and $J^P = 1.5^-$, $v = 0$ levels of the $X^2\Sigma^+$ state and the $J^P = 0.5^+$, $v = 0$ level of the $A^2\Pi_{1/2}$ state (the '+' and '−' refer to the parity of the state, P). The use of these spin-rotational states will eliminate rotational branching, as described in ref. 20. Given that the two levels in the $X^2\Sigma^+$ are separated by 263(4) MHz, a single laser with modulated frequency would be able to address both of them simultaneously. Two other lasers are used to re-pump molecules that decay to the $v = 1$ and $v = 2$ vibrational levels of the $X^2\Sigma^+$ state, back into the main cooling cycle. The described approach would allow each molecule to scatter more than 10^5 photons on average before it ends up in a dark state, at a rate greater than 10^6 photons per second (given by the lifetime of the excited $A^2\Pi_{1/2}$ state, $\tau < 50$ ns)[17].

While previous low-resolution measurements presented evidence for the existence of a laser cooling scheme of RaF[17], our results quantitatively provide the spin-rotation levels suitable for such a scheme, as well as the associated Franck–Condon factors, facilitating an unambiguous pathway to laser-cooling this molecule. This will allow future experimental developments aiming to laser cool and trap RaF molecules for fundamental physics studies[8]. In order to achieve laser cooling over reasonably short distances, as well as increase the population in the relevant rotational levels, developments of efficient production methods of cold RaF beams are needed[35]. Compared to other alkaline-earth monohalides, RaF is, to our knowledge, the most favourable molecule for laser cooling, in terms of the diagonality of Franck–Condon factors[20] and relatively simple energy-levels structure. The absence of any electronic manifolds between the two electronic states used for laser cooling in RaF, is a major advantage for laser cooling[17], in contrast to BaF (ref. 36), the heaviest stable alkaline-earth monohalide.

Due to the inherent complexity and heavy mass of RaF molecules, a large number of rovibronic transitions, originating from states with different J, can lie very close to each other. The first-step laser can therefore excite several of them simultaneously, even with a linewidth as narrow as a few tens of MHz. By properly adjusting the wavelength of the second-step laser, we introduce additional J-selectivity such that only molecules from a given initial rotational state are ionized. This enabled the observation of individual transitions with initial J values from 0.5 up to 40.5. An example of this J-selection is shown in Fig. 4 (more examples are shown in the Extended Data Fig. 4). Transitions containing J values between 0.5 and 3.5 can be isolated from a large background of higher-J transitions despite these states being populated much more strongly. In the upper part, the red dots represent the data, while the blue line is the result of a fit to the data using a sum of six peaks and a constant background. The dashed green lines show the individual fitted peaks. The same fitted spectrum is compared in the bottom part to the spectrum without the $J < 4$ cut (black dashed line). Without the additional second-step J-selectivity, the displayed wavelength region contains J values up to 15.5 (marked as the vertical black lines), making the investigation of low-J transitions virtually impossible. The rate of

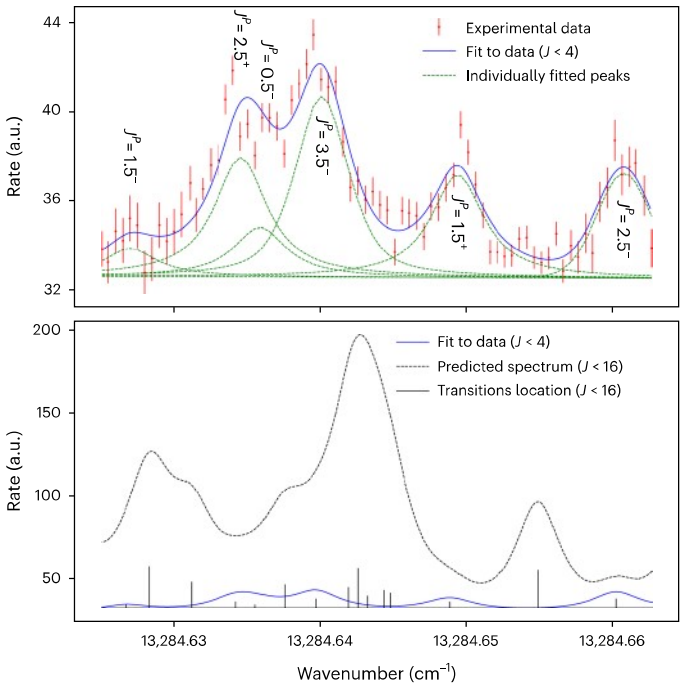

Fig. 4 | Measured spectra using second-step *J*-selectivity. In the upper part, the red dots represent the data while the blue continuous line is the result of a fit to the data, containing six peaks (shown in green) plus a constant background. The error bars show one standard deviation statistical uncertainty. For each peak we indicate the rotational quantum number, *J* and the parity of its ground rotational level. In the bottom part, the fit (blue line) is compared to the expected spectra without any cut on the *J* values range of the transitions (black dashed line). The black vertical lines mark the position of each transition (see the main text for the details of the fit).

molecules in the interaction region, populating states with $J < 4$ in our experiment was estimated to be between 50 and a few hundred per second. Hence, we can isolate and perform precision studies of particular transitions within a highly congested spectrum with high sensitivity, using the three-colour ionization scheme discovered herein.

Precision experiments using ^{226}RaF molecules, as well as the extension of such experiments to molecules containing Ra isotopes with nuclear spin larger than zero, such as ^{223,225}RaF, will enable highly sensitive studies of electroweak nuclear and leptonic properties. This will include searches for parity violation, through nuclear anapole moment measurements and combined parity and time-reversal violation searches, through investigations of the electron electric dipole moment, nuclear Schiff moment and nuclear magnetic quadrupole moment[5]. Such measurements can be performed using the lowest rotational and hyperfine levels of the ground electronic state[6,9].

The accuracy achieved in our experiment approaches what is required to guide astrophysical observations of radioactive molecules of importance in our understanding of stellar nucleosynthesis and astrochemistry, such as ^{26}AlF (ref. 37), ^{26}AlO (ref. 38) or ^{32}SiO (refs. 39,40). The rotational de-excitations of these molecules can be sensitively observed with a high spatial resolution using modern telescope facilities[41,42]. However, their identification requires a very precise knowledge of their rotational structure which can only be unambiguously obtained from laboratory measurements, achievable with the technique presented here.

In addition, several other radioactive molecules are predicted to possess an enhanced sensitivity to fundamental symmetry violations, such as RaOH (ref. 43), RaO (ref. 12), RaH (ref. 44), $RaOCH_3^+$ (refs. 45,46), PaF^{3+} (ref. 47) or $AcOH^+$ (ref. 48). However, their structure remains experimentally unknown. The described measurement technique can be used to investigate these and other short-lived radioactive molecules of fundamental physics interest. The extension of our current method to polyatomic molecules poses additional challenges, as extra degrees of freedom come into play. Further improvements in the resolution of the first-step transition (Methods), as well as the possibility of using the second-step laser to isolate individual transitions from complex molecular spectra, as described in this work, could allow the investigation of such species. The developments presented in this work are timely with respect to the current efforts to produce radioactive molecules for fundamental physics research at different facilities worldwide such as ISOLDE-CERN (Switzerland), the TRI-University Meson Facility (TRIUMF) (Canada), and the Facility for Rare Isotope Beams (FRIB) (US)[8].

Online content

Any methods, additional references, Nature Portfolio reporting summaries, source data, extended data, supplementary information, acknowledgements, peer review information; details of author contributions and competing interests; and statements of data and code availability are available at https://doi.org/10.1038/s41567-023-02296-w.

References

1. Tanabashi, M. et al. Review of particle physics: particle data groups. *Phys. Rev. D* **98**, 030001 (2018).
2. Hudson, J. J. et al. Improved measurement of the shape of the electron. *Nature* **473**, 493–496 (2011).
3. ACME collaboration. Order of magnitude smaller limit on the electric dipole moment of the electron. *Science* **343**, 269–272 (2014).
4. Cairncross, W. B. et al. Precision measurement of the electron's electric dipole moment using trapped molecular ions. *Phys. Rev. Lett.* **119**, 153001 (2017).
5. Safronova, M. S. et al. Search for new physics with atoms and molecules. *Rev. Mod. Phys.* **90**, 025008 (2018).
6. Altuntaş, E. et al. Demonstration of a sensitive method to measure nuclear-spin-dependent parity violation. *Phys. Rev. Lett.* **120**, 142501 (2018).
7. ACME Collaboration. Improved limit on the electric dipole moment of the electron. *Nature* **562**, 355–360 (2018).
8. Arrowsmith-Kron, G. et al. Opportunities for fundamental physics research with radioactive molecules. Preprint at *arXiv* https://doi.org/10.48550/arXiv.2302.02165 (2023).
9. Roussy, T. S. et al. An improved bound on the electron's electric dipole moment. *Science* **381**, 46–50 (2023).
10. Gaffney, L. P. et al. Studies of pear-shaped nuclei using accelerated radioactive beams. *Nature* **497**, 199–204 (2013).
11. Auerbach, N., Flambaum, V. V. & Spevak, V. Collective T-and P-odd electromagnetic moments in nuclei with octupole deformations. *Phys. Rev. Lett.* **76**, 4316–4319 (1996).
12. Flambaum, V. V. Electric dipole moments of actinide atoms and RaO molecule. *Phys. Rev. A* **77**, 024501 (2008).
13. Isaev, T. A., Hoekstra, S. & Berger, R. Laser-cooled RaF as a promising candidate to measure molecular parity violation. *Phys. Rev. A* **82**, 052521 (2010).
14. Kudashov, A. D. et al. Ab initio study of radium monofluoride (RaF) as a candidate to search for parity-and time-and-parity–violation effects. *Phys. Rev. A* **90**, 052513 (2014).
15. Sasmal, S., Pathak, H., Nayak, M. K., Vaval, N. & Pal, S. Relativistic coupled-cluster study of RaF as a candidate for the parity-and time-reversal-violating interaction. *Phys. Rev. A* **93**, 062506 (2016).
16. Gaul, K., Marquardt, S., Isaev, T. & Berger, R. Systematic study of relativistic and chemical enhancements of P, T-odd effects in polar diatomic radicals. *Phys. Rev. A* **99**, 032509 (2019).
17. Garcia Ruiz, R. F. et al. Spectroscopy of short-lived radioactive molecules. *Nature* **581**, 396–400 (2020).

18. Isaev, T.A. & Berger, R. Lasercooled radium monofluoride: a molecular all-in-one probe for new physics. Preprint at *arXiv* https://doi.org/10.48550/arXiv.1302.5682 (2013).
19. Udrescu, S. M. et al. Isotope shifts of radium monofluoride molecules. *Phys. Rev. Lett.* **127**, 033001 (2021).
20. Shuman, E. S., Barry, J. F. & DeMille, D. Laser cooling of a diatomic molecule. *Nature* **467**, 820–823 (2010).
21. Barry, J. F., McCarron, D. J., Norrgard, E. B., Steinecker, M. H. & DeMille, D. Magneto-optical trapping of a diatomic molecule. *Nature* **512**, 286–289 (2014).
22. Truppe, S. et al. Molecules cooled below the Doppler limit. *Nat. Phys.* **13**, 1173–1176 (2017).
23. Kozyryev, I. et al. Sisyphus laser cooling of a polyatomic molecule. *Phys. Rev. Lett.* **118**, 173201 (2017).
24. Anderegg, L. et al. Laser cooling of optically trapped molecules. *Nat. Phys.* **14**, 890–893 (2018).
25. Lim, J. et al. Laser cooled YbF molecules for measuring the electron's electric dipole moment. *Phys. Rev. Lett.* **120**, 123201 (2018).
26. Mitra, D. et al. Direct laser cooling of a symmetric top molecule. *Science* **369**, 1366–1369 (2020).
27. Jorapur, V., Langin, T.K., Wang, Q., Zheng, G. & DeMille, D. High density loading and collisional loss of laser cooled molecules in an optical trap. Preprint at *arXiv* https://doi.org/10.48550/arXiv.2307.05347 (2023).
28. Catherall, R. et al. The ISOLDE facility. *J. Phys. G* **44**, 094002 (2017).
29. Campbell, P., Moore, I. D. & Pearson, M. R. Laser spectroscopy for nuclear structure physics. *Prog. Part. Nucl. Phys.* **86**, 127–180 (2016).
30. Yang, X. F., Wang, S. J., Wilkins, S. G. & Garcia Ruiz, R. F. Laser spectroscopy for the study of exotic nuclei. *Prog. Part. Nucl. Phys.* **129**, 104005 (2022).
31. Athanasakis-Kaklamanakis, M. et al. Pinning down electron correlations in RaF via spectroscopy of excited states. Preprint at *arXiv* https://doi.org/10.48550/arXiv.2308.14862 (2023).
32. Western, C. M. PGOPHER: a program for simulating rotational, vibrational and electronic spectra. *J. Quant. Spectrosc. Radiat. Transf.* **186**, 221–242 (2017).
33. Zaitsevskii, A. et al. Accurate ab initio calculations of RaF electronic structure appeal to more laser-spectroscopical measurements. *J. Chem. Phys.* **156**, 044306 (2022).
34. Petrov, A. N. & Skripnikov, L. V. Energy levels of radium monofluoride RaF in external electric and magnetic fields to search for P-and T, P-violation effects. *Phys. Rev. A* **102**, 062801 (2020).
35. Hutzler, N. R., Lu, H. I. & Doyle, J. M. The buffer gas beam: an intense, cold, and slow source for atoms and molecules. *Chem. Rev.* **112**, 4803–4827 (2012).
36. Aggarwal, P. et al. Measuring the electric dipole moment of the electron in BaF. *Eur. Phys. J. D*, **72**, 197 (2018).
37. Kamiński, T. et al. Astronomical detection of radioactive molecule ^{26}AlF in the remnant of an ancient explosion. *Nat. Astron.* **2**, 778–783 (2018).
38. Chubb, K. L., Min, M., Kawashima, Y., Helling, C. & Waldmann, I. Aluminium oxide in the atmosphere of hot Jupiter WASP-43b. *Astron. Astrophys.* **639**, A3 (2020).
39. Fujiya, W., Hoppe, P., Zinner, E., Pignatari, M. & Herwig, F. Evidence for radiogenic sulfur-32 in type AB presolar silicon carbide grains? *Astrophys. J. Lett.* **776**, L29 (2013).
40. Cairnie, M., Forrey, R. C., Babb, J. F., Stancil, P. C. & McLaughlin, B. M. Rate constants for the formation of SiO by radiative association. *Mon. Notices Royal Astron. Soc.* **471**, 2481–2490 (2017).
41. Lacy, J. H., Richter, M. J., Greathouse, T. K., Jaffe, D. T. & Zhu, Q. Texes: a sensitive high-resolution grating spectrograph for the mid-infrared. *Publ. Astron. Soc. Pac.* **114**, 153–168 (2002).
42. Fomalont, E. B. et al. The 2014 ALMA long baseline campaign: an overview. *Astrophys. J. Lett.* **808**, L1 (2015).
43. Isaev, T. A., Zaitsevskii, A. V. & Eliav, E. Laser-coolable polyatomic molecules with heavy nuclei. *J. Phys. B* **50**, 225101 (2017).
44. Fazil, N. M., Prasannaa, V. S., Latha, K. V. P., Abe, M. & Das, B. P. RaH as a potential candidate for electron electric-dipole-moment searches. *Phys. Rev. A* **99**, 052502 (2019).
45. Yu, P. & Hutzler, N. R. Probing fundamental symmetries of deformed nuclei in symmetric top molecules. *Phys. Rev. Lett.* **126**, 023003 (2021).
46. Fan, M. et al. Optical mass spectrometry of cold $RaOH^+$ and $RaOCH_3^+$. *Phys. Rev. Lett.* **126**, 023002 (2021).
47. Zülch, C., Gaul, K., Giesen, S. M., Ruiz, R. F. G. & Berger, R. Cool molecular highly charged ions for precision tests of fundamental physics. Preprint at *arXiv* https://doi.org/10.48550/arXiv.2203.10333 (2022).
48. Oleynichenko, A. V., Skripnikov, L. V., Zaitsevskii, A. V. & Flambaum, V. V. Laser-coolable $AcOH^+$ ion for CP-violation searches. *Phys. Rev. A* **105**, 022825 (2022).

Methods

For this experiment, radium isotopes were produced by impinging 1.4-GeV protons onto a thick uranium-carbide target. By injecting CF_4 gas through a calibrated leak into the target container, radium-containing molecules were formed. Through surface ionization, RaF^+ was created and extracted using an electrostatic field. The isotopologue of interest for the present study, $^{226}Ra^{19}F^+$, was mass-selected using a high-resolution magnetic mass separator and then collisionally cooled in a radio-frequency quadrupole trap filled with room-temperature helium gas for up to 20 ms. After that, bunches of $^{226}Ra^{19}F^+$ were released, accelerated to an energy of 29.908(1) keV, and then sent to the Collinear Resonance Ionization Spectroscopy setup[49–53]. The energy of the molecular bunch allows a significant reduction of the measured transitions' linewidths[29,30]. This is possible because, during the acceleration, the initial energy spread of the ions is preserved, while their velocity increases, which leads to a reduction of the ion beam velocity spread along its axis of motion. At our acceleration voltage, the linewidths of the measured transitions can be reduced by up to three orders of magnitude, compared to a measurement performed on a thermal beam[29,30]. In practice, the observed linewidths are broader than this due to power broadening, variations in the acceleration voltage, collisions in the charge-exchange cell and the linewidth of the spectroscopy laser used. Reducing these effects will improve the resolution of the measured spectra.

Measured and fitted spectra, corresponding to $1' \leftarrow 1''$ rovibronic transitions, are presented in Extended Data Fig. 2, together with the rotational quantum numbers, J, that they contain. In the centre, we show the fitted spectrum simulated in PGOPHER for $J \leq 100$ and $T = 500$ K, over a region of ~70 cm^{-1}. The magnified views show different regions of the spectrum, with the red dots representing measured data, and the blue continuous line showing the best fit to the data. The x axis shows the wavenumber of the first-step laser, Doppler-corrected to the molecular rest frame and shifted by $T_{\Pi_{1/2},0} = 13284.427$ cm^{-1}. The y axis shows the rate in arbitrary units. During the experiment, the wavelength of the first-step Ti:Sa laser was measured with a wavemeter (WSU-2, HighFinesse) calibrated by measuring a reference wavelength provided by a rubidium-stabilized diode laser (DLC DL PRO 780, Toptica)[17]. Simultaneously, we measured the $5^2S_{1/2}, F = 2 \rightarrow 5^2P_{3/2}, F = 3$ transition in ^{87}Rb with the same wavemeter, as a reference, in order to correct for any measurement drifts. The wavenumbers shown in Fig. 2 and in Extended Data Fig. 2 were calculated using:

$$\tilde{\nu} = \tilde{\nu}_m - \left(\tilde{\nu}_m^{Rb} - \tilde{\nu}_0^{Rb}\right) \tag{1}$$

where $\tilde{\nu}_m$ and $\tilde{\nu}_m^{Rb}$ are the measured wavenumbers of the Ti:Sa laser and of the ^{87}Rb transition, respectively, while $\tilde{\nu}_0^{Rb}$ is the literature value of the reference ^{87}Rb transition[54]. Each peak used for the determination of the rotational Hamiltonian was fit with a Voigt profile plus a constant background, using the LMFIT Python package[55]. The number of peaks in a given scan was chosen based on the reduced χ^2 of the fit. The obtained central value of each peak, together with its associated uncertainty, were used as input in PGOPHER, in order to extract the rotational parameters.

The main sources of systematic uncertainties in our experimental setup were (the associated uncertainty in the measured wavenumber is given in brackets): variations in the ion beam's extraction voltage (1.2×10^{-4} cm^{-1}), changes in the beam energy during the charge-exchange process (<10^{-4} cm^{-1}), uncertainties in the measurement of the Rb reference frequency by the wavemeter (10^{-4} cm^{-1}), presence of stray magnetic and electric fields (<10^{-5} cm^{-1}) and AC Stark shifts due to the presence of the second- and third-step lasers (5×10^{-4} cm^{-1}). These uncertainties were added to the statistical uncertainty for each fitted line in the spectra, before performing the PGOPHER fit.

For the simulation of the spectrum in PGOPHER, the vibrational levels in the electronic ground state, $X^2\Sigma^+$, were described by the effective Hund's case (b) Hamiltonian:

$$H_{X^2\Sigma^+} = (B'' - D''\mathbf{N}^2)\,\mathbf{N}^2 + \gamma \mathbf{N}\cdot\mathbf{S} \tag{2}$$

where B'' is the rotational constant, D'' is the centrifugal distortion constant and γ is the spin-rotation constant. $\mathbf{N} = \mathbf{J} - \mathbf{S}$ and $\mathbf{S}$ are the molecular-rotational operator (excluding the electron spin) and electron-spin operator, respectively. The vibrational levels in the excited electronic state, $A^2\Pi$, were described by the effective Hund's case (a) Hamiltonian:

$$\begin{aligned} H_{A^2\Pi} &= T_\Pi - \tfrac{A_\Pi}{2} + (B' - D'\mathbf{N}^2)\,\mathbf{N}^2 - \\ &- \tfrac{1}{4}\{p + p_D\mathbf{N}^2, N_+S_+e^{-2i\phi} + N_-S_-e^{2i\phi}\} \end{aligned} \tag{3}$$

where $\{O,Q\} = OQ + QO$, T_Π represents the distance between the origins of the $v' = 0$ and $v' = 1$ vibrational levels of the $^2\Pi$ electronic manifold and the origins of the corresponding isovibrational levels of the $X^2\Sigma^+$ electronic manifold, while A_Π is the spin–orbit interaction. As rovibronic transitions to the $A^2\Pi_{3/2}$ electronic state were not measured, it wasn't possible to constrain both T_Π and A_Π simultaneously so A_Π was kept fixed at its previously measured value of 2067.6 cm^{-1} (ref. 17). p is the Λ-doubling parameter and p_D is the centrifugal distortion correction to p. $N_\pm$ and $S_\pm$ are the raising and lowering operators for the $\mathbf{N}$ and $\mathbf{S}$ operators defined above and ϕ is the electron orbital azimuthal angle. Because of the coupling between the rotation of the molecule and the electron orbital angular momentum, each level with a given quantum number J is split into two levels of opposite parity. Note that the terms in the Hamiltonians above are effective parameters, which include the small contributions of the other electronic states in the molecule[56]. The hyperfine splitting due to the fluorine nucleus is expected to be less than 100 MHz (ref. 33) and we were not able to observe this effect given our experimental resolution. The associated hyperfine Hamiltonian was therefore not included in the analysis. For laser cooling, the ground-state hyperfine sublevels of interest can be addressed using sidebands obtained from the modulation of the frequency of the laser used to pump the main cooling transition, similar to other laser-cooled molecules[20]. This will not influence the number of lasers needed, their frequencies or the calculated Franck–Condon factors.

From equations (2) and (3) we can see that in total there are nine parameters that we need to fit for, three for the ground and six for the excited state. Given the large parameter space, choosing initial values for the fit as close as possible to the true ones was crucial. It was also important to reduce the number of free parameters by using (approximate) theoretically and experimentally motivated constraints between them. These constraints were used only in the beginning of the fitting procedure, in order to have a fast convergence towards an optimal region of the parameter space. The only exception was for the A_Π parameter which was kept fixed at its previously measured value of 2,067.6 cm^{-1} (ref. 17).

We started the fitting procedure with $0' \leftarrow 0''$ rovibronic transitions. The rotational constants, B, of the $X^2\Sigma^+$ and $A^2\Pi_{1/2}$ electronic states were calculated in ref. 14 to be equal to 0.192 cm^{-1}. Based on the spacing between the well-separated measured peaks (located on the left and right side of the spectrum shown in Fig. 2), we were able to obtain two approximate constraints using combination differences:

$$\begin{aligned} B'' - B' &= 0.001\,\text{cm}^{-1} \\ p &= 6B' - \gamma - 1.552\,\text{cm}^{-1} \end{aligned} \tag{4.}$$

Hence, we set the initial rotational constants to $B'' = 0.192$ cm^{-1} and $B' = 0.191$ cm^{-1}. The initial value of T_Π was initially set to 14315 cm^{-1}, according to ref. 17, while γ was set to 0.006 cm^{-1} (ref. 33). For a Morse potential, the centrifugal distortion constant can be written in terms of the rotational constant as:

$$D = \frac{4B^3}{\omega^2} \tag{5}$$

where ω is the vibrational constant of the electronic level, which in our case for the $X^2\Sigma^+$ and $A^2\Pi_{1/2}$ states it is equal to $\omega_{X^2\Sigma^+} = 441.8\ cm^{-1}$ and $\omega_{A^2\Pi_{1/2}} = 435.5\ cm^{-1}$ (ref. 17). Together with the values of the rotational constants considered above, the initial values for the centrifugal distortion constants were set to: $D'' = 1.45 \times 10^{-7}\ cm^{-1}$ and $D' = 1.47 \times 10^{-7}\ cm^{-1}$. Initially p_D was set to zero.

Using these initial values of the parameters, we were able to assign the two bandheads present in the simulations and in the data to their respective transition branches. The location of the bandheads for the $0' \leftarrow 0''$ transitions is indicated with green arrows in the spectrum shown in Extended Data Fig. 3. Red dots represent the data, while the blue line is the fit to the data. The x axis corresponds to the wavenumber of the first laser used in the excitation-ionization scheme, Doppler-corrected to the molecular rest frame and shifted by $T_{\Pi_{1/2},0} = 13284.427\ cm^{-1}$. The y axis shows the rate in arbitrary units. This made the assignment of the measured transitions to the right branches substantially easier.

The fitting procedure started with only two free parameters: the rotational constant of the ground state, B'', and the centre of the excited state, T_Π. In PGOPHER, each measured transition is assigned to the closest transition in the simulated spectrum. Initially, only isolated lines, from the right and left sides of the simulated spectrum shown in Fig. 2, were used for the fit, as the assignment between the measured and simulated spectra was relatively easy. We then gradually removed the initial constraints, hence allowing other rotational parameters to vary, and we also added lines from the congested regions of the spectrum to the fit. In the end, all the molecular parameters were set as free parameters and 60 rovibronic transitions were used for the fit. For certain scans, extra peaks were present in the simulated spectrum relative to the measured ones. These extra peaks could be removed by placing simple cuts on the range of J values used in the simulation (as shown in Fig. 2), depending on the frequency of the second-step laser. We concluded that this effect is a consequence of the second-step J-selectivity described in the current work. An example of this effect is shown in Extended Data Fig. 4. We show three measurements (scans of the first-step laser) taken with the wavenumber of the second-step laser, Doppler-shifted to the molecular rest frame, being 15485.23(2) cm^{-1}, 15485.39(2) cm^{-1} and 15485.56(2) cm^{-1}. By increasing the frequency of the second-step laser, we are able to see transitions from levels with higher J values in the $A^2\Pi_{1/2} \leftarrow X^2\Sigma^+$ spectrum, increasing the maximum value of J from $J_{max} = 25.5$ to $J_{max} = 27.5$.

The second excited state used in the measurement scheme was tentatively assigned as a $^2\Pi_{1/2}$ state[31]. This was based on the shape of the spectrum of the second-step transition, obtained by scanning the frequency of the pulsed dye laser, while the frequency of the first-step laser was kept fixed. In order to make sure a wide range of J values was covered by the first step, the narrowband injection-seeded Ti:Sa laser, seeded by a Matisse 2 TS, was replaced with a grating Ti:Sa laser with a linewidth of 2 GHz for this study[17]. An example of such a scan is shown in Extended Data Fig. 1, for a wavenumber of the first-step laser of 13285.69(2) cm^{-1} (Doppler-corrected to the molecular rest frame). The red dots represent the measured data, while the blue line is the best fit to the data obtained in PGOPHER, assuming a $^2\Pi_{1/2}$ state for the second excited state. As seen in the figure, the fit is in good agreement with data over a frequency range of more than 30 cm^{-1}.

For the $1' \leftarrow 1''$ transitions we employed the same effective Hamiltonians mentioned above. We set the initial values of the parameters to the ones obtained from the fit to the $0' \leftarrow 0''$ transitions and we only allowed B'', B', p and T_Π to vary initially (A_Π was still kept fixed at 2,067.6 cm^{-1}). After several fitting iterations in PGOPHER, we allowed all the parameters to vary, including 32 rovibronic transitions in the final fit.

The parameters obtained for $v = 0$ and $v = 1$ vibrational levels of the $X^2\Sigma^+$ and $A^2\Pi_{1/2}$ electronic levels are reported in Table 1. For the location of the vibrational levels in the excited electronic state, relative to the isovibrational levels in the ground electronic state, we defined $T_{\Pi_{1/2}} = T_\Pi - \frac{A_\Pi}{2}$. Except for $T_{\Pi_{1/2}}$, all the other parameters have a dependence on the vibrational quantum number, v, which can be parameterized, to first order in v, as:

$$X_v = X_e - \alpha_X\left(v + \frac{1}{2}\right) \quad (6)$$

where X_e can be any of the rotational parameters considered and X_v is the extracted value of that parameter in the vibrational level v. The obtained values for X_e and α_X for all the rotational parameters are shown in Extended Data Table 1.

The locations in frequency space of the spin-rotational levels proposed for the laser cooling scheme (Fig. 3) were obtained directly from the effective Hamiltonians (equations (2) and (3)) using the fitted rotational parameters (Table 1). The associated Franck–Condon factors were calculated by approximating the ground and excited electronic states using a Morse potential (similar to ref. 20), which is a very good approximation in diatomic molecules, especially for low-lying electronic states. The potential for each level was parameterized using the rotational parameters B_e obtained in this work (Extended Data Table 1), together with the previously measured vibrational constant and dissociation energy[17]. The uncertainty on these parameters propagates to an uncertainty in the shape of the used potential and thus, to an uncertainty in the resulting Franck–Condon factors. The uncertainties associated with (or the upper bounds to) the calculated Franck–Condon factors are displayed in Fig. 3 and correspond to a 90% confidence interval.

Data availability

The processed spectra used for the analysis and supporting the findings of these studies are provided in ref. 57. The complete raw data is available from the corresponding authors upon request. Source data are provided with this paper.

Code availability

The Python script used for fitting individual peaks as well as a PGOPHER file containing a fitted spectra for the $0' \leftarrow 0''$ and $1' \leftarrow 1''$ rovibronic transitions are provided in ref. 57. The code used for processing the raw data is available from the corresponding authors upon request.

References

49. Flanagan, K. T. et al. Collinear resonance ionization spectroscopy of neutron-deficient francium isotopes. *Phys. Rev. Lett.* **111**, 212501 (2013).
50. De Groote, R. P. et al. Use of a continuous wave laser and pockels cell for sensitive high-resolution collinear resonance ionization spectroscopy. *Phys. Rev. Lett.* **115**, 132501 (2015).
51. Garcia Ruiz, R. F. et al. High-precision multiphoton ionization of accelerated laser-ablated species. *Phys. Rev. X* **8**, 041005 (2018).
52. Vernon, A. R. et al. Optimising the Collinear Resonance Ionisation Spectroscopy (CRIS) experiment at CERN-ISOLDE. *Nucl. Instrum. Methods. Phys. Res. B* **463**, 384–389 (2020).
53. Ágota, K. et al. Resonance ionization schemes for high resolution and high efficiency studies of exotic nuclei at the CRIS experiment. *Nucl. Instrum. Methods Phys. Res. B* **463**, 398–402 (2019).
54. Steck, D. A. Rubidium 87 D line data, revision 2.2.1 https://steck.us/alkalidata/ (21 November 2019).
55. Newville, M. et al. LMFIT: non-linear least-square minimization and curve-fitting for Python. *Zenodo* https://doi.org/10.5281/zenodo.11813 (2014).
56. Brown, J.M. & Carrington, A. *Rotational Spectroscopy of Diatomic Molecules* (Cambridge Univ. Press, 2003).
57. Udrescu, S.M. et al. Precision spectroscopy and laser cooling scheme of a radium-containing molecule. figshare https://doi.org/10.6084/m9.figshare.23703981 (2023).

Acknowledgements
This work was supported by the Office of Nuclear Physics, US Department of Energy, under grants DE-SC0021176 and DE-SC0021179 (S.M.U., S.G.W., R.F.G.R., A.J.B.); the MISTI Global Seed Funds (S.M.U.); Deutsche Forschungsgemeinschaft (DFG, German Research Foundation) – Projektnummer 328961117 – SFB 1319 ELCH (A.A.B., R.B., K.G., T.F.G.); STFC grants ST/P004423/1 and ST/V001116/1 (M.L.B., K.T.F., H.A.P., J.R.R., J.W.); Belgian Excellence of Science (EOS) project No. 40007501 (G.N.); KU Leuven C1 project No. C14/22/104 (M.A.-K., T.E.C., R.P.d.G., G.N.); FWO project No. G081422N (M.A.-K., G.N.); International Research Infrastructures (IRI) project No. I001323N (M.A.-K., T.E.C., R.P.d.G., A.D., S.G., L.L., G.N., B.v.d.B.); the European Unions Grant Agreement 654002 (ENSAR2); LISA: European Union's H2020 Framework Programme under grant agreement no. 861198 (M.A., D.H., M.N., J.W.); The Swedish Research Council (2016-03650 and 2020-03505) (D.H., M.N.). The National Key RD Program of China (No: 2022YFA1604800) (X.F.Y.) and the National Natural Science Foundation of China (No:12027809). (X.F.Y.). We thank R. Field, T. Isaev, L. Skripnikov and A. Zaitsevskii for insightful discussions.

Author contributions
S.M.U. and S.G.W. contributed equally to this work. S.M.U. led the data analysis and S.G.W. led the experiments. S.M.U., S.G.W., A.A.B., M.A.-K., R.F.G.R., M.A., I.B., R.B., M.L.B., C.L.B., A.J.B., K.C., T.E.C., A.D., S.F., K.G., S.G., T.F.G., R.H., A.K., S.K., L.L., M.N., H.A.P., J.R.R., S.R., B.v.d.B., A.R.V., Q.W., J.W. and C.Z. performed the experiment. S.M.U. and A.A.B. performed the data analysis. S.M.U. prepared the figures. S.M.U., S.G.W. and R.F.G.R. prepared the manuscript. All authors discussed the results and contributed to the manuscript at different stages.

Competing interests
The authors declare no competing interests.

Additional information
Extended data is available for this paper at https://doi.org/10.1038/s41567-023-02296-w.

Supplementary information The online version contains supplementary material available at https://doi.org/10.1038/s41567-023-02296-w.

Correspondence and requests for materials should be addressed to S. M. Udrescu, S. G. Wilkins or R. F. Garcia Ruiz.

Peer review information *Nature Physics* thanks Alec Owens, Aiko Takamine and the other, anonymous, reviewer(s) for their contribution to the peer review of this work.

https://doi.org/10.1038/s41567-023-02296-w

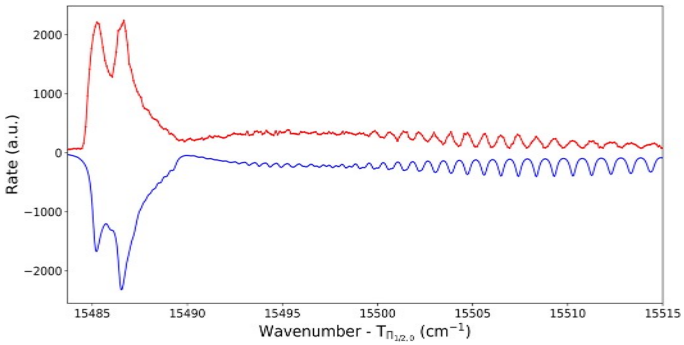

Extended Data Fig. 1 | Example of rovibronic spectra of the second step used in the experimental scheme. The red dots represent the measured data while the blue line is the best fit to the data. The x-axis corresponds to the wavenumber of the second laser used in the excitation-ionization scheme, Doppler-corrected to the molecular rest frame and shifted by $T_{\Pi_{1/2,0}} = 13284.427\ \mathrm{cm}^{-1}$ (see Methods for the details of the fit). The y-axis shows the rate in arbitrary units (a.u.). The errorbars show one standard deviation statistical uncertainty.

https://doi.org/10.1038/s41567-023-02296-w

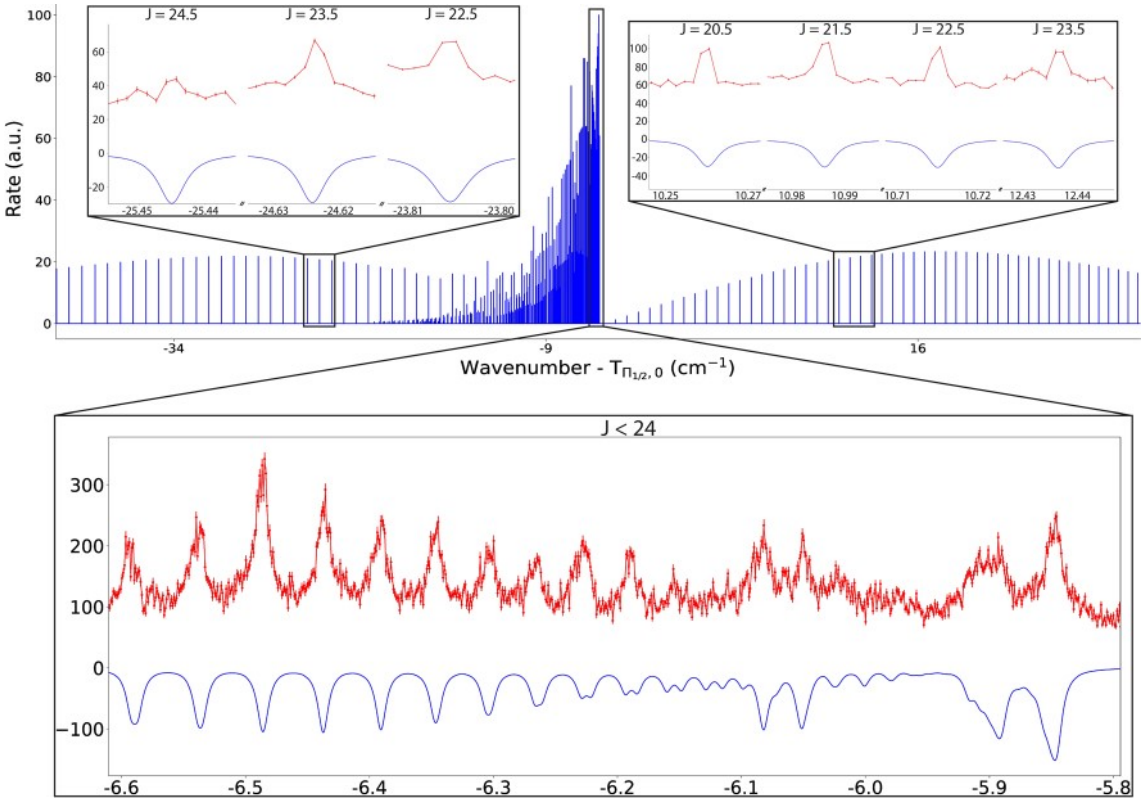

Extended Data Fig. 2 | Example of measured spectra for the $1' \leftarrow 1''$ transitions. In the centre, in blue, we present the simulated RaF spectrum for $J \leq 100$, over a range of ~ 70 cm^{-1} (J is the rotational quantum number of the rotational levels in the $X^2\Sigma^+$ electronic level). Figures in magnified views show measured spectra for different regions (note the broken x-axis present in some of the figures). The connected red dots show the experimental data, whereas the continuous blue line represents the best fit to the data. The errorbars indicate one standard deviation statistical uncertainty. For each spectrum we also show the covered range of J-values (see the main text and Methods for the details of the fit). The values on the x-axis correspond to the wavenumber of the first laser used in the excitation-ionization scheme, Doppler-corrected to the molecular rest frame and shifted by $T_{\Pi_{1/2,0}} = 13284.427\ cm^{-1}$. On the y-axis we show the rate in arbitrary units (a.u.).

https://doi.org/10.1038/s41567-023-02296-w

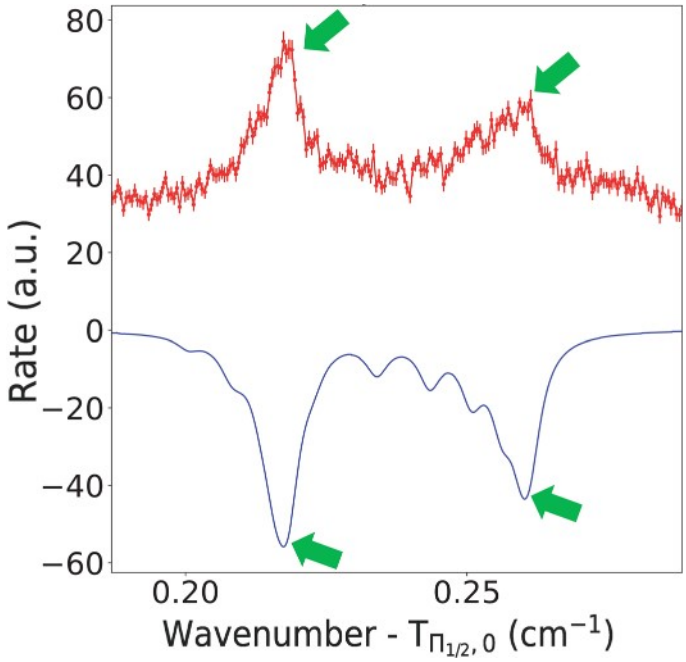

Extended Data Fig. 3 | Location of the bandheads in the $0' \leftarrow 0''$ rovibronic transitions. The bandhead locations are indicated with green arrows. The red dots represent the measured data while the blue line is the best fit to the data (see Methods for the details of the fit). The x-axis corresponds to the wavenumber of the first laser used in the excitation-ionization scheme, Doppler-corrected to the molecular rest frame and shifted by $T_{\Pi_{1/2,0}} = 13284.427\ cm^{-1}$. The y-axis shows the rate in arbitrary units (a.u.). The errorbars show one standard deviation statistical uncertainty.

https://doi.org/10.1038/s41567-023-02296-w

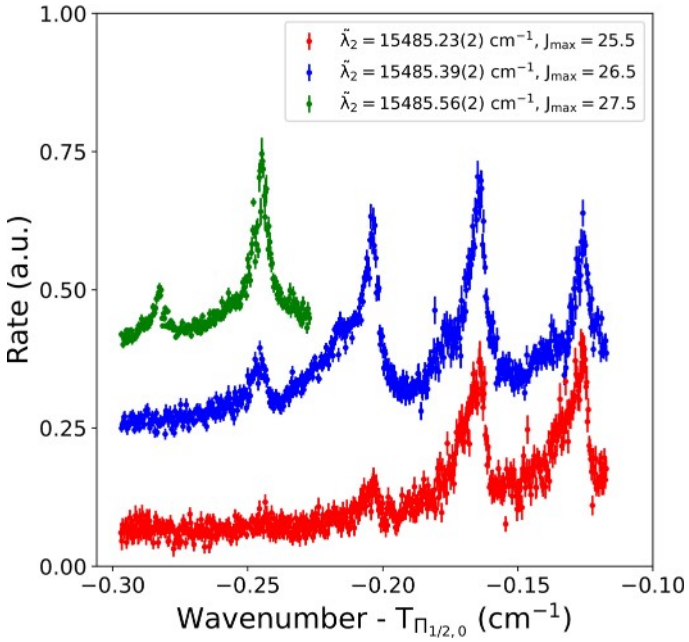

Extended Data Fig. 4 | Example of $0' \leftarrow 0''$ rovibronic spectra for different second-step laser wavenumbers. The red, blue and green dots correspond to separate scans of the first step laser, while the second-step laser wavenumber, Doppler-shifted to the molecular rest frame, was kept fixed at 15485.23(2) cm^{-1}, 15485.39(2) cm^{-1}, and 15485.56(2) cm^{-1}, respectively. Increasing the wavenumber of the second-step laser facilitated the observation of new transitions starting from levels with higher rotational quantum numbers, J, in the $A^2\Pi_{1/2} \leftarrow X^2\Sigma^+$ spectrum (the new peaks appearing on the left). The maximum J-value of the shown spectra increases from $J_{max} = 25.5$ to $J_{max} = 27.5$. The x-axis corresponds to the wavenumber of the first laser used in the excitation-ionization scheme, Doppler-corrected to the molecular rest frame and shifted by $T_{\Pi_{1/2,0}} = 13284.427$ cm^{-1}. The y-axis shows the rate in arbitrary units (a.u.). The errorbars show one standard deviation statistical uncertainty.

https://doi.org/10.1038/s41567-023-02296-w

Extended Data Table 1 | Vibrationally independent rotational constants of the $X^2\Sigma^+$ and $A^2\Pi_{1/2}$ electronic states

Parameter	This work
B''_e	0.19252(2)[4]
α''_B	0.00107(4)[6]
$10^7 \times D''_e$	1.50(17)[25]
$10^7 \times \alpha''_D$	0.20(31)[41]
γ_e	0.00587(5)[13]
α_γ	0.00004(6)[17]
B'_e	0.19154(2)[4]
α'_B	0.00105(4)[6]
$10^7 \times D'_e$	1.35(17)[25]
$10^7 \times \alpha'_D$	-0.10(31)[41]
p_e	-0.41118(7)[15]
α_p	-0.0009(1)[2]
$10^7 \times p_{D,e}$	0.7(10)[10]
$10^7 \times \alpha_{pD}$	-2.5(20)[16]

The first column shows the names of the parameters, while the second column shows their values in cm^{-1}. We show the 1σ statistical and systematic uncertainties in round and square brackets, respectively.

4.3 Article 3: Observation of the Distribution of Nuclear Magnetization in a Molecule

This article (S. Wilkins, S.-M. Udrescu, et al., "Observation of the distribution of nuclear magnetization in a molecule", arXiv preprint arXiv:2311.04121 (2023).) presents the first high-resolution, rotationally and hyperfine resolved spectroscopy of a radioactive molecule, ^{225}RaF, together with the observation of the effect of the distribution of the nuclear magnetization in a molecule. To our knowledge, this is the first time this effect has been observed in a molecule. By comparison with the measured hyperfine structure, the accuracy of *ab initio* many-body electronic structure calculations was confirmed at $< 1\%$ level. Similar calculations were then used to predict the magnitude of various nuclear effects on the molecular energy levels in RaF, confirming the high sensitivity of this molecule to such effects. For this article, under review in Science (2024), I was involved in the experiment, I led the data analysis and the analytical theoretical calculations, I prepared the figures and the different drafts of the manuscript, including the initially submitted version, as well as the subsequent, revised ones and I was involved in the submission process.

Observation of the distribution of nuclear magnetization in a molecule

S. G. Wilkins[1,*,†], S. M. Udrescu[1,*,‡], M. Athanasakis-Kaklamanakis[2,3], R. F. Garcia Ruiz[1,§], M. Au[4,5], I. Belošević[6], R. Berger[7], M. L. Bissell[8], A. A. Breier[9], A. J. Brinson[1], K. Chrysalidis[4], T. E. Cocolios[3], R. P. de Groote[3], A. Dorne[3], K. T. Flanagan[8,10], S. Franchoo[11], K. Gaul[7], S. Geldhof[3], T. F. Giesen[9], D. Hanstorp[12] R. Heinke[4], T. Isaev[13], Á. Koszorús[2], S. Kujanpää[14], L. Lalanne[3], G. Neyens[3], M. Nichols[12], H. A. Perrett[8], J. R. Reilly[8], L. V. Skripnikov[13], S. Rothe[4], B. van den Borne[3], Q. Wang[15], J. Wessolek[8], X. F. Yang[16], C. Zülch[7]

[1] *Massachusetts Institute of Technology, Cambridge, MA 02139, USA*
[2] *Experimental Physics Department, CERN, CH-1211 Geneva 23, Switzerland*
[3] *KU Leuven, Instituut voor Kern- en Stralingsfysica, B-3001 Leuven, Belgium*
[4] *Systems Department, CERN, CH-1211 Geneva 23, Switzerland*
[5] *Department Chemie, Johannes Gutenberg-Universitat Mainz, D-55099 Mainz, Germany*
[6] *TRIUMF, 4004 Wesbrook Mall, Vancouver, BC V6T 2A3, Canada*
[7] *Fachbereich Chemie, Philipps-Universität Marburg, Hans-Meerwein-Straße 4, 35032 Marburg, Germany*
[8] *School of Physics and Astronomy, The University of Manchester, Manchester M13 9PL, United Kingdom*
[9] *Laboratory for Astrophysics, Institute of Physics, University of Kassel, 34132 Kassel, Germany*
[10] *Photon Science Institute, The University of Manchester, Manchester M13 9PY, United Kingdom*
[11] *Laboratoire Irène Joliot-Curie, F-91405 Orsay, France*
[12] *Department of Physics, University of Gothenburg, SE-412 96 Gothenburg, Sweden*
[13] *Affiliated with an institute covered by a cooperation agreement with CERN*
[14] *Department of Physics, University of Jyväskylä, Survontie 9, Jyväskylä, FI-40014, Finland*
[15] *School of Nuclear Science and Technology, Lanzhou University, Lanzhou 730000, People's Republic of China*
[16] *School of Physics and State Key Laboratory of Nuclear Physics and Technology, Peking University, Beijing 100971, China*

Correspondence: [†]wilkinss@mit.edu, [‡]sudrescu@mit.edu, [§]rgarciar@mit.edu
[*]These authors contributed equally to this work.

Rapid progress in the experimental control and interrogation of molecules, combined with developments in precise calculations of their structure, are enabling new opportunities in the investigation of nuclear and particle physics phenomena. Molecules containing heavy, octupole-deformed nuclei such as radium are of particular interest for such studies, offering an enhanced sensitivity to the properties of fundamental particles and interactions. Here, we report precision laser spectroscopy measurements and theoretical calculations of the structure of the radioactive radium monofluoride molecule, ^{225}Ra^{19}F. Our results allow fine details of the short-range electron-nucleus interaction to be revealed, indicating the high sensitivity of this molecule to the distribution of magnetization, currently a poorly constrained nuclear property, within the radium nucleus. These results provide a direct and stringent test of the description of the electronic wavefunction inside the nuclear volume, highlighting the suitability of these molecules to investigate subatomic phenomena.

INTRODUCTION

Recent developments in the synthesis and manipulation of molecular systems are opening up a diverse range of opportunities in fundamental physics research [1–5]. Precision measurements in molecules [3–6], combined with the development of *ab initio* molecular theory [7–11], offer a compelling avenue for exploring various aspects of nuclear and particle physics [3, 4]. The structure of certain molecular states can be highly sensitive to subtle details of electron-nucleon and nucleon-nucleon interactions within the constituent nuclei of the molecule. As these effects scale rapidly with the proton number, nuclear size, nuclear spin, and nuclear deformation [3, 12–18] molecules containing heavy radioactive nuclei, such as radium monofluoride, RaF, are of particular interest for fundamental physics studies [14–16, 19, 20]. The radioisotope ^{225}Ra (half-life of 14.9 days), with 88 protons and 137 neutrons, is expected to possess a rare nuclear octupole deformation [21], boosting its sensitivity to both symmetry-conserving and symmetry-violating nuclear properties by more than three orders of magnitude with respect to stable isotopes [12–16, 19–23]. The former effects are critical to guide our understanding of the nuclear force and the emergence of collective nuclear phenomena, while the latter could provide answers to some of the most pressing questions in our understanding of the universe [3, 23]. Measurements of the breaking

of parity ($\mathcal{P}$)- and time-reversal ($\mathcal{T}$) symmetries could explain the nature of dark matter, the origin of the overwhelming imbalance between matter and anti-matter in the universe, or settle the decades-long search for charge-conjugation and parity ($\mathcal{CP}$)-violation in the strong force [3–5].

The ability to unravel nuclear and particle physics phenomena from experimental measurements on molecules is limited by the combined precision that can be achieved experimentally and theoretically. On the theoretical side, a detailed understanding of the electronic wavefunction inside of the nuclear volume is essential to reliably extract fundamental physics information from measurements [12–16]. Therefore, determining observables that are sensitive to the electron-nucleon interaction within the nucleus, such as the molecular hyperfine structure, is critical.

Here, we report precision laser spectroscopy measurements of the hyperfine structure of the ^{225}Ra^{19}F molecule. With a lifetime on the order of just days, our results represent a major milestone in precision studies of short-lived radioactive molecules. We combine these with state-of-the-art molecular structure calculations to reveal previously unknown details of the electron-nucleus interaction in this molecule. This enables a clear observation of the effect of the ^{225}Ra nuclear magnetization distribution on the molecular energy levels. This effect has been previously observed in atoms [24] but, to our knowledge, has never been measured before in a molecule. These findings exemplify the extreme sensitivity of the RaF molecule to properties of the Ra nucleus, and provide a direct and stringent test of the description of the electronic wavefunction within the nuclear volume.

EXPERIMENTAL SETUP

The experiment was performed using the Collinear Resonance Ionization Spectroscopy (CRIS) setup at ISOLDE-CERN [19, 20, 25]. A simplified version of the experimental setup is illustrated in Fig. 1A. The RaF molecules were created by impinging 1.4-GeV protons upon a uranium carbide target (UC), followed by the injection of CF_4 gas inside the target container at a temperature greater than 2000 K. The RaF^+ isotopologues of interest were extracted, mass selected, then trapped and bunched in a radiofrequency quadrupole (RFQ) trap filled with He gas at room temperature for up to 20 ms. Bunches of RaF^+ were subsequently released, accelerated to 29908(1) eV, neutralized in a charge-exchange cell filled with a Na vapor at a temperature of $T \approx$ 500 K and then entered the experimental interaction region.

There, they were collinearly overlapped with three pulsed lasers in a resonance ionization scheme. The first laser employed was a Ti:Sapphire with a linewidth of 20 MHz, which was used to excite transitions between rotational and hyperfine levels in the $X\ ^2\Sigma^+(v''=0)$ electronic ground state and the first excited $A\ ^2\Pi_{1/2}(v'=0)$ electronic state (Fig. 1B). v'' and v' label the vibrational quantum numbers in the two electronic manifolds. Then, a pulsed dye laser (PDL), with a linewidth of 15 GHz, was used to further excite the molecules to a higher-lying, $^2\Pi_{1/2}$, electronic state [26], from which the molecules were ionized by a third, high-power 532-nm Nd:YAG laser (40 mJ). The resulting RaF^+ ions were deflected from the neutral bunch and counted using an ion detector as a function of the first laser wavenumber, leading to the observed spectra (Fig. 1C). This laser ionization scheme allowed us to improve our resolution by more than two orders of magnitude and increase the signal-to-noise ratio by one order of magnitude compared to previous experiments [19, 20], achieving a transition linewidth of 150 MHz. This enabled an unambiguous observation of the hyperfine splitting in ^{225}RaF due to the ^{225}Ra nucleus (nuclear spin I = 1/2), despite its short lifetime and small rates in the interaction region (as low as 50 molecules per second in a given rotational state). A more detailed description of the experimental setup can be found in Ref. [26].

TABLE I. Rotational and hyperfine parameters in units of cm^{-1} for $X\ ^2\Sigma^+(v''=0)$ and $A\ ^2\Pi_{1/2}(v'=0)$ electronic manifolds of ^{225}Ra^{19}F. The 1σ statistical and systematic uncertainties are shown in round and square brackets, respectively. In the last two columns, values of these parameters obtained from previous experimental and theoretical studies are presented.

Parameter	This work	Exp. (Lit.)	Theory (Lit.)
B''	0.192070(5)[15]	0.19205(3)[5][a]	0.1910[b]
$A_\parallel$	-0.5692(5)[20]	-	-0.5690[55][c]
$A_\perp$	-0.5445(2)[8]	-	-0.5470[55][c]
T_Π	13284.532(5)[20]	13284.544(50)[20][d]	-
B'	0.191100(15)[45]	0.19108(3)[5][a]	0.1903[b]
p	-0.4109(15)[40]	-0.41087(9)[20][a]	-
$A_\perp$	-0.076(1)[2]	-	-0.074[1][c]

[a] Scaled from [26]
[b] Scaled from [27]
[c] Ref. [10]
[d] Ref. [20, 26]

RESULTS AND DISCUSSIONS

The measured transitions were fitted using a rotational and hyperfine Hamiltonian for each of the two electronic states involved, using the software PGOPHER [28]. The fit included 54 transitions (see Fig. 1C and Fig. 3) and the values of the fitted rotational and hyperfine parame-

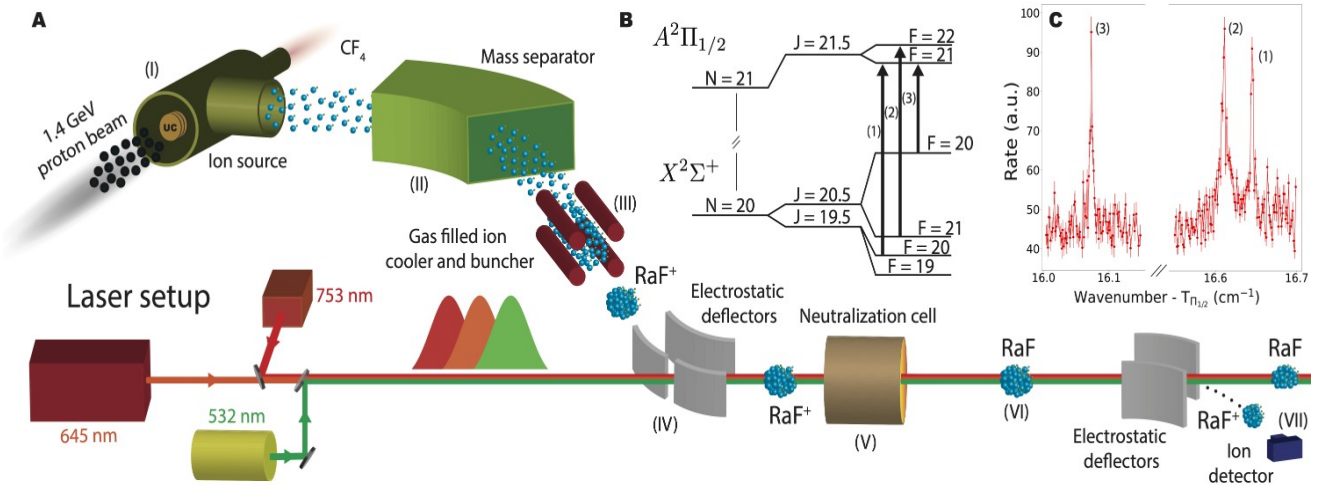

FIG. 1. **Experimental setup.** (**A**) Radium fluoride molecules are produced by impinging 1.4-GeV protons on a high-temperature (T= 2000 K) uranium carbide target, injected with CF_4 gas, then surfaced ionized and extracted using electrostatic fields (I). ^{225}RaF is mass-selected (II) and trapped in a He-filled radiofrequency quadrupole (T = 300 K) for up to 20 ms (III). The bunched RaF ions are guided using electrostatic deflectors (IV), neutralized in a Na-filled charge-exchange cell (V), then overlapped with 3 pulsed lasers in a collinear geometry (VI). The resulting RaF ions are deflected and detected using an ion detector (VII). (**B**) Example of energy levels involved in a transition between hyperfine levels in an R-branch (not to scale). N, J and F correspond to the rotational, electronic and total angular momentum quantum numbers of the molecule (N and J are not good quantum numbers when I > 0). Experimentally observed transitions are shown by upwards-pointing arrows and numbered. (**C**) Example of measured spectra showing the ion rate in arbitrary units (a.u.) as a function of the wavenumber of the first laser, Doppler corrected to the molecular rest frame and shifted by T_{Π}. The error bars show one standard deviation statistical uncertainty. Data points are connected by straight lines to guide the eye. The numbering on the individual peaks corresponds to the transitions shown in (**B**).

ters obtained are shown in Table I. These are in excellent agreement with previous experiments, as well as with *ab initio* theoretical calculations, from which they deviate by less than 1% (< 0.5 combined standard deviation). Examples of the measured spectra together with a detailed description of the data analysis and the quantum chemistry calculations can be found in the Supplementary Materials.

The hyperfine structure parameter of the ground state, $A_\perp$, which quantifies the strength of the coupling between the electron and the ^{225}Ra nuclear spin, can be written as the product between the magnetic dipole moment of the ^{225}Ra nucleus, $\mu(^{225}\mathrm{Ra})$, and an electronic form factor [10, 29]. Using available data for the $^{225}\mathrm{Ra}^+$ cation [30], this form factor has been calculated in Ref. [10] for $^{225}\mathrm{Ra}^{19}\mathrm{F}$ in two different ways: one in which $\mu(^{225}\mathrm{Ra})$ is treated as a point-like dipole moment and another one, in which the distribution of the nuclear magnetization within the ^{225}Ra nucleus is accounted for, in a model-independent manner. Details of the extraction of the effect of the nuclear magnetization distribution and the relation between Ra^+ and RaF are given in the Supplementary Materials. Using these two calculated values, together with our measured $A_\perp$ parameter, the value for $\mu(^{225}\mathrm{Ra})$ can be precisely extracted. The obtained results are shown in Fig. 2A, on the left, for the former case and on the right for the latter. The black error bars correspond to the experimental uncertainty, while the blue bands represent the combined theoretical and experimental uncertainty. The horizontal orange band represents the literature value of $\mu(^{225}\mathrm{Ra})$ and associated uncertainty, given by its thickness, obtained from an independent experiment performed on ^{225}Ra atoms [31]. It can be seen (Fig. 2A) that the effect of the distribution of nuclear magnetization inside of the Ra nucleus, $\mu_{BW}(^{225}\mathrm{Ra})$, amounts to almost 5% of the value of $\mu(^{225}\mathrm{Ra})$. The 1% uncertainty on the extracted value of $\mu(^{225}\mathrm{Ra})$ therefore corresponds to $\sim 20\%$ relative uncertainty on $\mu_{BW}(^{225}\mathrm{Ra})$. This level of uncertainty already has the potential to allow discrimination between simple models of the distribution of the nuclear magnetization inside the ^{225}Ra nucleus (see Supplementary Materials). The presence of this effect, known as the Bohr-Weisskopf effect (BW) in atoms [32], can only be clearly observed in $^{225}\mathrm{Ra}^{19}\mathrm{F}$ due to the combination of high experimental resolution and precise molecular theory (Fig. 2B).

The remarkable agreement between experiment and theory (see Table I), at below the 1% level, reflects the reliability of the *ab initio* quantum chemistry calculations, demonstrating that state-of-the-art theoretical methods

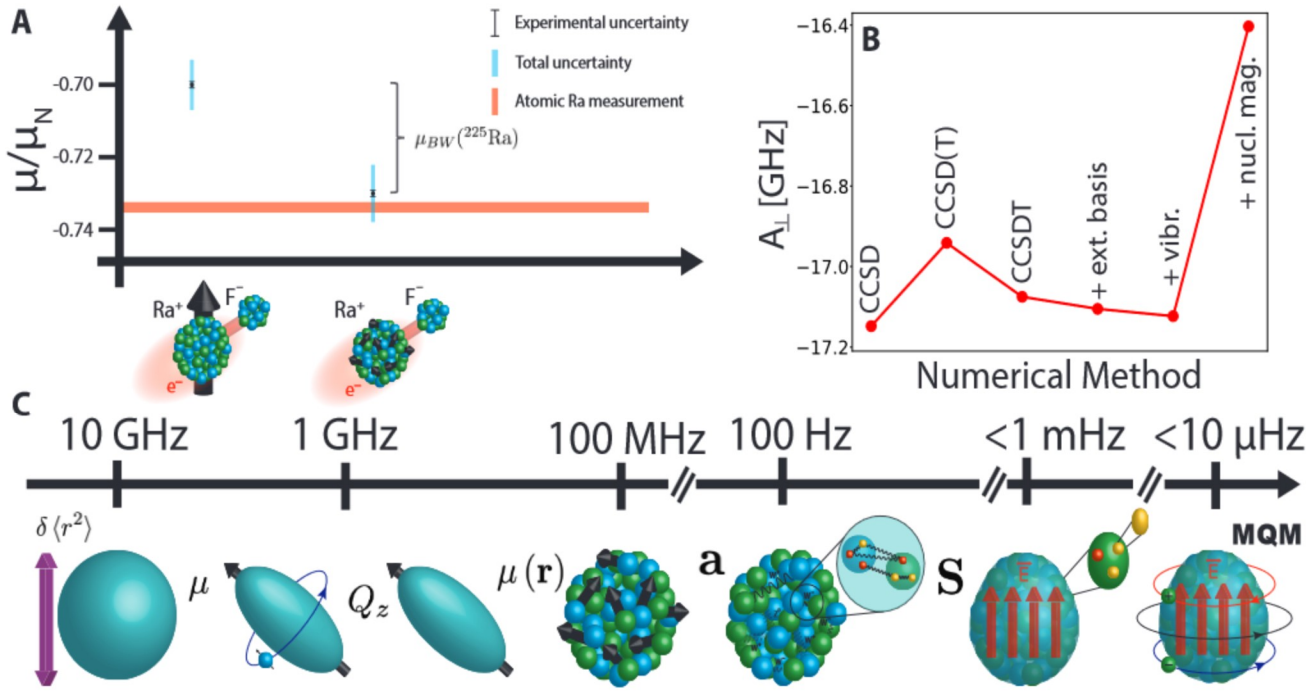

FIG. 2. **Nuclear effects in the RaF molecule due to the Ra nucleus.** (**A**) Extracted values of the magnetic moment of ^{225}Ra, $\mu\left(^{225}\mathrm{Ra}\right)$, in units of nuclear magnetons, μ_N, assuming the Ra nucleus is a point-like magnetic dipole (left) and accounting for the distribution of the nuclear magnetization inside of the Ra nucleus (right). The difference between the two, $\mu_{BW}(^{225}\mathrm{Ra})$, corresponds to the effect of the distribution of the nuclear magnetization and amounts to $\sim 5\%$ of the total value of $\mu\left(^{225}\mathrm{Ra}\right)$. The black and blue error bars are the experimental and total (experimental plus theoretical) uncertainties, respectively. The center and thickness of the orange band correspond to the previously measured value and associated uncertainty of $\mu(^{225}\mathrm{Ra})$ in an atom [31]. (**B**) Evolution of the calculated $A_\perp$ for increasing levels of theoretical sophistication (see main text and the Supplementary Materials for more details) [10]. (**C**) Order-of-magnitude estimation of nuclear effects due to Ra nucleus on the energy levels of ^{223,225}RaF. From left to right: changes in nuclear charge radius between Ra isotopes [20], point-like magnetic dipole moment, electric quadrupole moment [33], distribution of nuclear magnetization, anapole moment, nuclear Schiff moment [17, 34], magnetic quadrupole moment [35]. The electric and magnetic quadrupole moments are nonzero only for Ra isotopes with nuclear spin $\mathrm{I} > 1/2$, such as ^{223}Ra.

are able to provide an accurate description of the electronic wavefunction within the Ra nucleus. Molecular theory is an essential ingredient for extracting fundamental physics information from precision experiments [3, 10, 36, 37]. Using a computational scheme similar to that used in Ref. [10], the electronic parameters that provide the sensitivity of the ^{225}Ra^{19}F molecule to symmetry-violating phenomena were calculated: the effective electric field E_{eff} acting on the electron electric dipole moment (EDM); the molecular parameter $W_{P,T}$ that characterizes the $\mathcal{P},\mathcal{T}$-violating scalar-pseudoscalar nuclear-electron interaction; the molecular constant W_S that defines the interaction of the $\mathcal{P},\mathcal{T}$-violating Schiff moment of ^{225}Ra with the electronic cloud; and the molecular parameter W_a that captures the interaction between electrons and the $\mathcal{P}$-violating nuclear anapole moment (see Supplementary Materials for details). The obtained values are shown in Table II (second column). They are in good agreement with previous theoretical studies [15, 16, 38, 39] (third column of Table II), but are more precise, by as much as an order of magnitude, mainly due to a more complete treatment of correlation effects for all electrons of RaF.

The values of hyperfine structure (HFS) constants, $A_\perp$ and $A_\parallel$, as well as the symmetry-violating electronic form factors, E_{eff}, $W_{P,T}$, W_S, and W_a, strongly depend on the electronic density behaviour inside the ^{225}Ra nucleus [3]. However, unlike the HFS constants measured in this work, the other computed parameters, which provide the sensitivity to symmetry-violating phenomena, cannot be measured experimentally. Hence, HFS measurements are essential for benchmarking *ab initio* theoretical calculations, and critically, they allow a reliable prediction of the molecular sensitivity to symmetry-violating properties. As an illustrative example of the strong connection between the HFS constants and symmetry violating electronic form factor, it can be shown that the $A_\perp$ and $A_\parallel$ parameters can be directly related to E_{eff} using a semi-

TABLE II. Calculated symmetry-violating electronic form factors in ^{225}Ra^{19}F. The parameter names and their units are shown in the first column. The second and third columns show the values of the parameters calculated in this work and previous studies (see Supplementary Materials for details). The numbers in square brackets correspond to one standard deviation uncertainty (where available).

	This work	Previous work
E_{eff} (GV/cm)	-53.3[9]	-52.8[53][a] -52.5[52][b] -56.9[c] -50.8[d] -54.2[54][e]
$W_{P,T}$ (h kHz)	-144.3[14]	-139[14][a] -141.2[140][b] -152.5[c] -138[d]
W_a (h Hz)	1694[17]	1700[170][a] 1420[213][f] 1641[246][g]
W_S ($e/(4\pi\epsilon_0 a_0^4)$)	-20900[2100]	-22130[2213][a,h] -19148[d,g]

[a] Ref. [15], [b] Ref. [16], [c] Ref. [41], [d] Ref. [42], [e] Ref. [43], [f] Ref. [38], [g] Ref. [39], [h] Ref. [44]

empirical approximation [40], $E_{\text{eff}} = \alpha\sqrt{AA_d}$, where $A \equiv (A_\parallel + 2A_\perp)/3$, $A_d \equiv (A_\parallel - A_\perp)/3$ and $\alpha \approx 0.0313$ GV/(cm MHz) is an approximate proportionality constant that can be obtained by simple numerical calculations [40]. This approach provides a value of $E_{\text{eff}} = 63.2$ GV/cm, which is within 20% of our accurate state-of-the-art *ab initio* calculations, reported in Table II.

Using the calculated hyperfine and $\mathcal{P},\mathcal{T}$-odd electronic form factors, the contributions of various nuclear effects to the molecular spectra of ^{223,225}RaF are illustrated in Fig 2C. Electroweak nuclear properties related to W- and Z-boson exchange within the Ra nucleus, such as the anapole moment, are expected to be on the order of 100 Hz. Experiments on stable molecules are already able to achieve and exceed this level of precision [3]. Nuclear $\mathcal{CP}$-violation effects due to beyond the SM physics are predicted to produce shifts on the order of mHz, a level of precision that is within reach of existing atomic and molecular techniques [4, 5]. Molecules containing Ra nuclei therefore represent some of the most compelling systems for discovering $\mathcal{CP}$-violation in the strong force [3].

CONCLUSIONS AND OUTLOOK

The hyperfine structure of ^{225}Ra^{19}F was measured, revealing the high sensitivity of this molecule to the properties of the ^{225}Ra nucleus. The observation of the distribution of the nuclear magnetization effect in a molecule was possible thanks to the combined precision of our experiment and high accuracy of quantum chemistry calculations, which are now reaching the sub-percent level. Improving the precision of these calculations by a factor of $\sim 2-3$ would already enable different nuclear magnetization models to be distinguished between, at below the 10% level (see Ref. [10] and the Supplementary Materials), facilitating stringent tests of nuclear theory. We hope that our experimental results will motivate the development of higher-accuracy molecular and nuclear structure calculations.

Our findings lay the groundwork for using these molecules in future studies of higher-order symmetry-conserving nuclear moments such as the nuclear magnetic octupole moment [45, 46], electric hexadecapole [47, 48] or electric quadrupole shift (higher-order correction to the electric quadrupole interaction, due to electron penetration into the nucleus) [49]. The former has never been measured in a molecule, while the latter two have not been observed in any atom or molecule so far. All of these properties are enhanced in molecular systems containing heavy, octupole-deformed nuclei [3]. Together with the distribution of the nuclear magnetization, they can provide valuable information about the behaviour of protons and neutrons within atomic nuclei which is important for elucidating the microscopic origin of collective nuclear phenomena. Observables that are sensitive to the neutron distribution would be key to our understanding of nuclear matter and constrain properties of neutron stars [50]. Our measurements provide critical information on the rotational and hyperfine structure of ^{225}Ra^{19}F, which, complemented by the calculated electronic form factors, represent a major milestone towards future experimental developments that aim to use these molecules for fundamental physics studies [3].

[1] E. S. Shuman *et al.*, "Laser cooling of a diatomic molecule," Nature **467**, 820–823 (2010).
[2] S. Truppe *et al.*, "Molecules cooled below the Doppler limit," Nat. Phys. **13**, 1173–1176 (2017).
[3] M. S. Safronova *et al.*, "Search for new physics with atoms and molecules," Rev. Mod. Phys. **90**, 025008 (2018).
[4] ACME Collaboration *et al.*, "Improved limit on the electric dipole moment of the electron," Nature **562**, 355–360 (2018).
[5] T. S. Roussy *et al.*, "An improved bound on the electron's electric dipole moment," Science **381**, 46–50 (2023).
[6] E. Altuntaş *et al.*, "Demonstration of a sensitive method to measure nuclear-spin-dependent parity violation," Phys. Rev. Lett. **120**, 142501 (2018).
[7] T. Saue *et al.*, "The DIRAC code for relativistic molecular calculations," J. Chem. Phys. **152**, 204104 (2020).

[8] M. Kállay and J. Gauss, "Approximate treatment of higher excitations in coupled-cluster theory," J. Chem. Phys. **123**, 214105 (2005).

[9] M. Kállay *et al.*, "The MRCC program system: Accurate quantum chemistry from water to proteins," J. Chem. Phys. **152**, 074107 (2020).

[10] L. V. Skripnikov, "Nuclear magnetization distribution effect in molecules: Ra^+ and RaF hyperfine structure," J. Chem. Phys. **153**, 114114 (2020).

[11] L. V. Skripnikov *et al.*, "New nuclear magnetic moment of ^{209}Bi: Resolving the bismuth hyperfine puzzle," Phys. Rev. Lett **120**, 093001 (2018).

[12] N. Auerbach *et al.*, "Collective T-and P-odd electromagnetic moments in nuclei with octupole deformations," Phys. Rev. Lett. **76**, 4316 (1996).

[13] V. V. Flambaum, "Electric dipole moments of actinide atoms and RaO molecule," Phys. Rev. A **77**, 024501 (2008).

[14] T. A. Isaev *et al.*, "Laser-cooled RaF as a promising candidate to measure molecular parity violation," Phys. Rev. A **82**, 052521 (2010).

[15] A. D. Kudashov *et al.*, "Ab initio study of radium monofluoride (RaF) as a candidate to search for parity- and time-and-parity–violation effects," Phys. Rev. A **90**, 052513 (2014).

[16] S. Sasmal *et al.*, "Relativistic coupled-cluster study of RaF as a candidate for the parity-and time-reversal-violating interaction," Phys. Rev. A **93**, 062506 (2016).

[17] V. V. Flambaum, "Enhanced nuclear schiff moment and time-reversal violation in ^{229}Th-containing molecules," Phys. Rev. C **99**, 035501 (2019).

[18] K. Gaul *et al.*, "Systematic study of relativistic and chemical enhancements of P, T-odd effects in polar diatomic radicals," Phys. Rev. A **99**, 032509 (2019).

[19] R. F. Garcia Ruiz *et al.*, "Spectroscopy of short-lived radioactive molecules," Nature **581**, 396–400 (2020).

[20] S. M. Udrescu *et al.*, "Isotope shifts of radium monofluoride molecules," Phys. Rev. Lett. **127**, 033001 (2021).

[21] L. P. Gaffney *et al.*, "Studies of pear-shaped nuclei using accelerated radioactive beams," Nature **497**, 199–204 (2013).

[22] R. H. Parker *et al.*, "First measurement of the Atomic Electric Dipole Moment of ^{225}Ra," Phys. Rev. Lett. **114**, 233002 (2015).

[23] T. E. Chupp *et al.*, "Electric dipole moments of atoms, molecules, nuclei, and particles," Rev. Mod. Phys. **91**, 015001 (2019).

[24] G. Sanamyan *et al.*, "Empirical determination of the Bohr-Weisskopf effect in cesium and improved tests of precision atomic theory in searches for new physics," Phys. Rev. Lett. **130**, 053001 (2023).

[25] R. Catherall *et al.*, "The ISOLDE facility," J. Phys. G **44**, 094002 (2017).

[26] S.-M. Udrescu *et al.*, "Precision spectroscopy and laser cooling scheme of a radium-containing molecule," `https://www.researchsquare.com/article/rs-2648482/v1` (2023).

[27] A. Zaitsevskii *et al.*, "Accurate ab initio calculations of RaF electronic structure appeal to more laser-spectroscopical measurements," J. Chem. Phys. **156**, 044306 (2022).

[28] C. M. Western, "PGOPHER: A program for simulating rotational, vibrational and electronic spectra," J. Quant. Spectrosc. Radiat. Transf. **186**, 221–242 (2017).

[29] E. Fermi and E. Segrè, "Zur theorie der hyperfeinstruktur," Zeitschrift für Physik **82**, 729–749 (1933).

[30] K. Wendt *et al.*, "On the hyperfine structure and isotope shift of radium," Z. Phys. D. At., Mol. Clust. **4**, 227–241 (1987).

[31] E. Arnold *et al.*, "Direct measurement of nuclear magnetic moments of radium isotopes," Phys. Rev. Lett. **59**, 771 (1987).

[32] A. Bohr and V. F. Weisskopf, "The influence of nuclear structure on the hyperfine structure of heavy elements," Phys. Rev **77**, 94 (1950).

[33] A. N. Petrov and L. V. Skripnikov, "Energy levels of radium monofluoride RaF in external electric and magnetic fields to search for P-and T, P-violation effects," Phys. Rev. A **102**, 062801 (2020).

[34] B. Graner *et al.*, "Reduced limit on the permanent electric dipole moment of ^{199}Hg," Phys. Rev. Lett. **116**, 161601 (2016).

[35] V. V. Flambaum and A. J. Mansour, "Enhanced magnetic quadrupole moments in nuclei with octupole deformation and their C,P-violating effects in molecules," Phys. Rev. C. **105**, 065503 (2022).

[36] L. V. Skripnikov and A. V. Titov, "Theoretical study of ThF^+ in the search for T, P-violation effects: Effective state of a Th atom in ThF^+ and ThO compounds," Phys. Rev. A **91**, 042504 (2015).

[37] L. V. Skripnikov, "Combined 4-component and relativistic pseudopotential study of ThO for the electron electric dipole moment search," J. Chem. Phys. **145**, 214301 (2016).

[38] T. A. Isaev and R. Berger, "Electron correlation and nuclear charge dependence of parity-violating properties in open-shell diatomic molecules," Phys. Rev. A **86**, 062515 (2012).

[39] A. Borschevsky *et al.*, "Relativistic study of nuclear-anapole-moment effects in diatomic molecules," Phys. Rev. A **88**, 022125 (2013).

[40] M. G. Kozlov, "Enhancement of the electric dipole moment of the electron in the YbF molecule," J. Phys. B **30**, L607–612 (1997).

[41] A. Sunaga *et al.*, "Merits of heavy-heavy diatomic molecules for electron electric-dipole-moment searches," Phys. Rev. A **99**, 062506 (2019).

[42] K. Gaul and R. Berger, "Toolbox approach for quasi-relativistic calculation of molecular properties for precision tests of fundamental physics," J. Chem Phys. **152**, 044101 (2020).

[43] C Zhang *et al.*, "Calculations of time-reversal-symmetry-violation sensitivity parameters based on analytic relativistic coupled-cluster gradient theory," Phys. Rev. A **104**, 012814 (2021).

[44] V. V. Flambaum *et al.*, "Time-and parity-violating effects of the nuclear Schiff moment in molecules and solids," Phys. Rev. A **101**, 042501 (2020).

[45] R. P. De Groote *et al.*, "Magnetic octupole moment of ^{173}Yb using collinear laser spectroscopy," Phys. Rev. A **103**, 032826 (2021).

[46] R. P. de Groote *et al.*, "Precision measurement of the

magnetic octupole moment in ^{45}Sc as a test for state-of-the-art atomic-and nuclear-structure theory," Phys. Lett. B **827**, 136930 (2022).
[47] K. Beloy *et al.*, "Hyperfine structure of the metastable $^3P_2$ state of alkaline-earth-metal atoms as an accurate probe of nuclear magnetic octupole moments," Phys. Rev. A **77**, 012512 (2008).
[48] D. Xiao *et al.*, "Hyperfine structure of ^{173}Yb$^+$: Toward resolving the ^{173}Yb nuclear-octupole-moment puzzle," Phys. Rev. A **102**, 022810 (2020).
[49] K. Koch *et al.*, "Electron penetration into the nucleus and its effect on the quadrupole interaction," Phys. Rev. A **81**, 032507 (2010).
[50] X. F. Yang *et al.*, "Laser spectroscopy for the study of exotic nuclei," Prog. Part. Nucl. Phys. , 104005 (2022).
[51] M. Denis *et al.*, "Benchmarking of the Fock-space coupled-cluster method and uncertainty estimation: Magnetic hyperfine interaction in the excited state of BaF," Phys. Rev. A **105**, 052811 (2022).
[52] L. V. Skripnikov and S. D. Prosnyak, "Refined nuclear magnetic dipole moment of rhenium: ^{185}Re and ^{187}Re," Phys. Rev. C **106**, 054303 (2022).
[53] W. Neu *et al.* (ISOLDE"), "Quadrupole moments of radium isotopes from the 7p $^2P_{3/2}$ hyperfine structure in Ra II," Z. Phys. D **11**, 105–111 (1989).
[54] U. Dammalapati *et al.*, "Compilation of spectroscopic data of radium (Ra I and Ra II)," J. Phys. Chem. Ref. Data **45**, 013101 (2016).
[55] S. D. Prosnyak and L. V. Skripnikov, "Effect of nuclear magnetization distribution within the Woods-Saxon model: Hyperfine splitting in neutral Tl," Phys. Rev. C **103**, 034314 (2021).
[56] J. S. M. Ginges *et al.*, "Ground-state hyperfine splitting for Rb, Cs, Fr, Ba$^+$, and Ra$^+$," Phys. Rev. A **96**, 062502 (2017).
[57] R. A. Sen'kov and V. F. Dmitriev, "Nuclear magnetization distribution and hyperfine splitting in Bi^{82+} ion," Nucl. Phys. A **706**, 351 – 364 (2002).
[58] V. M. Shabaev *et al.*, "Ground-state hyperfine splitting of high-Z hydrogenlike ions," Phys. Rev. A **56**, 252 (1997).
[59] A. S. P. Gomes *et al.*, "DIRAC19. DIRAC, a relativistic ab initio electronic structure program, release DIRAC19 (2019)," (2019).
[60] K. G. Dyall, "Relativistic double-zeta, triple-zeta, and quadruple-zeta basis sets for the light elements H–Ar," Theor. Chem. Acc. **135**, 128 (2016).
[61] A. V. Titov and N. S. Mosyagin, "Generalized relativistic effective core potential: Theoretical grounds," Int. J. Quantum Chem. **71**, 359–401 (1999).
[62] N. S. Mosyagin *et al.*, "Shape-consistent relativistic effective potentials of small atomic cores," Int. Rev. At. Mol. Phys **1**, 63–72 (2010).
[63] N. S. Mosyagin *et al.*, "Generalized relativistic effective core potentials for actinides," Int. J. Quantum Chem. **116**, 301–315 (2016).
[64] L. V. Skripnikov *et al.*, "Relativistic coupled-cluster calculations of spectroscopic and chemical properties for element 120," Chem. Phys. Lett. **555**, 79–83 (2013).
[65] R. A. Kendall *et al.*, "Electron affinities of the first-row atoms revisited. Systematic basis sets and wave functions," J. Chem. Phys. **96**, 6796–6806 (1992).
[66] W. A. De Jong *et al.*, "Parallel Douglas–Kroll energy and gradients in NWChem: Estimating scalar relativistic effects using Douglas–Kroll contracted basis sets," J. Chem. Phys. **114**, 48–53 (2001).
[67] A.-M. Mårtensson-Pendrill and P. Öster, "Calculations of atomic electric dipole moments," Phys. Scr. **36**, 444 (1987).
[68] E. Lindroth *et al.*, "Order α^2 theory of the atomic electric dipole moment due to an electric dipole moment on the electron," J. Phys. B: At. Mol. Opt. Phys. **22**, 559 (1989).
[69] I. B. Khriplovich, *Parity nonconservation in atomic phenomena* (Philadelphia, PA (United States); Gordon and Breach Science Publishers, 1991).
[70] P. Sushkov and V. V. Flambaum, "Parity breaking effects in diatomic molecules," Zh. Eksp. Teor. Fiz **75**, 1208–1213 (1978).
[71] V. V. Flambaum and I. B. Khriplovich, "On the enhancement of parity nonconserving effects in diatomic molecules," Phys. Lett. A **110**, 121–125 (1985).
[72] L. V. Skripnikov and A. V. Titov, "Theoretical study of thorium monoxide for the electron electric dipole moment search: Electronic properties of $H^3\Delta_1$ in ThO," J. Chem. Phys. **142**, 024301 (2015).
[73] L. V. Skripnikov *et al.*, "Scalar-pseudoscalar interaction in the francium atom," Phys. Rev. A **95**, 022507 (2017).
[74] A. V. Titov *et al.*, "P,T-Parity Violation Effects in Polar Heavy-Atom Molecules," in *Recent Advances in the Theory of Chemical and Physical Systems* (Springer, 2006) pp. 253–283.
[75] L. V. Skripnikov and A. V. Titov, "LCAO-based theoretical study of $PbTiO_3$ crystal to search for parity and time reversal violating interaction in solids," J. Chem. Phys. **145**, 054115 (2016).
[76] L. Visscher and D. G. Dyall, "Dirac–Fock atomic electronic structure calculations using different nuclear charge distributions," Atomic Data and Nuclear Data Tables **67**, 207–224 (1997).
[77] V. M. Shabaev *et al.*, "Model operator approach to the lamb shift calculations in relativistic many-electron atoms," Phys. Rev. A **88**, 012513 (2013).
[78] L. V. Skripnikov, "Approaching meV level for transition energies in the radium monofluoride molecule RaF and radium cation Ra$^+$ by including quantum-electrodynamics effects," J. Chem. Phys. **154**, 201101 (2021).
[79] J. S. M. Ginges and V. V. Flambaum, "Violations of fundamental symmetries in atoms and tests of unification theories of elementary particles," Phys. Rep. **397**, 63–154 (2004).
[80] V. V. Flambaum and A. Kozlov, "Screening and finite-size corrections to the octupole and Schiff moments," Phys. Rev. C **85**, 068502 (2012).
[81] E. A. Hinds and P. G. H. Sandars, "Electric dipole hyperfine structure of TiF," Phys. Rev. A **21**, 471 (1980).
[82] O. P. Sushkov *et al.*, "Possibility of investigating P-and T-odd nuclear forces in atomic and molecular experiments," Zh. Eksp. Teor. Fiz **87**, 1521 (1984).
[83] L.V. Skripnikov *et al.*, "Actinide and lanthanide molecules to search for strong CP-violation," Phys. Chem. Chem. Phys. **22**, 18374–18380 (2020).
[84] A. D. Becke, "Density-functional thermochemistry. III.

The role of exact exchange," J. Chem. Phys. **98**, 5648–5652 (1993).
[85] C. Thierfelder *et al.*, "Relativistic coupled-cluster study of the parity-violation energy shift of CHFClBr," Phys. Rev. A **81**, 032513 (2010).
[86] N. J. Stone, "Table of nuclear magnetic dipole and electric quadrupole moments," Atomic Data and Nuclear Data Tables **90**, 75–176 (2005).
[87] P. Pyykkö, "Year-2008 nuclear quadrupole moments," Mol. Phys. **106**, 1965–1974 (2008).

SUPPLEMENTARY MATERIALS

A. Data analysis

Each peak used in the determination of the rotational and hyperfine Hamiltonian parameters was fit with a Voigt profile plus a constant background, using the LMFIT Python package. The number of peaks in a given scan was chosen based on the reduced-χ^2 of the fit. The obtained central value of each peak, together with its associated uncertainty, were input into PGOPHER where they were fit with the effective Hamiltonians described below. The main sources of systematic uncertainty in our experiment were (expressed as an uncertainty on the wavenumber in brackets): variations in the ion beam extraction voltage (1.2×10^{-4} cm^{-1}), changes in the beam energy during the charge-exchange process (10^{-4} cm^{-1}), uncertainties in the measurement of the Rb reference frequency by the wavemeter (10^{-4} cm^{-1}), presence of stray magnetic and electric fields ($<10^{-5}$ cm^{-1}) and AC Stark shifts due to the presence of the second- and third-step lasers (5×10^{-4} cm^{-1}). These uncertainties were added in quadrature to the statistical uncertainty for each fitted line in the spectra, before performing the PGOPHER fit.

For the $X\ ^2\Sigma^+$ electronic state, the employed rotational and hyperfine Hamiltonian is given by:

$$H^{\mathrm{rot}}_{X\ ^2\Sigma^+} = \left(B'' - D''\boldsymbol{N}^2\right)\boldsymbol{N}^2 + \gamma\boldsymbol{N}\cdot\boldsymbol{S} + b''\mathbf{I}\cdot\mathbf{S} + c''I_zS_z, \tag{1}$$

where B'' is the rotational constant, D'' is the centrifugal distortion constant, γ is the spin-rotation constant and b'' and c'' are hyperfine constants due to the ^{225}Ra nucleus. These parameters can be related to $A_\perp$ and $A_\parallel$ of the $X\ ^2\Sigma^+$ state from [10] using: $A_\perp = b''$ and $A_\parallel - A_\perp = c''$ [51]. $\boldsymbol{N} = \boldsymbol{J} - \boldsymbol{S}$, $\boldsymbol{S}$ and $\boldsymbol{I}$ are the molecular rotational operator (excluding the electron and nuclear spin), the electron spin operator and the nuclear spin operator, respectively, while S_z and I_z are the z-component of the latter two.

The excited electronic state, $A\ ^2\Pi$, was described by the effective rotational and hyperfine Hamiltonians:

$$\begin{aligned} H^{\mathrm{rot}}_{A\ ^2\Pi} = {} & T_\Pi + A_\Pi L_zS_z + \left(B' - D'\boldsymbol{N}^2\right)\boldsymbol{N}^2 - \\ & - \frac{1}{2}\left\{\frac{p}{2} + p_D\boldsymbol{N}^2, N_+S_+e^{-2i\phi} + N_-S_-e^{2i\phi}\right\} + \\ & + \frac{1}{2}d\left(e^{-2i\phi}I_+S_+ + e^{2i\phi}I_-S_-\right), \end{aligned} \tag{2}$$

where $\{O,Q\} = OQ + QO$, L_z is the z-component of the electron orbital momentum operator in the molecular rest frame, T_Π represents the energy difference between the origins of the $\nu' = 0$ vibrational level of the $^2\Pi$ electronic manifold and the origins of the corresponding isovibrational level of the $X\ ^2\Sigma^+$ electronic manifold, while A_Π is the spin-orbit interaction. The $^2\Pi$ electronic manifold, gets split, in a Hund case (a) picture, into a $^2\Pi_{1/2}$ and a $^2\Pi_{3/2}$ electronic levels due to the spin-orbit coupling, separated by A_Π. As rovibronic transitions to the $A^2\Pi_{3/2}$ electronic state were not measured, it was not possible to constrain both T_Π and A_Π simultaneously, therefore A_Π was kept fixed at its previously measured value of 2067.6 cm^{-1} [19]. p is the Λ-doubling parameter and p_D is the centrifugal distortion correction to p. Finally, d is a hyperfine structure constant due to the ^{225}Ra nucleus. In a $A^2\Pi$ state, this is related to the $A_\perp$ parameter from [10] by $A_\perp = d$ [51]. $N_\pm$, $S_\pm$ and $I_\pm$ are the raising and lowering operators for the $\boldsymbol{N}$, $\boldsymbol{S}$ and $\boldsymbol{I}$ operators defined above and ϕ is the polar angle around the molecular axis, defined in the molecule's rest frame. The molecular parameters, extracted from fitting the above Hamiltonians to the data, correspond to the ground vibrational level of each electronic manifold [26]. The hyperfine splitting due to the fluorine nucleus (I = 1/2) was predicted to be much below 100 MHz and hence was not observed given our current spectroscopic resolution. Therefore, the corresponding hyperfine Hamiltonian was not included in the analysis.

For the fitting procedure, γ, D', D'' and p_D parameters were each sampled from a Gaussian with mean and standard deviation given by the values of the corresponding parameters of the ^{226}Ra^{19}F molecule [26], scaled accordingly using the reduced mass of the two isotopologues. After sampling, these parameters were kept constant during the fitting procedure, and the values of the other rotational and hyperfine parameters were extracted. The sampling and subsequent fitting was repeated 1000 times, and the obtained average value and standard deviation of the fitted parameters are reported in Table I.

Examples of the measured spectra of ^{225}Ra^{19}F together with the obtained best fit are shown in Fig. 3, where the experimental data is shown in red, while the best fit is shown in blue. In the center, the full simulated spectrum of the transitions over a range of ~ 50 cm^{-1} is shown. The x-axis shows the wavenumber of the

first-step laser, Doppler corrected to the molecular rest frame, while the y-axis shows the rate in arbitrary units (a.u.). The splitting of each rotational line into 3 hyperfine components can be clearly observed in the R-branch spectra around 13300 cm^{-1}.

B. Nuclear magnetization distribution effect in Ra^+ and RaF

The magnetic dipole hyperfine structure (HFS) constant can be expressed using the following parametrization [32]:

$$A = A^{(0)} - A^{\rm BW}. \tag{3}$$

Here, $A^{(0)}$ represents the HFS constant in the point-like nuclear magnetic dipole moment approximation, and $A^{\rm BW}$ quantifies the contribution of the finite nuclear magnetization distribution to the HFS constant, commonly known as the Bohr-Weisskopf (BW) effect. In Ref. [10], it was demonstrated that the BW correction, $A^{\rm BW}$, for heavy atoms and molecules (including systems with complex electronic structures) can be factorized as follows (see Eq. (29) of Ref. [10] for details):

$$A^{\rm BW} \approx E B_s. \tag{4}$$

Here, E represents a pure electronic factor, which is independent of the nuclear magnetization distribution and is solely determined by the electronic structure. All information regarding the nuclear magnetization distribution can be encoded in the electronic state-independent parameter, B_s. This parameter has a well-defined physical meaning [10] being proportional to the BW effect contribution to the A constant of the hydrogen-like (H-like) ion. Therefore, in cases where measurements of H-like ions are available for a given isotope, B_s can be obtained almost directly [52] due to the very high accuracy of the theoretical description of such ions.

In Ref. [10], $A^{(0)}$ and E were computed for the ground electronic state $7s\ ^2S_{1/2}$ of the $^{225}Ra^+$ cation. By combining these theoretical values with the experimental value [30, 53, 54] of the A constant, the parameter B_s was determined. The electronic $A^{(0)}$ and E constants were also calculated for the excited electronic state $7p\ ^2P_{1/2}$ of $^{225}Ra^+$. Using these values, along with the extracted value of B_s, the BW contribution to the A constant for this state was computed according to Eq. (4). The resulting value of $A(7p\ ^2P_{1/2})$ was in good agreement with the available experimental value [30, 53, 54], with a deviation of about 0.1%, though the theoretical uncertainty was estimated at 1%. The BW effect contribution to $A(7p\ ^2P_{1/2})$ was 1.4%. Interestingly, the Bohr-Weisskopf effects for the $7s\ ^2S_{1/2}$ and $7p\ ^2P_{1/2}$ states are induced by different harmonics, $s_{1/2}$ and $p_{1/2}$, respectively [10]. However, as explained in Ref. [10], the same constant B_s can be utilized in both cases due to properties of the solutions to the Dirac equation and the symmetry of the magnetic dipole hyperfine interaction operator. This is particularly important for systems with complex electronic structures, where both harmonics contribute simultaneously. The validity of factorization (4) was also numerically confirmed by considering various nuclear magnetization distribution models [10, 55]. Finally, the semi-empirically extracted value of B_s was employed to predict the BW effect in the ^{225}RaF molecule for both the ground and first excited electronic states. The uncertainty on the deduced BW effects using this approach is limited by the uncertainty in the electronic structure calculation of $A^{(0)}$ and E of Ra^+, estimated to be 1% [10]. Given that the BW effect amounts to about 5% of the A value of the $7s\ ^2S_{1/2}$ ground state in Ra^+ [10], the uncertainty in the value of the BW effect obtained using this semi-empirical method is $\sim 20\%$.

TABLE III. The BW contribution to the hyperfine structure constants, $A_{||}$ and $A_\perp$, (in MHz) for the ground electronic state of the ^{225}RaF molecule, using different models of the nuclear magnetization.

Model	$A_{||}^{\rm BW}$	$A_\perp^{\rm BW}$
Ball	-537	-529
WS	-830	-818
Semi-empirical [10]	-730	-720

It is also possible to estimate the B_s parameter using simple nuclear magnetization distribution models. The simplest model is a uniformly magnetized sphere, while a more accurate model is a Woods-Saxon (WS) model. The WS model was used in Ref. [56] to calculate the BW effect in $^{225}Ra^+$. By combining the value of B_s^{Ball} with the data from Ref. [56] and using the factorization property (4), one can obtain B_s^{WS}. Using Eq. (4) and the values of the B_s parameter from different nuclear magnetization distribution models, one can calculate the value of the $A_{||}^{\rm BW}$ and $A_\perp^{\rm BW}$ constants for the ground electronic state of the ^{225}RaF molecule. The obtained results are given in Table III. The uncertainty of the BW effect depends on the nuclear model used [57, 58] and it is expected that future nuclear structure calculations, employing more realistic models, will allow a prediction of this effect with quantifiable uncertainties. An improvement in the accuracy of the electronic structure calculations by only a factor of $\sim 2-3$, combined with our experimental results, would allow the study of the distribution of the nuclear magnetization with a relative precision of better than 10%.

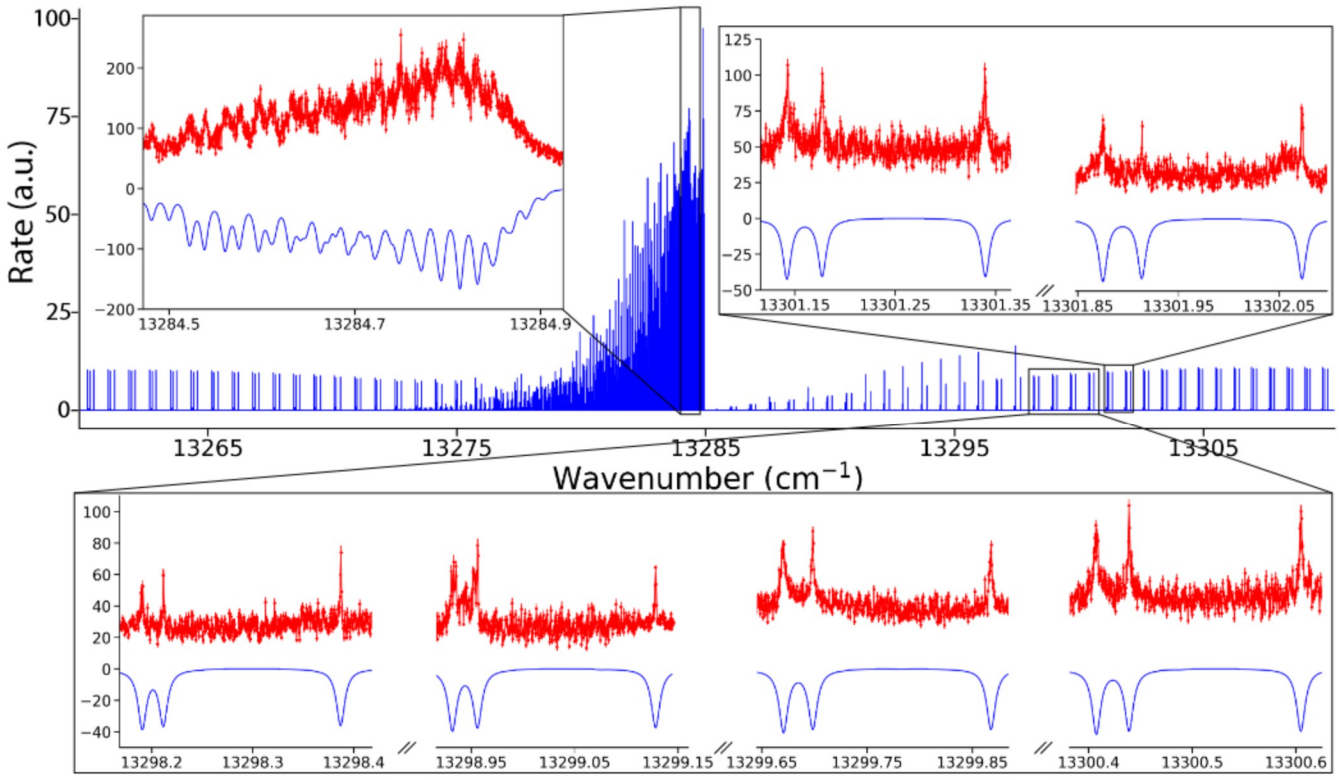

FIG. 3. **Example of measured spectra for the $0' \leftarrow 0''$ transitions.** In the center, in blue, the fitted combined hyperfine and rovibronic spectrum of ^{225}RaF obtained for $J \leq 100$, over a range of ~ 50 cm^{-1} is presented. Figures in magnified views show measured spectra for different regions in frequency space. The connected red dots show the experimental data, while the continuous blue lines represents the best fits to the data. The errorbars show one standard deviation statistical uncertainty. The values on the x-axis correspond to the wavenumber of the first laser used in the resonance ionization scheme, Doppler corrected to the molecular rest frame. The rate on the y-axis is given in arbitrary units (a.u.).

C. Computational methods

The Hund case (c) matrix elements $\langle ^2\Sigma_{1/2}|J^e_+|^2\Sigma_{-1/2}\rangle$ and $\langle ^2\Pi_{1/2}|J^e_+|^2\Pi_{-1/2}\rangle$, where J^e_+ is the $x + iy$ component of the body-fixed total electronic angular momentum, can be related to the spin-rotational and Λ-doubling parameters in Hund cases (b) and (a) in the above Hamiltonians as follows: $\langle ^2\Sigma_{1/2}|J^e_+|^2\Sigma_{-1/2}\rangle = 1 - \frac{\gamma_e}{2B''_e}$ and $\langle ^2\Pi_{1/2}|J^e_+|^2\Pi_{-1/2}\rangle = \frac{p_e}{2B'_e}$, where γ_e, p_e, B'_e and B''_e refer to vibrationally independent molecular parameters (see Ref. [26] for details). These matrix elements were calculated herein and the values obtained are reported in Table IV, exhibiting an excellent agreement with the experiment [26], at the 0.1% level (the values of these parameters are the same for ^{226}RaF [26] and ^{225}RaF). The following scheme was used for the calculations. First, correlation calculations were performed employing the relativistic coupled-cluster approach with single- and double-excitation amplitudes (CCSD) within the Dirac-Coulomb Hamiltonian [7, 59]. Here, 69 electrons of RaF were included in the correlation treatment and the extended uncontracted all-electron triple-zeta extAE3Z basis set (based on AE3Z [60] by Dyall) developed in Ref. [10] was used. It includes $[38s\,33p\,24d\,14f\,7g\,3h\,2i]$ Gaussian-type functions for Ra and corresponds to the uncontracted AE3Z [60] basis set on F. To account for effects of larger basis sets, a correction was taken as the difference between values of the matrix elements under consideration using the extended quadruple-zeta extAE4Z [10] basis set and the extAE3Z basis set. These calculations were performed at the 27-electron CCSD level using the valence part of the generalized relativistic effective-core potential approach [61–63]. Next, higher-order correlation effects were implemented through two contributions. The first of which was calculated as the difference between the results obtained within the CCSD and partial iterative triple-excitation amplitudes (CCSDT-3 [8]) model compared to the CCSD method. In this calculation, 35 electrons of RaF were correlated using the special compact basis set for Ra constructed using the approach developed in Refs. [10, 37, 64] and comprising $[8s\,8p\,7d\,7f\,4g\,2h]$ contracted Gaussian functions, while for F we used the aug-

TABLE IV. Contribution to the theoretically calculated $\langle {}^2\Sigma_{1/2}|J_+^e|{}^2\Sigma_{-1/2}\rangle$ and $\langle {}^2\Pi_{1/2}|J_+^e|{}^2\Pi_{-1/2}\rangle$ matrix elements. The associated experimental values extracted from [26] are shown in the last row. The numbers in round (square) brackets correspond to 1σ statistical (systematic) uncertainty.

Contribution	$\langle {}^2\Sigma_{1/2}\|J_+^e\|{}^2\Sigma_{-1/2}\rangle$	$\langle {}^2\Pi_{1/2}\|J_+^e\|{}^2\Pi_{-1/2}\rangle$
CCSD	0.98355	-1.05444
Basis correction	-0.00010	-0.00655
CCSDT-3 − CCSD	0.00050	-0.00728
CCSDT(Q) − CCSDT-3	0.00001	-0.00407
Gaunt	0.00057	0.00151
Total	0.98453[67]	-1.0708[97]
Experiment	0.98475(13)[34]	-1.07335(21)[45]

cc-pVDZ-DK [65, 66] basis set. Then, correlation effects up to the CC with full iterative triple- and perturbative quadruple-excitation amplitudes CCSDT(Q) [8, 9] approach were implemented. For this contribution, 27 electrons of RaF were correlated and the reduced compact basis set reduced for Ra to $[8s\,8p\,7d\,4f]$ contracted Gaussian functions was used. Finally, the effect of the Gaunt interelectron interaction at the self-consistent level was computed. In all of the calculations, the equilibrium Ra–F distance was used.

The $\mathcal{P},\mathcal{T}$-breaking interaction between an eEDM and electrons can be described by the following Hamiltonian [67, 68]:

$$H_d^{\rm eff} = d_e \sum_a 2ic\gamma_a^0\gamma_a^5 \boldsymbol{p}_a^2, \tag{5}$$

where index a denotes each electron, $\boldsymbol{p}$ is the electron momentum operator, c is the speed of light, d_e is the electron EDM and γ^0 and γ^5 are Dirac matrices defined according to Ref. [69]. These matrices are related through $\gamma^5 = -i\gamma_0\gamma_1\gamma_2\gamma_3$. This interaction can be characterized by the molecular constant W_d:

$$W_d = \frac{1}{\Omega}\langle\Psi|\frac{H_d}{d_e}|\Psi\rangle. \tag{6}$$

In these designations, the effective electric field acting on the eEDM is $E_{\rm eff} = W_d|\Omega|$. Another possible source of the $\mathcal{P},\mathcal{T}$-violation is the scalar-pseudoscalar nucleus-electron interaction given by the following Hamiltonian (see Ref. [70]):

$$H_{\rm s} = i\frac{G_F}{\sqrt{2}} Z k_{\rm s} \sum_a \gamma_a^0\gamma_a^5\rho_N(\mathbf{r}_a), \tag{7}$$

where $G_{\rm F} = 2.22249\cdot 10^{-14}$ $a.u$ is the Fermi-coupling constant, Z is the charge of the heavy nucleus ($Z = 88$ for ^{225}Ra in our case), $\rho_N(\mathbf{r})$ is the nuclear density normalized to unity and $\mathbf{r}$ is the electron radius vector with respect to the heavy atom nucleus under consideration. This interaction is characterized by the molecular parameter $W_{P,T}$:

$$W_{P,T} = \frac{1}{\Omega}\langle\Psi|\frac{H_{\rm s}}{k_{\rm s}}|\Psi\rangle. \tag{8}$$

The electron-nucleus $\mathcal{P}$-odd interaction Hamiltonian is defined as:

$$H_P = \kappa\frac{G_{\rm F}}{\sqrt{2}}\boldsymbol{\alpha}\cdot\boldsymbol{I}\rho_N(\mathbf{r}). \tag{9}$$

The main contributions to this effect in ^{225}RaF are the Z^0-boson exchange between the unpaired electron and the ^{225}Ra nucleus and the interaction of the unpaired electron with the nuclear anapole moment. These effects are characterized by the dimensionless constant κ. By averaging this Hamiltonian over the electronic wavefunction of the molecule, the following rotational and hyperfine effective Hamiltonian is obtained [71]:

$$H_{\rm eff} = (W_a\kappa)\mathbf{n}\times\mathbf{S}'\cdot\mathbf{I}, \tag{10}$$

where $\mathbf{n}$ is the unit vector directed from the Ra nucleus to F and W_a is a molecular parameter given by:

$$W_a = \frac{G_{\rm F}}{\sqrt{2}}\left\langle {}^2\Sigma_{1/2}\left|\rho_N(\mathbf{r})\alpha_+\right|^2\Sigma_{-1/2}\right\rangle. \tag{11}$$

To calculate $E_{\rm eff}$, $W_{P,T}$ and W_a, a similar scheme to that in Ref. [10] was used to calculate hyperfine structure constants. First, correlation calculations were performed employing the relativistic coupled-cluster approach with single-, double- and perturbative triple-excitation amplitudes, CCSD(T), within the Dirac-Coulomb Hamiltonian [7, 59]. All 97 electrons of RaF were included in the correlation treatment using the extAE3Z basis set. The virtual energy cutoff was set to 10,000 E_h. The significance of the high energy cutoff for properties that depend on the behavior of the wavefunction near the heavy-atom nucleus has been demonstrated and analyzed in detail in Refs. [72, 73]. Next, higher-order correlation effects were taken as the difference between values of the constants under consideration calculated within the CCSDT and CCSD(T) methods correlating 27 electrons of RaF and using the SBas basis set from Ref. [10]. Additionally, we calculated the contribution of even higher-order correlation effects by comparing the results obtained from CCSDT(Q) and CCSDT calculations, which correlate 27 electrons of RaF. We used the compact basis set comprising $[8s\,8p\,7d\,4f]$ contracted Gaussian functions for Ra, while for F, we employed the aug-cc-pVDZ-DK basis set [65, 66] and employed the two-component two-step approach within the generalized relativistic effective core potential (GRECP) theory [36, 74, 75]. Next, for the case of $E_{\rm eff}$, $W_{P,T}$, a basis set correction, calculated at

TABLE V. Theoretical contributions to the $E_{\rm eff}$ (in units of GV/cm), $W_{P,T}$ (in units of h kHz) and W_a (in units of h Hz) molecular parameters.

Contribution	$E_{\rm eff}$	$W_{P,T}$	W_a
CCSD(T)	-53.9	-145.2	1707
CCSDT(Q) − CCSD(T)	-0.1	-0.3	3
Basis correction	0.0	-0.1	-3
Gaunt	0.9	1.4	-16
Vibr.	-0.1	-0.4	4
Total	-53.3[9]	-144.3[14]	1694[17]

the 69e-CCSD(T) level within the Dirac-Coulomb Hamiltonian was added. Here, the extended number of basis functions in the extAE4Z basis set with respect to extAE3Z was accounted for. For the case of W_a, an equivalent correction was calculated in a similar way, but using the two-component 27e-CCSD(T) two-step approach [36, 74, 75]. To test the influence of further basis functions with high angular momentum for $E_{\rm eff}$, $W_{P,T}$, additional corrections were determined which capture the effect of [$15g\,15h\,15i$]-type basis functions within the scalar-relativistic two-step approach [36, 74, 75] and the 37e-CCSD(T) method. The Gaunt interelectron contribution was calculated at the self-consistent level and then rescaled by the factor 1.4 to account for correlation effects. The calculations described above were performed at a fixed internuclear distance of 2.24 Å, which corresponds to the equilibrium distance of the electronic ground state [10, 15]. Finally, a vibrational correction was implemented to the considered molecular constants for the ground vibrational levels of RaF using the two-step two-component 37e-CCSD(T) approach similar to Ref. [10]. In the calculations described above, a Gaussian nuclear charge distribution model [76] was used.

The calculated values of $E_{\rm eff}$, $W_{P,T}$ and W_a are given in Table V. High-order correlation effects given in the "CCSDT(Q) − CCSD(T)" lines can be seen to be quite small in addition to basis set corrections. These two sources of the theoretical uncertainty are therefore almost negligible for the present case. A special note should be made concerning the Gaunt interelectron interaction contribution to $E_{\rm eff}$. The one-electron operator (Eq. 5) is only valid within the Dirac-Coulomb Hamiltonian [68]. When the Gaunt interaction is included in the molecular Hamiltonian, the expression (Eq. 5) should be replaced by a two-electron operator. This is not trivial to realize computationally for molecules. Therefore, following a previous analysis [37], the whole "Gaunt" contribution was included in the uncertainty of $E_{\rm eff}$. This contribution represents the dominant source of uncertainty. The effect of this approximate method for calculating the Gaunt contribution was also included in the theoretical uncertainty of the other calculated constants. The final uncertainty estimation of $E_{\rm eff}$, $W_{P,T}$ and W_a values given in the main text includes: (i) contribution of higher-order correlation effects estimated as the value given in the "CCSDT(Q) − CCSD(T)" line of Table V; (ii) effects of further extending the basis set which are expected to be at the level of the values given in the "Basis correction" line of Table V and (iii) effects of the Gaunt (Breit) interelectron interaction described above; (iv) The contribution of quantum electrodynamics (QED) effects, which has been estimated as the difference in calculated values of $E_{\rm eff}$, $W_{P,T}$, and W_a obtained using the Dirac-Coulomb Hamiltonian with and without the inclusion of the model QED operator [77] in the formulation in Ref. [78]. It is important to note that we did not include the obtained QED contributions ($E_{\rm eff}$: 0.2 GV/cm, $W_{P,T}$: -0.2 kHz, W_a: 3 Hz) in the final values of the calculated constants, as the approach used is not a rigorous QED treatment. It can however still be used to estimate the order of magnitude of the QED effects. The final uncertainty is calculated as the root of the sum of the squares of these uncertainties. Contributions to these uncertainties from nuclear structure effects are not considered and included due to the lack of corresponding nuclear structure calculations.

The effective Hamiltonian of the $\mathcal{P},\mathcal{T}$-odd interaction of the nuclear Schiff moment with electrons that contains a finite nuclear size correction is given by the following expression [79, 80]:

$$H^{\rm eff,2} = W_S \mathbf{S}'' \cdot \mathbf{n}, \tag{12}$$

where S'' is the corrected nuclear Schiff moment [80] and W_S can be calculated as:

$$W_S = \langle\Psi|\sum_a \frac{3\mathbf{r_a}\cdot\mathbf{n}}{B}\rho_N|\Psi\rangle, \tag{13}$$

where $B = \int \rho_N(r) r^4 dr$. Direct use of Eq. (13) requires very large Gaussian-type basis sets. Alternatively, the relation $W_S \approx 6X/r^{sp}$ can be used, where the coefficient r^{sp} was calculated analytically in Ref. [44] and the molecular parameter X can be computed as follows [81, 82]:

$$X = -\frac{2\pi}{3}\langle\Psi|[\sum_i \nabla_{\mathbf{i}}\cdot\mathbf{n}, \delta(\mathbf{R})]|\Psi\rangle. \tag{14}$$

Following Ref. [83], the X parameter was calculated at the 2-component CCSD(T) level using the two-step approach [36, 74, 75], which allowed the use of the accurate asymptotic behaviour of the wavefunction inside the nucleus. 37 electrons were included in the correlation treatment using the extAE3Z basis set. According to this calculation, correlation effects reduced the relativistic Hartree-Fock value by a factor of 1.74. The Dirac-Hartree-Fock level of theory was also used to directly

calculate W_S according to Eq. (13) where it was possible to use a very large basis set. The latter was constructed by modifying the extAE3Z basis set where all $s-$ and $p-$type functions were replaced by even-tempered series of Gaussian functions. Here, the Gaussian exponential parameters β_i were calculated as $\beta_{i+1} = \beta_i \cdot 1.6$, where $\beta_1 = 1.0 \times 10^{-3}$ and the maximal $\beta_{i=64} = 7.3 \times 10^9$. The final value of W_S was obtained by applying the factor of 1.74 that takes into account correlation effects at the Dirac-Hartree-Fock value. The expected uncertainty of the final W_S is $\sim$ 10%, similar to that estimated in Ref. [83] for W_S constants for actinide-containing molecules.

The calculated values of the symmetry-violating electronic form factors are compared with literature values in the main text. Below, we provide a brief overview of the methods used in those studies (see the corresponding references for additional details). (i) In Ref. [15], the values of all molecular parameters of the $\mathcal{P}$-$\mathcal{P}$,$\mathcal{T}$-odd interactions were calculated for the ground electronic state of RaF using the 2-component two-step approach with the GRECP method [36, 74, 75]. Electronic correlation effects were treated using the relativistic Fock-Space coupled cluster method with single and double excitations, along with a correction for higher-order correlation effects within the scalar-relativistic CCSD(T) approach. In the calculation [15], 19 electrons were correlated. (ii) In Ref. [16], the authors calculated the values of $E_{\rm eff}$ and $W_{P,T}$ using the Dirac-Coulomb Hamiltonian and the CCSD method. They considered correlation effects for all electrons and set the virtual energy cutoff to 20 E_h. (iii) In Ref. [41], the authors calculated the values of $E_{\rm eff}$ and $W_{P,T}$ using the Dirac-Coulomb Hamiltonian and the CCSD method. They set the virtual energy cutoff to 80 E_h. In comparison to the results of Ref. [16], where the so-called Λ-equations were solved to determine the values of $E_{\rm eff}$ and $W_{P,T}$ as analytical derivatives of the coupled cluster energy with respect to the added perturbation (such as the interaction of the electron EDM with the effective electric field or the scalar-pseudoscalar nucleus-electron interaction), an expectation value approach was employed in Ref. [41]. There, the expectation value of a specific operator was calculated, considering only the linear terms in the CCSD wavefunction. (iv) In Ref. [42], the authors calculated the values of $E_{\rm eff}$, $W_{P,T}$, and W_S using quasi-relativistic wavefunctions obtained within the zeroth-order regular approximation (ZORA). They treated electronic correlation effects using the hybrid Becke three-parameter exchange functional and the Lee, Yang, and Parr correlation functional (B3LYP) [84]. A similar approach using the local density approximation functional was used in Ref. [38]. (v) In Ref. [43] the value of $E_{\rm eff}$ was calculated using the exact 2-component atomic mean-field Hamiltonian and the CCSD(T) method. The virtual energy cutoff was set to 100 E_h in the case of RaF. (vi) In Ref. [39], the value of W_a was calculated using the relativistic density functional method employing the Coulomb-attenuated B3LYP functional, the parameters of which were adjusted in Ref. [85].

The values of various nuclear effects of the ^{223,225}Ra isotopes presented in Fig. 2C were calculated as follows. The changes in mean-square charge radii $\delta\langle r^2\rangle$ were taken from [20]. The magnetic dipole moments μ and $\mu(\mathbf{r})$ are based on the measurements presented herein as well as electronic form factor calculations from Ref. [10]. The effect due to the electric quadrupole moment Q_z was estimated using electronic form factor calculations from Ref. [33] and the value of the ^{223}Ra nuclear electric quadrupole moment from Refs. [86, 87]. The expected contributions from the anapole $\mathbf{a}$ and Schiff $\mathbf{S}$ moments were estimated using the electronic form factors calculated in this work. The value of the ^{225}Ra anapole moment was calculated using the nuclear shell model [3, 79], while for the Schiff moment, the value from Ref. [17] was used:

$$S(^{225}\mathrm{Ra}) = 1.0\ \bar{\theta}\ \mathrm{e\ fm}^3, \tag{15}$$

where $\bar{\theta}$ is the $\mathcal{CP}$-violating phase of the QCD Hamiltonian. The upper limit on the Schiff moment in Fig. 2C, is based on the limit on $\bar{\theta}$ from Ref. [34]. Finally, the effect of the magnetic quadrupole moment, MQM, effect in ^{223}RaF is based on the calculations presented in Ref. [35].

The semi-empirical approximation

$$E_{\rm eff} = \alpha\sqrt{AA_d}, \tag{16}$$

assumes (see Ref. [40] for details) that there is a proportionality relation between $E_{\rm eff}$ and a function of the HFS constants of a heavy atom-containing diatomic molecules with a $^2\Sigma_{1/2}$ electronic state. This expression allowed an estimation of $E_{\rm eff}$ for the YbF molecule [40] using the experimental values of the HFS constants and a simple model of the electronic wavefunction, eliminating the need for large-scale calculations. To test this approach for RaF, $E_{\rm eff}$ and the HFS constants were calculated at the simple Dirac-Hartree-Fock level. A value of $\alpha = 0.0313$ GV/cm MHz using Eq. 16 was obtained. Next, Eq. 16 was used again to extract the value of $E_{\rm eff}$ substituting the estimated value of α and the experimental values of the HFS constants determined here. The obtained value of $E_{\rm eff}$ in this case was found to be overestimated by about 19% compared to the precise large-scale calculation presented here. It is however better than the pure Dirac-Hartree-Fock value of $E_{\rm eff}$, which is underestimated by 29%.

Acknowledgments

This work was supported by the Office of Nuclear Physics, U.S. Department of Energy, under grants DE-SC0021176 and DE-SC0021179 (S.M.U., S.G.W., R.F.G.R., A.J.B.); the MISTI Global Seed Funds (S.M.U.); Deutsche Forschungsgemeinschaft (DFG, German Research Foundation) – Projektnummer 328961117 – SFB 1319 ELCH (A.A.B., R.B., K.G., T.G.); STFC grants ST/P004423/1 and ST/V001116/1 (M.L.B., K.T.F., H.A.P., J.R.R., J.W.); Belgian Excellence of Science (EOS) project No. 40007501 (G.N.); KU Leuven C1 project No. C14/22/104 (M.A.K., T.E.C., R.P.dG, G.N); FWO project No. G081422N (M.A.K., G.N.); International Research Infrastructures (IRI) project No. I001323N (M.A.K., T.E.C., R.P.G., A.D., S.G., L.L., G.N., B.vdB.); the European Unions Grant Agreement 654002 (ENSAR2); LISA: European Union's H2020 Framework Programme under grant agreement no. 861198 (M.A., D.H., M.N., J.W.); The Swedish Research Council (2016-03650 and 2020-03505) (D.H., M.N.). The National Key RD Program of China (No: 2022YFA1604800) (X.F.Y.) and the National Natural Science Foundation of China (No:12027809). (X.F.Y.). Electronic structure calculations have been carried out using computing resources of the federal collective usage center Complex for Simulation and Data Processing for Mega-science Facilities at National Research Centre "Kurchatov Institute", http://ckp.nrcki.ru/, and partly using the computing resources of the quantum chemistry laboratory. Molecular electronic structure calculations performed at NRC "Kurchatov Institute" – PNPI have been supported by Grant No. 19-72-10019. Scalar-relativistic calculations performed at SPbU were supported by the foundation for the advancement of theoretical physics and mathematics "BASIS" grant according to Project No. 21-1-2-47-1.

4.4 Article 4: Ionization Potential of Radium Monofluoride

This article presents the measurement of the ionization potential of the ^{226}RaF molecule. The experimental results, combined with *ab initio* many-body electronic structure calculations, confirm the location of the ionization potential below the dissociation energy, proving the suitability for future studies of highly excited Rydberg states in these molecules. For this article, to be submitted to Physical Review Letters (2024), I was involved in the experiment, I contributed to the data analysis, the preparation of the figures and the initial draft of the manuscript.

Ionization potential of radium monofluoride

S. G. Wilkins,[1,*] H. A. Perrett,[2,†] S. M. Udrescu,[1,‡] A. A. Kyuberis,[3,§] L. F. Pašteka,[3,4] M. Au,[5,6] I. Belošević,[7,1] R. Berger,[8] C. L. Binnersley,[2] M. L. Bissell,[2] A. Borschevsky,[3] A. A. Breier,[9] A. J. Brinson,[1] K. Chrysalidis,[5] T. E. Cocolios,[10] B. S. Cooper,[2] R. P. de Groote,[10] A. Dorne,[10] E. Eliav,[11] R. W. Field,[1] K. T. Flanagan,[2,12] S. Franchoo,[13] R. F. Garcia Ruiz,[1] K. Gaul,[8] S. Geldhof,[10] T. F. Giesen,[9] F. P. Gustafsson,[10] D. Hanstorp,[14] R. Heinke,[5] Á. Koszorús,[15] S. Kujanpää,[16] L. Lalanne,[10] G. Neyens,[10] M. Nichols,[14] J. R. Reilly,[2] C. M. Ricketts,[2] S. Rothe,[5] A. Sunaga,[17,18] B. van den Borne,[10] A. R. Vernon,[2] Q. Wang,[19] J. Wessolek,[2] F. Wienholtz,[15] X. F. Yang,[20] Y. Zhou,[21] and C. Zülch[8]

[1]*Massachusetts Institute of Technology, Cambridge, MA 02139*
[2]*School of Physics and Astronomy, The University of Manchester, Manchester, M13 9PL, United Kingdom*
[3]*Van Swinderen Institute for Particle Physics and Gravity, University of Groningen, Groningen, 9747 AG, The Netherlands*
[4]*Department of Physical and Theoretical Chemistry, Faculty of Natural Sciences, Comenius University, Bratislava, 81806, Slovakia*
[5]*Systems Department, CERN, CH 1211 Geneva 23, Switzerland*
[6]*Department Chemie, Johannes Gutenberg-Universität Mainz, Mainz, 55099, Germany*
[7]*TRIUMF, Vancouver, BC V6T 2A3, Canada*
[8]*Fachbereich Chemie, Philipps-Universität Marburg, Marburg, 35032, Germany*
[9]*Laboratory for Astrophysics, Institute of Physics, University of Kassel, Kassel, 34132, Germany*
[10]*KU Leuven, Instituut voor Kern- en Stralingsfysica, Leuven, B-3001 , Belgium*
[11]*School of Chemistry, Tel Aviv University, Tel Aviv, 6997801, Israel*
[12]*Photon Science Institute, The University of Manchester, Manchester, M13 9PY, United Kingdom*
[13]*Laboratoire Irène Joliot-Curie, Orsay, F-91405, France*
[14]*Department of Physics, University of Gothenburg, Gothenburg, 41296, Sweden*
[15]*Experimental Physics Department, CERN, CH 1211 Geneva 23, Switzerland*
[16]*Department of Physics, Accelerator Laboratory, University of Jyväskylä, Jyväskylä, FI-40014, Finland*
[17]*Department of Physics, Graduate School of Science, Kyoto University, Kyoto 606-8502, Japan*
[18]*ELTE, Eötvös Loránd University, Institute of Chemistry, Pázmány Péter sétány 1/A 1117 Budapest, Hungary*
[19]*School of Nuclear Science and Technology, Lanzhou University, Lanzhou, 730000, China*
[20]*School of Physics and State Key Laboratory of Nuclear Physics and Technology, Peking University, Beijing, 100971, China*
[21]*Department of Physics and Astronomy, University of Nevada, Las Vegas, Las Vegas, Nevada 89154, USA*

(Dated: August 10, 2024)

The ionization potential (IP) of radium monofluoride (RaF) was measured to be 4.972(2)[14] eV, revealing a relativistic enhancement in the series of alkaline earth monofluorides. The results are in agreement with a relativistic coupled-cluster prediction of 4.978[6] eV, incorporating up to quantum electrodynamics corrections. Using the same computational methodology, an improved calculation for the dissociation energy (D_e) of 5.56[5] eV is presented. This confirms that radium monofluoride joins the small group of diatomic molecules for which $D_e >$ IP, paving the way for precision control and interrogation of its Rydberg states.

The ionization potential (IP), defined as the minimum energy required to release a bound electron, is a fundamental property of atoms and molecules, and is important in chemistry and physics. The IP is central to revealing rigorous and intuitively appealing interrelationships among all electronic structural properties of atoms and molecules [1]. Electronic states of these systems can be arranged into series, which differ in their principal quantum number, n, and excitation energy. The energy of states within each series increases with n and eventually converges at the IP.

Due to the highly non-linear scaling of atomic and molecular properties with n, states with $n \gg 1$ can exhibit remarkable properties when compared to their ground states. These 'Rydberg states' can have micrometer-sized atomic radii, extended lifetimes and extremely large transition dipole moments, thousands of times larger than those for their low-lying (low-n) states [2]. These exceptional characteristics make Rydberg states prominent systems for quantum computing and simulation [3], precision measurements [4] and the investigation of long-range interactions due to their high sensitivity to external electric fields and photon absorption.

For the majority of diatomic molecules, however, the dissociation energy (D_e) lies lower in energy than the

* wilkinss@mit.edu
† holly.perrett@manchester.ac.uk
‡ sudrescu@mit.edu
§ a.kiuberis@rug.nl

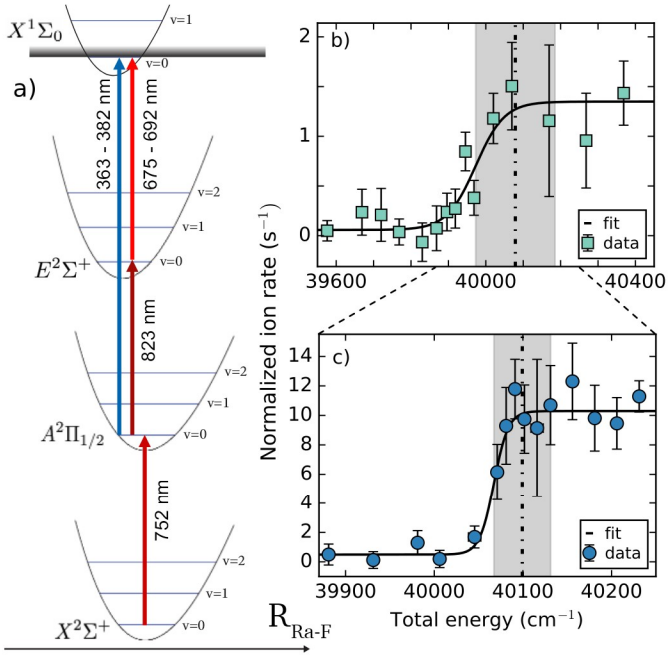

FIG. 1. (Color online) **a)** The two-step and three-step ionization schemes used in the experiments. Power-normalized, background-subtracted ion count rate as a function of total photon energy in $^{226}Ra^{19}F$ for the **b)** two-step scheme and **c)** three-step scheme. The determined IPs are shown as vertical dashed-and-dotted lines with their dominant 1σ systematic uncertainties as gray bands.

IP. This severely limits the ability of experiments to study and manipulate their high-lying Rydberg states, as the molecules can fragment following pre-dissociation in short (ns) timescales. A notable exception to this trend, with $D_e > \mathrm{IP}$, is BaF, which has been an important playground for the investigation of molecular Rydberg states owing to this extremely rare property [5–7].

Molecules containing isotopes of radium have been proposed as being promising systems in which to study the fundamental symmetries of the Universe [8, 9], particularly in the hadronic sector of the Standard Model, where the rare octupole deformation of certain radium isotopes significantly boosts their sensitivity to P,T-violating phenomena [10].

A notable example is the RaF molecule, which was theoretically predicted [8] and later experimentally confirmed to be directly laser-coolable [11–13]. Leveraging the unique properties of high-lying Rydberg states of RaF through manipulating them with external fields, could enable the sensitive control of these molecules [14, 15], offering complementary opportunities for future precision measurements. The realization of such techniques however relies upon the condition that $D_e > \mathrm{IP}$.

Here, we demonstrate that RaF possesses an exceptionally large dissociation energy that exceeds its ionization potential. We report the first measurement of the IP of $^{226}Ra^{19}F$, determined from the ionization threshold of its valence electron under multi-step laser excitation using both two-step and three-step ionization schemes. The obtained value is compared with *ab initio* calculations performed within the relativistic coupled-cluster (RCC) framework, corrected for higher-order effects, including QED contributions. The same computational method is used to calculate its dissociation energy, resulting in an improved value, thus confirming that RaF possesses the rare property in which $D_e > \mathrm{IP}$.

Experimental details: Bunches of $^{226}Ra^{19}F^+$ were produced at the ISOLDE radioactive ion beam facility at CERN and studied with the Collinear Resonance Ionization Spectroscopy (CRIS) experiment. Details on the production of RaF molecules at ISOLDE can be found in Refs. [12, 16]. Upon entering the CRIS beamline, the RaF^+ beam was neutralized in-flight after passing through a charge-exchange cell filled with a sodium vapor, where the neutral RaF molecules predominately populated the $X\ ^2\Sigma^+$ electronic ground state [17]. The non-neutralized residual ions were deflected away, while the neutral bunches entered an ultra high-vacuum interaction region ($\approx\ 10^{-10}$ mbar), where they were collinearly overlapped with either two or three pulsed laser beams.

The ionization threshold was measured during two separate experiments. The ionization schemes for these are shown in Fig. 1 a). In both experiments, the first laser excited the $A\ ^2\Pi_{1/2}(v=0) \leftarrow X\ ^2\Sigma^+(v=0)$ transition of the RaF molecules [12], transferring molecules residing in multiple rotational states from the vibronic ground state [11]. In the first experiment, the second laser was used to ionize molecules directly from the $A\ ^2\Pi_{1/2}(v=0)$ state, constituting a two-step resonance ionization scheme. In the second experiment, the discovery of the higher-lying $E\ ^2\Sigma^+$ state [18] allowed a three-step resonance ionization scheme to be employed. This resulted in a significantly improved signal-to-background ratio as the superior pulse energy and beam quality of the ionization laser operating in its fundamental wavelength range increased the ionization efficiency while simultaneously decreasing the non-resonant background. Additional details on the laser setups for each experiment can be found in the Supplemental Material.

The wavelengths of the ionization lasers were scanned and the resulting RaF^+ molecular ions were deflected onto an ion detector. The ion count rate was monitored as a function of ionization laser wavelength. The total excitation energy delivered to each molecule by the lasers was determined by Doppler-correcting the sum of the individual photon energies of the lasers in each ionization scheme. Two scans at each ionization laser wavelength were taken; one in which all lasers of each scheme were present in the interaction region and the other one where only the ionization laser was present such that any background resulting from the ionization laser could be accounted for. The ion rate was then determined as the difference between these two scans and linearly normal-

ized with respect to the ionization laser power.

The resulting thresholds are shown in Fig. 1 b) and c). In a similar fashion to Ref. [19], the two sets of data were fit using a Sigmoid function and the IPs determined from the energy at which the ion rate saturates. The ionization threshold measured using the three-step scheme (Fig. 1 c)) can be seen to increase more sharply when compared to the two-step scheme (Fig. 1 b)). This is due to the additional rotational angular momentum (J) selectivity introduced by having two sequential resonant excitations before the ionization step in the three-step scheme. This in turn reduced the number of high-lying Rydberg states populated by the ionization laser at energies below the IP, resulting in a sharper threshold. The ionization thresholds were determined to be 4.969(2)[13] eV and 4.972(1)[4] eV for the two-step and three-step scheme, respectively. A systematic uncertainty resulting from the fitting procedure and IP extraction is assigned by taking the energy difference between the inflection points of the curves and the extracted IPs. More details on the fitting and its justification can be found in the Supplementary Material.

The majority of each molecular bunch was present in a shielded interaction region when the ionization process took place. However, a fraction of the molecules at the tail-end of each bunch were outside of this region where stray fields are non-negligible. These molecules were gated out of the data set as a conservative measure to negate any systematic downward shift of the observed thresholds resulting from the electric fields present. See the Supplementary Material for more details on the time-of-flight gating.

The potential energy curves for the $A\ ^2\Pi_{1/2}$, $E\ ^2\Sigma^+$ states in RaF and the $X\ ^1\Sigma^+$ RaF^+ ground state calculated here have similar equilibrium bond lengths computed to be 2.246 Å, 2.191 Å and 2.167 Å, respectively. As no significant change in the molecular geometry or vibrational quantum number occurs, the observed ionization thresholds from the $A\ ^2\Pi_{1/2}$ and $E\ ^2\Sigma^+$ state represent the adiabatic IP of RaF. The final experimental value is given as 4.971(2)[14] eV, using the weighted standard deviation of the two-step and three-step scheme measurements to calculate the statistical error. The systematic errors from the two measurements were added in quadrature.

Computational method: The relativistic single-reference coupled-cluster approach with single, double (CCSD), and perturbative triple excitations (CCSD(T)) was employed in our calculations, as implemented in the DIRAC19 program package [20]. A zero-point energy (ZPE) correction of 5 meV is added to estimate the minimum vibrational energy of RaF and RaF^+ in the $^2\Sigma^+$ and $^1\Sigma^+$ states, respectively, using calculated harmonic vibrational frequencies. Relativistic core-valence-correlating Dyall basis sets [21, 22] of varying quality, cv$n$z ($n = 2-4$) augmented by a single layer of diffuse functions, were used (s-aug-cv$n$z). The calculated potential energy curves were extrapolated to the complete basis-set limit (CBSL) using the scheme in Ref. [23] for the Dirac-Hartree-Fock energy and the scheme in Ref. [24] for the correlation contribution. In the calculations, 49 electrons were correlated and the virtual space was cut off at 50 a.u.

To correct for the limited active space used, the difference between results obtained correlating 49 electrons with a 50 a.u. cutoff and those obtained correlating all (97) electrons with a virtual space cutoff of 2000 a.u was calculated. In order to capture the full active space effect and to account for inner-core correlations, the all-electron quality basis set was used in the latter calculation. The more modestly sized dyall-cv3z and dyall-ae3z basis sets were employed, as calculations were prohibitively computationally expensive at the 4z level. Furthermore, the possible lack of diffuse functions was accounted for by taking the difference between the d-aug-cv4z and the s-aug-cv4z results. The above corrections were calculated at a single geometry point and added to the potential energy curves.

The effect of perturbative triple excitations on the CBSL level was determined to be 51 meV. The effect of full triple excitations was evaluated to be around 1 meV by comparing the IP calculated at the CCSDT and CCSD(T) levels using the MRCC code [25, 26]. These calculations were performed using the dyall.v3z basis sets, 16 correlated electrons, and a 10 a.u. virtual cutoff. Higher-level excitations were not considered owing to the very small difference between the CCSD(T) and CCSDT results.

TABLE I. Experimental and calculated IP and D_e of RaF.

Method	IP (eV)	D_e (eV)
CBS-DC-CCSD[a]	4.932	5.454
CBS-DC-CCSD(T)[a]	4.983	5.547
+aug+ae.vs.cv	4.986	5.554
+ΔT	4.987	5.549
+Breit	4.985	5.547
+QED	4.978	5.556
Theoretical	4.978[6]	5.56[5]
Experimental	4.971(2)[14]	5.57(6)[22][b]

[a] ZPE correction is included.
[b] Scaled from Ref. [12].

In addition, the Breit and QED contributions were estimated. QED corrections were calculated using a development version of the DIRAC code [27]. Using this implementation, two effective QED potentials were added variationally to the DC Hamiltonian. The QED correction itself was obtained from a single-point calculation at the equilibrium geometry of neutral RaF. The Uehling potential [28] was employed for vacuum polarization and the effective potential of Flambaum and Ginges for the electron self-energy [29]. Our estimate of the size of the Breit effect relied on the fact that the electronic structure of RaF is very similar to that of Ra^+ and upon ionization, the valence electron is removed from a Rydberg orbital (atomic-like and non-bonding). Thus, the con-

tribution of the Breit interaction to the IP of RaF can be approximated by the effect calculated for the IP of Ra^+ (direct calculations of molecular Breit contributions are challenging at present). These calculations were performed within the Fock-space coupled-cluster approach (DCB-FSCC), using the Tel Aviv atomic computational package [30].

The various higher-order corrections are added to the adiabatic CBS-DC-CCSD(T) IP and the final theoretical value was determined to be 4.978[6] eV as shown in Table II. Using the same computational method, the dissociation energy D_e of RaF was calculated to be 5.56[5] eV. The uncertainty on the calculated IP and D_e was evaluated through further computational investigation using similar procedures that were previously employed for various properties of both atoms and molecules [31–34]. The details of the uncertainty treatment for both properties can be found in the Supplemental Material.

Discussion: Fig. 2 a) shows experimental determinations of the IP of the group II monofluorides from CaF to RaF and compared with theoretical calculations using the same method as for RaF described previously [35]. Experimental IP values measured using electron-impact [36–38] and laser spectroscopy methods [6, 39] are shown as yellow diamonds and turquoise circles, respectively, with theoretical calculations shown as dark blue squares. The error bars for the laser measurements and theoretical predictions are smaller than the markers. Fig. 2 b) shows the deviation, in units of standard deviations, between the theoretical predictions (dark blue squares) and experimental values (gray line). Where they exist, the experimental values used in the comparison are from laser spectroscopy methods using Rydberg states or ionization threshold measurements, owing to their higher precision. In SrF, where no laser measurements exist, an electron-impact measurement is used for comparison. Excellent agreement within 1 standard deviation is obtained for CaF, BaF, and RaF whereas SrF agrees within 2 standard deviations. Fig. 2 a) highlights the ability to determine the IP of RaF at a comparable or better precision than experiments on the homologues, despite the technical challenges imposed by its short-lived nature.

The IP of the group II monofluorides decreases progressively with increasing proton number, before increasing again in RaF. This enhancement in valence electron binding energy can be attributed to relativistic effects, which are significantly more pronounced in the heavier RaF. These effects result from the relativistic increase of the electron mass driven by the high velocity that bound electrons experience in atoms and molecules containing heavy elements [40]. This in turn spatially contracts orbitals with low angular momentum which increases their binding energies [41, 42]. The relativistic treatment required for correctly describing RaF is fully achieved in this study, yielding good agreement between theory and experiment as in the case of its homologues.

Fig. 2 c) shows how the calculated IP for RaF evolves with an increasing level of computational sophistication.

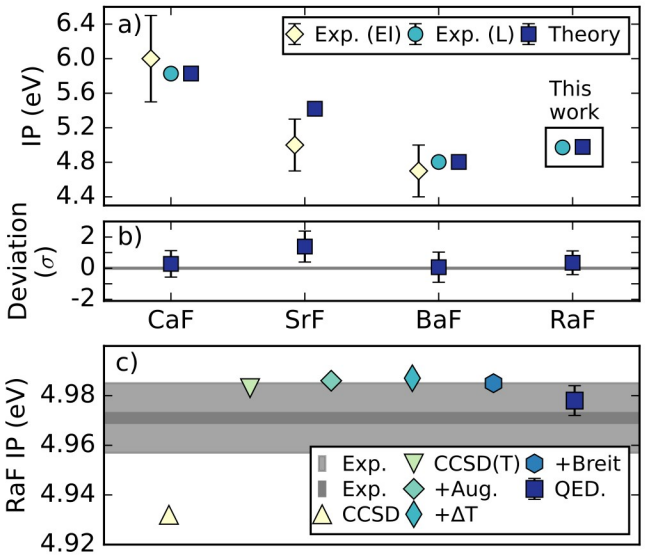

FIG. 2. (Color online) **a):** Comparison of predicted theoretical and measured values for the IP of Group II monofluorides. Electron-impact (EI) [36–38] and laser (L) measurements [6, 39] are denoted in the legend. The error bars for the laser measurements and theoretical predictions are smaller than the markers. **b):** Deviation, in standard deviations, between the theoretical predictions (dark blue squares) and experimental values (gray line). **c):** Comparison of experimental and theoretical values for the IP of ^{226}RaF for increasing computational sophistication (left to right). Error bars are shown only for the most accurate theoretical value. The thin dark gray band and thick light gray band correspond to the statistical and systematic uncertainties on the experimental value for the RaF IP.

An agreement within 1 standard deviation is found between experiment and CCSD(T) theory that incorporates a complete basis set-extrapolation correction, non-perturbative triple excitations, and Breit and QED corrections. The final theoretical uncertainty is 6 meV, owing to the extensive implementation of higher-order contributions.

Benchmarking the predictive power of molecular theory is crucial for the study of radioactive molecules, which is a prominent future avenue for precision tests of the Standard Model [43]. As most of the short-lived radioactive molecules of interest can only be made in small quantities at specialized facilities, none of their chemical properties are known experimentally even though knowledge of their chemical behavior is necessary to guide, or even enable altogether, their production and study [44, 45]. Therefore, while the calculated IP of RaF is accurate even for predictions of lower sophistication in Fig. 2, the ability to reduce the theoretical uncertainty by including higher-order contributions, up to the QED level, remains important to aid experiments attempting to perform the first spectroscopy of previously unexplored systems.

The previously calculated values of the dissociation energy, D_e, for RaF vary between 3.980 eV [8] and 5.282 eV

[46] with no corresponding uncertainties reported. Using the same computational method as for the IP, which achieves a more extensive and rigorous treatment of higher-order contributions compared to previous studies, an improved calculation of the RaF D_e equal to 5.56[5] eV is presented. This is in agreement with the RaF D_e extracted from Morse potential fits in Ref. [12], provided they are scaled by the ratio 1.55[6]. Dissociation energy determinations from Morse potential fits use linear extrapolations that significantly underestimate the true dissociation energy in molecules where ionic bonding is important [47, 48]. By taking the extrapolated D_e values in MgF, CaF, SrF and BaF, and comparing them to the true measured dissociation energies, the aforementioned scaling factor is obtained, which results in a RaF D_e of 5.57(6)[22] eV (using the $A\ ^2\Pi_{1/2}$ value from Ref. [12]). The resulting value and uncertainty of the computed D_e, corroborated by the agreement between experiment and theory for the IP, confirms that RaF joins BaF in the rare class of diatomic molecules for which $D_e >$ IP.

Conclusion: The ionization potential of radium monofluoride (RaF) was measured with the CRIS experiment at CERN-ISOLDE to be 4.971(2)[14] eV, through consistent observations of the ionization thresholds starting from two different excited electronic states. The experimental results were compared against predictions calculated with single-reference relativistic coupled-cluster theory that incorporates triple excitations, basis-set, Breit-effect and QED corrections. A good agreement is obtained between experiment and theory for RaF, in addition to its lighter homologues. The dissociation energy was found to lie above the IP, offering the possibility of accessing and utilizing Rydberg states in RaF, without loss due to pre-dissociation. This opens up several opportunities for controlling and manipulating the molecule via external fields [14, 15]. Additionally, these states can also offer an alternative window into probing the structure of radium nuclei [5].

Acknowledgments: The authors thank Michael Morse for his insights. This work was supported by the Office of Nuclear Physics, U.S. Department of Energy, under grants DE-SC0021176 and DE-SC0021179, the MISTI Global Seed Funds, Deutsche Forschungsgemeinschaft (DFG, German Research Foundation) – Projektnummer 328961117 – SFB 1319 ELCH; STFC grants ST/P004423/1 and ST/V001116/1, ERC Consolidator Grant no. 648381 (FNPMLS), Belgian Excellence of Science (EOS) project No. 40007501; KU Leuven C1 project No. C14/22/104, FWO project No. G081422N, International Research Infrastructures (IRI) project No. I001323N, the European Unions Grant Agreement 654002 (ENSAR2), LISA: European Union's H2020 Framework Programme under grant agreement no. 861198, The Swedish Research Council (2016-03650 and 2020-03505), The National Key RD Program of China (No: 2022YFA1604800) (X.F.Y.) and the National Natural Science Foundation of China (No:12027809), the Dutch Research Council (NWO) projects number VI.C.212.016 and Vi.Vidi.192.088, the Slovak Research and Development Agency projects APVV-20-0098 and APVV-20-0127, JSPS Overseas Challenge Program for Young Researchers, Grant No. 201880193, JST Moonshot R&D Grant No. JPMJMS2269 and NSF RII Track-4 (Grant No. 2327247). We thank the Center for Information Technology at the University of Groningen for their support and for providing access to the Peregrine and Hábrók high performance computing cluster.

[1] S. Ross, An MQDT Primer, AIP Conf. Proc. **225**, 73–110 (2008).
[2] T. F. Gallagher, Rydberg atoms, Rep. Prog. Phys. **51**, 143 (1988).
[3] M. Saffman, T. G. Walker, and K. Mølmer, Quantum information with Rydberg atoms, Rev. Mod. Phys. **82**, 2313–2363 (2010).
[4] U. D. Jentschura, P. J. Mohr, and J. N. Tan, Fundamental constants and tests of theory in Rydberg states of one-electron ions, J. Phys. B **43**, 074002 (2010).
[5] Y. Zhou, D. D. Grimes, T. J. Barnum, D. Patterson, S. L. Coy, E. Klein, J. S. Muenter, and R. W. Field, Direct detection of rydberg-rydberg millimeter-wave transitions in a buffer gas cooled molecular beam, Chem. Phys. Lett. **640**, 124 (2015).
[6] Z. J. Jakubek, Rydberg spectroscopy of barium monofluoride, PhD Thesis, Massachusetts Institute of Technology (1995).
[7] Z. J. Jakubek, N. A. Harris, R. W. Field, J. A. Gardner, and E. Murad, Ionization potentials of CaF and BaF, J. Chem. Phys. **100**, 622 (1994).
[8] T. A. Isaev, S. Hoekstra, and R. Berger, Laser-cooled RaF as a promising candidate to measure molecular parity violation, Phys. Rev. A **82**, 052521 (2010).
[9] T. A. Isaev and R. Berger, Lasercooled radium monofluoride: A molecular all-in-one probe for new physics, arXiv **1302.5682** (2020).
[10] N. Auerbach, V. V. Flambaum, and V. Spevak, Collective T- and P-odd electromagnetic moments in nuclei with octupole deformations, Phys. Rev. Lett. **76**, 4316–4319 (1996).
[11] S. M. Udrescu, S. G. Wilkins, A. A. Breier, M. Athanasakis-Kaklamanakis, R. F. G. Ruiz, M. Au, I. Belošević, R. Berger, M. L. Bissell, and C. L. Binnersley *et al.*, Precision spectroscopy and laser-cooling scheme of a radium-containing molecule, Nat. Phys. **20**, 202–207 (2024).
[12] R. F. Garcia Ruiz, R. Berger, J. Billowes, C. L. Binnersley, M. L. Bissell, A. A. Breier, A. J. Brinson, K. Chrysalidis, T. E. Cocolios, and B. S. Cooper *et al.*, Spectroscopy of short-lived radioactive molecules, Nature **581**, 396–400 (2020).
[13] M. Athanasakis-Kaklamanakis, S. G. Wilkins, P. Lassègues, L. Lalanne, J. R. Reilly, O. Ahmad,

M. Au, S. W. Bai, J. Berbalk, and C. Bernerd *et al.*, Radiative lifetime of the $A\ ^2\Pi_{1/2}$ state in RaF with relevance to laser cooling, Phys. Rev. A **110**, L010802 (2024).
[14] S. D. Hogan, P. Allmendinger, H. Saßmannshausen, H. Schmutz, and F. Merkt, Surface-electrode Rydberg-stark decelerator, Phys. Rev. Lett. **108**, 063008 (2012).
[15] S. D. Hogan, Rydberg-Stark deceleration of atoms and molecules, EPJ Techn. Instrum. **3**, 1–50 (2016).
[16] M. Au, M. Athanasakis-Kaklamanakis, L. Nies, J. Ballof, R. Berger, K. Chrysalidis, P. Fischer, R. Heinke, J. Johnson, and U. Köster *et al.*, In-source and in-trap formation of molecular ions in the actinide mass range at CERN-ISOLDE, Nucl. Instrum. Methods Phys. Res. B **541**, 375–379 (2023).
[17] T. A. Isaev, S. Hoekstra, L. Willmann, and R. Berger, Ion neutralisation mass-spectrometry route to radium monofluoride (RaF), arXiv **1310.1511** (2013).
[18] M. Athanasakis-Kaklamanakis, S. G. Wilkins, L. Skripnikov, A. Koszorús, A. A. Breier, M. Au, R. Berger, I. Belošević, M. L. Bissell, and A. Borschevsky *et al.*, Pinning down electron correlations in RaF via spectroscopy of excited states, arXiv **2308.14862** (2023).
[19] S. Rothe, A. N. Andreyev, S. Antalic, A. Borschevsky, L. Capponi, T. E. Cocolios, H. D. Witte, E. Eliav, D. V. Fedorov, and V. N. Fedosseev *et al.*, Measurement of the first ionization potential of astatine by laser ionization spectroscopy, Nat. Commun **4**, 1835 (2013).
[20] T. Saue, R. Bast, A. S. P. Gomes, H. J. A. Jensen, L. Visscher, I. A. Aucar, R. D. Remigio, K. G. Dyall, E. Eliav, and E. Fasshauer *et al.*, The DIRAC code for relativistic molecular calculations, J. Chem. Phys. **152**, 204104 (2020).
[21] K. G. Dyall, Relativistic double-zeta, triple-zeta, and quadruple-zeta basis sets for the light elements H–Ar, Theor. Chem. Acc. **135**, 128 (2016).
[22] K. G. Dyall, Relativistic double-zeta, triple-zeta, and quadruple-zeta basis sets for the 4s, 5s, 6s, and 7s elements, J. Phys. Chem. A **113**, 45 (2009).
[23] D. Feller, Application of systematic sequences of wave functions to the water dimer, J. Chem. Phys. **96**, 6104–6114 (1992).
[24] T. Helgaker, W. Klopper, H. Koch, and J. Noga, Basis-set convergence of correlated calculations on water, J. Chem. Phys. **106**, 9639–9646 (1997).
[25] M. Kállay, P. R. Nagy, D. Mester, Z. Rolik, G. Samu, J. Csontos, J. Csóka, P. B. Szabó, L. Gyevi-Nagy, and B. Hégely *et al.*, The MRCC program system: Accurate quantum chemistry from water to proteins, J. Chem. Phys. **152**, 074107 (2020).
[26] M. Kállay, P. R. Nagy, D. Mester, Z. Rolik, G. Samu, J. Csontos, J. Csóka, P. B. Szabó, L. Gyevi-Nagy, and B. Hégely *et al.*, MRCC, a quantum chemical program suite, https://www.mrcc.hu .
[27] A. Sunaga, M. Salman, and T. Saue, 4-component relativistic Hamiltonian with effective QED potentials for molecular calculations, J. Chem. Phys. **157**, 164101 (2022).
[28] E. A. Uehling, Polarization Effects in the Positron Theory, Phys. Rev. **48**, 55–63 (1935).
[29] V. V. Flambaum and J. S. M. Ginges, Radiative potential and calculations of qed radiative corrections to energy levels and electromagnetic amplitudes in many-electron atoms, Phys. Rev. A **72**, 052115 (2005).
[30] TRAFS-3C code (Tel-Aviv Relativistic Atomic Fock-Space coupled cluster code), written by E. Eliav, U. Kaldor and Y. Ishikawa (1990-2013), with contributions by A. Landau.
[31] Y. Hao, M. Iliaš, E. Eliav, P. Schwerdtfeger, V. V. Flambaum, and A. Borschevsky, Nuclear anapole moment interaction in BaF from relativistic coupled-cluster theory, Phys. Rev. A **98**, 032510 (2018).
[32] Y. Guo, L. F. Pašteka, E. Eliav, and A. Borschevsky, Chapter Five - Ionization potentials and electron affinity of oganesson with relativistic coupled cluster method, in *New Electron Correlation Methods and their Applications, and Use of Atomic Orbitals with Exponential Asymptotes*, Advances in Quantum Chemistry, Vol. 83, edited by M. Musial and P. E. Hoggan (Academic Press, 2021) pp. 107–123.
[33] P. A. Haase, E. Eliav, M. Iliaš, and A. Borschevsky, Hyperfine Structure Constants on the Relativistic Coupled Cluster Level with Associated Uncertainties, J. Phys. Chem. A **124**, 16 3157–3169 (2020).
[34] D. Leimbach, J. Karls, Y. Guo, R. Ahmed, J. Ballof, L. Bengtsson, F. B. Pamies, A. Borschevsky, K. Chrysalidis, and E. Eliav *et al.*, The electron affinity of astatine, Nat. Commun **11**, 3824 (2020).
[35] A. A. Kyuberis, L. F. Pasteka, E. Eliav, H. Perrett, A. Sunaga, S. M. Udrescu, S. G. Wilkins, R. F. G. Ruiz, and A. Borschevsky, Accurate theoretical determination of the ionization potentials of CaF, SrF, and BaF, Phys. Rev. A **109**, 022813 (2024).
[36] D. L. Hildenbrand, Dissociation energy of boron monofluoride from mass-spectrometric studies, J. Chem. Phys. **43**, 1400–1403 (1965).
[37] D. L. Hildenbrand, Mass-spectrometric studies of bonding in the group IIa fluorides, J. Chem. Phys. **48**, 3657–3665 (1968).
[38] K. H. Lau, R. D. Brittain, and D. L. Hildenbrand, High temperature thermodynamic studies of some gaseous thorium fluorides, J. Chem. Phys. **90**, 1158–1164 (1989).
[39] J. M. Berg, J. E. Murphy, N. A. Harris, and R. W. Field, Observation and analysis of core-penetrating Rydberg states of calcium monofluoride, Phys. Rev. A **48**, 3012 (1993).
[40] N. C. Pyper, Relativity and the periodic table, Philos. Trans. R. Soc. A **378:**, 20190305 (2020).
[41] P. Pyykko and J. P. Desclaux, Relativity and the periodic system of elements, Acc. Chem. Res. **12**, 276–281 (1979).
[42] P. Pyykko, Relativistic effects in structural chemistry, Chem. Rev. **88**, 563–594 (1988).
[43] G. Arrowsmith-Kron, M. Athanasakis-Kaklamanakis, M. Au, J. Ballof, J. J. Dobaczewski, R. F. G. Ruiz, N. R. Hutzler, A. Jayich, W. Nazarewicz, and J. Singh *et al.*, Opportunities for fundamental physics research with radioactive molecules, Rep. Prog. Phys (2024).
[44] R. Kirchner, Review of ISOL target–ion-source systems, Nucl. Instrum. Methods Phys. Res. B **204**, 179–190 (2003).
[45] U. Köster, O. Arndt, E. Bouquerel, V. N. Fedoseyev, H. Frånberg, A. Joinet, C. Jost, I. S. K. Kerkines, and R. Kirchner, Progress in ISOL target–ion source systems, Nucl. Instrum. Methods Phys. Res. B **266**, 4229–4239 (2008).
[46] T. A. Isaev, S. Hoekstra, L. Willmann, and R. Berger, Ion neutralisation mass-spectrometry route to radium monofluoride (RaF), arXiv **1310.1511** (2013).

[47] A. G. Gaydon, The determination of dissociation energies by the birge-sponer extrapolation, Proc. Phys. Soc. **58**, 525–538 (1946).
[48] C. L. Beckel, M. Shafi, and R. Engelke, Comparison of actual and linearly extrapolated dissociation energies of diatomic molecules, J. Mol. Spectrosc. **40**, 519–535 (1971).
[49] P. Naubereit, Weiterentwicklung eines weitabstimmbaren Titan:Saphir-Lasers und sein Einsatz zur Spektroskopie hochliegender Resonanzen in Holmium, Master's Thesis, Johannes Gutenberg-Universität Mainz (2014).
[50] M. Reponen, V. Sonnenschein, T. Sonoda, H. Tomita, M. Oohashi, D. Matsui, and M. Wada, Towards in-jet resonance ionization spectroscopy: An injection-locked Titanium:Sapphire laser system for the PALIS-facility, Nucl. Instrum. Methods Phys. Res. A **908**, 236 (2018).
[51] W. J. Huang, M. Wang, F. G. Kondev, G. Audi, and S. Naimi, The AME 2020 atomic mass evaluation (I). Evaluation of input data, and adjustment procedures, Chinese Phys. C **45**, 030002 (2021).
[52] S. Rothe, An all-solid state laser system for the laser ion source RILIS and in-source laser spectroscopy of astatine at ISOLDE, CERN, PhD Thesis, Johannes Gutenberg-Universität Mainz (2012).
[53] C. Linton, B. Simard, H. P. Loock, S. Wallin, G. K. Rothschopf, R. F. Gunion, M. D. Morse, and P. B. Armentrout, Rydberg and pulsed field ionization-zero electron kinetic energy spectra of YO, J. Chem. Phys. **111**, 5017–5026 (1999).
[54] W. A. Chupka, Factors affecting lifetimes and resolution of Rydberg states observed in zero-electron-kinetic-energy spectroscopy, J. Chem. Phys. **98**, 4520–4530 (1993).
[55] D. J. Manura and D. A. Dahl, SIMION 2020 (2020).
[56] J. M. Martin, Ab initio total atomization energies of small molecules — towards the basis set limit, Chemical Physics Letters **259**, 669 (1996).
[57] M. Lesiuk and B. Jeziorski, Complete Basis Set Extrapolation of Electronic Correlation Energies Using the Riemann Zeta Function, Journal of Chemical Theory and Computation **15**, 5398 (2019).

I. SUPPLEMENTAL MATERIAL

A. Experimental setup

Laser setup - two-step scheme: A pulsed grating-tunable Ti:Sa laser with a linewidth of several GHz [49] produced 752-nm light used to drive the $A\ ^2\Pi_{1/2}(v=0) \leftarrow X\ ^2\Sigma^+(v=0)$ transition [12] of the RaF molecules, exciting multiple rotational states from the vibronic ground state. A maximum pulse energy of 150 μJ was collimated through the interaction region with an 8 mm spot size. The wavelength of this laser was kept constant and measured using a HighFinesse WSU-2 wavelength meter.

A Sirah Cobra pulsed dye laser with a linewidth of 1.8 GHz produced 726-764 nm light which was frequency doubled to 363-382 nm. This light was used to ionize molecules from the $A\ ^2\Pi_{1/2}(v=0)$ state. The pulse energy of the second harmonic output of this laser varied between between 50-130 μJ and the light was collimated through the interaction region with a roughly 8-mm spot size. The wavelength and power of the ionization laser were measured using a HighFinesse WS6 wavelength meter and Thorlabs S120VC power sensor, respectively.

The relative timings of the laser pulses were adjusted to maximize the above-threshold ion rate using a Quantum Composers 9520 Digital Delay Generator.

Laser setup - three-step scheme: The 752-nm light used to drive the $A\ ^2\Pi_{1/2}(v=0) \leftarrow X\ ^2\Sigma^+(v=0)$ transition [12] of the RaF molecules was produced by a pulsed injection-seeded titanium-sapphire (Ti:Sa) laser [50] with a linewidth of around 20 MHz. A maximum pulse energy of 55 μJ was delivered in a spot size of approximately 8 mm collimated through the interaction region. The combined high photon density and transition strength caused significant power broadening, intentionally exciting multiple rotational levels centered around $J = 21.5$ from the vibronic ground state [11], despite the narrower linewidth of the laser. This was done to ensure the largest possible ion rate from which to determine the ionization threshold, given the challenges in studying such a small molecular beam intensity (10^5 s^{-1}).

A pulsed grating-tunable Ti:Sa laser with a linewidth of a several GHz [49] produced 823-nm light to further excite the molecules residing in $A\ ^2\Pi_{1/2}(v=0)$ to the $E\ ^2\Sigma^+(v=0)$ state. A maximum pulse energy of 130 μJ was collimated through the interaction region with an 8 mm spot size. The wavelengths of the lasers used for the first two excitation steps were kept constant and measured using a HighFinesse WSU-2 wavelength meter.

A Sirah Cobra pulsed dye laser with a linewidth of 1.8 GHz produced 675-692 nm light to ionize molecules from the $E\ ^2\Sigma^+(v=0)$ state. The pulse energy of this laser varied between 780-900 μJ across this wavelength range and the light was collimated through the interaction region with an 8-mm spot size. The wavelength and power of the ionization laser were measured using a HighFinesse WS6 wavelength meter and Thorlabs S370C power sensor, respectively.

The relative timings of the laser pulses were adjusted to maximize the above-threshold ion rate using a Quantum Composers 9520 Digital Delay Generator.

B. Data taking, processing and analysis

Doppler correction: The total excitation energy delivered to the molecules was determined by first adding the photon energies of the lasers in each scheme, as read by the two wavelength meters. This sum, E_{Lab}, was converted to the molecular rest frame energy, E, according to:

$$E = E_{\mathrm{Lab}} \frac{\sqrt{1-\beta^2}}{(1+\beta)}, \tag{1}$$

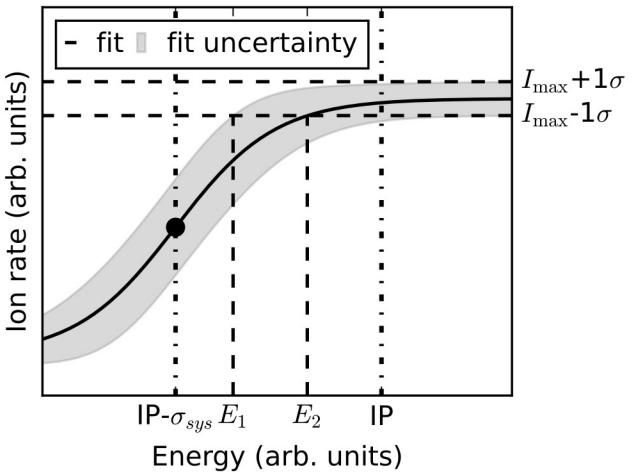

FIG. 3. Schematic representation of IP fitting procedure. See text for details.

with

$$\beta = \sqrt{1 + \frac{m^2c^4}{(eV + mc^2)^2}}, \tag{2}$$

where m is the combined masses of ^{226}Ra and ^{19}F [51], e is the charge of the electron and c is the speed of light and V is the acceleration voltage which averaged 39954(1) V for the two-step scheme experiment and 29614(1) V for the three-step scheme experiment. The uncertainty on the Doppler-corrected total photon energy, E, was determined to be much smaller than 1 cm^{-1}.

Scan procedure: Data was taken where the ion count rate was measured at discrete ionization laser wavelengths across the threshold region. Two scans at each set wavelength were taken after a measurement of the ionization laser power. In the first, all lasers for each ionization scheme were present in the interaction region and in the second, only the ionization lasers were present. This allowed any background resulting from the ionization laser to be accounted for. The ion rate was then determined as the difference between these two scans and was normalized with respect to the ionization laser power, which was measured prior to each scan. The data was then binned with respect to energy.

Fitting procedure: There is a lack of consistency in the literature on how to extract the ionization potential (IP) from observed ionization thresholds. Here, a similar procedure to Ref. [19] is followed where the IP is determined from the energy at which the ion rate saturates. The approach used in Ref. [19] is justified in Ref. [52], which contains an extended discussion of IP measurements derived from ionization thresholds obtained in resonance ionization experiments.

This method was chosen, instead using the onset energy where the first ions are observed or inflection point of the ion rate curve, because high-lying Rydberg states are expected to be populated by the laser ionization scheme in the experiment. These states can be subsequently ionized non-resonantly by absorption of another photon from the ionization laser or by the electric field generated by the deflection plates at the end of the interaction region with latter mechanism only being possible for states which lie sufficiently close in energy to the IP. The high-lying Rydberg states appear in series which increase in density as the IP is approached, forming a threshold. Once a certain energy is reached, all nearby photon energies result in a consistent ion rate, resulting from directly ionizing molecules from the excited states, which is interpreted as the IP.

The binned data was fitted using a Sigmoid function given by the following:

$$I(E) = B + \frac{I_{\max} - B}{1 + e^{(E_0 - E)/k}} \tag{3}$$

where $I(E)$ is the energy-dependent ^{226}RaF ion rate, B is the background, $I_{\max}$ is the maximum ion rate, k is the threshold width and E_0 is the inflection point of the curve.

The IP was taken as the point where the ion rate saturates. As the fitted curve strictly only reaches $I_{\max}$ at very large energies, the following procedure was undertaken to determine the IP, which is schematically depicted in Fig. 3. The fitted Sigmoid function, $I(E)$, was plotted in addition to its associated uncertainty, shown as the solid black line and gray band, respectively, in Fig. 3. Two constant ion rate limits corresponding to $I_{\max} \pm 1\sigma$ were also plotted (horizontal dashed lines).

Two energies were determined; the first of which where the $+1\sigma$ boundary of $I(E)$ intersects $I_{\max} - 1\sigma$ and the second where $I(E)$ meets the same limit. These two energies are denoted by E_1 and E_2 on the x-axis of Fig. 3. The IP was determined by adding the energy difference $E_2 - E_1$ to E_2. The systematic uncertainty, σ_{sys} resulting from the fitting and extraction procedure is taken as half of the width of the ionization threshold, namely the difference between the IP and the energy of the inflection point, E_0, shown as a black circle in Fig. 3.

Stray electric field impact: Electric fields present during ionization are known to decrease the observed IP according to $\Delta(\text{IP})\ (\text{cm}^{-1}) = 6.12\sqrt{\epsilon}$ where ϵ is the electric field in V/cm [53, 54]. The laser excitation and ionization process during both experiments predominately took place in a shielded interaction region. Outside of the shielded region are electrostatic elements held at high voltage including the non-neutral beam deflector (2000 V) on one side and the post-ionization deflection plates (±2600 V) on the other.

To estimate the magnitude of any fields that leak into the shielded region, SIMION [55] simulations were performed and the quantity $6.12\sqrt{\epsilon}$ was evaluated across the central axis of the vacuum chambers, in addition to 8 equidistant lines that follow the surface of a cylinder with a radius of 1 cm surrounding this. The simulated central-axis values are shown in Fig. 4 as a black line. From this, it is shown that the tail-end of the ^{226}RaF$^+$

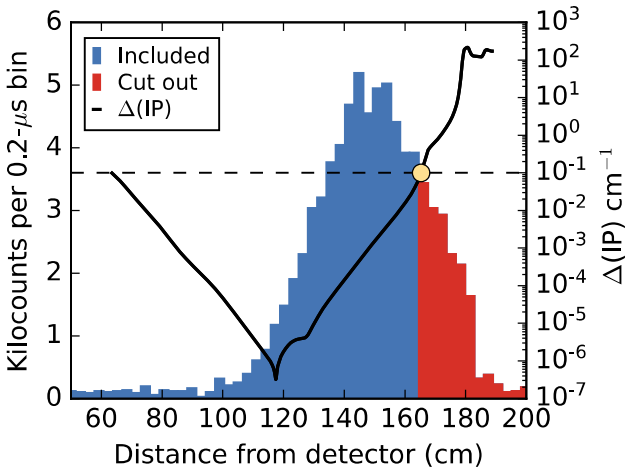

FIG. 4. Δ(IP) calculated as a function of distance from the ion detector (black line). The horizontal dashed line corresponds to the limit set at Δ(IP) = 0.1 cm^{-1}. Time-of-flight profile of ^{226}RaF$^+$ ions in the three-step scheme experiment is shown as a histogram. The blue portion of the histogram was included in the data analysis whereas the red portion was excluded.

bunches in each experiment were in a region with non-negligible electric fields. Within the shielded region, the simulated off-axis Δ(IP) values were in agreement with the on-axis value. However, outside of this region, the off-axis values varied significantly. As the exact beam profile and propagation axis were not known during the experiments, cutting the data with a conservative limit of Δ(IP) (cm^{-1}) > 0.1 was chosen in favor of applying a energy correction as a function ^{226}RaF$^+$ ion time of flight. This gating procedure shifted the extracted IPs by less than 1 meV and 1 meV, for the three-step and two-step scheme, respectively. The statistical uncertainty for the three-step scheme did not change but decreased from 3 meV to 2 meV for the two-step scheme, despite the decreased statistics. The systematic uncertainty reduced from 16 meV to 13 meV for the two-step scheme, remaining unchanged for the three-step scheme.

C. Computational method details

The final calculated IP and D_e of RaF are shown in Table II, where the size of different contributions to the final values is also presented. The zero-point energy (ZPE) correction for RaF and RaF$^+$ in the $^2\Sigma^+$ and $^1\Sigma^+$ states was based on the calculated vibrational frequencies of 438 cm^{-1} and 518 cm^{-1}, respectively.

The main sources of uncertainty in the calculations are the incompleteness of the employed basis set, the approximations in treating electron correlations and the missing higher-order relativistic effects. These are assumed to be largely independent of each other, and hence are investigated separately.

TABLE II. Experimental and calculated IP of RaF.

Method	IP (eV)	$D_e(eV)$
CBS-DC-CCSD[a]	4.932	5.454
CBS-DC-CCSD(T)[a]	4.983	5.547
+aug+ae.vs.cv	4.986	5.554
+ΔT	4.987	5.549
+Breit	4.985	5.547
+QED	4.978	5.556
Theoretical	4.978[6]	5.56[5]
Experimental	4.971(2)[14]	

[a] ZPE correction is included.

TABLE III. Summary of the main sources of uncertainty in the calculated IP and D_e of RaF.

Category	Error source	IP (meV)	D_e (meV)
Basis set	Cardinality	2.6	50.1
	Augmentation	0.5	3.3
Correlation	Core electrons	2.6	4.9
	Higher-order excitations	0.9	4.0
Relativity	QED	4.2	5.7
Uncertainty:		6	51

Basis set - cardinality: The final results were obtained through a complete basis-set limit (CBSL) extrapolation of the s-aug-cv$n$z basis sets following the H-CBSL scheme [24] for the correlation contribution. While this is a popular CBSL extrapolation approach, two additional schemes were tested; the Martin $(n+\frac{1}{2})^{-4}$ scheme [56] (M) and the scheme of Lesiuk and Jeziorski [57] (LJ).

The results obtained using the M and LJ schemes are consistent to within 1 meV with respect to the H-CBSL value, confirming the convergence of the calculated IP with respect to the basis-set cardinality. The uncertainty due to the incompleteness of the basis set is therefore estimated to be half the difference between the H-CBSL and s-aug-cv4z values.

Basis set - augmentation: The uncertainty due to the possible insufficient number of diffuse functions is evaluated as the difference between the results obtained using the doubly augmented and the singly augmented dyall.cv4z basis sets, see Table III.

Correlations - core: To account for the uncertainty due to incomplete size of the active space and any shortcomings in the treatment of core correlations, half the size of corrections applied in Tables II.

Correlations - Higher-order excitations: The contributions of ΔT in Tables II to estimate the uncertainty due to the missing higher-order excitations.

Relativity - QED effects: Higher-order QED contributions are assumed to be smaller than the calculated Lamb shift which is given as an conservative uncertainty estimate [35].

The magnitude of the various effects contributing to the total uncertainty on the calculated IP and D_e is given in Tables III. The dissociation energy is determined by the strength of the bonding, which is more sensitive to the basis set quality than the ionization potential, lead-

ing to a higher uncertainty. The total uncertainty is obtained by taking the Euclidean norm of the individual uncertainties, as these are assumed to be independent.

4.5 Experimental Setup

Given the challenges in studying radioactive molecules, the experiments described in this section were performed at the radioactive ion beam facility ISOLDE at CERN. A description of the facility as a whole can be found in Refs. [49, 182]. Our experiments were performed as part of the Collinear Resonance Ionization Spectroscopy (CRIS) experiment within ISOLDE [51, 183–187]. The experimental setup used is described in great detail in Articles 1, 2, 3 and 4, as well as in Refs. [51, 183–187] . This section presents a description of the CRIS technique and why it is able to fulfill the main requirements needed for the study of radioactive molecules, i.e., high sensitivity and selectivity while allowing for enough spectroscopic resolution to facilitate the observation of various nuclear effects that, to our knowledge, have not been observed before in a molecule.

4.5.1 Collinear Resonance Ionization Spectroscopy (CRIS) Method

For this experiment, several pulsed lasers were sent collinearly along the direction of propagation of the molecular beam, which was previously bunched and accelerated to ~ 40 keV (Articles 1 and 4) or ~ 30 keV (Articles 2, 3 and 4). For our experiments, we used two or three lasers to perform the spectroscopy. Usually (Articles 1, 2 and 3), the first one is used to drive the transition of interest, (although in Article 4 it was the last laser, as further discussed separately below). In our case, this is usually between vibrational, rotational, and hyperfine levels, between the ground ($X^2\Sigma^+$) and first excited ($A^2\Pi_{1/2}$) electronic levels. This first step laser is scanned over various ranges in frequency space, allowing us to record the molecular spectrum as shown, for example, in Fig. 1 of Article 1, Fig. 2 of Article 2, or Fig. 3 of Article 3. After this first resonant excitation step, we can either use a high-power laser to non-resonantly ionize the molecule (Article 1), such that the ionization happens only if the first step transition was successful, or have a second laser, usually of fixed frequency, drive resonantly a second transition in the molecule to another excited electronic level (Articles 2 and 3), from which a third laser ionizes the molecule only if these two first steps were resonant. In either case, if the first laser was resonant with a transition in the molecule, we would end up with an ion.

Radioactive molecules can only be produced in small numbers, with yields of less than 10^7 molecules per second. Only a small fraction of these molecules populate a given rotational level, leading to rates as low as 50 molecules per second in a specific quantum state [53, 54]. Therefore, detecting ions is a clear advantage compared to detecting photons (e.g., resulting from decays from the excited $A^2\Pi_{1/2}$ electronic level). On the one hand, ions can be easily guided towards the detector using simple electrostatic fields with almost 100% efficiency. At the same time, the detection efficiency of the ion detectors can be more than 90%, much higher than most photon detectors [51–54, 183–187]. Finally, the background rate is significantly reduced when detecting ions, without major technical complications, while reducing the background from photon scattering can be challenging [51–54, 183–187]. As we want to detect, ideally, every single molecule produced upon resonant interaction with the lasers and with the lowest possible background, detecting ions rather than photons is clearly a better option for our experiment.

While using two lasers is, in principle, enough to observe transitions in RaF, using

a three-step scheme provides a significantly better signal-to-background ratio, as shown in Articles 2 and 3 [53, 54]. On the one hand, each resonant laser significantly enhances the selectivity of the species of interest, which is very important when trying to detect single molecules among a large background of contaminants [188]. At the same time, using three lasers allows us to use a longer wavelength for the non-resonant ionization step, compared to the 2-step scheme, which further suppresses the background by reducing the rate of ionization events from levels other than the one of interest. In our experiment, we saw an increase in the signal-to-noise ratio of one order of magnitude when going from a 2-level scheme (Article 1) [52] to a 3-level scheme (Articles 2 and 3) [53, 54], and it was only with the 3 level scheme that the results in Articles 2 and 3 were possible.

The RaF molecules, before reaching the interaction region, are cooled to $T \approx 500$ K. At this temperature, the Doppler broadening in the frame of the molecular bunch, for a Maxwell-Boltzmann distribution at temperature T, is $\Delta f \approx 400$ MHz, using the formula:

$$\Delta f = \sqrt{\frac{8kT \ln 2}{mc^2}} f_0, \tag{4.2}$$

where f_0 is the rest frame transition frequency, k is the Boltzmann constant, c is the speed of light, and m is the mass of the molecule. This width would greatly complicate the observation of the rotational and hyperfine spectra. However, given that our molecules travel with high energies, the effective Doppler width in the lab frame is significantly reduced. This is because, during acceleration, the energy spread of the molecular bunch, ΔE, stays constant. If we write the energy of the beam as $E = mv^2/2$ (at our energies, we are in the non-relativistic regime), the spread in energy can be related to the spread in velocity, Δv, as:

$$\Delta E = mv\Delta v \implies \Delta v = \frac{\Delta E}{\sqrt{2mE}}. \tag{4.3}$$

This shows that, upon increasing the energy, the velocity spread, which depends on the temperature in the rest frame of the bunch and thus sets the Doppler linewidth, decreases as $1/\sqrt{E}$. At our energies, the effective Doppler linewidth is reduced by $2-3$ orders of magnitude compared to a stationary beam [15, 189, 190]. Note that our effective linewidth was, in the end, $100-150$ MHz [53, 54], which was a combination of the residual Doppler broadening, natural linewidth of the electronic transition, laser linewidth and power broadening, with the latter one being the dominant effect [53, 54]. While this resolution was enough to obtain the results presented herein, it can be improved by a factor of 3 or better.

4.6 Data Analysis

4.6.1 Processing the Raw Data

The data was taken in chunks, which will be called "scans" moving forward, of about $30-60$ mins each. During each scan, the frequency of the spectroscopy laser, which is usually the first step, was scanned, and the number of resulting counts was recorded. For each scan, several pieces of information were recorded, together with their timestamp: the number of events in each bunch, the spectroscopy/first step laser wavenumber and the reference

transition wavenumber, which corresponds to the $5^2S_{1/2}$, F= 2 $\rightarrow 5^2P_{3/2}$, F= 3 transition in ^{87}Rb. The acceleration voltage of the molecular bunch, which could drift over time, was also recorded. The bunching rate was higher than the rate at which the other three parameters were recorded, thus, for many bunches, there were no associated wavenumber, reference wavenumber or voltage measured. In such cases, for each missing parameter, a linear interpolation as a function of time was performed between the previous and next recorded value of the given parameter. Then, for each bunch recorded in between these two values, we associated the corresponding value of the given parameter obtained from a linear interpolation. Thus, in the end, for each bunch, we had the number of measured events, the associated spectroscopic frequency, the reference frequency, and the acceleration voltage.

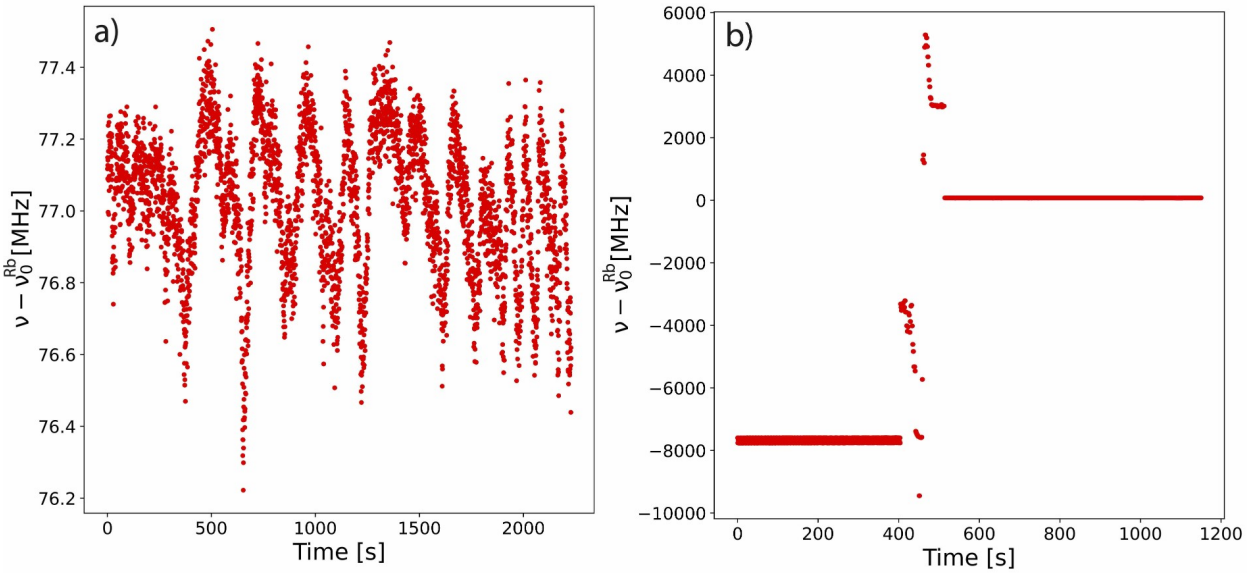

Figure 4.1: a) Example of the measured reference frequency as a function of time for a well-behaved scan. b) Example of the measured reference frequency as a function of time for a discarded scan (notice the sudden jump around 400 s). The literature value of the reference frequency was subtracted from the measured value.

Before proceeding with the analysis, we investigated, for each scan, the behavior of the three parameters mentioned above as a function of time. While a smooth variation is expected, any sudden, large change indicates something went wrong with that scan. In most cases like this, performing the needed corrections, as described below, was not possible, and therefore, such scans were discarded from the analysis. As an example, in Fig. 4.1 a) we show the reference frequency as a function of time for a well-behaved scan, while in Fig. 4.1 b) we show a situation in which a sudden, unphysical jump in the reference frequency value happened. This latter scan was discarded from the analysis. The next step was, for each measured bunch, to perform a correction to the measured first step laser wavenumber, $\tilde{\nu}_m$, based on the measured Rb reference transition, $\tilde{\nu}_m^{Rb}$ and its literature value, $\tilde{\nu}_0^{Rb}$. The used correction was obtained following the relation:

$$\tilde{\nu}' = \tilde{\nu}_m - (\tilde{\nu}_m^{Rb} - \tilde{\nu}_0^{Rb}), \tag{4.4}$$

which is used to calibrate the absolute value of the laser frequency, with a resolution of 2 MHz given by the used wavemeter, WSU-2, HighFinesse. Next, the adjusted frequency was Doppler corrected to the molecule's rest frame, based on the measured acceleration voltage, V, using:

$$\tilde{\nu} = \tilde{\nu}' \sqrt{\frac{1 - v/c}{1 + v/c}}, \tag{4.5}$$

with

$$v = \sqrt{\frac{2Ve}{m}}, \tag{4.6}$$

where e is the electron charge and m is the molecule's mass.

Finally, the data was binned using fixed-sized bins. Different sizes between 0.5 and 5 GHz, for Article 1 [52], and between 10 and 30 MHz, for Article 2 and 3 [53, 54] were used, without a significant change in the final result of the analysis for different binnings. For each wavenumber bin, the total number of counts, N, and the total measurement time, T, were recorded. The associated rate was calculated as N/T, while the uncertainty on the rate was $\sqrt{N}/T$. The central value of the wavenumber associated with that bin was the time-weighted average of all the measured wavenumbers within that bin. In the end, for each scan, a file was saved containing three columns corresponding to the first step wavenumber, the measured rate, and the associated uncertainty on the rate. Using such a file, spectra like the ones shown in Fig. 1 of Article 1, Fig. 2 of Article 2, and Fig. 3 of Article 3 were obtained.

The next step was fitting such spectra with the appropriate function and the extraction of the peak locations from each spectra together with their associated statistical uncertainty. While up to this point, the same steps were taken in the analysis for Articles 1, 2, and 3, given their vastly different resolutions, the following steps were different between the analysis performed in Article 1 and the one performed for Articles 2 and 3. We will treat them separately below. Article 4 will be discussed afterwards.

4.6.2 Analysis of the $X^2\Sigma^+ \leftarrow A^2\Pi_{1/2}$ Vibrational Transitions Data for $^{223-226,228}$RaF

For Article 1 [52], we show examples of the measured spectra, together with the fit to the data in Fig. 1 a) of that Article. Given the shape of the peaks, we decided to fit the data using a constant background plus four skewed Voigt profiles, defined as [191]:

$$f(x; A, \mu, \sigma, \gamma, s) = \text{Voigt}(x; A, \mu, \sigma, \gamma) \left\{ 1 + \text{erf}\left[\frac{s(x - \mu)}{\sigma\sqrt{2}} \right] \right\}, \tag{4.7}$$

where Voigt() is the usual Voigt function, erf() is the error function, A and μ are the amplitude and central value of the skewed Voigt profiles, σ and γ are the standard deviation and width of the Gaussian and Lorentzian components of the profile, respectively and s quantifies the skewing of the profile. The fit was performed using the publicly available package LMFIT: Non-Linear Least-Squares Minimization and Curve-Fitting for Python [191].

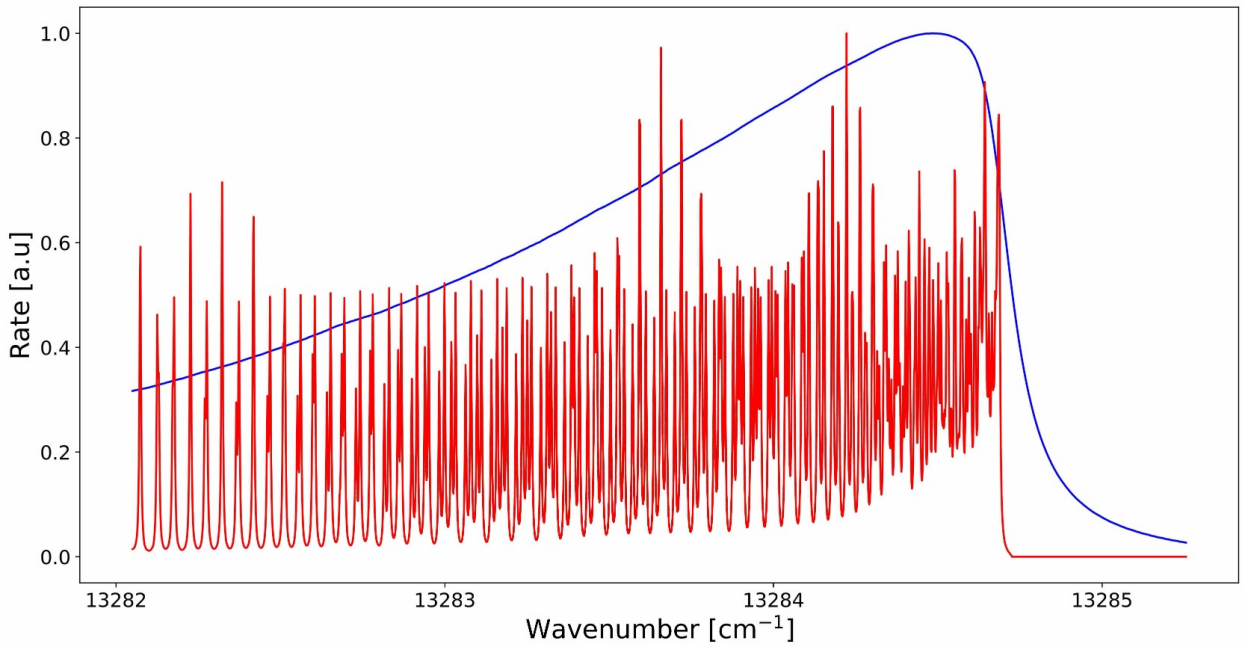

Figure 4.2: Simulated spectrum in PGOPHER, showing the rate in arbitrary units (a.u.) vs wavenumber in cm^{-1} for the $0 \leftarrow 0$ transitions in ^{226}RaF, for a transition linewidth of 150 MHz (red) and 5 GHz (blue).

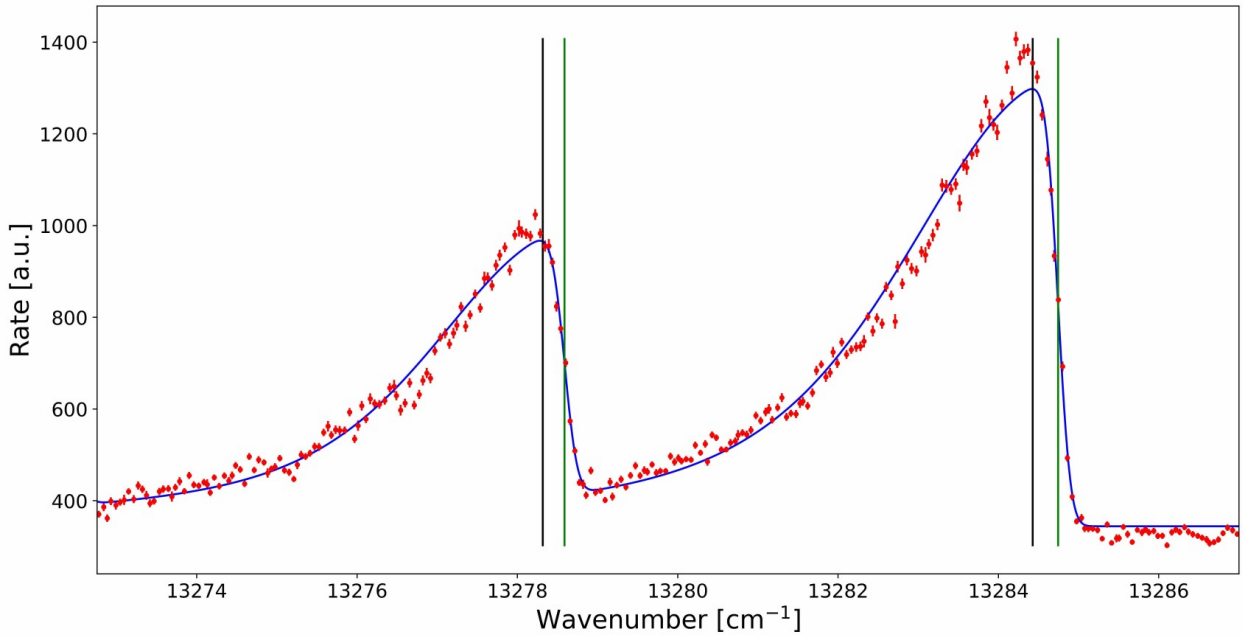

Figure 4.3: Example of a measured spectrum for the $0 \leftarrow 0$ (peak on the right) and $1 \leftarrow 1$ (peak on the left) vibrational transitions in ^{226}RaF (red data points), together with the obtained fit to the data (blue). The green lines mark the location of the μ parameter obtained from the fit (see Eq. 4.7), while in black, we show the location of $T_{\Pi} - \frac{A_{\Pi}}{2}$ for each of the two peaks (see main text for details).

At this point, it is worth explaining the apparently counter-intuitive shape of the observed transitions. The shape is related to the fact that, due to the effective linewidth of the first step laser used for this experiment ($\sim$ 5 GHz) being much larger than the distance between consecutive rotational and hyperfine transitions (on the order of 100 MHz, as shown in Fig. 2 of Article 2 and Fig. 3 of Article 3), all that could be observed was an envelope over all these transitions, instead of the individual rotational and hyperfine transitions. In addition, in this region in wavenumber space, to a good degree of approximation given our resolution, the energy of rotational levels is a second-order degree polynomial in J. In this case, J is taken to be the rotational quantum number of the ground electronic state. Thus, the monotonicity of energy as a function of J changes at a given value of J, mainly controlled by the difference between the rotational constants in the excited and ground electronic state, $B' - B''$ (see Eq. 4.12 and 4.13). For RaF, this point is around $J \approx 7.5$, and it is at this point where the sudden drop in counts vs. wavenumber happens in Fig. 1 a) of Article 1 (on the right side of the measured peaks). This effect is better shown in Fig. 4.2, for simulated data using the publicly available software PGOPHER, for the case of the $0 \leftarrow 0$ vibrational transition in ^{226}RaF, as well as in Fig. 1 d) of Article 2 for actually measured data. In Fig. 4.2, the blue line is the result of a simulated spectrum assuming a linewidth of the transitions of 5 GHz (similar to the resolution in Article 1), while in red, we show the same spectrum for a linewidth of 150 MHz, similar to the resolution in Articles 2 and 3.

The main challenge in the subsequent part of the analysis was to assign, to each measured peak in each isotope, a value for the vibrational transition frequency and an associated uncertainty. The most straightforward way to do so was to use the obtained μ parameter from the skewed Voigt profile fit (see Eq. 4.7). However, this value is not well-motivated from a physical point of view, as it doesn't correspond to the real value of the vibrational transition, defined as $T_\Pi - \frac{A_\Pi}{2}$ (see Eq. 4.12 and 4.13 below). But at the point this analysis was performed, the data in Articles 2 and 3 had not been measured yet, thus the "true" value of the transition was not known. We show in Fig. 4.3 the fit to the data corresponding to the $0 \leftarrow 0$ and $1 \leftarrow 1$ vibrational transitions in ^{226}RaF using a skewed Voigt profile, marking in green the value of the obtained μ parameter, and in black the value of $T_\Pi - \frac{A_\Pi}{2}$ (see Eq. 4.13 for the definitions of the T_Π and A_Π parameters) obtained from Article 2 [53]. It can be seen that they are very different (a few GHz apart, depending on the transition). Fortunately, this difference doesn't change much from one isotopologue to the other, and given that we are interested in differences in the transition frequencies between isotopologues and not in absolute transition values, this didn't represent a major issue, as described below. Moreover, as seen in Fig. 4.3, the location of $T_\Pi - \frac{A_\Pi}{2}$ is close to the location where the skewed Voigt profile reaches its maximum value. We were able to infer this even before the analysis performed in Articles 2 and 3, based on simulating the spectra of RaF using theoretically predicted rotational constants [192–195]. In the end, in order to extract the isotope shifts reported in TABLE I in Article 1, we used, for the central value, the differences between the fitted μ values for each pair of isotopologues and each transition. For the uncertainty, we proceeded as follows. For each calculated isotope shift, we combined in quadrature the uncertainty on the transition of the reference isotopologue, associated with the ^{226}RaF isotopologue, and the one from the isotopologue under consideration and denoted it as error1. We also computed the difference in the obtained isotope shift when using the μ value, and when using the difference in the maximum value of the skewed Voigt profile,

denoted as error2. In the end, we used as the error on the isotope shift the maximum value between error1 and error2. The obtained central values and associated uncertainties for the measured isotope shifts are reported in TABLE I of Article 1 [52].

4.6.3 Analysis of the $X^2\Sigma^+ \leftarrow A^2\Pi_{1/2}$ Rotational and Hyperfine Transitions Measurements for ^{225,226}RaF

This section discusses the statistical analysis performed for Articles 2 and 3 [53, 54]. For each scan, the obtained spectrum was fit using a linear function plus several pseudo-Voigt functions, defined as:

$$f(x; A, \mu, \sigma, \alpha) = (1-\alpha)A\frac{e^{\left[-(x-\mu)^2/2\sigma_1^2\right]}}{\sqrt{2\pi}\sigma_1} + \frac{\alpha A}{\pi}\frac{\sigma_2}{(x-\mu)^2+\sigma_2^2}, \tag{4.8}$$

where A is an overall normalization constant, μ is the center of the peak, σ_1 is the standard deviation of the Gaussian component, and σ_2 is half of the full width at half maximum (FWHM) of the Lorentzian component of the pseudo-Voigt function while α is the relative weight of the Lorentzian component versus the Gaussian one. The number of such functions was chosen for each spectrum based on the reduced χ^2 of the fit. The fit was performed using LMFIT [191] in Python. Using this approach, all the measured spectra were fit and the associated central peak values and statistical uncertainties were extracted. Examples of recorded spectra, together with the obtained fit, are shown in Fig. 4.4. The statistical uncertainty on the obtained peaks varied for different scans between 3 MHz and 15 MHz.

At this point, it is worth reiterating that the first goal of the analysis in Articles 2 and 3 was to extract the parameters of the rotational and hyperfine Hamiltonian, which will be discussed in more detail below (as well as in the Supplemental Materials of Articles 2 and 3). Before doing this, however, we also had to consider systematic uncertainties that can affect the value of the extracted peaks locations. Such uncertainties will be discussed next.

While there were no electrostatic elements in the interaction region, stray electric fields coming from the electrostatic benders located right after the neutralization cell, used to remove the non-neutralized molecules, and right after the interaction region, used to guide the ionized molecules towards the MagneTOF detector (from ETP Ion Detect, model 14925), can still reach the interaction region. Hence, the effect of these electric fields on the energy levels of the molecule needs to be taken into account. To estimate this, the electric fields in the interaction region, given our experimental setup, were simulated in SIMION 8.1. In order to map the electric field felt by the molecules traveling in this region, we generated neutral particles at different radial distances, between 0 and 15 mm away from the beamline axis, and let them propagate in the interaction region, recording the three components of the electric field at each step, every 0.25 mm. An example of electric field vs. distance for the three electric field components is shown in Fig. 4.5, for a particle located 1 mm away from the beamline axis. Note that only molecules ionized in this region along the z-axis were used for the analysis. Similar values of the electric field as a function of distance are obtained for particles produced at the other radii investigated. It can be seen that the maximum electric field felt by a molecule in this region is $< 10^{-3}$ V/cm (Fig. 4.5 a)), while most of the molecules, especially at the center of the interaction region, felt a significantly smaller

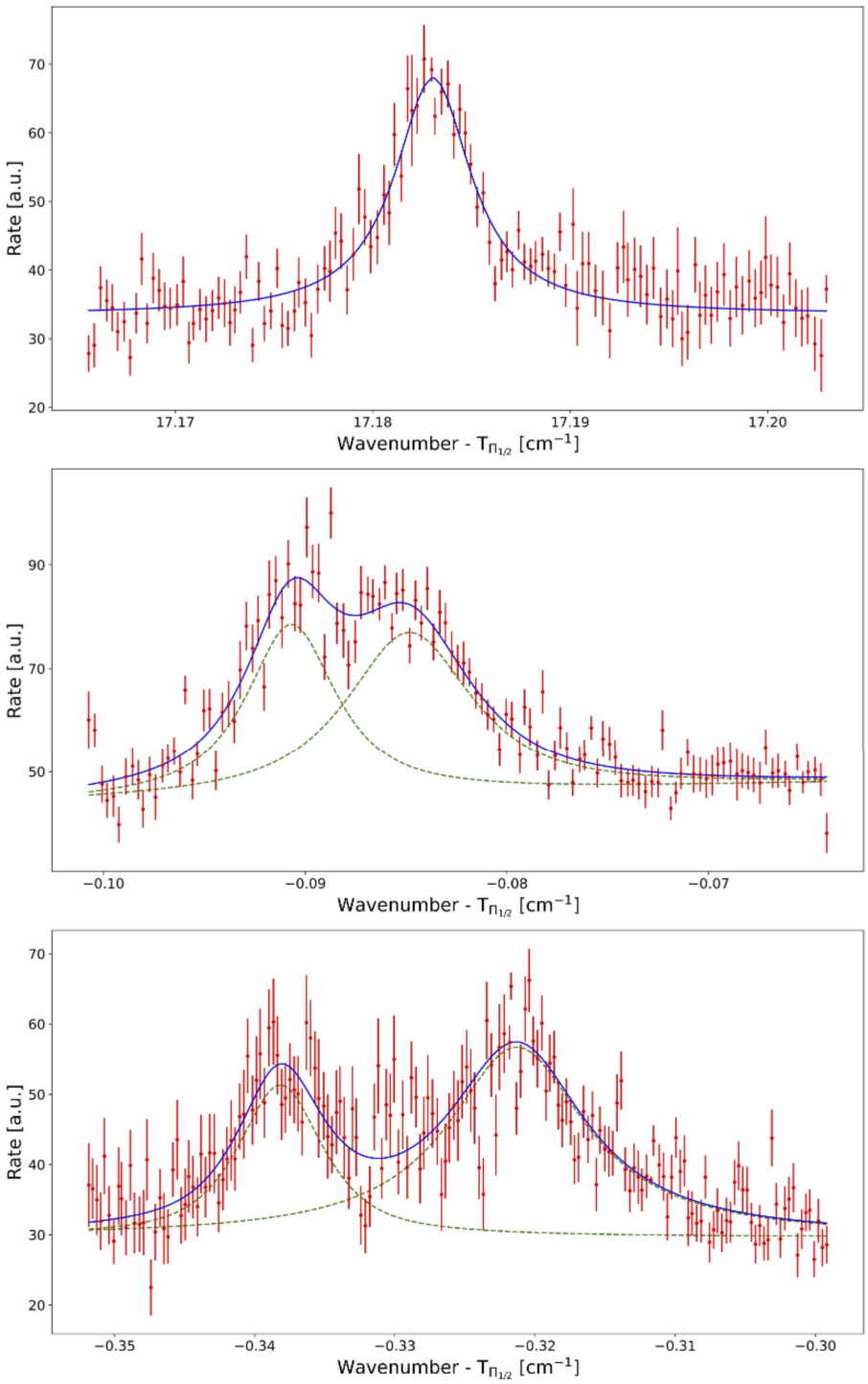

Figure 4.4: Example of measured spectra obtained after data processing (red), together with the obtained fit (blue). For the case where more than one pseudo-Voigt function was used for the fit, each individual fitted function is also shown (green dashed line).

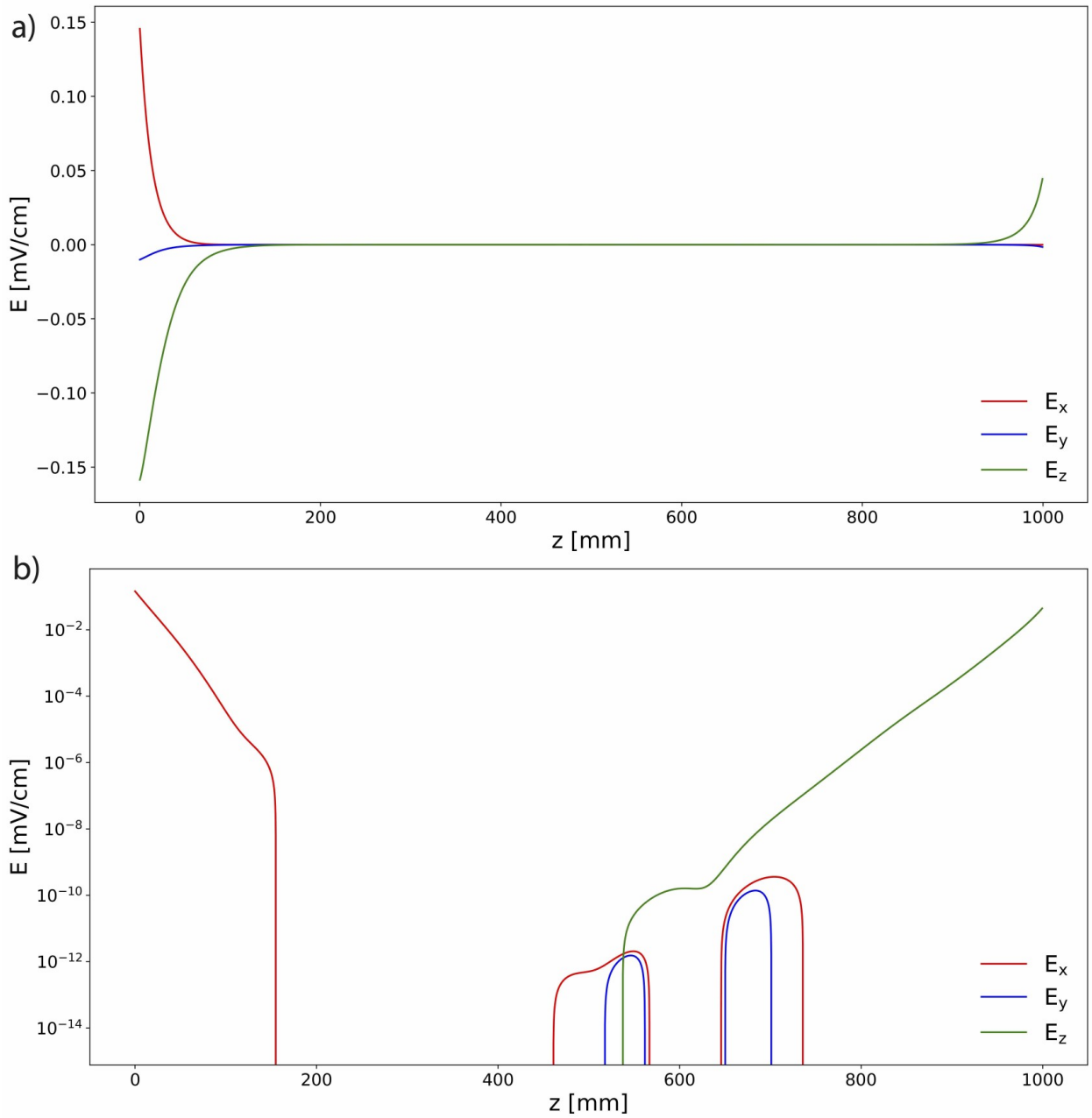

Figure 4.5: a) Electric field in the center of the interaction region of the CRIS experiment. The magnitude of each of the three components of the electric field, E_x, E_y, and E_z, is shown as a function of distance from the beginning of the interaction region, $z = 0$. b) Same as a), but the y-axis is logarithmic to see better the magnitude of the stray electric field at the center of the interaction region.

electric field (Fig. 4.5 b)). In this latter region, we expect the electric field to be higher than in these simulations due to other effects not accounted for, such as patch potentials formed on the beamline walls, but these are still expected to be below $< 10^{-3}$ V/cm. Taking this conservative value of 10^{-3} V/cm as the electric field felt by the molecules, its effect on the energy levels can be estimated, and it is on the order of $\sim \frac{(dE)^2}{\Delta E_{\pm}}$, where d is the dipole moment of the molecule in the electronic ground state, and $\Delta E_{\pm}$ is the energy difference between states of opposite parity in the molecule. Given that for RaF $\Delta E_{\pm} > 10$ GHz, and taking $d = -3.914$ D [195], we get that the effect due to stray electric field is $\ll 1$ MHz and thus negligible for our analysis. A similar value is obtained for the excited electronic state.

For the uncertainty in the extracted transition frequencies due to stray magnetic fields, we assumed a conservative value of such magnetic fields of $B = 1$ G. The main contributions to such shifts come from the unpaired electron's interaction with these fields, given by the Hamiltonian:

$$H_B = -g_{\perp}\mu_B \mathbf{B} \cdot \mathbf{S}, \tag{4.9}$$

where μ_B is the Bohr magneton, $g_{\perp} \approx -2$ [195] is related to the electron g-factor, and $\mathbf{S}$ is the electron spin. This leads to a shift of the measured energy levels in the ground electronic state of < 1.5 MHz. A much smaller value is expected from the excited electronic level.

A third systematic uncertainty comes from the uncertainty in the acceleration voltage, which in our case is $\Delta V = 1$ V [51, 53, 54]. Using this, together with Eq. 4.5 and 4.6, as well as the measured value of the acceleration voltage, we obtain an associated uncertainty in the measured transition frequencies of $3-4$ MHz. The uncertainty due to the wavemeter reading of the Rb reference frequency is assumed to be given by the uncertainty of the wavemeter, 2 MHz.

Finally, the last systematic uncertainty considered is due to AC Stark shifts produced by the lasers used in our experiment. The second and third-step lasers are delayed relative to the first-step laser, usually by ~ 50 ns. The exact delay was optimized online for different regions on the measured spectrum. However, the tail of their pulses, assumed to be Gaussian, can still have an overlap with the first step laser pulse, and thus it can lead to a shift of the measured energy levels. To estimate this effect, the temporal full width at half maximum (FWHM) of the first, second, and third laser were estimated, based on photodiode measurements, to be 50, 10, and 50 ns, respectively. The delay between the first step laser and the other two was 50 ns. Further delaying the third step laser by $10-20$ ns didn't change the results significantly. The powers of the three lasers were 2 μJ, 100 μJ and 40 mJ, respectively. The power of the first step laser was changed during the experiment, depending on the measured region in the molecular spectrum, but that didn't lead to significant changes in the estimated AC Stark shift effects.

The effect of the second-step laser (a similar approach was performed for the third-step laser) on the energy levels of interest in $X^2\Sigma^+$ and $A^2\Pi_{1/2}$ electronic manifolds was estimated as follows. For a given molecule, ignoring the molecule motion with respect to the laser pulses, we defined $t = 0$ as the time when the center of the first step laser overlaps with the molecule. We divided a time interval between -100 ns and 100 ns in steps of 0.1 ns. The actual interval length is negligible as long as it is longer than the temporal FWHM of the first-step laser. Similarly, the step size did not modify the results as long as it was

significantly smaller than the interval length. Then, at each time step, we computed the electric field experienced by the molecule due to the first-step and second-step lasers. As we knew the laser power at the location of the molecule (P_m), as well as the diameter of the laser beam (A), we obtained the magnitude of the electric field of each laser using the relation [196]:

$$E = \sqrt{\frac{2P_m/A}{c\epsilon_0}}, \tag{4.10}$$

where c is the speed of light, and ϵ_0 is the electric permittivity of the vacuum. For the second step laser, given its FWHM in frequency space of ~ 10 GHz, we divided an interval of -20 GHz to $+20$ GHz around the central value of the second step laser, in intervals of 100 MHz, and computed the electric field experienced by the molecule for each interval. Thus, for any energy level in the molecule, with an energy below $30,000$ cm^{-1} [197], connected by an electric dipole transition to the level we want to compute the AC Stark shift for, we were able to estimate a Rabi frequency. Depending on the nature of the electronic level, the transition dipole moment used in the Rabi frequency calculation was estimated from Ref. [198]. Then, for a fixed time bin, t, the AC Stark shift, $d\nu$, of the level of interest was calculated using:

$$d\nu = \sum_f \frac{\nu_l - \nu_0}{|\nu_l - \nu_0|} \left[\frac{\sqrt{\Omega_2^{f,t} + (\nu_l - \nu_0)^2}}{2} - \frac{|\nu_l - \nu_0|}{2} \right], \tag{4.11}$$

where ν_l is the second step laser central frequency, ν_0 is the transition frequency between the levels under consideration [197] and $\Omega_2^{f,t}$ is the second step Rabi frequency for the time bin t and frequency bin f. Using this, a Lorentzian lineshape was generated, with the central value of $d\nu$, and amplitude proportional to the square of the Rabi frequency of the first step laser. The transition linewidth was assumed to be similar to the one in the measured spectrum, ~ 100 MHz. The above steps were repeated for all time bins, and after each computation, the newly calculated Lorentzian lineshape was added to the previous one. In the end, the peak location of the resulted function was compared to the location of the peak in the absence of any AC Stark shift, and the difference between the two was used as a conservative estimate of the AC Stark shift due to the second step laser. The same was done for the third step laser, and the resulting AC Stark shift was added to the previously obtained one. The combined effect of the two lasers leads to a systematic uncertainty on the location of the measured transitions of $15 - 20$ MHz.

In the end, by combining all the systematic uncertainties considered above, we ended up with a total, conservative systematic uncertainty of 30 MHz. This value was assumed to be the same for all measured transitions.

4.6.4 Extraction of Rotational and Hyperfine Hamiltonian Parameters in ^{225,226}RaF

Now that we have the central values, statistical and systematic uncertainties for all measured transitions, the next step was to use these values to extract the parameters of the

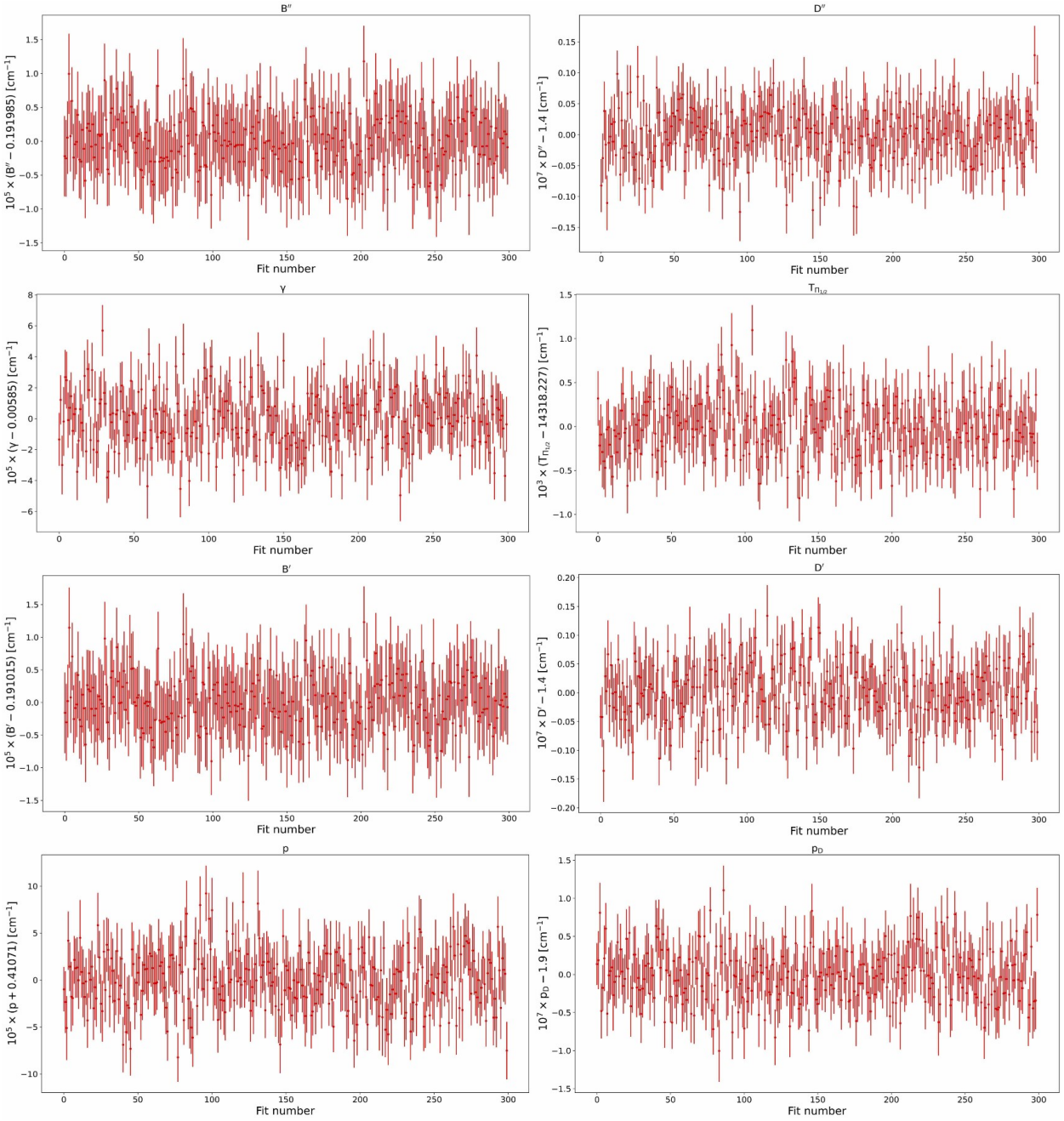

Figure 4.6: Example of obtained values of the rotational parameters of ^{226}RaF, upon subsequent fitting in PGOPHER, when accounting for the statistical uncertainty on the measured transitions.

rotational and hyperfine Hamiltonians for the ground, $X^2\Sigma^+$ and excited, $A^2\Pi_{1/2}$ electronic levels. These Hamiltonians for the ground electronic level, $X^2\Sigma^+$, are given by:

$$\begin{aligned} H^{\Sigma}_{rot} &= \left(B'' - D''\mathbf{N}^2\right)\mathbf{N}^2 + \gamma \mathbf{N}\cdot\mathbf{S} \\ H^{\Sigma}_{hyperfine} &= b''\mathbf{I}\cdot\mathbf{S} + c''I_zS_z, \end{aligned} \tag{4.12}$$

while for the excited state, $A^2\Pi_{1/2}$, we have:

$$\begin{aligned} H^{\Pi}_{rot} &= T_\Pi - \frac{A_\Pi}{2} + \left(B' - D'\mathbf{N}^2\right)\mathbf{N}^2 - \frac{1}{4}\left\{p + p_D\mathbf{N}^2, N_+S_+e^{-2i\phi} + N_-S_-e^{2i\phi}\right\} \\ H^{\Pi}_{hyperfine} &= \frac{1}{2}d\left(e^{-2i\phi}I_+S_+ + e^{2i\phi}I_-S_-\right), \end{aligned} \tag{4.13}$$

where B' and B'' are the rotational constants, D' and D'' centrifugal distortion constants, γ is the spin-rotational parameter, p is the Λ-doubling parameter, and p_D is its centrifugal correction. T_Π is the distance between the $X^2\Sigma^+$ and $A^2\Pi_{1/2}$ electronic levels, measured from the origin of the corresponding vibrational level under consideration. A_Π is the spin-orbit constant, and b'', c'', and d are hyperfine structure constants due to the ^{225}Ra nucleus [53, 54]. $\mathbf{N}$, $\mathbf{S}$ and $\mathbf{I}$ are operators associated to the molecular rotation, electron spin, and nuclear spin. O_+, O_-, and O_z are the raising, lowering, and z component associated to operator O, $\{O, Q\} = OQ + QO$ for any two operators O and Q, and ϕ is the electron orbital azimuthal angle [53, 54].

The molecular parameters appear in the form presented above in the Hamiltonian used by PHOPHER [65]. However, for the hyperfine structure parameters, it is useful to use a slightly different parameterization, which facilitates the comparison of the obtained values with the theoretical calculations. Therefore, for the ground electronic state we will use the parameters $A_\perp = b''$ and $A_\parallel = b'' + c''$, while for the excited electronic state we define $A_\perp = d$. It is worth mentioning that we should also have an $A_\parallel$ in the $A^2\Pi_{1/2}$ state. However, the effect of this state is about $2J + 1$ smaller than the one due to the $A_\perp$ term, for a given rotational level J [199]. Given the resolution of our measurements, and the fact that the levels we measured for ^{225}RaF were around $J > 15 - 20$, the contribution due to $A_\parallel$ was negligible. When we included it in the analysis, the values obtained were consistent with zero, therefore we decided to set it to zero from the beginning and remove it from the fitted hyperfine Hamiltonian. In addition, given that we didn't measure transitions to the $A^2\Pi_{3/2}$ state, we could not constrain both T_Π and A_Π simultaneously. Therefore, for the analysis, A_Π was always kept constant to its previously measured value $A_\Pi = 2067.6$ cm^{-1} [51]. Varying its fixed value over $\pm 3\sigma$ around its central value didn't significantly change the obtained Hamiltonian parameters upon fitting.

For the analysis performed in Article 2 [53], for the $0 \leftarrow 0$ transition of ^{226}RaF, the extraction of the above-mentioned molecular parameters was performed using the publicly available software PGOPHER [65]. Using this software, for user-specified values of the parameters of the molecular Hamiltonian, nuclear spin, and type of electronic levels ($X^2\Sigma^+$ and $A^2\Pi_{1/2}$ in our case), the expected spectra associated with transitions between the spin-rotational/hyperfine levels of the two electronic levels are displayed (e.g., Fig 2 in Article

2 and Fig. 3 in Article 3). In order to extract the molecular parameters, for a given line predicted in the PGOPHER spectrum, we associate the corresponding measured line (not all the predicted lines were measured). However, in the beginning, when the unknown molecular parameters used for the simulation were far from their true values, the simulated and measured spectra were very different, making the lines assignment virtually impossible. To simplify this task, previously theoretically predicted values of these parameters, as well as useful, approximate relationships between them, were used [31, 192–195], such that the initial simulated spectrum was more similar to the measured ones. This step is described in great detail in Articles 2 and 3 [53, 54]. After this, we were left with only two free parameters, B'' and T_{Π} and we started the fitting procedure by assigning isolated lines, such as those on the left and right of the spectrum in Fig. 2 of Article 2, where there was little ambiguity about the one-to-one correspondence between the location of the measured and simulated lines. After this initial fit and subsequent update of the free parameters, the simulated spectrum became even more similar to the measured one. Then, more lines were assigned for the fit, especially in the band-head, corresponding to the peaks located slightly higher than 0.00 cm^{-1} in Fig. 2 of Article 2, and more of the previously constrained parameters were allowed to vary. This process was repeated until all the measured lines were assigned to a corresponding line in the simulated spectrum, and all molecular parameters were free to vary.

Up to this point, we only used the central value of the measured transitions. The next step was to use the associated uncertainty for each line. By using the command line version of the PGOPHER software [65] using a custom-made Python function, we proceeded as follows. For each measured line, we sampled a value of the associated wavenumber from a Gaussian with mean given by the central value of that line and standard deviation given by its statistical uncertainty. Subsequently, we repeated these steps for the systematic uncertainty. With these newly generated values for the measured lines, and the previously obtained assignment for the PGOPHER simulated spectrum, we performed a fit, obtaining a set of rotational and hyperfine parameters. This was repeated 1000 times, and examples of the obtained values for the rotational parameters of ^{226}RaF are shown in Fig 4.6. The figure shows only the first 300 obtained values for each parameter, for clarity. Using these results, the central value of each parameter was calculated as the mean of all the 1000 values obtained, weighted by their variance, while the associated statistical uncertainty was calculated as the standard deviation of the 1000 values. The exact same steps were used for estimating the systematic uncertainties, but for each measured transition, we used the previously calculated systematic uncertainty instead of its statistical one. In the end, the obtained values for the parameters of the rotational Hamiltonians of ^{226}RaF are shown in TABLE I of Article 2 [53]. For the $1 \leftarrow 1$ transition in ^{226}RaF, a similar procedure to the one described above was followed, with the only difference being that the initial values of the rotational parameters before the fit, were set to the final values obtained for the $0 \leftarrow 0$ rotational spectrum.

The same steps as above were also followed for the analysis performed on the ^{225}RaF, with the addition of the parameters associated with the hyperfine Hamiltonian, see Eq. 4.12 and 4.13. The only difference was that in this case, for the initial line assignment, the values of γ, D_g, D_e and p_D were kept constant at the values obtained in ^{226}RaF, scaled by $\sqrt{\frac{\mu_{225}}{\mu_{226}}}$, with μ_{226} (μ_{225}) being the reduced mass of ^{226}RaF (^{225}RaF). Once the measured and

simulated spectrum were matched, the next step was also similar to the one performed in the case of the ^{226}RaF analysis, only that this time, besides sampling the line positions for each fit, we also sampled the values of the γ, D_g, D_e and p_D from a Gaussian with mean and standard deviation given by the central value and associated uncertainty obtained for ^{226}RaF (scaled by $\sqrt{\frac{\mu_{225}}{\mu_{226}}}$). Examples of the obtained parameters (for the parameters allowed to vary) are shown in Fig. 4.7 (only including the statistical uncertainty), with the final values and associated uncertainties obtained as in the case of ^{226}RaF, shown in TABLE I of Article 3 [54].

4.6.5 Analysis of the ^{226}RaF Ionization Potential Data

For Article 4, the initial processing of the raw data was similar to the one described above, except that it was the frequency of the last laser (and not the first one) that was scanned. It should be mentioned that, given that we were interested in the IP of RaF and thus the total laser energy needed to ionize the molecule, the Doppler correction to the molecular rest frame (Eq. 4.5 and 4.6) was performed after adding together the frequencies of all the lasers used. For each bin in wavenumber space, data was taken both with all lasers present and only with the ionization laser present, and then the rate in the former case was subtracted from the latter to remove any non-resonant background. Then, the obtained value for each wavenumber was normalized using the measured laser power. In the end, the spectra shown in Fig. 1 b) and c) of Article 4 were obtained, which show the clear shift from the region where the total laser energy was below the IP (on the left) to when it was above the IP (on the right). From this, the IP of RaF was extracted. The exact extraction procedure and further analysis details are described in great detail in Article 4 and its associated Supplemental Materials.

4.7 Results and Discussion

The results obtained from the RaF experimental campaign and the performed analysis presented above are described in detail in Articles 1, 2, 3 and 4. Here, I will briefly reiterate these results and their importance for future experiments aiming to study fundamental physics using RaF and other radioactive molecules.

4.7.1 Observation of the Nuclear Size Effect in a Radioactive Molecule

In Article 1 [52], we were able to observe, the effect of the nuclear size, parameterized using the nuclear mean-square charge radius, $\langle r^2 \rangle$, on the molecular energy levels. This is, to our knowledge, the first time that such effects are observed in a radioactive molecule. These results represented the first experimental proof of the high sensitivity of the RaF molecule to small nuclear effects, showing that by simply adding/removing a neutron to/from the Ra nucleus, the change of the nuclear size can shift the whole electronic spectrum of the molecule by as much as $2-3$ GHz. At the same time, it proved that our technique could be used to study very short-lived molecules, with a lifetime below 4 days (^{224}RaF), without any inherent limitation to further extend it to even shorter-lived species. Thus, our approach has the

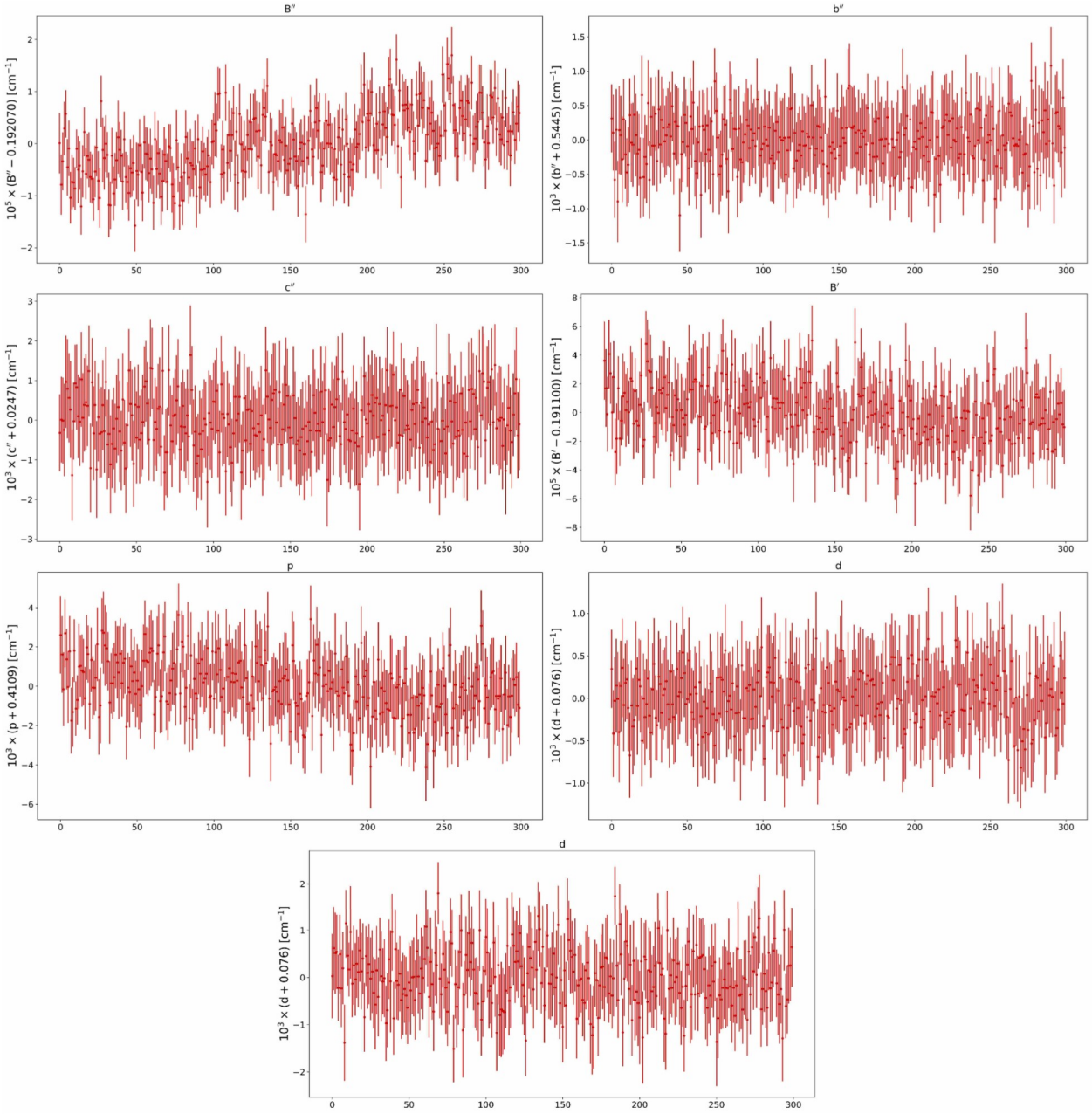

Figure 4.7: Example of obtained values of the rotational and hyperfine parameters of ^{225}RaF, upon subsequent fitting in PGOPHER, when accounting for the statistical uncertainty on the measured transitions.

potential to allow the exploration of a wide range of molecules, especially those containing nuclei in the actinide region, of interest for nuclear structure and studies of fundamental symmetries, but currently poorly known experimentally [47, 200–203].

Our result also provided a stringent test of molecular theory calculations applied to radioactive molecules. As described at length in Article 1 [52], from the slope of the measured isotope shift, $\delta\tilde{\nu}$, versus the change in the nuclear charge radius, $\delta\langle r^2\rangle$, we can extract the electron density inside the Ra nucleus, more specifically the difference in density between the excited $A^2\Pi_{1/2}$ and ground $X^2\Sigma^+$ electronic state, $\Delta\left(\bar{\rho}_e^A\right)^{\Pi-\Sigma}$. By comparing this experimentally obtained quantity with its theoretically predicted value, we were able to benchmark the molecular calculations at the 10% level, exhibiting an excellent agreement with the experiment. These results were very encouraging, proving that molecular theory can provide an accurate description of the electron density around and inside the Ra nucleus. This was exciting, given that, for many of the new physics and symmetry violation effects we are interested in measuring using RaF, the effect depends almost entirely on the behavior of the electron in inside the Ra nucleus, and our results confirm that we can rely on quantum chemistry calculations to extract the fundamental physics of interest from future measurements.

4.7.2 Laser Cooling Scheme of RaF Towards Future Precision Measurements

In Article 2 [53], we fully characterized the rotational Hamiltonian for the ground ($X^2\Sigma^+$) and excited ($A^2\Pi_{1/2}$) electronic manifolds of ^{226}RaF. This allowed us to clearly identify the spin-rotational energy levels ($N < 2$) that can be used for future fundamental physics measurements (e.g., electron electric dipole moment), while also facilitating the characterization of the spin-rotational and hyperfine Hamiltonian of ^{225}RaF. As described in Article 2 and shown in Fig. 4 of the same Article, the ability to change the frequency of the second step laser allowed us to see these levels of interest individually and not just infer their location in frequency space from the fitted Hamiltonian, giving us further confidence about our understanding of the rotational structure of this molecule. This was achieved by placing the second step laser in such a way that only a given range of J-values were excited from the $A^2\Pi_{1/2}$ electronic level (see Fig. 8 of Article 2). Thus, even if the first laser excited a wide range of rotational states, those with high J greatly dominating in intensity compared to the low-J ones at our temperature ($T \approx 500$ K), if the second step laser acted only on the low J states of $A^2\Pi_{1/2}$, it was only those who ended up being ionized and thus appeared in the measured spectrum. This led to spectra like the one shown in Fig. 4 top of Article 2, despite a more congested spectrum being expected without the second step J-selectivity (Fig. 4 bottom in Article 2).

The extraction of the rotational Hamiltonian also allowed us to propose and quantify a laser cooling scheme for the first time in a radioactive molecule, shown in Fig. 3 of Article 2. This is a significant step towards performing future precision measurements in this molecule, facilitating the slowing down of the molecular beam and its subsequent trapping, which is suitable for long coherence times and, thus, high spectroscopic resolution. The energy levels in Fig. 3 of Article 2 were obtained from the fitted rotational Hamiltonian (and can also be

seen in Fig. 4 a) of Article 2). In this work, we also showed that RaF is the most suitable molecule for laser cooling studied to date in terms of its Franck-Condon factors (see Chapter 2). These quantify the probability of a molecule decaying back to the same vibrational level it was excited from and represent one of the main factors that dictate the number of lasers needed to scatter a certain number of photons before the molecule ends up in a dark state [53]. From Fig. 3 of Article 2 it can be seen that even with only two lasers we can scatter more than 10^5 photons in ^{226}RaF. These factors were calculated by assuming that the Born-Oppenheimer (BO) electronic potential of the ground and excited electronic states can be described as a Morse potential, using the obtained rotational parameters and the previously measured vibrational constant and dissociation energy [51]. Using Mathematica, the eigenstate of these potentials, i.e., vibrational levels, ν, of the electronic level in the BO approximation, ψ^g_ν and ψ^e_ν were calculated and the Franck Condon factors $f_{\nu'\nu''}$ defined as $|\langle\psi^g_{\nu'}|\psi^e_{\nu''}\rangle|^2$.

Finally, it should be mentioned that the methods used in this experiment are quite general and can be extended to performing spectroscopic studies on other radioactive molecules of interest. Many other such molecules are expected to be highly sensitive to symmetry violations effects, such as RaO [200], RaOH [204], RaH [205], PaF^{3+} [206], $AcOH^+$ [207] or $RaOCH_3^+$ [181, 208], while others are of importance for astrophysics, in the quest for better understanding astrochemistry and stellar nucleosynthesis, such as ^{32}SiO [209, 210], ^{26}AlF [211] or ^{26}AlO [212]. However, for all these molecules, the rotational and hyperfine levels structure is currently completely unknown experimentally. Therefore, our method could represent a way to allow the detailed study of all these radioactive molecules. This opportunity is even more exciting in the context of various radioactive beam facilities worldwide actively working on producing radioactive molecules for fundamental physics studies [48–50].

4.7.3 First Observation of the Distribution of Nuclear Magnetization Effect in a Molecule

In Article 3 [54], the rotational and hyperfine structure of the ground ($X^2\Sigma^+$) and excited ($A^2\Pi_{1/2}$) electronic levels of ^{225}RaF were fully characterized. This molecule is a main candidate for future searches of symmetry violations at the nuclear level, and our characterization of the low-lying rotational and hyperfine states represents the first step toward building a concrete measurement scheme for such searches.

The observation of the hyperfine structure allowed us to measure nuclear spin-dependent phenomena, to our knowledge never observed before in a molecule: the effect of the distribution of the nuclear magnetization (inside the ^{225}Ra nucleus in our case) on the energy levels of the molecule. Unlike the common textbook picture of the nuclear dipole moment being a point-like effect, i.e., a compass needle pointing in space, in practice, the intricate motion of nucleons leads to a non-uniform distribution of the nuclear magnetization inside the nucleus [213]. When the electron enters the nucleus, it is able to sample these different regions with different magnetizations, and the resulting hyperfine splitting in the molecule can reflect this effect [104]. However, the effect can only be observed if the experimental measurement has a high enough resolution to allow its observation and if the electronic structure theoretical calculations needed to extract the effect from the measurement have a precision better

than the relative contribution of this effect to the total hyperfine structure splitting. With a relative experimental uncertainty of 0.1%, on the extracted magnetic dipole moment of ^{225}Ra [54], and a corresponding 1% relative theoretical uncertainty [54, 104], both of these conditions were fulfilled in Article 3. This was facilitated by the very large effect displayed by the ^{225}Ra nucleus, showcasing a distribution of the nuclear magnetization effect which represents 4% of the total hyperfine structure splitting [54, 104]. The extraction of this effect from the measurement, as well as the formalism used to do so, are described in great detail in Article 3 (as well as the SM of the same article) and Ref. [104]. The difference between the obtained dipole moment ^{225}Ra while accounting for the distribution of the nuclear magnetization and the same effect while treating the ^{225}Ra nucleus as a point dipole was extracted with 25% relative uncertainty (see Fig. 2 of Article 3). With an improvement of the electronic structure calculations by a factor of $2-3$, which is expected in the near future [104], our measurement would be able to tell apart various nuclear models aiming to describe the distribution of nuclear magnetization inside the ^{225}Ra nucleus, at the 10% level. Thus, our results also open the way for using molecules to perform stringent tests of nuclear models. Equally important, these results show the great sensitivity of RaF to phenomena happening inside of the nucleus, which is a major step towards using this molecule for future measurements of parity and time-reversal violating nuclear properties.

Benchmarking the *ab initio* molecular theory at the 1% level and confirming its precision and accuracy in computing the hyperfine structure electronic form factors prove the very good understanding and proper characterization of the electron behavior close to and inside the Ra nucleus. This is very important for symmetry violation studies, as similar electronic form factor calculations will be needed for extracting the physics of interest from such measurements in the future. The results of such electronic calculations, combined with nuclear physics calculations, are shown in Fig. 2 c) of Article 2, where the magnitude of the expected effect for different observables of interest is shown. As it can be seen, the P-odd, T-even anapole moment already contributes at the 100 Hz level, a level of precision which has already been achieved and surpassed using stable molecules [17]. Moreover, with measurements at the 1 mHz level or below, already achieved for stable molecules [28, 29], new bounds on hadronic C,P-violating constants can be set [179]. These numbers show the great promise of RaF and, in general, Ra-containing molecules for future hadronic symmetry-violating studies.

4.7.4 Ionization Potential of RaF

In Article 4, we measured the ionization potential (IP) of the ^{226}RaF molecule: $\mathrm{IP}_{\mathrm{exp}} = 4.972(2)[14]$ eV. This is a fundamental property of RaF, which can enable complementary opportunities in the study of this molecule, such as a highly reduced non-resonant background in the multi-step resonant ionization schemes or even quantum control via Rydberg states, using external electric fields. Our result, once again, confirmed the accuracy of *ab initio* quantum chemistry calculations able to predict this electronic property at the 0.1% level ($\mathrm{IP}_{\mathrm{th}} = 4.978[6]$ eV). By comparing the IP of RaF with other Group II monofluorides, we were able to observe an unexpected behavior, in which the IP of RaF doesn't continue the decreasing trend with atomic number observed in CaF, SrF and BaF (Fig. 2 a) in Article 4) [214]. This increase in IP is attributed to the highly relativistic behavior of the electronic

cloud around the Ra nucleus. This proves the need for relativistic calculations, performed in Article 4, for a proper characterization of the electronic behavior in the RaF molecule. In the same Article, similar calculations have also been performed for the dissociation energy of RaF, which was found to be bigger than the IP ($D_e = 5.56[5]$ eV). This unusual property for diatomic molecules facilitates the study of high-lying Rydberg states in RaF, which can be highly sensitive to external electric fields, relative to the low-lying electronic levels. This could offer exciting opportunities for using these molecules for future precision studies for fundamental physics research, with potential applications for quantum computing.

4.8 Outlook

Many opportunities lie ahead in the emerging field of radioactive molecules for fundamental physics. As we now have a concrete, quantitative laser cooling scheme for RaF, a natural next step is implementing it in practice. Our group is actively working towards performing transverse laser cooling on ^{226}RaF, produced in a buffer gas cell, with longitudinal laser cooling and trapping in a magneto-optical trap (MOT) following after that. These represent mandatory prerequisites for loading RaF in a conservative trap (e.g., optical dipole trap or magnetic trap) where it can be used for future precision experiments. For now, the focus is on ^{226}RaF, which doesn't showcase any complications to the laser cooling due to the hyperfine splitting of the Ra nucleus, but ultimately, the goal is to use molecules with a spinful Ra nucleus such as ^{223,225}RaF, where nuclear symmetry violation effects become visible. The most obvious choices for future symmetry violation experiments, where large enhancements are expected (see Fig. 2 c) in Article 3), are searches for the P-odd nuclear anapole moment (in ^{223,225}RaF), the P,T-odd nuclear Schiff moment (in ^{223,225}RaF) and the P,T-odd magnetic quadrupole moment (in ^{223}RaF).

Measuring symmetry-violation effects, in particular violations of the time-reversal invariance, would have profound consequences on our understanding of fundamental physics. Additionally, there are yet-to-be-explored symmetry-conserving properties of RaF that are of great interest. One such property is the intrinsic dipole moment of the ground electronic state $X^2\Sigma^+$ of RaF, which can be measured, for example, using laser-microwave double-resonance spectroscopy [215]. The dipole moment plays a key role for future symmetry violation searches, such as implementing a Stark interference technique for anapole moment measurements [26, 27, 43]. This property is also needed to estimate the electric field necessary to achieve a certain degree of polarization in an external electric field, required for P,T-odd searches [28, 29]. Another interesting property to be measured, specific to the ^{223}RaF isotopologue, is the nuclear magnetic octupole moment of ^{223}Ra, which hasn't been measured so far. This would represent the first measurement of this electromagnetic moment in a molecule and a powerful benchmark for nuclear theory.

Finally, the techniques applied here can be extended to other radioactive molecules of interest for fundamental physics [181, 200, 204–208, 216]. Our results confirmed the predicted high sensitivity of RaF to small nuclear effects, as well as the reliability of *ab initio* electronic many-body calculations for systems with a large number of electrons and where relativistic effects become important. These results have motivated other research groups around the world to explore other radioactive molecules. Work in this direction is already

under progress [181], with several other radioactive molecules, besides RaF, emerging as compelling candidates for searches for symmetry violations, but so far, very little is known about their energy level structure [181, 206, 208, 216]. Therefore, many opportunities exist in this newly emerging field. Currently, besides our attempt to laser cool RaF, our group is actively pursuing an experimental program at FRIB with the goal of studying Pa-containing molecular ions, such as PaF^{3+} [206]. The large enhancement in sensitivity from the ^{229}Pa nucleus to new physics effects at the nuclear level is expected to be 2 orders of magnitude higher than in ^{223,225}Ra [45, 46]. In addition, the ability to trap and quantum control ions, complementary to neutral species, makes PaF^{3+} a great candidate for future symmetry violation searches.

Chapter 5

Exploring Electroweak Nuclear Properties Using Molecular Ions

There has been a tremendous progress in the past decades in our understanding of the electromagnetic properties of nuclei, with laser spectroscopy playing a major role in this field (see Chapter 3 for more details) [15]. However, a lot less is known about the weak, parity violating nuclear properties [14, 17]. This chapter describes the efforts pursued during my PhD towards measuring nuclear spin-dependent parity violation effects using molecular ions. The proposed experiment is presented in Article 5 below, followed by a detailed description of the measurement protocol, theoretical calculations, and the progress made towards building this experiment.

5.1 Article 5: Electroweak Nuclear Properties from Single Molecular Ions in a Penning Trap

This article (J. Karthein, S.-M. Udrescu, S. Moroch, et al., "Electroweak nuclear properties from single molecular ions in a Penning trap", Phys. Rev. Lett. 133, 033003 (2024).) presents the proposal of a new experiment with the goal of studying nuclear electroweak properties using single molecular ions trapped in a Penning trap. The article describes the measurement protocol, the theory behind it, and the expected statistical and systematic uncertainties. The described technique should allow hadronic parity violation measurements over a wide range of isotopes, including short-lived, radioactive ones. For this article, published in Physical Review Letters (2024), I led the theoretical calculations and numerical simulations, I contributed to the preparation of the figures and the writing of the different drafts of the manuscript, including the initially submitted version, as well as the subsequent revisions.

Electroweak Nuclear Properties from Single Molecular Ions in a Penning Trap

J. Karthein,[1,*,†] S. M. Udrescu,[1,*,‡] S. B. Moroch,[1] I. Belosevic,[2] K. Blaum,[3] A. Borschevsky,[4] Y. Chamorro,[4] D. DeMille,[5,6,§] J. Dilling,[7,8] R. F. Garcia Ruiz,[1,‖] N. R. Hutzler,[9] L. F. Pašteka,[4,10] and R. Ringle[11]

[1]*Massachusetts Institute of Technology, Cambridge, Massachusetts 02139, USA*
[2]*TRIUMF, Vancouver, British Colombia V6T 2A3, Canada*
[3]*Max Planck Institute for Nuclear Physics, 69117 Heidelberg, Germany*
[4]*University of Groningen, 9747AG Groningen, The Netherlands*
[5]*Department of Physics and James Franck Institute at the University of Chicago, Chicago, Illinois 60637, USA*
[6]*Physics Division at Argonne National Laboratory, Lemont, Illinois 60439, USA*
[7]*Duke University, Durham, North Carolina 27708, USA*
[8]*Oak Ridge National Laboratory, Oak Ridge, Tennessee 37830, USA*
[9]*California Institute of Technology, Pasadena, California 91125, USA*
[10]*Comenius University, 84215 Bratislava, Slovakia*
[11]*Facility for Rare Isotope Beams, East Lansing, Michigan 48824, USA*

(Received 18 October 2023; revised 31 January 2024; accepted 18 April 2024; published 19 July 2024)

We present a novel technique to probe electroweak nuclear properties by measuring parity violation (PV) in single molecular ions in a Penning trap. The trap's strong magnetic field Zeeman shifts opposite-parity rotational and hyperfine molecular states into near degeneracy. The weak interaction-induced mixing between these degenerate states can be larger than in atoms by more than 12 orders of magnitude, thereby vastly amplifying PV effects. The single molecule sensitivity would be suitable for applications to nuclei across the nuclear chart, including rare and unstable nuclei.

DOI: 10.1103/PhysRevLett.133.033003

Introduction.—Of nature's four known fundamental forces, the weak force is the only one known to violate parity (P) and charge-parity (CP) symmetry. In this context, precision studies of the weak interaction provide powerful tests of the standard model, violations of the fundamental symmetries, and the existence of new physics [1–3]. Accelerator-based experiments and atomic parity violation studies have provided key insights into the weak interaction between the electrons and nucleons, mediated by Z^0-boson exchange [4–6]. However, the electroweak interactions between nucleons are only poorly understood [7–12]. A clear disagreement exists between measurements [1,13,14].

Recent progress in precision control and interrogation of molecules has demonstrated powerful routes for precision studies of symmetry-violating properties [1,15–18]. Parity violation (PV) can produce unique signatures in the molecular energy levels, enabling the isolation of weak force effects from the overwhelmingly dominant strong and electromagnetic forces [19–21]. The proximity of opposite parity molecular levels provides high sensitivity to symmetry-violating properties, which can be several orders of magnitude larger than in atomic systems. Moreover, external magnetic fields can drive these opposite-parity states into near degeneracy, enhancing their sensitivity to PV properties [22]. The possibility of about 11 orders of magnitude of enhancement of PV-induced state mixing was recently demonstrated with a neutral beam of ^{138}BaF [23].

In this Letter, we propose and analyze a new method for measuring PV nuclear properties using single molecular ions and a Penning trap, which allows for long coherence times ($\gg$1 ms) [20]. Combined with its well-controlled electric and magnetic fields, an enhancement in excess of 12 orders of magnitude in PV-induced state mixing relative to atoms can be achieved, thereby vastly increasing sensitivity to electroweak nuclear properties. The precision and versatility of our technique will enable measurements of many isotopes across the nuclear chart. These include species that may be difficult to manipulate and measure in neutral forms, such as short-lived nuclei [18,24,25].

In a diatomic molecule, PV properties are dominated by the nuclear-spin-dependent PV (NSD-PV) interactions. These primarily arise from the electron-vector and nucleon axial-vector (V_eA_N) Z^0-boson exchange [1], and the electron electromagnetic interaction with the nuclear anapole moment [1,26,27] (so far only detected in ^{133}Cs [4]). Another contribution could come from new interactions beyond the standard model between electrons and nucleons, mediated by yet-to-be-discovered gauge bosons [28–30].

Our proposed method should be highly general for various molecular ions. However, we will focus on $^{29}SiO^+$ due to practical and theoretical advantages for the initial demonstration: Its rotational and electronic structure is known [31], the ground electronic state is $^2\Sigma^+$, and it was demonstrated suitable for laser cooling [32,33].

Effective Hamiltonian and electroweak properties.—Our scheme builds on the concepts introduced in [20,34]. The effective Hamiltonian describing the lowest rotational and hyperfine energy levels of $^{29}SiO^+$, in the absence of PV effects, can be expressed as

$$H_0 = B_0 N^2 + D_0 N^4 + \gamma \boldsymbol{N}\cdot\boldsymbol{S} + b\boldsymbol{I}\cdot\boldsymbol{S} + c(\boldsymbol{I}\cdot\boldsymbol{n})(\boldsymbol{S}\cdot\boldsymbol{n}),$$

with $\boldsymbol{N} = \boldsymbol{R} + \boldsymbol{L}$, where $\boldsymbol{R}$ is the mechanical rotation of the molecular framework, $\boldsymbol{L}$ is the orbital angular momentum of the electron, $\boldsymbol{S}$ and $\boldsymbol{I}$ are the molecular frame electron and nuclear spin operator, respectively, and $\boldsymbol{n}$ is the unit vector along the internuclear axis. The rotational, centrifugal distortion, and spin-rotational constants are B_0, D_0, and γ. b and c are hyperfine structure constants associated with the ^{29}Si nucleus. The rotational constant of $^{29}SiO^+$ is far larger than all the other molecular parameters in H_0 [35]. Thus, N is a good quantum number for levels of energy $E_N \approx B_0 N(N+1)$ and parity $P_N = (-1)^N$.

When a magnetic field of a particular magnitude B is applied (see Fig. 1), sublevels of the $N^P = 0^+$ and 1^- states can be Zeeman shifted close to degeneracy. For $^{29}SiO^+$, this magnetic field strength is $B \approx [(E_1 - E_0)/2\mu_B] \approx 1.5$ T, since the coupling to the electron spin S dominates the Zeeman shift via the Hamiltonian $H_Z = -g\mu_B \boldsymbol{S}\cdot\boldsymbol{B}$ with g factor $g \approx -2$, the Bohr magneton μ_B, and the magnetic field aligned with the z axis $\boldsymbol{B} = B\boldsymbol{z}$ [23]. This field is strong enough to decouple $\boldsymbol{S}$ from $\boldsymbol{I}$ and $\boldsymbol{N}$. Hence, the rotational and hyperfine levels are better described in the decoupled basis used for the rest of the Letter: $|N, m_N\rangle|S, m_S\rangle|I, m_I\rangle$.

The NSD-PV interactions can mix opposite-parity levels. The Hamiltonian $H_{\mathrm{PV}} = \kappa'(G_F/\sqrt{2})(\boldsymbol{\alpha}\boldsymbol{I}/I)\rho(\boldsymbol{r})$ [26] describes such PV interactions, where κ' includes all the NSP-PV contributions. We denote the Fermi constant G_F, Dirac matrices vector $\boldsymbol{\alpha}$, nuclear spin $\boldsymbol{I}$, and nuclear density with respect to the nuclear center $\rho(\boldsymbol{r})$. An effective Hamiltonian acting only within the subspace of rotational and hyperfine levels can be obtained by averaging the previous Hamiltonian over the electronic wave function, given by $H_{\mathrm{eff}} = \kappa' W_{\mathrm{A}} C$, where W_{A} is a matrix element that includes the expectation value of H_{PV} over the electronic wave function in the $^2\Sigma$ state in the rotating frame of the molecule, which can be computed numerically using state-of-the-art quantum chemistry methods with uncertainties as low as a few percent [38]. $C = \{[(\boldsymbol{n}\times\boldsymbol{S})\cdot\boldsymbol{I}]/I\}$ contains the angular momentum dependence of H_{eff} and its matrix elements can be calculated analytically using angular momentum algebra [21].

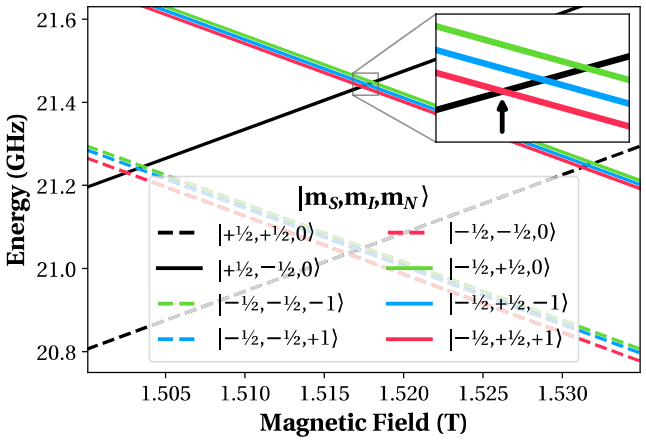

FIG. 1. Calculated energies of opposite parity rotational and hyperfine states in $^{29}SiO^+$ for different magnetic field strengths, based on the Hamiltonian H_0 and parameters given in [36,37]. The positive parity states $|\Psi^+_\uparrow\rangle$ are rising, while the negative ones $|\Psi^-_\downarrow\rangle$ are descending. For details, see text.

Measurement strategy.—Our proposed experiment will be performed in a Penning ion trap. This device is widely used in precision atomic and nuclear physics [39–42]. The trap consists of a strong magnetic and a weak electrostatic field, allowing three-dimensional trapping of ions (see Ref. [43] for a review on Penning traps). We use the trapping magnetic field to Zeeman shift two opposite parity states into near degeneracy (see arrow in Fig. 1). Moreover, the intrinsic trap design allows for various magnetic field strengths for maximal flexibility in the choice of ion species and rotational-hyperfine states.

Our experimental principle is identical to the one for neutral molecules in Refs. [20,23]. In the presence of axial (i.e., aligned with the magnetic field) and radial electric fields, E_z and E_r, the effective Hamiltonian of this two-level system is

$$H_\pm = \begin{pmatrix} \alpha_r E_r^2 + \alpha_z E_z^2 & iW + d\cdot E_z \\ -iW + d\cdot E_z & \Delta \end{pmatrix},$$

with the weak interaction matrix element $iW(m'_N, m'_I, m_N, m_I) \equiv \kappa' W_{\mathrm{A}} \langle \Psi^-_\downarrow(m'_N, m'_I)|C|\Psi^+_\uparrow(m_N, m_I)\rangle$, the expectation value d of the dipole moment operator, $\boldsymbol{D}$, between the two levels and the general wave function, $|\Psi(t)\rangle = c_+(t)|\Psi^+_\uparrow\rangle + e^{-i\Delta t}c_-(t)|\Psi^-_\downarrow\rangle$, of the two-level system with its eigenstates $|\Psi^P_{m_S}\rangle$ of parity P and spin projection m_S, and its time-dependent amplitudes $c_P(t)$ [see Refs. [20,23,44–46] and the Supplemental Material (SM)-B [47] for details]. Δ is a small detuning of the two levels from perfect degeneracy and depends on the applied magnetic field strength B; α_r and α_z represent the radial and axial contributions to the differential polarizability of the two levels [48], while E_r and E_z are any external radial and axial E fields.

In the ideal case of a single ion resting in a stable magnetic field B at $t_0 = 0$ with zero external electric fields prepared in the $|\Psi^+_\uparrow\rangle$ state in the center of our trap, we measure W using the Stark-interference procedure described

in Ref. [20]. Thereby, population transfer from the initial positive $|\Psi_{\uparrow}^{+}\rangle$ to the negative $|\Psi_{\downarrow}^{-}\rangle$ parity state occurs due to the PV matrix element and the interaction with a sinusoidal electric field. We repeat this measurement for several N_0 ions to determine the population transfer probability by measuring the average signal $S = N_0|c_{-}(t)|^2$ (see SM-B [47] and Refs. [44–46] for details). The existence of parity violation leads to a nonzero asymmetry, defined as $A_{\mathrm{PV}} \equiv \{[S(+E_{\mathrm{ext}}) - S(-E_{\mathrm{ext}})]/[S(+E_{\mathrm{ext}}) + S(-E_{\mathrm{ext}})]\}$ [23], where $S(+E_{\mathrm{ext}})$ and $S(-E_{\mathrm{ext}})$ refer to the signals obtained for measurements with zero (+) and π (−) phase shift in the sinusoidal field.

For $^{29}SiO^{+}$, the population transfer and, hence, the asymmetry can be estimated using first-order perturbation theory (see SM-B [47] and Refs. [44–46] for details). For interrogation times $t_{\mathrm{x}} \approx (2\pi N/\omega_{\mathrm{ext}}) \approx (\pi/\Delta)$ at integer N, the PV asymmetry becomes [20]

$$A_{\mathrm{PV}} = \frac{\frac{2W}{\Delta} \cdot \frac{\Omega_{\mathrm{R}}}{\omega_{\mathrm{ext}}}}{(\frac{W}{\Delta})^2 + (\frac{\Omega_{\mathrm{R}}}{\omega_{\mathrm{ext}}})^2}, \tag{1}$$

with $\Omega_{\mathrm{R}} = dE_{\mathrm{ext}}$. Ultimately, W is determined via the population transfer probability for different values of Δ, i.e., magnetic field strengths B we can easily scan in our setup. Its statistical uncertainty is

$$\delta W = \frac{\Delta}{4\sqrt{2N_0}\sin(\frac{\Delta t_{\mathrm{x}}}{2})} \frac{\sqrt{\eta^2+1}}{\eta} \tag{2}$$

using $\eta \equiv (\Omega_R/\omega_{\mathrm{ext}})/(W/\Delta)$ for the number of molecules N_0.

To reduce δW, we want to minimize Δ. Since we are technically limited in arbitrarily reducing Δ (as discussed in the following section), we set the interrogation time to $t_{\mathrm{x}} = (\pi/\Delta)$ once Δ is minimized. Thus, the precise control of the interrogation time t_{x} in our trap for a minimal uncertainty on δW and precise variation of t_{x} to check for systematic effects, are clear advantages we can leverage over experiments performed on molecular beams.

From our measurement of W and the calculated W_{A} and C, we can extract $\kappa' \approx \kappa_2' + \kappa_{\mathrm{a}}'$, encoding the physics of the weak interaction that leads to NSD-PV: κ_2', arising from the $V_e A_N$ term in the electron-nucleon-Z^0-boson exchange, and the electron electromagnetic interaction with the anapole moment, κ_{a}'. Applying our technique to a wide range of isotopic chains, including radioactive ones [18,24,25], could allow for a separation of κ_2' and κ_{a}' based on the dependence of κ_{a}' on the nuclear mass A and spin I [20,27].

Experimental details.—Trapped ions in a Penning trap move on three superimposed eigenmotions inside the trap. The eigenmotions' frequency, phase, and amplitude can be controlled and coupled through radio-frequency excitations on the ion trap's electrodes [43]. The eigenmotions can be further cooled by coupling to a resonance circuit at 1K. Once the ion is located in the trap center in equilibrium with the 1-K environment, it is decoupled from the resonance circuit using a cryogenic switch. It remains in a nominally zero E_{ext} field, allowing for the above assumptions on the Hamiltonian due to low reheating rates of ~ 65 mK/s [49].

An additional, significant advantage of our proposed method is that the magnetic field strength B experienced by the molecular ion with charge-to-mass ratio q/m can be precisely determined through a cyclotron frequency $\nu_c = (Bq/2\pi m)$ determination to the 10^{-11} level of precision or better [50,51].

In our proposed setup, neutral ^{29}SiO molecules are produced by laser ablating a silicon rod in the supersonic expansion of a mixture of oxygen and argon gas [52]. The molecules are photoionized using resonant laser light [53] into the ground electronic and vibrational states populating only low rotational levels [54]. The measurement scheme shown in Fig. 2 works as follows:

(i) The molecular ions are trapped in the Penning trap, and a single molecule is selected using the evaporative cooling technique [55]. Once the ion is located at the trap center in equilibrium with the 1-K environment (assumed as the kinetic temperature of the ions moving forward) and decoupled from the resonant circuit, it is optically pumped into its rotational ground state [94(3)% fidelity were shown in Ref. [32] for $^{28}SiO^{+}$]. This level is further split into four hyperfine substates. Given the large splitting between these substates (>100 MHz), they can be addressed individually after the rotational cooling using lasers or microwaves to transfer the population to the state of interest, $|\Psi_{\uparrow}^{+}\rangle$ (Fig. 1, solid black line), with >90% fidelity.

(ii) To ensure the molecule is not in the negative parity state $|\Psi_{\downarrow}^{-}\rangle$ (Fig. 1, colored lines) even after the state transfer, the molecule in $|\Psi_{\downarrow}^{-}\rangle$ is state-selectively dissociated via excitation to a higher-lying autodissociating state [32]. The timescale for this process is ~10 ns, i.e., short compared to all inverse frequencies in this measurement; thus, it corresponds to an instantaneous (but conditional) quantum projection onto unaffected states.

(iii) This step constitutes the starting point of the measurement. It will be executed after step (i) and in

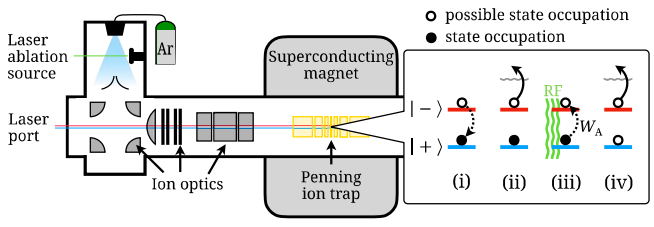

FIG. 2. Schematic layout and measurement principle with a laser port for the ionization, cooling, and dissociation lasers. Our measurement procedure, (i)–(iv), is described in the text.

parallel to step (ii) since $|\Psi_{\uparrow}^{+}\rangle$ would start to evolve in time even without an external electric field.

To induce Stark mixing, we have the ion experience, a sinusoidal electric field $E_z(t) = E_{\text{ext}} \cdot \sin(\omega_{\text{ext}} t)$ with $E_{\text{ext}} \approx 6$ V/cm and $\Omega_R/2\pi \approx 3$ kHz in its rest frame. This is achieved by exciting the ion to an axial amplitude of ~0.3 mm in the harmonic trapping potential with a ~20 V single cycle, resonant sinusoidal-wave "kick" to the trap's end caps as routinely achieved in practice [56].

(iv) The final state detection is performed by molecular dissociation of the negative parity state $|\Psi_{\downarrow}^{-}\rangle$, using the same autoionizing state as in step (ii) as soon as the oscillating field in step (iii) is switched "off" by reversing the sinusoidal "kick." Since the dissociation process is parity-state selective, we can perform a "double-dip" mass measurement [56] in search of $^{29}SiO^+$, $^{29}Si^+$, or $^{16}O^+$ as a measurement of the final parity state. If a dissociation had occurred, we can remove the $^{29}Si^+$ or $^{16}O^+$ ion from the trap and load a new $^{29}SiO^+$ ion. If no dissociation occurs, the measurement is restarted at step (i).

Figure 3 shows the simulated PV asymmetry, A_{PV}, in Eq. (1), as a function of Δ for a range of possible W values. For $^{29}SiO^+$, we assume $\Omega_R/2\pi = 3$ kHz, $\omega_{\text{ext}}/2\pi = 350$ kHz, and scan $\Delta/2\pi$ ranging from -150 Hz to 150 Hz in steps of 50 Hz. Measuring different values of Δ was shown to be effective in avoiding various systematic uncertainties [23,57]. Measuring at other relevant level crossings will also allow diagnosing systematics.

Heavier molecules with larger weak matrix elements comparable to Δ ($W \gtrsim 100$ Hz), such as the potentially laser-coolable TlF^+ [58] (see Table I), do not require additional external Stark mixing for amplifying the sought signal. As suggested in Ref. [34], the level crossing shown in Fig. 1 turns into a pseudocrossing, which can be measured directly. This approach requires an advanced level of systematic control which we plan to investigate in the future.

Uncertainty estimates.—Here, we estimate the primary sources and magnitude of uncertainty for $^{29}SiO^+$ with the calculated $W_A/2\pi = 16$ Hz from Table I, corresponding to $W/2\pi = 0.4$ Hz when assuming $\kappa' = 0.05$ and $C = 0.5$.

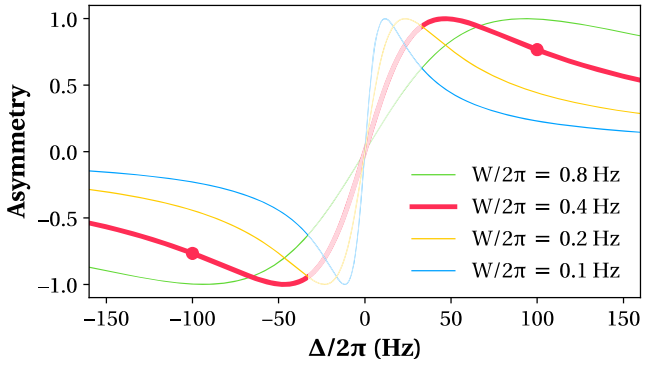

FIG. 3. Asymmetry for $^{29}SiO^+$ for different W and Δ. The assumed experimental condition is indicated in red with details provided in the text. The red dots show the expected asymmetry at $\Delta/2\pi = \pm 100$ Hz.

(i) Initial axial amplitude: The main contribution to the systematic uncertainty is expected to come from the ac Stark shift of the energy levels of interest due to the transverse and axial components of the electric field, with the effects proportional to $\alpha_r E_r^2$ and $\alpha_z E_z^2$, respectively. The uncertainty associated with this shift arising from the thermal distribution of ion positions and velocities is expected to be $\delta\Delta/2\pi \approx 30$ Hz (see SM-A [47] for details of the calculations). To clearly tell apart the two opposite parity levels of interest, we assume moving forward a value of $\Delta/2\pi \approx 100$ Hz, and therefore $t_x = \pi/\Delta = 5$ ms to minimize δW, leading to a maximum state transfer probability of the positive parity state's population of ~0.06% and an asymmetry of ~0.75 (red dots in Fig. 3).

A second major source of uncertainty is expected to derive from the thermal noise in the initial axial amplitude of cooled ions. Once cooled and resting in the center of the Penning trap, the ions' energy is Boltzmann distributed with an average initial axial amplitude of $z_0 = \sqrt{[2k_b T d_{\text{char}}^2/(q_{\text{ion}} U_0 C_2)]}$, where k_b is the Boltzmann constant, q_{ion} is the electron charge e, and we assume $T = 1$ K. Based on our trap design [56] optimized for E-field homogeneity of the electric trapping potential of depth $U_0 = -35$ V, characteristic trap length $d_{\text{char}} = \sqrt{0.5(z_{\text{trap}}^2 + r_{\text{trap}}^2/2)} = 3$ mm (with the central ring electrode's length z_{trap} and radius r_{trap}), and the dimensionless quadrupole constant $C_2 = -0.6$. The initial axial motion is then $z_0 \approx 10$ μm, which would result in an average thermal noise of $\delta E_{\text{th}} \approx 0.2$ V/cm, corresponding to $\delta W/W \approx 3\%$ for $^{29}SiO^+$. Both of these effects are statistical, i.e., they can be reduced by increasing the number of measurements.

(ii) Magnetic field: Short-term magnetic field instabilities (for the measurement time of up to many milliseconds) are expected to be $\delta B/B \lesssim 10^{-10}$ [59,60]. Observed temporal changes in the magnetic field tracked in a neighboring trap center will be used for live adjustment of slow magnetic field drifts on top of typical temperature and pressure stabilization of the magnet [56]. With this method, we anticipate $\delta B/B \approx 10^{-10}$ for the duration of the data taking [61]. Furthermore, deviations from spatial uniformity due to higher-order field effects not accounted for by shimming coils are expected to be $\delta B/B < 10^{-10}$ for the small probed volume of $\ll 0.1$ mm^3 [56]. All of these effects can be quantified based on precise measurements of ν_c for well-known species. These effects lead to a total systematic uncertainty from the magnetic field of $\delta B/B \approx 10^{-10}$, or $\delta\Delta/2\pi \approx 4$ Hz, i.e., $\delta W/W \approx 4\%$ for $^{29}SiO^+$.

(iii) Electric field: A relative electric field uncertainty of $\delta E/E \ll 1\%$, which can be routinely achieved in practice [56], would have negligible effect on δW.

TABLE I. Diatomic molecular ions with sizable weak matrix elements W_A (of the first-mentioned atom) in units of Hz and their bond lengths BL in units of Å. Data on additional molecular ions can be found in [62]. For details, see text.

System	W_A	BL	System	W_A	BL	System	W_A	BL
$^{11}B^{19}F^+$	1	1.21	$^{227}Ac^{79}Br^+$	1644	2.72	$^{261}Lr^{1}H^+$	11 295	1.89
$^{29}Si^{16}O^+$	13	1.52	$^{227}Ac^{127}I^+$	1677	2.94	$^{261}Lr^{7}Li^+$	2745	3.49
$^{205}Tl^{19}F^+$	4472	1.98	$^{229}Th^{16}O^+$	2506	1.8	$^{261}Lr^{19}F^+$	8826	1.93
$^{227}Ac^{1}H^+$	1649	2.23	$^{229}Th^{32}S^+$	1752	2.31	$^{261}Lr^{23}Na^+$	2425	3.8
$^{227}Ac^{19}F^+$	1655	2.08	$^{229}Th^{80}Se^+$	1588	2.45	$^{261}Lr^{35}Cl^+$	10 158	2.35
$^{227}Ac^{35}Cl^+$	1632	2.56	$^{229}Th^{126}Te^+$	1323	2.68	$^{261}Lr^{39}K^+$	1658	4.26

We thus anticipate a total systematic uncertainty of $\delta W/W < 5\%$ for $^{29}SiO^+$. To achieve a 10% statistical uncertainty on the proposed measurement, we need on the order of 10^5 trapped molecular ions. Given a measurement cycle of a few seconds (dominated by mass selection, cooling, and state preparation), a 10% relative uncertainty measurement would thus be feasible in about one week of measurement time for $^{29}SiO^+$.

Calculated sensitivity factors.—We calculated the molecular matrix element of the anapole moment W_A for the $^2\Sigma_{1/2}$ ground states of BF^+, $^{29}SiO^+$, and TlF^+ at the four-component relativistic Fock-space coupled-cluster (FSCC) level of theory using the finite field approach. This formalism includes H_{PV} as a perturbation to the Dirac-Coulomb Hamiltonian. The W_A factor is obtained as the first derivative of the total energy to this perturbation [38]. We used the dyall.cv4z basis sets [63,64] and correlated 13 (all), 21 (all), and 51 electrons for BF^+, $^{29}SiO^+$, and TlF^+, respectively. A Gaussian charge distribution represented the nucleus.

Furthermore, we calculated W_A for Ac, Th, and Lr-containing molecular ions. Here, we used the four-component relativistic Dirac-Hartree-Fock (DHF) level of theory. In this case, W_A was extracted from the off-diagonal matrix elements of the operator $\alpha\rho(r)$ acting on the degenerate $\Omega = |\pm 1/2\rangle$ states in the molecular spinor basis. We employed the dyall.cv4z basis set for all the elements [63–66].

The molecular geometries were optimized at the exact two-component [67,68] coupled-cluster level of theory, including single and double excitations in the parallel implementation of the Dirac program package [69]. The cutoff was set to −20 to 30 a.u. We used the dyall.v3z basis sets [64–66] for all the systems, except for $^{29}SiO^+$ (experimental bond length [70]), and BF^+/TlF^+ (s-aug-dyall.v4z basis sets [63,64]). All results are presented in Table I.

Besides $^{29}SiO^+$ [31–33], spectroscopic information in the literature among the presented molecular ions is not available to the best of our knowledge. Hence, prior studies of each molecular ion are necessary to find the needed rotational-hyperfine parameters and laser-cooling transitions.

Outlook.—We proposed a new technique that can provide a highly sensitive route to investigate yet-to-be-explored nuclear parity-violating properties using single molecular ions. These measurements will enable stringent tests of the weak interaction in stable and short-lived isotopes across the nuclear chart. This technique could be directly applied to light isotopes, for which PV nuclear properties can already be calculated on the lattice [71,72] and with *ab initio* methods [73]. For diatomic molecules containing elements as light as the deuteron, challenges with the required magnetic field strength could be overcome by using ground-rotational states in polyatomic molecules [20,25,74]. Furthermore, applying advanced cooling techniques already demonstrated in Penning traps would enable reducing the trapped molecule's kinetic energy to ∼1–100 mK [75–79], resulting in a reduction of the uncertainty on W by 1 to 2 orders of magnitude.

This work was supported by the U.S. Department of Energy (DOE), Office of Science (OS), and Office of Nuclear Physics under Awards No. DE-SC0021176 and No. DE-SC0021179. This research is partly based on work supported by Laboratory Directed Research and Development (LDRD) funding from Argonne National Laboratory, provided by the OS Director of the U.S. DOE under Contract No. DE-AC02-06CH11357. We thank the Center for Information Technology of the University of Groningen for its support and access to the Peregrine high-performance computing cluster. The INCITE program awarded computer time. This research also used resources from the Oak Ridge Leadership Computing Facility, a DOE-OS User Facility supported under Contract No. DE-AC05-00OR22725. We also acknowledge the support from High Sector Fock space coupled cluster method: benchmark accuracy across the periodic table (with Project No. VI.Vidi.192.088 of the research program Vidi, financed by the Dutch Research Council) and the 2020 Incite Award: "PRECISE: Predictive Electronic Structure Modeling of Heavy Elements." J. K. acknowledges the support of a Feodor Lynen Fellowship of the Alexander-von-Humboldt Foundation. S. B. M. acknowledges the support of a National Science Foundation Graduate Research Fellowship (NSF Grant No. 2141064)

and a Fannie and John Hertz Graduate Fellowship. The work of A. B. was supported by the project "High Sector Fock space coupled cluster method: benchmark accuracy across the periodic table" with Project No. Vi.Vidi.192.088 of the research program Vidis, financed by the Dutch Research Council (NWO). L. F. P. acknowledges the support from NWO Project No. VI.C.212.016 of the talent program VICI, and the support from the Slovak Research and Development Agency (Projects No. APVV-20-0098, No. APVV-20-0127). All sensitivity factor calculations were performed using an adapted version of the Dirac program package [80,81]. Simulations used NUMPY [82], SCIPY [83], PANDAS [84,85], and SIMION [86]. Figures were produced using MATPLOTLIB [87].

*These authors contributed equally to this work.
†Corresponding author: karthein@mit.edu
‡Corresponding author: sudrescu@mit.edu
§Corresponding author: ddemille@uchicago.edu
‖Corresponding author: rgarciar@mit.edu

[1] M. S. Safronova, D. Budker, D. DeMille, D. F. J. Kimball, A. Derevianko, and C. W. Clark, Search for new physics with atoms and molecules, Rev. Mod. Phys. **90**, 025008 (2018).
[2] H. Davoudiasl, H.-S. Lee, and W. J. Marciano, "Dark" z implications for parity violation, rare meson decays, and Higgs physics, Phys. Rev. D **85**, 115019 (2012).
[3] P. Langacker, The physics of heavy Z' gauge bosons, Rev. Mod. Phys. **81**, 1199 (2009).
[4] C. Wood, S. Bennett, D. Cho, B. Masterson, J. Roberts, C. Tanner, and C. E. Wieman, Measurement of parity nonconservation and an anapole moment in cesium, Science **275**, 1759 (1997).
[5] The Jefferson Lab PVDIS Collaboration, Measurement of parity violation in electron–quark scattering, Nature (London) **506**, 67 (2014).
[6] D. Androić *et al.* (Qweak Collaboration), Parity-violating inelastic electron-proton scattering at low Q^2 above the resonance region, Phys. Rev. C **101**, 055503 (2020).
[7] B. Desplanques, J. F. Donoghue, and B. R. Holstein, Unified treatment of the parity violating nuclear force, Ann. Phys. (N.Y.) **124**, 449 (1980).
[8] E. G. Adelberger and W. C. Haxton, Parity violation in the nucleon-nucleon interaction, Annu. Rev. Nucl. Part. Sci. **35**, 501 (1985).
[9] W. C. Haxton and B. R. Holstein, Hadronic parity violation, Prog. Part. Nucl. Phys. **71**, 185 (2013), fundamental Symmetries in the Era of the LHC.
[10] S. Gardner, W. Haxton, and B. R. Holstein, A new paradigm for hadronic parity nonconservation and its experimental implications, Annu. Rev. Nucl. Part. Sci. **67**, 69 (2017).
[11] J. de Vries, E. Epelbaum, L. Girlanda, A. Gnech, E. Mereghetti, and M. Viviani, Parity- and time-reversal-violating nuclear forces, Front. Phys. **8**, 218 (2020).
[12] S. Gardner and G. Muralidhara, Toward a unified treatment of $\delta\,\mathrm{s} = 0$ parity violation in low-energy nuclear processes, Phys. Rev. C **107**, 055501 (2023).
[13] M. J. Ramsey-Musolf and S. A. Page, Hadronic parity violation: A new view through the looking glass, Annu. Rev. Nucl. Part. Sci. **56**, 1 (2006).
[14] B. R. Holstein, Overview of hadronic parity violation, Eur. Phys. J. A **32**, 505 (2007).
[15] V. Andreev, D. G. Ang, D. DeMille, J. M. Doyle, G. Gabrielse, J. Haefner, N. R. Hutzler, Z. Lasner, C. Meisenhelder, B. R. OLeary, C. D. Panda, A. D. West, E. P. West, and X. Wu (ACME Collaboration), Improved limit on the electric dipole moment of the electron, Nature (London) **562**, 355 (2018).
[16] W. B. Cairncross, D. N. Gresh, M. Grau, K. C. Cossel, T. S. Roussy, Y. Ni, Y. Zhou, J. Ye, and E. A. Cornell, Precision measurement of the electron's electric dipole moment using trapped molecular ions, Phys. Rev. Lett. **119**, 153001 (2017).
[17] T. S. Roussy, L. Caldwell, T. Wright, W. B. Cairncross, Y. Shagam, K. B. Ng, N. Schlossberger, S. Y. Park, A. Wang, J. Ye, and E. A. Cornell, A new bound on the electron's electric dipole moment, Science **381**, 46 (2023).
[18] R. F. Garcia Ruiz *et al.*, Spectroscopy of short-lived radioactive molecules, Nature (London) **581**, 396 (2020).
[19] O. Sushkov and V. Flambaum, Parity breaking effects in diatomic molecules, Zh. Eksp. Teor. Fiz. **75**, 1208 (1978), http://www.jetp.ras.ru/cgi-bin/e/index/e/48/4/p608?a=list.
[20] D. DeMille, S. B. Cahn, D. Murphree, D. A. Rahmlow, and M. G. Kozlov, Using molecules to measure nuclear spin-dependent parity violation, Phys. Rev. Lett. **100**, 023003 (2008).
[21] V. Flambaum and I. Khriplovich, On the enhancement of parity nonconserving effects in diatomic molecules, Phys. Lett. A **110**, 121 (1985).
[22] M. G. Kozlov and L. N. Labzowsky, Parity violation effects in diatomics, J. Phys. B **28**, 1933 (1995).
[23] E. Altuntaş, J. Ammon, S. B. Cahn, and D. DeMille, Demonstration of a sensitive method to measure nuclear-spin-dependent parity violation, Phys. Rev. Lett. **120**, 142501 (2018).
[24] S. M. Udrescu *et al.*, Isotope shifts of radium monofluoride molecules, Phys. Rev. Lett. **127**, 033001 (2021).
[25] G. Arrowsmith-Kron *et al.*, Opportunities for fundamental physics research with radioactive molecules, arXiv: 2302.02165.
[26] V. Flambaum and I. Khriplovich, P-odd nuclear forces: A source of parity violation in atoms, Sov. Phys. JETP **52**, 835 (1980), http://www.jetp.ras.ru/cgi-bin/e/index/e/52/5/p835?a=list.
[27] V. Flambaum, I. Khriplovich, and O. Sushkov, Nuclear anapole moments, Phys. Lett. B **146**, 367 (1984).
[28] V. A. Dzuba, V. V. Flambaum, and Y. V. Stadnik, Probing low-mass vector bosons with parity nonconservation and nuclear anapole moment measurements in atoms and molecules, Phys. Rev. Lett. **119**, 223201 (2017).
[29] Y. Stadnik and V. Flambaum, Nuclear spin-dependent interactions: searches for WIMP, axion and topological defect dark matter, and tests of fundamental symmetries, Eur. Phys. J. C **75**, 110 (2015).
[30] Y. V. Stadnik and V. V. Flambaum, Axion-induced effects in atoms, molecules, and nuclei: Parity nonconservation, anapole moments, electric dipole moments, and spin-gravity

and spin-axion momentum couplings, Phys. Rev. D **89**, 043522 (2014).

[31] P. R. Stollenwerk, B. C. Odom, D. L. Kokkin, and T. Steimle, Electronic spectroscopy of a cold SiO^+ sample: Implications for optical pumping, J. Mol. Spectrosc. **332**, 26 (2016).

[32] P. R. Stollenwerk, I. O. Antonov, S. Venkataramanababu, Y.-W. Lin, and B. C. Odom, Cooling of a zero-nuclear-spin molecular ion to a selected rotational state, Phys. Rev. Lett. **125**, 113201 (2020).

[33] J. H. V. Nguyen and B. Odom, Prospects for doppler cooling of three-electronic-level molecules, Phys. Rev. A **83**, 053404 (2011).

[34] M. Kozlov, L. Labzovski, and A. Mitrushchenko, Parity nonconservation in diatomic molecules in a strong constant magnetic field, Zh. Éksp. Teor. Fiz. **100**, 749 (1991), http://www.jetp.ras.ru/cgi-bin/e/index/e/73/3/p415?a=list.

[35] G.-Z. Zhu, G. Lao, C. Ho, W. C. Campbell, and E. R. Hudson, High-resolution laser-induced fluorescence spectroscopy of $^{28}Si^{16}O^+$ and $^{29}Si^{16}O^+$ in a cryogenic buffer-gas cell, J. Mol. Spectrosc. **384**, 111582 (2022).

[36] L. B. Knight Jr, A. Ligon, R. Woodward, D. Feller, and E. R. Davidson, The generation and trapping of the high-temperature oxosilyliumyl cation radicals ($^{28}SiO^+$ and $^{29}SiO^+$) in neon matrixes at 4 K; an ESR and *ab initio* CI theoretical investigation, J. Am. Chem. Soc. **107**, 2857 (1985).

[37] G.-Z. Zhu, G. Lao, C. Ho, W. C. Campbell, and E. R. Hudson, High-resolution laser-induced fluorescence spectroscopy of $^{28}Si^{16}O^+$ and $^{29}Si^{16}O^+$ in a cryogenic buffer-gas cell, J. Mol. Spectrosc. **384**, 111582 (2022).

[38] Y. Hao, M. Iliaš, E. Eliav, P. Schwerdtfeger, V. V. Flambaum, and A. Borschevsky, Nuclear anapole moment interaction in BaF from relativistic coupled-cluster theory, Phys. Rev. A **98**, 032510 (2018).

[39] P. Filianin, C. Lyu, M. Door, K. Blaum, W. J. Huang, M. Haverkort, P. Indelicato, C. H. Keitel, K. Kromer, D. Lange, Y. N. Novikov, A. Rischka, R. X. Schüssler, C. Schweiger, S. Sturm, S. Ulmer, Z. Harman, and S. Eliseev, Direct q-value determination of the β^- decay of ^{187}Re, Phys. Rev. Lett. **127**, 072502 (2021).

[40] T. Sailer, V. Debierre, Z. Harman, F. Heiße, C. König, J. Morgner, B. Tu, A. V. Volotka, C. H. Keitel, K. Blaum, and S. Sturm, Measurement of the bound-electron g-factor difference in coupled ions, Nature (London) **606**, 479 (2022).

[41] M. Mougeot *et al.*, Mass measurements of $^{99-101}In$ challenge *ab initio* nuclear theory of the nuclide ^{100}Sn, Nat. Phys. **17**, 1099 (2021).

[42] M. Borchert, J. Devlin, S. Erlewein, M. Fleck, J. Harrington, T. Higuchi, B. Latacz, F. Voelksen, E. Wursten, F. Abbass *et al.*, A 16-parts-per-trillion measurement of the antiproton-to-proton charge–mass ratio, Nature (London) **601**, 53 (2022).

[43] L. S. Brown and G. Gabrielse, Geonium theory: Physics of a single electron or ion in a Penning trap, Rev. Mod. Phys. **58**, 233 (1986).

[44] D. Budker, D. F. Kimball, and D. P. DeMille, *Atomic Physics: An Exploration Through Problems and Solutions* (Oxford University Press, New York, 2004).

[45] S. Chattopadhyaya, A. Chattopadhyay, and K. K. Das, Electronic spectrum of SiO^+: A theoretical study, J. Mol. Struct. **639**, 177 (2003).

[46] G. Arfken, *Mathematical Methods for Physicists: Spherical Harmonics* (Academic Press, Orlando, 1985), Vol. 1, p. 680.

[47] See Supplemental Material at http://link.aps.org/supplemental/10.1103/PhysRevLett.133.033003 for a detailed investigation of the effects of time-varying electric fields as well as the derivation of the analytical formula in Eq. (1) for the parity violation asymmetry measured using the technique described in the Letter.

[48] S. B. Cahn, J. Ammon, E. Kirilov, Y. V. Gurevich, D. Murphree, R. Paolino, D. A. Rahmlow, M. G. Kozlov, and D. DeMille, Zeeman-tuned rotational level-crossing spectroscopy in a diatomic free radical, Phys. Rev. Lett. **112**, 163002 (2014).

[49] M. J. Jensen, T. Hasegawa, and J. J. Bollinger, Temperature and heating rate of ion crystals in Penning traps, J. Phys. Rev. A **70**, 033401 (2004).

[50] M. B. Comisarow and A. G. Marshall, Fourier transform ion cyclotron resonance spectroscopy, Chem. Phys. Lett. **25**, 282 (1974).

[51] R. X. Schüssler, H. Bekker, M. Braß, H. Cakir, J. R. Crespo L'opez-Urrutia, M. Door, P. Filianin, Z. Harman, M. W. Haverkort, W. J. Huang, P. Indelicato, C. H. Keitel, C. M. König, K. Kromer, M. Müller, Y. N. Novikov, A. Rischka, C. Schweiger, S. Sturm, S. Ulmer, S. Eliseev, and K. Blaum, Detection of metastable electronic states by Penning trap mass spectrometry, Nature (London) **581** (2020).

[52] A. J. Marr, M. Flores, and T. Steimle, The optical and optical/stark spectrum of iridium monocarbide and mononitride, J. Chem. Phys. **104**, 8183 (1996).

[53] P. R. Stollenwerk, I. O. Antonov, and B. C. Odom, IP determination and $1+1$ rempi spectrum of SiO at 210–220 nm in an ion trap: Implications for SiO^+ ion trap loading, J. Mol. Spectrosc. **355**, 40 (2019).

[54] X. Tong, A. H. Winney, and S. Willitsch, Sympathetic cooling of molecular ions in selected rotational and vibrational states produced by threshold photoionization, Phys. Rev. Lett. **105**, 143001 (2010).

[55] G. B. Andresen *et al.*, Evaporative cooling of antiprotons to cryogenic temperatures, Phys. Rev. Lett. **105**, 013003 (2010).

[56] S. Sturm, I. Arapoglou, A. Egl, M. Höcker, S. Kraemer, T. Sailer, B. Tu, A. Weigel, R. Wolf, J. C. López-Urrutia, and K. Blaum, The ALPHATRAP experiment, Eur. Phys. J. Spec. Top. **227**, 1425 (2019).

[57] E. Altuntaş, J. Ammon, S. B. Cahn, and D. DeMille, Measuring nuclear-spin-dependent parity violation with molecules: Experimental methods and analysis of systematic errors, Phys. Rev. A **97**, 042101 (2018).

[58] W. Chmaisani and S. Elmoussaoui, Theoretical study of laser cooling of the TlF^+ molecular ion, Phys. Chem. Chem. Phys. **23**, 1718 (2021).

[59] Y. Takeda, H. Maeda, K. Ohki, and Y. Yanagisawa, Review of the temporal stability of the magnetic field for ultra-high field superconducting magnets with a particular focus on superconducting joints between HTS conductors, Supercond. Sci. Technol. **35**, 043002 (2022).

[60] J. W. Britton, J. G. Bohnet, B. C. Sawyer, H. Uys, M. J. Biercuk, and J. J. Bollinger, Vibration-induced field fluctuations in a superconducting magnet, Phys. Rev. A **93**, 062511 (2016).
[61] C. Droese, M. Block, M. Dworschak, S. Eliseev, E. M. Ramirez, D. Nesterenko, and L. Schweikhard, Investigation of the magnetic field fluctuation and implementation of a temperature and pressure stabilization at SHIPTRAP, Nucl. Instrum. Methods Phys. Res., Sect. A **632**, 157 (2011).
[62] A. Borschevsky, M. Iliaš, V. A. Dzuba, K. Beloy, V. V. Flambaum, and P. Schwerdtfeger, Nuclear-spin-dependent parity violation in diatomic molecular ions, Phys. Rev. A **86**, 050501 (2012).
[63] K. G. Dyall, Relativistic quadruple-zeta and revised triple-zeta and double-zeta basis sets for the 4p, 5p, and 6p elements, Theor. Chem. Acc. **115**, 441 (2006).
[64] K. G. Dyall, Relativistic double-zeta, triple-zeta, and quadruple-zeta basis sets for the light elements H–Ar, Theor. Chem. Acc. **135**, 128 (2016).
[65] K. G. Dyall, Relativistic and nonrelativistic finite nucleus optimized triple-zeta basis sets for the 4p, 5p and 6p elements, Theor. Chem. Acc. **108**, 335 (2002).
[66] K. G. Dyall, Relativistic double-zeta, triple-zeta, and quadruple-zeta basis sets for the actinides Ac–Lr, Theor. Chem. Acc. **117**, 491 (2007).
[67] M. Iliaš and T. Saue, An infinite-order two-component relativistic Hamiltonian by a simple one-step transformation, J. Chem. Phys. **126**, 064102 (2007).
[68] T. Saue, Relativistic Hamiltonians for chemistry: A primer, ChemPhysChem **12**, 3077 (2011).
[69] J. V. Pototschnig, A. Papadopoulos, D. I. Lyakh, M. Repisky, L. Halbert, A. Severo Pereira Gomes, H. J. A. Jensen, and L. Visscher, Implementation of relativistic coupled cluster theory for massively parallel GPU-accelerated computing architectures, J. Chem. Theory Comput. **17**, 5509 (2021).
[70] A. Lagerqvist, I. Renhorn, and N. Elander, The spectrum of SiO in the vacuum ultraviolet region, J. Mol. Spectrosc. **46**, 285 (1973).
[71] T. Kurth, E. Berkowitz, E. Rinaldi, P. Vranas, A. Nicholson, M. Strother, and A. Walker-Loud, Nuclear parity violation from lattice QCD, Proc. Sci., LATTICE2015 (**2015**) 329.
[72] Z. Davoudi, W. Detmold, P. Shanahan, K. Orginos, A. Parreno, M. J. Savage, and M. L. Wagman, Nuclear matrix elements from lattice QCD for electroweak and beyond-standard-model processes, Phys. Rep. **700**, 1 (2021).
[73] Y. Hao, P. Navrátil, E. B. Norrgard, M. Iliaš, E. Eliav, R. G. E. Timmermans, V. V. Flambaum, and A. Borschevsky, Nuclear spin-dependent parity-violating effects in light polyatomic molecules, Phys. Rev. A **102**, 052828 (2020).
[74] E. B. Norrgard, D. S. Barker, S. Eckel, J. A. Fedchak, N. N. Klimov, and J. Scherschligt, Nuclear-spin dependent parity violation in optically trapped polyatomic molecules, Commun. Phys. **2**, 77 (2019).
[75] M. Bohman, V. Grunhofer, C. Smorra, M. Wiesinger, C. Will, M. Borchert, J. Devlin, S. Erlewein, M. Fleck, S. Gavranovic *et al.*, Sympathetic cooling of a trapped proton mediated by an LC circuit, Nature (London) **596**, 514 (2021).
[76] C. Will, M. Bohman, T. Driscoll, M. Wiesinger, F. Abbass, M. J. Borchert, J. A. Devlin, S. Erlewein, M. Fleck, B. Latacz, R. Moller, A. Mooser, D. Popper, E. Wursten, K. Blaum, Y. Matsuda, C. Ospelkaus, W. Quint, J. Walz, C. Smorra, and S. Ulmer, Sympathetic cooling schemes for separately trapped ions coupled via image currents, New J. Phys. **24**, 033021 (2022).
[77] C. Will, Image-current mediated sympathetic laser cooling of a single proton in a Penning trap down to 170 mK axial temperature, arXiv:2310.10208.
[78] W. M. Itano and D. J. Wineland, Laser cooling of ions stored in harmonic and Penning traps, Phys. Rev. A **25**, 35 (1982).
[79] S. B. Torrisi, J. W. Britton, J. G. Bohnet, and J. J. Bollinger, Perpendicular laser cooling with a rotating-wall potential in a Penning trap, Phys. Rev. A **93**, 043421 (2016).
[80] A. S. P. Gomes *et al.*, Dirac19, Zenodo, 10.5281/zenodo.3572669 (2019).
[81] T. Saue *et al.*, The Dirac code for relativistic molecular calculations, J. Chem. Phys. **152**, 204104 (2020).
[82] C. R. Harris, K. J. Millman, S. J. Van Der Walt, R. Gommers, P. Virtanen, D. Cournapeau, E. Wieser, J. Taylor, S. Berg, N. J. Smith *et al.*, Array programming with NUMPY, Nature (London) **585**, 357 (2020).
[83] P. Virtanen, R. Gommers, T. E. Oliphant, M. Haberland, T. Reddy, D. Cournapeau, E. Burovski, P. Peterson, W. Weckesser, J. Bright *et al.*, SCIPY1.0: Fundamental algorithms for scientific computing in Python, Nat. Methods **17**, 261 (2020).
[84] The Pandas Development Team, pandas-dev/pandas: Pandas, 10.5281/zenodo.10107975 (2023).
[85] Wes McKinney, Data structures for statistical computing in Python, in *Proceedings of the 9th Python in Science Conference*, edited by Stéfan van der Walt and Jarrod Millman (2010), pp. 56–61, 10.25080/Majora-92bf1922-00a.
[86] D. A. Dahl, simion for the personal computer in reflection, Int. J. Mass Spectrom. **200**, 3 (2000), volume 200: The state of the field as we move into a new millenium.
[87] J. D. Hunter, MATPLOTLIB: A 2d graphics environment, Comput. Sci. Eng. **9**, 90 (2007).

5.2 Measurement Protocol

Unlike atoms, where the main energy scale is the electronic one, in the eV range, molecules have a much more complex spectrum due to their additional vibrational and rotational degrees of freedom (see Chapter 2 for details about molecular structure) [31, 57, 58]. The spacing between two rotational energy levels of opposite parity, $\Delta E_{\pm}$, can be more than five orders of magnitude smaller than the spacing between opposite parity levels in atoms, which can lead to large enhancements of symmetry-violating phenomena [17, 31]. This is because many of the effects we are interested in, including the parity violating ones described in this section, are so much smaller than the other terms in the molecular Hamiltonian (Eq. 2.77) that they can be treated as small perturbations, in which case their effect scales as $\propto 1/\Delta E_{\pm}$ [14, 17]. Moreover, two opposite parity rotational levels can be brought even closer together using an external magnetic field of the right amplitude (usually on the order of a few Tesla [43]), leading to a PV-induced mixing between them that can be more than 11 orders of magnitude higher than in atoms [26, 43, 55]. A second advantage offered by diatomic molecules relative to atoms in the search for nuclear spin-dependent (NSD) PV is the fact that in molecules, the effect of the (nuclear spin independent) weak charge is significantly suppressed, being identically zero to first-order in perturbation theory [217]. Thus, any non-zero PV signal in a diatomic molecule will be dominated by the NSD effects, allowing a much cleaner investigation of such effects relative to the atomic case.

The NSD PV effects due to the interaction between electrons and the nucleus are characterized by the Hamiltonian (see Chapter 3 for a detailed derivation) [14, 17]:

$$H_{NSD}^{PV} = \frac{G_F}{\sqrt{2}} \eta \left(\boldsymbol{\alpha} \cdot \boldsymbol{I}\right) \rho(r), \tag{5.1}$$

where η is the fundamental physics parameter we are interested in measuring experimentally (e.g., containing contributions from the nuclear anapole moment [14, 17]). In molecules with a $^2\Sigma_{1/2}$ or $^2\Pi_{1/2}$ electronic state, this Hamiltonian can be rewritten, after averaging over the electronic wavefunction, as an effective Hamiltonian acting only on the spin-rotational/hyperfine levels of the molecule as [43, 155, 217]:

$$H_{NSD}^{PV,\text{eff}} = \eta W_{PV} \left(\hat{\mathbf{n}} \times \mathbf{S}_{\text{eff}}\right) \cdot \frac{\mathbf{I}}{I}, \tag{5.2}$$

where $\hat{\mathbf{n}}$ is the unit vector along the internuclear axis, pointing from the heavier to the lighter nucleus, and $\mathbf{S}_{\text{eff}}$ is the effective electron spin, which is simply $\boldsymbol{S}$ for a $^2\Sigma$ electronic state. $\boldsymbol{I}$ is the nuclear spin and W_{PV} is an electronic form factor defined as:

$$W_{PV} = \frac{G_F}{\sqrt{2}} \left\langle \Omega = \frac{1}{2} | \rho(\mathbf{r}) \alpha_+ | \Omega = -\frac{1}{2} \right\rangle, \tag{5.3}$$

where Ω is the projection of the electron angular momentum along the internuclear axis in the electronic state under consideration, and $\alpha_+ = \alpha_x + i\alpha_y$, with α_x and α_y being the x and y components of the $\boldsymbol{\alpha}$ Dirac matrix vector. For most molecules of practical interest, W_{PV} can be calculated with percent level accuracy using *ab initio* quantum chemistry calculations (see Article 5) [12, 55].

In the presence of the PV interaction and an appropriate magnetic field to bring the two levels of opposite parity, $|\psi^+\rangle$ and $|\psi^-\rangle$, close to degeneracy, the system of interest can be well described by a 2×2 Hamiltonian given by:

$$H_{PV} = \begin{pmatrix} 0 & iW \\ -iW & \Delta \end{pmatrix}, \tag{5.4}$$

where Δ is the splitting between the two levels, which depends on the magnetic field, and

$$iW \equiv \eta W_{PV} \langle \psi^- | \left(\hat{\mathbf{n}} \times \mathbf{S}_{\text{eff}} \right) \cdot \frac{\mathbf{I}}{I} | \psi^+ \rangle . \tag{5.5}$$

One way in which the PV parameter of interest, W, can be measured is by populating only one of the parity eigenstates considered above, letting the system evolve freely and then measuring the population transferred to the other state of opposite parity, which was initially depleted. In this case, the signal would be proportional to $\frac{W^2}{\Delta^2}$, which, for most systems of interest is prohibitively small, mainly because Δ can't be made arbitrarily small due to various systematic uncertainties present in the system (see Article 5 and Sec. 5.3 for details) [55]. One trick that can be used to further amplify this signal, based on Ref. [43], is to apply an external, blue-detuned, oscillatory electric field able to couple the two states of opposite parity. This is the so-called AC Stark interference technique. In this case, the Hamiltonian becomes:

$$H_{PV} = \begin{pmatrix} 0 & iW + dE \sin(\omega t) \\ -iW + dE \sin(\omega t) & \Delta, \end{pmatrix} \tag{5.6}$$

where E and ω are the magnitude and angular frequency of the applied field, while d is the effective dipole moment between the two levels of opposite parity. Given that in most cases $W < dE$, the extra off-diagonal term can further enhance the population transfer between the two levels of opposite parity, from which W can be extracted experimentally [26, 27, 55]. Assuming that population transfer is at the level of a few percent or lower over the duration of the measurement, the expected signal can then be calculated using time-dependent perturbation theory. This is the case for $^{29}SiO^+$, as described below. Assuming we start in the positive parity state, the probability of transferring the population to the opposite parity level is given by:

$$S(E) = |c_-(t)|^2 = \left| \frac{2W}{\Delta} e^{-i\frac{\Delta t}{2}} \sin\left(\frac{\Delta t}{2}\right) + i\frac{dE}{\omega} \left(\cos(\omega t) e^{-i\Delta t} - 1 \right) \right|^2 . \tag{5.7}$$

From this, it can be seen that we end up with an interference term, which is proportional to the product between W and dE, thus leading to an amplification of the effect due to W. By performing the same measurement using opposite directions for the electric field, i.e., $S(E)$ and $S(-E)$, we can build the asymmetry signal defined as:

$$A = \frac{S(E) - E(-E)}{S(E) + E(-E)} = \frac{2\frac{W}{\Delta}\frac{dE}{\omega}(1 + \cos(\omega t))(1 - \cos(\Delta t))}{2\left(\frac{W}{\Delta}\right)^2 (1 - \cos(\Delta t)) + \left(\frac{dE}{\omega}\right)^2 \left[1 + \cos^2(\omega t) - 2\cos(\omega t)\cos(\Delta t)\right]}, \tag{5.8}$$

which allows us to clearly isolate the effect due to W, as well as have better control over various systematic effects (see Article 5 and Refs. [26, 27] for details). If the measurement time t is chosen such that $t = \frac{2\pi N}{\omega} = \frac{\pi}{\Delta}$, the asymmetry signal takes the simple form [55]:

$$A = \frac{2\frac{W}{\Delta}\frac{dE}{\omega}}{\left(\frac{W}{\Delta}\right)^2 + \left(\frac{dE}{\omega}\right)^2}. \tag{5.9}$$

A first proof of the principle of using diatomic molecules for NSD PV effects, together with the method described above, has been performed in DeMille's group [26, 27] using a beam of neutral ^{138}Ba^{19}F molecules. In ^{138}Ba^{19}F, the ^{138}Ba nucleus has no nuclear spin, while the NSD PV effects from the ^{19}F nucleus ($I = 1/2$) were expected to be too small to be observed experimentally. However, the experiment was able to show a good control over various sources of systematic uncertainties. The results proved that a future measurement in ^{137}Ba^{19}F, where the effect due to the ^{137}Ba nucleus is non-zero and much larger than the one from the ^{19}F nucleus, should allow for a non-zero measured value of NSD PV effects.

Our experiment closely follows the concepts behind the method described above and applied to ^{138}Ba^{19}F. However, instead of using neutral molecules, we aim to use molecular ions inside a Penning trap. Performing measurements on single trapped molecular ions allows us to remove various systematic uncertainties present in the case of neutral molecular beams while facilitating much longer measurement times. For example, in Refs. [26, 27] the interaction time was ~ 100 μs, while in our setup, we expect to achieve more than tens or even hundreds of ms. Thus, a Penning trap seems like the ideal apparatus for such a measurement, as its magnetic and electric fields used for trapping ions (see Sec. 5.4.3) also naturally enhance the PV signal we aim to measure [55].

5.3 Theoretical Calculations and Uncertainty Estimation

To estimate the magnitude of the required magnetic and electric fields, as well as the PV effect and various systematic uncertainties, it is necessary to calculate the energies of different spin-rotational and hyperfine levels of the molecule of interest within the large magnetic field. Below, I will describe the calculations performed for our molecule of interest, ^{29}SiO$^+$, but the same formalism can be extended to other molecules in a $^2\Sigma$ electronic state and in a similar manner to $^2\Pi_{1/2}$ electronic levels.

The molecular Hamiltonian, in the presence of an external magnetic field, is given by [31, 43, 55]:

$$\begin{aligned} H &= H_{\text{eff}} + H_{\text{mag}} \\ H_{\text{eff}} &= B\boldsymbol{N}^2 + \gamma \boldsymbol{N}\cdot\boldsymbol{S} + b\boldsymbol{I}\cdot\boldsymbol{S} + c\,(\boldsymbol{I}\cdot\boldsymbol{n})\,(\boldsymbol{S}\cdot\boldsymbol{n}) \\ H_{\text{mag}} &= -g_\perp \mu_B \boldsymbol{S}\cdot\boldsymbol{B} - \left(g_\parallel - g_\perp\right)\mu_B\,(\boldsymbol{S}\cdot\boldsymbol{n})\,(\boldsymbol{B}\cdot\boldsymbol{n}) - g_I\mu_N \boldsymbol{I}\cdot\boldsymbol{B} - g_{rot}\mu_N \boldsymbol{N}\cdot\boldsymbol{B}, \end{aligned} \tag{5.10}$$

where $\boldsymbol{S}$ and $\boldsymbol{I}$ are the electron and nuclear spin operator, with $\boldsymbol{N} = \boldsymbol{R} + \boldsymbol{L}$. $\boldsymbol{L}$ is the orbital angular momentum of the electron, and $\boldsymbol{R}$ is the mechanical rotation of the molecular framework. $\boldsymbol{n}$ is the unit vector along the internuclear axis, and $\boldsymbol{B}$ is the externally applied magnetic field. B_0, D_0, and γ are the rotational, centrifugal distortion, and spin-rotational

constants, respectively. b and c are hyperfine structure constants associated with the ^{29}Si nucleus. $g_\perp$, $g_\parallel$, g_I, and g_{rot} are various g factors associated with the electron, nucleus, and the rotation of the molecule as a whole. μ_B and μ_N are the Bohr and nuclear magneton, respectively. The various spectroscopic parameters were taken from Refs. [218, 219]. Given that for $^{29}SiO^+$ the rotational parameter, B_0, is far larger than all the other parameters, N is a good quantum number for rotational levels of energy $E_N \approx B_0 N(N+1)$, and parity $P_N = (-1)^N$ [55].

The large magnetic field needed to bring the lowest two rotational levels of opposite parity close to degeneracy ($B \approx 1.5$ T for $^{29}SiO^+$) is able to decouple the electron spin, $\boldsymbol{S}$, from $\boldsymbol{I}$ and $\boldsymbol{N}$. Therefore, a convenient basis to describe the spin-rotational and hyperfine molecular levels is given by: $|N, m_N\rangle |S, m_S\rangle |I, m_I\rangle$, with m_N, m_S, and m_I being the projections of $\boldsymbol{N}$, $\boldsymbol{S}$, and $\boldsymbol{I}$ along the lab frame z-axis. Using this basis and the Hamiltonian operator in Eq. 5.10, we built the associated Hamiltonian matrix, for $N = 0, 1$ and 2, and diagonalized it to obtain the evolution of the energy levels as a function of the externally applied magnetic field, assumed to point along the lab frame z-axis. The obtained results for the levels of interest are shown in Fig. 1 of Article 5 [55], showing several energy level crossings around 1.5 T. Note that the PV Hamiltonian, Eq. 5.2, can only mix state with the same total angular magnetic moment projection along the lab frame z-axis, $m_F = m_N + m_S + m_I$.

Once two levels of opposite parity are chosen for the measurement and assuming they are much closer to each other than to any other energy levels inside the molecule, which is the case for our system, for the right magnetic field, we can apply the two-level system formalism described in the previous section to characterize our expected PV signal. Ways in which we can ensure that we have only a single $^{29}SiO^+$ ion trapped at a time and that the right initial energy level is populated are described in Sec. 5.4. In this section, we directly assume we start from the positive parity state with a single ion in the trap.

In a Penning trap, while we have a uniform magnetic field present, the electric field is not time-varying, as needed for our measurement, but it is harmonic in the axial direction, taken as the z-direction and also corresponding to the direction of the magnetic field: $\boldsymbol{E} = E_0 \boldsymbol{z}$ (see Sec. 5.4.3 for details). However, if the ion starts moving in the $\mathbf{z}$ direction, it will experience an oscillatory motion under this electric field. Thus, the stationary lab frame electric field will appear, in the frame of the ion, as an oscillatory electric field, with a frequency given by the axial frequency of the trap, $\omega_z/(2\pi) \approx 350$ kHz, for our trap (see Sec. 5.4.3). Thus, for our measurement protocol, in the ideal case, the starting point of the experiment is with the ion at the very center of the Penning trap, thus experiencing no electric field and being stationary. Then, by giving it an axial kick, we can have the ion experience a time-varying electric field for a while, after which we can measure our sought-for signal, i.e., the population transfer to the negative parity level, as described in Sec. 5.2.

However, in practice, due to the finite temperature of the system (taken to be 1 K in our case), the ion will have a random initial non-zero velocity and displacement both in the axial and radial directions. The contributions from the thermal noise in the axial direction will lead to a random phase ϕ_z, relative to the field experienced if the ion starts stationary from the trap's center. The radial part will lead to a radial electric field felt by the ion in its rest frame. This radial field has two main contributions: the radial part of the quadrupole electric potential at the trap center and a motional electric field due to the $\boldsymbol{v} \times \boldsymbol{B}$ term. For a fixed radius, the induced electric field due to the latter effect dominates, and thus, we will

only consider it moving forward. In the end, the electric field experienced by the ion can be approximately written as:

$$\boldsymbol{E}(t) = E_z \hat{\boldsymbol{z}} \cos\left(\omega_z t + \phi_z\right) + E_\perp \left(\hat{\boldsymbol{x}} \cos\left(\omega_\perp t\right) + \hat{\boldsymbol{y}} \sin\left(\omega_\perp t\right)\right), \tag{5.11}$$

where E_z and $E_\perp$ are the magnitude of the axial and radial field and $\omega_\perp/(2\pi) \approx 500$ kHz corresponds to the cyclotron frequency of our trap. The electric dipole interaction term is then:

$$\boldsymbol{d} \cdot \boldsymbol{E} = dE_z n_z \cos\left(\omega_z t + \phi_z\right) + \frac{dE_\perp}{2}\left(n_+ e^{-i\omega_\perp t} + n_- e^{i\omega_\perp t}\right), \tag{5.12}$$

where n_+ and n_- are the raising and lowering operators associated with the internuclear axis vector $\hat{\boldsymbol{n}}$. $\boldsymbol{d}$ is the rest frame dipole moment operator associated with the ground electronic level of $^{29}SiO^+$. Its magnitude was calculated to be $d = 4.147$ D in Ref. [220], which is the value we will use for our calculations. To calculate the expected signal, as well as various systematics, we need to compute the expectation value of this operator for different values of N and m_N, i.e., $\langle N, m_N|d|N', m_N'\rangle$. Given that the various angular momenta of the molecules are quantized along the laboratory z-axis, given by the direction of the magnetic field, it is useful to express the vector $\hat{\boldsymbol{n}}$ in the lab frame. This is given by [31]:

$$\hat{\boldsymbol{n}} = \sin\theta\cos\phi\hat{\boldsymbol{x}} + \sin\theta\sin\phi\hat{\boldsymbol{y}} + \cos\theta\hat{\boldsymbol{z}}, \tag{5.13}$$

which in spherical harmonics can be rewritten using:

$$\begin{aligned} n_z &= \cos\theta = 2\sqrt{\frac{\pi}{3}} Y_1^0\left(\theta,\phi\right) \\ n_+ &= n_x + i n_y = \sin\theta e^{i\phi} = -2\sqrt{\frac{2\pi}{3}} Y_1^1\left(\theta,\phi\right) \\ n_- &= n_x - i n_y = \sin\theta e^{-i\phi} = 2\sqrt{\frac{2\pi}{3}} Y_1^{-1}\left(\theta,\phi\right). \end{aligned} \tag{5.14}$$

Using the fact that:

$$\begin{aligned} |N, m_N\rangle &= Y_N^{m_N}\left(\theta,\phi\right) \\ \langle N, m_N| &= \overline{Y_N^{m_N}}\left(\theta,\phi\right) = (-1)^{m_N} Y_N^{-m_N}\left(\theta,\phi\right), \end{aligned} \tag{5.15}$$

the various electric dipole moment matrix elements needed will require the calculations of integrals of the form [221]:

$$\int_0^{2\pi}\int_0^{\pi} Y_{l_1}^{m_1} Y_{l_2}^{m_2} Y_{l_3}^{m_3} \sin\theta d\theta d\phi = \sqrt{\frac{(2l_1+1)(2l_2+1)(2l_3+1)}{4\pi}} \begin{pmatrix} l_1 & l_2 & l_3 \\ 0 & 0 & 0 \end{pmatrix} \begin{pmatrix} l_1 & l_2 & l_3 \\ m_1 & m_2 & m_3 \end{pmatrix}. \tag{5.16}$$

For this thesis, all such integrals have been calculated using the commercial software Mathematica. Calculating electric dipole moment matrix elements for our experiment is needed

for two main reasons. First, it allows us to compute the effective dipole moment between the two levels brought close to degeneracy. Second, it facilitates the calculation of AC Stark shifts of these two levels due to the presence of the other levels in the molecule. We will describe both below.

Two pairs of levels of opposite parity of interest for us, which the PV Hamiltonian can mix (Eq. 5.4) and can be brought close to degeneracy at a magnetic field of ~ 1.5 T are (see Fig. 1 of Article 5): $|m_S, m_I, m_N\rangle = |+1/2, -1/2, 0\rangle$ and $|-1/2, -1/2, +1\rangle$ as well as $|1/2, 1/2, 0\rangle$ and $|-1/2, 1/2, +1\rangle$. The first level in each pair corresponds to the $N = 0$ rotational state. Given that, for each pair, the two levels have different projections of the electron spin, m_S, and the dipole moment operator doesn't act on the nuclear spin, to first order in perturbation theory, the dipole moment matrix element between these two levels is exactly zero. However, the hyperfine and spin-rotational interactions present in the Hamiltonian lead to the mixture of these two levels with other molecular levels with opposite values of m_S, thus allowing a non-zero value of the electric dipole matrix element, on the order of $d_{\text{eff}} \sim \frac{(\gamma,b,c)}{B_e} d$. This scaling can be deduced by looking at the first pair of opposite parity levels considered above. We would like to change the electron spin projection of the $|-1/2, -1/2, +1\rangle$ state from $-1/2$ to $1/2$, without changing the nuclear spin projection, which is the same for both levels, as desired. This can be achieved through the $\gamma\mathbf{NS}$ operator which mixes the $|-1/2, -1/2, +1\rangle$ state with the $|1/2, -1/2, 0, N = 1\rangle$ one, giving an effect proportional to γ. However, as these two levels have opposite m_S values, they are split by $\approx 2B_e$. Thus, in the end, the contribution of the $|1/2, -1/2, 0, N = 1\rangle$ state, which will lead to a non-zero electric dipole moment coupling to the original $|1/2, -1/2, 0, N = 0\rangle$ state, is on the order of γ/B_e as initially claimed. The actual mixing can be calculated given the previously computed molecular Hamiltonian, giving an effective electric dipole moment of ~ 300 Hz/(V/cm) and ~ 500 Hz/(V/cm) for the two pairs of opposite parity levels considered above.

To gauge the needed external field for our measurement, E_z, we need to calculate the PV matrix element, W, as it is desirable to have $\frac{d_{\text{eff}} E_z}{\omega_z/(2\pi)} > \frac{W}{\Delta}$ in order to enhance the PV signal. To calculate W, we need three pieces of information, as shown in Eq. 5.2: $W_{PV} = 16$ Hz, calculated in Article 5 [55], $\eta \approx -0.06$, obtained using a nuclear shell model calculation (see Chapter 3) and the matrix element associated with the operator $(\hat{\boldsymbol{n}} \times \boldsymbol{S}) \cdot \frac{\boldsymbol{I}}{I}$. For the first pair of opposite parity levels considered above, the matrix element of this latter operator is equal to $0.39i$, giving a value of $W = -0.37$ Hz, while for the second pair, it is equal to $-0.41i$, leading to $W = 0.39$ Hz.

Given these values, we decided to choose an amplitude for the axial electric field of 6 V/cm, which corresponds to kicking the ion to an amplitude of ~ 0.3 mm in the axial direction. This value was chosen as a compromise between having $\frac{d_{\text{eff}} E_z}{\omega_z/(2\pi)} > \frac{W}{\Delta}$ and preventing the ion from moving too far from the trap center, where the uniformity of the magnetic and electric field is reduced (see Sec. 5.4.3 for details).

Using the same formalism as above, we can also calculate the AC Stark shifts of the two levels of interest due to the other molecular energy levels present. In this case, both the axial and radial fields contribute, depending on the m_N values of the nearby spin-rotational/hyperfine levels. In principle, if the external fields were well known, one could adjust for such AC Stark shifts by changing the value of the magnetic field. However, due to the non-zero temperature, the magnitude of E_z and $E_\perp$ are not perfectly known, thus

leading to an uncertainty in the energy splitting between the two levels. The effect due to E_z depends on the unknown random initial phase, ϕ_z, while the effect due to $E_\perp$ depends on the radius at which the ion is located when the measurement is performed. Both of these are because the ion will have a random energy associated with it being in thermal equilibrium with the trap at 1 K (see Sec. 5.4.3 for more details). For the AC Stark shift calculation, for the $N = 0$ level, we considered nearby levels in the $N = 1$ manifold, while for the $N = 1$ level, we considered levels in the $N = 0$ and $N = 2$ manifolds. Using calculated matrix elements between levels coupled by the present electric fields, using Eq. 5.11-5.16, as well as the spacing between these levels at the optimal magnetic field, computed as described above, the AC Stark shift was calculated using [222]:

$$\Delta E = \frac{(d_{\text{eff}} E)^2}{2} \frac{\omega_0}{\omega_0^2 - \omega_E^2}, \tag{5.17}$$

where d_{eff} is the dipole moment between any two considered levels, ω_0 is the energy difference between them, while E and ω_E are the magnitude and frequency of the external electric field (axial and radial in our case). For the two pairs of opposite parity levels considered above, the uncertainty in the AC Stark shift, due to the uncertainty in the axial electric field amplitude ($\delta E_z = 0.2$ V/cm) amounts to $\delta\Delta_{AC}^{axial}/2\pi \approx 20$ Hz, while the one due to the radial field is $\delta\Delta_{AC}^{radial}/2\pi \approx 10$ Hz. The latter one was obtained by assuming that the uncertainty in the ion's circular velocity is equal to the standard deviation of a Maxwell-Boltzman distribution with a temperature of 1 K. This shows that in practice, we can't bring the two levels closer than ~ 30 Hz, and ideally, we would like the stay a factor of a few greater than this. For our estimates below, we assume the splitting between the two levels of interest to be $\Delta/2\pi = 100$ Hz.

Besides the uncertainty in Δ through the AC Stark shift, the uncertainty on E_z also leads directly to an uncertainty in the Rabi frequency experienced by the ion, i.e. $\Omega_R = d_{\text{eff}} E_z$. At a temperature of 1 K, this uncertainty amounts to $\delta E_z \approx 0.2$ V/cm. Both of these directly lead to an uncertainty in extracting W from the measured asymmetry, A, and need to be accounted for when computing the signal expected from our measurement. It should be pointed out that these effects are random in nature, as their magnitude and sign change from one instance of the experiment to the next. Thus, their effect can be reduced by averaging over repeated measurements.

The main source of systematic uncertainty in our experiment is represented by variations in the magnitude of the magnetic field. As detailed in Article 5 [55], we expect a relative variation of the magnetic field of $\delta B/B \approx 10^{-10}$ during our measurement, which should have a contribution to the uncertainty on Δ of $\delta\Delta/2\pi = 4$ Hz, which leads, for the assumed $\Delta/2\pi = 100$ Hz, to a relative uncertainty on W (see Eq. 5.9) of $\delta W/W \approx 4\%$. Other sources of systematic uncertainties, such as variations in the voltages applied to the trap electrodes or the shimming coils for the magnet, are expected to be well below 1% [55].

Next, we estimate the number of molecules needed to achieve a 10% relative statistical uncertainty on the measured W value. For this we use the previously calculated values of W and d_{eff}, we take $E_z = 6$ V/cm, $\delta E_z = 0.2$ V/cm, $\Delta/2\pi = 100$ Hz, $\delta\Delta/2\pi = 30$ Hz and $\omega_z/2\pi = 350$ kHz. To estimate the uncertainty on W for a given number of measurements, N, we generated, for each measurement, a value of $\Delta/2\pi$ and one for $\Omega_R/2\pi$ from a Gaussian with mean and standard deviation given by the associated central value and uncertainty

mentioned above and a total measurement time of $t = 5$ ms. Then, the transition probability from one parity eigenstate to the other can be calculated using Eq. 5.7, and for each event, we associated a value of 1 (successful transition) or 0, based on a binomial distribution with probability given by the calculated transition probability. These numbers were then summed up over all N events, giving the measured signal for a given electric field orientation. The same was done for the opposite orientation of the electric field, and then the asymmetry was calculated using Eq. 5.8. We repeated this 1000 times, obtaining a distribution of the values of the asymmetry, from which the mean and standard deviation were extracted. Then, we sampled the asymmetry from this distribution 1000 times and calculated W, inverting Eq. 5.9. In the end, we obtained that $N \approx 3 \times 10^5$ events are needed to measure W with 10% relative uncertainty for each of the two orientations of the electric field. In our case, this corresponds to initial kicks of the ion in opposite directions. Note that the statistical uncertainty is largely independent of the used crossing, as it can be observed from the analytical expression for the statistical uncertainty:

$$\delta W = \frac{\Delta}{4\sqrt{2N_0}\sin\left(\frac{\Delta t}{2}\right)}\frac{\sqrt{\eta^2+1}}{\eta}, \tag{5.18}$$

where $\eta \equiv \frac{\Omega_R/\omega_z}{W/\Delta}$. This formula can be derived from the propagation of error on the number of counts, which is assumed to be Poissonian. While we assumed that Δ is kept constant, we can also perform measurements for different values of Δ (see Fig. 3 of Article 5), which can be favorable for further reducing the systematic uncertainties [26, 27]. A similar number of events as above is also needed in this case to reach 10% relative statistical uncertainty. Assuming ~ 1 second per measurement (e.g., the time needed to send a new ion to the trap, prepare it in the right quantum state, and cool its motional degrees of freedom), a 10% relative uncertainty measurement can be performed in about one week of integration time.

While in the calculation above, we used the theoretically calculated value of the dipole moment of $^{29}SiO^+$ [220], our setup allows us to measure it directly, in a straightforward manner. The ability to easily control the magnitude of the magnetic field (see Sec. 5.4) means that we can set the frequency difference between two levels of opposite parity to the same value as one of the Penning trap frequencies. If we look in the axial direction, this means that by putting the ion in motion along the z-axis, the oscillatory field felt in its rest frame will, in the ideal case, drive resonant Rabi oscillations between the two levels considered. By measuring the population transfer for different times, the Rabi frequency and, hence, the dipole moment can be extracted. This measurement can be easily extended to other molecular ions of interest without significant changes to the experimental setup. We estimate that with only 1000 measurements, assuming $\delta\Delta = 50$ Hz and $\delta E_z = 0.2$ V/cm, the dipole moment can be measured with a statistical uncertainty at the 1% level.

Before moving to the next section, it is worth mentioning that the $^{29}SiO^+$ molecular ion was chosen for our first experimental attempt because its ground and excited electronic energy levels have been investigated spectroscopically already, and their rotational and hyperfine parameters extracted [218, 219, 223, 224]. At the same time, effective rotational cooling was shown experimentally in $^{28}SiO^+$ [224]. However, other molecular ions, especially those containing a heavy nucleus, are expected to contain a much larger PV effect [14]. For example, based on TABLE I in Article 5, TlF^+ is a promising candidate, with an expected

value of $W \approx 300$ Hz, about three orders of magnitude higher than in the $^{29}SiO^+$ case. This value of W was calculated assuming a single particle model for the nuclear anapole moment. In this case, given the large magnitude of the PV effect, one can hope to directly measure the population transfer between two levels of opposite parity without the need for an external electric field, i.e., place the ion at the center of the trap, and wait for the PV interaction to transfer population on its own. While this will require further detailed experimental investigation to identify all sources of systematic uncertainties, it is worth noting that one of the main systematic uncertainties encountered in Ref. [26, 27] was given by stray electric field, able to mimic the sought for signal. In Ref. [26, 27], this effect was significantly reduced by building the asymmetry signal described above using an external sinusoidal electric field. However, in our case, the molecular ion will feel, on average, no external electric field in its rest frame, which could potentially allow a measurement without building the asymmetry signal. In this case, i.e., no external field applied, the population transfer can be calculated analytically, and it is given by:

$$S(t) = \frac{4W^2}{\Delta + 4W^2} \sin^2\left(\sqrt{\Delta^2 + 4W^2}t\right). \tag{5.19}$$

By performing a numerical calculation similar to the $^{29}SiO^+$ case described above, assuming $\Delta/(2\pi) = 100$ Hz and $\delta\Delta/(2\pi) = 30$ Hz, we obtain that with $\sim 10^4$ measurements we can reach 1% relative statistical uncertainty on W. This can be achieved in a few hours of total measurement time. While further detailed experimental investigation is needed for implementing such a measurement, these calculations show the great promise of our technique for measuring hadronic PV effects over a wide range of nuclei and even in relatively short periods.

5.4 Experimental Setup

This section describes the experimental setup currently being built in our lab on the MIT campus. I will provide details about the preparation of the initial and the readout of the final quantum states of the molecular ion inside the Penning trap and describe the simulations performed to choose the final design and dimensions for the Penning trap electrodes.

5.4.1 Beamline

A simplified diagram of the beamline to be used for this experiment is shown in Fig. 5.1. The source will produce neutral SiO molecules. More details about the source can be found in Sec. 5.4.2, but, briefly, it is based on ablating a Si rod with a high power Nd:YAG laser, followed by the release of a gas mixture of N_2O (5%) and Ar (95%) using a solenoid pulsed valve (Parker valve model number 009-0381-900). The reaction between the Si and N_2O will produce the molecules of interest, while Ar is used to cool them down through a supersonic expansion. A custom-made piece based on the design of Prof. Tim Steimle (Arizona State University) is used to mix the resulting Si ablation plume with the gas mixture (see Sec. 5.4.2 and Fig. 5.4). Based on previous studies [225], we expect a rotation temperature of the resulting SiO molecule of ~ 20 K. The molecules then pass

through a skimmer with an aperture of 2 mm, to reduce the gas load in rest of the setup and better collimate the molecular beam. A voltage can also be applied to the skimmer to remove any ions produced directly through ablation from the neutral molecules if needed.

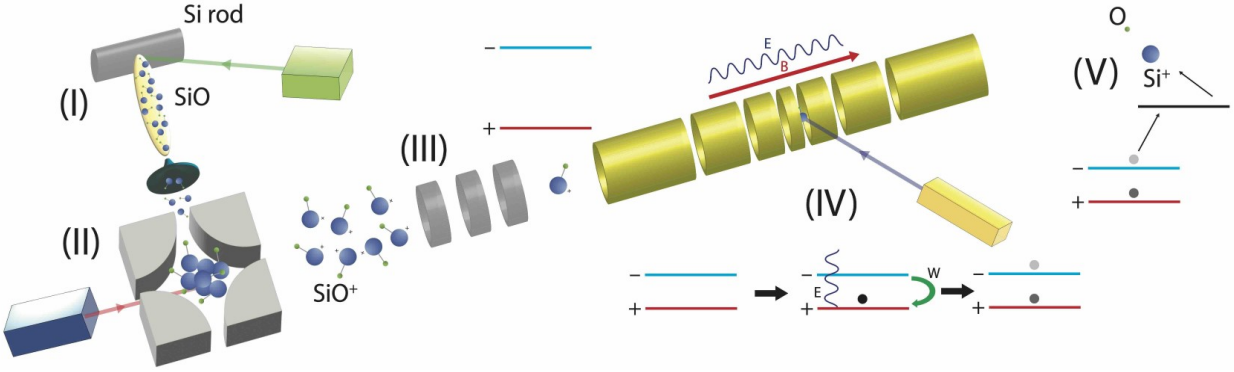

Figure 5.1: Simplified diagram of the beamline to be used for parity violation measurements. In the ablation source, we produce neutral SiO molecules (I). After passing through a skimmer, they are ionized at the center of a quadrupole bender, and the resulting SiO^+ molecular ions are sent toward the interaction region (II) at the center of the Penning trap. The ions are further guided towards the interaction region using electrostatic optics (III). At this step, the molecules are outside the magnetic field. Thus, the splitting between the opposite parity levels is ~ 21 GHz for SiO^+. The molecules then reach the center of the Penning trap, where they are optically prepared in the spin-rotational and hyperfine level of interest. We also ensure that only one molecule is present in the trap before the measurement protocol begins (IV). After the molecules experience the magnetic field (thus, the spacing between the two levels of opposite parity is on the order of 100 Hz) and the time-varying electric field for a fixed amount of time, they are state-selectively excited to an autodissociative state and the masses of the resulting products are detected by reading the induced current on one of the trap's electrodes (V).

Next, the SiO molecules are ionized inside a quadrupole bender, using a 1+1 REMPI scheme, at a wavelength of $210 - 220$ nm, as described in Ref. [223]. In our case, this will be achieved using the doubled light from a Sirah Cobra-Stretch Dye Laser Model CBST-D-30, pumped with a Continuum Surelite SLIII-10, perpendicular to the direction of motion of the molecules, though a VC234 Thorlabs viewport. This will populate the lowest ~ 15 rotational levels of the molecule [223, 224]. In the future, we aim to explore using 2-step resonant ionization schemes with two different lasers with tunable frequencies, with the goal of reducing the range of rotational levels populated in the resulting $^{29}SiO^+$ ion, ideally populating only the ground rotational state. This could be achieved using a custom-made injection-seeded Ti:Sa laser for the first step and a grating Ti:Sa laser for the second step, both of which are currently in our lab. These lasers are similar to the ones used for the RaF experiment (see Chapter 4), while the latter was used for the first resonant step in the results presented in Chapter 6.

The quadrupole bender [226] in which the molecules are ionized is located in a CF-160 6-way cross, and is used to bend the resulting SiO^+ ions by 90 degrees towards the Penning trap. Pictures of the quadrupole can be seen in Fig. 5.2 a) and b), while its installation in

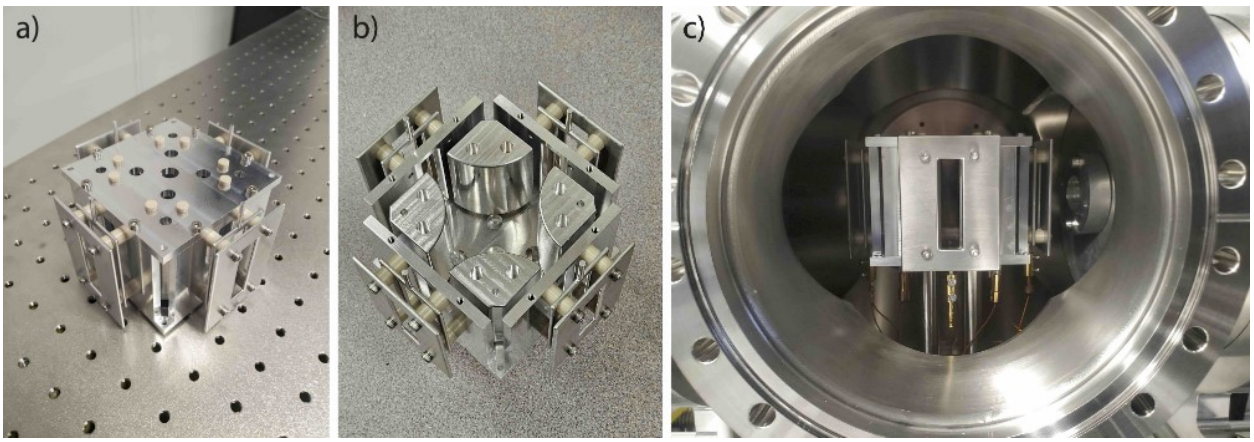

Figure 5.2: a) Assembled quadrupole bender. On each of the four faces, one of the aluminum plates has a pin to which a voltage can be applied. b) Assembled quadrupole bender with the top part removed. The four quarter cylinders used for bending can be observed. c) Quadrupole bender installed in the CF-160 6-way cross, with all the in vaccum electrical connections. The ions will come from the right, where we also see located the holder for the skimmer. In the current setup, a nipple was placed between the source chamber and the quadrupole bender; thus, the skimmer holder is further away from the bender and right before the nipple.

the vacuum chamber is shown in Fig 5.2 c). As shown in Fig. 5.2 b), the bender contains four quarter cylinders used for bending, each of them with an independent voltage connection. On each face of the quadrupole bender, there are also three plates in an Einzel lens setup, i.e., two of them are grounded while the middle one has its own voltage connection (Fig. 5.2 a)). These can be used to fine-tune the shape and focus of the ion beam if needed. After that, along the beamline, we have a manual valve to separate the interaction region from the source (not shown in Fig. 5.1) and two CF-160 6-way crosses that will host ion optics to better guide the ions toward the trap. As we only need one ion in the trap, SIMION electrostatic simulations showed minimal constraints on the parameters needed for such ion optics. Further simulations and ion optics design are currently in progress.

The ions then enter the magnet/trap region. We use a liquid-cryogen-free, superconducting magnet produced by SuperConducting Systems (the superconducting coils are cooled conductively using a Cryomech PT415 pulsed-tube cryocooler). The magnet can reach any value of the magnetic field between 0.05 T and 3 T. A passive ferro-shimmed tube placed inside the magnet bore is used to achieve higher magnetic field homogeneity at the center of the magnet for a prespecified magnetic field strength (around 1.5 T in our case). This tube is made of small iron plates placed in such a way as to cancel higher-order harmonics in the field generated by the main superconducting coil. This should achieve a field homogeneity of < 2 ppm in a 50 mm sphere at the magnet center. If needed (e.g., for using a different molecular ion and hence a different magnetic field strength for the energy levels crossing), a new ferro shim tube suitable for the new value of the magnetic field can be made upon request from SuperConducting Systems. For our experiment, to test different energy level crossings (see Fig. 1 in Article 5), we would need to change the magnetic field over a range

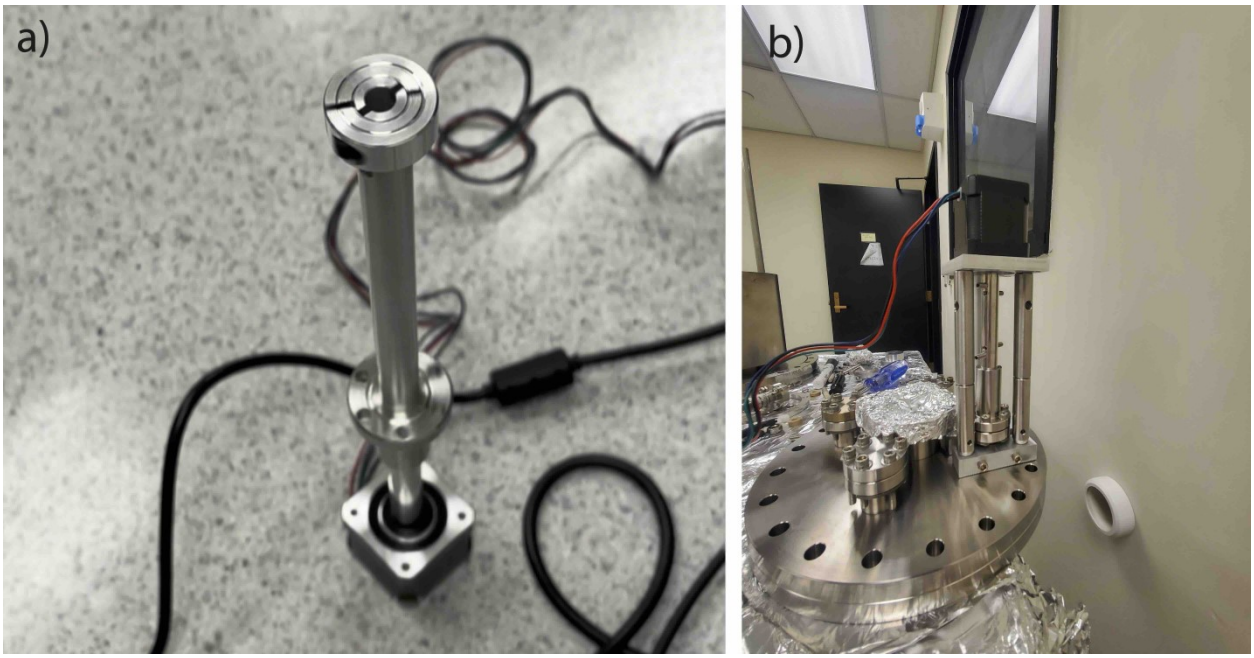

Figure 5.3: a) Full holder setup for the Si rod. At the bottom, we have the motor, which is connected with an aluminum rod to a CF-35 rotating feedthrough. The feedthrough is then directly connected to an aluminum rod with a cylindrical hole, with a slit through the middle at the other end and with a diameter approximately equal (but slightly bigger) to the diameter of the Si rod. At that end we also have a ring clamp used to fix the rod in place once inserted in the cylindrical hole. b) View of the Si rod holder from outside the flange, together with the custom-made holder for the motor itself.

of $\sim \pm 200$ G. The magnetic field can be easily changed, with a resolution of ~ 2 G, using a user-interface, which, according to the manufacturing company, would change the previously mentioned uniformity from 2 to 5 ppm, for the same ferro-shimmed tube. To reduce this and achieve a better control over the mangetic field (ideally at the 1 mG level) around a certain energy levels crossing, an additional resistive shim coil tube was added inside the ferro-shimmed tube. This new tube contains a "B_0 coil", able to change the magnitude at the center by ± 5 G, as well as a "B_2 coil" and a "B_4 coil", used to correct for higher order field inhomogeneities. With these, the expected field uniformity at the magnet center should be ~ 1 ppm in a 50 mm sphere. Note, however, that in our case, the ion will be in a region $\ll 1$ mm^3 at the trap center, so the uniformity is expected to be significantly higher than this [91]. Work towards mapping the magnetic field at the magnet's center is underway. The Penning trap itself will be described in more detail in Sec. 5.4.3. Initially, multiple ions will end up in the trap. We can ensure that only one is left in the end using the evaporative cooling technique [227]. The Penning trap used for measurement will be connected to a cryogenic resonant circuit, kept at a temperature of ~ 1 K, and the ion's three motional degrees of freedom will be brought in thermal equilibrium with this circuit, after which the resonant circuit will be decoupled (e.g., by changing its resonant frequency or its Q-factor) [91].

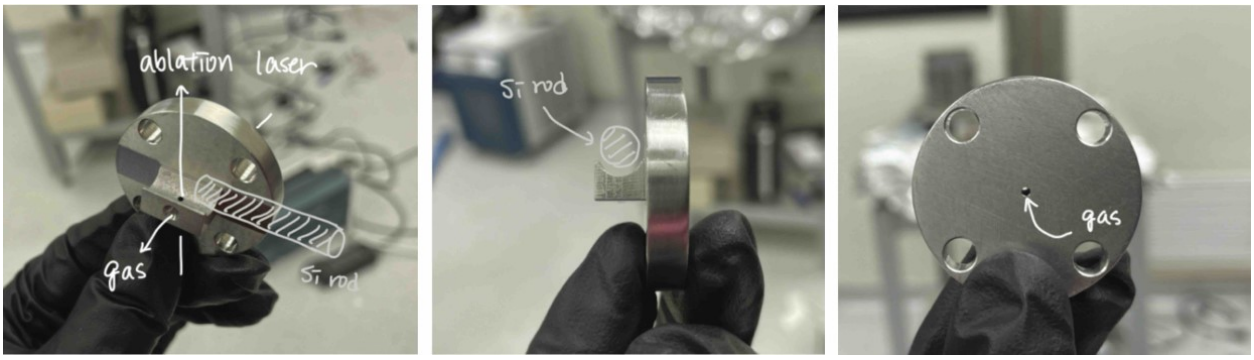

Figure 5.4: Custom-made piece for creating SiO molecules by combining the plume resulting from the Si rod ablation and the gas mixture produced by the solenoid valve. The rod is placed in the indicated curved region of the piece, with the direction of the ablation laser marked. The gas from the valve will flow along a cylindrical hole perpendicular to the direction of the ablation. The piece will be directly attached to the solenoid valve using the four holes on the big diameter. Annotation thanks to H. Kakioka.

As mentioned above, at this point, several rotational energy levels are expected to be populated. Therefore, we need to perform rotational cooling to populate only the lowest rotational level of the molecule. Ref. [224] showed that optically pumping to the lowest rotational level is possible with a fidelity of 94(3)% for ^{28}SiO, and a similar value is expected for ^{29}SiO. In our case, we want to initially populate the positive parity state close to the crossing, so care must be taken to ensure this is achieved before the measurement begins. To make sure we are not populating the $N = 1$ state, we could drive transition to the $N = 0$ or $N = 2$ rotational states in the $B^2\Sigma^+$ electronic level [228], followed by a second transition to the autodissociative $C^2\Pi$ electronic state [224]. The molecule will dissociate if starting

from the $N = 1$ state but not from the $N = 0$ one. This can be done before the evaporative cooling stage, and we expect the remaining molecules to be in the $N = 0$ rotational state with high probability ($> 95\%$). This level is further split into four spin-rotational/hyperfine components: $|m_S, m_I, m_N\rangle = |+1/2, -1/2, 0\rangle$ and $|+1/2, +1/2, 0\rangle$ with an energy of $\sim B_0$, and a splitting between them of ~ 400 MHz and $|-1/2, -1/2, 0\rangle$ and $|+1/2, +1/2, 0\rangle$ with an energy of $\sim -B_0$ and a splitting between them of ~ 400 MHz. Given the large splitting between them, the other levels besides the one of interest can be selectively excited, and then the molecule dissociated as above, leaving only molecules in the desired energy state in the trap. As we need only one molecular ion in this state per measurement cycle, we expect this to be easily achieved with $> 90 - 95\%$ fidelity [55].

At this point, the molecule is in the desired internal spin-rotational/ground state, and its motional degrees of freedom are cooled down. We then apply a "kick" to the molecule, for example, by increasing the voltage on one of the trap electrodes (e.g., Ref. [229]), which represents the beginning of our measurement protocol, as described in Sec. 5.2. In the end, we apply the same "kick" in the opposite direction to bring the molecule back to the trap center and check the population transfer to the other parity state using state-selective dissociation. We can investigate if the molecule was dissociated by checking if the trapped ion's mass corresponds to $^{29}SiO^+$ or one of its dissociation products. If we induce a dissociation, we repeat the whole process described above, starting from the ablation source. Otherwise, we keep the ion trapped, confirm it is in the right spin-rotational level and redo the measurement without any new loading cycle.

On the other side of the magnet, we will have a CF200 6-way cross, which will host the cryocooler (SRDK-415 Ultra Low Vibrations Cryocooler system from ColdEdge) used to cool down the Penning trap and the associated resonant circuit and amplifiers. Currently, this chamber hosts a MagneTOF ion detector (from ETP Ion Detect, model 14925) for initial beam tuning tests inside the magnetic field (not shown in Fig. 5.1).

5.4.2 Ion Source

For the first version of our experiment, we are planning to use $^{29}SiO^+$ molecular ions [55]. The SiO molecules will be produced as follows. First, a high power, 532 nm Nd:YAG laser is used to ablate a Si rod (0.25″ diameter, 3″ length, 6N purity, from ESPI Metals). The rod is attached to a feedthrough that allows it to rotate using an external motor (see Fig. 5.3). This ensures that different regions on the rod are ablated uniformly, and thus, the rate of SiO production varies less over time compared to the case of always ablating the same spot. The ablation is done through a 1 mm diameter hole in the custom-made aluminum piece shown in Fig. 5.4, while the rod will be placed in the curved region of the same piece, almost in contact with the piece itself. This is needed such that the rod can rotate freely while making sure the ablation plume is forced to move through the mentioned piece cylindrical holes as described below. The piece also contains a 1.2 mm diameter hole along the direction perpendicular to the ablation, and the two holes intersect in the region where the ablation plume is expected to be produced. This ensures that some of the ablation plume will be forced to exit through this second hole. Right after the ablation (the optimal delay will be determined in practice), a solenoid pulsed valve (not shown in Fig. 5.1) will release a gas mixture of N_2O (5%) and Ar (95%) which will overlap with the ablation plume inside

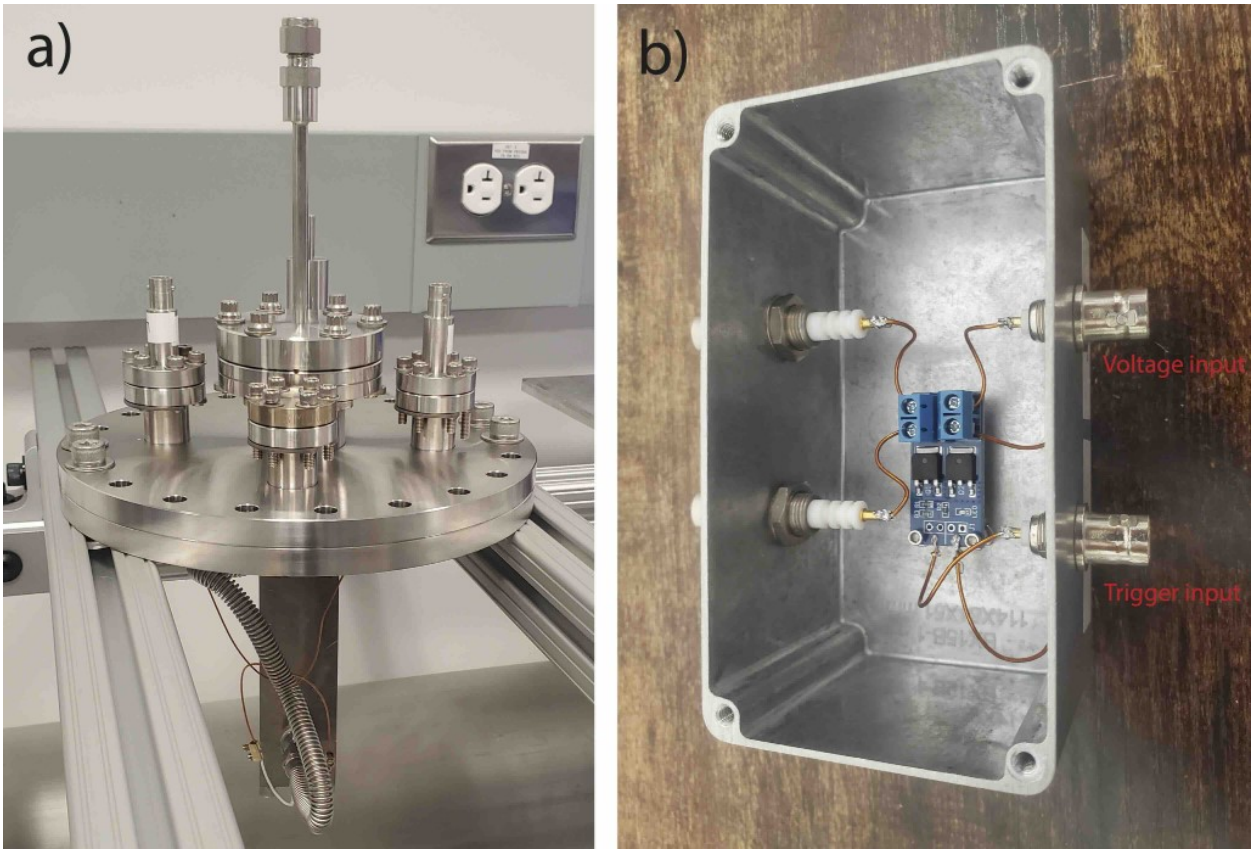

Figure 5.5: a) Flange containing the source for the experiment. The gas connection (DN40CF LIQUID FEEDTHROUGH 1 x 1/4" TUBE / SWAGELOK FITTING from LEWVAC) and the two SHV connections to the valve are shown. b) MOSFET switch and corresponding electrical connections used to control the solenoid valve.

the second cylindrical hole. The N_2O gas will react with the Si, producing, among others, SiO, while the Ar gas will cool down the rotational and translational degrees of freedom through a supersonic expansion. Previous studies [225] showed that this design should lead to rotational temperatures around $\sim$ 20 K, which is enough as the starting point of our experiment. The pulsed valve is controlled using a high power (400 W) MOSFET shown in Fig. 5.5 (together with the electrical connections to the pulsed valve). A voltage of at least 15 V is needed to trigger the valve, while an independent input sets the repetition rate and the length of each pulse using a TTL signal, both of which are used as inputs to the MOSFET, as shown in Fig. 5.5 b). The best pulse length and amplitude values will need to be optimized experimentally. The MOSFET output is then sent to the two connections of the pulsed valve, whose outside vacuum feedthroughs are shown in Fig. 5.5 a). The entire ion-source setup and its installation in the source chamber are shown in Fig. 5.6.

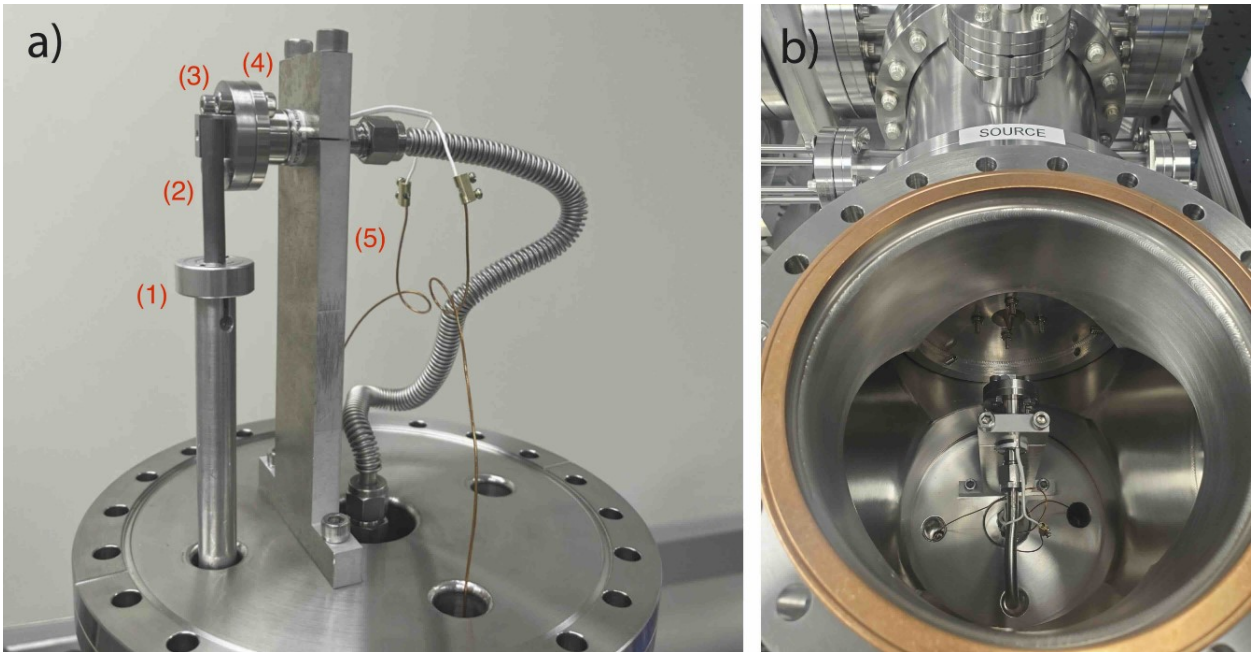

Figure 5.6: a) Assembled ion source setup. On the left, we have the Si rod holder (1) and the rod itself (2). This is close to the piece used to mix the ablation plume with the gas (3) from the solenoid pulsed valve (4). This piece is attached to the valve, held in place by a custom-made T-shaped piece (5) directly connected to the stainless steel flange. The electrical connections to the valve and the bellow used to connect the valve to the gas source are shown. b) Ion source setup placed inside a CF-160 flange. The setup was designed such that the gas is produced along a line passing through the skimmer located in front of the valve, also shown in this figure.

5.4.3 Penning Trap Theory and Simulations

The Penning trap is the main tool behind our measurement strategy. A Penning trap is a device that uses electrostatic and magnetostatic fields to trap ions in 3 dimensions [90, 91]. In its simplest, hyperbolic form, it contains a ring electrode and two endcap electrodes,

as shown in Fig. 5.7 a). The confinement along the axial directions, which we will consider to be along the $\boldsymbol{z}$ axis of the laboratory frame and along the magnetic field direction, is achieved by a quadrupolar potential of the form [90, 91]:

$$U(r,z) = U_0 \frac{C_2}{2d^2}\left(z^2 - \frac{r^2}{2}\right), \tag{5.20}$$

where U_0 is the voltage difference between the ring electrode and the end caps, C_2 is a dimensionless parameter, d is a characteristic trap length defined as:

$$d = \sqrt{\frac{z_0^2 + \frac{r_0^2}{2}}{2}}, \tag{5.21}$$

where r_0 is the trap radius, z_0 its half length along the z-axis and $r = \sqrt{x^2+y^2}$ is the distance in the radial direction (perpendicular to the magnetic field direction). The radial trapping is achieved by the application of a large magnetic field (on the order of 1 T) along the axial direction, which leads to the existence of a Lorentz force:

$$\overrightarrow{F}_L = q\overrightarrow{v} \times \overrightarrow{B}, \tag{5.22}$$

resulting in a free-space cyclotron frequency of the ion of:

$$\omega_c = \frac{q}{m}B_0, \tag{5.23}$$

where q and m are the charge and mass of the trapped particle. In the end, the ion trajectory becomes a superposition of three oscillatory motions (Fig. 5.7 b)), which can be calculated from the differential equation [90, 91]:

$$\begin{pmatrix}\ddot{x}\\ \ddot{y}\\ \ddot{z}\end{pmatrix} - \frac{qB_0}{m}\begin{pmatrix}\dot{y}\\ -\dot{x}\\ 0\end{pmatrix} - \frac{q}{m}\frac{U_0 C_2}{2d^2}\begin{pmatrix}x\\ y\\ -2z\end{pmatrix} = 0. \tag{5.24}$$

Note that this formula is classical and non-relativistic. This approximation is suitable for our experiment where the ion velocity is expected to be on the order of a few thousand meters per second while the expected quantum numbers at our temperature ($\sim$ 1 K) are on the order of 10^4. Extending this formalism to the relativistic or quantum regime can be done straightforwardly [90]. From Eq. 5.24, we obtain a frequency for the axial motion given by:

$$\omega_z = \sqrt{\frac{q}{m}\frac{U_0 C_2}{d^2}}, \tag{5.25}$$

which is decoupled from the radial motions. In the radial direction, we obtain two independent oscillatory motions with frequencies given by:

$$\omega_\pm = \frac{\omega_c}{2} \pm \frac{1}{2}\sqrt{\omega_c^2 - 2\omega_z^2}. \tag{5.26}$$

The lower frequency among the two, ω_-, corresponds to the so-called magnetron motion, while ω_+ corresponds to the modified cyclotron motion. Overall, these three modes lead to a relatively complicated ion trajectory in the Penning trap, as shown in Fig. 5.7 b). However,

as mentioned in Sec. 5.2, in our case the goal is to reduce the radial amplitude as much as possible, in order to reduce the effect of the AC Stark shifts. Thus, the trajectory of the ion can be thought of, to a good degree of approximation, as a simple harmonic motion in the z-direction. The stability criterion for the Penning trap follows from the requirement that the radial motion frequencies are real, which means:

$$\omega_c > \sqrt{2}\omega_z, \tag{5.27}$$

which is equivalent to

$$B_0 > \sqrt{2\frac{m}{q}\frac{U_0 C_2}{d^2}}. \tag{5.28}$$

One important relationship among the trap's eigenfrequencies is given by:

$$\omega_c^2 = \omega_+^2 + \omega_-^2 + \omega_z^2, \tag{5.29}$$

which implies that measuring the three frequencies of an ion allows the extraction of the free space cyclotron frequency, which facilitates, using Eq. 5.23, to precisely measure the magnetic field using an ion with known mass and charge (e.g., ^{12}C). This could also be used to calibrate the magnetic field in our experiment. The advantage of Eq. 5.29 is that it holds even when imperfections are present, such as machining errors on the electrodes or misalignments between the magnetic and electric fields [90, 230].

Finally, the energies of the three modes are given by [90, 231]:

$$\begin{aligned} E_z &= \frac{1}{2}m\omega_z^2 z_{max}^2 \\ E_+ &= \frac{1}{2}m\left(\omega_+^2 r_+^2 - \frac{1}{2}\omega_z^2 r_+^2\right) \\ E_- &= \frac{1}{2}m\left(\omega_-^2 r_-^2 - \frac{1}{2}\omega_z^2 r_-^2\right) \approx -\frac{1}{4}m\omega_z^2 r_-^2, \end{aligned} \tag{5.30}$$

where z_{max} is the amplitude of the axial motion and r_+ and r_- are the radii of the modified cyclotron and magnetron motion, respectively. It is worth noting that, while the axial and modified cyclotron frequencies have energies that decrease with the radius, thus, extracting energy from the system brings the ion towards the central region of the trap, the magnetron radius increases with decreasing energy.

While the conventional shape of a Penning trap is the one shown in Fig. 5.7 a), such a shape can pose several practical issues [91, 231]. Machining parabolical electrodes and aligning them with high precision so that the electric field felt by the ion is as quadrupolar as possible can be very challenging. This shape can also lead to significant limitations in terms of laser access, which is a major issue for our setup. Moreover, even if a trap with this shape is used, a perfect quadrupolar field can be achieved only for infinitely long electrodes. A commonly used alternative is that of a cylindrical trap, which can overcome most of the issues present in a parabolical trap [91, 231]. While such a trap can be, in principle, implemented with only three electrodes, most experiments use five or seven electrodes, some

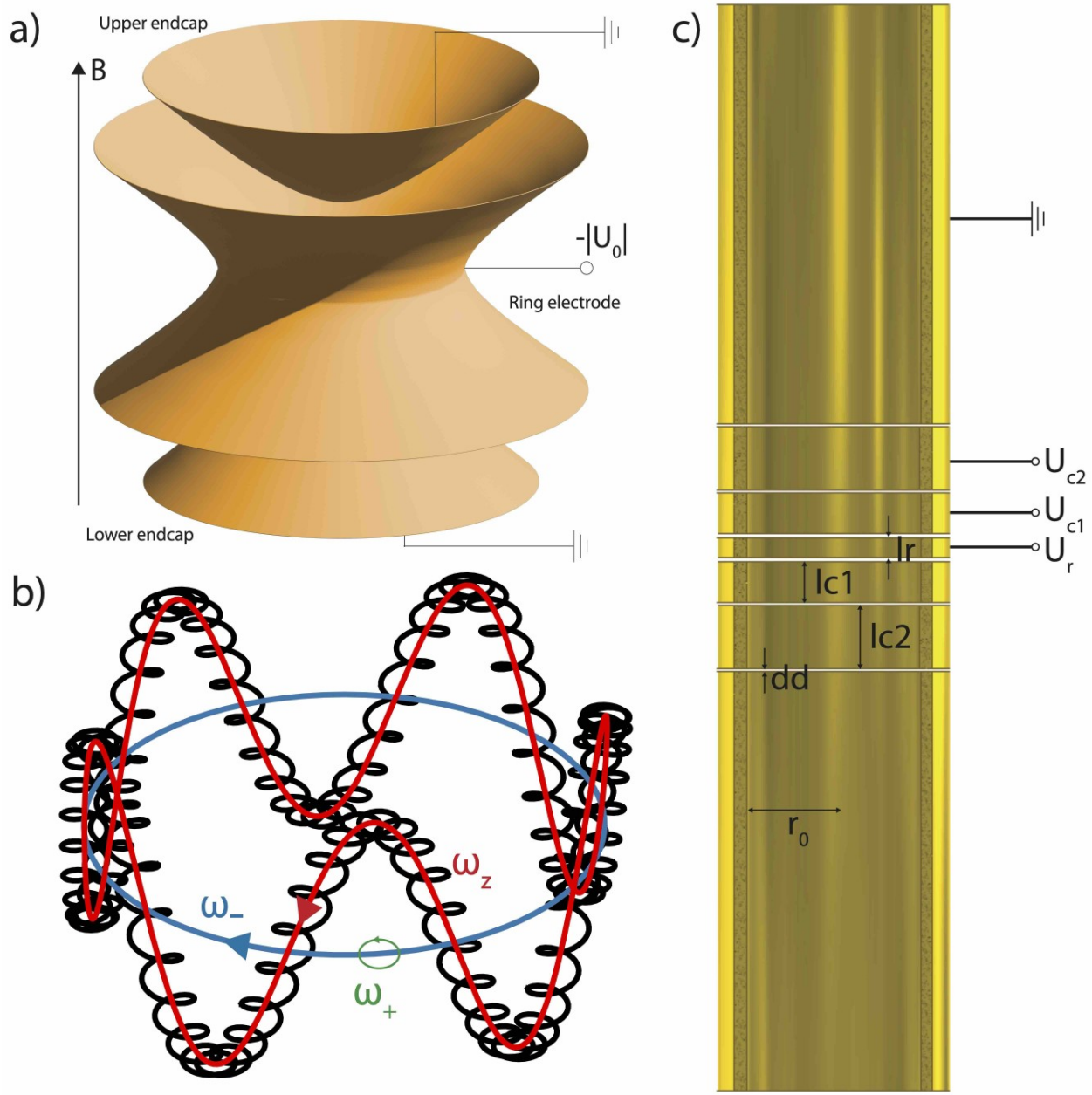

Figure 5.7: a) Classical design for a Penning trap containing two endcaps and a ring electrode. b) Trajectory of an ion inside a Penning trap (black). The three individual degrees of freedom of the ion are shown in red (axial motion), green (modified cyclotron motion), and blue (magnetron motion). Amplitudes of the three motions are amplified for display purposes and not shown to scale. c) Cylindrical trap with seven electrodes. The naming convention for the voltages and dimensions of the electrodes is shown.

of which can be used for correcting various imperfections, thus leading to a more quadrupolar field at the center of the trap [91, 231]. Such a seven electrodes trap, together with the labels for electrodes lengths and voltages, is shown in Fig. 5.7 c). However, even if using such a trap can significantly reduce experimental challenges compared to a hyperbolic one, one still has to deal with an imperfect potential at the trap's center. In general, the potential experienced by the ion can be expanded in terms of Legendre polynomials, $P_n(\cos\theta)$ as [90, 91, 231]:

$$V(r,\theta,z) = \frac{U_0}{2}\sum_{n=0}^{\infty} C_n \left(\frac{r}{d}\right)^n P_n(\cos\theta), \tag{5.31}$$

where U_0 is the potential difference between the central electrode and the grounded endcaps, C_n are expansions coefficients, and d is the characteristic length of the trap. In the ideal case, we want $C_n = 0$ for $n > 2$, as higher order terms in the potential expansion can lead to energy-dependent frequency shifts, limiting the precision of our measurements. Note that due to the mirror symmetry of the setup (ignoring possible slits in the electrodes), the odd coefficients are identically zero. Therefore, it is important to design a trap such that the higher order even coefficients in Eq. 5.31 are as close as possible to zero.

l_r	0.5723 mm
l_{c1}	1.1456 mm
l_{c_2}	1.9575 mm
U_{c1}	-34.684941 V
U_{c2}	-29.351721 V

Table 5.1: Parameters of the optimized Penning trap setup: lengths of the central ring electrode, l_r and the two corrections electrodes, l_{c1} and l_{c2} and the voltages applied on the correction electrodes, U_{c1} and U_{c2}.

As previously mentioned, the trap we use contains seven electrodes, as shown in Fig. 5.7 c): a central electrode, two upper and two lower correction electrodes, and two end cap electrodes. The diameter of the trap's electrodes was fixed to 6 mm, which was small enough in order to allow the reading of the ion motion using a resonant circuit but large enough to reduce the effect of trap imperfections, patch potentials, and image charge shifts (which scale as $\frac{1}{r^3}$, where r is the trap's radius) [55, 91]. The spacing between electrodes was also fixed to 0.14 mm, according to Ref. [231], and the voltage on the central electrode was fixed to -36 V to reach close to the maximum value of the axial frequency allowed by the Penning trap stability criterion, Eq. 5.27. This is needed for the AC Stark interference technique, as described in Sec. 5.2. The length of the end cap electrodes was also fixed at 20 mm and was assumed to be grounded. The length and voltages of the other electrodes, five parameters in total, were then optimized as described below. Given the cylindrical symmetry of the problem (ignoring any vertical slits and assuming that the endcap electrodes are long enough, ideally infinite), this optimization can be performed analytically [232–235]. Given that we have five parameters to optimize for: the length of the central electrode, l_r, and the lengths and voltages of the two correction electrodes, l_{c1}, U_{c1}, l_{c2} and U_{c2}, one can in principle aim to bring C_4, C_6, C_8, C_{10} and C_{12} as close as possible to zero. However, one other thing we need to account for is the C_2 parameter to be independent of any changes in

voltages made to the corrections electrodes, which are expected once the trap is implemented in practice. Therefore, one can write:

$$C_2 = D_{21}\frac{U_{c1}}{U_r} + D_{22}\frac{U_{c2}}{U_r} + E_2, \tag{5.32}$$

and aim to minimize $D_2' \equiv D_{21}\frac{U_{c1}}{U_r} + D_{22}\frac{U_{c2}}{U_r}$ in addition to C_4, C_6, C_8, C_{10}, without any explicit constraints on C_{12}. See Ref. [231] for deriving the analytical expressions for these parameters, expressions used in our custom-made optimization program in Python. In the end, the minimized function in our case was:

$$L = C_4^2 + C_6^2 + C_8^2 + w_1 C_{10}^2 + w_2 D_2'^2, \tag{5.33}$$

where $w_1 \approx 10^{-2}$ and $w_2 \approx 10^{-3}$ were weights used to give more importance to the first three parameters without completely neglecting the final two. The optimization was implemented in Python 3.8.9 using the Nelder-Mead method of the scipy.optimize.minimize package.

The optimal parameters obtained are shown in Table 5.1 and the final values of the minimized parameters are: $C_2 = -0.60152$, $C_4 = -1.3 \times 10^{-9}$, $C_6 = 5.0 \times 10^{-10}$, $C_8 = -9.3 \times 10^{-10}$, $C_{10} = -3.9 \times 10^{-10}$ and $D_2' = -4.1 \times 10^{-10}$. Note that the half-length of the central electrode is ~ 0.3 mm, which sets the limit on the maximum amplitude kick we can give the ion when placing it on its axial motion at the beginning of the measurement protocol (see Sec. 5.2). The suitability of these parameters for creating a quadrupolar potential even in the presence of slits in the electrodes, as well as the stability of C_2 to changes in the correction electrodes potentials, were confirmed based on independent COMSOL simulations. The trap for our experiment, built using these parameters, is currently under construction at the Max Planck Institute for Nuclear Physics in Heidelberg, Germany. The electrodes will be made of copper, with a 10μm layer of gold deposited on top. In between the copper and gold, a 2μm layer of silver will also be deposited to act as a diffusion barrier between the copper and gold. The resulting frequencies for this trap are: $\frac{\omega_z}{2\pi} = 354$ kHz, $\frac{\omega_+}{2\pi} = 311$ kHz, $\frac{\omega_-}{2\pi} = 201$ kHz and $\frac{\omega_c}{2\pi} = 512$ kHz.

5.5 Outlook

The first step toward measuring NSD PV effects in a molecule is to test our SiO source. As we expect to produce ions (and not only SiO^+), we can use these to adjust the various electrostatic optics in our setup, such as the focusing lenses and the quadrupole bender. We also have the possibility to accelerate the ions to a few keV of energy, which would allow us to perform a time-of-flight measurement. This could tell us about the amount of $^{29}SiO^+$ ions produced directly from the source. It should be mentioned that if enough such ions are produced, and if they are distributed only among the lowest rotational level (ideally $N < 5$), we could use them directly for our experiment without the need to perform the 1+1 REMPI step described in Sec. 5.2. At this step, it is worth focusing on optimizing the various experimental parameters available, such as the ablation laser power, timings of the pulsed valve, gas pressure, and voltages on the electrodes to maximize the number of produced $^{29}SiO^+$ ions.

If this number is considered not high enough for future measurements, the next step is the implementation of the 1+1 REMPI scheme from Ref. [223]. Again, we will aim to maximize the number of produced $^{29}SiO^+$ ions. As we have laser access through the quadrupole bender, we can, in principle, also perform in-flight, collinear laser spectroscopy on these ions to measure the distribution of their population among the rotational levels. This can be done by exciting the $X^2\Sigma^+ \rightarrow B^2\Sigma^+$ transition using our $\sim$ 20 MHz linewidth injection seeded Ti:Sa laser (see Chapter 4 and 5.2) followed by laser excitation to the auto dissociative state $2^2\Pi$ using, for example, our Ti:Sa grating laser (see Chapters 4 and 6) and then detecting the resulting products.

On the Penning trap side, we are currently working on mapping the magnetic field inside the magnet and its temporal stability using an NMR probe. The designed Penning trap and the associated resonant circuit (see Sec. 5.4.3) are currently being built at the Max Planck Institute for Nuclear Physics in Heidelberg, Germany, and they are expected to be delivered to MIT in the coming months. Once they arrive and are installed inside the magnet, the next step is to perform the first ion trapping. This will allow us to calibrate the various voltages on the trap electrodes to reduce the higher order terms in the electrostatic potential (see Sec. 5.4.3), as well as to map the magnetic field with higher precision than just using an NMR probe. It will also facilitate a better alignment of the trap with the magnetic field axis. All these can be achieved by exciting one of the ion's motional modes and measuring the frequency of the mode as a function of motional amplitude using the resonant circuit. In the ideal case, no dependence of the frequencies on the motional amplitude should be observed [90, 91, 231].

Once these preliminary tests are done, we can begin our first measurements. Our first goal is to prove that we can control the various energy levels of opposite parity (and hence the magnetic field) at the level of 10 Hz. Once the levels are close enough, ideally $\sim$ 100 Hz apart, we can aim to measure induced population transfer between them due to external electric fields as a function of various parameters, such as spacing between the levels or magnitude of the external field. For this proof of principle, both the radial and axial electric fields can be used, as well as both $^{28}SiO^+$ and $^{29}SiO^+$. This should also allow us to measure the dipole moment of SiO^+ as described in Sec. 5.3.

Once this is achieved, the next step is to attempt an actual PV measurement using $^{29}SiO^+$. Based on the discussion in Sec. 5.3, we expect a measurement at the 10% level for the W (and hence η) parameter in about one week of total measurement time [55]. Once this is achieved, the next goal is to extend our measurement to other molecular ions of interest, TlF^+ being a promising candidate, as mentioned in Sec. 5.3. This method can also be applied to light isotopes, whose properties can be calculated with much higher accuracy and thus provide a stronger comparison between experiment and theory [12, 236]. Using diatomic molecules for such measurements might require magnetic fields beyond the current technological capabilities [31], but using polyatomic molecular ions could represent a feasible alternative [43, 237]. Finally, the Penning trap temperature could be further reduced from $\sim$ 1 K down to $10 - 100$ mK [238–240] or as low as $\sim$ 1 mK [241, 242] using already demonstrated cooling techniques, which could reduce the uncertainty on the measured physics parameters of interest by as much as two orders of magnitude compared to the calculations performed in Sec. 5.3 [55].

Chapter 6

Towards Measurements of Sub-Millisecond Lifetime Radioactive Isotopes

Collinear laser spectroscopy has proved to be extremely successful over the past few years, allowing us to measure the electromagnetic properties of nuclei at the extremes of the nuclear chart (see Chapter 4 for details on the CRIS method) [15, 16, 19, 20, 23, 52, 54, 123, 243, 244]. These measurements have played a major role in our understanding of the nuclear many-body problem, guiding the development of the nuclear theory [11–13, 83–86]. However, despite many successes, state-of-the-art techniques such as the collinear resonant ionization spectroscopy (CRIS) technique still have various limitations, making it particularly challenging to apply them in the study of highly reactive (e.g. F), light (e.g. Be, B) or very short-lived elements, with lifetimes on the millisecond level and below [48, 50, 53, 245, 246]. However, such elements are highly critical in connecting the description of nuclei with the underlying theory of the strong interaction, QCD [15]. One limitation of the current CRIS technique (see Chapter 4) [15, 51, 247] is the need for pre-cooling and bunching of ions. This can take more than 10 ms, which makes the study of some short-lived elements, produced at low rates, virtually impossible. At the same time, extracting, trapping, and cooling light elements have additional challenges [246]. One proposed solution is to create and extract these elements as molecules. After extraction, the desired atom or ion can be obtained from the dissociation of the molecules. However, during dissociation, the desired atom/ion can have a large energy spread, on the order of a few to 10's of eV, preventing the use of the existing collinear laser spectroscopy techniques [246]. At the same time, the CRIS method, despite its high sensitivity and selectivity, still has sources of background that can hinder the study of specific elements or transitions of interest. To list a few, we can have dark counts due to the ion detector, which can be ~ 20 per minute for some of the commonly used detectors [51–54], ionization events from states previously excited in non-resonant processes (e.g., due to collisions inside the bunched beam, with the buffer gas in the radio-frequency buncher or the charge exchange cell), or two-photon ionization events, with both photons coming from the ionizing laser [51]. The latter ones are considerably higher for short wavelength lasers (e.g., 532 nm or 355 nm) due to the large power needed for the non-resonant ionization step [51–53].

This chapter discusses the experimental efforts to overcome all the challenges described above. Article 6 [56], which is added below, contains a detailed theoretical investigation of a proposed experimental scheme, with the ultimate goal being the study of isotopes with lifetime below 1 ms and produced in rates as low as 1 per minute. Following the Article, I will present the progress made towards implementing this proposal in practice, using a novel setup named Photo-Resonance Excitation and Cavity Ionization Spectroscopy Apparatus (PRECIOSA), together with very encouraging preliminary results. The main idea behind the experiment is to perform the ionization step in a direction perpendicular to the trajectory of the atoms. This would lead to a well-defined ionization region with a length below 1 cm, in contrast to the current CRIS technique where the interaction and ionization regions are larger than $\sim$ 1 m [51], which can allow an efficient collection of the produced electrons. This has several major implications for the sensitivity of the experiment. On the one hand, performing a coincidence measurement between the produced ions and electrons obtained during an ionization event can significantly reduce the non-resonant background. At the same time, by performing the ionization inside an electric field and recording not just the time but also the position where the ions and electrons hit two independent position-sensitive detectors, one can reconstruct the initial energy of the atom before ionization, on an event by event-basis [53]. This means that a Doppler correction of the laser frequency to the rest frame of the atom can be performed for each atom individually, thus bypassing the need to cool down the whole ion bunch/beam. Bypassing the cooling step would, therefore, extend the reach of our experimental capabilities to very short-lived and reactive elements. Finally, one can further reduce the background of this technique by measuring the energy of the electrons and thus discarding events in which the electrons are ionized from a level different from the one of interest or are produced from a non-resonant multi-photon process. This can be achieved by using a Velocity Map Imagning (VMI) device [248–253] as described in detail in Sec 6.3. Thus, combining some or all of these techniques can allow us to overcome the current limitations of the CRIS approach, enabling the study of nuclei further away from the valley of stability [15, 53].

6.1 Article 6: Precision Spectroscopy of Fast, Hot, Exotic Isotopes Using Machine-Learning-Assisted Event-by-Event Doppler Correction

This article (S.-M. Udrescu, D. A. Torres, and R. F. Garcia Ruiz, "Precision spectroscopy of fast, hot, exotic isotopes using machine-learning-assisted event-by-event Doppler correction", Phys. Rev. Res. 6, 013128 (2024)) presents the proposal of a novel experiment aiming to study specific short-lived isotopes (lifetimes $<$ 1 ms) of high interest for nuclear structure, astrophysics, and even new physics searches, expected to be produced at the various radioactive ion beam facilities worldwide, such as FRIB [48], ISOLDE [49] and RIKEN [50]. Many short-lived, light elements, already produced in these facilities, are currently out of reach for the existing laser spectroscopy techniques. For this article, published in Physical Review Research (2024), I performed all the theoretical calculations and numerical simulations, I prepared all the figures and wrote the different drafts of the manuscript, including

the initially submitted version and subsequent revisions. I was in charge of the submission process.

Precision spectroscopy of fast, hot, exotic isotopes using machine-learning-assisted event-by-event Doppler correction

S. M. Udrescu [1,*] D. A. Torres [2] and R. F. Garcia Ruiz [1]
[1]Massachusetts Institute of Technology, Cambridge, Massachusetts 02139, USA
[2]Departamento de Física, Universidad Nacional de Colombia, Bogotá 111321, Colombia

(Received 23 April 2023; revised 21 November 2023; accepted 21 December 2023; published 31 January 2024)

We propose an experimental scheme for performing sensitive, high-precision laser spectroscopy studies on fast exotic isotopes. By inducing a stepwise resonant ionization of the atoms traveling inside an electric field and subsequently detecting the ion and the corresponding electron, time-, and position-sensitive measurements of the resulting particles can be performed. Using a mixture density network, we can leverage this information to predict the initial energy of individual atoms and thus apply a Doppler correction of the observed transition frequencies on an event-by-event basis. We conduct numerical simulations of the proposed experimental scheme and show that kHz-level uncertainties can be achieved for ion beams produced at extreme temperatures ($>10^8$ K), with energy spreads as large as 10 keV and nonuniform velocity distributions. The ability to perform in-flight spectroscopy, directly on highly energetic beams, offers unique opportunities to study short-lived isotopes with lifetimes in the millisecond range and below, produced in low quantities, in hot and highly contaminated environments, without the need for cooling techniques. Such species are of marked interest for nuclear structure, astrophysics, and new physics searches.

DOI: 10.1103/PhysRevResearch.6.013128

I. INTRODUCTION

With the advent of new radioactive beam facilities worldwide, short-lived nuclei that hitherto have only existed in stellar explosions are being created artificially in the laboratory, extending our exploration of the nuclear chart to extreme proton-to-neutron ratios [1–3]. These unstable isotopes, typically with lifetimes of just a fraction of a second, are critical for our fundamental understanding of nuclei and nuclear matter [2]. The major challenge of current experimental nuclear physics is to develop sensitive and precise techniques to enable the study of these exotic isotopes, commonly produced at high temperature and with yields of just a few isotopes per second [1–3].

Laser spectroscopy has long been established as an important tool for studying the properties of unstable nuclei [2]. This technique allows the extraction of nuclear spins, electromagnetic moments, and changes in the nuclear root-mean-square charge radii [2,3]. These observables are key for understanding the atomic nucleus and guiding developments of nuclear theory [4–10]. To extract nuclear properties from atomic spectra, high experimental sensitivity and precision are critical. Laser cooling and trapping techniques represent some of the most precise experimental methods [11,12], but they are not universally applicable to all elements of the periodic table and cannot be employed directly to study short-lived nuclei, typically produced at high temperatures, high energies (>30 keV), and with subsecond lifetimes [2].

A highly successful approach to overcome these challenges is the collinear laser spectroscopy technique applied on bunched ion beams [13]. Unstable isotopes, typically produced from nuclear reactions, can be mass separated as ions, trapped, and then cooled in gas-filled radio-frequency ion traps [13,14]. Buffer gas collisions are then used to reduce the temperature of the initial beam down to the temperature of the gas. These methods have allowed high-precision measurements of a wide range of radioactive nuclei [2] and have recently been extended to study radioactive molecules [15–18]. However, the lifetime of the systems that can be studied with such experiments is limited by the cooling and trapping time, which are typically on the order of tens or hundreds of milliseconds [13]. Moreover, trapping becomes impractical when large amounts of contaminants are present, overfilling the trap, and preventing the capture of the ion of interest. New-generation radioactive beam facilities, such as the Facility for Rare Isotopes Beams (FRIB) [19] in the U.S. and RIKEN in Japan [20], are already producing isotopes at the extreme of stability, but due to their short lifetimes (<5 ms) they cannot be studied with the current laser spectroscopy techniques. Therefore, spectroscopy methods that could be directly applied to fast, hot, short-lived isotopes need to be developed [21,22].

Here, we propose a simple, versatile method for performing high-precision laser spectroscopy studies of fast atomic beams in a way that allows the energy of the atoms of interest to be measured in flight on an event-by-event basis.

*sudrescu@mit.edu

By performing coincidence measurements of the resonant ions and ejected electrons produced during a resonant laser ionization process, the vector velocity of each initial atom can be reconstructed, enabling accurate measurements of the transitions of interest. This setup would enable precision laser spectroscopy measurements directly on isotopes produced by in-flight reactions, with energy spreads as large as 10 keV and lifetimes bellow one millisecond or on ions produced after molecular breakup reactions. We demonstrate that precision measurements can be achieved even for arbitrary energy distributions of the initial particles, without the need for cooling mechanisms.

To highlight the broad applicability of our proposed method, we present three different physics scenarios:

(i) *Atomic spectroscopy of Sn isotopes*. Sn is the element with the largest number of stable isotopes (ten). Precision isotope shift measurements over this long isotope chain could provide complementary studies to constrain the possible existence of new fundamental forces and particles [23]. Having a proton magic number, $Z = 50$, Sn isotopes possess a relatively simple nuclear structure and thus exhibit reduced sensitivity to Standard Model effects, such as nuclear deformation [23,24], facilitating a clear identification of any new physics signals.

(ii) *Charge radii measurement of Boron isotopes*. Located along the proton drip-line, the ^{8}B isotope is of particular interest for nuclear structure studies, being a main candidate for displaying a proton halo [25–28]. This behavior would manifest as an increased value of the charge radius of ^{8}B, which can be extracted, in a model independent way, through isotope shifts measurements. ^{8}B is also of interest for solar neutrino physics [29,30]. Its production in the sun, through the proton capture on a ^{7}Be nucleus, is accompanied by a high-energy neutrino emission [26,29]. The rate of this process depends on the structure of the ^{8}B nucleus [26,29,30]. Despite having a relatively long lifetime ($\tau = 770$ ms) its spectroscopic investigation has not been possible so far, mainly due to its high reactivity in forming molecules, and the low efficiency of deceleration and trapping for elements with small mass [28].

(iii) *Charge radii measurements of Ni isotopes at the extreme of stability*. With both neutron and proton magic numbers at $N = 20$ and $Z = 28$, respectively, ^{48}Ni is of marked interest for nuclear structure and the study of exotic nuclear phenomena at the edge of stability [31,32]. Although this isotope can be produced at the current radioactive beam facilities, its short lifetime ($\tau = 2.1$ ms) prevents its study using available laser spectroscopy techniques. ^{48}Ni is the mirror nucleus of the stable doubly magic ^{48}Ca, hence a measurement of the nuclear charge radii difference between these two isotopes can be highly sensitive to constrain parameters of the equation of state of nuclear matter [33].

II. EXPERIMENTAL APPROACH

A schematic of our proposed method is shown in Fig. 1. An ion beam, whose energy and energy spread depend on the isotopic production mechanism, is neutralized in-flight and then sent towards the experimental interaction region. There, after the non-neutralized ions are removed, the remaining atoms are overlapped collinearly with a continuous-wave laser, such that they are resonantly excited to a particular electronic state. The laser power and beam diameter will depend on the properties of the atomic beam under investigation, such as its spatial and energy spread. After this, the atoms can be ionized by a different continuous-wave laser beam, perpendicular to the atoms' propagation direction. As this second step can be a non-resonant process, power densities on the order of tens to thousands of kW/cm^2 can be required for efficient ($50\% - 100\%$) ionization [34]. This can be achieved by using a standing-wave laser built inside an optical cavity [35]. Similar to the excitation step case, the ionization laser beam diameter will depend on the properties of the atomic beam. We expect that a diameter of a few mm [35] will be suitable for an effective ionization. Below we briefly describe possible experimental implementations for the study of the considered isotopes:

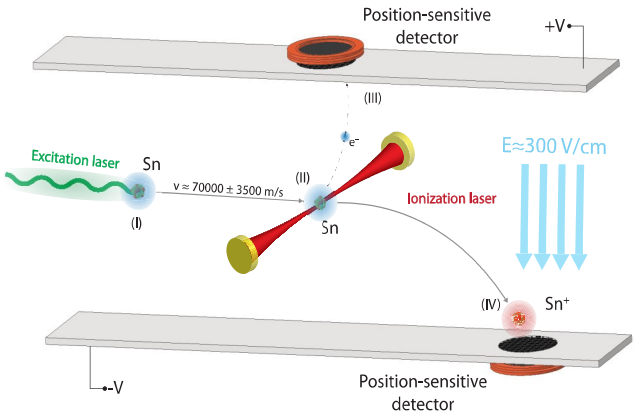

FIG. 1. Illustration of the experimental setup. The neutral atoms resulting from the neutralization process (not shown) enter the interaction region where they are excited to a higher-lying electronic state by a collinear laser (I). The excited atoms are then ionized by a standing-wave laser inside an optical cavity (II). The resulting electrons are detected by a position-sensitive detector located above the ionization point (III), while the ions continue their trajectories in the electric field produced in between two parallel plates, until they reach a second position-sensitive detector (IV). The direction and magnitude of the electric field experienced by the ions is shown in light blue.

(i) Singly charged ^{120}Sn ions can be produced by laser ablation at relatively low energies in large amounts ($>10^9$ ions/s). This element can be neutralized with high efficiency by collisions with alkali metals [36,37]. To highlight the ability of our proposed method to perform precision experiments on ion beams of large energy spread, we assume an initial energy of 10 ± 1 keV.

(ii) ^{8}B isotopes can be produced by impinging a ^{6}Li beam on a ^{3}He target [38]. After passing through a gas catcher, significantly reducing their energies, ^{8}B emerges mainly as molecular ions, which then enter an radio frequency quadrupole cooler and buncher [28]. From here, the molecular ions can be sent towards the interaction region with an energy on the order of tens of keV, a cross section of a few mm, and an energy spread of <1 eV [14,28,39–41]. The molecular ions can be passed through a nanometer-thin carbon foil [28] to cause molecular breakup and produce the desired atoms of

^{8}B. The energy of the resulting beam, as well as its charge state, depends on the initial energy of the molecular ions as well as the thickness of the carbon foil [28,42]. For an output energy on the order of 1 keV, 90% of the output beam can contain neutral boron [28,42]. In our setup, such a carbon foil can be placed a few centimeters in front of the interaction region with ionization laser. This ensures that the optical cavity performance is not affected (the radius of the laser beam inside the ionization cavity is expected to be <5 mm) and that the resulting ^{8}B ions are deflected from the neutral beam. The energy spread of the ^{8}B atoms is expected to be on the order of the molecular dissociation energy, which can be in the range of 1 to few tens of eV [43]. Here, we assume a conservative value of 100 eV energy spread for the ^{8}B atomic beam, ending up with a total energy of 1000 ± 100 eV. Given the proximity of the carbon foil to the ionization point, as well as the higher longitudinal (along the beamline axis) energy (∼1000 eV), relative to the transverse energy (<100 eV), the spatial spread of the ions is expected to be on the order of one centimeter, thus most of the ions can be overlapped with the laser beams. Assuming an excitation laser linewidth of 100 MHz [34], an overall efficiency of ∼0.1% can be expected [2], defined as the number of ^{8}B ions detected in coincidence with their respective electron after ionization, over the number of atoms produced after the interaction with the carbon foil.

(iii) ^{48}Ni isotopes can be produced by in-flight nuclear reactions with energies on the order of hundreds of MeV/u [19,20,44]. This can be reduced down to ∼1 MeV by collisions with solid targets [44]. The transverse diameter of the beam at this stage is expected to be on the order of a few centimeters [45]. From here, we assume the ion beam can be decelerated to 100 keV. To maximize the transmission efficiency during the deceleration step, a custom deceleration setup needs to be implemented, which will strongly depend on the initial beam properties and thus requires a detailed experimental investigation for each specific experimental setup. The energy spread of the beam also depends on the deceleration stages. For the analysis below, we assume an energy spread of 10% of the total beam energy, leading to a final value for the the energy of the ^{48}Ni beam to be 100 ± 10 keV. The produced ions can be highly charged, thus they need to be neutralized by collisions with a gas [36] or solid targets [46–48], which can lead to species with +1 or 0 charge states on nanoseconds timescales [46–48]. The optimal neutralization setup as well as its efficiency will depend on the properties of the initial ion beam. Assuming a 100 MHz linewidth for the first step laser [34], we expect, given the energy and energy spread considered, an excitation efficiency of 10^{-3}. A further reduction in efficiency of about two orders of magnitude is expected from the laser-atom overlap, assuming a diameter of the atomic beam on the order of a few centimeters [45], which is a factor of 10 larger than the expected laser beam diameter. Finally, based on particle trajectory simulations, we expect a transmission efficiency higher than ∼0.1% to the interaction region during the deceleration process to 100 keV. Hence, the total experimental efficiency, defined as the ratio of the number of ions detected in the interaction region in coincidence with an electron to the number of ions produced at ∼1 MeV, is estimated to be higher than 10^{-8} for our proposed method. It should be noted that the efficiency losses are dominated by the large energy spread and spatial dispersion introduced during the deceleration process. A detailed investigation of these effects is beyond the scope of our paper. For comparison with current techniques, at FRIB [19], the overall efficiency of decelerating and cooling ^{48}Ni isotopes for laser spectroscopy experiments, such as the BECOLA facility [14], is expected to be less than 10^{-15}, seven orders of magnitude smaller than the lower limit expected from our proposed method. ^{48}Ni is an extreme example, presented here as a pedagogical illustration to highlight the orders of magnitude in sensitivity gain that our proposed method can provide for short-lived isotopes at the very extreme of existence. Independent developments in efficient deceleration and beam transport should be addressed to be able to perform any laser spectroscopy measurement with this isotope. A realistic estimation of the expected rates of ^{48}Ni requires an experimental characterization of beam properties and stopping efficiencies at the existing RIB facilities [19,20,44]. Below we investigate the energy reconstruction efficiency and resolution for ^{48}Ni isotopes, assuming they are able to reach the interaction region.

The ionization step takes place within the electric field created between two parallel plates. The voltage between the plates, as well as their dimensions, will depend on the energy of the atomic beam. The frequency of the ionization laser can be selected to either directly ionize the atom to the continuum or to excite it to a Rydberg state, from where it can be ionized by the electric field. A position-sensitive detector, located right above the interaction region, can be used to detect individual electrons produced during the ionization process [49–51]. The region on the position sensitive detector where the electrons will be observed is expected to be of similar size to the diameter of the ionization laser beam. Thus, a position sensitive active area of ∼10 mm would be suitable. This will allow the extraction of the atom's initial position and time at the moment of the ionization. After that, the ion will move in the existing electric field until it reaches a second position-sensitive detector, such that the ion's final position and time of flight can also be recorded. The diameter of this position sensitive detector will depend on the energy spread of the beam and the voltage applied between the two electrode plates. The location of the two detectors can be chosen such that virtually all the produced electrons and ions are detected (up to the intrinsic efficiency of the detectors, which can be above 80% [52,53]). Using the initial and final position of the ions, as well as their time of flight, the initial ion velocity can be inferred as described below.

In the ideal case of a charged particle moving in an uniform field created by two parallel plates, one can analytically compute the particle trajectory and hence extract its initial velocity. In reality, different experimental uncertainties need to be accounted for, such as edge effects due to the finite size of the electrodes or uncertainties in the applied potentials and geometry of the experimental array. The effect of these uncertainties can be overcome by using a reference atom with a well-known electronic transition. To provide a realistic example, ^{40}Ca and its $^1S_0(4s^2) \rightarrow {}^3P_1(4s4p)$ transition at 657 nm [54,55] can be used as a reference. For each ionization event, given the known frequency of the excitation step, ν_{laser}, as well as the real frequency in the atom's rest-frame, ν_{atom}, the

ion velocity, v, and thus energy, E can be extracted using the Doppler correction formula. The uncertainty on the measured energy for each event is given by $dE = m_r v c(1 - \frac{v}{c})\frac{d\nu_{\text{atom}}}{\nu_{\text{atom}}}$, where $d\nu_{\text{atom}}$ is the linewidth of the transition, m_r is the atom's mass, and c is the speed of light. The experiment will then be repeated with the atom of interest, labeled as the target atom, recording its initial and final position, time of flight, and the laser frequency measured during an ionization event.

For a system of nonrelativistic particles experiencing only electrostatic fields, two ions with different masses but the same charge state follow identical trajectories. Moreover, the time of flight between two given points is related simply by the square root of the mass ratios of the two species, $R \equiv \sqrt{m_r/m_t}$, where m_t is the mass of the target atom. Thus, the energy of the atom of interest can be obtained by comparing its time of flight, initial, and final positions with those of the reference atom. By predicting the energy of each individual target atom, while knowing the frequency of the laser used during an ionization event, the transition frequency in the atom's rest frame can be obtained on an event-by-event basis by using a neural network (NN).

As the parameter space of the two species is almost identical, NNs are ideally suited for the task, given their well-known power of interpolation. The main drawback of standard, feed-forward NN is that there is no statistically consistent way of estimating the uncertainties associated with the predicted values, which is critical for high-precision experiments. To overcome this challenge, a mixture density network (MDN) can be used [56]. Similar to regular NNs, MDNs take a vector as input, which in this case is $\mathbf{x} = (x_i, x_f, t)$ for each individual ion, which is then passed through one or more hidden layers. However, unlike standard NNs, where the output is a deterministic function of the input, the output of an MDN is represented by a mixture of Gaussian functions:

$$\mathbf{y}(\mathbf{x}) = \sum_{i=1}^{N} \alpha_i(\mathbf{x})\mathcal{N}(\mu_i(\mathbf{x}), \sigma_i(\mathbf{x})), \tag{1}$$

where $\mu_i(\mathbf{x})$, $\sigma_i(\mathbf{x})$ and $\alpha_i(\mathbf{x})$ are functions learnt during the NN training, and N is the number of Gaussian components. In addition, the loss function of an MDN is a log-likelihood loss,

$$\mathcal{L} = -\ln\left(\sum_{i=1}^{N} \frac{\alpha_i(\mathbf{x})}{(2\pi)^{m/2}\sigma_i(\mathbf{x})} \exp\left[-\frac{|\mathbf{E} - \mu(\mathbf{x})|^2}{2\sigma_i(\mathbf{x})^2}\right]\right), \tag{2}$$

where $\mathbf{E}$ is the vector of energies of the training data. Thus, after training the network using the reference atom measurements, the energy value and the associated uncertainty can be predicted for each event measured for the atom of interest.

III. RESULTS AND DISCUSSION

To illustrate the overarching capabilities of our approach, we have selected as the isotopes of interest: ^{120}Sn with its transition $^3P_0(5s^25p^2) \rightarrow {}^1S_0(5s^25p^2)$ at 583 nm [23], ^{8}B with its transition $^2P_{1/2}(2s^22p) \rightarrow {}^2S_{1/2}(2s^23s)$ at 250 nm [57], and ^{48}Ni with the transition $^3F_3(4s^2) \rightarrow {}^5P_2(4s4p^2)$ at 255 nm [58], respectively. Precision isotope shift measurements for the isotopic chains of Sn, Ni, and B are of marked interested for nuclear structures [6,25–27,37,59,60], nuclear matter [33,61], astrophysics [29,30], and new physics searches [23,62,63]. These elements have not been laser cooled yet, consequently, achieving precision measurements with the current laser spectroscopy techniques is particularly challenging.

Numerical simulations of electric fields and ion beam trajectories were performed using the software SIMION [64]. To prove our ability to properly reconstruct the correct rest frame transition frequencies of interest, the ions and electrons are produced in between the two parallel plates, just below a position-sensitive detector. The plates are rectangular, of dimensions 50 cm (along the atoms propagation direction) $\times$ 8 cm. The second position sensitive detector is assumed to have a diameter of 40 mm for the case of ^{120}Sn and ^{8}B and 60 mm for the case of ^{48}Ni (a diameter of 10 mm is suitable for the first position sensitive detector in both cases). The distance between the position sensitive detectors is set to 20 cm for ^{120}Sn, 11 cm for ^{8}B, and 63 cm for ^{48}Ni. These parameters allow virtually all the simulated ions to be detected. The ions' initial position is assumed to be distributed according to a 3D Gaussian with a standard deviation of 1 mm. This is a reasonable value given the laser beam diameters that can be achieved in high-power optical cavities [35]. The simulations were performed with a potential difference between the two plates, located 20 cm apart, of 6 kV for ^{8}B and 20 kV for ^{120}Sn and ^{48}Ni. The electrons are assumed to be produced with nearly zero kinetic energy, which can be achieved by setting the ionization laser close to the IP of the atom or by exciting the atom to a Rydberg state and then performing field ionization. The time-of-flight of the electrons was calculated, resulting in a distribution with a standard deviation of less than 30 ps, which is below the resolution of typical position-sensitive detectors (which we assume in this paper to be 50 ps [52,53]). This uncertainty was added in quadrature to the time-of-flight uncertainty due to detectors' resolution, dt. The uncertainties on the initial, dx_i and final, dx_f position are given by the detector's resolution, which is assumed to be 10 μm. For the reference atom, for each event, a Gaussian noise of mean zero and standard deviation given by the above-mentioned uncertainties (dx_i, dx_f, dt, dE) was added to the values of the initial and final position, time of flight, and initial ion energy, which are then recorded. The same steps were followed for the target atom, except that the initial energy information was assumed to be unknown.

For our numerical simulations, for each of the two considered cases, 2×10^8 ions were generated, corresponding to the reference atom. Half of them were used for training and the other half for validation, allowing us to optimize the hyperparameters of the MDN. The MDN used in this work was implemented in PyTorch [65] and its architecture is shown in Fig. 2. It had one hidden layer of ten nodes and one Gaussian component. This allowed us to achieve the desired level of prediction accuracy, without using a large number of model parameters and thus avoid overfitting. The nonlinearity used for the hidden layer was an exponential linear unit (ELU) activation function, as suggested in Ref. [66], given by

$$\text{ELU}(x) \equiv \begin{cases} x & \text{if } x > 0 \\ e^x - 1 & \text{if } x \leqslant 0. \end{cases} \tag{3}$$

The MDN was trained for 6000 epochs with a starting learning rate of 10^{-2}, which was reduced by a factor of 10

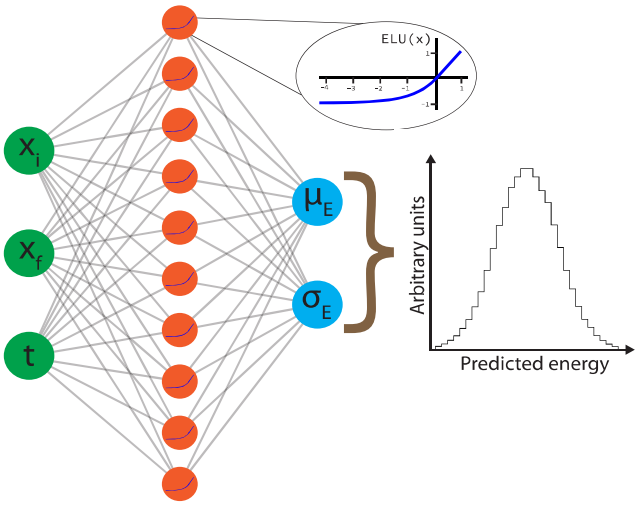

FIG. 2. Architecture of the employed MDN. The initial (x_i) and final (x_f) positions of the ions as well as their time of flight (t) are used as inputs (green disks). They are passed to a hidden layer containing ten nodes (orange disks), each with an exponential linear unit (ELU) activation function, shown in the magnified view. For each input, the MDN predicts a mean and standard deviation for the energy distribution (blue disks), from which the energy of the event can be sampled.

every 1000 epochs. This learning schedule was chosen based on numerical experiments using the validation data, being suitable for achieving the prediction accuracy presented below. To further reduce the risk of overfitting, we used the Adam optimizer [67], which is a stochastic gradient descent method, with a batch size of 1024. Using the trained NN, we predicted the energy and associated rest frame transition frequency uncertainty for each event of the target atom. Figure 3 shows the obtained results. For the simulations involving ^{120}Sn, Fig. 3(a) displays a histogram of the MDN's prediction error defined as $E_{\text{pred}} - E_{\text{real}}$ in eV, having a standard deviation of 2.3 eV. This is a significant uncertainty reduction relative to the initial spread of 1000 eV. For ^{8}B, the energy uncertainty is reduced from 100 eV to 0.4 eV [Fig. 3(c)], while for ^{48}Ni, the energy uncertainty was reduced from 10 keV to only 77 eV [Fig. 3(e)]. In all three cases, ∼95% of the MDN's predictions are within two standard deviations from the true energy value, proving the reliability of the MDN's estimation of individual energies and associated uncertainties.

Using the predicted mean and standard deviation of the energy, as well as the laser frequency used when an event was observed, we can calculate the transition frequency in the rest frame of the target atom, together with its associated uncertainty on an event-by-event basis. In our simulation, this is done as follows. For each event, we sample the true rest-frame frequency using a Lorentzian distribution with mean and linewidth given by the transition of interest mentioned above. We Doppler shift it to the laboratory frame using the real energy of the ion, taken from SIMION, thus obtaining the laser frequency at which the given event was observed. Finally, we Doppler correct back to the ion's rest frame using the MDN predicted energy. The final value of the transition, obtained from N measured events, will be given

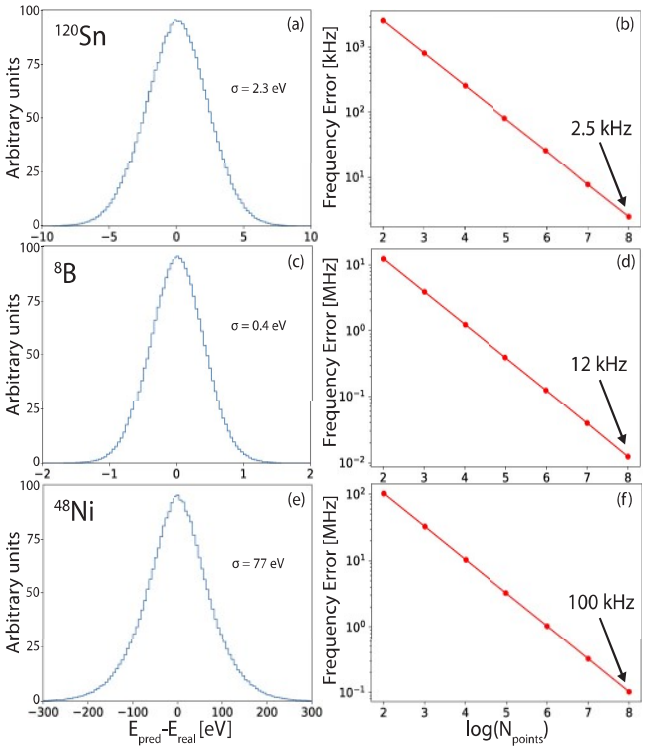

FIG. 3. Results of the energy and frequency reconstruction. The predicted energy error for ^{120}Sn over all events is normally distributed with a standard deviation of 2.3 eV (a). This corresponds to an event-by-event reconstructed rest frame transition frequency with an error around 2 MHz when 100 target atoms events are detected, which is further decreased to only 2.5 kHz for 10^8 events (b). For ^{8}B, an energy spread of 0.4 eV is obtained (c), corresponding to an uncertainty on the rest frame transition frequency of ∼1.2 MHz for 10^4 events (d). For ^{48}Ni, the energy uncertainty is reduced to 77 eV (e), leading to a reconstructed rest frame transition frequency uncertainty at the MHz level, for 10^6 events (f).

by $\nu_{\text{pred}} = \sum_i^N \frac{\nu_i}{d\nu_i^2} / \sum_i^N \frac{1}{d\nu_i^2}$ and its associated uncertainty: $d\nu_{\text{pred}} = 1/\sum_i^N \frac{1}{d\nu_i^2}$, where ν_i and $d\nu_i$ are the predicted frequency and uncertainty, respectively, for the ith target atom event. In Fig. 3, we show the error in the calculated frequency as a function of the number of target atom events for the considered isotopes. For ^{120}Sn, we can correctly predict the true value of the rest-frame transition frequency with an uncertainty of about 2 MHz with as little as 100 events and reach a precision at the 1 kHz level when 10^8 events of the target atom are measured. For ^{8}B, 10^4 events are needed to reach an uncertainty of ∼1 MHz on the measured transitions. This will allow the extraction of the charge radius of ^{8}B with 10% relative uncertainty [28,57]. Finally, for ^{48}Ni, an uncertainty of ∼100 MHz can be achieved for only 10^2 events. This level of precision will be enough for the extraction of the charge radius of ^{48}Ni with 10% relative uncertainty [2,60]. We emphasize that performing spectroscopic measurements on light elements, such as boron, is challenging and currently impossible for ^{8}B [28], while studying very short lived isotopes, such as ^{48}Ni is completely out of the reach using available experimental techniques [14,20,44].

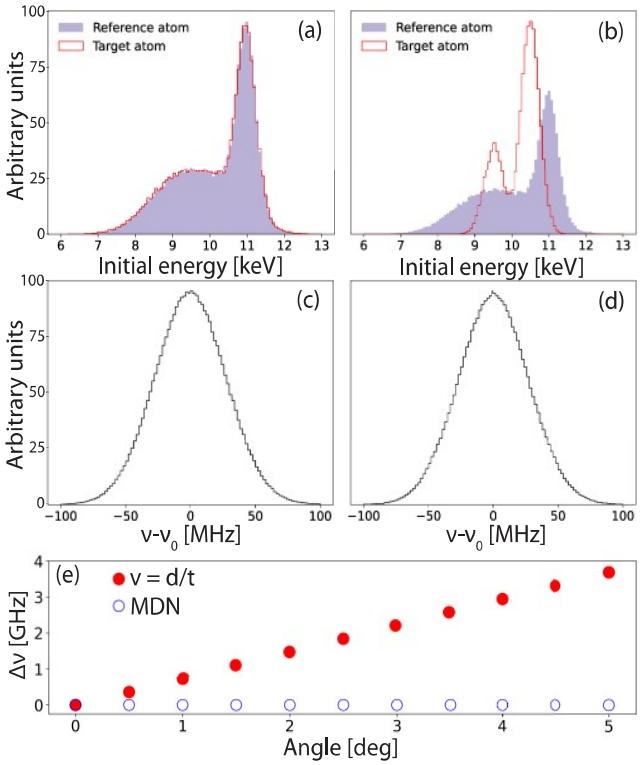

FIG. 4. Results of the frequency extraction for ions with non-Gaussian distributed initial energies for the ^{120}Sn case. The energy histograms when the reference and target atom having the same and different initial energy distributions are shown in (a) and (b), while the associated reconstructed rest-frame frequency of the target atom using our proposed method, relative to the true rest-frame frequency, ν_0, is shown in (c) and (d). (e) Difference, $\Delta\nu$, between true and reconstructed frequency, when using an MDN (blue circles) and when inferred from the distance and time information of the target atom only (red filled circles). The results are shown for different tilt angles of one electrode plate relative to the other (see main text for details).

To further explore the robustness of our approach in the case where the initial energy is not symmetrically distributed, we performed simulations assuming an arbitrary energy distribution, as shown in Fig. 4(a). This is particularly interesting as it indicates that our proposed scheme can be applied universally, for atoms and/or ions produced by diverse physical processes. For such a situation, simply applying a regular Doppler shift to the entire atomic ensemble, assuming a fixed acceleration voltage, would lead to distorted line shapes and add significant systematic uncertainties to the value of the extracted transition. However, as our method can recover the energy and hence the rest-frame frequency of individual atoms, using only the recorded parameters, it allows the scheme to be independent of the original energy distribution and produce consistent results for arbitrary distributions. This is shown in Fig. 4(c) for the case of ^{120}Sn, where the distribution of the reconstructed rest-frame transition frequency has a well-behaved shape, from which the correct value of the frequency can be extracted with uncertainties at the 100 kHz level, with only 10^4 events.

Finally, we explore the situation in which the reference and target atoms have different initial energy distributions [Fig. 4(b)]. This is of interest when the production mechanism is a particularly violent one, as is often the case at radioactive beam facilities. The results obtained in this case are shown in Fig. 4(d). Again, we can recover the correct rest-frame transition frequency with similar uncertainties as described above, using arbitrary distributions for the initial energy. Similar results are obtained for the cases of ^{8}B and ^{48}Ni atoms with initial energies on the order of ∼1 keV and ∼100 keV, respectively, being able to reconstruct the rest frame transition frequencies with uncertainties comparable to those displayed in Fig. 3.

To study possible systematic uncertainties, numerical simulations under the following experimental conditions were performed: (i) one of the plates was tilted with respect to the beam propagation direction at different angles between 0 and 5 degrees, (ii) both plates were simultaneously tilted with respect to the horizontal at angles between 0 and 2 degrees, (iii) up to 10% relative uncertainties on the voltage applied to the two plates as well as on the distance between the plates were assumed, (iv) up to 5 millimeters of uncertainty on the vertical location of the ionization was assumed, (v) up to 5 millimeters of uncertainty on the distance between the two position sensitive detectors was assumed, and (vi) an additional transverse energy component of up to 1 keV to the ions was introduced. These values are significantly larger than one would expect from a properly implemented experimental setup. However, these uncertainties do not have a significant effect on the energy reconstruction of events. This is expected, as described above, given that during training, the MDN is able to learn all these variations of the experimental parameters which are encoded in the trajectories of the reference atoms and account for them in the predictions of the energies of the target atom.

A simple reconstruction of the target atom's velocity, taken as the ratio between the traveled distance and the time of flight, would be sensitive to the above-mentioned systematic uncertainties, leading to a wrong value of the rest frame transition frequency of the atom. The result of this approach is illustrated in Fig. 4(e), where the error in the reconstructed frequency is shown for different tilt angles between the two electrode plates. It can be seen that the shift in the reconstructed frequency is on the order of a few GHz with respect to the true rest-frame frequency (red filled circles). Moreover, this shift can't be reduced by increasing the accumulated statistics, thus being a limiting factor in extracting the physics of interest for most experiments. Additional experimental unknowns, such as an uncertainty in the distance between the two position-sensitive detectors, can lead to errors of similar magnitude, with ∼1 GHz frequency shifts for an uncertainty of two millimeters. On the other hand, it can be seen in Fig. 4(e) that the use of an MDN is largely insensitive to such experimental uncertainties (blue circles).

The main conditions that need to be fulfilled for the energy reconstruction to be successful with our proposed method are (i) the parameter space of the target atom needs to be contained within the parameter space of the reference one and (ii) enough events need to be recorded during the reference atom measurement for any region of interest in the parameter space. The first condition should be fulfilled by the geometric

constraints of the setup, i.e., the electron and ion should hit the position-sensitive detector for both ions. Moreover, one can easily compare the spatial and temporal information of the two species and confirm the validity of this assumption. The second condition depends only on the statistics accumulated while measuring the reference atom, which can be easily increased by several orders of magnitude if needed.

IV. CONCLUSION

We proposed a simple, versatile, and powerful experimental technique, suitable for performing high-resolution spectroscopy on fast, hot, short-lived isotopes produced with arbitrary energy distributions and large energy spreads. Using the temporal and spatial information of ions and corresponding electrons produced in a laser ionization process, the atoms' initial vector velocity can be reconstructed on an event-by-event basis, enabling precision measurements of the rest-frame transition frequency of the species of interest.

The described method is very efficient in terms of computing time, as the MDN needs to be trained initially, only once for a given energy range, using a reference atom. After that, predictions can be made for any other atom and transitions of interest. By increasing the number of events for the atom of interest, N_t, the uncertainty on the measured transition frequency, which scales as $\frac{1}{\sqrt{N_t}}$, can be further reduced. This can also be achieved by using detectors with better spatial and temporal resolutions compared to the ones considered here. Possible NN prediction biases can be estimated using the validation data set of the reference atom. The MDN predictions could potentially be further improved by using different learning rate schedules or trying more complex architectures (in terms of layers, nodes per layers, or number of Gaussian components), compared to the one presented in this paper. The performance of other types of NN, able to estimate uncertainties for the predicted results, such as Bayesian NN [68], can also be investigated. Non-NN based methods could also offer a possible pathway for estimating the energies of interest. For example, for each target event, the energy and the associated uncertainty could be estimated in terms of the mean and standard deviation of the energy of the closest reference events in parameter space, where the number of such events would be optimized using the validation data.

The ability to perform precision measurements on fast beams with large energy spreads opens the way to studying short-lived isotopes at the extreme of existence, with lifetimes on the order of milliseconds or less. Such species can already be produced at different radioactive beam facilities worldwide, but their laser spectroscopic investigation is currently impossible with the available techniques. The proposed approach also opens the possibility to study isomeric states with sub-millisecond lifetimes that can be produced in flight by nuclear reactions.

ACKNOWLEDGMENTS

The authors thank the discussions with S. G. Wilkins, C. S. Sumithrarachchi, P. Mueller, F. C. Pastrana Cruz, and M. Paula Montes. This work was supported by the Office of Nuclear Physics, U.S. Department of Energy, under Grants No. DE-SC0021176 and No. DE-SC0021179, and the Jarve Seed fund. D.A.T. thanks the Laboratory of Nuclear Science at MIT for their hospitality during the sabbatical year when this work was performed, and the Universidad Nacional de Colombia for support under Grants No. 51111 and No. 51119.

[1] G. Arrowsmith-Kron, M. Athanasakis-Kaklamanakis, M. Au, J. Ballof, R. Berger, A. Borschevsky, A. A. Breier, F. Buchinger, D. Budker, L. Caldwell *et al.*, Opportunities for fundamental physics research with radioactive molecules, arXiv:2302.02165.

[2] X. F. Yang, S. J. Wang, S. G. Wilkins, and R. F. Garcia Ruiz, Laser spectroscopy for the study of exotic nuclei, Prog. Part. Nucl. Phys. **129**, 104005 (2023).

[3] M. Block, M. Laatiaoui, and S. Raeder, Recent progress in laser spectroscopy of the actinides, Prog. Part. Nucl. Phys. **116**, 103834 (2021).

[4] R. F. Garcia Ruiz, M. L. Bissell, K. Blaum, A. Ekström, N. Frömmgen, G. Hagen, M. Hammen, K. Hebeler, J. D. Holt, G. R. Jansen *et al.*, Unexpectedly large charge radii of neutron-rich calcium isotopes, Nat. Phys. **12**, 594 (2016).

[5] A. J. Miller, K. Minamisono, A. Klose, D. Garand, C. Kujawa, J. D. Lantis, Y. Liu, B. Maaß, P. F. Mantica, W. Nazarewicz *et al.*, Proton superfluidity and charge radii in proton-rich calcium isotopes, Nat. Phys. **15**, 432 (2019).

[6] C. Gorges, L. V. Rodríguez, D. L. Balabanski, M. L. Bissell, K. Blaum, B. Cheal, R. F. Garcia Ruiz, G. Georgiev, W Gins, H. Heylen *et al.*, Laser spectroscopy of neutron-rich tin isotopes: A discontinuity in charge radii across the N= 82 shell closure, Phys. Rev. Lett. **122**, 192502 (2019).

[7] R. P. de Groote, J. Billowes, C. L. Binnersley, M. L. Bissell, T. E. Cocolios, T. Day Goodacre, G. J. Farooq-Smith, D. V. Fedorov, K. T. Flanagan, S. Franchoo *et al.*, Measurement and microscopic description of odd–even staggering of charge radii of exotic copper isotopes, Nat. Phys. **16**, 620 (2020).

[8] M. Reponen, R. P. de Groote, L. Al Ayoubi, O. Beliuskina, M. L. Bissell, P. Campbell, L. Cañete, B. Cheal, K. Chrysalidis, C. Delafosse *et al.*, Evidence of a sudden increase in the nuclear size of proton-rich silver-96, Nat. Commun. **12**, 4596 (2021).

[9] A. Koszorús, X. F. Yang, W. G. Jiang, S. J. Novario, S. W. Bai, J. Billowes, C. L. Binnersley, M. L. Bissell, T. E. Cocolios, B. S. Cooper *et al.*, Charge radii of exotic potassium isotopes challenge nuclear theory and the magic character of $N = 32$, Nat. Phys. **17**, 439 (2021).

[10] A. R. Vernon, R. F. Garcia Ruiz, T. Miyagi, C. L. Binnersley, J. Billowes, M. L. Bissell, J. Bonnard, T. E. Cocolios, J. Dobaczewski, G. J. Farooq-Smith *et al.*, Nuclear moments of indium isotopes reveal abrupt change at magic number 82, Nat. Commun. **607**, 260 (2022).

[11] T. Manovitz, R. Shaniv, Y. Shapira, R. Ozeri, and N. Akerman, Precision measurement of atomic isotope shifts using a two-isotope entangled state, Phys. Rev. Lett. **123**, 203001 (2019).

[12] J. Hur, D. P. L. Aude Craik, I. Counts, E. Knyazev, L. Caldwell, C. Leung, S. Pandey, J. C. Berengut, A. Geddes, W. Nazarewicz

et al., Evidence of two-source king plot nonlinearity in spectroscopic search for new boson, Phys. Rev. Lett. **128**, 163201 (2022).

[13] R. Neugart, J. Billowes, M. L. Bissell, K. Blaum, B. Cheal, K. T. Flanagan, G. Neyens, W. Nörtershäuser, and D. T. Yordanov, Collinear laser spectroscopy at ISOLDE: New methods and highlights, J. Phys. G: Nucl. Part. Phys. **44**, 064002 (2017).

[14] K. Minamisono, P. F. Mantica, A. Klose, S. Vinnikova, A. Schneider, B. Johnson, and B. R. Barquest, Commissioning of the collinear laser spectroscopy system in the BECOLA facility at NSCL, Nucl. Instrum. Methods Phys. Res., Sect. A **709**, 85 (2013).

[15] R. F. Garcia Ruiz, R. Berger, J. Billowes, C. L. Binnersley, M. L. Bissell, A. A. Breier, A. J. Brinson, K. Chrysalidis, T. E. Cocolios, B. S. Cooper *et al.*, Spectroscopy of short-lived radioactive molecules, Nature (London) **581**, 396 (2020).

[16] S. M. Udrescu, A. J. Brinson, R. F. Garcia Ruiz, K. Gaul, R. Berger, J. Billowes, C. L. Binnersley, M. L. Bissell, A. A. Breier, K. Chrysalidis *et al.*, Isotope shifts of radium monofluoride molecules, Phys. Rev. Lett. **127**, 033001 (2021).

[17] S.-M. Udrescu, S. G. Wilkins, A. Breier, R. F. Garcia Ruiz, M. Athanasakis-Kaklamanakis, M. Au, I. Belosevic, R. Berger, M. Bissell, C. L. Binnersley C *et al.*, Precision spectroscopy and laser-cooling scheme of a radium-containing molecule, Nat. Phys. (2024).

[18] S. G. Wilkins, S.-M. Udrescu, M. Athanasakis-Kaklamanakis, R. F. Garcia-Ruiz, M. Au, I. Belosevic, R. Berger, M. Bissell, A. A. Breier, A. J. Brinson *et al.*, Observation of the distribution of nuclear magnetization in a molecule, arXiv:2311.04121 (2023).

[19] T. Glasmacher, B. Sherrill, W. Nazarewicz, A. Gade, P. Mantica, J. Wei, G. Bollen, and B. Bull, Facility for rare isotope beams update for nuclear physics news, Nucl. Phys. News **27**, 28 (2017).

[20] Y. Yano and T. Motobayashi, Radioactive Isotope Beam Factory at RIKEN (RIBF), Nucl. Phys. News **17**, 5 (2007).

[21] R. F. Garcia Ruiz, A. R. Vernon, C. L. Binnersley, B. K. Sahoo, M. Bissell, J. Billowes, T. E. Cocolios, W. Gins, R. P. de Groote, K. T. Flanagan *et al.*, High-precision multiphoton ionization of accelerated laser-ablated species, Phys. Rev. X **8**, 041005 (2018).

[22] J. Jovanović and R. F. Garcia Ruiz, Modeling of transient interference phenomena in colinear laser spectroscopy, Phys. Rev. A **107**, 013104 (2023).

[23] D. R. Leibrandt, S. G. Porsev, C. Cheung, and M. S. Safronova, Prospects of a thousand-ion Sn^{2+} Coulomb-crystal clock with sub-10^{-19} inaccuracy, arXiv:2205.15484.

[24] D. T. Yordanov, L. V. Rodríguez, D. L. Balabanski, J. Bieroń, M. L. Bissell, K. Blaum, B. Cheal, J. Ekman, G. Gaigalas, R. F. Garcia Ruiz *et al.*, Structural trends in atomic nuclei from laser spectroscopy of tin, Commun. Phys. **3**, 107 (2020).

[25] M. H. Smedberg, T. Baumann, T. Aumann, L. Axelsson, U. Bergmann, M. J. G. Borge, D. Cortina-Gil, L. M. Fraile, H. Geissel, L. Grigorenko *et al.*, New results on the halo structure of ^{8}B, Phys. Lett. B **452**, 1 (1999).

[26] G. A. Korolev, A. V. Dobrovolsky, A. G. Inglessi, G. D. Alkhazov, P. Egelhof, A. Estradé, I. Dillmann, F. Farinon, H. Geissel, S. Ilieva *et al.*, Halo structure of ^{8}B determined from intermediate energy proton elastic scattering in inverse kinematics, Phys. Lett. B **780**, 200 (2018).

[27] A. V. Dobrovolsky, G. A. Korolev, A. G. Inglessi, G. D. Alkhazov, G. Coló, I. Dillmann, P. Egelhof, A. Estradé, F. Farinon, H. Geissel *et al.*, Nuclear-matter distribution in the proton-rich nuclei ^{7}Be and ^{8}B from intermediate energy proton elastic scattering in inverse kinematics, Nucl. Phys. A **989**, 40 (2019).

[28] Bernhard Maaß, Laser spectroscopy of the boron isotopic chain, Ph.D. thesis, Technische Universität Darmstadt, 2020.

[29] J. N. Bahcall, F. H. Walter S. H. Lubow, P. D. Parker, and R. K. Ulrich, Standard solar models and the uncertainties in predicted capture rates of solar neutrinos, Rev. Mod. Phys. **54**, 767 (1982).

[30] K. Riisager and A. S. Jensen, The radius of ^{8}B and solar neutrinos, Phys. Lett. B **301**, 6 (1993).

[31] B. Blank, M. Chartier, S. Czajkowski, J. Giovinazzo, M. S. Pravikoff, J.-C. Thomas, G. de France, F. de Oliveira Santos, M. Lewitowicz, C. Borcea *et al.*, Discovery of doubly magic ^{48}Ni, Phys. Rev. Lett. **84**, 1116 (2000).

[32] L. V. Grigorenko, R. C. Johnson, I. G. Mukha, I. J. Thompson, and M. V. Zhukov, Theory of two-proton radioactivity with application to ^{19}Mg and ^{48}Ni, Phys. Rev. Lett. **85**, 22 (2000).

[33] S. V. Pineda, K. König, D. M. Rossi, B. A. Brown, A. Incorvati, J. Lantis, K. Minamisono, W. Nörtershäuser, J. Piekarewicz, R. Powel *et al.*, Charge radius of neutron-deficient ^{54}Ni and symmetry energy constraints using the difference in mirror pair charge radii, Phys. Rev. Lett. **127**, 182503 (2021).

[34] W. Demtröder, *Laser Spectroscopy 2: Experimental Techniques* (Springer, New York, 2015).

[35] H. Carstens, S. Holzberger, J. Kaster, J. Weitenberg, V. Pervak, A. Apolonski, E. Fill, F. Krausz, and I. Pupeza, Large-mode enhancement cavities, Opt. Express **21**, 11606 (2013).

[36] A. R. Vernon, J. Billowes, C. L. Binnersley, M. L. Bissell, T. E. Cocolios, G. J. Farooq-Smith, K. T. Flanagan, R. F. Garcia Ruiz, W. Gins, R. P. de Groote *et al.*, Simulation of the relative atomic populations of elements $1 \leqslant Z \leqslant 89$ following charge exchange tested with collinear resonance ionization spectroscopy of indium, Spectrochim. Acta, Part B **153**, 61 (2019).

[37] F. P. Gustafsson, C. M. Ricketts, M. L. Reitsma, R. F. Garcia Ruiz, S. W. Bai, J. C. Berengut, J. Billowes, C. L. Binnersley, A. Borschevsky, T. E. Cocolios *et al.*, Tin resonance-ionization schemes for atomic- and nuclear-structure studies, Phys. Rev. A **102**, 052812 (2020).

[38] A. P. Galván *et al.*, Status update on the β-ν Correlation Measurement in the β Decay of ^{8}B, in *Proceedings of the Conference on Advances in Radioactive Isotope Science (ARIS2014)* (Tokyo, Japan, 2015), p. 030071.

[39] J. Dilling, R. Krücken, and G. Ball, ISAC overview, Hyperfine Interact. **225**, 1 (2014).

[40] I. D. Moore, P. Dendooven, and J. Ärje, *The IGISOL technique—three decades of developments*, Three decades of research using IGISOL technique at the University of Jyväskylä A Portrait of the Ion Guide Isotope Separator On-Line Facility in Jyväskylä (Berlin, Germany, 2014), pp. 15–60.

[41] M. J Borge and B. Jonson, ISOLDE past, present and future, J. Phys. G: Nucl. Part. Phys. **44**, 044011 (2017).

[42] R. Kallenbach, M. Gonin, P. Bochsler, and A. Bürgi, Charge exchange of B, C, O, Al, Si, S, F and Cl passing through thin carbon foils at low energies: Formation of negative ions, Nucl. Instrum. Methods Phys. Res., Sect. B **103**, 111 (1995).

[43] J. M. Brown and A. Carrington, *Rotational Spectroscopy of Diatomic Molecules* (Cambridge University Press, Cambridge, 2003).

[44] K. Cooper, C. S. Sumithrarachchi, D. J. Morrissey, A. Levand, J. A. Rodriguez, G. Savard, S. Schwarz, and B. Zabransky, Extraction of thermalized projectile fragments from a large volume gas cell, Nucl. Instrum. Methods Phys. Res., Sect. A **763**, 543 (2014).

[45] C. Sumithrarachchi (private communication).

[46] T. Schenkel, M. A. Briere, H. Schmidt-Böcking, K. Bethge, and D. H. Schneider, Electronic sputtering of thin conductors by neutralization of slow highly charged ions, Phys. Rev. Lett. **78**, 2481 (1997).

[47] T. Schenkel, A. V. Hamza, A. V. Barnes, and D. H. Schneider, Interaction of slow, very highly charged ions with surfaces, Prog. Surf. Sci. **61**, 23 (1999).

[48] R. A. Wilhelm, E. Gruber, J. Schwestka, R. Heller, S. Fascko, and F. Aumayr, Neutralization dynamics of slow highly charged ions in 2D materials, Appl. Sci. **8**, 1050 (2018).

[49] R. Dörner, V. Mergel, O. Jagutzki, L. Spielberger, J. Ullrich, R. Moshammer, and H. Schmidt-Böcking, Cold target recoil ion momentum spectroscopy: A 'momentum microscope' to view atomic collision dynamics, Phys. Rep. **330**, 95 (2000).

[50] J. Ullrich, R. Moshammer, A. Dorn, R. Dörner, L. P. H. Schmidt, and H. Schmidt-Böcking, Recoil-ion and electron momentum spectroscopy: Reaction-microscopes, Rep. Prog. Phys. **66**, 1463 (2003).

[51] W. Jiang, X. Wang, S. Zhang, R. Dong, Y. Guo, J. Feng, Z. Shen, Z. Zhu, and Y. Jiang, A reaction microscope for AMO science at Shanghai soft X-ray free-electron laser facility, Appl. Sci. **12**, 1821 (2022).

[52] X. Gong, P. He, Q. Song, Q. Ji, H. Pan, J. Ding, F. He, H. Zeng, and J. Wu, Two-dimensional directional proton emission in dissociative ionization of H_2, Phys. Rev. Lett. **113**, 203001 (2014).

[53] U. S. Sainadh, H. Xu, X. Wang, A. Atia-Tul-Noor, W. C Wallace, N. Douguet, A. Bray, I. Ivanov, K. Bartschat, A. Kheifets *et al.*, Attosecond angular streaking and tunnelling time in atomic hydrogen, Nature (London) **568**, 75 (2019).

[54] A. Lurio, R. L. de Zafra, and R. J. Goshen, Lifetime of the first $^1P_1$ state of zinc, calcium, and strontium, Phys. Rev. **134**, A1198 (1964).

[55] R. Engleman and E. S. Chang, High-resolution spectroscopy of Ca, Sr and Ba hollow cathodes, in *Fourier Transform Spectroscopy* (Optica Publishing Group, Washington DC, 1999).

[56] C. M. Bishop, Mixture density networks, *Neural Computing Research Group, Aston University*, Technical Report NCRG/94/004, 1994.

[57] B. Maaß, T. Hüther, K. König, J. Krämer, J. Krause, A. Lovato, P. Müller, K. Pachucki, M. Puchalski, R. Roth *et al.*, Nuclear charge radii of ^{10,11}B, Phys. Rev. Lett. **122**, 182501 (2019).

[58] M. C. E. Huber and R. J. Sandeman, Oscillator strengths of ultraviolet NI I lines from hook-method and absorption measurements in a furnace, Astron. Astrophys. **86**, 95 (1980).

[59] L. V. Rodríguez, D. L. Balabanski, M. L. Bissell, K. Blaum, B. Cheal, G. De Gregorio, J. Ekman, R. F. Garcia Ruiz, A. Gargano, G. Georgiev *et al.*, Doubly-magic character of ^{132}Sn studied via electromagnetic moments of ^{133}Sn, Phys. Rev. C **102**, 051301(R) (2020).

[60] S. Malbrunot-Ettenauer, S. Kaufmann, S. Bacca, C. Barbieri, J. Billowes, M. L. Bissell, K. Blaum, B. Cheal, T. Duguet, R. F. Garcia Ruiz *et al.*, Nuclear charge radii of the nickel isotopes $^{58-68,70}$Ni, Phys. Rev. Lett. **128**, 022502 (2022).

[61] J. Tanaka, Z. Yang, S. Typel, S. Adachi, S. Bai, P. van Beek, D. Beaumel, Y. Fujikawa, J. Han, S. Heil *et al.*, Formation of α clusters in dilute neutron-rich matter, Science **371**, 260 (2021).

[62] P.-G. Reinhard, W. Nazarewicz, and R. F. Garcia Ruiz, Beyond the charge radius: The information content of the fourth radial moment, Phys. Rev. C **101**, 021301(R) (2020).

[63] R. A. Müller, V. A. Yerokhin, A. N. Artemyev, and A. Surzhykov, Nonlinearities of King's plot and their dependence on nuclear radii, Phys. Rev. A **104**, L020802 (2021).

[64] D. A. Dahl, SIMION 3D Version 7.0, computer program, Idaho National Engineering and Environmental Laboratory.

[65] A. Paszke, S. Gross, F. Massa, A. Lerer, J. Bradbury, G. Chanan, T. Killeen, Z. Lin, N. Gimelshein, L. Antiga *et al.*, PyTorch: An imperative style, high-performance deep learning library, in *Advances in Neural Information Processing Systems*, 32 ed. (Curran Associates, Inc., 2019), pp. 8024–8035.

[66] A. B. Guillaumes, Mixture density networks for distribution and uncertainty estimation, Ph.D. thesis, Universitat Politècnica de Catalunya. Facultat d'Informàtica de Barcelona, 2017.

[67] D. P. Kingma and J. Ba, Adam: A method for stochastic optimization, arXiv:1412.6980.

[68] R. M. Neal, *Bayesian Learning for Neural Networks* (Springer Science & Business Media, 2012), Vol. 118.

6.2 Optical Cavity

Given the different geometry for the ionization step compared to our previous experiments (see Chapter 4), several challenges had to be overcome. On the one hand, because we aim to bypass the cooling and bunching step, we expect to have a continuous beam of atoms in our interaction region. As the ionization is performed perpendicularly, using a pulsed laser means that even for high repetition rates ($10-100$ kHz), most of the atoms will miss the laser pulses. Thus, a continuous wave (CW) laser is clearly preferred. However, given that in most cases, the ionization step is non-resonant, a high spectral power density is needed, which is difficult to achieve with commercially available CW laser, and it can also pose challenges in terms of the damage threshold of the windows required to send the light inside the vacuum chamber and ways in which the power can be safely and efficiently damped. The efficiency of the non-resonant ionizing process for an excited atom, ϵ, can be written as [188]:

$$\epsilon \propto \frac{1}{1 + R_e/(\sigma_i n_L)}, \tag{6.1}$$

where R_e is the relaxation rate of the excited level, σ_i is the non-resonant ionization cross-section, and n_L is the photon flux density for the ionization laser. Usual values for σ_i for atoms are on the order of $\sigma_i \sim 10^{-17}$ cm^2 [188]. For an excited state with a life time of 50 ns, the relaxation rate is $R_e = 2 \times 10^7$ s^{-1}. Thus, to achieve $\sim 70\%$ ionization efficiency (this is only the intrinsic efficiency of the process, and it ignores other effects, such as the ion detection efficiency), we would need a CW laser of power 10 kW at a wavelength of 1064 nm, focused to an area of 1 mm^2 (see below for details of the laser parameters). The approach we decided to pursue to achieve such a high CW power density is using an enhancement cavity placed perpendicularly to the atom's trajectories. This can allow high enough power for efficient ionization, as described below, while ensuring that the high-power light travels only inside the cavity, which can be placed entirely inside the vacuum chamber. In addition, to further reduce the number of ionization events coming from excited levels other than the ones of interest (e.g., previously excited in the charge exchange cell), a 1064 nm laser will be used for the ionization step, unlike the RaF experiment (see Chapter 4) where 355 nm and 532 nm lasers were used [51–54].

In order to be able to spectroscopically address as many atoms as possible among these reaching the interaction region, which is especially desirable for species produced in very small amounts (< 1/s), a large laser beam diameter, on the order of 1 mm, is needed. Going larger than this, while possible, is not desirable as the resolution of the VMI setup degrades if atoms are produced from a too wide area (bigger than a few mm), as described in Sec 6.3. To achieve a mm size beam diameter, a bow-tie cavity was chosen, instead of a two mirror Fabry–Pérot (FP) cavity. The latter one would require a total length on the order of 1 meter (distance between the 2 mirrors) for a ~ 1 mm beam diameter, which is impractical for our experimental setup, given that we aim to fit the whole cavity inside the ultra-high vacuum (UHV) chamber in which the laser-atom interaction takes place. There are 2 main designs for a bow-tie cavity: one having all 4 mirrors concave, and one having 2 concave and 2 flat mirrors [254]. We decided to pursue the second option, as it has a bigger parameter space (given by the location of the 4 mirrors and the curvature of the 2 concave mirrors)

over which the cavity is stable, and hence, it is more robust to external perturbations, such as vibrations or temperature variation [254].

6.2.1 Gaussian Beams

In order to properly describe the behavior of the laser inside the optical cavity, a Gaussian beam model is used [255]. This will allow us to easily and accurately compute various parameters needed for our setup, such as the laser beam diameter needed to mode match the optical cavity mode or the focal length and location of the lenses needed to achieve that diameter for an initial laser diameter (see Sec. 6.2.2).

Using the paraxial approximation, a Gaussian beam solution to the source-free wave equation, based on Maxwell's equations, for a wave moving in the z-direction can be written as [255]:

$$u(x,y,z) = \exp\left\{-i\left(P(z) + \frac{k}{2q(z)}\left(x^2+y^2\right)\right)\right\}e^{-ikz}, \tag{6.2}$$

where u can be any electric or magnetic field component, k is the magnitude of the wave vector, and $q(z)$ is the complex beam parameter, which is crucial for computing the changes in the Gaussian beam properties as it travels through various optical media, as shown below. This parameter can be written as:

$$\frac{1}{q} = \frac{1}{R} - i\frac{\lambda}{n\pi\omega^2}, \tag{6.3}$$

which, upon substituting in Eq. 6.2 leads to:

$$u(x,y,z) = \exp\left\{-i\left(P(z) + kz + k\frac{r^2}{2R}\right) - \frac{r^2}{\omega^2}\right\}, \tag{6.4}$$

with $r^2 = x^2 + y^2$. Thus, the field components of the wave are characterized by a phase shift given by the terms in the round brackets and a Gassian-shaped amplitude in the radial direction, given by the second term in the exponential. From this, it becomes clear that w gives the radial intensity profile of the Gaussian beam, while R is the wavefront radius of the beam. These properties of the Gaussian beam are shown diagrammatically in Fig. 6.1 a). An important parameter coming from this formalism and also shown in Fig. 6.1 a) is the minimum diameter the beam can achieve, called the beam waist and usually denoted as w_0, which is obtained when the R becomes infinite. From Eq. 6.2 and 6.3 we can then get the important relationships [255]:

$$\begin{aligned} w(z) &= w_0\left[1 + \left(\frac{\lambda z}{n\pi\omega_0^2}\right)^2\right]^{1/2} = w_0\left[1 + \left(\frac{z}{z_R}\right)^2\right]^{1/2} \\ R(z) &= z\left[1 + \left(\frac{n\pi\omega_0^2}{\lambda z}\right)\right] = z + \frac{z_R^2}{z}. \end{aligned} \tag{6.5}$$

giving the change in the beam diameter and wavefront radius when moving away from the waist, where we defined the Rayleigh length:

$$z_R \equiv \frac{n\pi\omega_0^2}{\lambda}, \tag{6.6}$$

as the distance from the waist where the spot size increases by $\sqrt{2}$ (see Fig. 6.1 a)).

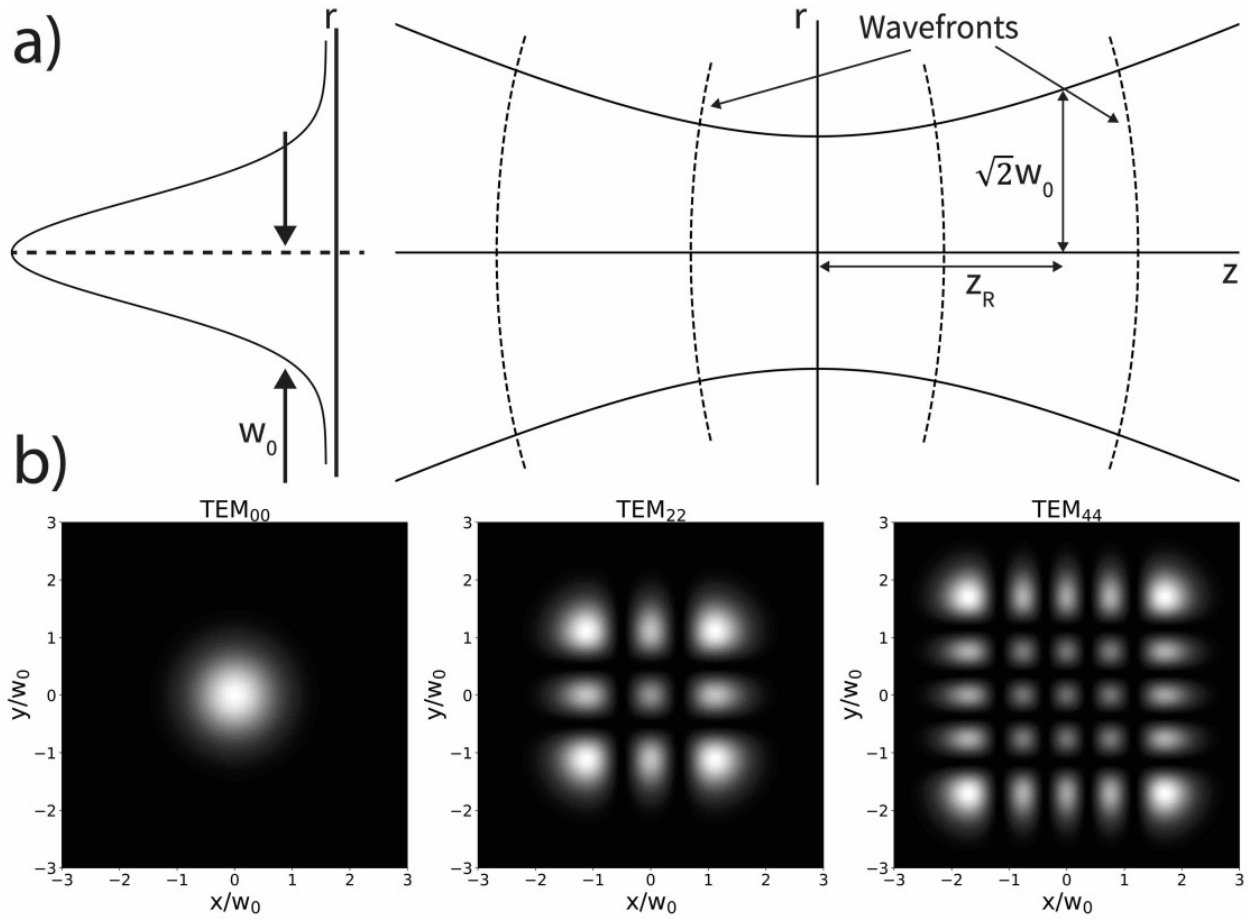

Figure 6.1: a) On the left, the intensity profile of a Gaussian beam is shown (TEM_{00} Hermite-Gaussian mode) along the radial direction when the beam has its smallest diameter. The location of the waist, defined as twice the standard deviation of the Gaussian intensity distribution, is marked. On the right, we show the propagation of a Gaussian beam along the z-axis (along the direction of propagation of the beam). We show examples of wavefronts at different values along the z-axis, as well as the location of the Raylength length (z_R). The increment of the radial profile away from the waist ($z = 0$) is clear. b) Example of Hermite-Gaussian 2D distributions. We show the case of TEM_{00}, TEM_{22} and TEM_{44} modes.

It can be shown that the other parameter in Eq. 6.2, $P(z)$, is given by [255]:

$$P(z) = -i \ln \sqrt{1 + \left(\frac{z}{z_R}\right)^2} + \tan^{-1}\left(\frac{z}{z_R}\right). \tag{6.7}$$

The first term on the right leads to a decrease of the field amplitude with z. The second one leads to an additional phase shift in the field of the Gaussian beam (see Eq. 6.2), called

the Gouy phase, which is important for determining the location in frequency space of the optical cavity resonances for different transverse modes, as explained in Sec. 6.2.2.

As mentioned above, the complex beam parameter, q, is very useful in describing the behavior of the beam as it passes through optical media. This is usually calculated using the ABCD matrix formalism [255]. While usually applied to ray optics, it can be easily extended to Gaussian beams. In this approach, a given optical element has associated to it a 2×2 matrix, $\begin{pmatrix} A & B \\ C & D \end{pmatrix}$. The value of the q parameter after the optical element, q_2, is related to the one before, q_1, by [255]:

$$q_2 = \frac{Aq_1 + B}{Cq_1 + D}. \tag{6.8}$$

The matrices associated with some common optical elements: free-space propagation over a distance d, propagation through a thin lens of focal length f, reflection from a mirror of curvature R, and propagation through a slab of thickness d and index of refraction n are given by [255]:

$$\begin{aligned} \text{Free} - \text{space} : & \begin{pmatrix} 1 & d \\ 0 & 1 \end{pmatrix} \\ \text{Thin lens} : & \begin{pmatrix} 1 & 0 \\ -1/f & 1 \end{pmatrix} \\ \text{Mirror} : & \begin{pmatrix} 1 & 0 \\ -2/R & 1 \end{pmatrix} \\ \text{Slab} : & \begin{pmatrix} 1 & d/n \\ 0 & 1 \end{pmatrix}. \end{aligned} \tag{6.9}$$

The value of q, after propagating through several optical elements, is obtained by calculating the 2×2 matrix coming from multiplying all the matrices associated with these elements and then using Eq. 6.8 with this matrix. After this, by looking at the real and imaginary parts of q, w and R can be obtained for any set of optical elements.

We end this section by mentioning that Eq. 6.2 describes one particular field configuration with cylindrical symmetry, satisfying Maxwell's equations in paraxial approximation. While this configuration is the one we are interested in, in general, an arbitrary field configuration can be written in terms of a linear combination of a complete set of functions satisfying the specified conditions/equations. It can be shown that these functions, called Hermite-Gaussian modes, have the following form in cartesian coordinates [255]:

$$u(x,y,z)_{nm} = \frac{1}{\sqrt{1 + \left(\frac{z}{z_R}\right)^2}} H_n\left(\sqrt{2}\frac{x}{w}\right) H_m\left(\sqrt{2}\frac{y}{w}\right) \times \exp\left\{-i(kz - \Phi_{nm}(z)) - i\frac{k}{2q}(x^2 + y^2)\right\}, \tag{6.10}$$

with n and m integers, H_n the Hermite polynomials of order n, $\Phi_{nm}(z) = (n + m + 1)\tan^{-1}(z/z_R)$ is the Gouy phase for the nm mode and the origin in z-direction is located

at the waist. Note that for $n = m = 0$, we get back Eq. 6.2. Examples of several Hermite-Gaussian modes are shown in Fig. 6.1 b).

6.2.2 Cavity Design

A simplified diagram of a bow-tie cavity, similar to the one used in our experiment, is shown in Fig. 6.2. Our goal is to allow the electric field of the incoming light (injected through one of the mirrors) to replicate itself after one round-trip inside the cavity, which leads to constructive interference and, hence, to a large power buildup inside the cavity after many round-trips. In order to design the right cavity, several parameters need to be optimized. We did this by performing a grid search over the distance between the plane (d_1) and concave mirrors (d_3), the curvature of the concave mirrors (R), and the angle between the mirrors and the vertical axis (α). The index of refraction n was kept constant at 1, given that the cavity will be placed inside the vacuum. During the optimization, we aimed for a beam diameter between the plane mirrors of ~ 1 mm and a distance between them of 50 cm or below to limit the size of the chamber in which the cavity will be placed. In general, the resonant frequencies of a bow-tie cavity are given by [255]:

$$\nu_{nm} = \left(q + (n + m + 1) \frac{\cos^{-1}(\pm\sqrt{g_1 g_2})}{\pi} \right) \frac{c}{L}, \tag{6.11}$$

where $L = d_1 + 2d_2 + d_3$ is the total length of the cavity, q is an integer, n and m define the Gaussian-Hermite mode and:

$$\begin{aligned} g_1 &= 1 - \frac{d_1 + 2d_2}{R} \\ g_2 &= 1 - \frac{d_3}{R}. \end{aligned} \tag{6.12}$$

Note that the second term in the bracket in Eq. 6.11 comes from the Gouy phase introduced in Sec. 6.2.1. The parameter $\frac{c}{L}$ is called the free spectral range (FSR) of the cavity and gives the spacing in frequency space between consecutive cavity resonances of the same Hermite-Gaussian mode (i.e., different q values, but the same m and n values).

By enforcing the complex beam parameter, q, to replicate itself after one round trip inside the cavity, which is required for reaching constructive interference, the beam waist between the 2 flat mirrors, obtained by using the ABCD matrix formalism introduced in Sec. 6.2.1, is given by [255]:

$$\omega_0^2 = \left(\frac{\lambda R}{2n\pi} \right) \frac{\sqrt{g_1 g_2 (1 - g_1 g_2)}}{|g_1|}, \tag{6.13}$$

where λ is the wavelength of the laser used, and R is the radius of the curved mirrors, chosen to be the same for both mirrors. The small waist, located between the curved mirrors, is given by [255]:

$$\omega'^2_0 = \left(\frac{\lambda R}{2n\pi} \right) \frac{\sqrt{g_1 g_2 (1 - g_1 g_2)}}{|g_2|}, \tag{6.14}$$

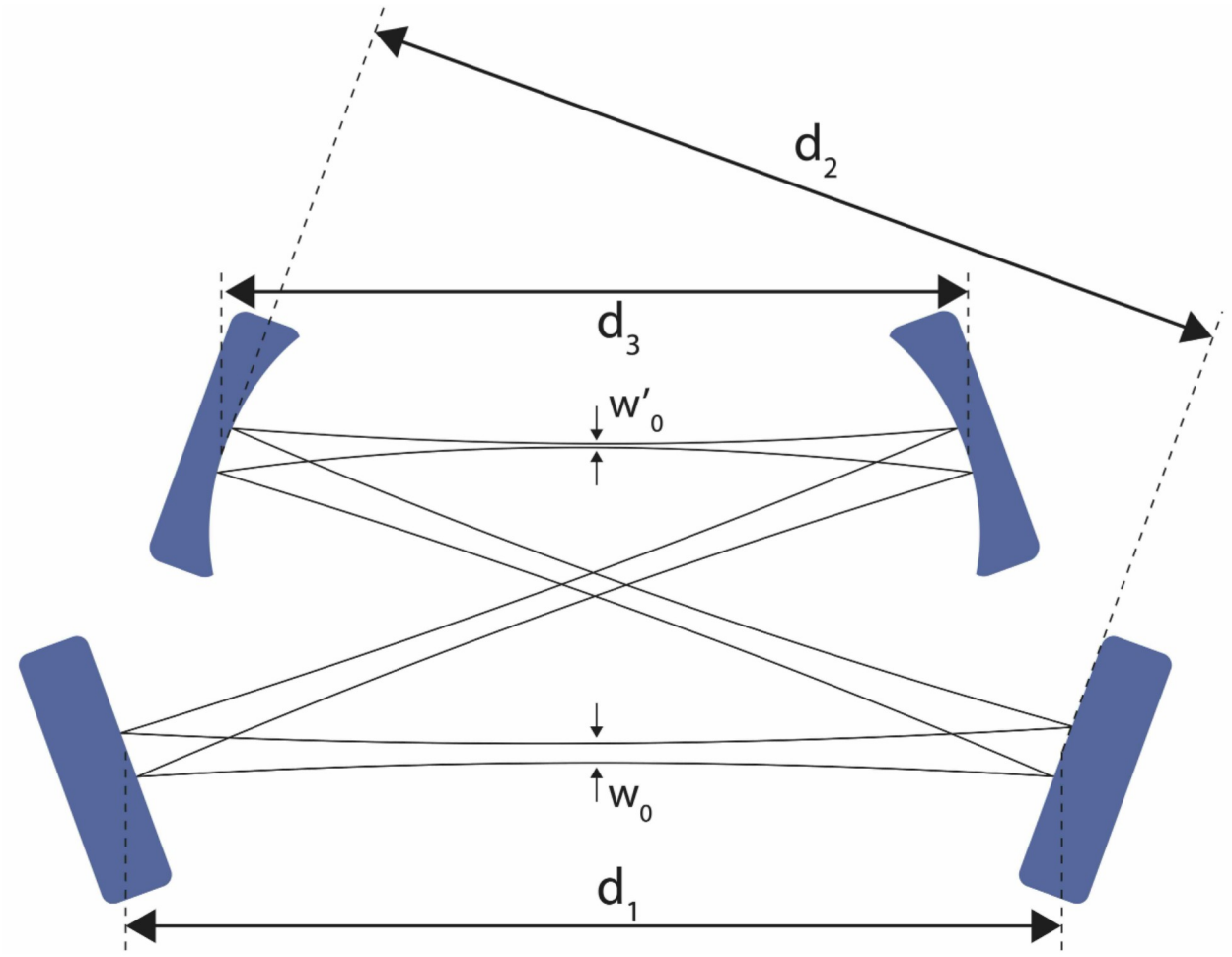

Figure 6.2: Diagram of a bow tie cavity with two plane (lower) and two concave (upper) mirrors. The distances between the two plane mirrors (d_1), the two curved mirrors (d_3), and between the plane and the curved mirrors (d_2) are shown. A simplified diagram of a Gaussian beam propagation inside the cavity is shown, together with the beam waist between the two plane (ω_0) and curved (ω_0') mirrors.

From Eq. 6.13 and 6.14, the stability criterion for the bow tie cavity can also be obtained:

$$0 \leq g_1 g_2 \leq 1. \tag{6.15}$$

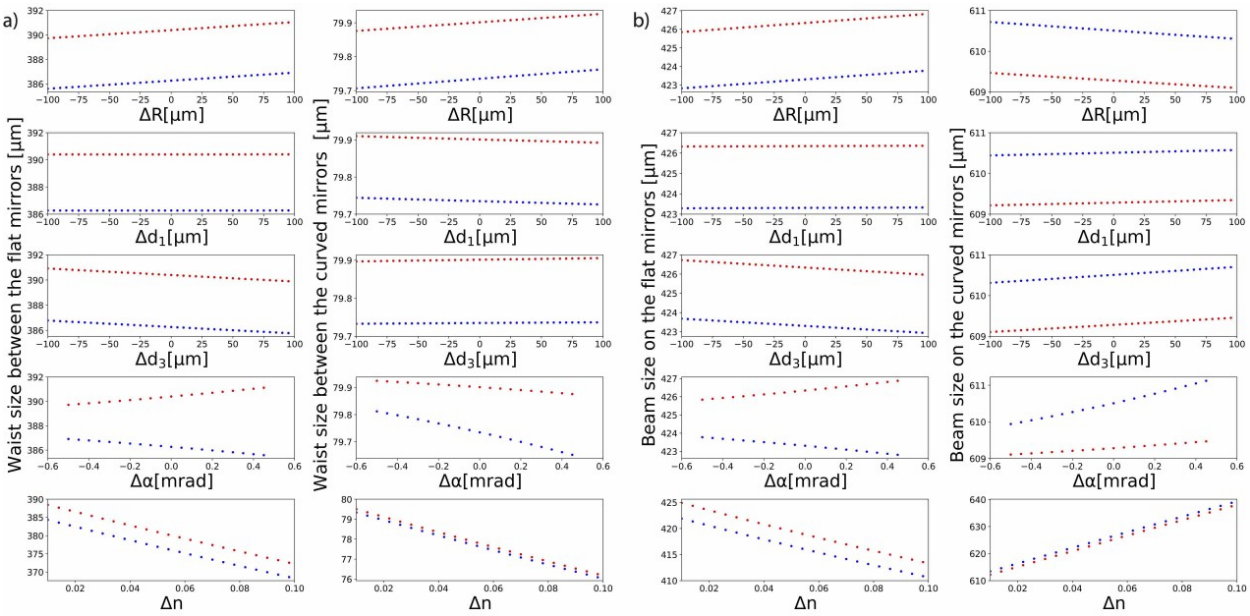

Figure 6.3: Laser beam size stability inside the cavity. a) Variation of the beam waist between the two flat mirrors (left column) and the two curved mirrors (right column) for the sagittal (red dots) and tangential (blue dots) direction when various experimental parameters are varied. From top to bottom, the parameters investigated are changes in the radius of curvature of the two curved mirrors (ΔR), variations of the distance between the two planes (Δd_1) and curved (Δd_3) mirrors, variations in the orientation angle of the mirrors with respect to the vertical ($\Delta\alpha$) and variations in the index of refraction of the medium between the two mirrors (Δn). b) Same as a), but looking at the size of the laser beam (half diameter) on the flat (right column) and curved (left column) mirrors.

The equations above are correct, ignoring the effects of astigmatism. Given that in a bow-tie cavity, the mirrors are tilted at an angle α from the vertical, the effective radius of the curved mirrors is different in the tangential and sagittal plane, and the shape of the beam at the waits changes from circular to elliptical. The effective radii of the mirrors that should be used in the equations above in order to extract the beam waist in the sagittal and tangential direction, accounting for astigmatism, are [255]:

$$\begin{aligned} R_{sag} &= \frac{R}{\cos\alpha} \\ R_{tan} &= R\cos\alpha. \end{aligned} \tag{6.16}$$

Upon optimization, the parameters chosen for the cavity were: $d_1 = 39.5$ cm, $d_3 = 28.5$ cm, $R = 25$ cm, and $\alpha = 2.86°$. Given that we will use a laser of wavelength $\lambda = 1064$ nm, the waists of the beam between the flat mirrors are: $w_{\text{sag}} = 0.390$ mm and $w_{\text{tan}} = 0.386$

mm, while between the curved mirrors we get: $w_{\text{sag}} = 80\ \mu m$ and $w_{\text{tan}} = 80\ \mu m$. These parameters were chosen such that the beam diameter (twice the waist) is around 1 mm, while the cavity is well inside the stability region, and the astigmatism is minimized, making the initial alignment of the cavity easier. Increasing the waist can be easily achieved by reducing the distance between the two curved mirrors, which we can do experimentally if needed, as described in Sec. 6.2.3. Next, we investigated the stability of the cavity to small changes in these parameters, which can result in practice from sources such as vibrations or temperature variations in the laboratory.

Figure 6.3 a) shows the variation of the waist size between the flat (right column) and curved mirrors (left mirror) for the sagittal (red dots) and tangential (blue dots) directions due to variations of different parameters of the cavity (from top to bottom): the radius of curvature of the concave mirrors (ΔR), the distance between the flat mirrors (Δd_1), the distance between the concave mirrors (Δd_3), the inclination angle of the mirrors relative to the vertical ($\Delta\alpha$), and the index of refraction of the medium (Δn). As it can be seen, for a wide range of parameters, larger than the expected experimental variations, the size of the two waists varies by less than 5%, showing the stability of this setup to external perturbations.

Another important consideration in designing the cavity is the size of the beam (using its half diameter in the radial direction) on the mirrors. To avoid losses due to diffraction coming from the finite size of the mirrors, it is desirable for the beam size to be at least 3-4 times smaller than the radius of the mirrors [255]. Moreover, one needs to check that the beam's diameter on the mirrors is large enough to prevent mirror damage. The mirror beam size can be calculated using Eq. 6.5. Plugging in the optimized values for the cavity parameters mentioned above, the obtained beam sizes are ~ 0.4 mm on the curved mirrors and ~ 0.6 mm on the flat ones. In order to account for the possible need for larger beam sizes in the future (e.g., due to the need for a higher overlap of the laser beam with the atomic beam), we decided to use 1" diameter mirrors. To check the stability of the beam spot size on the mirrors to perturbations, we again varied the same cavity parameters as above over the same ranges. The results are displayed in Figure 6.3 b) for the beam size on the flat (right column) and curved (left column) mirrors, for sagittal (red dots) and tangential (blue dots) directions, showing the stability of the waist's size around 0.4 mm and 0.6 mm, respectively.

Once the geometrical properties of the cavity were analyzed, an investigation of the power enhancement and cavity finesse was performed. Assuming a well-aligned and mode-matched cavity, these properties depend mainly on the reflection coefficients of the mirrors, as well as other possible losses inside the cavity. The power enhancement at resonance is given by [255]:

$$\frac{I_c}{I_0} = \frac{1 - r_1^2}{(1 - r_1 r_m)^2}, \tag{6.17}$$

where $r_1 = \sqrt{1 - T_1}$, with T_1 the transmission of the input mirror and $r_m = r_2 r_3 r_4 t$, where r_i for $i = 2, 3, 4$ is defined in the same way as r_1 for the other three mirrors (which will be taken to have the same transmission coefficient) and $t = \sqrt{1 - L}$, where L represents all the other losses in the cavity, beside the transmission of the mirrors. The linewidth of the cavity (defined as the full width at half maximum of the circulating power) is given by [255]:

$$\Delta\nu_{1/2} = \frac{2(1 - r_1 r_m)}{\sqrt{r_1 r_m}}, \tag{6.18}$$

while the finesse of the cavity, $\mathcal{F}$, defined as the ratio between the FSR and the linewidth of the cavity, is given by [255]:

$$\mathcal{F} = \frac{\pi\sqrt{r_1 r_m}}{1 - r_1 r_m}. \tag{6.19}$$

The laser sent inside the cavity will have a power of 20 W and we aim for a cavity enhancement factor in vacuum of ~ 1000. This value should allow for the ionization of a large faction of the already excited atoms while preventing any damage to the mirrors. Based on Eq. 6.1, assuming a lifetime of the excited atomic state used in the transition of 50 ns and an input power to the cavity of 20 W, the ionization efficiency will be $\sim 80\%$. The transmission coefficients were also chosen such that the linewidth of the cavity (~ 25 kHz) is large enough compared to the linewidth of the used laser (~ 5 kHz) to allow a proper locking of the laser to the cavity (see Sec. 6.2.3).

In order to achieve the enhancement mentioned above, high-reflectivity mirrors are needed. After a parameter space search, we decided to use a transmission coefficient of 3×10^{-4} for the input coupling mirror, which will be one of the flat mirrors, and 10^{-4} for the other three mirrors. The mirrors were custom-made by Layertech. Assuming a total loss of 10^{-4}, which can be obtained in vacuum conditions, the total enhancement factor becomes 2500, corresponding to a finesse of 9000 and a linewidth of the cavity of 25 kHz, which should allow a proper locking of the laser to the cavity.

We investigated the stability of the enhancement factor to variation in the values of T_1, T_2, and L. Here, T_2 is the transmission coefficient for all the other three mirrors besides the input coupling one. Such variations can come from factors like not perfect laser polarization, mirror imperfections, or diffraction losses. The results are presented in Figure 6.4. There is a clear dependence of the power inside of the cavity on the parameters under considerations, however, for relative changes in these parameters of up to 50% (much larger than expected in practice), the enhancement factor is still above the desired value of 1000.

6.2.3 Cavity Alignment and Locking

The cavity was first aligned and locked outside the vacuum chamber, and it is shown in Fig. 6.5. For the rest of this section, the mirrors are labeled as shown in this figure, with mirror 1 being the input coupler and the others labeled in numerical order after that. The laser used is a Model RIO0175-5-07-3 from RIO Lasers, lasing at 1064 nm, with a power of 20 mW and a linewidth of ≤ 5 kHz. The output is sent through a fiber to a high-power fiber amplifier Model ALS-IR-1064-20-A-CC from Azurlight Systems. The amplifier output maintains the wavelength and linewidth of the seed but increases the power to anywhere between 0.5 W and 20 W. This light is then sent towards the optical cavity. For the tests done outside the vacuum, the maximum power used after the amplifier was 0.5 W. The mirrors used to send the laser light inside the cavity are all Throlabs NB1-K14. A periscope is placed right after the amplifier head to adjust the height of the outside of the vacuum setup

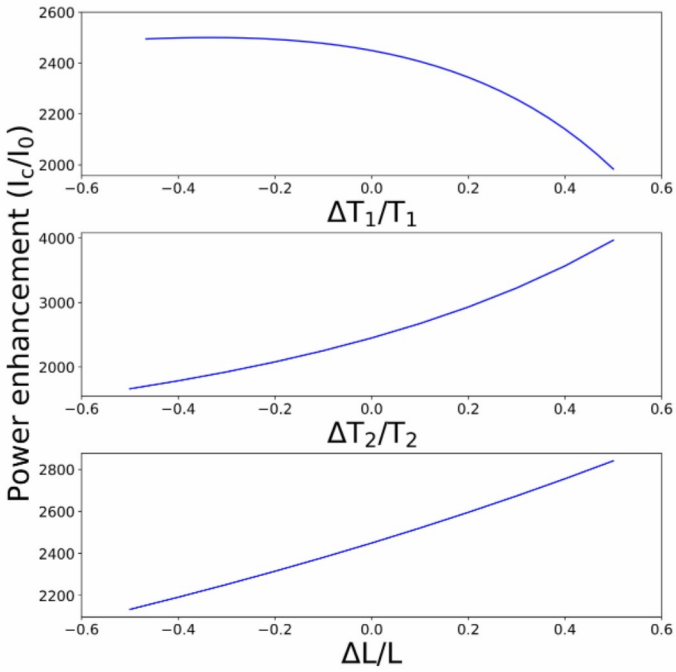

Figure 6.4: Power enhancement inside the cavity as a function of relative changes in various parameters. From top to bottom, these parameters are the transmission of the input coupler mirror (T_1), the transmission of the other three mirrors (T_2), and other losses inside the cavity (L).

to the height of the main experimental chamber. A zero-order half-wave plate (WPH05M-1064 from Thorlabs) and a polarizing beamsplitter cube (CCM1-PBS255 from Thorlabs) are used to adjust the power coming out of the laser, as well as select the correct polarization to be sent towards a resonant electric optical modulator (EOM) placed after the beamsplitter cube. This is a resonant (resonant frequency at 4 MHz) free space EOM, Model PM7-NIR_4 from QUBIG, and it will be used for Pound–Drever–Hall (PDH) locking [256]. After that, a telescope is used for mode matching the laser transverse profile to the previously calculated TEM_{00} mode of the cavity. The first lens is divergent, with $f = -1000$ mm, and located 910 mm away from the laser head. The second one is convergent, with $f = 750$ mm, located 150 mm after the first one. Their focal lenses and locations were chosen based on simulations using the GaussianBeam software. After this, two mirrors are used to send the laser light to the input coupler mirror of the cavity. Once the laser spot location was relatively close to the center of the input coupler, the alignment of the cavity was performed as described below. Behind mirror 4, a 2° round wedge prism acting as a beam splitter ($\sim 500:1$) is placed that sends most of the laser power to a photodiode (DET10N2 from Thorlabs), while the rest is sent to a CMOS camera (CS165MU from Thorlabs) to monitor the transverse modes being enhanced inside the cavity.

For the cavity alignment, the laser frequency was scanned by changing the laser current using a triangular ramp signal of amplitude between 0.5 and 3 V and frequency of 500 Hz, produced using the D2-125 Laser Servo from Vescent. Mirrors 1 and 2 were removed from their mounts and replaced with previously machined aluminum disks of 1" diameter, with

Figure 6.5: Bow-tie optical cavity used in our setup. The mirrors are labeled from 1 to 4, starting from the input coupler mirror. They are placed in THORLABS POLARIS mounts, with the two mounts holding the plane mirrors having piezos for fine adjustments of the cavity alignment once the setup is placed under vacuum. The cavity is placed on an invar plate (various holes in the plate are used to help with the initial alignment).

a 2 mm hole in the center. The two mirrors before the cavity were used to align the laser light such that it passes through the two holes. Once this was achieved, the mirrors 1 and 2 were put back in place, mirror 3 was replaced with one of the aluminum disks, and the mirror 2 mount adjusted such that the light passed through the disk's hole. Mirror 3 was then put back in place, and the same was done for the mount containing mirror 4. Once this initial alignment was done, the mounts containing mirrors 4 and 1 were adjusted such that the second pass of the light between the flat mirrors overlaps with the initial one. A faint signal from the photodiode was seen at this point in transmission on the oscilloscope. From there, all 4 mirrors were adjusted iteratively, with the goal of maximizing the signal on the oscilloscope. At the same time, the beam spot size on the camera was monitored. Besides adjusting the four cavity mirrors, the distance between the 2 telescope lenses was also adjusted to maximize the TEM_{00} mode built up inside the cavity and minimize all the other transverse modes. This can also be confirmed by ensuring that no other peaks are seen on the oscilloscope while scanning the laser frequency beside the main one, corresponding to the TEM_{00} mode. A picture of the transverse mode obtained after optimization, as well as the peaks seen on the oscilloscope while scanning the laser current, are shown in Fig. 6.6. After this, the Side Lock mode on the Vescent laser servo was turned on. A lock was initially achieved which was further improved by adjusting the proportional gain and the integrator on the lock box. In the end, the lock was stable, and the maximum power enhancement obtained in the cavity was ~ 100. This enhancement factor was obtained by measuring the power transmitted through mirror 4, using its transmission coefficient and the known input power to the cavity. Following this, a PDH locking was also pursued. For this, we switched on the Peak Lock mode on the Vescent laser servo. A 4 MHz sinusoidal signal produced by the Vescent box was sent to the resonant EOM and the reflected instead of transmitted signal was used for locking. Using this approach, an enhancement factor of 200 was achieved. Moving forward, the PDH locking approach will be pursued due to its

higher stability to external perturbations and ability to reach higher power enhancements. The main experimental chamber, where the cavity is located, was then placed under the vacuum. Under these conditions, an enhancement factor of 500 was obtained using the PDH locking, with input powers as high as 2.5 W. From the decay of the transmission peaks (Fig. 6.6 a)), the linewidth of the cavity was measured to be 30(5) kHz, in agreement with the theoretically predicted value of 25 kHz. The achieved power inside the cavity is enough for preliminary tests and can be further increased if needed.

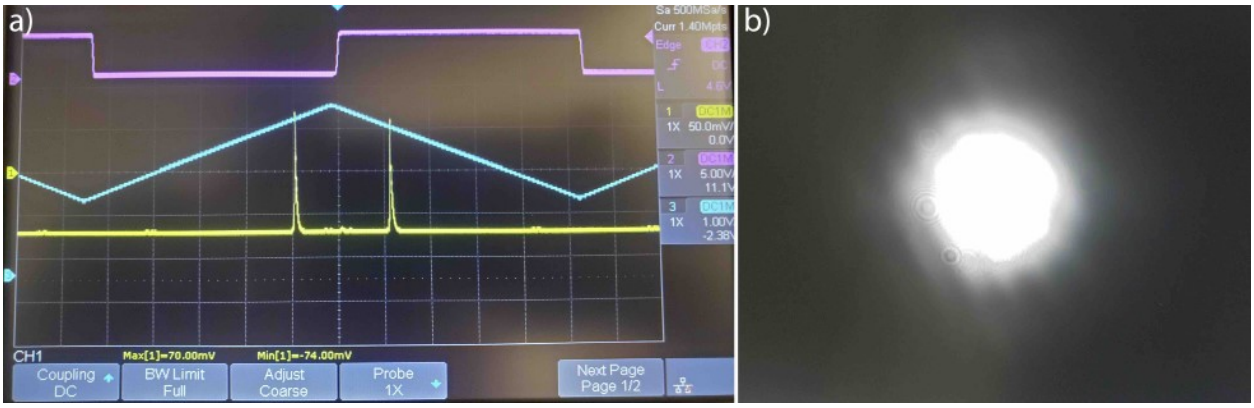

Figure 6.6: a) Example of the signal obtained from the cavity transmission on an oscilloscope. The yellow line represents the transmitted signal, while the blue and pink lines are the ramp applied to scan the laser frequency and the TTL signal associated with the ramp. b) Example of the transverse mode of the cavity measured in transmission on the CMOS camera.

6.3 Velocity Map Imaging

As mentioned at the beginning of this chapter, being able to detect the electrons and ions in coincidence, as well as the energy of the electrons produced during an ionization event, can significantly reduce the background of our measurements. While detecting the timing of the ionization is relatively straightforward, extracting the electron's energy (which is on the order of 1 eV in most atoms) requires a more complex apparatus. For this purpose, we decided to use the Velocity Map Imaging (VMI) technique. This was developed in 1997 [248], leading to a significant improvement in electron imagining compared to previous methods [257]. The VMI working principle is based on using non-uniform electric fields, produced by electrodes acting as electrostatic lenses, to project a 3D volume of charged particles resulting from the photoionization event on a 2D position sensitive detector [258]. The main idea behind this technique is that, for properly chosen voltages and geometry, charged particles with the same mass and velocity are projected on the same point of the 2D detector, regardless of their initial position. This allows a high-resolution measurement of the electrons' energy ($\sim$ 10 meV energy resolution), as well as of their angular distribution, which can provide further information about the orbitals from which the electrons are ionized. In practice, the energy resolution starts to degrade for electron sources bigger than a few millimeters, but it can still be enough to clearly tell apart different electronic energy levels in most atoms. This

technique is widely used in photofragmentation [249, 259–266], photoelectron spectroscopy [267–276], and scattering [277–279] experiments.

6.3.1 Velocity Map Imagining Simulations

Given that the ionizing laser has a wavelength of 1064 nm, corresponding to ~ 1 eV, the VMI setup was optimized for photoelectrons with energies below this value. Several designs have been considered in the past [252, 253, 258, 280–284], taking into account the electron energy, the required energy resolution, the shape of the source from which the electrons are produced, the size of the detector, as well as the complexity of the electrodes stack (e.g. sizes and number of electrode plates). In the end, a design similar to Ref. [253] was chosen, and its parameters were optimized to match the needs of our experiment. The final dimensions and applied voltages for the VMI setup used in our experiment are shown in Table 6.1. Besides the main electrodes usually used in a traditional VMI design [248]: L_R - the repeller plate, L_1, L_2 and L_3 lenses, we placed two extra lenses in between L_1 and L_2 (L_{12}), and L_2 and L_3 (L_{23}), respectively, to prevent any significant fringe effects. We also added three shielding electrodes beside L_3 to produce a better focusing [253]. The thickness and outer radius of each electrode were set in our simulations to 1 mm and 70 mm, respectively. The latter value was the largest one allowed by the space constraints of our setup, and it was chosen to avoid any edge effects and shield the electrons from any external electric fields.

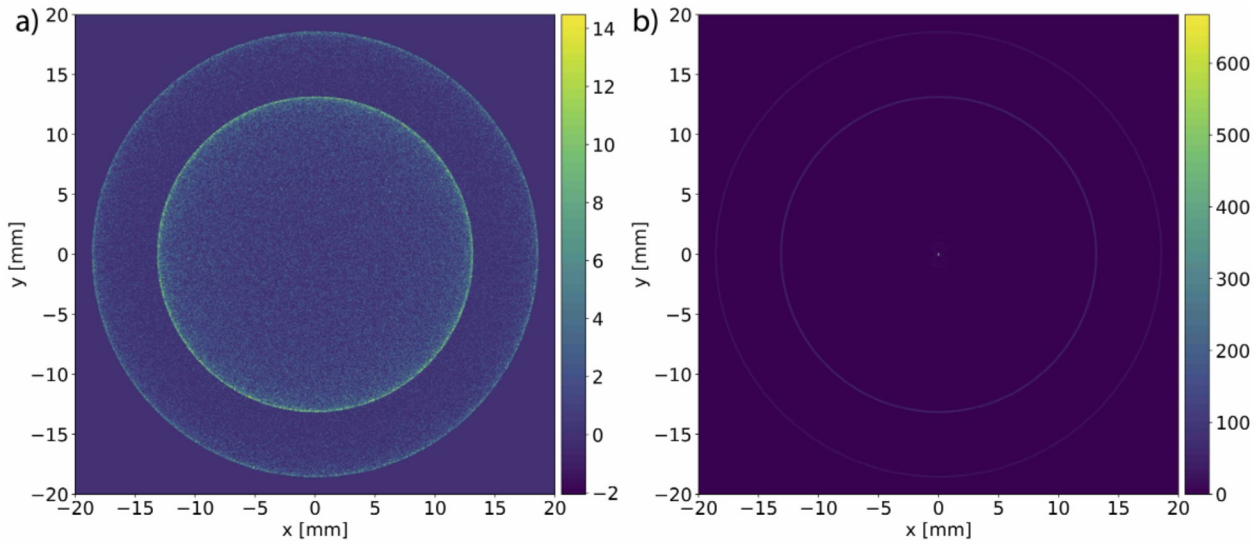

Figure 6.7: a) Example of the simulated pattern (in SIMION 8.1) observed on the 2D screen of the VMI setup for electrons produced isotropically from a Gaussian source of $\sigma = 0.5$ mm, with energies of 0.5 eV and 1 eV. b) Results of the Inverse Abel transformation applied to the 2D pattern in a). The two circles corresponding to electrons with 0.5 eV (inner circle) and 1 eV (outer circle) are clear (see main text for details).

The working principle of the VMI is based on using a laser with a polarization parallel to a position-sensitive detector, a microchannel plate detector (MCP) in our case. This leads to the electrons being emitted with a cylindrical symmetry around the polarization axis, their

3D distribution is well described by spherical harmonics based on the angular momentum of the orbital from which the electron is ejected [248–253]. Setting the polarization of the ionization laser parallel to the position sensitive detector, the original 3D angular and energy distribution of the electrons at the ionization point can be reconstructed, from the 2D projection on the detector plate, using an inverse-Abel transformation [251]. This transformation turns the 2D projection on the screen into a slice through the middle of the initial 3D electron distribution parallel to the detector. As the original distribution has cylindrical symmetry, this slice contains all the necessary information about the initial kinematic properties of the emitted electrons. An example of a simulated image of the expected measured 2D pattern (obtained using the optimized setup in SIMION 8.1), as well as the associated inverse-Abel transformed image, can be seen in Fig. 6.7, for electrons emitted with an S-wave, spherically symmetric distribution, with initial energies of 0.5 and 1 eV and produced from a Gaussian source with $\sigma = 0.5$ mm (corresponding to a waist of 1 mm). The radii of the two circles in the inverse-Abel transformed image correspond to the two different electron energies, while their thickness sets the resolution of the reconstructed energy.

Given the cylindrical symmetry of the problem, optimizing the parameters of the VMI setup, which amounts to improving the achievable energy resolution, can be done by only considering electrons emitted parallel to the detector [285]. All electrons with a given initial kinetic energy will be projected on a circle on the screen, and the goal of parameter optimization is to reduce the thickness of these circles as much as possible, which is equivalent to improving the energy resolution. We define the circle thickness associated with a given initial kinetic energy as the standard deviation of the radii on the 2D screen corresponding to electrons with that initial kinetic energy.

The electrons are produced at the interaction between the laser and atomic beam, which, for a VMI setup, must be between the L_R and L_1 electrode plates. The initial parameters of the simulations (voltages, electrodes inner diameter and distances between electrodes) were set to the values in Ref. [253]. They were then varied to optimize the simulation's resolution for photoelectrons with an initial energy of 1 eV. All the simulations were done using the SIMION 8.1 software [286]. The adjusted parameters were the voltage on the repeller plate V_R, the ratio between the voltage on L_1 and the repeller plate, the ratio between the voltage on L_2 and the repeller plate, the distances between L_R and L_1, L_1 and L_2, L_2 and L_3, L_3 and the first shielding electrode, respectively and the inner diameters of L_1, L_2, L_3, and the shielding electrodes. L_{12} (L_{23}) was always located halfway between L_1 (L_2) and L_2 (L_3), had an inner diameter equal to the average of the L_1 (L_2) and L_2 (L_3) inner diameters and a potential equal to the average of L_1 (L_2) and L_2 (L_3) potentials. The shielding electrodes had all the same inner diameter during optimization, and the distance between them was kept equal to the distance between L_3 and the closest shielding electrode. The potentials of the shielding electrodes, as well as that of L_3, were all kept to zero. The distance between the source (halfway between L_1 and L_R) and the detector plate remained constant at 400 mm. The larger this value is, the better the energy resolution, thus we chose it as roughly the largest one allowed such that electrons with energies up to 1 eV can still hit the position-sensitive detector. The electron cloud expands as it travels toward the detector, so placing it too far would lead to electrons missing its active area.

The optimization was done iteratively in 3 steps. In the first step, the distances between the electrodes varied by 2 mm at a time while ensuring that the correct order of the

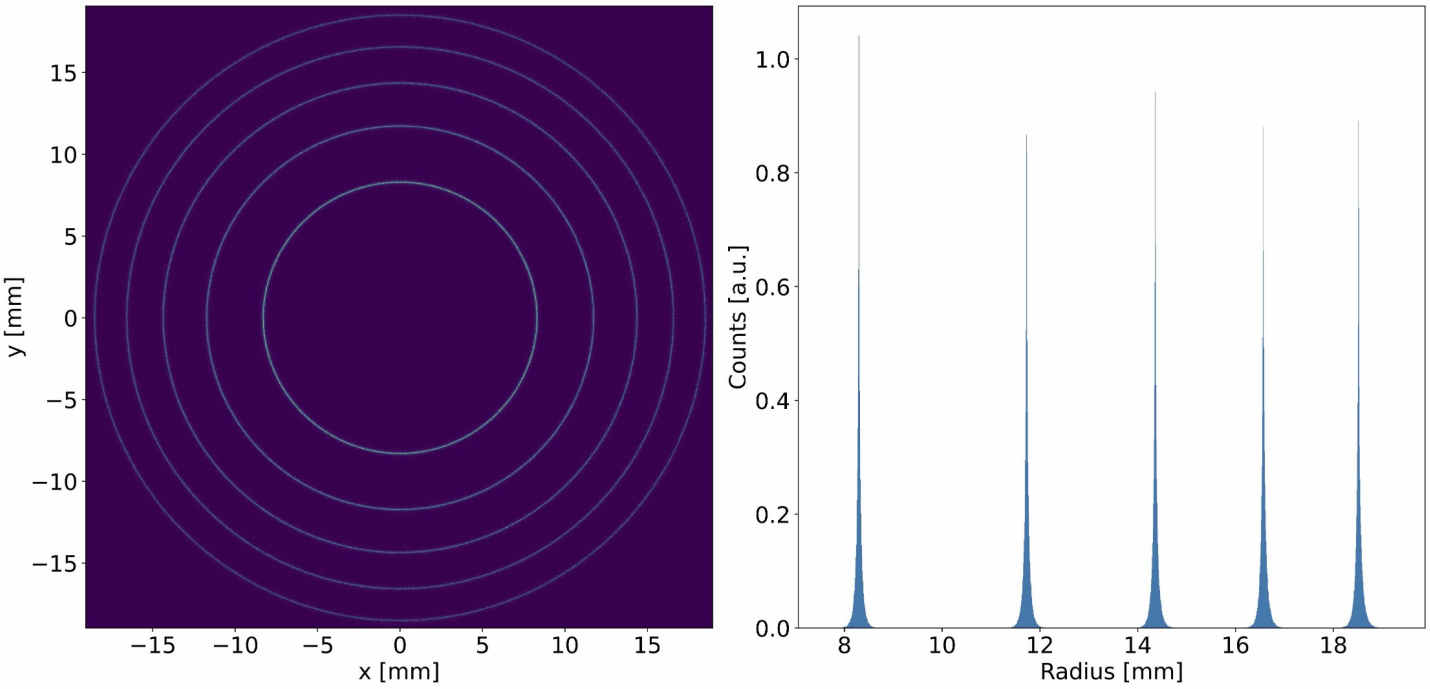

Figure 6.8: Left: Electrons distribution on the 2D detector plate after the VMI optimization. Right: Histogram of the radii of the electrons on the detector plate. The source was a 3D Gaussian with a standard deviation of 0.75 mm. The energies of the electrons are, from the inside out: 0.2, 0.4, 0.6, 0.8, and 1 eV.

electrodes was still kept. For each increment, 100 electrons were generated. The electrons were produced, during all steps of the optimization process, from a Gaussian source of $\sigma = 0.75$ mm and with an energy of 1 eV. The configurations with the best resolution among the tested simulations, usually the best 50, were kept and re-run with 1000 electrons. Only the best configuration was kept this time, and the new distances between electrodes were set to the optimized values. In the second step, the same process was repeated for the inner diameter of the electrodes. Finally, in the last step, the voltages were adjusted. The voltage on the repeller was adjusted in steps of 5 V, while the ratios V_1/V_R and V_2/V_R in steps of 0.02, separately. The best configuration was kept. This was run using the 2D cylindrical symmetry configuration of SIMION 8.1, which is significantly faster than a full 3D simulation at a resolution of 1 mm/g.u. (g.u. is the graphical unit) and using a fractional surface. All these three steps were then repeated at a resolution of 0.5 mm/g.u., the length increments going all down to 1 mm per step, the V_R voltage increments to 2 V, while the voltage ratios were kept at 0.02. The best configuration at each step was again kept and used at the next iteration. Finally, the process was repeated at a SIMION resolution of 0.1 mm/g.u., with length increments of 0.5 mm per step, V_R voltage increments of 1 V per step, and V_1/V_R and V_2/V_R increments of 0.01. The best geometrical configuration and optimized voltages are shown in Table 6.1.

For these VMI parameters, Fig. 6.8 a) shows the distribution of the electrons on the detector screen for electrons initially emitted parallel to the screen, while Fig. 6.8 b) shows

	Electrode spacing [mm]	Inner diameter [mm]	Voltage sim. [V]	Voltage exp. [V]
L_R	0	0	-930	-935
L_1	16	21	-771.9	-760
L_{12}	10	41.5	-646.35	-630
L_2	10	62	-520.8	-500
L_{23}	9	44	-260.4	-250
L_3	9	26	0	0
Shield 1	17	34	0	0
Shield 2	17	34	0	0
Shield 3	17	34	0	0

Table 6.1: Parameters of the optimized VMI setup. For each electrode (first column), we show the distance relative to the previous one (second column). The electrodes are listed in the order in which they appear in the setup, with the ionization point being in the middle in between L_R and L_1. In the third column, we show the inner diameter of the electrodes, and in the fourth column, we show the optimal voltages according to the SIMION 8.1 simulation. The last column shows the optimal voltages obtained experimentally (see text for details).

a histogram of the radii of the electrons on the detector screen. The source simulated in SIMION 8.1 to generate Fig. 6.8 was a 3D Gaussian with a standard deviation of 0.75 mm, and the initial kinetic energies of the electrons were 0.2, 0.4, 0.6, 0.8 and 1 eV. For each energy, 10^4 electrons were simulated. As it can be seen, the circles corresponding to different initial kinetic energies are well separated, and the standard deviation of the radii associated with each circle is around 50 μm, indicating a good spatial and, hence, energy resolution of the VMI setup.

Figure 6.9 shows the relative energy resolution of the VMI as a function of the initial electron energy for different standard deviations of the 3D Gaussian source. The energy resolution can be directly obtained from the radii of the circles in Fig. 6.8. A given initial kinetic energy is related to a radius on the detector by $KE = aR^2$, where a is some calibration constant [285]. Thus, it can be shown that $\frac{dKE}{KE} = 2\frac{dR}{R}$, where KE is the initial kinetic energy of the electron, dKE is the kinetic energy standard deviation, R is the mean radius on the detector screen corresponding to that energy and dR is the radial standard deviation. As shown in Fig. 6.9, the energy resolution stays below 3% for all the considered source sizes relevant to our experiment.

Given that we are using a bow-tie cavity for ionization, the atomic beam will interact with the laser not only between the two plane mirrors but also in 2 more places: in the middle between the two concave mirrors and at the intersection of the two beams of light moving on the diagonal of the cavity. Given the geometry of our cavity, these points are shifted relative to the main interaction point by 25 mm and 34 mm, respectively. As the inner radius of the L_1 plate is 10.5 mm, the electrons emitted at these 2 other points should not be able to reach the MCP. This was confirmed by our simulations with Gaussian sources with standard deviations of up to 2.5 mm. Thus, any signal reaching the electron detector is expected to come from the main interaction region.

A 3D model of the setup located in the main interaction chamber, made using Autodesk

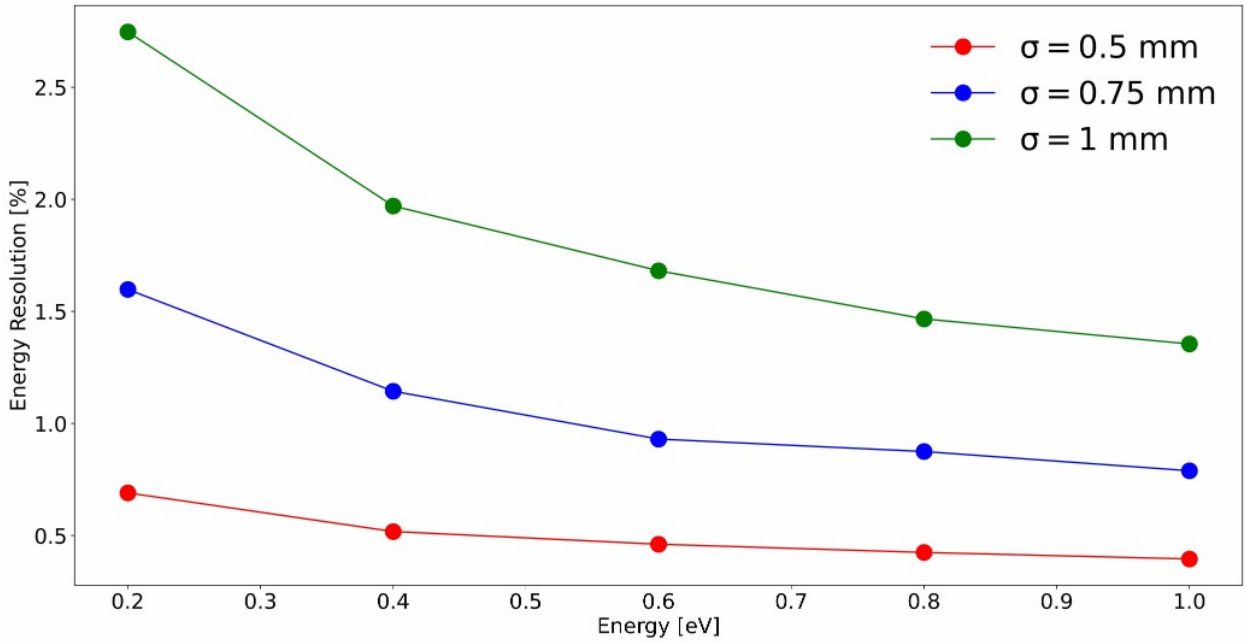

Figure 6.9: Energy resolution of the optimized VMI setup as a function of the initial photoelectron energy, for 3D Gaussian sources with three different standard deviations: 0.5 mm (red), 0.75 mm (blue) and 1 mm (green).

Inventor Professional 2023 using the optimized dimension for the VMI and cavity setup, is shown in Fig. 6.10. Further details of the setup are shown, such as the holders for the electrode plates and the cavity, as well as several CF100 ports for extra access needed for aligning the cavity once inside the chamber (see Sec. 6.2.2 and 6.2.3 for further details) and for feedthroughs for the voltage connections. Simulations of electron trajectories inside the chamber have also been performed in SIMION 8.1 to check if any of the extra elements added to the setup compared to the initial simplified simulation would affect the performance of the VMI setup. No significant difference was observed between the two simulations, confirming the VMI electrode configuration's robustness.

6.3.2 Micro Channel Plate Assembly

For the detection of electrons produced during ionization, we used an MCP-based detector with a helical wire delay-line anode, model DLD40 from RoentDek, with high 2D-imaging (< 100 μm) and timing (< 100 ps) resolution. A pair of thin (0.72 mm) MCPs are placed in a chevron configuration to increase detection efficiency. The delay-line anode is made of two helical wires, one for each spatial dimension (labeled x and y moving forward). For each dimension, there is a signal wire (collecting the electrons) and a reference wire, with a voltage difference between them of $20 - 50$ V. This leads to an increased efficiency of detecting the electron cloud produced by the MCPs on the signal wires.

Before its installation in the main experimental chamber, the detector had to be assembled. This was done in a clean room using powder-free gloves, following the instructions in the official manual. The anode holder, on which the detector would be assembled, had

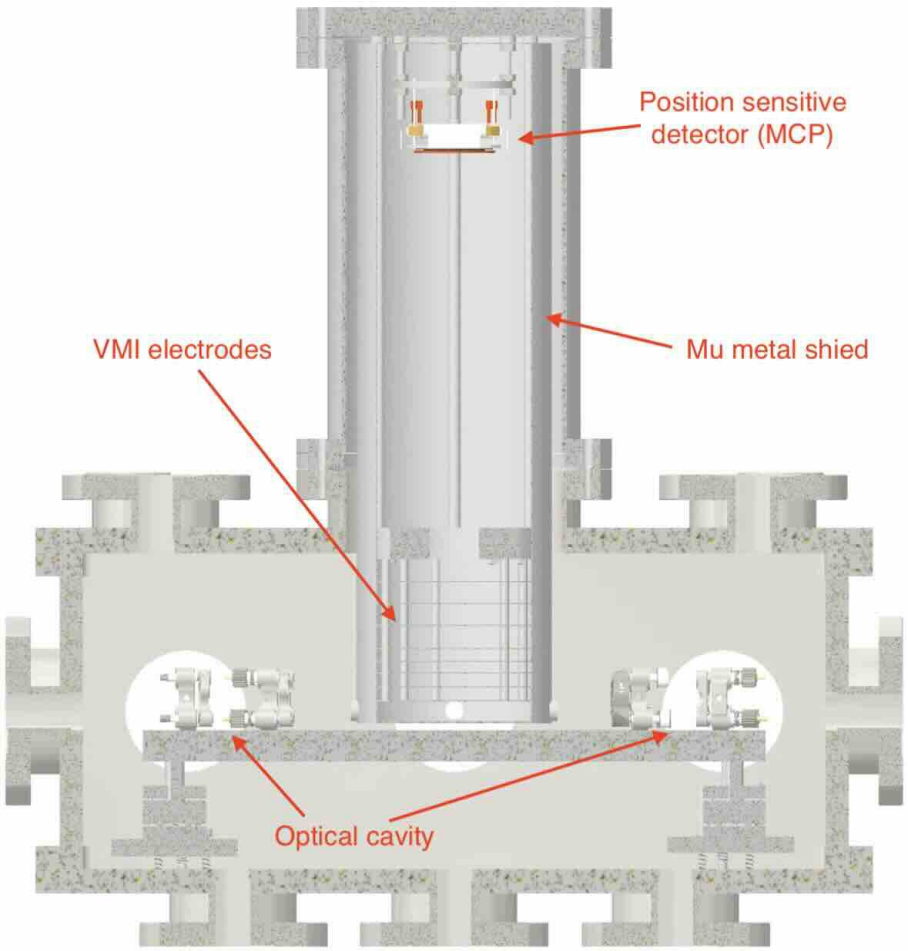

Figure 6.10: 3D model of the main experimental chamber made in Autodesk Inventor Professional 2023. The main components of the apparatus are shown: The optical cavity, the VMI electrodes, the position-sensitive (MCP) detector, and the mu-metal shield.

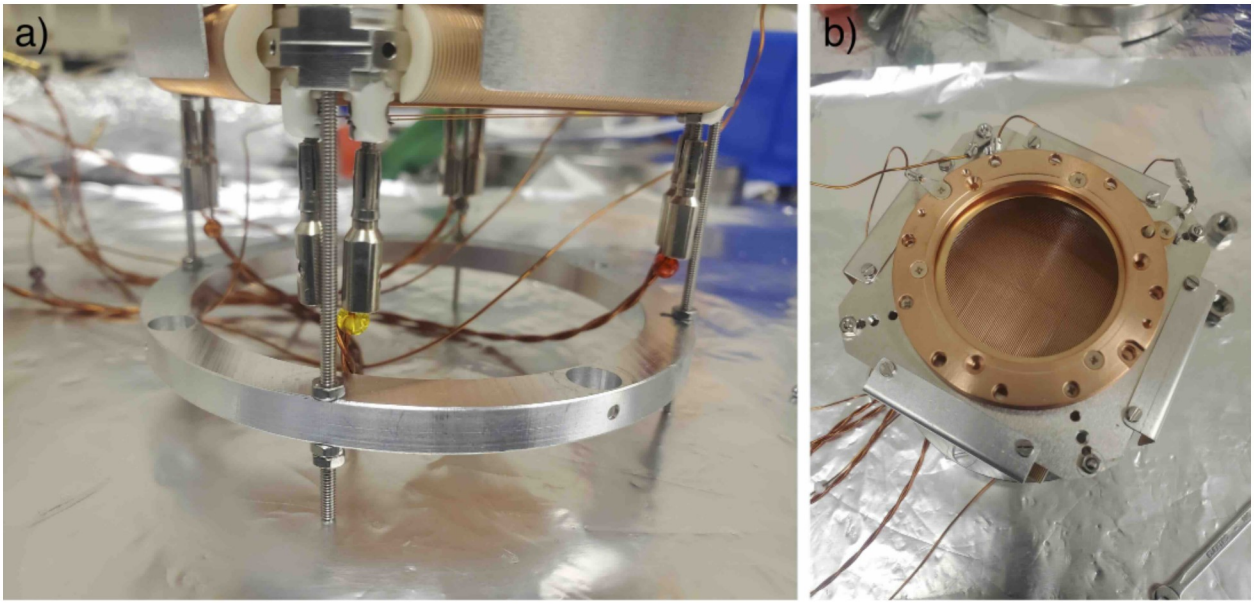

Figure 6.11: a) Ring holder for the MCP stack. The MCP/anode stack is attached to the ring using two pairs of M2 nuts on four threaded rods. The ring also has 4 0.25" holes used to attach the whole MCP setup above the interaction region (see main text for details). In the four corners of the anode, two electrical connections are made through a pair of twisted wires. These connections correspond to the reference and signal wires of the two ends of the x and y directions. b) Top view of the anode before installing the MCPs. Electrical connections to different rings holding the MCPs, as well as to the anode holder, can be seen.

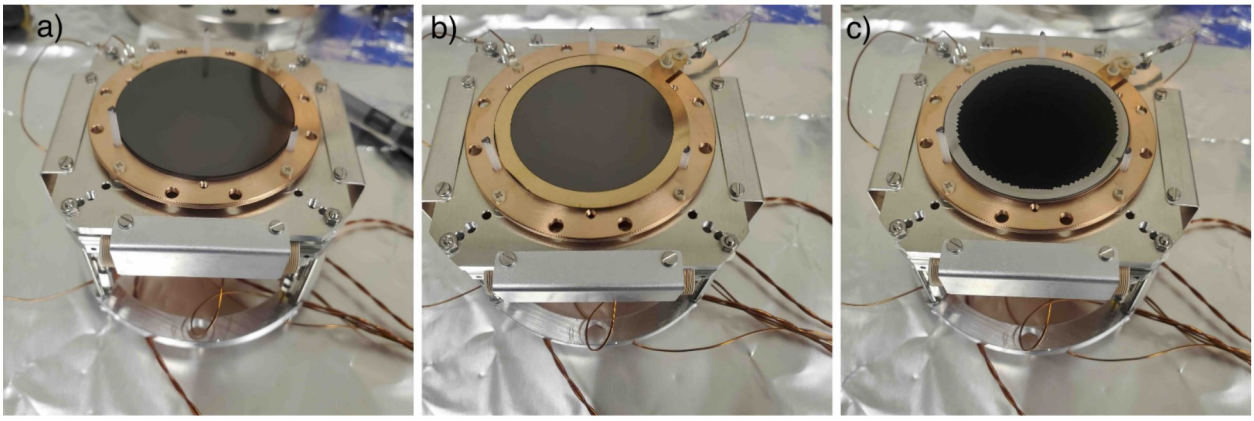

Figure 6.12: a) The bottom MCP plate is placed on top of the MCP Back metal ring and aligned using three threaded PEEK rods. b) On top of this, a bias ring is added together with a separate electrical connection. c) The top MCP disk is added to the setup and aligned using the same three threaded rods as above. Care must be taken that the 2 MCPs are at the right orientation with respect to each other, provided by small marks placed on their sides.

the two anode helical wires preinstalled (see Fig. 6.11 a)). The holder was attached to an aluminum ring using four long threaded rods and two aluminum M2 nuts for each rod. The aluminum ring has four extra holes (of $\sim 1/4''$ diameter) that will be used to attach the MCP setup in its final position for the experiment (see Sec. 6.3.3). For the anode connection to the vacuum feedthroughs, four cable pairs in a helical configuration are needed, 2 for each end of the signal and reference pair in both x and y directions. For each pair, it was ensured that the cables have the same length to within 1 mm, and they were twisted to about $3-4$ turns per 10 cm for proper signal transmission (see Fig. 6.11 b)). They were connected to M2 stub terminals of the delay-line wires, located in the rear part of the anode holder, using 2 mm connector pins. Electrical connections to the anode holder, the front, back, and the shim ring (located in between the 2 MCP disks) were also made as shown in Fig. 6.12 and 6.13. The cables were attached in their proper location using M2 PEEK screws to avoid any short between different components of the detector.

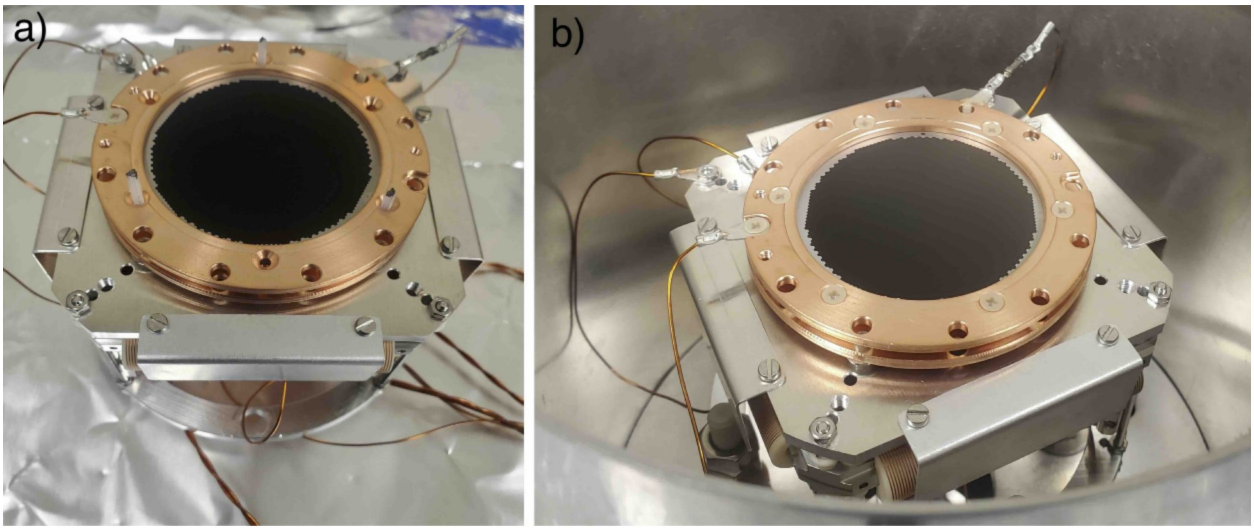

Figure 6.13: a) The MCP Front plate is added on the top of the MCPs. b) The three threaded PEEK rods used for alignment are removed, and the MCP setup is tightened in place using 6 M2 PEEK screws.

Before starting the assembly of the detector, the resistance between different anode wires (both between different directions and between the signal and reference for each direction) and between the cables and the anode holder were tested to confirm that they were not electrically shorted (e.g., by dust particles). The MCP assembly proceeded as follows. The rear MCP was placed on the metal ring attached to the anode holder. The connection between this ring (referred to as MCP Back) and the anode holder is made using four M2 PEEK screws and nuts for electrical insulation. The MCP disk is centered on the metal ring using three M2 PEEK threaded rods (see Fig. 6.12 a)). Then, a metal shim ring was placed on top of the rear MCP and fixed in place on the MCP Back ring using a PEEK nut (Fig. 6.12 b)). This ring can allow for an intermediate MCP bias, improve the total gain of the detector, and facilitate the resistance matching of the two MCPs (see Sec. 6.3.3). The second front MCP was placed on top of the shim metal ring, aligned using the same three PEEK threaded rods mentioned before (Fig. 6.12 c)). Its angular orientation relative

to the rear MCP was based on marks made on the edge of the MCPs, ensuring they were placed in a chevron configuration. Great care was taken to ensure that no dust particles are present between the two MCPs, which can permanently damage them by blowing dry air on their surface. Finally, a metal ring (referred to as MCP Front) was added on top (Fig. 6.13 a)). All three metal rings had individual electrical connections for the vacuum feedthroughs, which will be used to apply the required voltages. Lastly, the three PEEK threaded rods used for alignment were removed, and six M2 PEEK screws were installed to fix the whole setup in place (Fig. 6.13 b)).

6.3.3 Velocity Map Imagining Assembly

The VMI setup, which needs to be located above the plate containing the large mode optical cavity to detect the electrons produced during ionization, is attached to a CF200 stainless steel flange. To reduce the influence of external magnetic fields on the electrons' trajectories, the VMI setup was surrounded by a cylindrical mu-metal shield. Due to space constraints, the mu-metal shield itself (in particular, its bottom part) was used as the repeller plate for the VMI (see Sec. 6.3). The mu-metal shield is made of two independent parts, connected together by six M3 screws (see Fig. 6.19 c)). The assembly and commissioning of the VMI setup was implemented as follows:

1. We attached eight PEEK threaded rods to the top CF200 flange, using previously made 1/4-20 threaded holes (Fig. 6.14 a)). The inner four rods of length 4" are used to hold the MCP setup, while the outer ones of length 2" are used to hold the VMI stack as described below. On each of them, a PEEK spacer of 5 mm was inserted to isolate the mu-metal shield from the rest of the chamber, as the mu-metal shield will be kept at a voltage on the order of -1 kV with respect to the chamber.

2. Due to a machining error, the mu-metal shield was 1" shorter than designed therefore an aluminum ring of 1" thickness was added in between the PEEK spacers and the top part of the mu-metal shield (Fig. 6.14 b)).

3. The mu-metal shield was then added and fixed in place using four stainless steel nuts on the four threaded rods on the outside (Fig. 6.14 c) and Fig. 6.15 a)). The top part of the mu-metal shield holes, through which the rods pass, has an elongated shape in order to allow for the rotation of the whole setup for further alignment. The central hole (Fig. 6.15 b)) is used for the electrical connections to the vacuum feedthroughs.

4. The previously assembled MCP stack (see Sec. 6.3.2) was attached to the inner PEEK rods using the metal ring shown in Fig. 6.15 c) by pressing it against the golden spacers using stainless steel nuts (Fig. 6.15 b)). The vertical position of the VMI was adjusted using the M2 nuts on the threaded rods attaching the MCP to the metal ring (see Sec. 6.3.2). The final position of the front plate of the MCP was about 400 mm from the ionization point of the atoms. The exact location is not very important, as it can be easily calibrated using electrons with known energy (e.g., produced from an atom with well-known ionization potential).

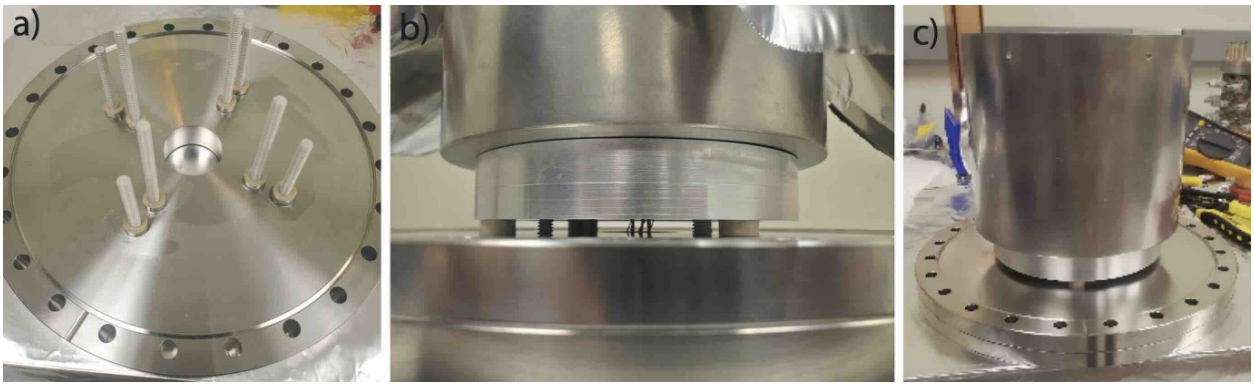

Figure 6.14: a) CF200 flange used to attach the VMI setup above the optical cavity. Four inner (4" long) and four outer (2" long) PEEK threaded rods are attached to the flange using previously made 1/4-20 threaded holes. 5 mm PEEK spacers are used to separate the flange (which is grounded) from the mu-metal shield (which is kept at a voltage of ~ -1 kV). b) An aluminum ring of 1" thickness is added between the flange and the mu-metal ring to compensate for a machining error on the length of the mu-metal shield. c) Top part of the mu-metal shield attached to the CF200 flange.

5. The electrical connections to the MCP were passed through the open hole in the top part of the mu-metal shield (Fig. 6.16 a) and c)) to the corresponding pins on the provided 12-pin vacuum feedthrough (Fig 6.16 b)). The connections on the feedthrough are such that they can be directly connected to the FT12TP signal decoupler electronic box from RoentDek (see Sec. 6.3.2). The box contains six SHV connections used to apply voltage to the MCP Front, MCP Back, the shim ring, the anode holder and the bias for the reference and signal wires (labeled on the box as Front, Back, X, Holder, Ref. and Signal), as well as six LEMO 00 connections for signal readout from the two ends of the anode in the x and y direction (labeled on the box as x1, x2, y1 and y2) and from the MCP Front and MCP Back rings (labeled on the box as Front and Back). The box contains the needed electronics to decouple the high voltage ($\sim 1-2$ keV) needed for the MCP operation from the weak signal from electrons hitting the detector. Also, the decoupling box is compatible with the RoentDek amplifier and constant fraction discriminator (CFD) needed for signal processing, as described below. As only one of the MCP Front and MCP Back signal outputs is needed as reference for any given event, the one not used (MCP Back in our case) was terminated with a 50 Ω resistance for a better signal shape.

6. Before attaching the VMI stack and the bottom part of the mu-metal shield, the current setup was placed inside the main vacuum chamber to test the proper functionality of the MCP, and the chamber was placed under vacuum. The used scroll pump had a valve attached to it, which was slowly opened after turning on the pump. This was done to avoid sudden changes in pressure, which can damage the MCP (ideally, the pressure increase/decrease should be < 50 mbar/s). After about 10 mins of slowing opening the valve, it was fully open and the pressure was $\sim 10^{-1}$ mbar. At this point, the turbo pump was turned on. Once the pressure reached 10^{-6} mbar, the MCP was

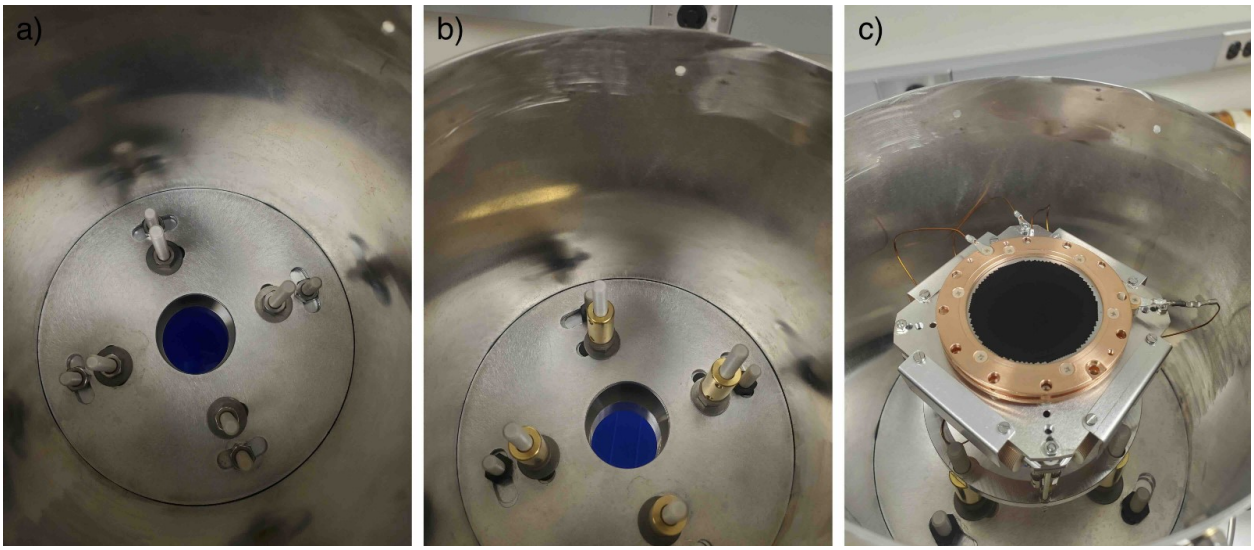

Figure 6.15: a) The top part of the mu-metal shield is attached to the CF200 flange using eight aluminum nuts of 0.25" thickness. b) On top of the nuts, for the four inner PEEK threaded rods, metal spacers of 1" thickness are added for better horizontal alignment of the MCP detector. c) The MCP detector is attached on top of the metal spacers using a previously mounted aluminum ring (see Sec. 6.3.2 for details).

not turned on for an extra 24 hours. After this period, the pressure in the vacuum chamber was $\sim 10^{-7}$ mbar and remained approximately constant for the rest of the experimental tests. Note that any vacuum gauge needs to be turned off during the MCP operation, as it might act as a large electron source which can damage the MCP permanently.

7. The first test performed investigated the proper electrical connection in vacuum. Using a signal generator (RoentDek APG1) producing pulses of 10 mV amplitude and 20 ns width, signals were sent through the x1 channel and readout through the x2 channel (similar tests have been done for the y1, y2, MCP Front, and MCP Back). The results of such a test are shown in Fig. 6.17 a) where the pink line is the input signal, blue is the readout signal and green is the y1 signal (which shouldn't see this input). The delay between the input and output (< 100 ns) for the x1 and x2 signals was consistent with MCP specifications. This confirmed the proper wiring.

8. The resistance between the different channels on the decoupling box was measured to be > 40 MOhm (limited by the multimeter readout), confirming that no cross-talk existed between the channels. The only value smaller than this was between MCP front and the shim ring, at 14.8 MOhm, which was within the expected specifications. However, before the MCP could be properly used, this resistance had to be matched to the one between the MCP back and the shim ring (which was > 40 MOHm). Thus, a resistance was needed in parallel to the latter two channels. The HVT4+ box provided by Roentdek, with a resistance of 25 MOhm, was initially used, giving a total resistance between MCP Back and the shim ring of 16.6 MOhm, still bigger

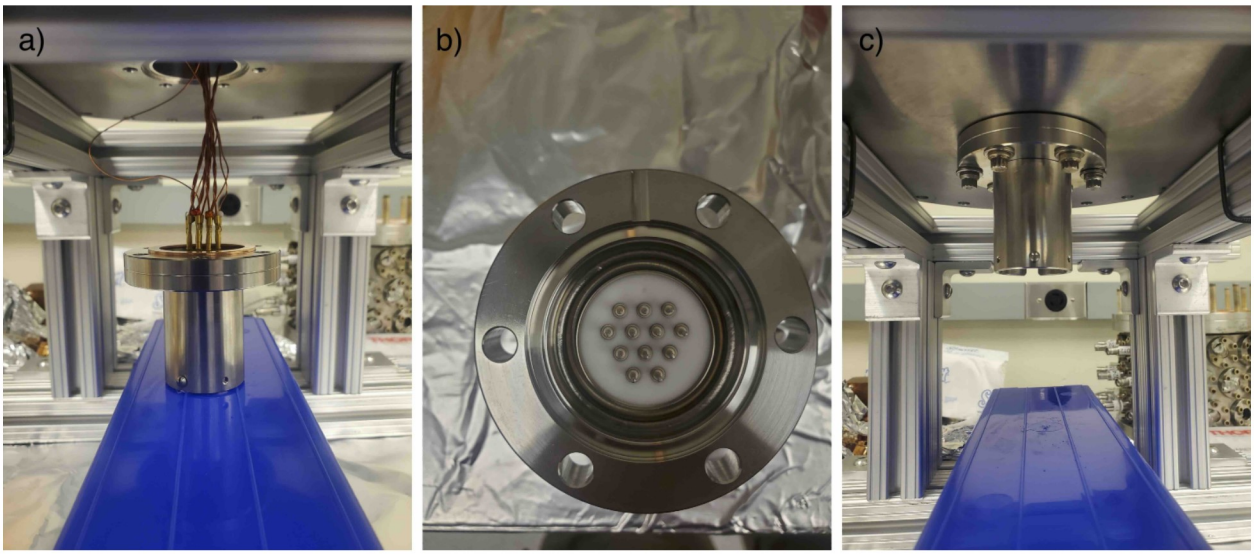

Figure 6.16: a) Electrical connections of the anode wires and MCP rings (see Sec. 6.3.2) to the vacuum feedthrough flange. b) Pins on the vaccum feedthrough flange, used for connection to the FT12TP signal decoupler electronic box. c) Vacuum feedthrough with all connections attached to the CF200 flange.

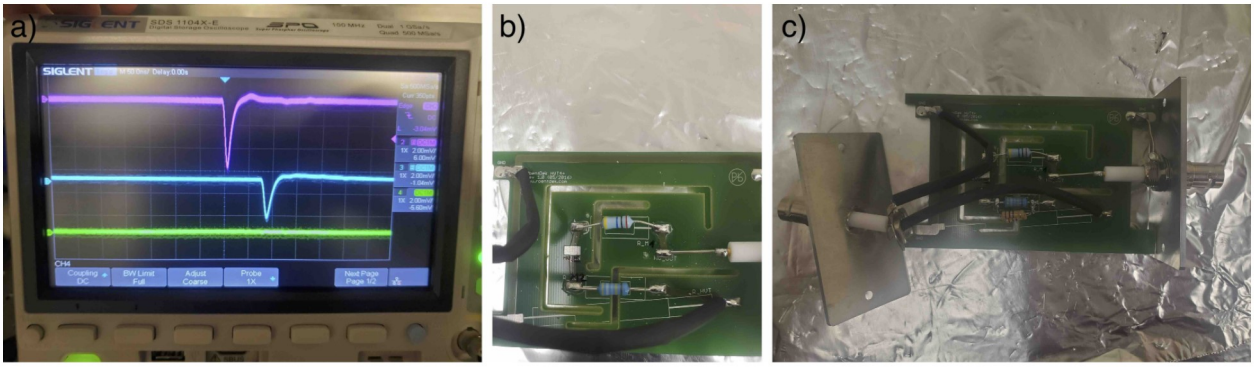

Figure 6.17: a) Sample of signal on the oscilloscope when a pulse of 10 mV amplitude and 20 ns width was sent on the x1 channel of the decoupling box. The pink line is the original signal, the blue line is the signal readout from the x2 channel (the other end of the x-position encoding wire), and the green line is the signal from the y1 channel. b) Resistances present in the HVT+ box delivered by RoentDek (5 MOhm and 20 MOhm in series). c) Final resistance configuration after 2 10 MOhm resistances were added in parallel to the 5 MOhm resistance.

than needed. To calculate the needed resistance more precisely, a 400 V potential difference, using an NHQ 205M high voltage module, was applied between the MCP Front and the X channel (corresponding to the shim ring), and the resulting current was read with a 1 μA resolution. The obtained resistance was 15.0(5) MOHm. Using the same method, a 45.0(5) MOhm resistance was obtained between MCP Back and the X channel. Thus, a 22.5 MOhm was needed in parallel with MCP Back and the X channel. The HVT4+ box contained two resistances of 5 and 20 MOHm in series, therefore, two more resistances of 10 MOhm were added in parallel to the 5 MOhm one (see Fig. 6.17 b) and c)), leading to the desired final resistance between MCP Back and the X channel. The resistance matching was confirmed by applying a voltage and measuring the current as described above.

9. The next step was to perform the MCP startup procedure, which required slowly increasing the voltage on the MCP Front and MCP Signal inputs up to the desired values. As for the initial test we wanted to check the ion background, the recommended final values were −2000 V for MCP Front and +270 V for MCP Signal. We started by increasing the MCP Signal value to +270 V and reducing the MCP Front to −730 V (for a difference of 1000 V) using NHQ 205M high voltage modules. Then, the voltage on the MCP front was reduced by 50 V every 10 mins until it reached −2000 V. For some increment steps, the current went over the limit imposed using the high voltage module (0.2 mA), which triggered the voltage to drop to zero. When this happened, the voltage was quickly brought to the last stable value, and the process continued until the final value on the MCP Front was achieved. At each step, the current was also recorded, showing the expected linear trend as a function of voltage (Fig. 6.18 a)) and further confirming the proper working of the MCP. Once −2000 V was reached on the MCP Front, we waited for 30 minutes before making all the electrical connections outside the vacuum. For future operations of the MCP, the voltages can be directly increased/decreased to the desired voltage as long as the ramp is below 500 V/s.

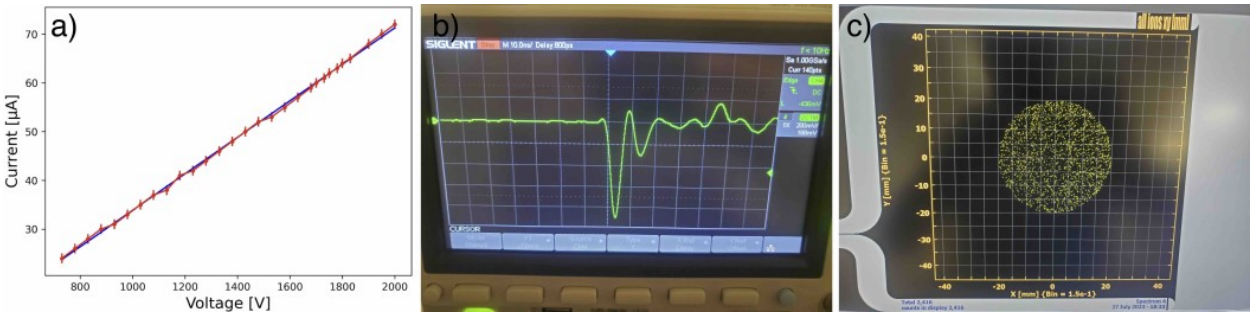

Figure 6.18: a) Recorded current vs input voltage from the ISEG HV NHQ 205M module during the starting procedure of the MCP. Red dots represent the data, while the blue line results from a linear fit to the data. b) Example of background signal from MCP Front recorded on the oscilloscope after amplification using FAMP1. c) Example of recorded 2D distribution of background events using the CoboldPC software.

10. We began by connecting the four anode outputs (x1, x2, y1, y2) and the MCP Front output to an amplifier (FAMP1+ or ATR19-2 from RoentDek) and observing their

analog output on an oscilloscope in order to check for background events. The resulting shape, as well as the rate ($\sim$ 50/s) of the events, were as expected (Fig. 6.18 b)). The height of all five outputs was adjusted to about 150 mV on average after amplification.

11. The signals from the decoupler box were then connected to the provided RoentDek analog electronics. The signals from x1, x2, y1, and y2 were each sent to one of the input channels of the ATR19-2 module, which acts both as an amplifier and a constant fraction discriminator (CFD). The MCP Front signal was first sent to an amplifier (FAMP1+) and then to a separate CFD (CFD1c). The NIM outputs from the CFDs are subsequently sent to a RoentDek 8 channels TDC card (TDC8HPi) attached to a PCI2PCIe adapter crate. The data is recorded on a Windows PC using a PCIe card. The TDC card has a $<$ 100 ps resolution, allowing $<$ 100 μm 2D position resolution and rates $>$ 2 MHz per channel. Then, the first 2D spectrum was recorded using the provided CoboldPC software, as shown in Fig. 6.18 c). The background data was uniformly distributed over the whole area of the MCP, as expected.

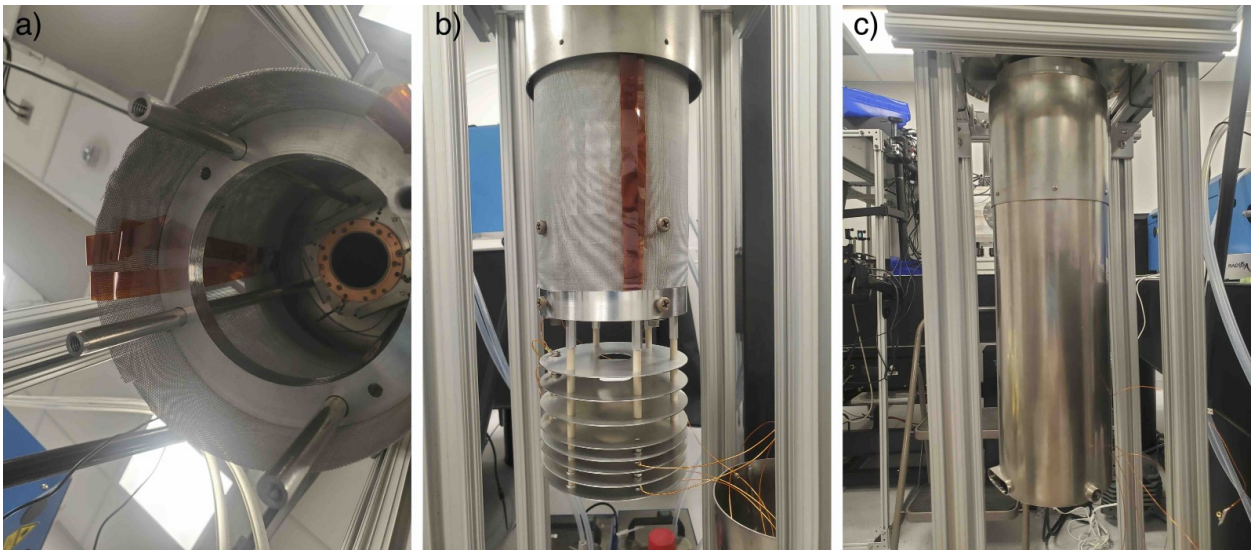

Figure 6.19: a) 4 aluminum rods (40 cm long) are attached to the outer four PEEK spacers on the CF200 flange. A 1" thick aluminum ring is used to add further stability and better alignment for the rods, as well as ease the attachment of an aluminum mesh around the rods (see Sec. 6.3.3 for details). b) The previously assembled VMI setup is attached to the four aluminum rods using a 1" aluminum ring. c) Fully assembled mu-metal shield. The top and bottom parts are attached together using M3 aluminum screws.

12. Once the preliminary results of testing the proper functionality of the MCP were complete, the vacuum was turned down in the chamber, and the top flange with the MCP and the top part of the mu-metal shield attached removed in order for the rest of the VMI setup, as well as the bottom part of the mu-metal shield to be attached.

13. Four aluminum rods of equal length (40 cm), used to hold the VMI stack containing the electrodes, were attached to the four outer PEEK threaded rods (Fig. 6.19 a)). As

in the final setup the mu-metal shield will be kept at a non-zero voltage (on the order of -1 kV), an aluminum mesh was placed around the rods in order to shield the electrons traveling towards the MCP from this voltage (Fig. 6.19 b)). An aluminum rod of 1″ thickness was added about halfway in between the electrodes stack and the MCP in order to add more stability to the aluminum rods, as well as ease the attachment of the aluminum mesh (Fig. 6.19 a)). A Kapton tape was placed around the region where the two ends of the aluminum mesh were connected in order to prevent any sharp edges from producing a voltage drop between the mu-metal shield and the mesh.

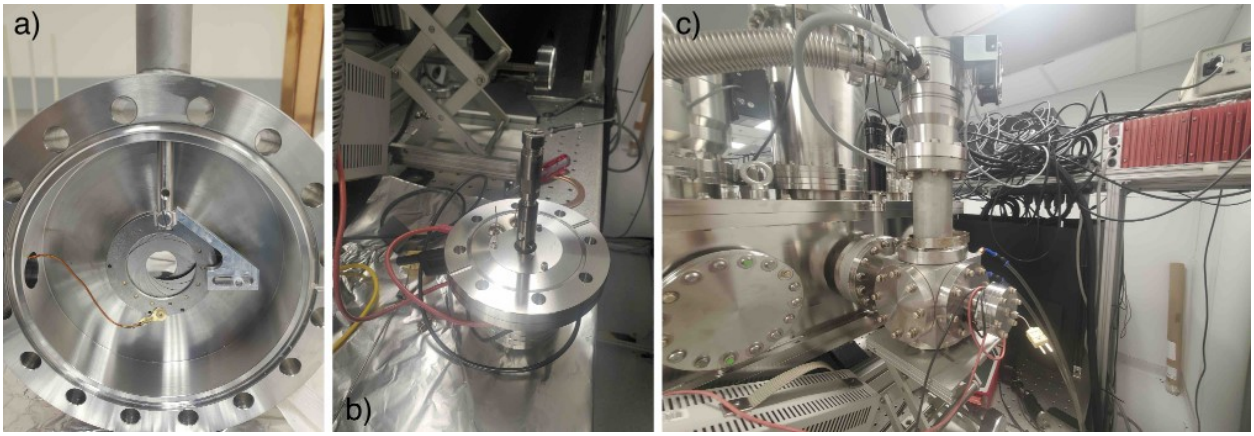

Figure 6.20: a) Assembled iris attached to a linear feedthrough that allows for adjusting of the inner diameter between 3 and 25 mm. An electrical connection is made to the iris to allow for its use as a Faraday cup in the future, for ion beam alignment and calibration. b) Crucible used to load the Yb in the oven. c) Iris and oven attached to the main interaction chamber. A vacuum pump is added on top of the oven for differential pumping.

14. Finally, the VMI electrode stack was attached at the bottom of the aluminum rods using another aluminum ring of 1″ thickness (Fig. 6.19 b)). This ring was attached to the aluminum rods using M6 PEEK screws. The electrode stack was attached to the ring using aluminum screws. The ring and the top 4 electrodes were connected to each other and kept at the ground potential. The other electrodes had individual connections (kapton-covered wires in Fig. 6.19 b)) that were attached to individual SHV connectors on the vacuum feedthrough, allowing the application of individual voltages. The electrode disks were attached to each other using PEEK spacers. The M6 PEEK screws were used to adjust the electrodes stack horizontally in order for it to be parallel to the MCP. The alignment was achieved using an electronic level meter by comparing the inclination of the top flange (to which the MCP was previously aligned) with the inclination of the top disk of the VMI stack. Previously, the alignment of all the electrodes with respect to the top one was done using an analog level meter. The bottom part of the mu-metal shield was then connected to the top part using M3 screws as shown in Fig. 6.19 c), and the electrical connection cables to the VMI electrodes were brought outside the mu-metal shield through previously made holes on the side. Two bigger circular holes in the bottom part of the mu-metal shield will be used for the ions/atoms path, while the two elongated holes will be used for laser path

access.

15. The fully assembled setup was placed again at the top of the main experimental chamber, and the cables to the VMI electrodes connected to SHV pins on the vacuum feedthroughs.

16. A previously assembled iris was attached between the oven atomic source and the main interaction chamber (Fig. 6.20 a)). This ensured a better collimation of the atoms while preventing too many atoms from reaching the interaction region, which could negatively impact the vacuum level. The oven was loaded with Yb (Fig. 6.20 b)) and then attached to the main interaction chamber, and a small turbo pump was placed on top of the oven chamber for differential pumping relative to the main chamber (Fig. 6.20 c)). The oven is equipped with a water cooling system able to keep it at 20º C. Its inner element is heated by applying a current to built-in connector pins, and the resulting temperature inside can be readout using a type K thermocouple.

17. For the initial tests, a thermal source of Yb was used. Given the low energy of the atom expected from this source (a few 1000 m/s), the ions produced upon ionization inside the mu-metal shield will not be able to exit the shield and will hit its bottom part. Thus, for the initial test, only the electron detection was possible. Current developments are being made to allow the use of atoms with energies of up to 20 keV, which would allow the detection of both the electrons and ions produced upon ionization in coincidence.

6.4 Results

The whole setup was put under vacuum following the procedure described in Sec. 6.3.3. For the initial tests, with the goal of testing the proper functionality of the VMI electron detector, the ${}^1S_0(4f^{14}6s^2) \rightarrow {}^3P_1(4f^{14}6s7p)$ transition of Yb, at 262 nm [287], was studied using a 2-step resonant ionization process. For this, two pulsed lasers were sent perpendicularly to the direction of motion of the atoms, using previously mounted VC234 Thorlabs viewports on the sides of the main experimental chamber. The first laser was a home-built grating titanium-sapphire (Ti:Sa) laser with a linewidth of ~ 2 GHz and tunable wavelength [51, 247]. In order to reach the required frequency for the first step in the 2-step resonant-ionization process, the frequency of the light produced by this laser was first doubled using a BBO crystal and then tripled using a second BBO crystal by summing the initial and doubled frequencies. The second laser, used for the non-resonant ionization, was a commercial BigSky 532 nm Nd:YAG laser. For these tests, the optical cavity was not placed in the main experimental chamber.

The Nd:YAG laser polarization was adjusted using a zero-order half-wave plate (see Sec. 6.2.3). This was needed in order to ensure that the polarization direction was parallel to the plane of the MCP detector (see Sec. 6.3.1). Both lasers were injected inside the experimental chamber through the same viewport using a bichromatic mirror. A second viewport, located on the other side of the chamber relative to the injection point, was used

to dump the laser power to a beam dump, as well as perform the initial laser alignment, using an iris on each of the 2 viewports.

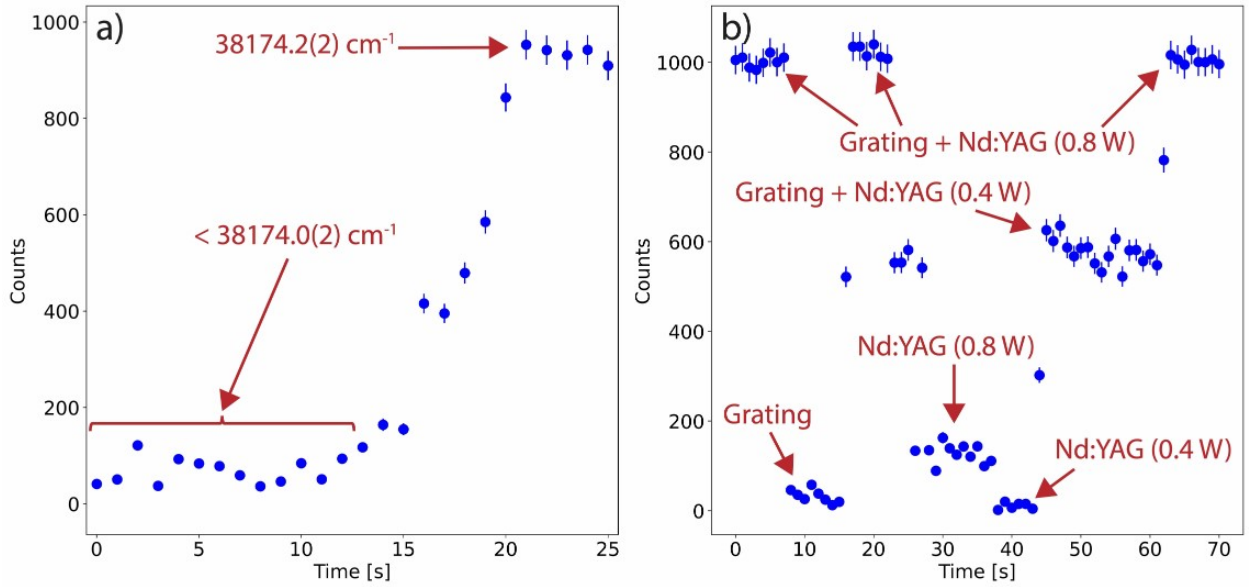

Figure 6.21: a) Number of counts as a function of time for different values of the wavenumber of the first step laser, from below resonance ($<$ 38174.0(2) cm^{-1}) to the resonance value (38174.2(2) cm^{-1}). The first and second step laser powers were kept constant at 50 μW and 0.8 W, respectively. b) Number of counts as a function of time for different changes in the laser setup. For all cases where the Grating laser was on, its power was at the optimized value of 50 μW.

For the used Yb transition, the wavenumber of the first step laser was set based on the literature resonance value of 38174.17 cm^{-1} [287]. The oven current was increased to 3 A (corresponding to $\sim$ 300^{o} C), the maximum value allowed by the oven specifications. The grating laser power after the tripling unit was set to 10 μW and the green laser to 900 V, corresponding to a power of 2.1 W. The delay between the 2 lasers was set to 100 ns. The MCP signals were recorded if they occurred in a time window of 100 ns after the Nd:YAG laser pulse. An increment in the MCP counts signal with both lasers on, in the above-mentioned configuration, was observed relative to the case of only one of them being on. This initial signal was optimized by adjusting the various available parameters, reaching the best parameters at a voltage of the Nd:YAG laser of 850 V (0.8 W), a power of the grating laser of 50 μW and a delay between the 2 lasers of 100 ns. The resonant nature of the signal was tested by changing the frequency of the laser, in which case the signal dropped significantly, or by blocking one or both of the lasers, which had a similar effect. In Fig. 6.21 a), we can see a clear, significant increment in the number of counts when the frequency is increased from below 38174.0(2) cm^{-1} to the resonant frequency, 38174.2(2) cm^{-1}. Due to DAQ-related issues, we could not record the laser wavelength as a function of time. Thus, the quantity on the x-axis in Fig. 6.21 is time instead of wavenumber. This issue is being addressed in the current, improved version of the experiment. In Fig. 6.21 b), we also show the signal variation when changes to the laser setup are made, such as blocking one of the

two lasers or reducing their power, further proving the resonant signal observed. From Fig. 6.21, it can be seen that a large SNR ($\sim$ 10) can be achieved for the right experimental parameters. By further reducing the power of the two lasers, we were able to achieve a background as low as $<$ 1 count per minute at the cost of a reduced number of events when on resonance. We note that detecting the ions in coincidence with the electrons should keep the background at the $<$ 1 count per minute level while allowing a significant increase in the SNR. This path is currently pursued in the improved version of the experiment (see Sec. 6.5).

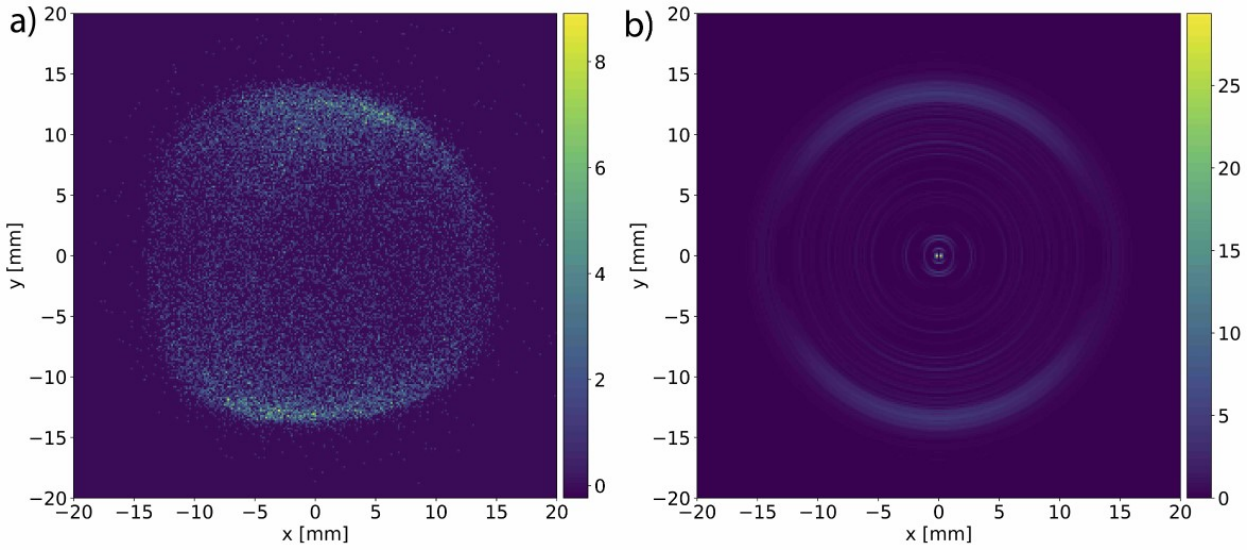

Figure 6.22: a) 2D VMI raw image obtained using the optimized electrode voltages (see Table 6.1). The color code is shown in the color bar on the right and corresponds to the number of counts in each 0.15 $\times$ 0.15 mm pixel. b) 2D image obtained after performing an inverse Abel transform on the raw image. The color code is shown in the color bar on the right and corresponds to the number of counts in each 0.15 $\times$ 0.15 mm pixel.

With the first step laser frequency fixed on the resonant transition, a 2D image of the electrons on the MCP was recorded. Starting with and adjusting the values of the voltages obtained from SIMION simulations (see Sec. 6.3.1), the 2D pattern obtained on the position-sensitive detector was optimized, aiming to improve the spatial/energy resolution of the signal. The voltages giving the best result are shown in the last column of Table 6.1, and the obtained 2D image is displayed in Fig. 6.22 a). Two lobes, corresponding to a p-wave electron, can be clearly seen, with their thickness setting the energy resolution of the setup. We believe that the deviation of the 2D pattern from a circular shape is mainly due to the extended and non-symmetrical distribution (along the direction of the lasers) of the thermal atomic beam in the interaction region. This effect should be significantly reduced once we switch to an ablation target ion source and increase the ions' energy to $\sim$ 20 kV, as planned for the improved version of the experiment (see Sec. 6.5). In order to extract the energy resolution of the setup, an inverse Abel transform was performed using the rBasex algorithm [288] and the obtained pattern is shown in Fig. 6.22 b). The existence of the two lobes is even more apparent than in the raw image, while the background events have a minor effect,

as expected [251].

From the obtained inverse-Abel transformed image, the achieved energy resolution can be obtained by fitting the radial distribution with a Gaussian plus a constant function. This is shown in Fig. 6.23. Given the known ionization potential of Yb [289] and the frequencies of the two lasers used, the location of the Gaussian mean, $\mu = 13.8(1)$ mm, corresponds to an electrons energy of 0.74 eV. Then, the width of the Gaussian distribution, $\sigma = 0.97(1)$ mm, leads to an energy resolution of the VMI setup of $\Delta E = 100(10)$ meV. This resolution is already enough to clearly distinguish between different electronic energy levels in most atoms, and we expect to improve it by at least a factor of ~ 5 in the updated version of the experimental setup.

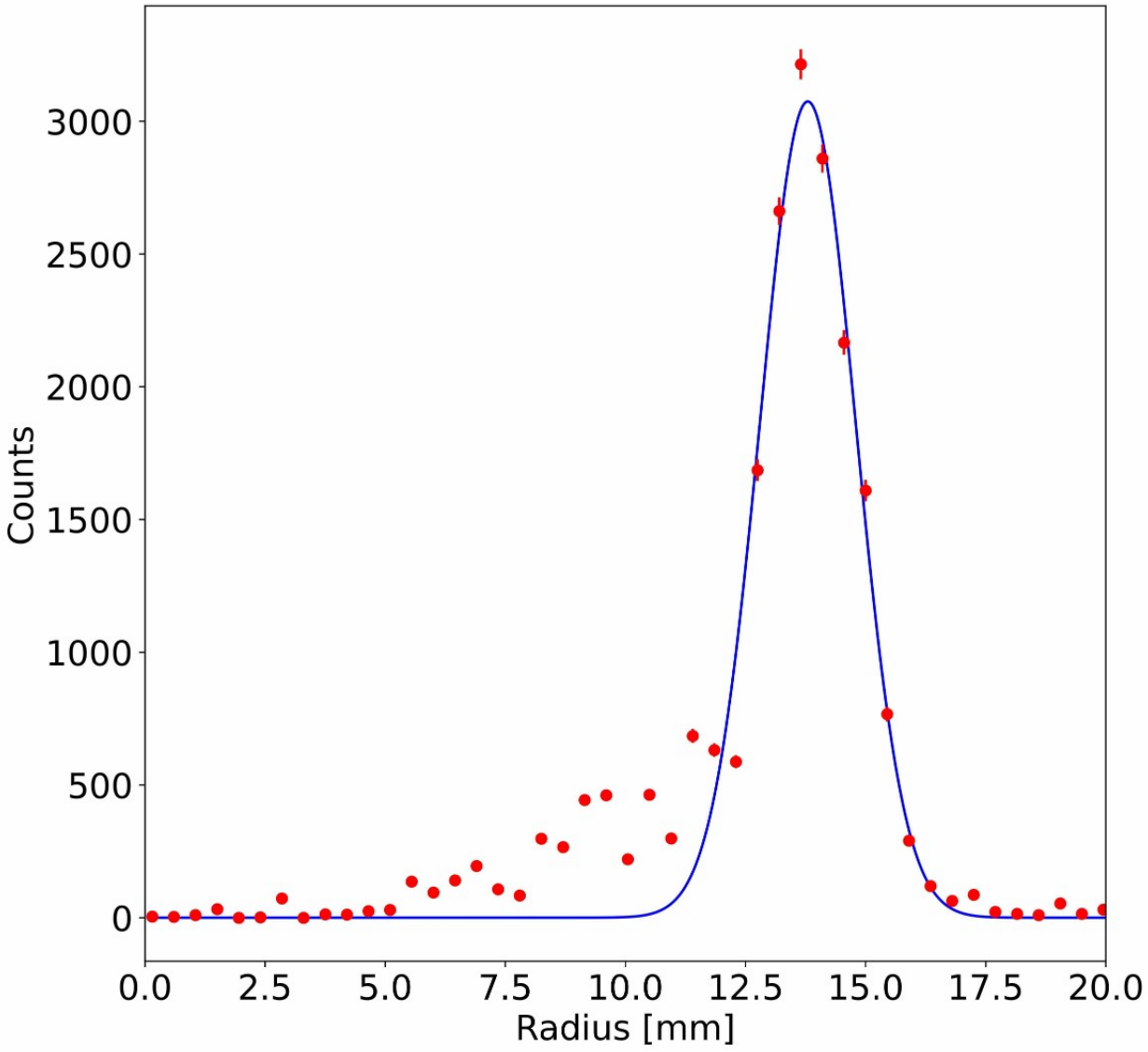

Figure 6.23: Measured counts as a function of the radial distance from the center of the position-sensitive detector. The red dots represent the data, while the blue line is the fit to the data.

6.5 Outlook

Now that the VMI setup and the cavity locking were successfully tested under vacuum, there are several directions to be pursued moving forward. The first obvious next step is reproducing the obtained results using the actual cavity for the ionization step instead of the Nd:YAG laser. Placing the cavity in the experimental chamber will prevent us from sending the first step laser perpendicularly to the direction of motion of the atoms, and an anti-collinear direction will be used.

As the ionization step now has a wavelength of 1064 nm, no transitions in Yb can be studied with only one excitation step (using multi-step resonant steps in the future is also being considered). Therefore, we decided to test the setup using a Cs source, and drive the $^2S_{1/2}(5p^6 6s) \rightarrow^2 P_{3/2}(5p^6 8p)$ transition at 387.7 nm [290] as the first step, which can be achieved by doubling the light produced by our grating Ti:Sa laser using a BBO crystal. Using a CW laser for the first step in the future, instead of the grating Ti:Sa laser, will also be explored. This transition will take us 0.7 eV away from the IP of Cs [291], from which we can induce non-resonant ionization with a 1064 nm (1.17 eV) laser.

In the proof of principle experiment, the ions reaching the interaction region had too little energy to escape the mu-metal shield. This was because they were produced using a thermal source. While for the initial test of inducing ionization using the optical cavity we will also use a thermal source (but of Cs instead of Yb), we aim to switch to a laser ablation target ion source. This will allow us to produce ions instead of neutral Cs atoms. The ions obtained from ablating a solid Cs target (e.g., using a BigSky Nd:YAG 532 nm laser) can be accelerated to high energies (we aim for 20 keV kinetic energy), deflected by 90 degrees towards the interaction region, then neutralized in a charge exchange cell. The non-neutralized Cs ions will be deflected, while the neutral ones will be able to reach the interaction region inside the mu-metal shield. A Rb-based charge exchange cell is already in our lab, and its installation and characterization are underway. Importantly, given that we can control the ions electrostatically before neutralization, we can have a much more focused atomic beam in the interaction region compared to the one produced from the oven source, which should allow for a significantly higher energy resolution (see Sec. 6.4). The 90 degrees bender has already been assembled and is ready to be installed (see Fig. 5.2). Its design allows ample laser access, which is needed both for ablation and for the alignment of the first step resonant laser. After the interaction region, a 6-way cross will be placed with a MagneTOF ion detector to detect the ions exiting the mu-metal shield, which is now possible given their high kinetic energy. This new setup will allow us to test the cavity inside the vacuum, the new Rb charge exchange cell, as well as various background reduction techniques by using the time and position information of the electrons and ions produced during the ionization event. Using a position-sensitive detector instead of a MagnetTOF to detect the ions can further allow background reduction and even an event-by-event reconstruction of the initial energy of the atoms before ionization (see more details in Article 6 [56]). Once these tests are successful, the setup is expected to be taken to a radioactive beam facility for online study of short-lived isotopes.

Chapter 7

Conclusion and Outlook

In this thesis, I presented pioneering results in the field of radioactive molecules, opening the way for future precision measurements of fundamental physics using these systems. Taking advantage of the high sensitivity, selectivity, and spectroscopic resolution of the Collinear Resonant Ionization Spectroscopy (CRIS) technique, we achieved the first precision spectroscopic study of a radioactive molecule, radium monofluoride (RaF), opening the way for similar studies in other radioactive systems of interest, while proving the predicted high sensitivity of RaF to various nuclear structure properties.

In Article 1 [52], we performed a systematic investigation of an isotopologue chain of RaF molecules, being able to measure the vibrational spectrum of RaF molecules containing Ra isotopes with lifetimes of less than 4 days (^{224}RaF). These results revealed the isotope shift effect related to changes in the nuclear charge radius of the Ra nucleus and allowed us to quantify the changes in the RaF vibronic spectrum upon isotopic substitutions of the Ra nucleus. These measurements proved, for the first time, the high sensitivity of RaF molecules to small nuclear effects, while confirming the reliability of many-body electronic structure calculations at the $< 10\%$ level. These results were the first of their kind performed on radioactive molecules, providing empirical evidence for the suitability of these systems for future fundamental physics studies.

While very encouraging results were obtained in the work presented in Article 1, the spectroscopic resolution prevented the observation of the finer details of the energy structure of the RaF molecules. The resolution of the experiments was improved in a second experimental campaign, allowing us to resolve the rotational and hyperfine structure of these molecules. Article 2 [53] describes the first rotational spectroscopy of a radioactive molecule, ^{226}RaF, which allowed us to observe molecules in rotational levels with production rates as low as 50 molecules per second. The measured data was fit with an effective Hamiltonian, from which the rotational energy levels, useful for future precision spectroscopy studies, can be determined. The measurements also allowed us to quantify, for the first time, an efficient laser cooling scheme for RaF, proving the suitability of this molecule for future precision measurements.

Article 3 [54] reports the advances made to observe the rotational and hyperfine structure of the ^{225}RaF molecule. This allowed us to study the magnetic dipole moment of the ^{225}Ra nucleus and observe, for the first time in a molecule, the effect of the distribution of the nuclear magnetization in one of the constituent nuclei on the energy levels of the molecule.

This result further highlighted the high sensitivity of RaF molecules to minuscule nuclear effects, even nuclear-spin dependent ones, while confirming the accuracy and precision of *ab initio* quantum chemistry many-body calculations at below 1% level of accuracy. In the same article, using electronic structure and single particle nuclear shell model calculations, we predicted the expected effect of various nuclear symmetry-violating effects in RaF molecules. The obtained results proved that by applying advanced quantum sensing techniques already used for stable molecules to RaF, one could set world-record bounds on symmetry-violating effects.

Article 4 presents a measurement of the ionization potential (IP) of the RaF molecule. This is the first IP measurement performed on a short-lived, radioactive molecule. The obtained value of the IP was in excellent agreement with *ab initio* quantum chemistry many-body calculations, proving the critical contribution of relativistic effects in understanding the properties of this molecule. We showed that, unlike most molecules, the IP of RaF is below the dissociation energy, which should allow the investigation, with high precision, of high-lying Rydberg states in RaF. These states can facilitate an enhanced control of these molecules using external electric fields, which can be a valuable tool for future precision measurement studies. Concurrently, knowing the precise value of the IP can allow for the development of laser ionization schemes with improved signal-to-background ratio.

These results have stimulated different research directions, as described in detail in Chapter 4. Developments to implement the laser cooling scheme presented in Article 2 [53] are underway. Starting with laser cooling and trapping of ^{226}RaF, the experimental scheme will be extended to ^{225}RaF molecules, and other RaF isotopologues containing Ra isotopes with nuclear spin, such as ^{223}Ra. Once cooled and trapped, precision measurement of nuclear symmetry violating effects can be performed. Concurrently, efforts are being made to measure other symmetry-conserving properties of RaF molecules, such as the rest frame electric dipole moment, needed for the symmetry violation measurements [26, 28, 29], or the nuclear magnetic octupole moment of ^{223}Ra, which can provide us with a better understanding of the nucleon distribution inside the Ra nucleus [15]. At the same time, the techniques presented in Articles 1, 2, 3, and 4 [52–54] can be extended to other radioactive molecules of interest for symmetry violation searches as well as for astrophysics [181, 200, 204–208, 216]. A letter of intent for the development of Pa beams for future experiments using Pa atoms and molecules has already been approved at FRIB. Studies of these species should begin in the coming years. ^{229}Pa is expected to have an enhanced sensitivity to nuclear symmetry violating effects, which is two orders of magnitude higher than for Ra isotopes [45, 46, 206].

Following the results achieved in the RaF molecule, Article 5 [55] presents a different experiment with the goal of measuring hadronic parity violation using single molecular ions in a Penning trap. The experiment is well suited for molecules containing short-lived, radioactive nuclei and should allow the investigation of parity-violating properties at the nuclear level in a wide range of nuclei across the entire nuclear chart. This will provide critical information to understand the weak interaction between protons and neutrons. Moreover, it will allow us to measure some of the least well-known parameters of the Standard Model [26, 43, 55]. Improvements in nuclear structure calculations could potentially facilitate the use of such measurements for searches for beyond the Standard Model physics, too [17]. The current status of the experiment is presented in Chapter 5, with the following steps being the

trapping of ions in our new Penning trap, the proof of principle for the AC Stark interference technique inside the trap, and, ultimately, a non-zero measurement of parity violation effects. Once these goals are achieved on the MIT campus, the setup can also be taken to radioactive beam facilities in order to perform measurements in molecules containing radioactive nuclei, where the sought-for effects can be significantly enhanced [14, 54].

Finally, Chapter 6 presents a new experimental setup, with the goal of measuring isotopes with lifetime on the order of 1 ms and below. The experiment will be applicable to isotopes produced with small rates ($<$ 1 ion per minute) and in the presence of highly contaminated environments. This will enable measurements of the electromagnetic properties of key isotopes at the extreme of stability, which are of particular interest for nuclear structure, astrophysics, and beyond the Standard Model physics [15, 56]. Such species can't be studied currently with existing laser spectroscopy techniques. Article 6 [56] proposes a new experimental setup that could overcome most of the shortcomings of the existing methods and will allow the study of a wide range of nuclei at the limits of stability. Chapter 6 presents the status of this experiment, together with preliminary results, showing the ability of this technique to achieve very low background levels ($<$ 1 event per minute), with ample room for improvement in the future. Once all the components of the experiment are proved to work together, and a proof of principle measurement is performed at MIT, the goal is to take the setup to a radioactive beam facility and apply it to the study of short-lived isotopes of interest [56].

The study of radioactive molecules is an emergent field of research, with a wide variety of species, diatomic and polyatomic, neutral and ionic, waiting to be investigated. Currently, many molecules with complementary advantages have been proposed for studies of fundamental symmetries and new physics searches [181, 200, 204–208, 216]. The results presented in this thesis, as well as in the articles published as the result of this PhD work [52–56] are expected to motivate and guide future progress in this emerging field of research. Radioactive molecules offer unprecedented sensitivity to study various parity and time-reversal violating effects, with great promise to discover new physics beyond the Standard Model.

Bibliography

[1] M. Tanabashi, P. D. Grp, K. Hagiwara, K. Hikasa, K. Nakamura, Y. Sumino, F. Takahashi, J. Tanaka, K. Agashe, G. Aielli, et al., "Review of particle physics", Phys. Rev. D **98** (2018).

[2] X. Fan, T. G. Myers, B. Sukra, and G. Gabrielse, "Measurement of the electron magnetic moment", Phys. Rev. Lett. **130**, 071801 (2023).

[3] G. Aad, T. Abajyan, B. Abbott, J. Abdallah, S. A. Khalek, A. A. Abdelalim, R. Aben, B. Abi, M. Abolins, O. S. AbouZeid, et al., "Observation of a new particle in the search for the Standard Model Higgs boson with the ATLAS detector at the LHC", Phys. Lett. B **716**, 1–29 (2012).

[4] S. Chatrchyan, V. Khachatryan, A. M. Sirunyan, A. Tumasyan, W. Adam, E. Aguilo, T. Bergauer, M. Dragicevic, J. Erö, C. Fabjan, et al., "Observation of a new boson at a mass of 125 GeV with the CMS experiment at the LHC", Phys. Lett. B **716**, 30–61 (2012).

[5] F. Feruglio, "Pieces of the flavour puzzle", EPJ C **75**, 1–18 (2015).

[6] J. L. Feng, "Naturalness and the status of supersymmetry", Annu. Rev. Nucl. Part. Sci. **63**, 351–382 (2013).

[7] M. Dine and A. Kusenko, "Origin of the matter-antimatter asymmetry", Rev. of Mod. Phys. **76**, 1 (2003).

[8] R. Machleidt and D. R. Entem, "Chiral effective field theory and nuclear forces", Physics Reports **503**, 1–75 (2011).

[9] A. Obertelli and H. Sagawa, *Modern nuclear physics* (Springer, 2021).

[10] H.-W. Hammer, "Three-body forces: from cold atoms to nuclei.", Acta Physica Polonica B **46** (2015).

[11] J. De Vries, E. Epelbaum, L. Girlanda, A. Gnech, E. Mereghetti, and M. Viviani, "Parity-and time-reversal-violating nuclear forces", Frontiers in Physics **8**, 218 (2020).

[12] Y. Hao, P. Navrátil, E. B. Norrgard, M. Iliaš, E. Eliav, R. G. Timmermans, V. V. Flambaum, and A. Borschevsky, "Nuclear spin-dependent parity-violating effects in light polyatomic molecules", Phys. Rev. A **102**, 052828 (2020).

[13] B. Hu, W. Jiang, T. Miyagi, Z. Sun, A. Ekström, C. Forssén, G. Hagen, J. D. Holt, T. Papenbrock, S. R. Stroberg, et al., "Ab initio predictions link the neutron skin of ^{208}Pb to nuclear forces", Nat. Phys. **18**, 1196–1200 (2022).

[14] G. Arrowsmith-Kron, M. Athanasakis-Kaklamanakis, M. Au, J. Ballof, J. J. Dobaczewski, R. F. Garcia Ruiz, N. R. Hutzler, A. Jayich, W. Nazarewicz, and J. Singh, "Opportunities for fundamental physics research with radioactive molecules", Reports on Progress in Physics (2023).

[15] X. Yang, S. Wang, S. Wilkins, and R. G. Ruiz, "Laser spectroscopy for the study of exotic nuclei", Progress in Particle and Nuclear Physics **129**, 104005 (2023).

[16] R. F. Garcia Ruiz, M. L. Bissell, K. Blaum, A Ekström, N. Frömmgen, G. Hagen, M. Hammen, K. Hebeler, J. D. Holt, G. R. Jansen, et al., "Unexpectedly large charge radii of neutron-rich calcium isotopes", Nat. Phys. **12**, 594–598 (2016).

[17] M. S. Safronova, D. Budker, D. DeMille, D. F. J. Kimball, A. Derevianko, and C. W. Clark, "Search for new physics with atoms and molecules", Rev. of Mod. Phys. **90**, 025008 (2018).

[18] C. Abel, S. Afach, N. J. Ayres, C. A. Baker, G. Ban, G. Bison, K. Bodek, V. Bondar, M. Burghoff, E. Chanel, et al., "Measurement of the permanent electric dipole moment of the neutron", Phys. Rev. Lett. **124**, 081803 (2020).

[19] A. R. Vernon, R. F. Garcia Ruiz, T. Miyagi, C. Binnersley, J. Billowes, M. Bissell, J. Bonnard, T. Cocolios, J. Dobaczewski, G. Farooq-Smith, et al., "Nuclear moments of indium isotopes reveal abrupt change at magic number 82", Nature **607**, 260–265 (2022).

[20] Á. Koszorús, X. Yang, W. Jiang, S. Novario, S. Bai, J. Billowes, C. Binnersley, M. Bissell, T. E. Cocolios, B. Cooper, et al., "Charge radii of exotic potassium isotopes challenge nuclear theory and the magic character of N= 32", Nat. Phys. **17**, 439–443 (2021).

[21] M. Reponen, R. de Groote, L. Al Ayoubi, O. Beliuskina, M. Bissell, P. Campbell, L. Cañete, B. Cheal, K. Chrysalidis, C. Delafosse, et al., "Evidence of a sudden increase in the nuclear size of proton-rich silver-96", Nat. Comm. **12**, 4596 (2021).

[22] K. König, S. Fritzsche, G. Hagen, J. D. Holt, A. Klose, J. Lantis, Y. Liu, K. Minamisono, T. Miyagi, W. Nazarewicz, et al., "Surprising charge-radius kink in the Sc isotopes at N= 20", Phys. Rev. Lett. **131**, 102501 (2023).

[23] J. Karthein, C. Ricketts, R. Ruiz, J. Billowes, C. Binnersley, T. Cocolios, J. Dobaczewski, G. Farooq-Smith, K. Flanagan, G. Georgiev, et al., "Electromagnetic properties of indium isotopes elucidate the doubly magic character of ^{100}Sn", arXiv preprint arXiv:2310.15093 (2023).

[24] D. Antypas, A. Fabricant, J. E. Stalnaker, K. Tsigutkin, V. Flambaum, and D. Budker, "Isotopic variation of parity violation in atomic ytterbium", Nat. Phys. **15**, 120–123 (2019).

[25] C. Wood, S. Bennett, D. Cho, B. Masterson, J. Roberts, C. Tanner, and C. E. Wieman, "Measurement of parity nonconservation and an anapole moment in cesium", Science **275**, 1759–1763 (1997).

[26] E. Altuntaş, J. Ammon, S. B. Cahn, and D. DeMille, "Demonstration of a sensitive method to measure nuclear-spin-dependent parity violation", Phys. Rev. Lett. **120**, 142501 (2018).

[27] E. Altuntaş, J. Ammon, S. B. Cahn, and D. DeMille, "Measuring nuclear-spin-dependent parity violation with molecules: Experimental methods and analysis of systematic errors", Phys. Rev. A **97**, 042101 (2018).

[28] ACME Collaboration, "Improved limit on the electric dipole moment of the electron", Nature **562**, 355–360 (2018).

[29] T. S. Roussy, L. Caldwell, T. Wright, W. B. Cairncross, Y. Shagam, K. B. Ng, N. Schlossberger, S. Y. Park, A. Wang, J. Ye, et al., "An improved bound on the electron's electric dipole moment", Science **381**, 46–50 (2023).

[30] P. Sandars, "Electric dipole moments of charged particles", Contemporary Physics **42**, 97–111 (2001).

[31] J. M. Brown and A. Carrington, *Rotational spectroscopy of diatomic molecules* (Cambridge university press, 2003).

[32] K.-K. Ni, S. Ospelkaus, M. De Miranda, A. Pe'Er, B. Neyenhuis, J. Zirbel, S. Kotochigova, P. Julienne, D. Jin, and J. Ye, "A high phase-space-density gas of polar molecules", Science **322**, 231–235 (2008).

[33] E. S. Shuman, J. F. Barry, and D. DeMille, "Laser cooling of a diatomic molecule", Nature **467**, 820–823 (2010).

[34] J. Barry, D. McCarron, E. Norrgard, M. Steinecker, and D. DeMille, "Magneto-optical trapping of a diatomic molecule", Nature **512**, 286–289 (2014).

[35] L. De Marco, G. Valtolina, K. Matsuda, W. G. Tobias, J. P. Covey, and J. Ye, "A degenerate fermi gas of polar molecules", Science **363**, 853–856 (2019).

[36] L. Anderegg, L. W. Cheuk, Y. Bao, S. Burchesky, W. Ketterle, K.-K. Ni, and J. M. Doyle, "An optical tweezer array of ultracold molecules", Science **365**, 1156–1158 (2019).

[37] L. Anderegg, S. Burchesky, Y. Bao, S. S. Yu, T. Karman, E. Chae, K.-K. Ni, W. Ketterle, and J. M. Doyle, "Observation of microwave shielding of ultracold molecules", Science **373**, 779–782 (2021).

[38] N. B. Vilas, C. Hallas, L. Anderegg, P. Robichaud, A. Winnicki, D. Mitra, and J. M. Doyle, "Magneto-optical trapping and sub-doppler cooling of a polyatomic molecule", Nature **606**, 70–74 (2022).

[39] A. Schindewolf, R. Bause, X.-Y. Chen, M. Duda, T. Karman, I. Bloch, and X.-Y. Luo, "Evaporation of microwave-shielded polar molecules to quantum degeneracy", Nature **607**, 677–681 (2022).

[40] L. Anderegg, N. B. Vilas, C. Hallas, P. Robichaud, A. Jadbabaie, J. M. Doyle, and N. R. Hutzler, "Quantum control of trapped polyatomic molecules for eedm searches", Science **382**, 665–668 (2023).

[41] L. Christakis, J. S. Rosenberg, R. Raj, S. Chi, A. Morningstar, D. A. Huse, Z. Z. Yan, and W. S. Bakr, "Probing site-resolved correlations in a spin system of ultracold molecules", Nature **614**, 64–69 (2023).

[42] N. Bigagli, W. Yuan, S. Zhang, B. Bulatovic, T. Karman, I. Stevenson, and S. Will, "Observation of Bose–Einstein condensation of dipolar molecules", Nature, 1–5 (2024).

[43] D. DeMille, S. B. Cahn, D. Murphree, D. A. Rahmlow, and M. G. Kozlov, "Using molecules to measure nuclear spin-dependent parity violation", Phys. Rev. Lett. **100**, 023003 (2008).

[44] O. Sushkov, V. Flambaum, and I. Khriplovich, "Possibility of investigating P-and T-odd nuclear forces in atomic and molecular experiments", Zh. Eksp. Teor. Fiz **87**, 1521 (1984).

[45] N. Auerbach, V. Flambaum, and V. Spevak, "Collective T-and P-odd electromagnetic moments in nuclei with octupole deformations", Phys. Rev. Lett. **76**, 4316 (1996).

[46] V. Spevak, N. Auerbach, and V. Flambaum, "Enhanced T-odd, P-odd electromagnetic moments in reflection asymmetric nuclei", Phys. Rev. C **56**, 1357 (1997).

[47] J. Dobaczewski, J. Engel, M. Kortelainen, and P. Becker, "Correlating Schiff moments in the light actinides with octupole moments", Phys. Rev. Lett. **121**, 232501 (2018).

[48] T. Glasmacher, B. Sherrill, W. Nazarewicz, A. Gade, P. Mantica, J. Wei, G. Bollen, and B. Bull, "Facility for rare isotope beams update for nuclear physics news", Nuclear Physics News **27**, 28–33 (2017).

[49] M. J. Borge and B. Jonson, "Isolde past, present and future", Journal of Physics G: Nuclear and Particle Physics **44**, 044011 (2017).

[50] Y. Yano and T. Motobayashi, "Radioactive isotope beam factory at RIKEN (RIBF)", Nuclear Physics News **17**, 5–10 (2007).

[51] R. F. Garcia Ruiz, R. Berger, J. Billowes, C. Binnersley, M. Bissell, A. Breier, A. Brinson, K. Chrysalidis, T. Cocolios, B. Cooper, et al., "Spectroscopy of short-lived radioactive molecules", Nature **581**, 396–400 (2020).

[52] S.-M. Udrescu, A. Brinson, R. G. Ruiz, K. Gaul, R. Berger, J. Billowes, C. Binnersley, M. Bissell, A. Breier, K. Chrysalidis, et al., "Isotope shifts of radium monofluoride molecules", Phys. Rev. Lett. **127**, 033001 (2021).

[53] S.-M. Udrescu, S. Wilkins, A. Breier, M Athanasakis-Kaklamanakis, R. Garcia Ruiz, M. Au, I. Belošević, R. Berger, M. Bissell, C. Binnersley, et al., "Precision spectroscopy and laser-cooling scheme of a radium-containing molecule", Nature Physics **20**, 202–207 (2024).

[54] S. Wilkins, S.-M. Udrescu, M Athanasakis-Kaklamanakis, R. F. Garcia Ruiz, M. Au, I. Belošević, R. Berger, M. Bissell, A. Breier, A. Brinson, et al., "Observation of the distribution of nuclear magnetization in a molecule", arXiv preprint arXiv:2311.04121 (2023).

[55] J. Karthein, S.-M. Udrescu, S. B. Moroch, I. Belosevic, K. Blaum, A. Borschevsky, Y. Chamorro, D. DeMille, J. Dilling, R. F. G. Ruiz, et al., "Electroweak nuclear properties from single molecular ions in a Penning trap", Phys. Rev. Lett. **133**, 033003 (2024).

[56] S.-M. Udrescu, D. A. Torres, and R. G. Ruiz, "Precision spectroscopy of fast, hot, exotic isotopes using machine-learning-assisted event-by-event Doppler correction", Phys. Rev. Res. **6**, 013128 (2024).

[57] W. Demtröder, *Molecular physics: theoretical principles and experimental methods* (John Wiley & Sons, 2008).

[58] R. W. Field, *Spectra and dynamics of small molecules: Alexander von Humboldt lectures*, Vol. 900 (Springer, 2015).

[59] E. Wigner, *Group theory: and its application to the quantum mechanics of atomic spectra*, Vol. 5 (Elsevier, 2012).

[60] E. P. Wigner, "On the matrices which reduce the kronecker products of representations of sr groups", in *The collected works of Eugene Paul Wigner: Part A: The Scientific Papers* (Springer, 1993), pp. 608–654.

[61] G. Herzberg, *Molecular spectra and molecular structure* (D. van Nostrand, 1945).

[62] V. Aquilanti, S. Cavalli, and G. Grossi, "Hund's cases for rotating diatomic molecules and for atomic collisions: angular momentum coupling schemes and orbital alignment", Zeitschrift für Physik D Atoms, Molecules and Clusters **36**, 215–219 (1996).

[63] J. F. Barry, "Laser cooling and slowing of a diatomic molecule", PhD thesis (2013).

[64] D. DeMille, F. Bay, S. Bickman, D. Kawall, L. Hunter, D. Krause Jr, S. Maxwell, and K. Ulmer, "Search for the electric dipole moment of the electron using metastable PbO", in Aip conference proceedings, Vol. 596, 1 (American Institute of Physics, 2001), pp. 72–83.

[65] C. M. Western, "PGOPHER: A program for simulating rotational, vibrational and electronic spectra", Journal of Quantitative Spectroscopy and Radiative Transfer **186**, 221–242 (2017).

[66] R. Kronig, *Band spectra and molecular structure* (CUP Archive, 1930).

[67] J. Van Vleck, "On the isotope corrections in molecular spectra", J. Chem. Phys. **4**, 327–338 (1936).

[68] M. Born and R. Oppenheimer, "On the quantum theory of molecules", in *Quantum chemistry: classic scientific papers* (World Scientific, 2000), pp. 1–24.

[69] P. M. Morse, "Diatomic molecules according to the wave mechanics. II. Vibrational levels", Phys. Rev. **34**, 57 (1929).

[70] J. Dunham, "The energy levels of a rotating vibrator", Phys. Rev. **41**, 721 (1932).

[71] J. K. Watson, "The inversion of diatomic vibration-rotation expectation values", J. Mol. Spectrosc. **74**, 319–321 (1979).

[72] J. K. Watson, "The isotope dependence of diatomic dunham coefficients", J. Mol. Spectrosc. **80**, 411–421 (1980).

[73] J. Franck and E. Dymond, "Elementary processes of photochemical reactions", Transactions of the Faraday Society **21**, 536–542 (1926).

[74] E. Condon, "A theory of intensity distribution in band systems", Phys. Rev. **28**, 1182 (1926).

[75] E. U. Condon, "Nuclear motions associated with electron transitions in diatomic molecules", Phys. Rev. **32**, 858 (1928).

[76] H. Gegier and E. Marsden, "On a diffuse reflection of the α-particles", Proceedings of the Royal Society of London. Series A, Containing Papers of a Mathematical and Physical Character **82**, 495–500 (1909).

[77] E. Rutherford, "The scattering of α and β particles by matter and the structure of the atom", The London, Edinburgh, and Dublin Philosophical Magazine and Journal of Science **21**, 669–688 (1911).

[78] C. F. Weizsäcker, "On the theory of nuclear masses", Journal of Physics **96**, 431–458 (1935).

[79] E. Wigner, "On the consequences of the symmetry of the nuclear Hamiltonian on the spectroscopy of nuclei", Phys. Rev. **51**, 106 (1937).

[80] M. G. Mayer, "On closed shells in nuclei. II", Phys. Rev. **75**, 1969 (1949).

[81] O. Haxel, J. H. D. Jensen, and H. E. Suess, "On the magic numbers in nuclear structure", Physical Review **75**, 1766 (1949).

[82] M. Mougeot, D. Atanasov, J. Karthein, R. Wolf, P. Ascher, K. Blaum, K. Chrysalidis, G. Hagen, J. Holt, W. Huang, et al., "Mass measurements of $^{99-101}$In challenge ab initio nuclear theory of the nuclide ^{100}Sn", Nat. Phys. **17**, 1099–1103 (2021).

[83] P. Froese and P. Navrátil, "Ab initio calculations of electric dipole moments of light nuclei", Phys. Rev. C **104**, 025502 (2021).

[84] C.-Y. Seng, "Model-independent determination of nuclear weak form factors and implications for standard model precision tests", Phys. Rev. Lett. **130**, 152501 (2023).

[85] T. Miyagi, X. Cao, R. Seutin, S. Bacca, R. Garcia Ruiz, K. Hebeler, J. Holt, and A. Schwenk, "Impact of two-body currents on magnetic dipole moments of nuclei", Phys. Rev. Lett. **132**, 232503 (2024).

[86] S. J. Novario, D. Lonardoni, S. Gandolfi, and G. Hagen, "Trends of neutron skins and radii of mirror nuclei from first principles", Phys. Rev. Lett. **130**, 032501 (2023).

[87] R. P. Feynman, "The feynman lectures on physics", **1**, 46 (1963).

[88] W. H. King, *Isotope shifts in atomic spectra* (Springer Science & Business Media, 1984).

[89] W. Nörtershäuser and C. Geppert, "Nuclear charge radii of light elements and recent developments in collinear laser spectroscopy", The Euroschool on Exotic Beams, Vol. IV, 233–292 (2014).

[90] L. S. Brown and G. Gabrielse, "Geonium theory: physics of a single electron or ion in a penning trap", Rev. of Mod. Phys. **58**, 233 (1986).

[91] S. Sturm, I. Arapoglou, A. Egl, M. Höcker, S. Kraemer, T. Sailer, B. Tu, A. Weigel, R. Wolf, J. C. López-Urrutia, et al., "The ALPHATRAP experiment", The European Physical Journal Special Topics **227**, 1425–1491 (2019).

[92] P.-G. Reinhard, W. Nazarewicz, and R. G. Ruiz, "Beyond the charge radius: The information content of the fourth radial moment", Phys. Rev. C **101**, 021301 (2020).

[93] I. Counts, J. Hur, D. P. Aude Craik, H. Jeon, C. Leung, J. C. Berengut, A. Geddes, A. Kawasaki, W. Jhe, and V. Vuletić, "Evidence for nonlinear isotope shift in Yb^+ search for new boson", Phys. Rev. Lett. **125**, 123002 (2020).

[94] J. Hur, D. P. Aude Craik, I. Counts, E. Knyazev, L. Caldwell, C. Leung, S. Pandey, J. C. Berengut, A. Geddes, W. Nazarewicz, et al., "Evidence of two-source king plot nonlinearity in spectroscopic search for new boson", Phys. Rev. Lett. **128**, 163201 (2022).

[95] A. Arima and H. Horie, "Configuration mixing and magnetic moments of odd nuclei", Progress of Theoretical Physics **12**, 623–641 (1954).

[96] T. Otsuka, T. Suzuki, R. Fujimoto, H. Grawe, and Y. Akaishi, "Evolution of nuclear shells due to the tensor force", Phys. Rev. Lett. **95**, 232502 (2005).

[97] R. Neugart and G. Neyens, "Nuclear moments", The Euroschool Lectures on Physics with Exotic Beams, Vol. II, 135–189 (2006).

[98] E. Fermi, "Über die magnetischen momente der atomkerne", Zeitschrift für Physik **60**, 320–333 (1930).

[99] J. Grossman, L. Orozco, M. Pearson, J. Simsarian, G. Sprouse, and W. Zhao, "Hyperfine anomaly measurements in francium isotopes and the radial distribution of neutrons", Phys. Rev. Lett. **83**, 935 (1999).

[100] J. R. Persson, "Table of hyperfine anomaly in atomic systems", Atomic Data and Nuclear Data Tables **99**, 62–68 (2013).

[101] J. Zhang, M. Tandecki, R. Collister, S. Aubin, J. Behr, E. Gomez, G. Gwinner, L. Orozco, M. Pearson, G. Sprouse, et al., "Hyperfine anomalies in Fr: boundaries of the spherical single particle model", Phys. Rev. Lett. **115**, 042501 (2015).

[102] B. Roberts and J. Ginges, "Hyperfine anomaly in heavy atoms and its role in precision atomic searches for new physics", Phys. Rev. A **104**, 022823 (2021).

[103] G. Sanamyan, B. Roberts, and J. Ginges, "Empirical determination of the Bohr-Weisskopf effect in cesium and improved tests of precision atomic theory in searches for new physics", Phys. Rev. Lett. **130**, 053001 (2023).

[104] L. V. Skripnikov, "Nuclear magnetization distribution effect in molecules: Ra^+ and RaF hyperfine structure", J. Chem. Phys. **153** (2020).

[105] D. Rossi, K. Minamisono, H. Asberry, G. Bollen, B. Brown, K. Cooper, B. Isherwood, P. Mantica, A. Miller, D. Morrissey, et al., "Charge radii of neutron-deficient ^{36}K and ^{37}K", Phys. Rev. C **92**, 014305 (2015).

[106] Á. Koszorús, X. Yang, J. Billowes, C. Binnersley, M. Bissell, T. Cocolios, G. Farooq-Smith, R. de Groote, K. Flanagan, S. Franchoo, et al., "Precision measurements of the charge radii of potassium isotopes", Phys. Rev. C **100**, 034304 (2019).

[107] F. Touchard, P. Guimbal, S. Büttgenbach, R. Klapisch, M. De Saint Simon, J. Serre, C. Thibault, H. T. Duong, P. Juncar, S. Liberman, et al., "Isotope shifts and hyperfine structure of $^{38-47}$K by laser spectroscopy", Phys. Lett. B **108**, 169–171 (1982).

[108] K. Kreim, M. L. Bissell, J. Papuga, K. Blaum, M. De Rydt, R. G. Ruiz, S. Goriely, H. Heylen, M. Kowalska, R. Neugart, et al., "Nuclear charge radii of potassium isotopes beyond N= 28", Phys. Lett. B **731**, 97–102 (2014).

[109] J. Papuga, M. Bissell, K. Kreim, C. Barbieri, K. Blaum, M. De Rydt, T. Duguet, R. Garcia Ruiz, H. Heylen, M. Kowalska, et al., "Shell structure of potassium isotopes deduced from their magnetic moments", Phys. Rev. C **90**, 034321 (2014).

[110] V. Kellö and A. J. Sadlej, "The quadrupole moment of the ^{39}K and ^{41}K nuclei from microwave data for KF and KCl", Chem. Phys. Lett. **292**, 403–410 (1998).

[111] I. Khriplovich, "Parity nonconservation in atomic phenomena", (1991).

[112] W. Marciano and A. Sanda, "Parity violation in atoms induced by radiative corrections", Phys. Rev. D **17**, 3055 (1978).

[113] R. N. Cahn and G. L. Kane, "Parity violations in hydrogen and the fundamental structure of the weak current", Phys. Lett. B **71**, 348–352 (1977).

[114] J. Erler and S. Su, "The weak neutral current", Progress in Particle and Nuclear Physics **71**, 119–149 (2013).

[115] L. Skripnikov, A. Petrov, A. Titov, and V. Flambaum, "HfF^+ as a candidate to search for the nuclear weak quadrupole moment", Phys. Rev. A **99**, 012517 (2019).

[116] V. Flambaum, V. Dzuba, and C. Harabati, "Effect of nuclear quadrupole moments on parity nonconservation in atoms", Phys. Rev. A **96**, 012516 (2017).

[117] V. Flambaum, "Enhancing the effect of Lorentz invariance and Einstein's equivalence principle violation in nuclei and atoms", Phys. Rev. Lett. **117**, 072501 (2016).

[118] B. G. Lackenby and V. V. Flambaum, "Weak quadrupole moments", Journal of Physics G: Nuclear and Particle Physics **45**, 075105 (2018).

[119] L. Skripnikov, A. Petrov, A. Titov, and V. Flambaum, "HfF^+ as a candidate to search for the nuclear weak quadrupole moment", Phys. Rev. A **99**, 012517 (2019).

[120] G. Penyazkov, L. V. Skripnikov, A. V. Oleynichenko, and A. V. Zaitsevskii, "Effect of the neutron quadrupole distribution in the TaO^+ cation", Chemical Physics Letters **793**, 139448 (2022).

[121] B. A. Brown, A. Derevianko, and V. Flambaum, "Calculations of the neutron skin and its effect in atomic parity violation", Phys. Rev. C **79**, 035501 (2009).

[122] S. V. Pineda, K. König, D. M. Rossi, B. A. Brown, A. Incorvati, J. Lantis, K. Minamisono, W. Nörtershäuser, J. Piekarewicz, R. Powel, et al., "Charge radius of neutron-deficient ^{54}Ni and symmetry energy constraints using the difference in mirror pair charge radii", Phys. Rev. Lett. **127**, 182503 (2021).

[123] K. König, J. C. Berengut, A. Borschevsky, A. Brinson, B. A. Brown, A. Dockery, S. Elhatisari, E. Eliav, R. F. G. Ruiz, J. D. Holt, et al., "Nuclear charge radii of silicon isotopes", Phys. Rev. Lett. **132**, 162502 (2024).

[124] E. Fortson, Y. Pang, and L Wilets, "Nuclear-structure effects in atomic parity nonconservation", Phys. Rev. Lett. **65**, 2857 (1990).

[125] S. Pollock, E. N. Fortson, and L. Wilets, "Atomic parity nonconservation: Electroweak parameters and nuclear structure", Phys. Rev. C **46**, 2587 (1992).

[126] W. Marciano and A. Sirlin, "Radiative corrections to atomic parity violation", Phys. Rev. D **27**, 552 (1983).

[127] W. Marciano and A. Sirlin, "Some general properties of the O(α) corrections to parity violation in atoms", Phys. Rev. D **29**, 75 (1984).

[128] A. Czarnecki and W. J. Marciano, "Electroweak radiative corrections to polarized moller scattering asymmetries", Phys. Rev. D **53**, 1066 (1996).

[129] J. Erler, A. Kurylov, and M. J. Ramsey-Musolf, "Weak charge of the proton and new physics", Phys. Rev. D **68**, 016006 (2003).

[130] H. Davoudiasl, H.-S. Lee, and W. J. Marciano, "Muon anomaly and dark parity violation", Phys. Rev. Lett. **109**, 031802 (2012).

[131] H. Davoudiasl, H.-S. Lee, and W. J. Marciano, ""Dark" Z implications for parity violation, rare meson decays, and Higgs physics", Phys. Rev. D **85**, 115019 (2012).

[132] S. Andreas, "Update on hidden sectors with dark forces and dark matter", arXiv preprint arXiv:1211.5160 (2012).

[133] A. Derevianko, "Detecting dark-matter waves with a network of precision-measurement tools", Phys. Rev. A **97**, 042506 (2018).

[134] C. Bouchiat and C. Piketty, "Parity violation in atomic cesium and alternatives to the standard model of electroweak interactions", Phys. Lett. B **128**, 73–78 (1983).

[135] C. Bouchiat and P. Fayet, "Constraints on the parity-violating couplings of a new gauge boson", Phys. Lett. B **608**, 87–94 (2005).

[136] S. Porsev, K. Beloy, and A. Derevianko, "Precision determination of electroweak coupling from atomic parity violation and implications for particle physics", Phys. Rev. Lett. **102**, 181601 (2009).

[137] R. Diener, S. Godfrey, and I. Turan, "Constraining extra neutral gauge bosons with atomic parity violation measurements", Phys. Rev. D **86**, 115017 (2012).

[138] H. Davoudiasl, H.-S. Lee, and W. J. Marciano, "Muon g-2, rare kaon decays, and parity violation from dark bosons", Phys. Rev. D **89**, 095006 (2014).

[139] H. Davoudiasl, H.-S. Lee, and W. J. Marciano, "Low Q^2 weak mixing angle measurements and rare higgs decays", Phys. Rev. D **92**, 055005 (2015).

[140] W. J. Marciano and J. L. Rosner, "Atomic parity violation as a probe of new physics", Phys. Rev. Lett. **65**, 2963 (1990).

[141] J. L. Rosner, "Role of present and future atomic parity violation experiments in precision electroweak tests", Phys. Rev. D **65**, 073026 (2002).

[142] Y. Stadnik and V. Flambaum, "Axion-induced effects in atoms, molecules, and nuclei: parity nonconservation, anapole moments, electric dipole moments, and spin-gravity and spin-axion momentum couplings", Phys. Rev. D **89**, 043522 (2014).

[143] B. Roberts, Y. Stadnik, V. Dzuba, V. Flambaum, N. Leefer, and D. Budker, "Limiting P-odd interactions of cosmic fields with electrons, protons, and neutrons", Phys. Rev. Lett. **113**, 081601 (2014).

[144] B. Roberts, Y. Stadnik, V. Dzuba, V. Flambaum, N. Leefer, and D. Budker, "Parity-violating interactions of cosmic fields with atoms, molecules, and nuclei: Concepts and calculations for laboratory searches and extracting limits", Phys. Rev. D **90**, 096005 (2014).

[145] M. Macpherson, K. Zetie, R. Warrington, D. Stacey, and J. Hoare, "Precise measurement of parity nonconserving optical rotation at 876 nm in atomic bismuth", Phys. Rev. Lett. **67**, 2784 (1991).

[146] D. M. Meekhof, P. Vetter, P. Majumder, S. Lamoreaux, and E. Fortson, "High-precision measurement of parity nonconserving optical rotation in atomic lead", Phys. Rev. Lett. **71**, 3442 (1993).

[147] S. Phipp, N. Edwards, P. Baird, and S. Nakayama, "A measurement of parity non-conserving optical rotation in atomic lead", Journal of Physics B: Atomic, Molecular and Optical Physics **29**, 1861 (1996).

[148] N. Edwards, S. Phipp, P. Baird, and S. Nakayama, "Precise measurement of parity nonconserving optical rotation in atomic thallium", Phys. Rev. Lett. **74**, 2654 (1995).

[149] P. Vetter, D. Meekhof, P. Majumder, S. Lamoreaux, and E. Fortson, "Precise test of electroweak theory from a new measurement of parity nonconservation in atomic thallium", Phys. Rev. Lett. **74**, 2658 (1995).

[150] B. Sahoo, B. Das, and H. Spiesberger, "New physics constraints from atomic parity violation in ^{133}Cs", Phys. Rev. D **103**, L111303 (2021).

[151] S. Porsev, K. Beloy, and A. Derevianko, "Precision determination of weak charge of ^{133}Cs from atomic parity violation", Phys. Rev. D **82**, 036008 (2010).

[152] V. Novikov, O. Sushkov, V. Flambaum, and I. Khriplovich, "Possibility of studying the structure of weak neutral currents in optical transitions in heavy atoms", Zh. Eksp. Theo. Fiz **73**, 802 (1977).

[153] V. Flambaum and I. Khriplovich, "P-odd nuclear forces: a source of parity violation in atoms", Sov. Phys.-JETP (Engl. Transl.);(United States) **52** (1980).

[154] V. Flambaum, I. Khriplovich, and O. Sushkov, "Nuclear anapole moments", Phys. Lett. B **146**, 367–369 (1984).

[155] V. Flambaum and I. Khriplovich, "On the enhancement of parity nonconserving effects in diatomic molecules", Phys. Lett. A **110**, 121–125 (1985).

[156] J. Ginges and V. V. Flambaum, "Violations of fundamental symmetries in atoms and tests of unification theories of elementary particles", Physics Reports **397**, 63–154 (2004).

[157] M. Buckley and M. Ramsey-Musolf, "Precision probes of a leptophobic Z' boson", Phys. Lett. B **712**, 261–265 (2012).

[158] C. Bouchiat and C. Piketty, "Nuclear spin dependent atomic parity violation, nuclear anapole moments and the hadronic axial neutral current", Zeitschrift für Physik C Particles and Fields **49**, 91–107 (1991).

[159] W. Haxton and C. E. Wieman, "Atomic parity nonconservation and nuclear anapole moments", Annual Review of Nuclear and Particle Science **51**, 261–293 (2001).

[160] V. Flambaum and D. Murray, "Anapole moment and nucleon weak interactions", Phys. Rev. C **56**, 1641 (1997).

[161] B. Desplanques, J. F. Donoghue, and B. R. Holstein, "Unified treatment of the parity violating nuclear force", Annals of Physics **124**, 449–495 (1980).

[162] E. Adelberger and W. Haxion, "Parity violation in the nucleon-nucleon interaction", Annual Review of Nuclear and Particle Science **35**, 501–558 (1985).

[163] W. Haeberli and B. R. Holstein, "Parity violation and the nucleon-nucleon system", Symmetries and fundamental interactions in nuclei, 17–66 (1995).

[164] V. Flambaum, "Dynamical enhancement of weak interactions and quantum chaos", Physica Scripta **1993**, 198 (1993).

[165] S.-L. Zhu, C. M. Maekawa, B. R. Holstein, M. Ramsey-Musolf, and U. Van Kolck, "Nuclear parity violation in effective field theory", Nuclear Physics A **748**, 435–498 (2005).

[166] M. J. Ramsey-Musolf and S. A. Page, "Hadronic parity violation: a new view through the looking glass", Annu. Rev. Nucl. Part. Sci. **56**, 1–52 (2006).

[167] L. Girlanda, "Redundancy in the parity-violating 2-nucleon contact lagrangian", Phys. Rev. C **77**, 067001 (2008).

[168] W. C. Haxton and B. R. Holstein, "Hadronic parity violation", Progress in Particle and Nuclear Physics **71**, 185–203 (2013).

[169] W. Haxton, C.-P. Liu, and M. J. Ramsey-Musolf, "Nuclear anapole moments", Phys. Rev. C **65**, 045502 (2002).

[170] W. Johnson, M. Safronova, and U. Safronova, "Combined effect of coherent Z exchange and the hyperfine interaction in the atomic parity-nonconserving interaction", Phys. Rev. A **67**, 062106 (2003).

[171] W. Haxton, C.-P. Liu, and M. Ramsey-Musolf, "Anapole moment and other constraints on the strangeness conserving hadronic weak interaction", Phys. Rev. Lett. **86**, 5247 (2001).

[172] I. Kozyryev and N. R. Hutzler, "Precision measurement of time-reversal symmetry violation with laser-cooled polyatomic molecules", Phys. Rev. Lett. **119**, 133002 (2017).

[173] N. R. Hutzler, "Polyatomic molecules as quantum sensors for fundamental physics", Quantum Science and Technology **5**, 044011 (2020).

[174] J Engel, J. L. Friar, and A. Hayes, "Nuclear octupole correlations and the enhancement of atomic time-reversal violation", Phys. Rev. C **61**, 035502 (2000).

[175] V. Flambaum and J. Ginges, "Nuclear Schiff moment and time-invariance violation in atoms", Phys. Rev. A **65**, 032113 (2002).

[176] V. Flambaum, D. DeMille, and M. Kozlov, "Time-reversal symmetry violation in molecules induced by nuclear magnetic quadrupole moments", Phys. Rev. Lett. **113**, 103003 (2014).

[177] D. E. Maison, L. V. Skripnikov, and V. V. Flambaum, "Theoretical study of ^{173}YbOH to search for the nuclear magnetic quadrupole moment", Phys. Rev. A **100**, 032514 (2019).

[178] C. Ho, J. Lim, B. Sauer, and M. Tarbutt, "Measuring the nuclear magnetic quadrupole moment in heavy polar molecules", Frontiers in Physics **11**, 1086980 (2023).

[179] B. Graner, Y. Chen, E. Lindahl, and B. Heckel, "Reduced limit on the permanent electric dipole moment of ^{199}Hg", Phys. Rev. Lett. **116**, 161601 (2016).

[180] L. P. Gaffney, P. A. Butler, M. Scheck, A. B. Hayes, F. Wenander, M. Albers, B. Bastin, C. Bauer, A. Blazhev, S. Bönig, et al., "Studies of pear-shaped nuclei using accelerated radioactive beams", Nature **497**, 199–204 (2013).

[181] M. Fan, C. Holliman, X. Shi, H. Zhang, M. Straus, X. Li, S. Buechele, and A. Jayich, "Optical mass spectrometry of cold $RaOH^+$ and $RaOCH_3^+$", Phys. Rev. Lett. **126**, 023002 (2021).

[182] R. Neugart, J. Billowes, M. Bissell, K. Blaum, B. Cheal, K. Flanagan, G. Neyens, W. Nörtershäuser, and D. Yordanov, "Collinear laser spectroscopy at ISOLDE: new methods and highlights", Journal of Physics G: Nuclear and Particle Physics **44**, 064002 (2017).

[183] K. Flanagan, K. Lynch, J. Billowes, M. Bissell, I. Budinčević, T. E. Cocolios, R. De Groote, S. De Schepper, V. Fedosseev, S. Franchoo, et al., "Collinear resonance ionization spectroscopy of neutron-deficient francium isotopes", Phys. Rev. Lett. **111**, 212501 (2013).

[184] R. De Groote, I. Budinčević, J. Billowes, M. Bissell, T. E. Cocolios, G. J. Farooq-Smith, V. Fedosseev, K. Flanagan, S. Franchoo, R. G. Ruiz, et al., "Use of a continuous wave laser and pockels cell for sensitive high-resolution collinear resonance ionization spectroscopy", Phys. Rev. Lett. **115**, 132501 (2015).

[185] R. G. Ruiz, A. Vernon, C. Binnersley, B. Sahoo, M. Bissell, J. Billowes, T. E. Cocolios, W. Gins, R. De Groote, K. Flanagan, et al., "High-precision multiphoton ionization of accelerated laser-ablated species", Phys. Rev. X **8**, 041005 (2018).

[186] A. Vernon, R. de Groote, J. Billowes, C. Binnersley, T. Cocolios, G. Farooq-Smith, K. Flanagan, R. G. Ruiz, W. Gins, Á Koszorús, et al., "Optimising the collinear resonance ionisation spectroscopy (CRIS) experiment at CERN-ISOLDE", Nuclear Instruments and Methods in Physics Research Section B: Beam Interactions with Materials and Atoms **463**, 384–389 (2020).

[187] A. Koszorús, J. Billowes, C. Binnersley, M. Bissell, T. Cocolios, B. Cooper, R. De Groote, G. Farooq-Smith, V. Fedosseev, K. Flanagan, et al., "Resonance ionization schemes for high resolution and high efficiency studies of exotic nuclei at the CRIS experiment", Nuclear Instruments and Methods in Physics Research Section B: Beam Interactions with Materials and Atoms **463**, 398–402 (2020).

[188] W. Demtröder, *Laser spectroscopy 2: experimental techniques* (Springer, 2015).

[189] S. Kaufman, "High-resolution laser spectroscopy in fast beams", Optics Communications **17**, 309–312 (1976).

[190] W. H. Wing, G. A. Ruff, W. E. Lamb Jr, and J. J. Spezeski, "Observation of the infrared spectrum of the hydrogen molecular ion HD^+", Phys. Rev. Lett. **36**, 1488 (1976).

[191] M. Newville, T. Stensitzki, D. B. Allen, M. Rawlik, A. Ingargiola, and A. Nelson, "LMFIT: Non-linear least-square minimization and curve-fitting for Python", Astrophysics Source Code Library, ascl–1606 (2016).

[192] T. Isaev, S. Hoekstra, and R Berger, "Laser-cooled RaF as a promising candidate to measure molecular parity violation", Phys. Rev. A **82**, 052521 (2010).

[193] T. Isaev and R. Berger, "Lasercooled radium monofluoride: A molecular all-in-one probe for new physics", arXiv preprint arXiv:1302.5682 (2013).

[194] A. Kudashov, A. Petrov, L. Skripnikov, N. Mosyagin, T. Isaev, R. Berger, and A. Titov, "Ab initio study of radium monofluoride, RaF, as a candidate to search for P-and T, P-violation effects", arXiv preprint arXiv:1405.6391 (2014).

[195] A. Petrov and L. Skripnikov, "Energy levels of radium monofluoride RaF in external electric and magnetic fields to search for P-and T, P-violation effects", Phys. Rev. A **102**, 062801 (2020).

[196] J. Jackson, *Classical electrodynamics* (John Wiley & Sons, 2021).

[197] M. Athanasakis-Kaklamanakis, S. Wilkins, L. Skripnikov, A. Koszorus, A. Breier, M. Au, I. Belosevic, R. Berger, M. Bissell, A. Borschevsky, et al., "Pinning down electron correlations in RaF via spectroscopy of excited states", arXiv preprint arXiv:2308.14862 (2023).

[198] A. Zaitsevskii, L. V. Skripnikov, N. S. Mosyagin, T. Isaev, R. Berger, A. A. Breier, and T. F. Giesen, "Accurate ab initio calculations of RaF electronic structure appeal to more laser-spectroscopical measurements", J. Chem. Phys. **156** (2022).

[199] M. Denis, P. A. Haase, M. C. Mooij, Y. Chamorro, P. Aggarwal, H. L. Bethlem, A. Boeschoten, A. Borschevsky, K. Esajas, Y. Hao, et al., "Benchmarking of the Fock-space coupled-cluster method and uncertainty estimation: Magnetic hyperfine interaction in the excited state of BaF", Phys. Rev. A **105**, 052811 (2022).

[200] V. Flambaum, "Electric dipole moments of actinide atoms and RaO molecule", Phys. Rev. A **77**, 024501 (2008).

[201] J. Engel, M. J. Ramsey-Musolf, and U. Van Kolck, "Electric dipole moments of nucleons, nuclei, and atoms: the standard model and beyond", Progress in Particle and Nuclear Physics **71**, 21–74 (2013).

[202] V. Flambaum, "Enhanced nuclear Schiff moment and time-reversal violation in ^{229}Th-containing molecules", Phys. Rev. C **99**, 035501 (2019).

[203] L. V. Skripnikov, N. S. Mosyagin, A. V. Titov, and V. V. Flambaum, "Actinide and lanthanide molecules to search for strong CP-violation", Physical Chemistry Chemical Physics **22**, 18374–18380 (2020).

[204] T. Isaev, A. Zaitsevskii, and E Eliav, "Laser-coolable polyatomic molecules with heavy nuclei", Journal of Physics B: Atomic, Molecular and Optical Physics **50**, 225101 (2017).

[205] N. Fazil, V. Prasannaa, K. Latha, M. Abe, and B. Das, "RaH as a potential candidate for electron electric-dipole-moment searches", Phys. Rev. A **99**, 052502 (2019).

[206] C. Zülch, K. Gaul, S. M. Giesen, R. F. G. Ruiz, and R. Berger, "Cool molecular highly charged ions for precision tests of fundamental physics", arXiv preprint arXiv:2203.10333 (2022).

[207] A. V. Oleynichenko, L. V. Skripnikov, A. V. Zaitsevskii, and V. V. Flambaum, "Laser-coolable $AcOH^+$ ion for CP-violation searches", Phys. Rev. A **105**, 022825 (2022).

[208] P. Yu and N. R. Hutzler, "Probing fundamental symmetries of deformed nuclei in symmetric top molecules", Phys. Rev. Lett. **126**, 023003 (2021).

[209] W. Fujiya, P. Hoppe, E. Zinner, M. Pignatari, and F. Herwig, "Evidence for radiogenic sulfur-32 in type AB presolar silicon carbide grains?", The Astrophysical Journal Letters **776**, L29 (2013).

[210] M. Cairnie, R. Forrey, J. Babb, P. Stancil, and B. McLaughlin, "Rate constants for the formation of SiO by radiative association", Monthly Notices of the Royal Astronomical Society **471**, 2481–2490 (2017).

[211] T. Kamiński, R. Tylenda, K. M. Menten, A. Karakas, J. M. Winters, A. A. Breier, K. T. Wong, T. F. Giesen, and N. A. Patel, "Astronomical detection of radioactive molecule ^{26}AlF in the remnant of an ancient explosion", Nat. Astron. **2**, 778–783 (2018).

[212] K. L. Chubb, M. Min, Y. Kawashima, C. Helling, and I. Waldmann, "Aluminium oxide in the atmosphere of hot Jupiter WASP-43b", Astronomy & Astrophysics **639**, A3 (2020).

[213] A. Bohr and V. F. Weisskopf, "The influence of nuclear structure on the hyperfine structure of heavy elements", Phys. Rev. **77**, 94 (1950).

[214] A. Kyuberis, L. Pasteka, E. Eliav, H. Perrett, A. Sunaga, S. Udrescu, S. Wilkins, R. Ruiz, and A Borschevsky, "Accurate theoretical determination of the ionization potentials of CaF, SrF, and BaF", arXiv preprint arXiv:2309.01705 (2023).

[215] W. Ernst, J. Kändler, and T. Törring, "Hyperfine structure and electric dipole moment of BaF $X^2\Sigma^+$", J. Chem. Phys. **84**, 4769–4773 (1986).

[216] J. Kłos, H. Li, E. Tiesinga, and S. Kotochigova, "Prospects for assembling ultracold radioactive molecules from laser-cooled atoms", New Journal of Physics **24**, 025005 (2022).

[217] M. G. Kozlov and L. N. Labzowsky, "Parity violation effects in diatomics", Journal of Physics B: Atomic, Molecular and Optical Physics **28**, 1933 (1995).

[218] L. B. Knight Jr, A. Ligon, R. Woodward, D. Feller, and E. R. Davidson, "The generation and trapping of the high-temperature oxosilyliumyl cation radicals ($^{28}SiO^+$ and $^{29}SiO^+$) in neon matrixes at 4K; an ESR and ab initio CI theoretical investigation", Journal of the American Chemical Society **107**, 2857–2864 (1985).

[219] G.-Z. Zhu, G. Lao, C. Ho, W. C. Campbell, and E. R. Hudson, "High-resolution laser-induced fluorescence spectroscopy of $^{28}Si^{16}O^+$ and $^{29}Si^{16}O^+$ in a cryogenic buffer-gas cell", J. Mol. Spectrosc. **384**, 111582 (2022).

[220] S. Chattopadhyaya, A. Chattopadhyay, and K. K. Das, "Electronic spectrum of SiO^+: a theoretical study", Journal of Molecular Structure: THEOCHEM **639**, 177–185 (2003).

[221] G. Arfken, "Spherical harmonics", Mathematical methods for physicists, 680–685 (1985).

[222] D. Budker, D. F. Kimball, and D. P. DeMille, *Atomic physics: an exploration through problems and solutions* (Oxford University Press, USA, 2004).

[223] P. R. Stollenwerk, I. O. Antonov, and B. C. Odom, "IP determination and 1+1 REMPI spectrum of SiO at 210-220 nm in an ion trap: Implications for SiO^+ ion trap loading", J. Mol. Spectrosc. **355**, 40–45 (2019).

[224] P. R. Stollenwerk, I. O. Antonov, S. Venkataramanababu, Y.-W. Lin, and B. C. Odom, "Cooling of a zero-nuclear-spin molecular ion to a selected rotational state", Phys. Rev. Lett. **125**, 113201 (2020).

[225] D. L. Kokkin, T. Ma, T. Steimle, and T. J. Sears, "Detection and characterization of singly deuterated silylene, SiHD, via optical spectroscopy", J. Chem. Phys. **144** (2016).

[226] T. Steinsberger, "Microwave injection for the ALPHATRAP experiment and developments of the multi-reflection time-of-flight technique of the ISOLTRAP experiment", PhD thesis (Heidelberg U., 2018).

[227] G. B. Andresen, M. Ashkezari, M. Baquero-Ruiz, W. Bertsche, P. D. Bowe, E. Butler, P. Carpenter, C. Cesar, S. Chapman, M. Charlton, et al., "Autoresonant excitation of antiproton plasmas", Phys. Rev. Let.. **106**, 025002 (2011).

[228] S. Chattopadhyaya, A. Chattopadhyay, and K. K. Das, "Electronic spectrum of SiO^+: a theoretical study", Journal of Molecular Structure: THEOCHEM **639**, 177–185 (2003).

[229] S. Sturm, I. Arapoglou, A. Egl, M. Höcker, S. Kraemer, T. Sailer, B. Tu, A. Weigel, R. Wolf, J. C. López-Urrutia, et al., "The ALPHATRAP experiment", The European Physical Journal Special Topics **227**, 1425–1491 (2019).

[230] L. S. Brown and G. Gabrielse, "Precision spectroscopy of a charged particle in an imperfect Penning trap", Phys. Rev. A **25**, 2423 (1982).

[231] F. Köhler, "Bound-electron g-factor measurements for the determination of the electron mass and isotope shifts in highly charged ions", PhD thesis (Ruprecht-Karls-Universität Heidelberg, 2015).

[232] G. Gabrielse, L. Haarsma, and S. Rolston, "Open-endcap Penning traps for high precision experiments", International Journal of Mass Spectrometry and Ion Processes **88**, 319–332 (1989).

[233] C. Roux, C. Böhm, A. Dörr, S. Eliseev, S. George, M. Goncharov, Y. N. Novikov, J. Repp, S. Sturm, S. Ulmer, et al., "The trap design of PENTATRAP", Applied Physics B **107**, 997–1005 (2012).

[234] C.-E. Roux, "High-resolution mass spectrometry: the trap design and detection system of pentatrap and new Q-values for neutrino studies", PhD thesis (Ruprecht-Karls Universität Heidelberg, 2012).

[235] S. Ulmer, "First observation of spin flips with a single proton stored in a cryogenic Penning trap", PhD thesis (Ruprecht-Karls-Universität Heidelberg, Germany, 2011).

[236] Z. Davoudi, W. Detmold, P. Shanahan, K. Orginos, A. Parreno, M. J. Savage, and M. L. Wagman, "Nuclear matrix elements from lattice QCD for electroweak and beyond-standard-model processes", Physics Reports **900**, 1–74 (2021).

[237] E. B. Norrgard, D. S. Barker, S. Eckel, J. A. Fedchak, N. N. Klimov, and J. Scherschligt, "Nuclear-spin dependent parity violation in optically trapped polyatomic molecules", Comm. Phys. **2**, 77 (2019).

[238] M. Bohman, V. Grunhofer, C. Smorra, M. Wiesinger, C. Will, M. Borchert, J. Devlin, S. Erlewein, M. Fleck, S. Gavranovic, et al., "Sympathetic cooling of a trapped proton mediated by an LC circuit", Nature **596**, 514–518 (2021).

[239] J. J. He, Y. Tanaka, and N. Nagaosa, "A phenomenological theory of superconductor diodes", New Journal of Physics **24**, 053014 (2022).

[240] C. Will, M. Wiesinger, P. Micke, H. Yildiz, T. Driscoll, S. Kommu, F. Abbass, B. Arndt, B. Bauer, S. Erlewein, et al., "Image-current mediated sympathetic laser cooling of a single proton in a penning trap down to 170 mK axial temperature", arXiv preprint arXiv:2310.10208 (2023).

[241] W. M. Itano and D. Wineland, "Laser cooling of ions stored in harmonic and Penning traps", Phys. Rev. A **25**, 35 (1982).

[242] S. B. Torrisi, J. W. Britton, J. G. Bohnet, and J. J. Bollinger, "Perpendicular laser cooling with a rotating-wall potential in a Penning trap", Phys. Rev. A **93**, 043421 (2016).

[243] F. Sommer, K. König, D. M. Rossi, N. Everett, D. Garand, R. P. de Groote, J. D. Holt, P. Imgram, A. Incorvati, C. Kalman, et al., "Charge radii of ^{55,56}Ni reveal a surprisingly similar behavior at N=28 in Ca and Ni isotopes", Phys. Rev. Lett. **129**, 132501 (2022).

[244] J. Cubiss, A. Andreyev, A. Barzakh, P. Van Duppen, S. Hilaire, S Péru, S. Goriely, M. Al Monthery, N. Althubiti, B. Andel, et al., "Deformation versus sphericity in the ground states of the lightest gold isotopes", Phys. Rev. Lett. **131**, 202501 (2023).

[245] J. Dilling, R. Krücken, and G. Ball, "ISAC overview", Hyperfine Interactions **225**, 1–8 (2014).

[246] B. Maaß, "Laser spectroscopy of the boron isotopic chain", PhD thesis (2020).

[247] V. Sonnenschein, "Laser developments and high resolution resonance ionization spectroscopy of actinide elements", PhD thesis (University of Jyväskylä, 2014).

[248] A. T. Eppink and D. H. Parker, "Velocity map imaging of ions and electrons using electrostatic lenses: application in photoelectron and photofragment ion imaging of molecular oxygen", Review of Scientific Instruments **68**, 3477–3484 (1997).

[249] M. N. Ashfold, N. H. Nahler, A. J. Orr-Ewing, O. P. Vieuxmaire, R. L. Toomes, T. N. Kitsopoulos, I. A. Garcia, D. A. Chestakov, S.-M. Wu, and D. H. Parker, "Imaging the dynamics of gas phase reactions", Physical Chemistry Chemical Physics **8**, 26–53 (2006).

[250] V. Papadakis and T. N. Kitsopoulos, "Slice imaging and velocity mapping using a single field", Review of Scientific Instruments **77** (2006).

[251] R. Mabbs, E. R. Grumbling, K. Pichugin, and A. Sanov, "Photoelectron imaging: an experimental window into electronic structure", Chemical Society Reviews **38**, 2169–2177 (2009).

[252] N. Kling, D. Paul, A. Gura, G. Laurent, S. De, H. Li, Z. Wang, B. Ahn, C. Kim, T. K. Kim, et al., "Thick-lens velocity-map imaging spectrometer with high resolution for high-energy charged particles", Journal of Instrumentation **9**, P05005 (2014).

[253] I. León, Z. Yang, H.-T. Liu, and L.-S. Wang, "The design and construction of a high-resolution velocity-map imaging apparatus for photoelectron spectroscopy studies of size-selected clusters", Review of Scientific Instruments **85**, 083106 (2014).

[254] H. Carstens, S. Holzberger, J. Kaster, J. Weitenberg, V. Pervak, A. Apolonski, E. Fill, F. Krausz, and I. Pupeza, "Large-mode enhancement cavities", Optics express **21**, 11606–11617 (2013).

[255] B. E. Saleh and M. C. Teich, *Fundamentals of photonics* (john Wiley & sons, 2019).

[256] E. D. Black, "An introduction to Pound Drever Hall laser frequency stabilization", American journal of physics **69**, 79–87 (2001).

[257] D. W. Chandler and P. L. Houston, "Two-dimensional imaging of state-selected photodissociation products detected by multiphoton ionization", J. Chem. Phys. **87**, 1445–1447 (1987).

[258] S. J. Kregel, G. K. Thurston, J. Zhou, and E. Garand, "A multi-plate velocity-map imaging design for high-resolution photoelectron spectroscopy", J. Chem. Phys. **147**, 094201 (2017).

[259] H. Cruse and T. Softley, "Velocity-map imaging study of the photodissociation of acetaldehyde", J. Chem. Phys **122**, 124303 (2005).

[260] D. Holland and D. Shaw, "The design and performance of a velocity map imaging spectrometer for the study of molecular photoionisation dynamics", Chemical Physics **409**, 11–22 (2012).

[261] M. Ryazanov and H. Reisler, "Improved sliced velocity map imaging apparatus optimized for H photofragments", J. Chem. Phys. **138**, 144201 (2013).

[262] Z. Lu, Y. C. Chang, Q.-Z. Yin, C. Ng, and W. M. Jackson, "Evidence for direct molecular oxygen production in CO_2 photodissociation", Science **346**, 61–64 (2014).

[263] I. S. Parry, A. C. Hermes, A. Kartouzian, and S. R. Mackenzie, "Imaging the photodissociation dynamics of neutral metal clusters: copper dimer, Cu_2, and copper oxide, CuO", Physical Chemistry Chemical Physics **16**, 458–466 (2014).

[264] J. Maner, D. Mauney, and M. Duncan, "Velocity map ion imaging study of Ar_2^+ photodissociation", Chem. Phys. Lett. **671**, 182–185 (2017).

[265] D. W. Chandler, P. L. Houston, and D. H. Parker, "Perspective: advanced particle imaging", The Journal of chemical physics **147**, 013601 (2017).

[266] B. W. Toulson, K. M. Kapnas, D. A. Fishman, and C. Murray, "Competing pathways in the near-uv photochemistry of acetaldehyde", Physical Chemistry Chemical Physics **19**, 14276–14288 (2017).

[267] A. Sanov and W. C. Lineberger, "Cluster anions: structure, interactions, and dynamics in the sub-nanoscale regime", Physical Chemistry Chemical Physics **6**, 2018–2032 (2004).

[268] D. M. Neumark, "Slow electron velocity-map imaging of negative ions: applications to spectroscopy and dynamics", The Journal of Physical Chemistry A **112**, 13287–13301 (2008).

[269] A. Sanov and R. Mabbs, "Photoelectron imaging of negative ions", International Reviews in Physical Chemistry **27**, 53–85 (2008).

[270] C. Bartels, C. Hock, J. Huwer, R. Kuhnen, J. Schwöbel, and B. von Issendorff, "Probing the angular momentum character of the valence orbitals of free sodium nanoclusters", Science **323**, 1323–1327 (2009).

[271] G. A. Garcia, H. Soldi-Lose, and L. Nahon, "A versatile electron-ion coincidence spectrometer for photoelectron momentum imaging and threshold spectroscopy on mass selected ions using synchrotron radiation", Review of Scientific Instruments **80**, 023102 (2009).

[272] D. A. Horke, G. M. Roberts, J. Lecointre, and J. R. Verlet, "Velocity-map imaging at low extraction fields", Review of Scientific Instruments **83**, 063101 (2012).

[273] S.-B. Cheng, C. Berkdemir, J. J. Melko, and A. Castleman Jr, "SP coupling induced unusual open-shell metal clusters", Journal of the American Chemical Society **136**, 4821–4824 (2014).

[274] R. Otto, J. Ma, A. W. Ray, J. S. Daluz, J. Li, H. Guo, and R. E. Continetti, "Imaging dynamics on the $F + H_2O \rightarrow HF + OH$ potential energy surfaces from wells to barriers", Science **343**, 396–399 (2014).

[275] L.-S. Wang, "Perspective: electrospray photoelectron spectroscopy: From multiply-charged anions to ultracold anions", J. Chem. Phys. **143**, 040901 (2015).

[276] O. Kostko, B. Xu, M. Jacobs, and M. Ahmed, "Soft X-ray spectroscopy of nanoparticles by velocity map imaging", J. Chem. Phys. **147**, 013931 (2017).

[277] D. Townsend, W. Li, S. K. Lee, R. L. Gross, and A. G. Suits, "Universal and state-resolved imaging of chemical dynamics", The Journal of Physical Chemistry A **109**, 8661–8674 (2005).

[278] S. J. Greaves, R. A. Rose, and A. J. Orr-Ewing, "Velocity map imaging of the dynamics of bimolecular chemical reactions", Physical Chemistry Chemical Physics **12**, 9129–9143 (2010).

[279] R. Wester, "Velocity map imaging of ion–molecule reactions", Physical Chemistry Chemical Physics **16**, 396–405 (2014).

[280] S. Skruszewicz, J. Passig, A. Przystawik, N. Truong, M. Köther, J. Tiggesbäumker, and K.-H. Meiwes-Broer, "A new design for imaging of fast energetic electrons", International Journal of Mass Spectrometry **365**, 338–342 (2014).

[281] H. Fukuzawa, T. Tachibana, K. Motomura, W. Xu, K. Nagaya, S. Wada, P. Johnsson, M. Siano, S. Mondal, Y. Ito, et al., "Electron spectroscopy of rare-gas clusters irradiated by X-ray free-electron laser pulses from sacla", Journal of Physics B: Atomic, Molecular and Optical Physics **49**, 034004 (2016).

[282] Z. Qu, C. Li, Z. Qin, X. Zheng, G. Yao, X. Zhang, and Z. Cui, "The design of double electrostatic-lens optics for resonance enhanced multiphoton ionization and photoelectron imaging experiments", Review of Scientific Instruments **86**, 063106 (2015).

[283] D. Schomas, N. Rendler, J. Krull, R. Richter, and M. Mudrich, "A compact design for velocity-map imaging of energetic electrons and ions", J. Chem. Phys. **147**, 013942 (2017).

[284] A. Vredenborg, W. G. Roeterdink, and M. H. Janssen, "A photoelectron-photoion coincidence imaging apparatus for femtosecond time-resolved molecular dynamics with electron time-of-flight resolution of σ= 18 ps and energy resolution Δ E/E= 3.5%", Review of Scientific Instruments **79**, 063108 (2008).

[285] M. Eklund, H. Hultgren, I. Kiyan, H. Helm, and D. Hanstorp, "Tomography of photoelectron distributions produced through strong-field photodetachment of Ag^-", Phys. Rev. A **102**, 023114 (2020).

[286] D. J. Manura and D. A. Dahl, *Simion 2020*, 2020.

[287] A. Kramida, Yu. Ralchenko, J. Reader, and NIST ASD Team, NIST Atomic Spectra Database (ver. 5.11), [Online]. Available: `https://physics.nist.gov/asd` [2024, April 9]. National Institute of Standards and Technology, Gaithersburg, MD. 2023.

[288] S. Gibson, D. D. Hickstein, R. Yurchak, M. Ryazanov, D. Das, and G. Shih, *Pyabel/pyabel: v0.9.0*, version v0.9.0, Dec. 2022.

[289] M. Aymar, A. Debarre, and O. Robaux, "Highly excited levels of neutral ytterbium. II. Multichannel quantum defect analysis of odd-and even-parity spectra", Journal of Physics B: Atomic and Molecular Physics **13**, 1089 (1980).

[290] K.-H. Weber and C. J. Sansonetti, "Accurate energies of nS, nP, nD, nF, and nG levels of neutral cesium", Phys. Rev. A **35**, 4650 (1987).

[291] J. Deiglmayr, H. Herburger, H. Saßmannshausen, P. Jansen, H. Schmutz, and F. Merkt, "Precision measurement of the ionization energy of Cs I", Phys. Rev. A **93**, 013424 (2016).